eman ta zabal zazu

Universidad del País Vasco
Euskal Herriko Unibertsitatea

Hybrid Polyoxometalates: Synthesis, Crystal Structures, Thermostructural Behavior and Anchoring to Tailored Polymeric Surfaces

Memoria para optar al Grado de Doctor por la Universidad del País Vasco (UPV/EHU) presentada por

Jagoba Martín Caballero

Leioa, Septiembre 2017

BASQUE CENTER FOR
MATERIALS, APPLICATIONS
& NANOSTRUCTURES

ehugroup

eman ta zabal zazu

Universidad
del País Vasco

Euskal Herriko
Unibertsitatea

FACULTY
OF SCIENCE
AND TECHNOLOGY
UNIVERSITY
OF THE BASQUE
COUNTRY

Este trabajo de investigación para optar al Grado de Doctor por la Universidad del País Vasco (UPV/EHU) se ha realizado en colaboración entre el BERC BCMATERIALS, Basque Center for Materials, Applications and Nanostructures y los Grupos MOF-POM y LABQUIMAC de los departamentos de Química Inorgánica y Química Física, respectivamente, de la Facultad de Ciencia y Tecnología de la UPV/EHU.

Ambas entidades desean agradecer al Departamento de Educación del Gobierno Vasco (Ayudas para apoyar las actividades de los grupos de investigación del sistema universitario vasco IT-477-10 y IT-718-13) y al Departamento de Desarrollo Económico e Infraestructuras del Gobierno Vasco (Proyecto ELKARTEK FRONTIERS) por su financiación. Así mismo agradecen al Ministerio de Economía y Competitividad su financiación mediante el subprograma de Generación de conocimiento “Excelencia” 2013 (proyecto MAT2013-48366-C2-2-P).

I want to express my most sincere gratitude to all of you.

A mis directores, los Doctores Juan M. Gutiérrez-Zorrilla y José Luis Vilas, Catedráticos de Química Inorgánica y Química-Física de la Facultad de Ciencia y Tecnología de la Universidad del País Vasco UPV/EHU, respectivamente. Al primero por aceptarme con los brazos abiertos en su grupo de investigación desde el primer día y "*engañarme*" para realizar la Tesis Doctoral, por sus ideas, su disposición y guía. Al segundo, por todo su apoyo, conocimiento, actitud y motivación. Gracias a ambos, por los innumerables cafés/zuritos y los buenos momentos.

Al Dr. Beñat Artetxe, por motivarme a "*pensar*" en el laboratorio y fuera de él. Por sus consejos y los buenos momentos por Bilbao, Astrabu y NewCastle. Al Dr. Santiago Reinoso, por su extenso conocimiento, sin olvidar sus correcciones hasta altas horas de la madrugada y, sobre todo, la farra en época de congresos. Todos ellos fueron momentos duros, pero merecieron la pena.

A la Dra. Leire San Felices, Dr. Aitor Larrañaga, Dr. Fco. Javier Sangüesa y Pablo Vitoria, por las medidas de difracción de rayos X y toda la ayuda proporcionada durante estos años. Su experiencia, trabajo diario y apoyo han sido indispensables para no sólo la realización de este trabajo, sino también mi formación como investigador. Así mismo, quisiera aprovechar esta oportunidad para agradecer el trabajo de todas las personas que han realizado las medidas presentadas en este trabajo, especialmente a los técnicos de los Servicios Generales de Investigación de la UPV/EHU (SGIker).

I wish to express my deepest gratitude to Prof. Tatsumi Ishihara-*sensei* for allowing me to expend three months working in his research group at I^{2}CNER at Kyushu University, Fukuoka, Japan. ありがとうございます! Similarly, I would like to thank Dr. Helena Téllez, Dr. John Druce, Dr. Henning Schraknepper and Dr. Kuan-Ting Wu for all their support, friendliness and for introducing me in the fields of LEIS and SIMS techniques. *Arigato gozaimasu!*

Al Dr. Pascual Román, director del departamento y en general, a todos los miembros que actualmente componen y/o que han formado parte del departamento de Química Inorgánica de la Facultad de Ciencia y Tecnología de la UPV/EHU durante estos últimos cuatro años, especialmente al Dr. Xabier Lasheras, Dra. Mónica Lanchas y Leire Idoiaga. De la misma forma, quisiera agradecer el apoyo de la Dra. Nuria García-Huete y Dra. Leire Ruiz-Rubio del departamento de Química física, a la primera por todos esos cafés, TGs y desatinos varios; a la segunda por su valiosa ayuda en todo lo referente a síntesis de polímeros, su caracterización y a la preparación de superficies poliméricas.

Eskerrak eman nahiko nituzke azken urte hauetan zehar lankide izan ditudan Beñat, Santi, Amaia, Aroa, Iñigo "Iron", Estitxu, Carlos, Nerea, Leti, Estibaliz, Aitor eta Markel.

Agradecer especialmente a mi amigo y Dr. Javi Salado que, aunque no fuéramos parte del mismo grupo, para mí era uno más del *labo*.

A todos mis compañeros del BCMaterials, en particular a Maite, Anabel y Ariane.

A mis amigos de la carrera e integrantes del *Quinteto Mágico* o *Magic Five (*como dicen algunos), Dr. Iván Sasselli, Iker Chasco, Dr. Edu Sánchez y Dr. Liher Prieto, inmejorables momentos en pintxo-potes varios por Vitoria esos jueves salvajes.

A mi cuadrilla, ya que me han aguantado muchas penurias y quejas en los poteos durante la redacción de esta tesis y, sobre todo, porque sin ellos no sería quién soy. Muchas gracias Ander, Casti, Mikel, Orive, Xabo y a las chicas también por supuesto, Rubi, Silvia, Xandra, Tamara, Amaia, Lexuri, Sara y June. Sigo respirando (*Free Jagoba*). A mi otra cuadrilla, Luke, Rubio, David y Roko, por todos esos momentos que me habéis dado y que seguiréis dándome, cabrones. Mención especial para el barman/cocinero por amenizar todas esas largas y arduas tardes.

Por último, a mi familia, que quiero y que siempre querré: Ama, Aita y June; Aiti y Yaya; Tia y Tio; Iñi, Maitane y Unax; Kay and Michael. En particular, quiero agradecer a Ama y a mi hermana June (sin olvidar al pequeño último integrante de la familia) todo su apoyo y comprensión durante estos largos años, ya que son y siempre serán mi mundo, aunque no lo demuestre todo lo que me gustaría o se mereciesen. Zuengatik eta zuentzako delako egiten dudan guztia.

Benetan, **ESKERRIK ASKO** nire mundua osatzen duzuen guztioi,

Jago

A TI, TARUGO

Dedicated to the memory of Aita

TABLE OF CONTENTS

GENERAL INTRODUCTION

Chapter 1

The nanometric metal–oxo anionic species known as polyoxometalates (POMs) are amongst the most remarkable families of metal clusters, due to their rich solution equilibria as well as their unique compositional, electronic, reactive and structural diversity. They possess an intrinsic multifunctional nature, and thus, POMs have found applications in a wide range of fields involving technology, health, energy, or environment. As a result, they are considered exceptional candidates for the construction of functional inorganic–organic hybrid materials, which could potentially display enhanced or unusual properties born from synergistic effects. One of such could be the capacity to undergo single–crystal–to–single–crystal (SCSC) transformations leading to new crystalline phases upon applying an external triggering stimulus. In this introductory chapter, a brief view on the complex POM chemistry is given. The four main methods to carry out the organic derivatization of POMs that lead to the formation of hybrid POMs are discussed, as well as the metalorganic building blocks employed in this work. Synthetic strategies for constructing high dimensional POM–based networks are mentioned, followed up by the unusual occurrence of the SCSC phenomena in all known stimuli–responsive POMs to date, the relevance of which is also briefly discussed. Later, basic notions regarding the preparation of tailored "breath figures" polymeric surfaces composed of amphiphilic diblock copolymers and their potential to act as platforms to immobilize POM clusters are given. The introductory chapter ends with the aim of this work.

GENERAL INTRODUCTION

1.1 POLYOXOMETALATES

1.1.1 Definition

Polyoxometalates (POMs) are a well–known class of anionic metal oxide nanoclusters that exhibit a huge compositional, structural and electronic versatility as well as an intrinsic multifunctional nature.[1] A great variety of anions can be found within this unique inorganic family which range from simple and small dimetalates and oligomeric species to larger and more complex heterometallic clusters and even giant macrostructures with sizes close to those shown by some proteins (Figure 1.1). A contemporary huge impetus in the systematic design and controllable syntheses of POM-based multifunctional materials has been developed not just because of their stunningly varied compositions, diversified architectures and fascinating topologies, but also due to their versatile potential applications in a wide range of fields such as catalysis,[2] magnetism,[3] biomedicine[4] and material science,[5] among others. Since the seminal work carried out by M. T. Pope,[1] POM chemistry has undergone an outstanding growth over the last two decades[6,7] and thus, it can be considered as one of the most active and promising fields within Inorganic Chemistry.

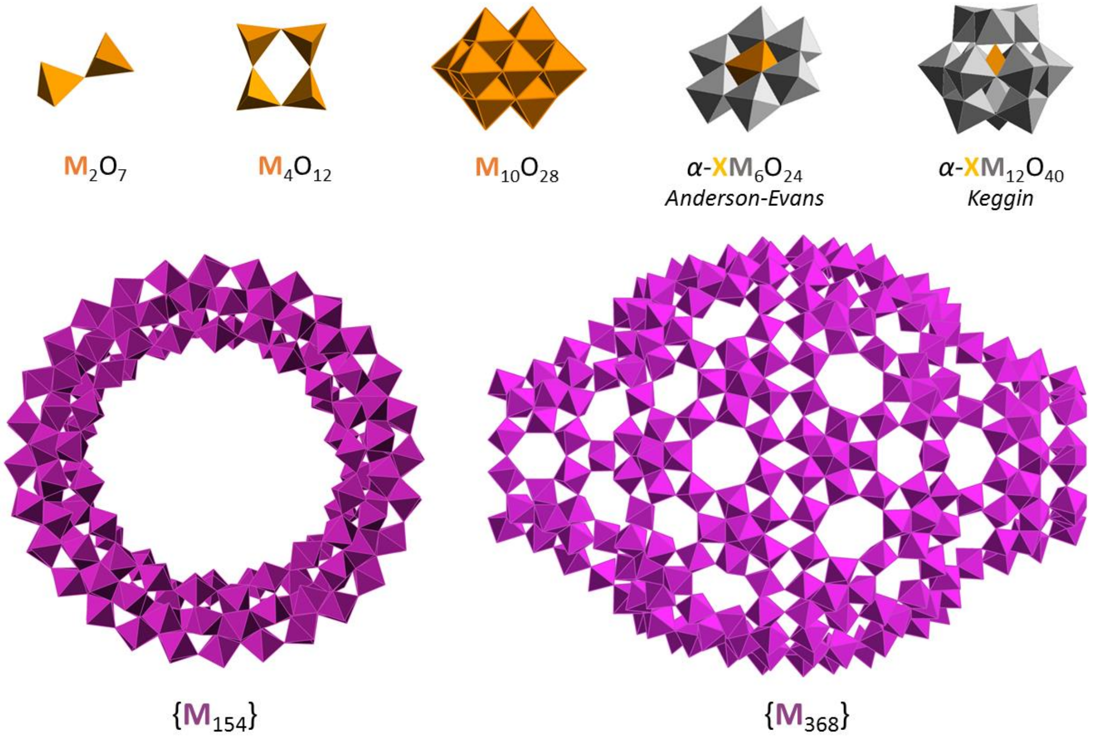

Figure 1.1. Structural diversity in POMs.

POMs are formed by the acidic condensation of a variable number of MO_x polyhedra, where M stands for early transition metals from groups 5 and 6, traditionally V, Mo or W but also Nb or Ta,[8] usually in their highest oxidation states, although some examples of noble metal POMs including polyoxopalladates, –platinates and –aurates have emerged as well during the last few years.[9] These *addenda* metals, as they are called, show a suitable charge and ionic radius ratio as well as empty and accessible d orbitals for the required back–donation to form π M–O bonds. The coordination numbers of the *addenda* metallic centers range from 4 to 7, being the octahedral the most common geometry by far (Figure 1.2). The condensation of {MO_6} subunits may occur by either corner– or edge–sharing and exceptionally via face–sharing. Regarding the common linkages modes, corner–sharing confers flexibility to the polyanion while edge–sharing mode results in a more rigid cluster. Nevertheless, the condensation of the polyhedra must be such that no more than two oxygen atoms per octahedron are free (Limpscomb's rule), which minimizes the strong *trans*–effect of the terminal M–O bonds in order to avoid the dissociation of the cluster.[10] Due to the participation of the d orbitals in the formation of the π M–O bonds, all subunits inevitably show distorted geometries. This way, all *addenda* metals in each {MO_x} polyhedra result oriented towards the terminal oxygen atoms of their immediate coordination environment which lead to two classes of polyoxoanions with different electronic properties: *class I*, if the π M–O bonds are polarized toward a single terminal O atom and *class II*, where the polarization takes place toward two atoms locates in *cis* relative configuration. Since the LUMO orbital of the former is of non–bonding nature, they can accept and release specific numbers of electrons reversibly under chemical, electrochemical and/or photochemical procedures, which result in the formation of mixed valence species with marginal structural rearrangement.[1a] In contrast, *class II* POMs possess an anti–bonding LUMO orbital and thus, they are electrochemically inactive and/or difficult to be reduced.[11] Because of the polarization that the *addenda* metals sustain toward the outer oxygen shell, the d orbitals permit the formation of the π M–O bonds which in turn prevents the formation of more bridges with additional octahedra limiting the polycondensation process.

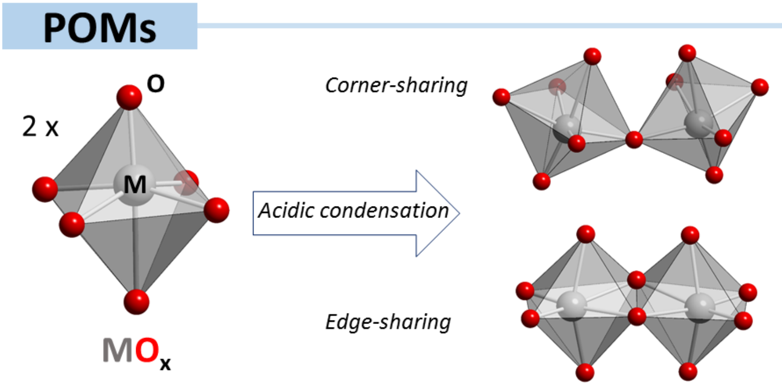

Table 1.1. Shannon & Prewitt ionic radii for 4, 5 and 6 group of transition metals in CN = 6.

4	5	6
Ti(IV) 0.74	V(V) 0.68	Cr(VI) 0.58
Zr(IV) 0.86	Nb(V) 0.78	**Mo(VI)** **0.73**
Hf(IV) 0.85	Ta(V) 0.78	W(VI) 0.74

S&P ionic radii (CN = 6)

Table 1.2. Coordination polyhedra of MO_x metal centers making POMs.

Coordination number (CN)	4	5	6	7
	Tetrahedron	Square pyramid	Octahedron	Pentagonal bipyramid
Polyhedron	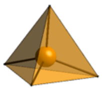		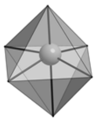	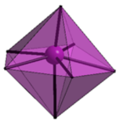
Found in	Metavanadates	Polyvanadates	Majority of POMs	Mo-blues

Figure 1.2. Polyhedral representation of the two main linkage modes between two {MO_6} octahedra that form POMs as well as typical coordination polyhedra of MO_x addenda metals and their S&P ionic radii (Tables 1.1–1.2).

In spite of the vast compositional, topological and structural diversity, most POM usually exhibit some common properties:[1] a) They possess high charge, size and symmetry as well as thermal and solution stability; b) the equilibria involving the formation of POMs are modified to a great extent by several variables like concentration of the reactants, pH, ionic strength, presence of extra ligands, employed counterions, temperature or pressure (hydrothermal synthesis, microwave assisted reactions, etc.). Several solution studies confirm the coexistence of various species in equilibrium for a given range of pH. Furthermore, usually the less soluble specie (which may not be the predominant specie) is isolated in solid state, evidencing the crucial role that the pH of the reaction medium fulfill in the formation and consequent isolation of these nanoclusters; c) species containing alkaline counterions are water soluble whereas protonated organic amines or bulky counterions confer a higher solubility in organic solvents; and d) they can act as multidentate inorganic ligands toward a wide variety of electrophiles through the oxygen atoms located at the cluster surface.

1.1.2 Classification of Polyoxometalates

Two main groups can be distinguised attending to the composition of the POM skeleton.

a) Isopolyoxometalates (isoPOMs), the general formula of which is $[M_mO_y]^{q-}$, as they only contain metal and oxygen atoms. The structures of most isoPOMs originate from the removal of some octahedral subunits from the parent decametalate cluster, which is formed by the condensation of ten $\{MO_6\}$ octahedra linked to each other through their edges in an ideal D_{2d} symmetry. The most common representatives of this group are the α– or β–M_8O_{26} octa–, M_7O_{24} hepta– (parametalate–A) and M_6O_{19} hexametalate (Lindqvist–type structure) species (Figure 1.3). It should be noted that meta– and cyclic polyvanadate species are also considered isoPOMs and thus, they belong in this group.

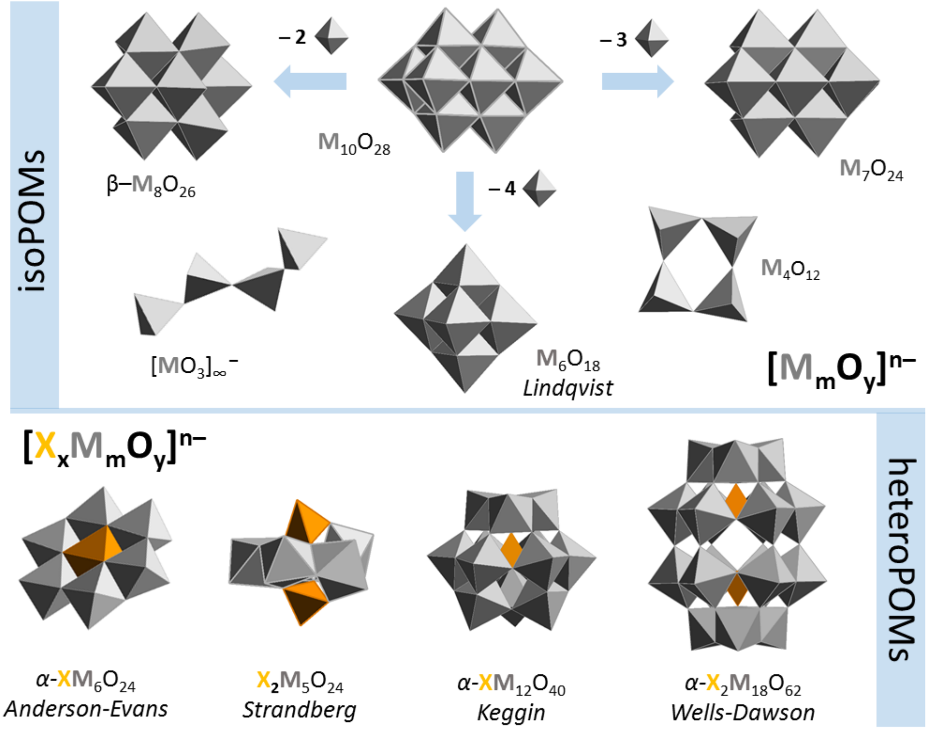

Figure 1.3. Polyhedral representation of archetypal isoPOMs, as well as some common HeteroPOMs architectures.

b) Heteropolyoxometalates (heteroPOMs), of general formula $[X_xM_mO_y]^{q-}$, are composed not only by metal and oxygen but also by other elements *X* in their frameworks, which are denominated heteroatoms. As opposed to the *addenda* M centers, the nature of X is not restricted as most of the elements of the periodic table can fulfill the role of heteroatom with the exception of noble gases. Typical examples of heteroPOMs include the Keggin–type anion $[XW_{12}O_{40}]^{n-}$ with a tetrahedral heterogroup (X = Si^{IV}, Ge^{IV}, P^{V}), the Wells–Dawson specie $[X_2W_{18}O_{62}]^{n-}$derived from the Keggin anions that contains two tetrahedral heteroatoms (X = P^{V}, As^{V}) and the Anderson–Evans $[XM_6O_{24}]^{n-}$ cluster, which shows an octahedral heteroatom where X denotes a 1st row transition metals (Figure 1.3).

1.1.3 The Keggin–type Anion: Isomeric, Lacunary and Substituted species

While it is common knowledge that J. J. Berzelius was responsible for the synthesis of the first polyoxometalate back in 1826,[12] the Elhuyar brothers were the first chemists that had successfully prepared a tungsten–containing POM almost 40 years before Berzelius' work in 1783.[13] However, it was not until 1933 that J. F. Keggin determined the structure of that first POM, the $H_3[PMo_{12}O_{40}]$ heteropolyacid, using powder X–ray diffraction technique.[14] From then on, the worldwide interest in POM discipline and the rate of discovering novel species have steadily increased over the years.

The $\{XM_{12}O_{40}\}$ Keggin–type structure is one of the most important type of POMs and it is formed by the condensation of $\{MO_6\}$ octahedral subunits in the presence of a tetrahedral $\{XO_4\}^{n-}$ anion in acidic medium. The Keggin anion is composed of four $\{M_3O_{13}\}$ trimers, each one constituted by three edge–sharing $\{WO_6\}$ octahedra linked to each other and to the central $\{XO_4\}$ tetrahedron by corner–sharing in an ideal T_d symmetry (Figure 1.4). Keggin–type HeteroPOMs show up to five structural isomers (Baker–Figgis isomers) that originate from the parent $\{\alpha\text{–}XM_{12}O_{40}\}$ anion by the 60° rotation of one (β), two (γ), three (δ) or four (ε) M_3O_{13} trimers (Figure 1.4). While the α, β *and* γ isomers have been widely observed in the silicontungstate subfamily,[15] reports on compounds containing the much less stable δ– and ε– are limited to just one example each, which are the aluminum–based $[(AlO_4)Al_{12}(OH)_{24}(H_2O)_{12}]^{7+}$ cationic cluster [16] and the lanthanum–stabilized $[\varepsilon\text{–}PMo_{12}O_{36}(OH)_4\{La(H_2O)_4\}_4]^{4+}$ phosphomolybdate,[17] respectively.

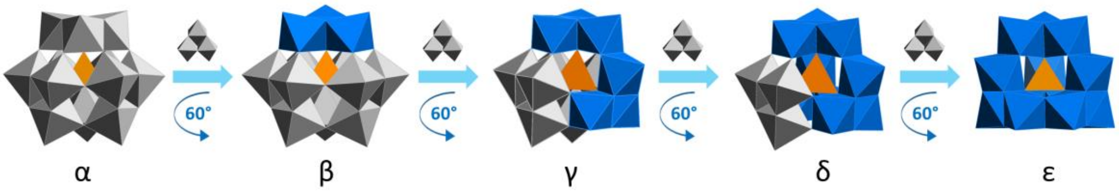

Figure 1.4. Baker–Figgis isomers of the Keggin–type structure.

Increasing the pH of the reaction medium promotes the removal of some $\{MO_6\}$ octahedra from the parent plenary Keggin anion leaving vacancies in the inorganic framework. The resulting lacunary POMs have higher charges, hence increased basicity and nucleophility than their parent complete species. Consequently, they react quite easily with a variety of electrophilic groups in water or in non–aqueous solvents. In this sense, up to nine different lacunary species can be prepared starting from the plenary Keggin {α–$XM_{12}O_{40}$} cluster (X = Si, Ge) as seen in Figure 1.5. This way, the removal of one or three subunits from the α–keggin generates the mono–(α–$XM_{11}O_{39}$) and trilacunary {α–XM_9O_{34}} species, respectively. Depending on the connectivity of the removed trimer, both α– and β–trilacunary anions exhibit two possible isomers: {A–α–/A–β–XM_9O_{34}} if the lost trimer is an edge–sharing one, or alternatively, {B–α–/B–β–XM_9O_{34}} isomers when a corner–sharing trimer (a triad) is eliminated. In contrast, three different monolacunary β–isomers can be formed depending on the position of the resulting vacancy because of the lower symmetry of the {β–$XM_{11}O_{39}$} cluster compared to that of the {α–$XM_{11}O_{39}$} isomer. This way, the β_1–monolacunary shows the vacancy in the triad opposite to the 60° rotated trimer, β_2 in the central belt and β_3 in the rotated trimer. As opposed to the former isomers, only one divacant specie {$XM_{10}O_{36}$} have been reported so far for the γ isomer. In certain conditions, lacunary species can suffer further condensation reactions resulting in new interesting structures. One such well–known heteroPOM is the {α–$X_2M_{18}O_{62}$} Wells–Dawson structure, which is formed by the assembly of two {A–α–XM_9O_{34}} trilacunary Keggin fragments by corner sharing as can be seen in Figure 1.1. Interestingly, the lacunary derivatives of Keggin or Dawson–Wells HeteroPOMs exhibit the ability to act as multidenate inorganic ligands toward a wide variety of metallic centers such as transition metal or lanthanide atoms, which result in the formation of 3d– or 4f– substituted species, respectively.[18]

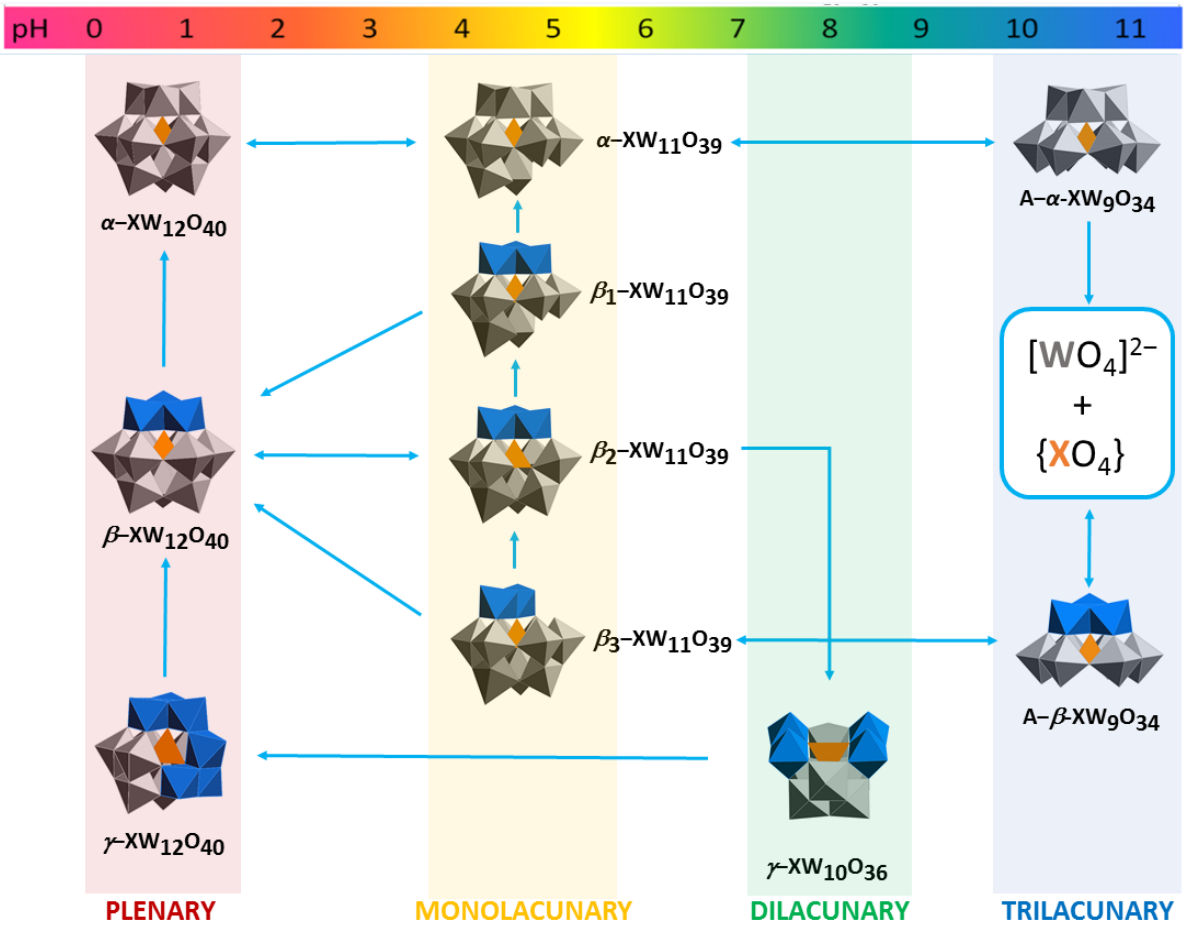

Figure 1.5. Scheme of the chemical equilibria between the different plenary and lacunary species in aqueous solution for the heteropolyoxotungstate family (X = Si, Ge).

1.2 HYBRID POMs: ORGANIC FUNCTIONALIZATION

The combination of organic moieties and inorganic POM clusters represents one of the current hot topics in synthetic POM chemistry due to the possibility of combining two components with different characteristics into a single material to obtain unusual properties born from the synergy that could result in novel applications. The resulting hybrid POMs are considered a key factor for the incorporation of these nanoclusters into not only functional materials like carbon nanotubes or polymeric matrixes, but also to interact with diverse surfaces (oxides such as alumina or silica, and highly oriented pyrolytic graphite) and even with metallic nanoparticles.[19,20] Hybrid POMs can be classified into two groups attending to the nature of the interaction forces that exist between the two different building blocks, namely, non–covalent and covalent interactions, respectively. The first group (*class I*) consist on systems where only electrostatic interactions are involved while in the second group the organic and inorganic moieties are covalently attached to each other (*class II*).[20] In this sense, the covalent approach offers several advantages since covalent bond improves the stability of the resulting hybrid and might enhance the interaction between the inorganic and organic components facilitating the construction of novel POM–based integrated systems.[19b] Indeed, it has been widely demonstrated that the presence of covalently bonded organic ligands can bring new functionalities to the system allowing the elaboration of unique materials and devices,[20] as evidenced by the characterization of surfaces patterned with POMs,[21] as well as the synthesis of fluorescent[22] and catalytic[23] POM–based functional materials, among others. Considering the latter route, four different approaches have been stablished that allow the synthesis of covalent hybrid POMs at a precursor scale.[20] These synthetic strategies are based on the nucleophilic character of the terminal oxygen atoms, the substitution of oxo groups of the POM by organic ligands and/or the use of 3d– or 4f metallic centers (transition metal or lanthanides) as well as other electrophilic groups bearing specific organic groups.

1.2.1 p–block Organoderivatives

One of the most studied methods to achieve the organic functionalization of POMs consist on reacting p–block organoderivatives such as organosilyl, –germyl, –phosphoryl, –stibyl or –stannil moieties with lacunary polyoxotungstates. Compared to the reactivity of the terminal oxygen atoms of the plenary anion, the higher nucleophilic character of the O atoms delimiting the lacuna facilitates the reaction toward electrophile groups. Two main synthetic strategies have been developed so far for the preparation of these types of hybrid POMs. The first approach requires the POM to be phase transferred to an appropriate organic solvent like DMF or acetonitrile, after which is reacted with a fitting reactant such as organotrichlorosilane. In the second approach however, no prior phase transfer is required as the reaction between the lacunary heteroPOM and the organoderivative is carried out in a mixed water/organic solvent such as CH_3CN/H_2O or CH_3OH/H_2O in the presence of an acid. The organoderivative moieties are either preformed or they can be further postfunctionalized after their incorporation into the lacuna of the vacant cluster. It must be highlighted that most of the work concerning these types of hybrids fall back into the RSi, RP and RSn derivatives, as few reports exist for RGe and RSb functionalized POMs (Figure 1.7.).

The first organosilyl derivatives, namely $[SiW_{11}O_{39}\{O(SiR)_2\}]^{4-}$ (R = C_2H_5, C_6H_5, $NC(CH_2)_3$, C_3H_5), were not reported until 1979 by Knoth and coworkers.[24] Following this pioneering work, a large variety of organosilyl groups have been successfully attached to monolacunary Keggin– or Dawson–Wells–type clusters by numerous authors.[25] In a similar fashion, several studies describing the incorporation of organosilyl fragments into di– or tri–lacunary Keggin units have been also reported.[26] Some of such compounds have been linked to gold or latex nanoparticles, combined with polymers and even post–functionalized to add new organic groups.[27] While the combination of organosilyl and lacunary POMs have been well documented, comparatively far less studies have been carried out regarding organogermyl derivatives, as just a handful of papers describing such compounds can be found.[28]

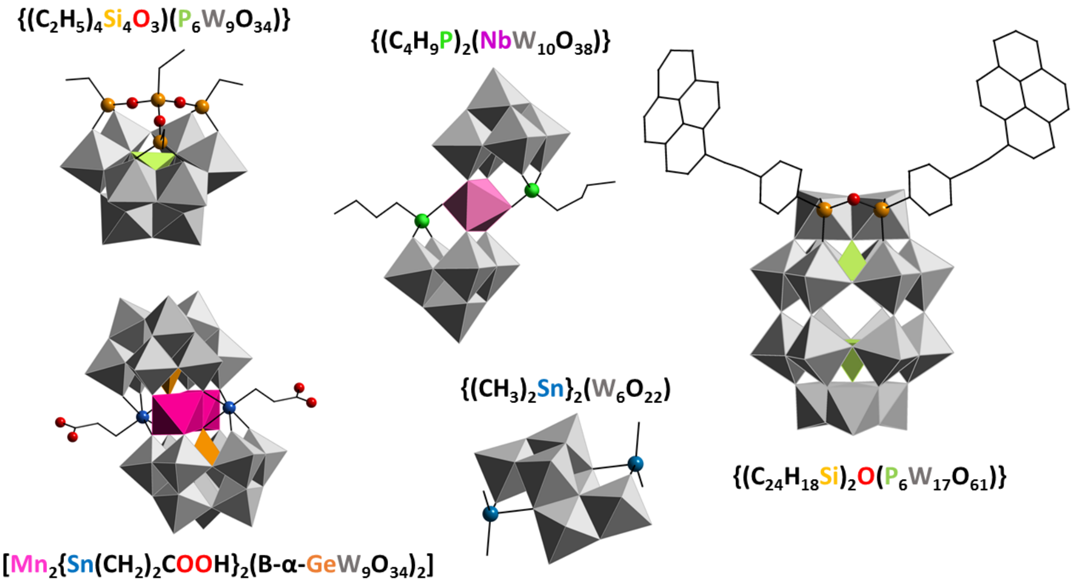

Figure 1.6. Some representative and structurally diverse examples of hybrid POMs with p–block organoderivatives.

Alternatively, organophosphonates have been mostly employed in the organic derivatization of lacunary polyoxotungstates, Strandberg–type diphosphopentamolybdates and various polyoxovanadates, with a strong focus on optical activity.[29] In comparison, organotins have been extensively used in the past few years due to several factors which include the high stability of the Sn–C bond in aqueous media, the capacity of Sn^{IV} to substitute *addenda* W^{VI} centers in POM skeletons owing to their similar sizes and the possibility to easily characterize the resulting hybrid species in solution using ^{119}Sn–NMR spectroscopy. These syntheses are usually carried out in aqueous medium by reacting organotrichlorotin reagents with preformed lacunary POMs, as exemplified by the studies initiated by Knoth et al., and later on followed up by Liu's group, regarding the reactivity of monoorganotin groups with mono–, di– and trivacant Keggin or monovacant Wells–Dawson polyoxotungstates.[30] Pope et al. reported sandwich–type organotin–derivatives starting from trilacunary $[\alpha\text{–}XW_9O_{33}]^{9-}$ (X = As^{III}, Sb^{III}) polyoxotungstates[31] whereas Hasenknop's group successfully reacted lacunary Dawson–Wells POMs with organotin moieties carrying pendant reactive groups (carboxylic acids, alkynes or azides) which allowed them to graft a huge variety of additional organic groups by amide formation or click chemistry.[32] Hussain et al. used phenyl– and dimethyltin moieties in combination with polylacunary POM clusters which led to the formation of large structures.[33] Similarly, Kortz and coworkers reported the dodecameric ball–shaped $[\{SnMe_2(H_2O)\}_{24}\{SnMe_2\}_{12}(A–XW_9O_{34})_{12}]^{36-}$ (Me = CH_3 and X^V = P, As) macroanion by using diorganotin linkers with trilacunary heteropolyoxotungstates.[34] In contrast, much like organogermyl derivatives, only a couple of works have been reported regarding organostibil moieties, which show organometallic moieties trapped between two trilacunary fragments. The potential biological activity as antimicrobial agents was evaluated for such hybrids.[35]

1.2.2 Replacement of Shell Oxygen Atoms

This second approach consists on the substitution of surface oxygen atoms of the POM cluster with those belonging to either O– or N–donor ligands. Typical examples following this procedure are the covalent attachment of trisalkoxo–ligands to Anderson–Evans type polyoxomolybdates, Lindqvist–type hexavanadates or trivanadium–capped Well–Dawson phosphotungstate derivatives, as well as the reaction of organoimido/diazenido ligands toward Lindqvist–type hexamolybdates.

In the case of Anderson–type POMs,[36] the general formula of which is $[H_yXM_6O_{24}]^{n-}$ (y = 0–6; n = 2–8; M = Mo^{VI} or W^{VI}; X = central heteroatom), the organic moieties are linked to both sides of the plane defined by the metal atoms where the trisalkoxo ligand caps the two opposite triangular faces of the central $\{XO_6\}$ octahedron (δ–*c*oordination mode). Organic functionalization of Anderson–type clusters have succeeded so far exclusively for trivalent transition metal (X^{III} = Cr^{III}, Mn^{III}, Fe^{III}) polyoxomolibdates with a wide diversity of organic groups such as alkyl chains, alkenes, alcohols, amines and nitro groups, or even polycyclic molecules such as pyrene or terpyridine.[37] Some of the latter have been further derivatized by linking to active catalytic metal centers like Pd or Ru, whereas others exhibited photoactive properties or the ability to self–assemble into vesicles in solution.[38] Remarkably, both single–side and asymmetric organic functionalization of anderson type polyanion have been recently achieved by Wei's and Cronin's groups.[39] In 2002, Hasenknopf and coworkers reported the only known example to date of a divalent metal containing polyoxomolibdates (X^{II} = Ni, Zn) where the tris(alkoxo) ligands caps a tetrahedral cavity (χ–coordination mode) instead of being bound to the central heteroatom $\{XO_6\}$ of the heteropolyoxomolybdate[40] (Figure 1.7).

Trisalkoxo ligands have been also used to prepare several difunctionalyzed hybrid Lindqvist–type hexavanadates, the postfunctionalization of which resulted in fluorescent compounds or coordination polymers with catalytic activity.[41] The grafting of the trisalkoxo ligands occurs almost exclusively in a *trans* fashion, although a few examples have been reported where a *cis*–coordination mode is observed, as published firstly by Müller and coworkers back in 1995.[42] Kortz et al. reported lone–pair heteroatom containing hexamolybdates in which the inner O atoms of the clusters were substituted by the carboxylic oxygen atoms of amino acid ligands.[43] The organic derivatization of V_3–Dawson–Wells clusters have been also achieved by using tris(hydroxymethyl) ligands capping the $\{V_3O_{13}\}$ trimmer,[44] resulting in some hybrids which can self–assemble into vesicles in acetone/water solutions.[45] Relatively small organic molecules carrying amide and diol groups $\{RCONHC_5H_9(OH)_2\}$ have been used to replace the shell O–atoms of the V_3–Wells–Dawson POM, as well.[46]

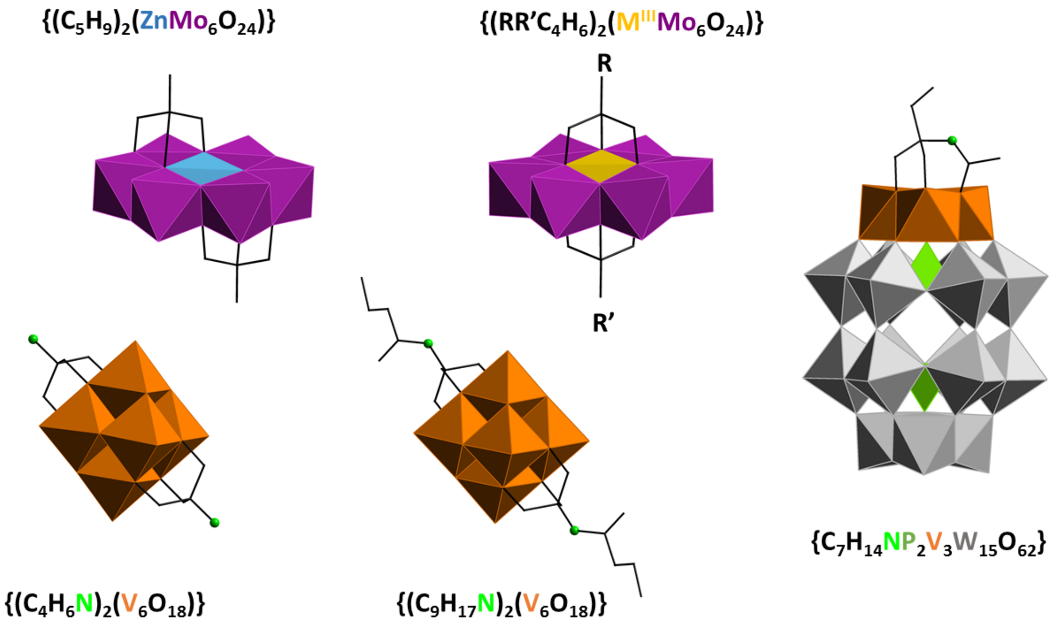

Figure 1.7. Some representative examples of hybrid POMs with substituted shell O–atoms (R = R' symmetric functionalization; R ≠ R' asymmetric functionalization).

The organic functionalization of Lindqvist–type hexamolybdates with N–donor ligands was initiated by the pioneering work conducted by Zubieta and Maata, who reported the first example of a polyoxomolybdate–based organoimido derivative.[47] The general method for the preparation of such hybrid polyoxomolybdates consisted on the refluxing of the hexamolybdate precursor in pyridine together with variable equivalents of isocyanates, which yielded both mono–or di–organoimido derivatives.[48] Later, Peng designed a more efficient synthetic process involving the use of dicyclohexylcarbodiimide in acetonitrile, which has become the conventional method for the functionalization of Lindqvist–type POMs.[49] Interestingly, Gao et al. demonstrated that not only terminal but also bridging oxo ligands are susceptible to be replaced by organic imido–type ligands.[50] Several studies have exposed the potential applicability of this type of hybrids as antitumoral and herbicidal agents, while non–linear optical activities for some of them were also observed and evaluated by Xue and coworkers.[51] Recently, Zhang et al. reported the synthesis of unusual chiral rod–like molecular triads constituted by two Lindqvist–type molibdates that are connected to a central Anderson cluster through bridging trisalkoxo organic ligands. While the trisalkoxo ligands reacts with the Anderson cluster from both sides, the pendant amino groups forms an imide bond with the Lindqvist units.[52] Closely related but far less studied organodiazenido derivatives are usually synthetized starting from a phosphazine.[53]

1.2.3 Organic Derivatization of 3d–/4f–Metal Substituted POMs

As opposed to the modern methods described above, the incorporation of metallic or lanthanide centers into the vacancies of lacunary derivatives is the oldest and consequently, the most extensively studied reactions in synthetic POM chemistry. Three main methods can be distinguished within this strategy and they consist in: a) replacing labile solvent or small molecules (like acetate anions or aqua ligands) with organic ligands; b) adding transition metal complexes to lacunary POMs; c) using one–pot procedures by mixing a tungstate salt, a heteroatomic source, the transition metal and the organic ligand.

Unfortunately, the first route requires the use of solution stable 3d or 4–f metal substituted POMs with exposed metallic centers in order to achieve the ligand exchange reaction, which is rather difficult and hence, this approach remains mostly unexplored compared to the other two routes. The first attempts to apply this method were carried out by replacing the water molecule of 3d–monosubstituted Keggin–type $[M(H_2O)(XW_{11}O_{39})]^{n-}$ anions with N–donor ligands such as imidazole or pyridine derivatives. Latter on, substitution of that same water molecule with more sophisticated ligands like 4,4'–bipyridine under hydrothermal conditions was achieved.[54] Alternatively, ruthenium monosubstituted POMs have been widely studied due to their catalytic properties as well as their capacity to form Ru–C bonds.[55] Monodentate N–donor ligands like pyridine, imidazole as well as ethylendiamine ligands have been also reported to be able to exchange water molecules of several Weakley $[M_4(H_2O)_2(XW_9O_{34})_2]^{n-}$ and Hervé–type $[M_3(H_2O)_3(XW_9O_{33})_2]^{n-}$ sandwich structures.[56] The first examples of a POM showing embedded chelated metals were reported by Pope, which consist in ethylendiamine chelated Co metal centers encapsulated between two $\{PW_9O_{34}\}$ or $\{PW_{10}O_{38}\}$ lacunary Keggin units or lacunary hexamolybdates[57] (Figure 1.8). In a similar fashion, Wang et al. prepared a hexamethylenetetramine bridged decanuclear Fe^{III} cluster sandwiched by two $\{P_2W_{13}O_{51}\}$ clusters.[58] The one–pot reaction of tungstate and phosphate together with a Ni^{II} salt and N,N'–bis(2–hydroxyethyl)piperazine (bhep) ligand resulted in the encapsulation of a metal chelate within a dilacunary Keggin POM. In addition, the formation of a dimeric cluster constituted by two trilacunary Keggin–type $\{PW_9O_{34}\}$ fragments containing nine divalent Co ions bridged by three bhep ligands was observed in similar reaction when the pH of the reaction medium was increased.[59]

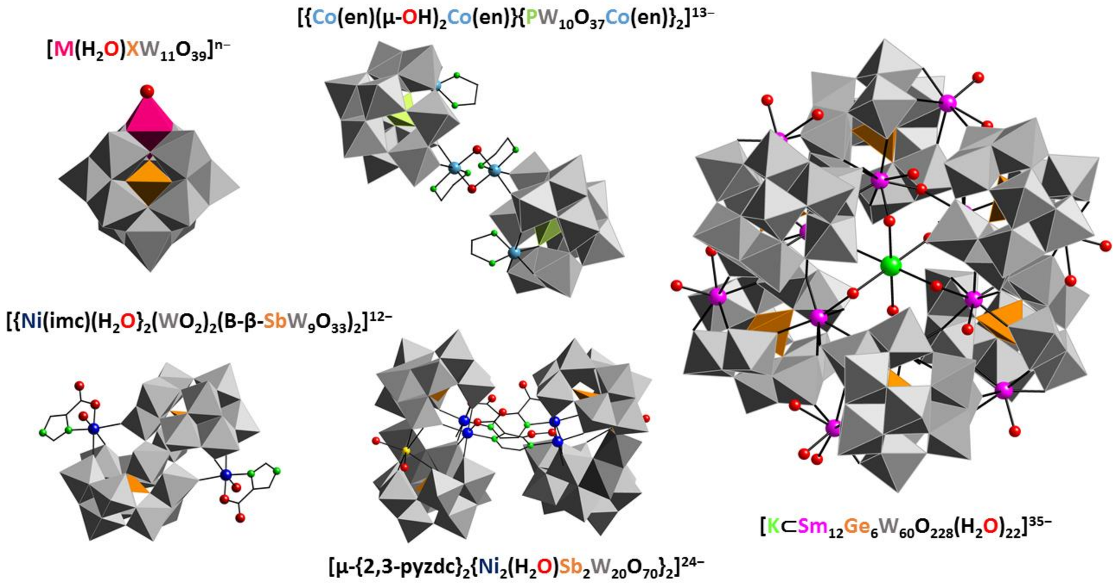

Figure 1.8. A generic transition metal monosubstituted Keggin–type polyoxotungstate together with some representative and structurally diverse 3d–metal substituted hybrid polyoxoanions. Organic ligands: imc = 1 H–imidazole–4–carboxylate, en = ethylendiamine, 2,3–pyzdc = pyrazine–2,3–dicarboxylate. A hexameric giant 4f–substituted POM with accesible water molecules susceptible for organic derivatization is also shown. Small green spheres of the organic ligands stand for N atoms.

In 2005, Hill's group prepared two enantiomerically pure compounds formed by malate or tartrate ligands coordinated to Zr^{IV}–substituted polyanions, where the metal centers bridge two lacunary $\{P_2W_{15}O_{46}\}$ Wells–Dawson subunits.[60] It is also worth highlighting the outstanding work carried out by B. Artetxe. Within this work, a well–documented systematic study on the organic functionalization under mild conditions of transition–metal–disubstituted Krebs–type $[\{M(H_2O)_3\}_2\{WO_2\}_2(Sb^{III}W_9O_{33})_2]^{10-}$ (M^{II} = Mn, Co, Ni, Zn) POMs with several N,O–chelating and N,O–bis(bidentate) bridging organic ligands is described, as well as the synthesis and full characterization of some new 4f–metal containing clusters or 3d–4f heterometallic species[61] (Figure 1.8). Analogously, Rousseau et al. performed systematic studies under bench conditions in order to develop a general method for the functionalization of 3d–substituted POMs containing carboxylate ligands. This work resulted in the preparation of hybrids with varied dimensionalities constructed from $[B\text{–}\alpha\text{–}XW_9O_{33}]^{9-}$ Keggin clusters substituted by multiple Cu or Ni metal centers which were linked to several different carboxylate ligands[62] (3–thiopheneacetate, p–phenilenediacetate, glutarate as well as β–alanine and γ–aminobutyric aminoacids).

Finally, it must be noted that the synthesis of organically derivatized POMs in organic solvents have been successfully carried out, even though only a handful of such studies have been reported to date.[63] In comparison, hydrothermal methods have been identified as an excellent alternative for the preparation of such type of hybrids as evidenced by the formation of high dimensional POM–based metalorganic frameworks by Yang and coworkers.[64]

1.2.4 Grafting of Transition Metal Complexes at the POM Surface

In the previous section, the transition–metal ions (or lanthanide cations) were coordinated to lacunary polyoxometalate fragments via M–O bonds with the nucleophilic oxygen atoms delimiting the vacancy, but these electrophilic groups can also be attached although more weakly to saturated POM clusters through terminal or bridging oxygen atoms located at the polyanion surface. Since the 3d–metal center is bonded only to one or two terminal oxygen atoms, several positions in the coordination sphere of the metal remain available to coordinate to an organic ligand. Thus, this approach allows the possibility of decorating POM clusters with more sophisticated organic ligands results in hybrids with varied dimensionality, which depends on the chemical nature and structure of the organic ligand.

Although this kind of syntheses were traditionally performed under bench conditions, a huge number of hybrid structures have been prepared using hydrothermal methods in the last decades. This work was initiated by Zubieta et al. on polyoxomolibdates and in particular –vanadates, and was later expanded to the –tungstate family.[65] Since then, several groups have studied the synthesis of hybrid species by grafting different 3d–metal moieties at POM surfaces to incorporate additional catalytically or magnetically active centers in the system, which resulted in the formation of hybrid POMs with varied topologies and structural motifs. In this sense, systematic studies include those carried out in our group under both mild bench and hydrothermal conditions. The former includes the rational self–assembly of *in situ* generated plenary Keggin–type silicotungstates or copper(II)–monosubstituted $[SiW_{11}O_{39}Cu(H_2O)]^{6-}$ species and dinuclear Cu^{II}–bridging caboxylate cationic complexes $[\{Cu(phen)(H_2O)_2OAc\}_2]^{2+}$ and $[\{CuL(H_2O)_2\}_2ox]^{2+}$ (L = phenantroline, 2,2'–bipyridine), which led to discrete molecular polyanions, monodimensional hybrid arrangements or even extended 3D coordination networks.[66] Hydrothermal conditions were successfully applied in the preparation of novel organic–inorganic compounds based on Keggin–type silico– or germanotungstates and copper complexes as well. Organic ligands include the N–donor bidentate 2,2'–bipyridine, 1,10–phenantroline and 2,9–dimethyl–1,10–phenantroline, bridging 4,4'–bipyridine and 1,2–bis(4–pyridil)ethane, or tetradentate cyclam, diamino–dipyridin–type species and their methylated derivatives.[67] Some remarkable examples of these types of hybrids structures have been reported by other groups within the last two decades, such as the "porphyrin hamburger" formed by a plenary keggin cluster decorated by two porphyrin metalorganic complexes in a *trans*–fashion; porous structures with uncommon sorption properties, hybrids showing accessible catalytic Ag or Ru metallic centers; or even compounds generated by the inclusion of chiral neutral ligands like L–proline into chiral POMs exhibiting applications in asymmetric catalysis.[68]

The general synthetic method is pretty straightforward, as it usually consist on preparing a solution for each building block and mixing them under appropriate experimental conditions of pH, temperature, pressure (hydrothermal), stoichiometry, reaction time, ionic strength and so on. Depending on the inorganic precursor, two slightly different synthetic strategies may be distinguished within this general functionalization procedure. The first one consist in dissolving crystals of the preformed POM precursor whereas the other is carried out by mixing appropriate amounts of the adequate reactants at a suitable pH to form *in situ* the desired cluster precursor in solution before adding the complexing metalorganic units. Usually, the former approach results in better yields. One must take into consideration the total charge of the POM and that of the metalorganic building blocks to assure that enough quantities of the latter are used for charge compensation purposes. This way, the incorporation of other cations present in the medium to the POM structure can be avoided, and thus, extended hybrid structures usually arise from the interaction between the building blocks when ligands with various free vacant coordination sites are used. Alternatively, small quantities of the metalorganic component favors the formation of low dimensional hybrids such as molecular 0D and 1D arrangements as the functionalization degree is lower. In the same fashion, the pH plays a vital role in maintaining the desired POM structure in solution and should be always monitored before and after adding the metalorganic units to the reaction medium to assure the cluster stability. Regarding the organic components, steric effects and electrostatic repulsion between anionic ligands and the polyoxoanions sometimes make the functionalization challenging. Overall, neutral or positively charged and relatively small ligands will react more easily than larger anionic ligands. The ionic strength of the medium also seems to affect greatly the degree of the functionalization in some cases as evidenced by great differences in yield when using aqueous saline solutions instead of simple water. In a similar fashion, buffered reaction medium is sometimes required to achieve the desired functionalization in some specific synthetic systems.

These types of hybrid compounds derived from grafting metal complexes at surface oxygen atoms of the clusters usually display a significant drawback in terms of predictability, which is originated from the limited control of the anchoring position, as there are several oxygen atoms per cluster susceptible for coordination. However, this approach provides several advantages compared to the other methods. In this sense, usually no harsh conditions are required as temperatures below 50 °C and even room temperature confers enough energy to achieve the organic functionalization in numerous cases. Similarly, there is no need to employ organic solvents and/or complicated and tedious multistep procedures since most of the time the functionalization takes place in simple aqueous solution and even with low reaction times (1 or 2 hours). Because of all this, this method can be considered an excellent option to carry out the organic functionalization of POMs to construct new hybrid architectures that could display novel or enhanced properties compared to those of the individual building blocks.

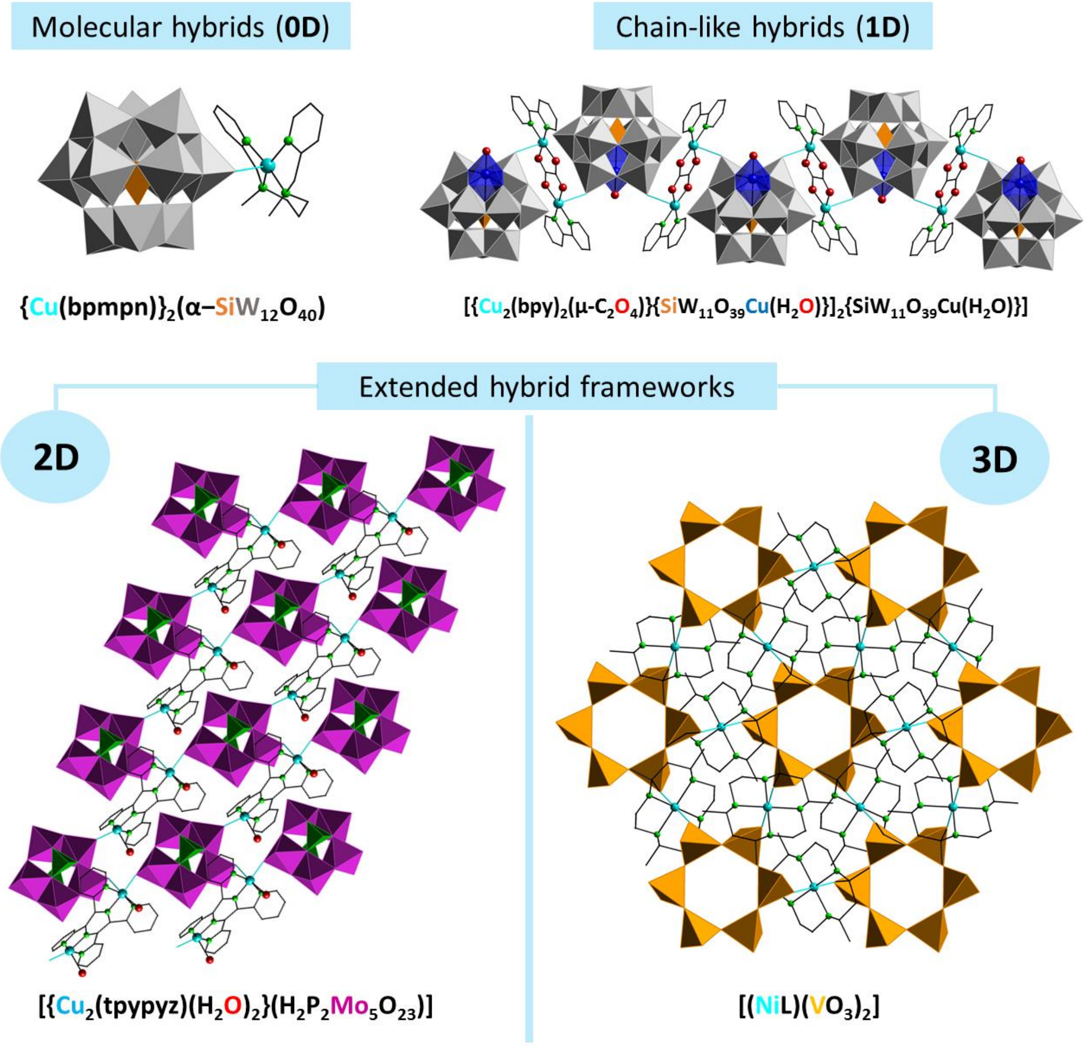

Molecular hybrids (**0D**)

$\{Cu(bpmpn)\}_2(\alpha\text{–}SiW_{12}O_{40})$

Chain-like hybrids (**1D**)

$[\{Cu_2(bpy)_2(\mu\text{-}C_2O_4)\}\{SiW_{11}O_{39}Cu(H_2O)\}]_2\{SiW_{11}O_{39}Cu(H_2O)\}]$

Extended hybrid frameworks

2D

$[\{Cu_2(tpypyz)(H_2O)_2\}(H_2P_2Mo_5O_{23})]$

3D

$[(NiL)(VO_3)_2]$

Figure 1.9. Dimensional diversity of some hybrid POMs with grafted transition metal 3d–complexes. Organic ligands: bpmpn = N,N'–dimethyl–N,N'–bis(pyridin–2–ylmethyl)–1,3–diaminopropane, bpy = 1,4–bipyridine, tpypyz = tetra–2–pyridylpyrazine, L = 5,5,7,12,12,14–hexamethyl–1,4,8,11–tetraazacyclotetradecane. Green spheres of the organic ligands stands for N atoms.

1.3 COMPLEXES OF MACROCYCLIC POLYAMINES: THE CYCLAM LIGAND

Macrocyclic polyamine ligands have been generating continuous interest due to their biological relevance, as there are many examples of metal complexes of naturally occurring macrocyclic ligands such as porphyrin or corrin ring derivatives, and their importance in coordination chemistry.[69] In this sense, saturated macrocyclic polyamines exhibit a different chemical behavior compared to that of mere assemblies of amines or linear polyamines.[70] For example, Hancock et al. demonstrated that the protonation constants (*pK*) of tetraaza macrocycles differ greatly from those of open–chain tetraamine analogues.[71] Macrocyclic structures are also extremely favorable for metal complexation, so much in fact that the effect of increased stability of a macrocyclic polyamine complex over that of similar linear tetraamine ligands is known as *macrocyclic effect*.[69,72] The strong affinity as well as the selective binding of certain metals shown by tetradentate macrocylic polyamines has allow them to be used as models for molecular carriers in biological systems,[73] as catalysts with active sites that mimic metalloenzymes,[74] and as anti–HIV agents,[75] among others.

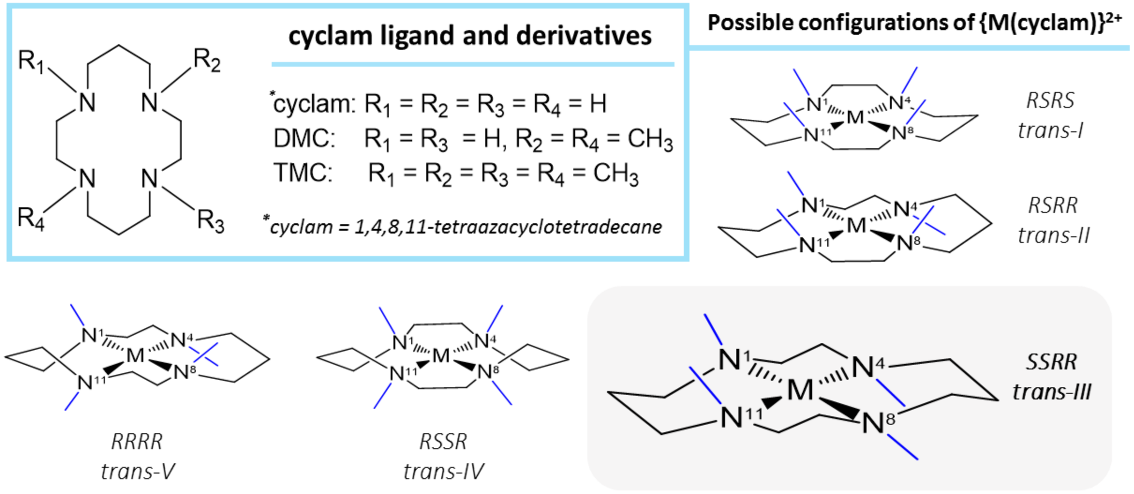

Figure 1.10. Chemical structure of the cyclam ligand and its methyl derivatives along with the five possible configurations that the cyclam ligand can adopt. The most common *trans–III* configuration is highlighted (DMC = 1,8–dimethyl–1,4,8,11–tetraazacyclotetradecane; TMC = 1,4,8,11–tetramethyl–1,4,8,11–tetraazacyclotetradecane).

As one of the most used tetraazamacrocycles, the fourteen–membered cyclic tetraamine cyclam[76] (1,4,8,11–tetraazacyclotetradecane) ligand is flexible enough to bind various cations including transition metals, often leading to complexes with very high thermodynamic and kinetic stability with respect to metal ion dissociation. The cyclam molecule was first synthetized in 1937 by Van Alphen through the reaction of 1,3–dibromopropane and ethylenediamine.[77] It is a white solid with formula $C_{10}H_{24}N_4$, a molar mass of 200.33 g mol^{-1} and highly soluble in water and chloroform, whereas it is insoluble in acetonitrile. Complexes of the cyclam ligand feature four secondary chiral amines with alternating five and six–membered chelate rings (Figure 1.10). Even though most of the studies concerning transition metal complexes of cyclam derivatives reside within the fields of biology and biomedicine,[78] Ni–cyclam derivatives have shown a promising activity towards the catalytic reduction of CO_2. These studies were initiated by Fischer and Eisenberg[79] in 1980, although it was not until six years later when Sauvage and coworkers demonstrated that $[Ni(cyclam)]^{2+}$ was unique in its efficiency and selectivity for CO_2 reduction in aqueous solutions with minimal production of H_2.[80] Because of that, up until now several studies have been reported regarding the catalytic behaviour of Ni–cyclam complexes, which is a topic that still attracts significant attention nowadays.[81]

Most first row transition–metals can bind to the cyclam ligand as metallocyclam complexes of V, Cr, Mn, Fe, Co, Ni, Cu and Zn can be found in the Cambridge Structural Database (CSD) as well as some 4d (Tc, Ru, Rh and Pd, Ag, Cd) and even 5d–containing structures (Re and Pt). Upon metal coordination, there are five possible configurations for metallocyclam complexes depending on the ligand conformation, and more specifically, on whether the N–H bonds of the four chiral nitrogen atoms are located above or below the MN_4 plane: *RSRS*, *RSRR*, *SSRR*, *RSSR*, and *RRR*; which are designated as *trans–I* to *trans–V*, respectively[82] (Figure 1.10). The energies of the different configurations have been estimated on the basis of molecular models and calculated using semi–empirical methods, molecular mechanics as well as local density functional theory. The semiquantitative estimates of the relative strain energies for each of the five isomers were calculated by Bosnich and coworkers[82] and later corroborated by Whimp et al., which have shown that the most favorable configuration of a Ni^{II}–cyclam complex with octahedral geometry is the *trans–III* one.[83] Molecular mechanics calculations have also demonstrated that the *trans–I* configuration gains stability over the *trans–III* when going from an octahedral Ni(II) environment to square–planar, square–pyramidal and trigonal–bipyramidal geometries in Ni^{II}–cyclam complexes.[84] From the analysis of all the nickel complexes containing the cyclam backbone in CSD, Donnelly and Zimmer observed that the most commonly found configuration and thus, the most stable one, is indeed the *trans–III* (*SSRR*).[85] The vast majority (77.8%) of octahedral nickel(II) complexes with a 1,4,8,11–tetrasubstituted cyclam derivatives adopt a *trans–III* configuration, while just 22.2% exhibit the *trans–I*. For the square–planar, square–pyramidal, and trigonal–bipyramidal molecules, however, the situation is reversed. Only 26.7% adopt the *trans–III* configuration while the other 73.3% prefer the *trans–I* conformation. These results are in perfect agreement with the molecular mechanical calculations. Similar results were reported for Cu(II) complexes by Bakaj and Zimmer.[86]

Regarding the stability of such complexes, there are both enthalpy and entropy contributions to the *macrocyclic effect* mentioned above compared to the complexes formed by the analogous open–chain 1,4,8,11–tetraazaundecane.[78b] In this sense, the alkylation of the N atoms of the cyclam ligand leads to a reduction in the complexing ability, as evidenced by the decrease of the *pK* values corresponding to the TMC (TMC = 1,4,8,11–tetramethyl–1,4,8,11–tetraazacyclotetradecane) derivative compared to those obtained for the non–methylated cyclam (Table 1.3). For example, *log K* drops significantly from 27.2 for Cu(II) cyclam complex to 18.3 in the case of the TMC methylated derivative. This fact can be explained taking into account the large increase in steric strain that results from the incorporation of methyl groups to the cyclic tetraamine. Variables such as pH and the oxidation state of the metal also affect the stability of metallocyclam complexes, which may very well lead to their demetallation.[87] For instance, at low pH the free cyclam ligand is easily protonated which induces a shift in the equilibrium towards dissociation.[87a] The hole size provided by the macrocyclic ligand has a major influence on the stability of cyclam complexes regarding the oxidation state of the metal, since variations of the latter alter the size of a given metal center. In some cases, the changes in the metal radii can result in a mismatch between the size of the cyclam ring and the metal, decreasing the overall stability of the resulting cyclam complex.[87b] The conformation of the tetraazaligands also show an important influence over the stability, as metal exchange reactions may or not occur depending on the conformation of the starting metallocyclam complex.[88]

Table 1.3. Stability constants (log K) for cyclam and TMC complexes and ionic radii (r) of selected transition metals.

Ref[78b]	Co^{2+}	Ni^{2+}	Cu^{2+}	Zn^{2+}	Cd^{2+}	Hg^{2+}
r (pm)	75	69	72	74	97	110
Log K (cyclam)	12.7	22.4	27.2	15.5	11.7	23
Log K (TMC)	7.9	8.6	18.3	10.4	9.0	20.3

TMC = 1,4,8,11–tetramethyl–1,4,8,11–tetraazacyclotetradecane).

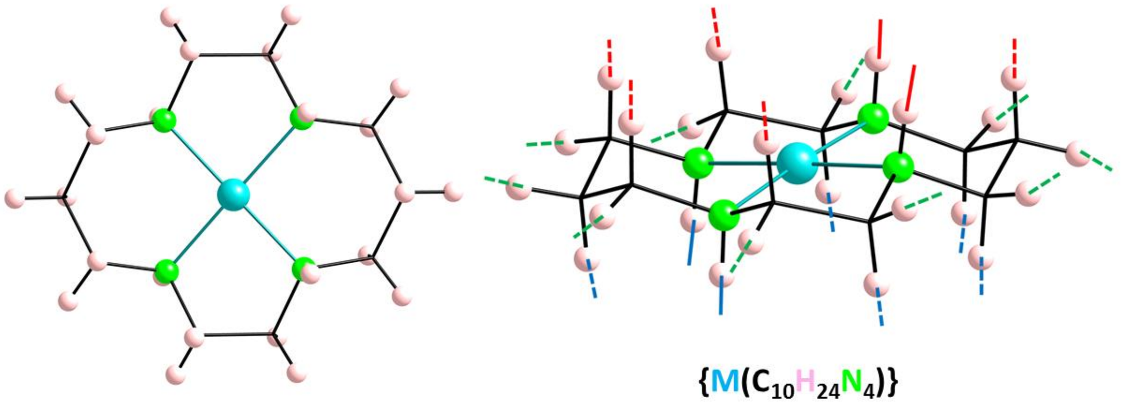

Figure 1.11. Top and lateral view of the ball&sticks representation of a *trans–III* M(cyclam)}$^{2+}$ building block showing the potential H–bonds that it can form. N–H···X contacts are depicted as straight lines whereas C–H···X interactions are shown as dashed lines. Color code: H···X contacts above (red) and below the MN_4 plane (blue), and those in the laterals (green).

In regards to their capacity as building blocks, transition metal complexes of macrocyclic polyamines such as metallocyclam are excellent candidates for the constructions of high–dimensional hybrid frameworks, as four of six–coordination sites of the metal ions are blocked by the ligand, only the two axial coordination sites are vacant for coordination, and hence the geometries of the metal ions are easier to control. Moreover, since POMs often exhibit large negative charge, the number of {M(cyclam)}$^{2+}$ complexes required to achieve electroneutrality is usually high, which in turn increases the number of coordination sites between clusters, raising the possibility of generating extended covalent networks. In addition, the high tendency shown by the cyclam ligand to establish extensive H–bonding systems with the inorganic building blocks significantly contributes to the overall stability of the resulting hybrid framework. In this context, the cyclam ligand can form up to 24 H–bonds, 4 of them being N–H···X while the remaining bonds involve C–H···X contacts. The four hydrogen atoms of the secondary amines (–NH–) are located above and below the MN_4 plane (Figure 1.11). The other 20 H atoms form $–CH_2$···X bonds and they are located in both axial and equatorial positions in such a way that 10 are located above and below the MN_4 plane while the remaining 10 H are oriented towards the periphery of the ligand. This way, metallocyclam complexes can form 7 hydrogen bonds above and another 7 below the MN_4 plane, whereas 10 more H–contacts arise in the laterals.

The metallorganic building blocks can adopt up to three different roles within the hybrid crystal structure depending on the coordination sphere of the metal in the resulting hybrid structure (Figure 1.12), which are: a) bridging ligand, when the metal center is coordinated to two adjacent clusters, that is, both axial positions become occupied by O atoms belonging to different POMs. In this case, the metal adopts a distorted octahedral geometry (MN_4O_2); b) antenna ligands, when the metal is monocoordinated to a single POM, leaving the remaining axial position free. The complex is grafted to one POM subunit and the 3d–metal adopts a distorted square–pyramidal geometry (MN_4O); c) countercations, when the metal center is not coordinated to any oxygen atoms of POM clusters. In this case, the metal adopts a square–planar geometry (MN_4). These non–coordinated complexes help reinforce the hybrid crystal packing through a significant network of supramolecular forces via N–H···X as well as C–H···X interactions, as mentioned above. The first two roles mentioned above involves the formation of a coordinative role and thus, they lead to the formation of *class II* materials, whereas compounds showing metalorganic blocks only fulfilling the latter role result in *class I* hybrids, as there are no covalent interactions.

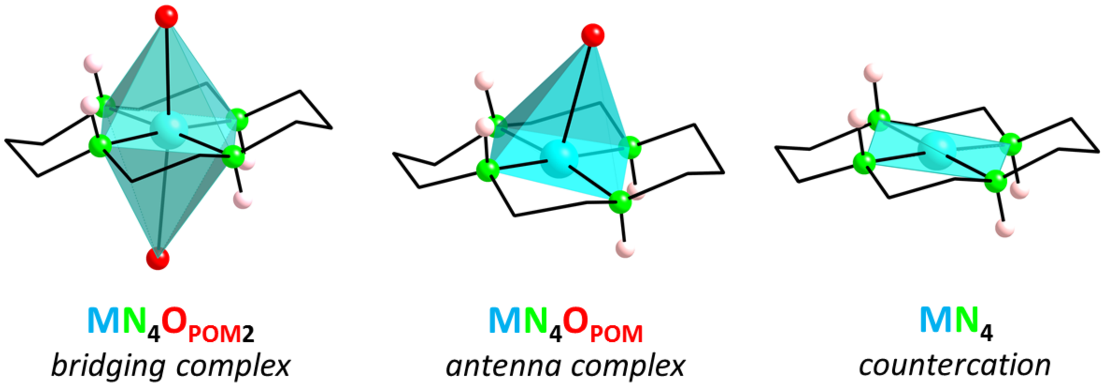

Figure 1.12. Ball&sticks representations of M(cyclam)}$^{2+}$ building blocks with the typical *trans–III* configuration showing the different geometries and roles that they adopt in the hybrid structures described in this dissertation.

Despite all this, it is shocking to realize that no POM–based compounds containing {M(cyclam)} buiding blocks in their crystal structures were reported until 2015. To our knowledge, these studies were limited to just three examples which consist in *type II* discrete bimetallic hybrids built from simple $[MoO_4]^{2-}$ and $[WO_4]^{2-}$ oxoanions and M(cyclam) (M = Cr^{III}, Rh^{III}) moieties.[89] In 2015 and 2016, however, we reported the first studies regarding the grafting of {Cu(cyclam)}$^{2+}$ complexes into some polyoxovanadates, namely meta– and decavanadate species, respectively[90] (which will be covered in the following Chapter 2). Later, Ou's group prepared a series of polyoxovanadates using {Ni(cyclam)}$^{2+}$ moieties ranging from meta– to decahexavanadates.[91] In contrast, several combinations of POMs and metalorganic complexes built from cyclam–derived ligands (such as 5,5,7,12,12,14–hexamethyl–1,4,8,11–

tetraazacyclotetradecane) can be found in crystallographic databases. Most of them were reported recently and they consist in various types of POM archetypes like octamolybdates, Strandberg–type diphosphopentamolybdates as well as various polyoxovanadates (meta–, deca–, dodeca–, hexadecavanadate and the large $[V_{34}O_{82}]^{10-}$ cluster) with exclusively Cu^{II} or Ni^{II} metal centers, which display a wide range of different dimensionalities.[92] A closely cyclam–related organic ligand, namely 5,7,7,12,14,14–hexamethyl–1,4,8,11–tetraazacyclotetradeca–4,11–diene (known as *transdiene*) has been also used recently by Sarma and coworkers to organically modify Lindqvist–type hexamolybdates and hexatungstates clusters (M = Co^{II}, Ni^{II}, Cu^{II} and Zn^{II}) resulting exclusively in *type I* hybrids.[93]

The interesting properties, chemical nature and its potential capacity as a bridging building block and H–bonding reinforcing unit as well as the absence of any reports concerning M(cyclam)–containing POM–based compounds motivated us to use metalorganic complexes of this tetraazamacrocyclic ligand to attempt to construct novel functional high–dimensional porous polyoxometalate hybrids with a strong focus on catalytic and/or sorption–related properties.

1.4 POM–BASED OPEN–FRAMEWORKS

In the last decades, porous crystalline materials such as metal–organic frameworks (MOFs) have attracted great attention due to their wide range of relevant applications.[94] These materials are constructed by coordination of metal ions or metal–containing units (nodes) to organic bridging ligands (linkers) to form open crystalline frameworks with permanent porosity. This feature qualifies them as suitable candidates for gas storage and separation, ion exchange, host–guest chemistry, magnetism, biomedicine and catalysis.[95] However, the synthesis of MOFs usually requires harsh conditions (e.g. high temperature or pressure, prolonged reaction times, harmful solvents, etc.), and removal of guest molecules from their cavities can often lead to the collapse of the porous structure when flexible linkers are used. In this context, the incorporation of rigid and voluminous species such as metal clusters could increase the overall mechanical and thermal stability of the hybrid network leading to the generation of robust frameworks.

Among metal clusters, polyoxometalates have been identified as excellent building blocks for the construction of such robust, high–dimensional open structures.[96] Moreover, POM–based crystalline solids with permanent porosity are of great interest because inherent features of POMs such as reversible redox properties or high catalytic site density can be combined with the characteristics derived from open–framework structures.[97] Several examples have been reported during the last few years including both supramolecular ionic compounds and covalent extended lattices (POMOFs). The former can be exemplified by Mizuno's series of hybrid salts in which $[M_3O\{RCO_2\}_6L_3]^+$ macrocations (M^{III} = Cr, Fe; L = terminal ligand) are combined with Keggin–type $[XM_{12}O_{40}]^{n-}$ (X = B^{III}, Si^{IV}, P^{V}; M = W^{VI}) heteropolyanions in microporous structures with tunable shape–selective sorption ability.[97] Among POMOFs, four different approaches for assembling clusters into extended lattices can be identified according to Wang et al.:[98] a) organically derivatized POM units linked by metal ions;[99] b) POM clusters directly connected by metal ion linkers in fully inorganic open–

frameworks;[100] c) metal–substituted POMs connected through organic bridging ligands;[101] d) POMs connected through metal–organic ligand–metal linking fragments.[102] Compared to MOFs, the synthetic requirements for the assembly of POMOFs usually involve milder conditions, aqueous reaction media and easier counterion exchange. Moreover, configurable and more diverse architectures can be achieved in the resulting compounds because POM building blocks possess specific topological and chemical information that can be transferred to the final product.[96] A fifth subclass closely related to type b) above could also be proposed: that in which the metal ion linkers belong to discrete coordination complexes with peripheral organic ligands[97,19c] (Scheme 1.1).

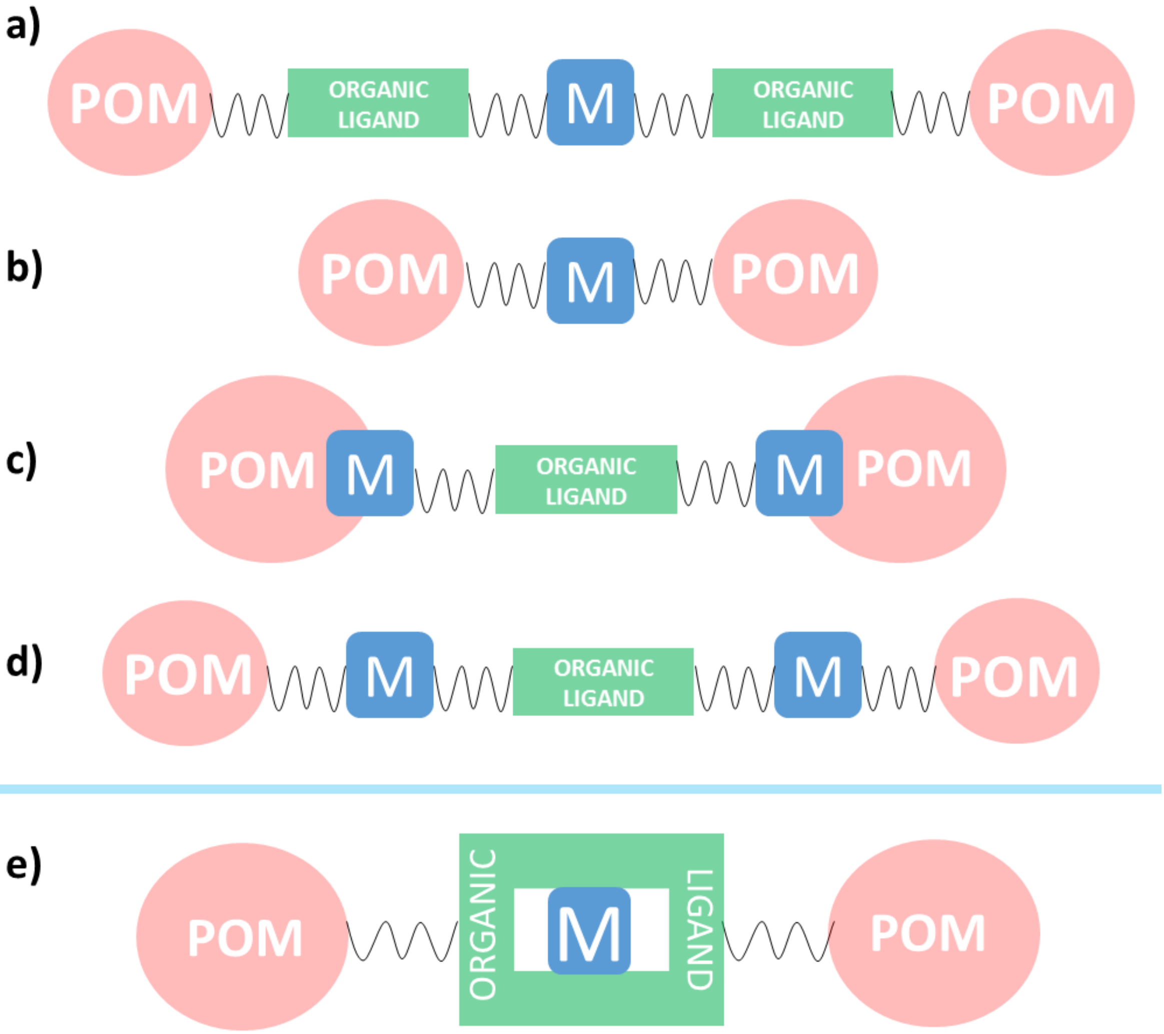

Scheme 1.1. Schematic representation of the four main approaches to connect POMs according to Wang and co–workers (a to d). A fifth approach using cyclic organic ligands is proposed in (e). M: transition metal ions.

Even though a considerable number of covalent extended networks based on POM clusters connected through metalorganic moieties have been prepared so far, to the best of our knowledge none of such hybrid compounds have exhibited genuine functions associated with porosity (e.g. adsorption, separation). This fact might be mainly due to the presence of pores with small sizes and/or inaccessible voids or dynamic frameworks that collapse under the activation of the sample. Thus, the preparation of such type of functional porous open–frameworks is still a challenging issue in current synthetic POM chemistry.

1.5 SINGLE–CRYSTAL–TO–SINGLE–CRYSTAL TRANSFORMATIONS

Solid state reactions and transformations induced by a given external stimulus applied on a responsive material have been long considered an attracting topic within material science because of the possibility of obtaining products with compositions, architectures as well as bulk physical properties different from those achievable by following alternative routes. Controlling the applied stimulus may open the possibility of tuning such responsive materials making them suitable for a wide range of potential applications including switches, storing devices or sensors.

Among solid–state phase transitions, those in which the crystalline order and integrity are maintained along the process are known as single–crystal–to–single–crystal transformations (SCSC). The occurrence of SCSC phase transitions is a powerful tool to characterize the structure of the functional materials that result from applying a given external stimulus (heat, light, pressure, etc.), which are usually not accessible by conventional direct synthetic routes.[103] They allow the exact monitoring of how the location of atoms and molecules change within the structure as a result of the external stimulus and hence, detailed structural information can be achieved for a better understanding of the transformation mechanisms and their relationship with the properties subject of interest.[104] In rare cases, transient intermediate phases coexisting with the initial and/or final stages of the SCSC transformation can even be detected and its structure fully determined.[105] These type of responsive materials can be classified into two main groups depending on their structural behavior upon applying the external stimulus: dynamic and robust frameworks. For dynamic materials, SCSC transformations usually involve the cleavage and formation of coordination or covalent bonds, as well as rearrangement of the network of intermolecular interactions that stabilize the crystal packing, and hence they often are accompanied by dramatic structural modifications with changes in properties like the color, magnetism, luminescence or the ability to adsorb different molecules. In comparison, the SCSC transformations on robust frameworks do not result in significant structural modifications regardless of the compositional and functional changes that the latter may undergo when promoted by evacuation, incorporation or exchange of solvent or guest molecules, or even by variations in the oxidation states of the constituent atoms or changes in the overall charge. A third class of materials may also be proposed, in which compounds for which different interconvertible crystalline polymorphic forms exist as a result of order–disorder transitions belong, as well as cases where atoms suffer slight motions that can change or even break the crystal symmetry.

In recent years, SCSC transformation processes triggered by different types of external applied stimuli have been reported for numerous systems, both purely organic[106] and inorganic.[107] Compared to the vast number of studies developed for compounds of metalorganic nature, such as metalorganic frameworks (MOFs) or porous coordination polymers (PCPs),[108] reports on POM–containing compounds are much less common. In fact, up to date just 28 POM–based structures have been identified as being able to undergo SCSC transformations. Related compounds may include a recent family of lanthanide–based MOFs with the 4,4′–bipyridyl–N,N′–dioxide ligand that are able to incorporate Lindqvist–type POMs upon post–synthetic functionalization involving anion exchange.[109] Recent examples of such studies for which the initial and final stages of the process have been characterized by single–crystal XRD techniques include: (a) the sandwich $[\{Zn(OH_2)(OH)\}_2\{Zn(OH_2)_2\}_2\{HSiW_{10}O_{36}\}_2]^{8-}$ anion,[110] which leads to two isomeric forms of the $[\{Zn_2W(O)O_3\}_2H_4\{SiW_9O_{33}\}_2]^{8-}$ cluster[111] upon thermal treatment through the isomerization of the *γ*–type $\{HSiW_{10}O_{36}\}$ subunits into either α– or β–forms and consequent rearrangement of the sandwiched metal core from a planar, rhomblike assembly of four oxo–bridged zinc centers to a hexaprismatic moiety of two tungsten and four zinc atoms; (b) or the sandwich $[Co_4(OH)_4(H_4SiW_{10}O_{36})_2]^{8-}$ anion,[112] the cubane–type tetracobalt sandwiched core of which transforms into a planar, rhomblike moiety upon exposure to water to result in the $[\{Co(H_2O)\}_2(OH)_2\{Co(H_2O)_2\}_2(H_2SiW_{10}O_{36})_2]^{8-}$ specie. To our knowledge, the first report on a SCSC transformation involving single–crystal XRD measurements of the initial and final stages carried out for the same POM–containing crystal dates back to 2004.[113] This seminal report by Mizuno et al. consisted in the comparative structural descriptions of the robust microporous ionic crystal $Cs_5[Cr_3O(OOCH)_6(H_2O)_3][CoW_{12}O_{40}]\cdot 7.5H_2O$[113a] and the heptahemihydrate derivative $Cs_5[Cr_3O(OOCH)_6(H_2O)_3][CoW_{12}O_{40}]\cdot 3.5H_2O$ obtained by partial thermal dehydration of the former.

The scarce number of reports on SCSC transformations associated with POM–based compounds is certainly surprising taking into account the exponential growth that POM chemistry has been experiencing during the last decade. Nevertheless, these reports cover a wide range of compositionally and structurally diverse systems and they already include examples of dynamic thermostructural behavior and examples of robust frameworks, as well as compounds showing polymorphism: from molecular clusters such as the $H_5PV_2Mo_{10}O_{40}\cdot 36H_2O$ heteropolyacid to 3D covalent assemblies like the family of $[H_mM_{12}X_7W_{72}O_{268}]^{n-}$ lattices, and from purely inorganic compounds (e.g., $[H_3O]_4[Mn_4(H_2O)_{18}][WZnMn_2(H2O)_2(ZnW_9O_{34})_2]\cdot 18H_2O$) to organic salts represented by $(TBA)_4[SiV_2W_{10}O_{39}]\cdot 2DCE$, as well as a relevant number of inorganic–metalorganic hybrid materials such as the collection of microporous ionic crystals based on trinuclear $[M^{III}{}_3O(OOCR)_6(L)_3]^+$ macrocations or the different examples including N–donor tetradentatate ligands. Regarding the inducing effect that triggers the SCSC transformations in POMs–containing compounds, several different external stimuli have been applied such as light[114] (1 report), temperature[115] (4 reports), redox processes[116] (4 reports), removal of solvent/guest molecules[90,91,117] (12 reports, 2 of them from chapter 2 of this work) or postsynthetic functionalization[118] *via* cations/ligands exchange reactions (4 reports). Taking into account all these facts, it can be deduced that the occurrence of SCSC transformations in POMs rather than being an exceptional phenomenon, it might be a relatively common feature in polyoxometalates, and hence, it should be worth analyzing. A few months ago, Cronin and coworkers prepared what they call the first “flexi–crystal”, namely $Li_9K_7W_1Co_{10}[H_2P_8W_{48}O_{186}]\cdot 132\ H_2O$, the denomination of which stands for a flexible crystalline transition metal oxide compound that is dynamically switchable between many phases and capable of performing SCSC transformations.[119] Indeed, this fully inorganic POM–based material formed by doughnut–shaped molecular metal oxide rings $[P_8W_{48}O_{184}]^{40-}$that are connected to each other by cobalt(II) linkers can undergo at least eight different SCSC transformations, with huge crystal volume contraction and expansion changes ranging from –2,170 to +1,720 $Å^3$ with preservation of crystallinity.

1.6 TAILORED POLYMERIC SURFACES

Highly ordered honeycomb structures on polymer–based films has attracted significant attention in the last few years due to their potential applications in fields such as tissue engineering, electronics, catalysis and separation.[120] Unfortunately, the fabrication of this type of polymeric surfaces usually require time–consuming and expensive methods like lithography,[121] plasma–etching[122] and emulsions.[123] In comparison, breath figure (BF) patterning method has been emerged as a promising and cost–effective strategy to obtain highly ordered films for advanced applications. For instance, breath figures have been applied as separation membranes,[124] photonic band gaps,[125] supports for cell culture,[126] antibiofilm formation,[127] antireflective coatings,[128] and catalyst supports.[129]

The fabrication of BF surfaces consists in drop–casting a small volume of a polymer solution in a highly volatile solvent onto a solid substrate under a highly humid environment. The mechanism behind the formation of BF patterning is shown in Figure 1.13, which involves: a) a cold surface created by the evaporation of the solvent of the polymer solution; b) water condensation from the humid environment; c) movement and arrangement of the condensed water droplets into organized islands with hexagonal packing; d) stabilization of the droplets through the precipitation of the polymer (that is, the polymer envelopes around the droplets and thus, the water droplets act as templates for the pores); e) total evaporation of the solvent followed up by a pressure increase results in the bursting of the polymer envelope forming the pores and f) total evaporation of water.[130a] The formation of BF films is strongly affected by numerous parameters such as the nature of the polymer and its concentration, solvent, relative humidity, temperature, presence of additives and so on.[130] Various approaches to prepare BF polymeric films currently exist such as dip–coating, spin coating and solvent cast techniques (dynamic and static).[130a] Several studies have been devoted to obtain honeycomb structures by using wide variety of polymers, such as polymers with modified terminal groups, cellulose, and block copolymers, among others.[131] When amphiphilic copolymers are used, the breath figure patterning naturally results in the migration of the hydrophilic block towards the cavities formed by the condensation of the water droplets. This way, highly ordered polymeric surfaces with functionalized pores can be fabricated.

The latter type BF surfaces are particularly interesting since they could potentially allow the incorporation of other components that could interact with the functional groups located in the cavities. For instance, using organically modified POMs and polymers bearing complementary functionalities for covalent bond formation (e.g. amino and carboxylic groups).[132] Thus, the preparation of such novel functionalized hybrid polymeric surfaces that could exhibit new or enhanced properties compared to those shown by their individual components generates considerable interest. Even though POMs have been successfully combined in the past with amphiphilic molecules or cationic surfactants to construct several discrete architectures (micelles, capsules, vesicles, cones), fibers and wires, or highly ordered bidimensional arrays,[133] reports on their immobilization on such type of polymeric films are scarce. To our knowledge, only one example of hybrid film composite involving POMs and diblock copolymers has been described in the literature up to now, in which the formation of aggregates in solution is employed to direct the self–assembly of highly ordered films with inverse hexagonal topology.[134]

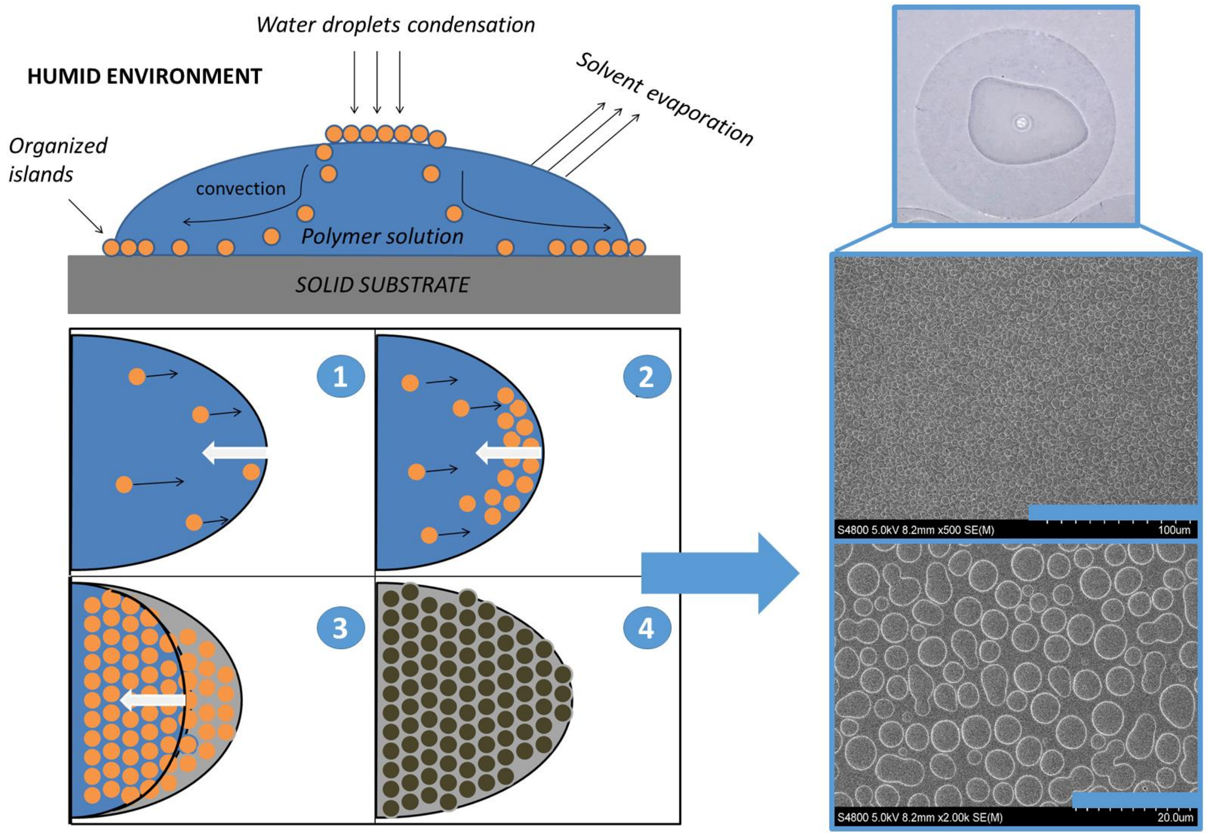

Figure 1.13. Mechanism of the formation of breath figures (BF) polymeric surfaces, along with a digital photograph of a BF sample and SEM images showing the cavities.

1.7 AIM OF THE WORK

The experimental work carried out in this dissertation have been performed at *BCMaterials: Basque Center for Materials, Applications & Nanostructures* in collaboration with the *Departamento de Química Inorgánica* and *Departamento de Química–Física* at the *Facultad de Ciencia y Tecnología* at the *University of the Basque Country* (UPV/EHU). This research consist in the synthesis and structural characterization of organic–inorganic compounds based on covalent interactions between polyoxometalate clusters and transition–metal tetraazacomplexes leading to the formation of hybrid compounds exhibiting new or enhanced properties and/or structural architectures to enrich the field of POM chemistry. The main objectives of this thesis can be divided as follows:

–Synthesis and characterization of high–dimensional and/or porous POM–based inorganic–metalorganic hybrids by grafting 3d–metal complexes of macrocyclic tetraamines at POM surfaces for potential catalytic, sorption–related applications and/or novel architectures and topologies. The resulting hybrid extended frameworks are susceptible to SCSC transformations, and hence, new crystalline phases have been obtained by heating. These new crystalline phases were structurally characterized by means of high–temperature single–crystal X–Ray Diffraction techniques and the structural modifications promoted by thermal evacuation of guest molecules from the initial hybrid frameworks have been analyzed and discussed. The reversibility of such transformations was also evaluated. These hybrid compounds have been classified attending to the nature of the *addenda* atoms that constitute the POM skeleton (V, W or Mo). This way, studies regarding polyoxovanadates are found in **Chapter 2** (6 compounds) whereas **Chapters 3** involves compounds based on polyoxotungstates (21 compounds). Similarly, polyoxomolybdate–based hybrids are grouped in **Chapter 4** (7 compounds). All synthetized and characterized hybrid POM structures are listed in Table 1.4.

Table 1.4. Summary of all the hybrid structures prepared and characterized in this dissertation.

CODE		COMPOUND
Chapter 2	**1–CuV**	$[\{Cu(cyclam)\}(VO_3)_2]\cdot5H_2O$
	2–CuV	$[\{Cu(cyclam)\}(VO_3)_2]\cdot3H_2O$
	3–CuV	$[\{Cu(cyclam)\}(VO_3)_2]\cdot1.3H_2O$
	4–CuV	$[\{Cu(cyclam)\}(VO_3)_2]$
	1–CuV10	$[Cu(cyclam)][\{Cu(cyclam)\}_2(V_{10}O_{28})]\cdot10H_2O$
	1a–CuV10	$[Cu(cyclam)][\{Cu(cyclam)\}_2(V_{10}O_{28})]$
Chapter 3	**1–CuW7**	$[\{Cu(cyclam)\}_3(W_7O_{24})]\cdot15.5\ H_2O$
	2–CuW7	$[\{Cu(cyclam)\}_3(W_7O_{24})]\cdot12H_2O$
	3–CuW7	$[Cu(cyclam)]_{0.5}[\{Cu(cyclam)\}_{2.5}(W_7O_{24})]$
	1–La	$[Cu(cyclam)]_2[\{Cu(cyclam)\}_4\{(\alpha\text{–}GeW_{11}O_{39})La(H_2O)(\mu\text{–}CH_3COO)\}_2]\cdot18H_2O$
	1–Ce	$[Cu(cyclam)]_2[\{Cu(cyclam)\}_4\{(\alpha\text{–}GeW_{11}O_{39})Ce(H_2O)(\mu\text{–}CH_3COO)\}_2]\cdot18H_2O$
	1–Pr	$[Cu(cyclam)]_2[\{Cu(cyclam)\}_4\{(\alpha\text{–}GeW_{11}O_{39})Pr(H_2O)(\mu\text{–}CH_3COO)\}_2]\cdot17H_2O$
	1–Nd	$[Cu(cyclam)]_2[\{Cu(cyclam)\}_4\{(\alpha\text{–}GeW_{11}O_{39})Nd(H_2O)(\mu\text{–}CH_3COO)\}_2]\cdot18H_2O$
	1–Sm	$[Cu(cyclam)]_2[\{Cu(cyclam)\}_4\{(\alpha\text{–}GeW_{11}O_{39})Sm(H_2O)(\mu\text{–}CH_3COO)\}_2]\cdot19H_2O$
	1–Eu	$[Cu(cyclam)]_2[\{Cu(cyclam)\}_4\{(\alpha\text{–}GeW_{11}O_{39})Eu(H_2O)(\mu\text{–}CH_3COO)\}_2]\cdot17H_2O$
	1–Gd	$[Cu(cyclam)]_2[\{Cu(cyclam)\}_4\{(\alpha\text{–}GeW_{11}O_{39})Gd(H_2O)(\mu\text{–}CH_3COO)\}_2]\cdot18H_2O$
	1–Tb	$[Cu(cyclam)]_2[\{Cu(cyclam)\}_4\{(\alpha\text{–}GeW_{11}O_{39})Tb(H_2O)(\mu\text{–}CH_3COO)\}_2]\cdot18H_2O$
	1–Dy	$[Cu(cyclam)]_2[\{Cu(cyclam)\}_4\{(\alpha\text{–}GeW_{11}O_{39})Dy(H_2O)(\mu\text{–}CH_3COO)\}_2]\cdot18H_2O$
	1–Ho	$[Cu(cyclam)]_2[\{Cu(cyclam)\}_4\{(\alpha\text{–}GeW_{11}O_{39})Ho(H_2O)(\mu\text{–}CH_3COO)\}_2]\cdot19H_2O$
	1–Er	$[Cu(cyclam)]_2[\{Cu(cyclam)\}_4\{(\alpha\text{–}GeW_{11}O_{39})Er(H_2O)(\mu\text{–}CH_3COO)\}_2]\cdot18H_2O$
	1–Tm	$[Cu(cyclam)]_2[\{Cu(cyclam)\}_4\{(\alpha\text{–}GeW_{11}O_{39})Tm(H_2O)(\mu\text{–}CH_3COO)\}_2]\cdot18H_2O$
	1–Yb	$[Cu(cyclam)]_2[\{Cu(cyclam)\}_4\{(\alpha\text{–}GeW_{11}O_{39})Yb(H_2O)(\mu\text{–}CH_3COO)\}_2]\cdot18H_2O$
	1–Lu	$[Cu(cyclam)]_2[\{Cu(cyclam)\}_4\{(\alpha\text{–}GeW_{11}O_{39})Lu(H_2O)(\mu\text{–}CH_3COO)\}_2]\cdot17H_2O$
	2–Eu	$[Cu(cyclam)]_{0.5}[\{Cu(cyclam)\}_{5.5}\{(\alpha\text{–}GeW_{11}O_{39})Eu(\mu\text{–}CH_3COO)\}_2]$
	2–Er	$[Cu(cyclam)]_{0.5}[\{Cu(cyclam)\}_{5.5}\{(\alpha\text{–}GeW_{11}O_{39})Er(\mu\text{–}CH_3COO)\}_2]$
	3–Ce	$[\{Cu(cyclam)\}_6\{(\alpha\text{–}GeW_{11}O_{39})Ce(H_2O)(\mu\text{–}CH_3COO)\}_2]\cdot4H_2O$
	3–Eu	$[\{Cu(cyclam)\}_6\{(\alpha\text{–}GeW_{11}O_{39})Eu(H_2O)(\mu\text{–}CH_3COO)\}_2]\cdot4H_2O$
Chapter 4	**1–CuMo5**	$[\{Cu(cyclam)\}_2(H_2P_2Mo_5O_{23})].4.5H_2O$
	1–NiMo5	$[\{H_2(cyclam)\}_{0.3}\{Ni(cyclam)\}_{0.7}][\{Ni(cyclam)\}(H_2P_2Mo_5O_{23})].5H_2O$
	1a–CuMo5	$[\{Cu(cyclam)\}_2(H_2P_2Mo_5O_{23})]$
	1a–NiMo5	$[H_2(cyclam)]_{0.3}[\{Ni(cyclam)\}_{1.7}(H_2P_2Mo_5O_{23})]$
	1–CuMo6	$[\{Cu(cyclam)\}_3(H_6CrMo_6O_{24})_2].18H_2O$
	1–NiMo6	$[\{Ni(cyclam)\}_2][\{Ni(cyclam)\}(H_6CrMo_6O_{24})_2].18H_2O$
	1–ZnMo6	$[\{H_2(cyclam)\}_{1.3}\{Zn(cyclam)\}_{0.3}][\{Zn(cyclam)\}_{1.4}(H_6CrMo_6O_{24})_2].18H_2O$

–The first steps in a new research line stablished by the collaboration of *Departamento de Química–Física* and *Departamento de Química Inorgánica* have been also carried out within this dissertation. The main objective of this new research line consist in the incorporation of POM clusters into tailored polymeric surfaces to fabricate smart POM/Polymer hybrid surface materials for a wide range of potential applications. The preliminary work in this new research line constitutes the final **Chapter 5**, the scope of which is limited to the validation of the anchoring method to different surfaces made of PS–*b*–PAA diblock amphiphilic copolymers and {Cu(cyclam)}–functionalized POM compounds through a Cu(II)–carboxylate coordination approach. Several prototype surfaces were fabricated and their characterization was performed at IC^{2}NER located in Kyushu University, Fukuoka (Japan) during a short stay (3 months) by advanced sophisticated surface analysis techniques such as Time–of–Flight Secondary Ion Mass Spectroscopy (ToF–SIMS) and Low–Energy Ion Scattering (LEIS).

1.8 REFERENCES

---

[1] (a) Pope, M. T. *Heteropoly and Isopoly Oxometalates*; Springer-Verlag: Berlin, **1983**. (b) Pope, M. T. Isopolyanions and Heteropolyanions. In *Comprehensive Coordination Chemistry*, Wilkinson, G., Gillard, R.D., McCleverty, J.A., Eds.; Pergamon Press, New York, NY, USA, **1987**; pp. 1023-1058. (c) *Polyoxometalates: from Platonic Solids to Anti Retroviral Activity*; Pope, M. T., Müller, A, Eds.; Kluwer, Dordrecht, The Netherlands, **1994**. (d) Pope, M. T. Polyoxoanion. In *Encyclopedia of Inorganic Chemistry*; King, R. B., Ed.; John Wiley & Sons, Chichester, UK, **1994**; pp. 3361-71.

[2] (a) Neumann, R.; Dahan, M. *Nature* **1997**, *388*, 353. (b) *Catalysts for Fine Chemical Synthesis (Volume 2): Catalysis by Polyoxometalates;* Kozhevnikov, I. ; Wiley-VCH, Wenheim, Germany, **2002** (c) Kamata, K.; Yonehara, K.; Sumida, Y.; Yamaguchi, K.; Hikichi, S.; Mizuno, N. *Science* **2003**, *300*, 964. (d) Yin, Q.; Tan, J. M.; Besson, C.; Geletti, Y. V.; Musaev, D. G.; Kuznetsov, A. E.; Luo, Z.; Hardcastle, K. I.; Hill, C. L. *Science* **2010**, *328*, 342. (e) Carraro, M.; Sartorel, A.; Ibrahim, M.; Nsouli, N.; Jahier, C.; Nlate, S.; Kortz, U.; Bonchio, M. Polyoxometalates as Homogeneous Oxidation Catalysts, In *Innovative Catalysis in Organic Synthesis: Oxidation, Hydrogenation, and C–X Bond Forming Reactions*, Andersson, P. G., Ed.; Wiley-VCH, Wenheim, Germany, **2012**. (f) Misono, M.; Catalysis of Heteropoly Compounds, In *Heterogeneous Catalysis of* Mixed *Oxides*; Elsevier Ltd., Oxford, UK, **2013**; pp. 97-155. (g) Sun, M.; Zhang, J.; Putaj, P.; Lefebvre, F.; Pelletier, J.; Basset, J.-M. *Chem. Rev.* **2014**, *114*, 981.

[3] (a) Müller, A.; Peters, F.; Pope, M. T.; Gatteschi, D. *Chem. Rev.* **1998**, *98*, 239. (b) Clemente-Juan, J. M.; Coronado, E. *Coord. Chem. Rev.* **1999**, *193-195*, 1776. (c) Kortz, U.; Müller, A.; van Slageren, J.; Schnack, J.; Dalal, N. S.; Dressel, M. *Coord. Chem. Rev.* **2009**, *253*, 2315. (d) Clemente-Juan, J. M.; Coronado, E.; Gómez-García, C. J. *Chem. Soc. Rev.* **2012**, *41*, 7464.

[4] (a) Rhule, J. T.; Hill, C. L.; Judd, D. A.; Schinazi, R. F. *Chem. Rev.* **1998**, *98*, 327. (b) Hasenknopf, B.; *Front. Biosci*., 2005, *10*, 275. (c) Yamase, T. *Prog. Mol. Subcell. Biol.* **2013**, *54*, 65.

[5] (a) Coronado, E.; Gómez-García, C. J. *Chem. Rev.* **1998**, *98*, 273. (b) Long, D.-L.; Burkholder, E.; Cronin, L. *Chem.* Soc. *Rev.* **2007**, *36*, 105. (c) Miras, H. N.; Yan, J.; Long, D.-L.; Cronin, L. *Chem. Soc. Rev.* **2012**, *41*, 7403. (d) Song, Y.-F.; Tsunashima, R. *Chem. Soc. Rev.* **2012**, *41*, 7384.

[6] (a) *Polyoxometalate Chemistry: From Topology via Self-Assembly to Applications*; Pope, M. T., Müller, A., Eds.; Kluwer, Dordrecht, The Netherlands, **2001**. (b) *Polyoxometalate Chemistry for Nano-Composite Design*; Yamase, T., Pope, M. T., Eds.; Kluwer, Dordrecht, The Netherlands, **2002**. (c) *Polyoxometalate Molecular Science*; Borrás-Almenar, J. J., Coronado, E., Müller, A., Pope, M. T., Eds.; Kluwer: Dordrecht, The Netherlands, **2003**. (d) Pope, M. T. Polyoxo Anions: Synthesis and structure. In *Comprehensive Coordination Chemistry II*; McCleverty, J. A., Meyer, T. J. Eds.; Elsevier Ltd., Oxford, UK, **2004**; pp. 1023-1058. (e) *Complexity in Chemistry and Beyond: Interplay Theory and Experiments;* Hill, C. L., Musaev, D. G., Eds.; Springer, Dordrecht, **2012**. (e) *Polyoxometalate Chemistry: Some Recent Trends*; Sécheresse, F., Ed.; World Scientific, Singapore, **2013.**

---

[7] Special issues on POMs: (a) Hill, C. L., Ed. *Chem. Rev.* **1998**, *98*(1). (b) Kortz, U., Ed. *Eur. J. Inorg. Chem.* **2009**, *34.* 5259-5266. (c) De-Liang, L.; Cronin, L. Eds. *Dalton Trans.* **2012**, *41*(33). (d) Cronin, L.; Müller, A. Eds. *Chem. Soc. Rev.* **2012**, 41. (e) Kortz, U.; Liu, T. Eds. *Eur. J. Inorg. Chem.* **2013**, *10-11.* 1556-1967.

[8] (a) Lindqvist, I.; Aronsson, B. *Ark. Kemi*, **1953**, *7*, 49. (b) Filopwitz, M.; Ho, R. K. C.; Klemperer, W. G.; Shum, W. *Inorg. Chem*. **1979**, *18*, 93. (c) Nyman, M.; Bonhomme, F.; Alam, T. M.; Rodriguez, M. A.; Cherry, B. R.; Krumhansl, J. L.; Nenoff, T. M.; Sattler, A. M. *Science* **2002**, *297*, 996. (e) Nyman, M. *Dalton Trans.* **2011**, *40*, 8049.

[9] Izarova, N. V.; Pope, M. T; Kortz, U. *Angew. Chem. Int. Ed.* **2012**, *51*, 9492.

[10] Lipscomb, W. N. *Inorg. Chem.* **1965**, *4*, 132.

[11] Yamase, T. *J. Chem. Soc., Dalton Trans.* **1991**, 3055.

[12] Berzelius, J. J. Poggend*. Ann. Phys. Chem.* **1826**, *6*, 369.

[13] De Luyart, F.; De Luyart, J. J. *Extractos de las Juntas Generales celebradas por la R.S.B.A.P.*, **1783**, 46.

[14] Keggin, J. F. *Nature* **1933**, *132*, 351.

[15] Tézé, A.; Hervé, A. G. *Inorg. Synth.* **1990**, *27*, 85.

[16] Casey, W. H. *Chem. Rev.* **2006**, *106*, 1.

[17] Rowsell, J.; *Naza*, L. F. *J. Am. Chem. Soc.* **2000**, *122*, 3777.

[18] (a) Pope, M. T. In *Handbook on Physics and chemistry of the Rare Earths*; **2007**, *38*, 337. (b) Bassil, B. S.; Kortz, U. *Z. Anorg. Allg. Chem*. **2010**, *636*, 2222. (c) Oms, O.; Dolbecq, A.; Mialane, P. *Chem. Soc. Rev*. **2012**, *41*, 7497. (d) Zheng, S.-T.; Yang, G.-Y. *Chem. Soc. Rev.* **2012**, *41*, 7623.

[19] (a) Gouzerh, P.; Proust, A. *Chem. Rev.* **1998**, *98*, 77. (b) Proust, A.; Thouvenot, R.; Gouzerh, P. *Chem. Commun.* **2008**, 1837. (c) Dolbecq, A.; Dumas, E.; Mayer, C. R.; Mialane P. *Chem. Rev.* **2010**, *110*, 6009.

[20] Proust, A.; Matt, B.; Villanneau, R.; Guillemot, G.; Gouzerh, P.; Izzet, G. *Chem. Soc. Rev.* **2012**, *41*, 7605.

[21] (a) Musumeci, C.; Luzio, A.; Pradeep, C.P.; Miras, H.N.; Rosnes, M.H.; Song, Y.-F.; Long, D.-L.; Cronin, L.; Pignataro, B. *J. Phys. Chem. C* **2011**, *115*, 4446. (b) Errington, R. J.; Petkar, S. S.; Horrocks, B. R.; Houlton, A.; Lie, L. H.; Patole, S. N. *Angew. Chem. Int. Ed.* **2005**, *44*, 1254.

[22] Geisberger, G.; Gyenge, E.B.; Hinger, D.; Bösiger, P.; Maake, C.; Patzke, G.R. *Dalton Trans.* **2013**, *42*, 9914.

[23] Li, J.; Huth, I.; Chamoreau, L.M.; Hasenknopf, B.; Lacôte, E.; Thorimbert, S.; Malacria, M. *Angew. Chem. Int. Ed.* **2009**, *48*, 2035.

[24] Knoth, W. H. *J. Am. Chem. Soc*. **1979**, *101*, 759.

[25] (a) Bar-Nahum, I.; Neumann, R. *Chem. Commun.* **2003**, 2690. (b) Duffort, V.; Thouvenot, R.; Alfonso, C.; Izzet, G.; Proust, A. *Chem. Commun.* **2009**, 6062. (c) Odobel, F.; Séverac, M.; Pellegrin, Y.; Blart, E.; Fosse, C.; Cannizzo, C.; Mayer, C. R.; Elliot, K. J.; Harriman, A. *Chem. Eur. J.* **2009**, *15*, 3130. (d) Matt, B.; Renaudineau, S.; Chamoreau, L.-M.; Afonso, C.; Izzet, G.; Proust, A. *J. Org. Chem.* **2011**, *76*, 3107. (e) Aoki, S.; Kurashina, T.; Kasahara, Y.; Nishijima, T; Nomiya, K. *Dalton Trans.* **2011**, *40*, 1243.

[26] (a) Mazeaud, A.; Ammari, N.; Robert, F.; Thouvenot, R. *Angew. Chem. Int. Ed.* **1996**, *35*, 1961. (b) Mayer, C. R.; Fournier, I.; Thouvenot, R. *Chem. Eur. J.* **2000**, *6*, 105. (c) Agustin, D.; Coelho, C.; Mazeaud, A.; Herson, P. Proust, A.; Thouvenot, R. *Z. Anorg. Allg. Chem*. **2004**, *630*, 2049.

[27] (a) Mayer, C. R.; Cabuil, V.; Lalot, T.; Thouvenot, R. *Angew. Chem. Int. Ed.* **1999**, *38*, 3672. (b) Mayer, C. R.; Neveu, S.; Cabuil, V. *Angew. Chem. Int. Ed.* **2002**, *41*, 501. (c) Canizzo, C.; Mayer, C. R.; Sécheresse, F.; Larpent, C. *Adv. Mater.* **2005**, 2888. (D) Matt, B.; Renaudineau, S.; Chamoreau, L.-M.; Afonso, C.; Izzet, G.; Proust, A. *J. Org. Chem.* **2011**, *76*, 3107.

[28] (a) Sazani, G.; Pope, M. T. *Dalton Trans.* **2004**, 1989. (b) Joo, N.; Renaudineau, S.; Delapierre, G.; Bidan, G.; Chamoreau, L.-M.; Thouvenot, R.; Gouzerh, P.; Proust, A. *Chem. Eur. J.* **2010**, *16*, 5043. (c) Nomiya, K.; Togashi, Y.; Kasahara, Y.; Aoki, S.; Seki, H.; Noguchi, M.; Yoshida, S. *Inorg. Chem.* **2011**, *50*, 9606.

[29] (a) Kwak, W.; Pope, M. T.; Scully, T. F. *J. Am. Chem. Soc.* **1975**, *97*, 5735. (b) Kim, G.-S.; Hagen, K. S.; Hill, C. L. *Inorg. Chem.* **1992**, *31*, 5316. (c) Mayer, C. R.; Thouvenot, R. *Dalton. Trans.* **1998**, 7. (d) Mayer, C. R.; Herson, P.; Thouvenot, R. *Inorg. Chem.* **1999**, *38*, 6152. (e) Yamase, T.; Makino, H.; Naruke, H.; Wéry, A. M. S. J. *Chem. Lett*.

2000, *12*, 1350. (f) Carraro, M.; Sartorel, A.; Scorrano, G; Maccato, C.; Dickman, M. H.; Kortz, U.; Bonchio, M. *Angew. Chem. Int. Ed*. **2008**, *47*, 7275. (f) Breen, J. M.; Schmitt, W. *Angew. Int. Ed*. **2008**, *47*, 6904.

[30] (a) Knoth, W. H. *J. Am. Chem. Soc.* **1979**, *101*, 2211. (b) Knoth, W. H.; Domaille, P. J.; Roe, D. C. *Inorg. Chem*. **1983**, *22*, 818. (c) Wang, X. H.; Dai, H. C.; Liu, J. F. *Polyhedron* **1999**, *18*, 2293. (d) Wang, X. H.; Liu, J. F. *J. Coord. Chem.* **2000**, *51*, 73.

[31] (a) Zonnevijlle, F.; Pope, M. T. *J. Am. Chem. Soc.* **1979**, *101*, 2211. (b)) Xin, F.; Pope, M. T.; Long, G. J.; Russo, U. *Inorg. Chem.* **1996**, *35*, 1207. (c) Sazani, G.; Dickman, M. H.; Pope, M. T. *Inorg. Chem.* **2000**, *39*, 939. (d) Belai, N.; Pope, M. T. *Polyhedron*, **2006**, *25*, 2015.

[32] (a) Bareyt, S.; Piligkos, S.; Hasenknopf, B.; Gouzerh, P.; Lacôte, E.; Thorimbert, S.; Malacria, M. *Angew. Chem. Int. Ed.* **2003**, *42*, 3404 (b) Bareyt, S.; Piligkos, S.; Hasenknopf, B.; Gouzerh, P.; Lacôte, E.; Thorimbert, S.; Malacria, M. *J. Am. Chem. Soc.* **2005**, *127*, 6788. (c) Micoine, K.; Hasenknopf, B.; Thorimbert, S.; Lacôte, E.; Malacria, M. *Angew. Chem. Int. Ed.* **2009**, *48*, 3466.

[33] (a) Hussain, F.; Kortz, U.; Clark, R. J. *Inorg. Chem.* **2004**, *43*, 3237. (b) Hussain, F.; Kortz, U. *Chem. Commun*. **2005**, 1191. (c) Hussain, F.; Kortz, U.; Keita, B.; Nadjo, L.; Pope, M. T. *Inorg. Chem*. **2006**, *45*, 761. (e) Reinoso, S.; Dickman, M. H.; Praetorius, A.; Piedra-Garza, L. F.; Kortz, U. *Inorg. Chem*. **2008**, *47*, 8798.

[34] (a) Kortz, U.; Hussain, F.; Reicke, M. *Angew. Chem. Int. Ed.* **2005**, *44*, 3773. (b) Keita, B.; de Oliveira, P.; Nadjo, L.; Kortz, U. *Chem. Eur. J*. **2007**, *13*, 5480.

[35] (a) Piedra-Garza, L. F.; Dickman, M. H.; Moldovan, O.; Breunig, H. J.; Kortz, U. *Inorg. Chem.* **2009**, *48*, 411. (b) Barsukova-Stuckart, M.; Piedra-Garza, L. F.; Gautam, B.; Alfaro-Espinoza, G.; Izarova, N. V.; Banerjee, A.; Bassil, B. S.; Ullrich, M. S.; Breuning, H. J.; Silvestru, C.; Kortz, U. *Inorg. Chem.* **2012**, *51*, 12015.

[36] Blazevic, A.; Rompel, A. *Coord. Chem. Rev.* **2016**, *307*, 42.

[37] (a) Marcroux, P. R.; Hasenknopf, B.; Vaissermann, J.; Gouzerh, P. *Eur. J. Inorg. Chem.* **2003**, 2406. (b) Song, Y.-F.; Long, D.-L.; Cronin, L. *Angew. Chem. Int. Ed.* **2007**, *46*, 3900. (c) Song, Y.-F.; McMillan, N.; Long, D.-L.; Thiel, J.; Ding, Y.; Chen, H.; Gadegaard, N.; Cronin, L. *Chem. Eur. J.* **2008**, 1*4*, 2349. (d) Song, Y.-F.; Long, D.-L.; Cronin, L. *CrystEngComm.* **2010**, *12*, 109 (e) Santoni, M.-P.; Pal, A. K.; Hanan, G. S.; Proust, A.; Hasenknopf, B. *Inorg. Chem.* **2011**, *50*, 6737. (f) Thiel, J.; Yang, D.; Rosnes, M. H.; Liu, X.; Yvon, C.; Kelly, S. E.; Song, Y.-F.; Long, D.-L.; Cronin, L. *Angew. Chem. Int. Ed.* **2011**, 50, 8871.

[38] (a) Favette, S.; Hasenknopf, B.; Vaissermann, J.; Gouzerh, P.; Roux, C. *Chem. Commun*. **2003**, 2664. (b) Allain, C.; Favette, S.; Chamoreau, L.-M.; Vaissermann, J.; Ruhlmann, L.; Hasenknopf, B. *Eur. J. Inorg. Chem.* **2008**, 3433. (c) Zhang, J.; Song, Y.-F.; Cronin, L.; Liu, T. *J. Am. Chem. Soc.* **2008**, *130*, 14409. (d) He, Z.; Yan, Y. Y.; Li, B.; Ai, H.; Wang, H.; Li, H.; Wu, L. *Dalton Trans.* **2012**, *41*, 10043.

[39] (a) Song, Y.-F.; Long, D.-L.; Kelly, S. E.; Cronin, L. *Inorg. Chem.* **2008**, *47*, 9137. (b) Rosnes, M. H.; Musumeci, C.; Pradeep, C. P.; Mathieson, J. S.; Long, D.-L.; Song, Y.-F.; Pignataro, B.; Cogdell, R.; Cronin, L. *J. Am. Chem. Soc.* **2010**, *132*, 15490. (c) Wu, P.; Yin, P.; Zhang, J.; Hao, J.; Xiao, Z.; Wei, Y. *Chem. Eur. J.* **2011**, *17*, 12002. (d) Oms, O.; Hakouk, K.; Dessap, R.; Deniard, P.; Jobic, S.; Dolbecq, A.; Palacin, T.; Nadjo, L.; Keita, B.; Marrot, J.; Mialane, P. *Chem. Commun.* **2012**, *48*, 12103.

[40] Hasenknopf, B.; Delmont, R.; Herson, P.; Gouzerh, P. *Eur. J. Inorg. Chem.* **2002**, 1081.

[41] (a) Chen, Q.; Goshorn, D. P.; Scholes, C. P.; Tan, X.-L.; Zubieta, J. *J. Am. Chem. Soc.* **1992**, *114*, 4667. (b) Han, J. W.; Hill, C. L. *J. Am. Chem. Soc.* **2007**, *129*, 15094. (c) Wu, P.; Xiao, Z.; Zhang, J.; Hao, J.; Chen, J.; Yin, P.; Wei, Y. *Chem.* Commun. **2011**, *47*, 5557. (d) Yin, P.; Wu, P.; Xiao, Z.; Li, D.; Bitterlich, E.; Zhang, J.; Cheng, P.; Vezenov, D. V.; Liu, T.; Wei, Y. *Angew. Chem. Int. Ed.* **2011**, *50*, 2521. (e) Li, D.; Song, J.; Yin, P.; Simotwo, S.; Bassler, A. J.; Aung, YY, Roberts, J. E.; Hardcastle, J. I.; Hill, C. L.; Liu, T. *J. Am. Chem. Soc.* **2011**, *133*, 14010. (f) Santoni, M.-P.; Pal, A. K.; Hanan, G. S.; Tang, M.-C.; Venne, K.; Furtos, A.; Ménard-Tremblay, P.; Malveau, C.; Hasenknopf, B. *Chem. Commun.* **2012**, *48*, 200.

[42] Müller, A.; Meyer, J.; Mögge, H.; Stammler, A.; Botar, A. *Z. Anorg. Allg. Chem.* **1995**, *621*, 1818.

[43] Kortz, U.; Savelieff, M. G.; Ghali, F. Y. A.; Khalil, L. M.; Maalouf, S. A. ; Sinno, D. I. *Angew. Chem. Int. Ed.* **2002**, *41*, 4070.

[44] Pradeep, C. P.; Long, D.-L.; Newton, G. N.; Song, Y.-F.; Cronin, L. *Angew. Chem. Int. Ed.* **2008**, *47*, 4388.

---

[45] Pradeep, C. P.; Misdrahi, M. F.; Li, F.-Y.; Zhang, J.; Xu, L.; Long, D.-L.; Liu, T.; Cronin, L. *Angew. Chem. Int. Ed.* **2009**, *48*, 8309.

[46] Li, J.; Huth, I.; Chamoreau, L.-M.; Hasenknopf, B.; Lacôte, E.; Thorimbert, S.; Malacria, M. *Angew. Chem. Int. Ed.* **2009**, *48*, 2035.

[47] (a) Kang, H.; Zubieta, J. *J. Chem. Soc, Chem. Commun.* **1988**, 1192. (b) Du, Y.; Rheingold, A. L.; Maata, E. A. *J. Am. Chem. Soc.* **1992**, *114*, 345.

[48] Strong, J. B.; Yap, G. P.A.; Ostrander, R.; Liable-Sands, L. M.; Rheingold, A. L.; Thouvenot, R.; Gouzerh, P.; Maata, E. A. *J. Am. Chem. Soc.* **2000**, *122*, 639.

[49] (a) Wei, Y.; Xu, B.; Barnes, C. L.; Peng, Z. *J. Am. Chem. Soc.* **2001**, *123*, 4083. (b) Xu, B.; Wei, Y.; Barnes, C. L.; Peng, Z. *Angew. Chem. Int. Ed.* **2001**, *40*, 2290. (c) Xu, L.; Lu, M.; Xu, B.; Wei, Y.; Peng, Z.; Powell, D.R. *Angew. Chem. Int. Ed.* **2002**, *41*, 4129. (d) Lu, M.; Wei, Y.; Xu, B.; Cheung, C. F.-C.; Peng, Z.; Powell, D. R. *Angew. Chem. Int. Ed.* **2002**, *41*, 1566. (e) Kang, J.; Xu, B.; Peng, Z.; Zhu, X.; Wei, Y.; Powell, D. R. *Angew. Chem. Int. Ed.* **2005**, *44,* 6902. (f) Li, Q.; Wei, Y.; Hao, J.; Zhu, Y.; Wangm L. *J. Am. Chem. Soc.* **2007**, *129*, 5810.

[50] Hao, J.; *Xia*, Y.; Wang, L.; Ruhlmann, L.; Zhu, Y.; Li, Q.; Yin, P.; Wei, Y.; Guo, H. *Angew. Chem. Int. Ed.* **2008**, *47*, 2626.

[51] (a) Xue, S.; Ke, S.; Yan, L.; Cai, Z.; Wei, Y. *J. Inorg. Biochem.* **2005**, *99*, 2276. (b) Xue, S.; Chai, A.; Cai, Z.; Wei, Y.; Xiang, C.; Bian, W.; Shen, J. *Dalton Trans*. **2008**, 4770. (c) Xue, S.; Xiang, C.; Wei, Y.; Tao, Z.; Chai, A.; Bian, W.; Xu, Z. *Cryst. Growth Des.* **2008**, *8*, 2437.

[52] (a) Zhang, J.; Hao, J.; Wei, Y.; Xia, F.; Yin, P.; Wang, L. *J. Am. Chem. Soc.* **2010**, *132*, 14. (b) Zhang, J.; Yin, P.; Hao, J.; Xiao, F.; Chen, L.; Wei, Y. *Chem. Eur. J.* **2012**, *18*, 135096.

[53] (a) Hsieh, T.-C.; Zubieta, J. *Inorg. Chem.* **1985**, *24*, 1287. (b) Kwen, H.; Young, V. G.; Maatta, E. A. *Angew. Chem. Int. Ed.* **1999**, *38*, 1145. (c) Bustos, C.; Hasenknopf, B.; Thouvenot, R.; Vaissermann, J.; Proust, A.; Gouzerh, P. *Eur. J. Inorg. Chem.* **2003**, 2757.

[54] (a) Baker, L. C. W.; Figgis, J. S. *J. Am. Chem. Soc.* **1970**, *92*, 3794. (b) Liu, H.; Gómez-García, P.; Peng, J.; Sha, J.; Li, Y.; Yan, Y. *Dalton Trans.* **2008**, 6211. (c) Liu, H.; Gómez-García, C. J.; Peng, J.; Sha, J.; Wang, L.; Yan, Y. *Inorg. Chim. Acta* **2009**, *362*, 1957.

[55](a) Rong, C.; Pope, M. T. J. Am. Chem. Soc. 1992, 114, 2932. (b) Rong, C. C.; So, H.; Pope, M. T. Eur. J. Inorg. Chem. 2009, 5211. (c) Lahootun, V. L.; Besson, C.; Villanneau, R.; Villain, F.; Chamoreau, L.-M.; Boubekeur, K.; Blanchard, S.; Thouvenot, R.; Proust, A. J. Am. Chem. Soc. 2007, 129, 7127.

[56] (a) Zheng, S.-T.; Wang, M.-H.; Yang, G.-Y. *Chem. Asian J.* **2007**, *2*, 1380. (b) Zhao, J.-W.; Li, B.; Zheng, S.-T.; Yang, G.-H. *Cryst. Growth Des*. **2007**, *7*, 2658. (c) Cui, R.-R.; Wang, H.-L.; Yang, X.-Y.; Ren, S.-H.; Hu, H.-M.; Fu, F.; Wang, J.-W.; Xue, G.-L. *Chin. J. Chem*. **2007**, *25*, 176. (d) Liu, H.; Qin, C.; Wei, Y.-G.; Xu, L.; Gao, G.-G.; Li, F.-Y.; Qu, X.-S. *Inorg. Chem*. **2008**, *47*, 4166.

[57] (a) Belai, N.; Pope, M. T. *Chem. Commun.* **2005**, 5760. (b) Belai, N.; Kapoor, P. N.; Dickman, M. H.; Butcher, R. J.; Pope, M. T. *Eur. J. Inorg. Chem.* **2009**, 5215.

[58] Shi, Q.; Zhang, Z.-M.; Li, Y.-G.; Wu, Q.; Yao, S.;Wang E. *Inorg. Chem. Commun.* **2009**, *12*, 293.

[59] Ritchie, C.; Boyd, T.; Long, D.-L.; Ditzel, E.; Cronin, L. *Dalton Trans.* **2009**, 1587.

[60] (a) Fang, X.; Anderson, T. M.; Hill, C. L. *Angew. Chem. Int. Ed.* **2005**, *44*, 3540. (b) Fang, X.; Anderson, T. M.; Hou, Y.; Hill, C. L. *Chem. Commun*. **2005**, 5044.

[61] Artetxe, B. *ChemistryOpen* **2016**, *5*, 261 –266.

[62] (a) Rousseau, G.; Oms, O.; Dolbecq, A.; Marrot, J.; Mialane, P. *Inorg. Chem*. **2011**, *50*, 7376. (b) Rousseau, G., Rivière, E.; Dolbecq, A.; Marrot, J.; Oms, O.; Mialane, P. *Eur. J. Inorg. Chem*. **2013**, 1793.

[63] (a) Errington, J. R.; Petkar, S.S.; Middleton, P. S.; McFarlane, W; Clegg, W.; Coxall, R. A.; Harrington, R. W. J. Am. Chem. Soc. **2007**, *129*, 12181. (b) Errington, J. R.; Petkar, S.S.; Middleton, P. S.; McFarlane, W; Clegg, W.; Coxall, R. A.; Harrington, R. W. *Dalton Trans.* **2007**, 5211. (c) Falber, A.; Burton-Pye, B. P.; Radivojevic, I.; Todaro, L.; Saleh, R.; Francesconi, L. C.; Drain, C. M. et al. *Eur. J. Inorg. Chem*. **2009**, 2459. (d) Hirano, T.; Uehara, K.; Uchida, S.; Hibino, M.; Kamata, K.; Mizuno, N. *Inorg. Chem*. **2013**, *52*, 2662.

---

[64] (a) Zheng, S.-T.; Zhang, J.; Yang, G.-Y. *Angew. Chem. Int. Ed.* **2008**, *47*, 3909. (b) Zheng, S.-T., Zhang, J.; Li, X.-X.; Fang, G.-Y. *J. Am. Chem. Soc.* **2010**, *132*, 15102.

[65] (a) Warren, C. J.; Haushalter, R. C.; Rose, D. J.; Zubieta, J. *Chem. Mater.* **1997**, *9,* 2694. (b) Zapf, P.; Haushalter, R. C.; Zubieta, J. *Chem. Mater*. **1997**, *9,* 2019. (c) D. Hagrman, C. Zubieta, D. J. Rose, J. Zubieta, R. C. Haushalter, *Angew. Chem. Int. Ed. Engl.* **1997**, *36*, 873. (d) Hagrman, P. L.; Hagrman, D.; Zubieta, J. *Angew. Chem. Int. Ed.* **1999**, *38*, 2638.

[66] (a) Reinoso, S. Complejos *dinucleares cobre(II)-carboxilato Puente soportados sobre polioxometalatos tipo Keggin* Ph.D., UPV/EHU, Leioa, **2005.** (b) Reinoso, S.; Vitoria, P.; San Felices, L.; Lezama, L.; Gutiérrez-Zorrilla, J. M.. *Chem. Eur. J.* **2005**, *11,* 1538. (c) Reinoso, S.; Vitoria, P.; Gutiérrez-Zorrilla, J. M.; Lezama, L.; San Felices, L.; Beitia, J. I. *Inorg. Chem*. **2005**, *44*, 9731. (d) Reinoso, S.; Vitoria, P.; San Felices, L.; Lezama, L.; Gutiérrez-Zorrilla, J. M. *Inorg. Chem.* **2006**, *45*, 108. (e) Reinoso, S.; Vitoria, P.; Gutiérrez-Zorrilla, J.-M.; Lezama, L.; Madariaga, J. M.; San Felices, L.; Iturrospe, A. *Inorg. Chem.* **2007**, *46*, 4010. (f) Reinoso, S.; Vitoria, P.; San Felices, L.; Montero, A; Lezama, L.; Gutiérrez-Zorrilla, J. M. *Inorg. Chem.* **2007**, *46*, 1237.

[67] (a) San Felices, L. *Interacción de heteropolianiones de wolframio y silicio, germanio o fósforo con complejos de cobre: Síntesis, caracterización química y estructural y estudio topológico* Ph.D., UPV/EHU, Leioa, **2009.** (b) San Felices, L.; Vitoria, P.; Gutiérrez-Zorrilla, J. M.; Lezama, L.; Reinoso, S. *Inorg. Chem.* **2006**, *45*, 7748. (c) Iturrospe, A. *Síntesis, caracterización química y estudio estructural de sistemas basados en* heteropolianiones *de wolframio y silicio o germanio y complejos de cobre con ligandos N4-tetradentados.* Ph. D., UPV/EHU, Leioa, **2013.**

[68] (a) Rhule, J. T.; Neiwert, W. A.; Hardcastle, K. I.; Do, T.; Hill, C. L. *J. Am. Chem. Soc.* **2001**, *123*, 12101. (b) Bi, L.; Hussain, F.; Kortz, U.; Sadakane, M.; Dickman, M. H. *Chem. Commun*. **2004**, 1420. (c) An, H.-Y.; Wang, E.-B.; Xiao, D.-R.; Li, Y.-G.; Su, Z. M.; Xu, L. *Angew. Chem. Int. Ed.* **2006**, *45*, 904. (d) Streb, C.; Ritchie, C.; Long, D.-L.; Kögerler, P.; Cronin, L. *Angew. Chem. Int. Ed.* **2007**, *46*, 7579. (e) Yokoyama, A.; Kojima, T.; Ohkubo, K.; Fukuzumi, S. *Chem. Commun.* **2007**, 3997. (f) Uchida, S; Mizuno, N. *Coord. Chem. Rev.* **2007**, *46*, 7579. (g) Gao, G.-G.; Cheng, P.-S.; Mak, T. C. W. *J. Am. Chem. Soc.* **2009**, *131*, 18257.

[69] (a) Christensen, J. J.; Eatough, D. J.; Izatt, R. M. *Chem. Rev.*, 1974, **74**, 351. (b) Wainwright, K. P. *Coord. Chem. Rev.* **1997**, *166*, 35. (c) Barefield, E. K. *Coord. Chem. Rev*. **2010**, *254*, 1607.

[70] Kimura, E. *Tetrahedron* **1992**, *48*, 6175.

[71] Hancock, R. D.; Ramunas, J. M.; Mashishi, J.; Cukrowski, I.; Reibenspies, J. H.; Martell, A. E. *J. Chem. Soc., Perkin Trans. 2* **1996**, *9*, 1925.

[72] (a) Cabbiness, D. K.; Margerum, D. W. *J. Am.* Chem. *Soc.*, 1969, **91**, 6540.

[73] (a) E. Kimura, C. A. Dalimunte, A. Yamashita, R. Machida, *J. Chem. Soc., Chem. Commun.* **1985**, 1041. (b) E. Kimura, M. Sasada, M. Shionoya, T. Koike, H. Kurosaki M. Shiro, *J. Biol. Inorg. Chem*. 1997, **2**, 74. (c) E. Kimura, M. Shionoya, T. Mita, Y. Iitaka, *J. Chem. Soc., Chem. Commun.* 1987, 171..

[74] (a) Bolm, C.; Meyer, N.; Raabe, G.; Weyhermüller, T.; Bothe, E. *Chem. Commun.* **2000**, 2435. (b) Grenz, A. Ceccarelli, S.; Bolm, C. *Chem. Commun.*, 2001, 1726. (c) R. Breslow, D. Berger, D. L. Huang, *J. Am. Chem. Soc.*, 1990, **112**, 3686–3687; (d) K. Mochizuki, S. Manaka, I. Takeda and T. Kondo, *Inorg. Chem.*, 1996, **35**, 5132.

[75] (a) Volkert, W. A.; Hoffmann, T. J. *Chem. Rev.* **1999**, *99*, 2269. (b) Inouye, Y.; Kanamori, T.; Yoshida, T.; Bu, X.; Shionoya, M.; Koike, T.; Kimura, E. *Biol. Pharm. Bull*. **1994**, *17*, 243.

[76] (a) Martell, A. E.; Hancock, R. D. *Metal Complexes in Aqueous Solutions*, Plenum Press, New York, **1996**. (b) Wainwright, K. P. *Coord. Chem. Rev*., **1997**, *166*, 35. (c) Lincoln, S. F. *Coord. Chem. Rev*. **1997**, *166*, 255. (d) Meyer, M.; Dahaoui-Ginderey, V.; Lecomte, C.; Guilard, R. *Coord. Chem. Rev.* **1998**, *178*, 1313. (e) Lindoy, L. F. *Adv. Inorg. Chem.* **1998**, *45*, 75. (f) Elias, H. *Coord. Chem. Rev*. **1999**, *187*, 37.

[77] Van Alphen, J. *Rec. Trav. Chim*. **1937**, *56*, 1343.

[78] (a) Martell, A. E.; Hancock, R. D.; Motekaitis, R. J. *Coord. Chem. Rev.* **1994**, *133*, 39. (b) Liang, X.-G.; Sadler, P. J. *Chem. Soc. Rev.* **2004**, *33*, 234.

[79] Fisher, B. J.; Eisenberg, R., *J. Am. Chem. Soc.* **1980**, *102*, 7361.

[80] Beley, M.; Collin, J. P.; Ruppert, R.; Sauvage, J. P. *J. Am. Chem. Soc.* **1986**, *108*, 7461.

[81] (a) Froehlich, J. D.; Kubiak, C. P. *Inorg. Chem*. **2012**, *51*, 3932. (b) Song, J.-S.; Klein, E. L.; Neese, F.; Ye, S.-F. *Inorg. Chem.* **2014**, *53*, 7500. (c) Neri, G.; Walsh, J. J.; Wilsom, C.; Reynal, A.; Lim, J. Y. C.; Li, X.; White, A. J. P.; Long, N. J.;

Durrani, J. R.; Cowan, A. *J. Phys. Chem. C.* **2015**, *17*, 1562. (c) Kang, S.-J.; Dale, A.; Sarkar, S.; Yoo, J.-S.; Lee, H. J. *Electrochem. Sci. Technol.* **2015**, *6*, 106. (d) Murase, M.; Kitahara, G.; Suzuki, T. M.; Ohta, R. *ACS Appl. Mater. Interfaces* **2016**, *8*, 24315.

[82] Bosnich, B.; Poon, C. K.; Tobe, M. L. *Inorg. Chem.*, **1965**, *4*, 1102.

[83] Whimp, P. O.; Bailey, M. F.; Curtis, N. F. *J. Chem. Soc. A* **1970**,1956.

[84] Connolly, P. J.; Billo, E. J. *Inorg. Chem.* **1987**, *26*, 3224.

[85] Donnelly, M. A.; Zimmer, M. *Inorg. Chem*. **1999**, *38*, 1650.

[86] Bakaj, M.; Zimmer, M. *J. Mol. Struct*. **1999**, *508*, 59.

[87] (a) X. Liang, J. A. Parkinson, S. Parsons, M. Weishäupl and P. J. Sadler, *Inorg. Chem.*, 2002, **41**, 4539. (b) Lalitham; J.; Vijayaraghavan, V. R. *Proc. Indian Acad. Sci.* **2000**, *112*, 507.

[88] Bang, H.; Lee, E. J.; Lee, E. Y.; Suh, J.; Suh, M. P. *Inorg. Chim. Acta*,**2000**, *308*, 150.

[89] Glerup, J.; Hazell, A.; Michelsen, K.; Weihe, H. *Acta Chem. Scand.* **1994***, 48***,** 618.

[90] a) Martín-Caballero, J.; San José Wéry, A.; Reinoso, S.; Artetxe, B.; San Felices, L.; Vilas, J. L.; Gutiérrez-Zorrilla, J. M. *CrystEngComm* **2015**, *17*, 8915. (b) Martín-Caballero, J.; San José Wéry, A.; Reinoso, S.; Artetxe, B.; San Felices, L.; El Bakkali, B.; Trautwein, G.; Alcañiz-Monge, J.; Vilas, J. L.; Gutiérrez-Zorrilla, J. M. *Inorg. Chem*. **2016**, *55*, 4970.

[91] Ou, G.-C.; Yuan, X.-Y.; Li, Z.-Z.; Li, W.-Y.; Zeng, F.; Deng, J.-H.; Zhong, D.-C. *Eur. J. Inorg. Chem.* **2016**, 3500.

[92] (a) Ou, G.-C.; Jiang, L.; Feng, X.-L.; Lu, T.-B. *Dalton Trans.* **2009**, 71. (b) Ou, G.-C.; Yuan, X.-Y.; Li, Z.-Z.; Ding, M.-H. *J. Coord. Chem.* **2013**, *66*, 2065. (c) Ou, G.-C.; Yuan, X.-Y.; Li, Z.-Z. *Transition Met. Chem.* **2012**, *37*, 705. (d) Ou, G.-C.; Yuan, X.-Y.; Li, Z.-Z.;*Chin. J. Struct. Chem.* **2013**, *32*, 375. (e) Huang, Z.-W.; Pan, Z.-Y.; Zhou, D.-L.; Ou, G.-C. *Asian J. Chem*. **2015**, *27*, 2579.

[93] (a) Sarma, M.; Chatterjee, T.; Das, S. K. *Dalton Trans.* **2011** *,40*, 2954. (b) Sarma, M.; Chatterjee, T.; Das, S. K. *J. Mol. Struct.* **2011***, 1004*, 31. (c) Sarma, M.; Chatterjee, T.; Vindhya, H.; Das, S. K. *Dalton Trans.* **2012***, 41*, 1862.

[94] (a) Furukawa, H.; Cordova, K. E.; O'Keeffe, M.; Yaghi, O. M. *Science* **2013**, *341*, 974. (b) Guest. Eds. Zhou, H.-C.; Long, J. R.; Yaghi, O. M. *Chem. Rev.* **2012**, *112*, thematic issue 2. (c) Liu, J.; Thallapally, P. K.; McGrail B. P.; Brown, D. R.; Liu, J. *Chem. Soc. Rev.* **2012**, *41*, 2308. (d) Long. J. R.; Yaghi, O. M. *Chem. Soc. Rev.* **2009**, *38*, thematic issue 5.

[95] See for example: (a) Qin, J.-S.; Du, D.-Y.; Li, W.-L.; Zhang, J.-P.; Li, S.-L.; Su, Z.-M.; Wang, X.-L.; Xu, Q.; Shao, K.-Z.; Lan, Y.-Q. *Chem. Sci*. **2012**, *3*, 2114. (b) Horcajada, P.; Chalati, T.; Serre, C.; Gillet, B.; Sebrie, C.; Baati, T.; Eubank, J. F.; Heurtaux, D.; Clayette, P.; Kreuz, C.; Chang, J.-S.; Hwang, Y. K.; Marsaud, V.; Bories, P.-N.; Cynober, L.; Gil, S.; Férey, G.; Couvreur P.; Gref, R. *Nat. Mater.* **2010**, *9*, 172.

[96] (a) Miras, H. N.; Vilà-Nadal, L.; Cronin, L. *Chem. Soc. Rev*. **2014**, 43, 5679. (b) Du, D.-Y.; Qin, J.-S.; Li, S.-L.; Su, Z.-M.; Lan, Y.-Q. *Chem. Soc. Rev.* **2014**, 43, 4615.

[97] (a) Uchida, S.; Mizuno, N. *Coord. Chem. Rev.* **2007**, *251*, 2537 and references therein. (b) Eguchi, R.; Uchida, S.; Mizuno, N. *J. Phys. Chem. C* **2012**, *116*, 16105. (c) Eguchi, R.; Uchida, S.; Mizuno, N. *Angew. Chem., Int. Ed.* **2012**, *51*, 1635. (d) Kawahara, R.; Uchida, S.; Mizuno, N. *Inorg. Chem.* **2014**, *53*, 3655.

[98] Wang, Y.; Ye, L.; Wang, T.-G.; Cui, X.-B.; Shi, S.-Y.; Wang, G.-W.; Xu, J. Q. *Dalton Trans*. **2010**, 39, 1916.

[99] Han, J. W.; Hill, C. L. *J. Am. Chem. Soc*. **2007**, *129*, 15094.

[100] (a) Liu, D.; Lu, Y.; Tan, H.-Q.; Chen, W.-L.; Zhang, Z.-M.; Li, Y.-G.; Wang, E.-B. *Chem. Commun.* **2013**, *49*, 3673. (b) Zhang, Z.; Sadakane, M.; Murayama, T.; Izumi, S.; Yasuda, N.; Sakaguchi, N.; Ueda, W. *Inorg. Chem.* **2014**, *53*, 903. (c) An, H.; Hu, Y.; Wang, L.; Zhou, E.; Fei, F.; Su, Z. *Cryst. Growth Des.* **2015**, *15*, 164. (d) Zhang, Z.; Sadakane, M.; Noro, S.; Murayama, T.; Kamachi, T.; Yoshizawa, K.; Ueda, W. *J. Mater. Chem. A*, **2015**, *3*, 746.

[101] (a) Nohra, B.; El Moll, H.; Rodriguez Albelo, L. M.; Mialane, P.; Marrot, J.; Mellot-Draznieks, C.; O'Keeffe, M.; Biboum, R. N.; Lemaire, J.; Keita, B.; Nadjo, L.; Dolbecq, A. *J. Am. Chem. Soc.* **2011**, *133*, 13363. (b) Qin, J.-S.; Du, D.-Y.; Guan, W.; Bo, X.-J.; Li, Y.-F.; Guo, L.-P.; Su, Z.-M.; Wang, Y.-Y.; Lan, Y.-Q.; Zhou, H.-C. *J. Am. Chem. Soc*. **2015**, *137*, 7169. (c) Zheng, S.-T.; Zhang, J.; Yang, G.-Y. *Angew. Chem. Int. Ed.* **2008**, *47*, 3909.

---

[102] (a) Fu, H.; Qin, C.; Lu, Y.; Zhang, Z.-M.; Li, Y.-G.; Su, Z.-M.; Li, W.-L.; Wang, E.-B. *Angew. Chem. Int. Ed.* **2012**, *51*, 7985. (b) Wang, X.; Hu, H.; Liu, G.; Lin, H.; Tian, A. *Chem. Commun.* **2010**, *46*, 6485. (c) An, H.-Y.; Wang, E.-B.; Xiao, D.-R.; Li, Y.-G.; Su, Z.-M.; Xu, L. *Angew. Chem. Int. Ed.* **2006**, *45*, 904.

[103] (a) Zhang, Y. J.; Liu, T.; Kanegawa, S.; Sato, O. *J. Am. Chem. Soc*. **2009**, *131*, 7942. (b) Wriedt, M.; Yakovenko, A. A.; Halder, G. J., Prosvirin, A. V.; Dunbar, K. R.; Zhou, H. C. *J. Am. Chem. Soc.* **2013**, *135*, 4040.

[104] (a) Halasz, I. *Cryst. Growth Des*. **2010**, *10*, 2817 and references therein. (b) Friščić, T.; MacGillivray, L. R. *Z. Kristallogr,* **2005**, *220*, 351. (c) Hao, Z.-M; Zhang, X.-M. *Dalton Trans.* **2011**, *40*, 2092. (d) Coronado, E.; Mínguez Espallargas, G. *Chem. Soc. Rev.* **2013**, *42*, 1525. (e) Ke, S.-Y; Wang, C.-C. *CrystEngComm* **2015**, *17*, 8776.

[105] Aromí, G.; Beavers, C. M; Sánchez Costa, J.; Craig, G. A.; Mínguez Espallargas, G.; Orera, A.; Roubeau, O. *Chem. Sci*. **2016**, *7*, 2907.

[106] (a) Centore, R.; Capitolino, V.; Cerciello, F.; Tuzi, A.; Borbone, F.; Carella, A.; Roviello, R. *CrystEngComm* **2015**, *17*, 8864. (b) Takahashi, H.; Tamura, R. *CrystEngComm* **2015**, *17*, 8888. (c) Hagihara, R.; Harada, N.; Karasawa, S.; Koga, N. *CrystEngComm* **2015**, *17*, 8825–8834. (d) Mouchaham, G.; Gualino, M.; Roques, N.; Duhayon, C.; Brandès, S.; Sutter, J. P. *CrystEngComm* **2015**, *17*, 8906. (e) Khorasani, S.; Botes, D. S.; Fernandes, M. A.; Levendis, D. C. *CrystEngComm* **2015**, *17*, 8933.

[107] (a) Zakharov, B. A; Marchuk, A. S; Boldyreva, E. V. *CrystEngComm* **2015**, *17*, 8812. (b) Avdeeva, V. V; Buzin, M. I; Malinina, E. A; Kuznetsov, N. T; Vologzhanina, A. V. *CrystEngComm* **2015**, *17*, 8870.

[108] (a) Li, Q.-Q; Ren, C.-Y; Huang, Y.-Y; Li, J.-L; Ping, L.; Liu, B.; Liu, Y.; Wang, Y. Y. *Chem. Eur. J.* **2015**, *21*, 4703. (b) Coronado, E.; Giménez-Marqués, M.; Mínguez Espallargas, G.; Brammer, L. *Nat. Commun*. **2012**, *3*, 828. (c) Ren, H.-Y; Yao, R.-X; Zhang, X.-M. *Inorg. Chem*. **2015**, *54*, 6312. (d) Manna, B.; Desai, A. V.; Kumar, N.; Karmakar, A.; Ghosh, S. K. *CrystEngComm* **2015**, *17*, 8796–8800. (e) Lee, J.-H; Kim, T.-K; Suh, M.-P; Moon, H. R. *CrystEngComm* **2015**, *17*, 8807. (f) Tahier, T.; Oliver, C. L. *CrystEngComm* **2015**, *17*, 8946.

[109] (a) Baldoví, J. J.; Coronado, E.; Gaita-Ariño, A.; Gamer, C.; Giménez-Marqués, M.; Mínguez Espallargas, G. *Chem. Eur. J.* **2014**, *20*, 10695. (b) López-Cabrelles, J.; Mínguez Espallargas, G.; Coronado, E. *Polymers*, **2016**, *8*, 171.

[110] Kikukawa, Y.; Yamaguchi, K.; Mizuno, N. *Angew. Chem. Int. Ed*. **2010**, *49*, 6096.

[111] Kikukawa, Y.; Yamaguchi, K.; Mizuno, N. *Inorg. Chem.* **2010**, *49*, 8194.

[112] Kuriyama, Y.; Kikukawa, Y.; Suzuki, K.; Yamaguchi, K.; Mizuno, N. *Chem. Eur. J*. **2016**, *22*, 3962.

[113] Uchida, S.; Mizuno, N. *J. Am. Chem. Soc*. **2004**, *126*, 1602.

[114] Zhang, L.-Z.; Gu, W.; Liu, X.; Dong, Z.; Li, B. *CrystEngComm* **2008**, *10*, 652.

[115] (a) Don, A.; Weakley, T. J. R. *Acta Crystallogr.* **1981**, *B37*, 451. (b) Reinoso, S.; Dickman, M. H.; Praetorius, A.; Kortz, U. *Acta Crystallogr.* **2008**, *E64*, m614. (c) Zhang, L.-Z.; Gu, W.; Dong, Z.; Liu, X.; Li, B. *CrystEngComm* **2008**, *10*, 1318. (d) Fernández de Luis, R.; Urtiaga, M. K.; Mesa, J. L.; Orive Gómez de Segura, J.; Rojo, T.; Arriortua, M. I. *CrystEngComm* **2011**, *13*, 6488. (e) Barats-Damatov, D.; Shimon, L. J.V.; Feldman, Y.; Bendikov, T.; Neumann, R. *Inorg. Chem*. **2015**, *54*, 628.

[116] (a) Ritchie, C.; Streb, C.; Thiel, J.; Mitchell, S. G.; Miras, H. N.; Long, D.-L.; Boyd, T.; Peacock, R. D.; McGlone, T.; Cronin, L. *Angew. Chem. Int. Ed*. **2008**, *47*, 6881. (b) Thiel, J.; Ritchie, C.; Streb, C.; Long, D.-L.; Cronin, L. *J. Am. Chem. Soc*. **2009**, *131*, 4180. (c) Thiel, J.; Ritchie, C.; Miras, H. N.; Streb, C.; Mitchell, S. G.; Boyd, T.; Corella Ochoa, M. N.; Rosnes, M. H.; McIver, J.; Long, D.-L; Cronin, L. *Angew. Chem Int. Ed.* **2010**, *49*, 6984.

[117] (a) Uchida, S.; Mizuno, N. *J. Am. Chem. Soc*. **2004**, *126*, 1602. (b) Uchida, S.; Kawamoto, R.; Mizuno, N. *Inorg. Chem*. **2006**, *45*, 5136. (c) Kawamoto, R; Uchida, S; Mizuno, N. *J. Am. Chem. Soc*. **2005**, *127*, 10560. (d) Lesbani, A.; Kawamoto, R.; Uchida, S.; Mizuno, N. *Inorg. Chem*. **2008**, *47*, 3349. (e) Chen, C.-L.; Goforth, A. M.; Smith, M. D.; Su, C.-Y.; zur Loye, H. C. *Angew. Chem. Int. Ed.* **2005**, *44*, 6673. (f) Iturrospe, A.; Artetxe, B.; Reinoso, S.; San Felices, L.; Vitoria, P.; Lezama, L.; Gutiérrez-Zorrilla, J. M. *Inorg. Chem*. **2013**, *52*, 3084. (g) Iturrospe, A.; San Felices, L.; Reinoso, S.; Artetxe, B.; Lezama, L.; Gutiérrez-Zorrilla, J. M. *Cryst. Growth Des*. **2014**, *14*, 2318. (h) Pache, A.; Reinoso, S.; San Felices, L.; Iturrospe, A.; Lezama, L.; Gutiérrez-Zorrilla, J. M. *Inorganics* **2015**, *3*, 194.

[118] (a) Shi, L.-X.; Zhao, W.-F.; Xu, X.; Tang, J.; Wu, C.-D. *Inorg. Chem*. **2011**, *50*, 12387. (b) Uehara, K.; Mizuno, N. *J. Am. Chem. Soc*. **2011**, *133*, 1622. (c) Eguchi, R.; Uchida, S.; Mizuno, N. *Angew. Chem. Int. Ed*. **2012**, *51*, 1635. (d) Eguchi, R.; Uchida, S.; Mizuno, N. *J. Phys. Chem. C* **2012**, *116*, 16105. (e) Uchida, S.; Takahashi, E.; Mizuno, N. *Inorg.*

Chem. **2013**, *52*, 9320. (c) Uchida, S.; Eguchi, R.; Mizuno, N. *Angew. Chem. Int. Ed*. **2010**, *49*, 9930. (f) Uchida, S.; Mizuno, K.; Kawahara, R.; Takahashi, E.; Mizuno, N. *Chem. Lett*. **2014**, *43*, 1192.

[119] Zhan, C.; Cameron, J. M.; Thomas-Boyd, D.-G.; Winter, R. S.; Vilá-Nadal, L.; Mitchell, S. G.; Glatzel, S.; Breternitz, J.; Gregory, D. H.M; Long, D.-L.; Macdonell, A.; Cronin, L. *Nat. Commun.* **2017**, *8*, 14185.

[120] Zhou, C. M.; Gall, D. *Thin Solid Films* **2007**, *516*, 433.

[121] (a) Xu, B.; Arias, F.; Whitesides, G. M. *Adv. Mater.* **1999**, *11*, 492. (b) Acikgoz, C.; Hempenius, M. A.; Huskens, J. G.; Vancso, J. *Eur. Polym. J.* **2011**, *47*, 2033

[122] Akinoglu, E. M.; Morfa, A. J.; Giersig, M. *Langmuir* **2014**, *38*, 563.

[123] Pine, D. J.; Imhof, A. *Nature* **1997**, *389*, 948.

[124] (a) Tripathi, B. K.; Pandey, P. J. Membr. Sci. **2014**, *471*, 201. (b) Ou, Y.; Lv, C.; Yu, W.; Mao, Z.; Wan, L.; Xu, Z. *ACS Appl. Mater. Interfaces* **2014**, *6*, 22400.

[125] Ma, H.; Cui, J.; Chen, J.; Hao, J. *Chem. A: Eur. J.* **2011**, *17*, 655.

[126] (a) Chen, S.; Lu, X.; Hu, Y.; Lu, Q. Biomater. Sci. 2014, 3, 85. (b) Kawano, T.; Nakamichi, Y.; Fujinami, S.; Nakajima, K.; Yabu, H.; Shimomura, M. *Biomacromolecules* **2013**, *14*, 1208.

[127] Manabe, K.; Nishizawa, S.; Shiratori, S. *ACS Appl. Mater. Interfaces* **2013**, *5*, 11900

[128] Nielsen, K. H.; Kittel, T.; Wondraczek, K.; Wondraczek, L. *Sci. Rep*. **2014**, *4*, 6595.

[129] Kon, K.; Brauer, C. N.; Hidaka, K.; L€ohmannsr€oben, H. G.; Karthaus, O. *Langmuir* **2010**, 26, 12173.

[130] (a) Hernández-Guerrero, M.; Stenzel, M. H. *Polym. Chem*. **2012**, *3*, 563. (b) Ruiz-Rubio, L.; Azpitarte, I.; Garcıa-Huete, N.; Laza, J. M.; Vilas, J. L.; Leon, L. M. J. *Appl. Polym. Sci.* **2016**, DOI: 10.1002/APP.44004.

[131] (a) Hernández-Guerrero, M.; Davis, T. P.; Barner-Kowollik, C.;Stenzel, M. H. *Eur. Polym. J.* **2005**, *41*, 2264. (b) Tung, P.-H.; Huang, C.-F.; Chen, S.-C.; Hsu, C.-H.; Chang, F.-C. *Desalination* **2006**, *200*, 55. (c) de León, A. S.; del Campo, A.; Fernández-García, M.; Rodríguez-Hernández, J.; Muñoz-Bonilla, A. *ACS Appl. Mater. Interfaces* **2013**, *5*, 3943. (d) Liu, C.; Wang, G.; Zhang, Y.; Huang, J. *J. Appl. Polym. Sci.* **2008**, *108*, 777. (e) Zhu, L.; Ou, Y.; Wan, L.; Xu, Z. *J. Phys. Chem.* **2014**, *118*, 1.

[132] (a) Mercier, D.; Boujday, S.; Annabi, C.; Villanneau, R.; Pradier, C.-M.; Proust, A. *J. Phys. Chem. C* **2012**, *116*, 13217. (b) Villanneau, R.; Marzouk, A.; Wang, Y.; Djamaa, A. B.; Laugel, G.; Proust, A.; Launay, F. *Inorg. Chem*. **2013**, *52*, 2958. (c) Song, Y.-F.; McMillan, N.; Long, D.-L.; Kane, S.; Malm, J.; O Riehle, M.; Pradeep, C. P.; Gadegaard, N.; Cronin, L. *J. Am. Chem. Soc*. **2009**, *131*, 1340.

[133] See for example: (a) Liu, S. Q.; Tang, Z. Y. *Nano Today* **2010**, *5*, 267 and references therein. (b) Li, D.; Yin, P.; Liu, T. *Dalton Trans*. **2012**, *41*, 2853. (c) Nisar, A.; Lu, Y.; Zhuang, J.; Wang, X. *Angew. Chem. Int. Ed.* **2011**, *50*, 318. (d) Kurth, D. G.; Lehmann, P.; Volkmer, D.; Cölfen, H.;Müller, A.; Du Chesne, A. *Chem. Eur. J*. **2000**, *6*, 385. (e) Li, H.; Sun, H.; Qi, H.; Xu, M.; Wu L. *Angew. Chem. Int. Ed*. **2007**, *46*, 1300. (f) Landsmann, S.; Lizandara-Pueyo, C.; Polarz, S. *J. Am. Chem. Soc*. **2010**, *132*, 5315. (g) Zhang, J.; Song, Y. F.; Cronin, L.; Liu, T. *J. Am. Chem. Soc*. **2008**, *130*, 14408. (h) Rosnes, M. H.; Musumeci, C.; Pradeep, C. P.; Mathieson, J. S.; Long, D.-L.; Song, Y.-F.; Pignataro, B.; Cogdell, R.; Cronin, L. *J. Am Chem. Soc*. **2010**, *132*, 15490.

[134] Lunkenbein, T.; Kamperman, M.; Li, Z.; Bojer, C.; Drechsler, M.; Förster, S.; Wiesner, U.; Müller, A. H. E.; Breu, J. *J. Am. Chem. Soc*. **2012**, *134*, 12685.

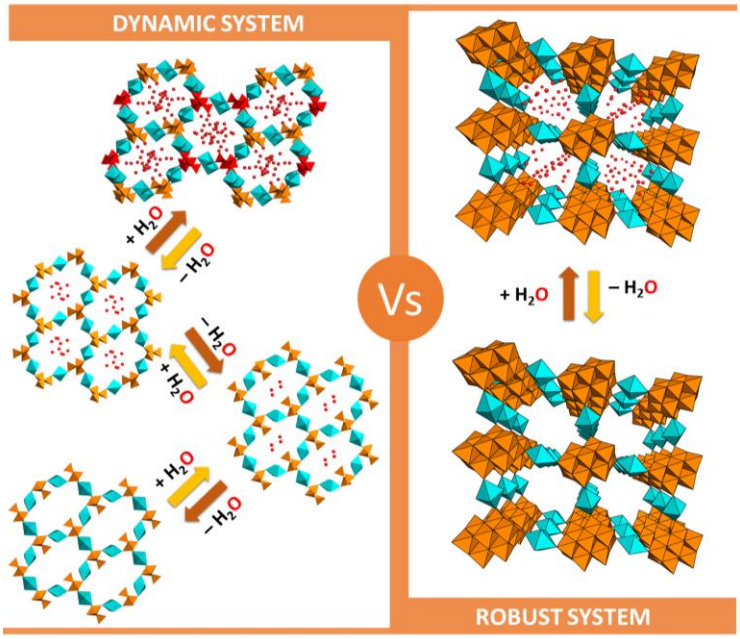

THERMOSTRUCTURAL STUDIES IN POLYOXOVANADATE–METALORGANIC HYBRID COMPOUNDS: DYNAMIC VS. ROBUST OPEN–FRAMEWORKS

Chapter 2

*The reaction of $[VO_3]^-$ anions and $[Cu(cyclam)]^{2+}$ complex cations (cyclam = 1,4,8,11–tetraazacyclotetradecane) results in the $[\{Cu(cyclam)\}(VO_3)_2]\cdot 5H_2O$ (**1–CuV**) and $[Cu(cyclam)][\{Cu(cyclam)\}_2(V_{10}O_{28})]\cdot 10H_2O$ (**1–CuV10**) compounds at pH > 6 and pH 4–6, respectively. **1–CuV** consists in a covalent 3D structure formed by metavanadate chains linked by {Cu(cyclam)} moieties in a hybrid open–framework with two different types of hexagonal channels where water molecules of hydration are hosted. In comparison, **1–CuV10** exhibits a POMOF–like supramolecular porous structure built up of covalent decavanadate/metalorganic layers with square–like voids, the stacking of which is aided by interlamellar cementing complexes and generates water–filled channels. The dynamic structure of **1–CuV** undergoes up to three sequential and totally reversible single–crystal–to–single–crystal transitions triggered by thermal dehydration to lead to the anhydrous form $[\{Cu(cyclam)\}(VO_3)_2]\cdot$(**4–CuV**) through the intermediate phases $[\{Cu(cyclam)\}(VO_3)_2]\cdot 3H_2O$ (**3–CuV**) and $[\{Cu(cyclam)\}(VO_3)_2]\cdot 1.3H_2O$ (**2–CuV**). In contrast, the robust supramolecular framework of **1–CuV10** remains virtually unaltered upon thermal evacuation of guest solvent molecules, resulting in the anhydrous phase **1a–CuV10**, which shows accessible and fully operative micropores. As opposed to the dynamic metavanadate hybrid and its thermal derivatives, the robust nature together with the permanent microporosity renders interesting functionalities to **1–CuV10**, such as the selective adsorption of CO_2 over N_2 gas as well as a remarkable activity as heterogeneous catalyst toward the H_2O_2–based oxidation of the highly–stable, tricyclic alkane adamantane.*

THERMOSTRUCTURAL STUDIES IN POLYOXOVANADATE–METALORGANIC HYBRID COMPOUNDS: DINAMIC VS. ROBUST OPEN–FRAMEWORK MATERIALS

2.1 INTRODUCTION

2.1.1 Polyoxovanadates: A Brief Introduction

Polyoxovanadates (POVs), as a relevant subfamily of polyoxometalates (POMs), have attracted an increasing attention over the years owing to the variable oxidation states that vanadium can adopt and the diverse coordination spheres shown by vanadium oxide polyhedra, which confers them the capacity to form an outstanding variety of different architectures.[1]

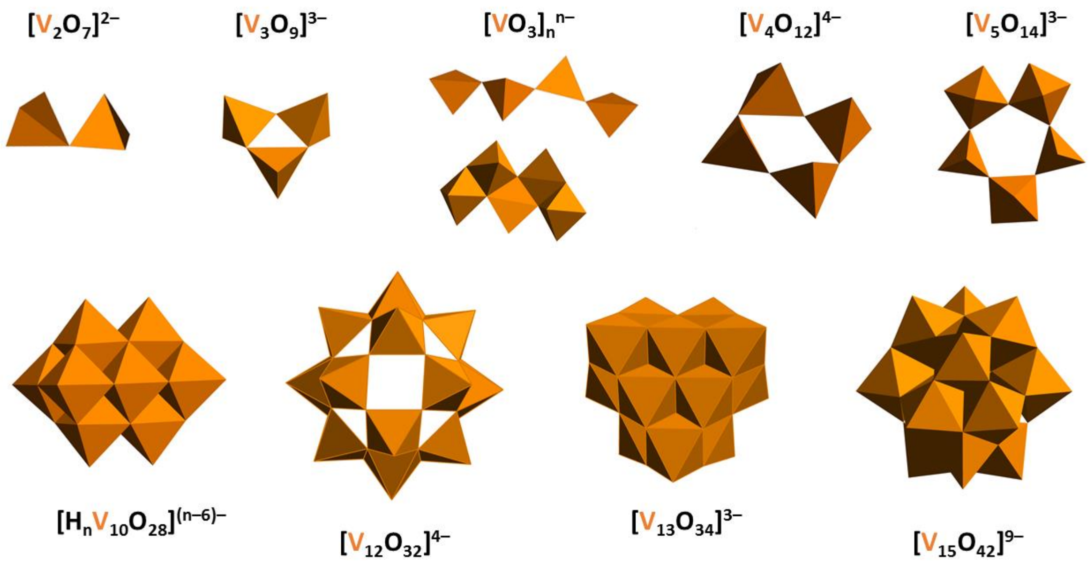

Figure 2.1. Structural diversity in typical fully–oxidized isoPOVs (V^V).

POVs are formed in pH–dependent condensation reactions in which small $[VO_n]^{q-}$ fragments aggregate to build a large variety of high– and low– nuclearity clusters with diverse coordination geometries of the vanadium polyhedra (Figure 2.1). These polyhedra consist of homo– or heterovalent V atoms which can show tetrahedral $\{V^{IV}O_4\}^{3-}$, square pyramidal $\{V^{V}O_5\}^{5-}$ and $\{V^{IV}O_5\}^{9-}$, and octahedral $\{V^{V}O_6\}^{7-}$coordination geometries, which differs greatly from the predominantly octahedral environments shown by Mo and W atoms in polyoxomolybdates and –tungstate compounds. In highly alkaline conditions, the monovanadate $[VO_4]^{3-}$ anion is the only stable specie in aqueous solution, although it can condensate to form the divanadate $[V_2O_7]^{4-}$ specie (pyrovanadate) for high vanadium concentrations. When the solution is slightly acidified, the protonation of the oxido group of the monovanadate begins which lead to the formation of the protonated $[HVO_4]^{2-}$, $[H_2VO_4]^{-}$, and H_3VO_4 species as intermediates. The fully protonated H_3VO_4 is suggested to be a minor species as it is easily converted to $[VO_2]^+$ with increasing coordination number.[2] As the solution becomes more acidic, however, condensation reactions between monovanadate units begin to take place resulting in the generation of various oxovanadate species. In the pH range 8–13, monovanadates, $[VO_4]^-$, divanadates, $[V_2O_7]^{4-}$, as well as metavanadates, $[VO_3]_n^{n-}$ and cyclovanadates $[V_4O_{12}]^{4-}$ are particularly stable (Figure 2.2). The pH range 3–8 is known as the *unstability zone*, where the condensation degree is significant even for low vanadium concentrations. Within this region, the predominant POVs in aqueous solution are the metavanadate species with no longer than five $[VO_n]^{q-}$ units, as POVs larger than the pentameric species (other than decavanadates) do not occur to any great extent in aqueous solution) in the basic zone,[3] while the predominant species in the acidic region are the $[H_nV_{10}O_{28}]^{(n-6)-}$ decavanadate anions. Depending on the vanadium concentration and the ionic strength of the medium, five predominant metavanadate species can be found, which are $[VO_3]_n^{n-}$, $[V_2O_6]^{2-}$, $[V_3O_9]^{3-}$ and the cyclic $[V_4O_{12}]^{4-}$ and $[V_5O_{15}]^{5-}$ anions. For low vanadium concentrations, the polymeric and oligomeric anions are favored whereas higher concentration of the metal leads to the predominance of the cyclic tetra– and pentameric vanadate species. The equilibrium between the different isopolyoxovanadate species have been well investigated by potenciometric and ^{51}V–NMR techniques.[4]

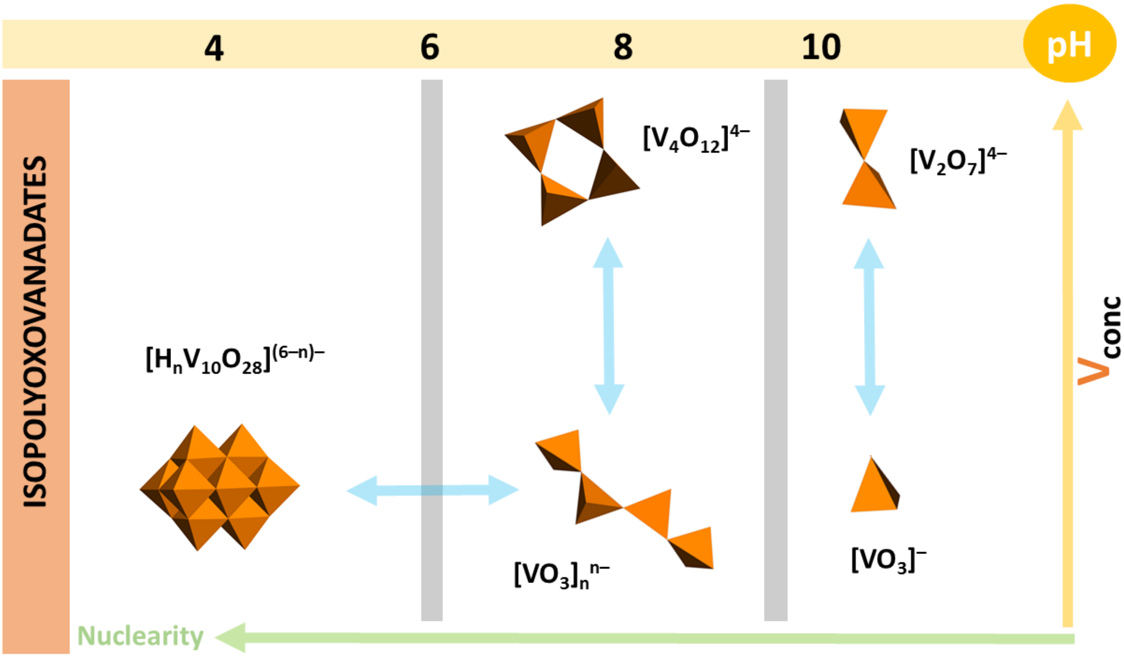

Figure 2.2. General scheme showing the stability range of the predominant isoPOV species of different nuclearity in aqueous solution as a function of the pH and concentration.

POVs can be divided into four general subfamilies attending to the oxidation state of their constituent V atoms, which are the fully–oxidized (V^V), mixed–valent (V^V/V^{IV} or V^{IV}/V^{III}), ''*fully–reduced*'' (V^{IV}) and ''*highly–reduced*'' (V^{III}) categories. The following crystallographically characterized isoPOVs $[V_2O_7]^{4-}$, $[V_3O_9]^{3-}$, $[V_4O_{12}]^{4-}$, $[V_5O_{14}]^{3-}$, $[V_{10}O_{28}]^{6-}$, $[V_{12}O_{32}]^{4-}$, $[V_{13}O_{34}]^{3-}$, $[V_{15}O_{42}]^{9-}$ and $[V_{16}O_{42}]^{4-}$ constitute the class of fully–oxidized vanadium polyanions[5] (Figure 2.1). Up to date, single–crystal X–ray diffraction has allowed the elucidation of various isoPOV structures belonging to the class of the mixed–valent V^V/V^{IV} species such as $[V^{IV}_2V^V_8O_{26}]^{4-}$,

$[V^{IV}_{8}V^{V}_{7}O_{36}]^{5-}$, $[V^{IV}_{11}V^{V}_{5}O_{38}]^{7-}$, $[V^{IV}_{3}V^{V}_{13}O_{42}]^{7-}$, $[V^{IV}_{5}V^{V}_{12}O_{42}]^{4-}$, $[V^{IV}_{16}V^{V}_{2}O_{42}]^{10-}$, $[V^{IV}_{10}V^{V}_{8}O_{42}]^{4-}$, $[V^{IV}_{8}V^{V}_{10}O_{44}]^{6-}$, $[V^{IV}_{6}V^{V}_{13}O_{49}]^{9-}$, $[V^{IV}_{8}V^{V}_{14}O_{54}]^{6-}$, $[V^{IV}_{16}V^{V}_{18}O_{82}]^{10-}$ (disregarding encapsulated supramolecular guest species).[6] In contrast, the mixed–valent V^{IV}/V^{III}– as well as the ''*highly–reduced*'' V^{III}–POVs consist mostly on alkoxide–substituted species such as $[V^{III}V^{IV}_{5}O_6(OCH_3)_8(calix)(CH_3OH)]^-$ (calix = p–tert–butylcalix[4]arene) for the former and $[V^{III}_{4}(\mu\text{–}CH_3COO^-)_4\text{–}(\mu\text{–}OH)_4(H_2O)_8]^{4-}$ cluster for the latter case.[7] The most renowned representative cluster in the ''*fully–reduced*'' class is the archetypal $[V^{IV}_{18}O_{42}]^{12-}$ anion, whose chemical and structural characterization was reported for the first time by Johnson and Schlemper[8] back in 1978 (Figure 2.3).

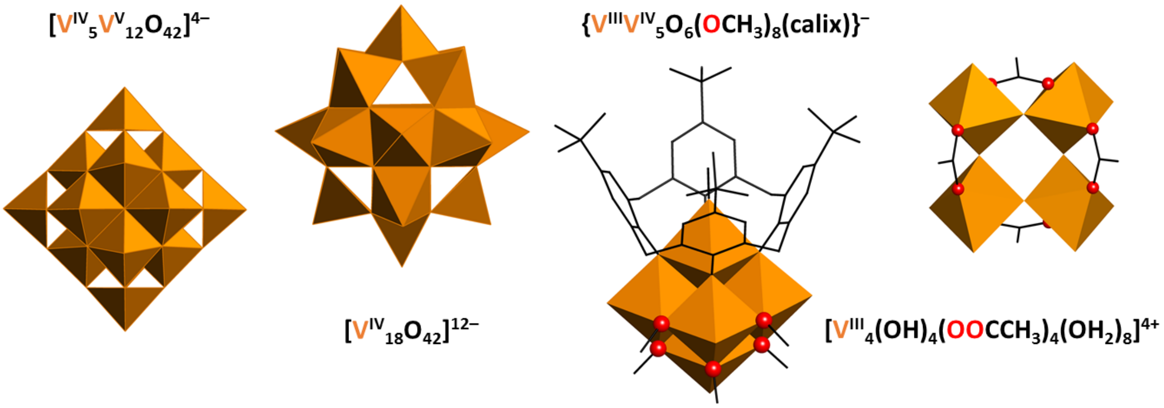

Figure 2.3. Polyhedral representation of some representative mixed–valence (V^{IV}–V^{V}/V^{III}–V^{IV}) as well as highly–reduced (V^{IV}) and fully–reduced (V^{III}) POV clusters. Organic ligands: calix = p–tert–butylcalix[4]arene.

Besides the huge structural variety shown by isopolyoxovanadates, POV chemistry is even more diversified by the incorporation of heteroatoms which results in the formation of heteroPOVs,[9] such as $[PV_{14}O_{42}]^{9-}$, $[Mn_2V_{22}O_{64}]^{10-}$, $[Mn_3H_3V_{12}O_{40}]^{5-}$, and $[MV_{13}O_{38}]^{7-}$ (M = Mn, Ni, Ln^{3+}),[10] among many others. In this sense, even though metavanadate ring sizes larger than the $[V_5O_{15}]^{5-}$ pentamer are unknown to date, the addition of a transition metal cation as heteroatom promotes the formation of larger disk–shaped cyclic species that can adjust to the size of the metallic ion, as exemplified by $[PdV_6O_{18}]^{4-}$, $[Cu_2V_8O_{24}]^{4-}$ and $[Ni_2(OH_2)_2V_{10}O_{30}(H_2O)_6]^{6-}$ heteromacrocycles[11] (Figure 2.4). The positive charge of the cationic heterometal at the center compensates the high negative charge of the larger cyclic polyoxovanadates. Another relevant example consists in the incorporation of anionic heteroatoms resulting in the generation of cage– or sphere–like high–nuclearity lacunary POVs whose specific shape enables them to entrap small guest species.[12] These type of POV spheres are formed through linkages of multiple square–pyramidal $\{VO_5\}^{7-}$ units, with the bottoms of all the pyramids pointing towards the center of the sphere where the guest heteroanion is hosted, whose interactions with the cationic vanadium atoms stabilize the whole spherical framework. The removal of a few V–O units from the spherical framework forms a lacunary POV, which is required in order to make the guest anion accessible from the outside. For example, the reaction of the reduced decavanadate $[V^{IV}_{2}V^{V}_{8}O_{26}]^{4-}$ with two F^- template anions yield the monolacunary undecavanadate, $[HV^{V}_{11}O_{29}F_2]^{4-}$.[13] This lacunary HeteroPOV consists on a belt layer composed of five $\{VO_5\}^{7-}$ units and two capping layers composed of $\{V_3\}$ units sandwiching the belt layer. In contrast, the incorporation of a Cl^- guest anion by oxidation of the reduced decavanadate affords a protonated trilacunary dodecavanadate, $[HV_{12}O_{32}(Cl)]^{4-}$ (Figure 2.4). These type of anionic cages were extensively studied by Müller's group and usually consist of V atoms showing mixed–valence or a fully–reduced state, as seen in $[V_{15}O_{36}(Cl)]^{5-}$, $[V_{18}O_{42}(X)]_n^-$ (X = H_2O, Cl^-, Br^-, I^-) and $[V_{22}O_{54}(ClO_4)]^{7-}$ cluster anions.[12,14] Moreover, the addition of transition metal complexes to these reduced cores can produce layered solid materials, as exemplified by the family of isostructural 2D hybrids constructed from the connection of the container cluster molecules $\{V_{18}O_{42}(X)\}$ (X = H_2O, Br–, Cl–) and the 3d–metalorganic moieties $\{M(H_2N(CH_2)_2NH_2)_2\}$ (M = Zn, Cd), among others.[15] In recent years, much effort has been oriented toward the preparation of silicato–, germanato–, arsenato–, and antimonato–derivatised heteroPOVs and their hybrid derivatives with middle and late transition metals.[16] The fully–oxidized (V^V), mixed–valent (V^V/V^{IV} and V^{IV}/V^{III}), ''*fully–reduced*'' (V^{IV}), and ''*highly–reduced*'' (V^{III}) heteroPOVs show an astonishing tendency for organic and transition metal/lanthanide functionalization granting access to multifunctional inorganic–organic supramolecular hybrid materials, and hence, offers potential applications in catalysis, surface science, and information technology.[16]

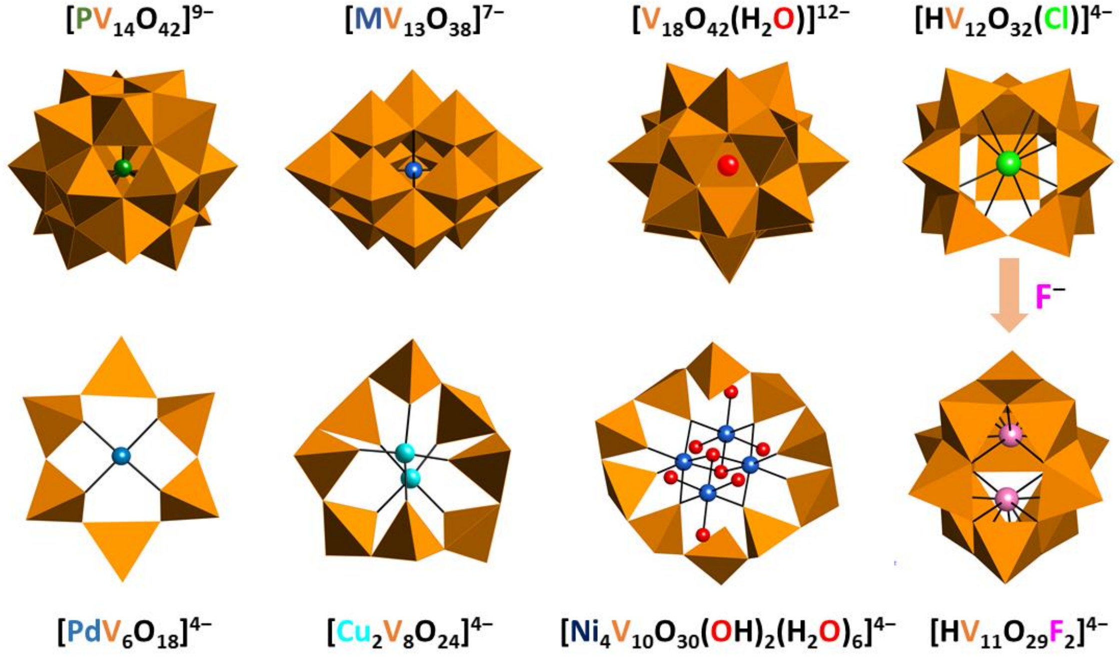

Figure 2.4. Polyhedral representation of some HeteroPOVs, along with the $[V_{18}O_{42}(H_2O)]^{12-}$ cage–type isoPOV.

2.1.2 Hybrid Vanadates

One of the main directions in POM chemistry over the last few years is the modification by assembling and interconnection of POM clusters with transition metal complexes, targeting the generation of novel structural types of hybrid materials with potential alteration or enhancement of their properties. As a subclass of POVs, hybrid vanadates are considered a promising candidate to construct such POV–based hybrid materials due to their structural heterogeneity and rich coordination chemistry, which allows not only for their diverse coordination environments but also for a wide variety of valence states.[17] Since the pioneering work of Zubieta et al.,[18] a huge number of hybrid low–nuclearity oxovanadates have been prepared,[17] most of them through hydrothermal methods. In such compounds, the most common coordination geometries shown by vanadium atoms are the regular tetrahedron and the distorted square pyramid, the oxidation state of which usually being V^V. In this sense, the most frequent inorganic building blocks in hybrid oxovanadates are the polymeric metavanadate $[VO_3]_n^{n-}$ chains and the $[V_4O_{12}]^{4-}$ cycles, both formed by corner–sharing $\{VO_4\}^{3-}$ tetrahedral units (Figure 2.1). The latter anion shows flexible nature and can be isolated in either planar or bent (boat or chair) conformations depending on the requirements of the crystal packing in terms of the establishment of coordinative bonds or networks of weak intermolecular interactions. The metavanadate subunit also possess a certain degree of adaptability to the crystal environment due to the reorientation and reorganization ability of the $\{VO_4\}^{3-}$ tetrahedra that form the chains. Only one type of metavanadate specie constructed from five–coordinated vanadium has been reported so far, which consists on edge–sharing square pyramids[19] (Figure 2.1).

There are two different but complementary ways to classify hybrid vanadates: Zavalij and Wittingham proposed a classification based on the coordination environment of the vanadium centers composed of seven categories according to the presence of tetrahedral (T), square–pyramid (SP) and/or octahedra (O) in the hybrids.[20] In contrast, the assortment made by Zubieta and coworkers[18] takes into account the role of the metalorganic building block in the crystal structure of the hybrid, which lies within the general classification described previously by Cheetam et al. for organic–inorganic hybrid materials in which a code I^nO^m is proposed.[21] This code is based on the dimensionality of both the inorganic and organic substructures within the hybrid crystal, where I^n and O^m refers to the dimensionality for each array (n, m = 0, 1, 2, 3). Nowadays, a huge library of hybrid vanadates showing an enormous structural and dimensional variety can be found in crystallographic databases. The analyses of those oxovanadate–based crystal structures reveals that I^3O^2, I^3O^1, I^2O^2 and I^2O^1 architectures are the most common ones.[17] This indicates that the crystal structures of most vanadate hybrids usually contain metalorganic mono– or bidimensional sublattices within the 3D or 2D covalent inorganic framework, that is, both frameworks show a tendency to organize into high dimensional packings.

Regarding the metalorganic building blocks, up to now Mn(II), Fe(II), Co(II), Ni(II), Cu(II), Cu(I), Zn(II) 3d–metal centers have been employed in conjunction with simple, bi–, tri– and tetrapodal N– and/or O–donor ligands to construct hybrid vanadates, as well as Ag(I) and Cd(II) 4d–metallic ions. In this sense, Mn(II), Co(II), Ni(II) and Cd(II) cations usually show regular octahedral coordination environments, even though a few examples of hybrids with five coordinated Co(II) cations are known. The great variety of coordination modes displayed by Cu(II) and Zn(II) atoms (CN = 4–6) makes more difficult the prediction of the structural archetypes that result from their interaction with vanadate building blocks, but at the same time enlarges the rich structural diversity of Zn(II) and Cu(II) vanadates in comparison with those obtained from cations possessing regular octahedral coordination spheres. For Cu(I) and Ag(I), however, the coordination spheres are less predictable, although they can favor the formation of monodimensional metalorganic subnets with certain types of ligands due to their linear coordination. The chemical nature of the organic ligand as well as its length, geometry and relative position of the donor groups within it heavily determine the final structure and crystal dimensionality of the resulting hybrid vanadate. In this sense, several organic ligands such as 2,2–bipyridine, 1,10–phenanthroline and terpyridine have been used to organically functionalize vanadate units, resulting in I^nO^m (n = 1–3, m = 0) structures with discrete metalorganic building blocks.[22] In contrast, bidentate ligands like pyrazine, pyrimidine, 4,4'–bipyridine, and dipodal 1,2–di(4–pyridyl)ethylene and 1,2–di(4–pyridyl)ethane, as well as 1,4–bis(imidazol–1–yl)butane and 1,4–bis(triazol–1–ylmethyl)benzene, usually lead to the formation of high–dimensional architectures both for the inorganic main framework and the metalorganic substructure (I^nO^m where n=2–3, m=0–3) because of their capability to act as bridging ligands.[23] In close analogy, the use of multipodal amino ligands such as 1,2,4–triazole, 5–(pyrimidin–2–yl)tetrazole, tetra–2–pyridylpyrazine, 2,4,6–tri(4–pyridyl)–1,3,5–triazine and 6',6''–bis(2–pyridyl)–2,2':4',4'':2'',2'''–quaterpyridine, among others, show a similar tendency for extended inorganic and organic architectures for the resulting hybrid vanadates.[24] Besides amines, multipodal ligands carrying the carboxylic function have been also employed, as exemplified by oxalate or terephthalate ligands.[25] Another strategy to obtain organic–inorganic vanadates with varied dimensionality consist in using ligands containing both amino and carboxylate donor groups like 2–pyrazinecarboxylate and 4,4'–bipyridine–2–carboxylate.[26]

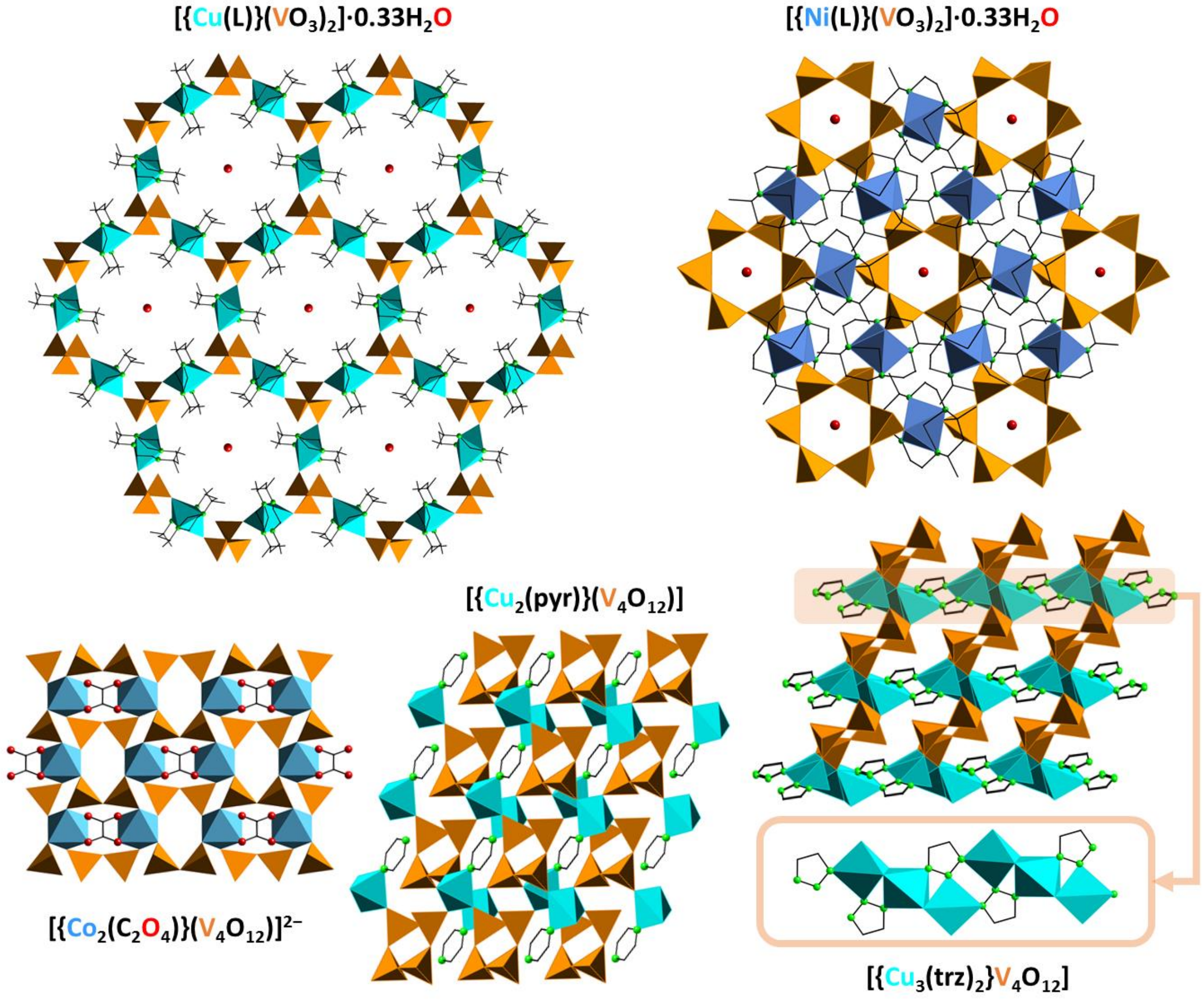

Figure 2.5. Structural diversity in some representative 3D covalent hybrid vanadates. Organic ligands: L = 5,5,7,12,12,14–hexamethyl–1,4,8,11–tetraazacyclotetradecane; pyr = pyrazine; trz = 1,2,3–triazolate.

One of the many types of extended high–dimensional IsoPOV–based hybrids are those that are characterized by a 3D covalent inorganic network constructed from the linkage between the transition metal centers of discrete metalorganic complexes and the vanadate polyhedra,[27] and hence, belong to the I^3O^0 group. The hybrid $[\{Ni(L)\}(VO_3)_2]\cdot 0.33H_2O$ and $[\{Cu(L)\}(VO_3)_2]\cdot 0.33H_2O$ (L = 5,5,7,12,12,14–hexamethyl–1,4,8,11–tetraazacyclotetradecane) vanadates prepared by Ou and coworkers[27] constitute two representative examples of this group (Figure 2.5). In these compounds, the equatorial plane of the metal centers is occupied by four N atoms belonging to the L ligand while the axial oxygen atom is shared with the metavanadate chains (Ni) or hexanuclear $[V_6O_{18}]^{6-}$ rings (Cu). This connectivity generates a porous 3D covalent framework with hexagonal channels in which water molecules of hydration are hosted. Similarly, Zubieta et al. synthetized a $[\{Cu_2(pyr)\}(V_4O_{12})]$ cyclotetravanadate–based hybrid under hydrothermal conditions with Cu–organonitrogen bridging complexes (pyr = pyrazine), which is built from binuclear subunits of two square piramidal $\{CuO_4N\}$ sites linked through the pyr ligand[28] (Figure 2.5). This way, the cyclic clusters serve to connect eight neighboring $\{Cu_2(pyr)\}^{4+}$ subunits which provides the three–dimensional covalent connectivity. Two interesting examples of hybrids also belonging to the I^3O^0 group are $(H_2en)[\{Co_2(Ox)\}(V_4O_{12})]$ and $(H_2pn)[Mn_2(Ox)(V_4O_{12})]$ extended compounds (en = ethylendiamine; pn = 1,3–diaminopropane, ox = oxalate), both of them containing bridging ox ligands.[29] These hybrid vanadates are formed by discrete metal–oxalate dimers which are linked through the $\{V_4O_{12}\}^{4-}$ cyclic anions resulting in 3D inorganic–organic arrangements, where the protonated amines act as templates compensating for the negative charge of the hybrid net (Figure 2.5). Within this category, a great number of extended hybrid vanadates have been prepared using chelating ligands as linkers between the building blocks, such as ethylenediamine, N,N–*bis*(3–aminopropyl)ethylenediamine, and 1,3–diaminopropane.[30] It must be noted that almost all of these types of hybrids have been synthetized using hydrothermal methods.

As mentioned before, the organic ligand can act as a bridge between adjacent metal centers, and thus, a polymeric metal–organic substructure is generated within the 3D inorganic framework. When the mentioned substructure generates chains, the resulting hybrid crystal architectures are classified as I^3O^1. For example, the 3D $[\{Cu_3(trz)\}_2V_4O_{12}]$ hybrid (trz = 1,2,3–triazolate) reported by Zubieta et al. is constructed from metalorganic $\{Cu_3(trz)_2\}_n^{+4n}$ chains, each constituted by trinuclear Cu(II) clusters connected to tridentate trz ligands, that are linked through cyclic $\{V_4O_{12}\}^{4-}$ clusters forming a hybrid 3D framework[28] (Figure 2.5). In close analogy to the previous case, if the linkage between metal centers and bridging ligands generates layers instead of chains, a I^3O^2 type hybrid is obtained. Such is the case observed for $[\{M_2(H_2O)_2(4,4'\text{–}Bpy)_3\}(VO_3)_4]\cdot 2.5H_2O$ (M = Ni^{II}, Co^{II}), where the metal centers are connected along two different directions through the bidentate 4,4'–bipyridine ligand, generating rectangular–like interpenetrated metal–organic sheets.[31] The metavanadate chains are located between the metal centers of different metal–organic layers, connecting them to generate the three–dimensional I^3O^2 type inorganic framework. Despite the interpenetration, not all I^3O^2 hybrids show this kind of structural phenomenon although it must be noted that it is common for hybrid vanadates within this category.[17] Finally, the I^3O^3 archetype is characterized by the coexistence of both 3D inorganic and metal–organic substructures as exemplified by [{Ni₈(4,4'–

$Bpy)_{16}\}(V_{24}O_{68})]\cdot 8.5H_2O$ hybrid oxovanadate.[32] The metal–organic substructure consists on the polycatenation of a “CdS”–like 3D metal–organic net with two square–like metal–organic layers, where the vanadium oxide chains are located and linked via corners to the Ni(II) metal cations (Figure 2.6). As in metal–organic framework materials (MOFs), the transition metal hybrid vanadates constructed from di– or multipodal ligands often leads to the generation of high–dimensional metal–organic sub–structures through the linkage of the metal atoms and the organic ligands.[17] The occurrence of the high dimensionality of the metalorganic subnet could originate because of the small sizes and notable flexibility of the inorganic building blocks in these hybrids vanadates, as metalorganic extended assemblies built from larger and more rigid POM clusters usually do not usually exhibit this type of interpenetration phenomenon.

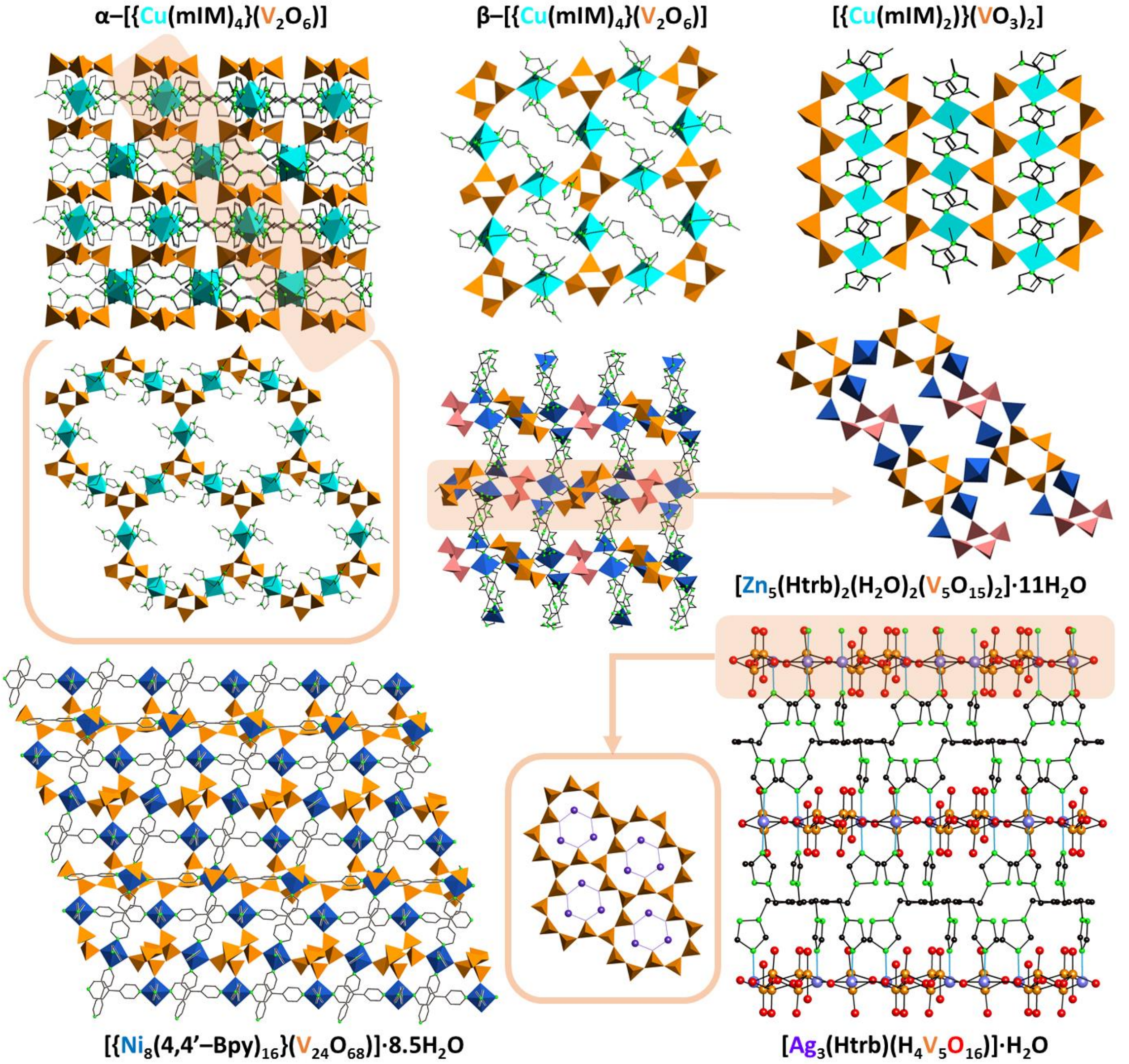

Figure 2.6. Structural diversity in some representative extended hybrid vanadates. Organic ligands: mIM = 1–methylimidazole; Htrb = hexakis(1,2,4–triazol–ylmethy1)benzene; 4,4’–Bpy = 4,4’–bipyridine.

The organic derivatization of vanadates with 3d–metalorganic moieties to construct extended open–frameworks constitutes a promising strategy for the preparation of new functional hybrid materials.[17,33] Recently, Li et al. prepared a series of extended hybrid copper vanadates: α–[{Cu(mIM)$_4$}(V$_2$O$_6$)] cyclotetravanadate which shows a 3D covalent framework with an interpenetrating diamond topology, and two layered metavanadate hybrids, namely β–[{Cu(mIM)$_4$}(V$_2$O$_6$)], and [{Cu(mIM)$_2$)}(VO$_3$)$_2$] (mIM = 1–methylimidazole, Figure 2.6). While all three compounds exhibit excellent catalytic performance in the oxidation of sulfides in heterogeneous phase with H_2O_2 as oxidant, the catalytic activity of the α–tetravanadate isomer outperforms the others and can be reused without losing its activity. The authors attributed this difference to the 3D interpenetrating framework of the cyclotetravanadate derivative that may result in more exposure of the active sites than 2D network structures of the latter, and thus, enhance the catalytic activity. The activity of the former was also investigated in the oxidation of various alcohols, and excellent results were obtained as well. Among others, compounds [Zn$_5$(Htrb)$_2$(H$_2$O)$_2$(V$_5$O$_{15}$)$_2$]·11H$_2$O and [Ag$_3$(Htrb)(H$_4$V$_5$O$_{16}$)]·H$_2$O has been hydrothermally synthesized using a multidentate N–containing hexakis(1,2,4–triazol–ylmethy1)benzene (Htrb) by Zhang and coworkers.[33b] The former consist on unusual inorganic layers containing both tetranuclear $[V_4O_{12}]^{4-}$ and hexanuclear $[V_6O_{18}]^{6-}$ rings linked through bridging Zn–complexes, which are further pillared by chains of Htrb ligands (I^2O^1, Figure 2.6). In comparison, the structure of yet another extended hybrid prepared by the same authors can be described as an unique 2D inorganic layers formed by adjacent 12–membered vanadium rings built of {VO$_4$} tetrahedra and $\{VO_5\}^-$ trigonal bipyramids and Ag(I) centers, where the layers are further extended by Htrb ligands and Ag(I) centers into a 3D framework (Figure 2.6). These hybrid POVs show high photocatalytic activity towards the degradation of methylene blue and methyl orange organic pollutants under UV light irradiation, as well as a remarkable capacity as fluorescent probe for Cr^{3+} ions, showing strong and selective emission quenching effects for the former over other metal ions such as Zn^{2+}, Al^{3+}, Co^{2+}, K^+, Na^+, and Pb^{2+}. These examples nicely illustrate the potential occurrence of new interesting properties born from the synergy of the different building blocks that ultimately lead to hybrid extended functional frameworks with novel architectures and expanded applicability.

2.1.3 Decavanadate–based Hybrid Compounds

Decavanadate $(H_nV_{10}O_{28})^{n-6}$ (n = 0–4) polyanions, which are the predominant POV species in the acidic pH range, have recently attracted significant attention due to their intriguing role in biomedicine, as they have been proven to impact proteins, lipidic structures and also cellular functions.[34] The structure of the decavanadate anion, which was reported for the first time back in 1956, consists in an arrangement of 10 edge–shared {VO$_6$} octahedra with ideal D_{2h} symmetry. This arrangement can be described as a central {V$_6$O$_{12}$} cluster built of six {VO$_6$} octahedra arranged in a 2 × 3 rectangular array and capped with two additional {VO$_6$} units on both sides (Figure 2.1).

While the coordinative role of small polyoxovanadates like the metavanadate species toward transition–metal metalorganic moieties has been extensively investigated,[17] hybrids consisting of $[H_nV_{10}O_{28}]^{(6-n)-}$ clusters covalently linked to 3d–metal complexes have been rarely reported up to now. Moreover, most of the decavanadate–metalorganic hybrids known at present consists in *class I* hybrids,[35–44] in which the structural stability of the crystal lattice simply relies on electrostatic forces and weak intermolecular interactions between the different components. In this sense, several 3d–metal (Fe^{II} to Zn^{II}) containing organic building blocks have been used resulting in various decavanadate–containing ionic crystals with imidazole–type complexes such as $[Co(pyim)_3]_2[V_{10}O_{28}]\cdot7H_2O$ and $[Ni(pyim)_3]_2[H_2V_{10}O_{28}]\cdot4H_2O$[35] (pyim = 2–(2–pyridyl)–imidazole) while the use of aminoacids like glycine and β–alanine led to $(NH_4)_2[Mn_2(HGly)(H_2O)_{10}][V_{10}O_{28}].(HGly).2H_2O$, $(NH_4)[Mn(\beta\text{–}HAla)(H_2O)_5]_2[V_{10}O_{28}].2H_2O$[36] as well as $(NH_4)_2[Zn(H_2O)_5(\beta\text{–}HAla)]_2[V_{10}O_{28}].4H_2O$ and $(NH_4)_2[Mn(H_2O)_5(\beta\text{–}HAla)]_2[V_{10}O_{28}].2H_2O$ (HGly = glycine, β–HAla = β–alanine) hybrid salts.[37] Chelating ligands like *salen* have been also incorporated as charge compensating units to decavanadate ionic assemblies as seen in $(NH_4)_2[Mn(salen)(H_2O)_2]_4[V_{10}O_{28}].6H_2O$ hybrid (salen = N,N'–ethylene–bis(salicylideneiminate)[38] and the use of zinc complexes of bis–triazol ligands resulted in various *class I* hybrids like $[Zn(bte)(H_2O)_4][Zn_2(bte)(H_2O)_{10}][V_{10}O_{28}]\cdot8H_2O$ as well as $[Zn_2(btp)_4(H_2O)_6][H_2V_{10}O_{28}]\cdot4H_2O$, $[Zn_2(bth)(H_2O)_{10}][H_2V_{10}O_{28}].6H_2O$ and $[Zn_3(Htrz)_6(H_2O)_6][V_{10}O_{28}]\cdot10H_2O\cdot Htrz$ compounds[39] (bte = 1,2–bis(1,2,4–triazol–1–yl)ethane, btp = 1,3–bis(1,2,4–triazol–1–y1)propane, bth = 1,6–bis(1,2,4–triazol–1–y1)hexane, Htrz = 1,2,4–triazole). The non–covalent interaction between decavanadates and bicyclic diazaalkene was also studied in the isostructural $(NH_4)_2[M(dod)(H_2O)_4]_2[V_{10}O_{28}].6H_2O$ (M = Mn, Zn; dod = 1,4–diazoniabicyclo[2,2,2]octane–1,4–diacetate) salts[40] whereas the use of heterocyclic ligands like phenantroline in conjunction with divalent copper or iron metals yielded $[Cu(H_2O)_3(phen)]_2[H_4V_{10}O_{28}].4H_2O$ and $[Fe(phen)_3]_2[V_{10}O_{28}].15H_2O$ (phen = 1,10–phenantroline) derivatives.[41] Ionic crystals containing both decavanadates and Cu^{II} and Ni^{II} complexes of pyrazine have been also reported in $(H_3O)_2\{[Cu(pyr)(H_2O)_4]_2[V_{10}O_{28}].13.5H_2O$ and $\{[Ni(pyr)(H_2O)_4]_2(H_3O)_2[V_{10}O_{28}].9.5H_2O$ (pyr = pyrazine) compounds, respectively.[42]

Besides transition metals belonging to the first row, other metalorganic cations that contain 4d– or 5d–metals acting as structure–directing agents in decavanadate assemblies have been also evaluated. For example, Jansen et al. used a bulky cationic gold clusters $[Au_9(PPh_3)_8]^{3+}$ (PPh_3 = triphenylphosphine) resulting in a supramolecular assembly of the ionic $[Au_9(PPh_3)_8]_2[V_{10}O_{28}H_3]_2$ crystal, which is governed by intermolecular hydrogen bonds and C–H/π interactions between the POVs and the phenyl rings of the ligands of the cationic gold cluster complexes.[43] The latter interactions arise from adjacent phenyl groups being in edge–to–face orientation, which is a common structure–directing motif in inorganic supramolecular chemistry, as this disposition has shown to contribute substantially to the overall lattice energy. Meyer et al. developed a new strategy for the preparation of Ag(I)–POM hybrids which allowed them to synthetize a decavanadate specie, namely $[Ag(thb)_2]_2(H_4V_{10}O_{28})\cdot3H_2O$ (thb = theobromine).[44] This elegant method takes advantage of the ability of purine bases to build robust non–covalent networks of hydrogen bonds and stacking interactions using them as ligands to silver(I). This way, the H–bonding framework of the hybrid POV is dominated by amide–to–amide theobromine dimers and amide–to–POM/H_2O hydrogen bonds, as well as π–π and anion–π stacking interactions that contribute to the overall structural stabilization for the resulting decavanadate–based hybrid (Figure 2.7).

Concerning decavanadate *class II* hybrids, the first crystal structure involving metalorganic complex moieties covalently linked to the surface of decavanadate anions was not reported until 2007,[45] which consisted in a discrete hybrid built from a diprotonated decavanadate cluster grafted to Cu(II) complexes of 2,2'–bipyridine moieties, namely

$[\{Cu(bipy)_2\}]_2\{H_2V_{10}O_{28}\}].bipy.H_2O$. In this covalent molecular compound, the copper(II) exhibits distorted trigonal bipyramidal geometry, where the equatorial plane is defined by the oxo–bridge to the vanadium core and a nitrogen atom from each bipyridine ligand, while the axial positions are occupied by the remaining nitrogen donors. Since the coordination sphere of the copper does not have any free positions, the dimensionality of the crystal is limited to a 0D architecture (I^0O^0). Compared to the extensive low–nuclearity isoPOV hybrids, the coordination of 3d transition–metal containing metalorganic moieties to the larger decavanadate clusters has met limited success. Moreover, almost all hybrid covalent decavanadate–containing hybrids that have been prepared later on consist in low dimensionality crystal packings, that is, either similar discrete decorated molecular clusters (I^0O^0)[46,39,47,48] or mono–dimensional arrangements (I^1O^n with n = 0–2).[27,39,44,49–51] It is worth mentioning that only Cu(II) and Zn(II)–based 3d–metalorganic moieties have been successfully grafted so far to the surface of a decavanadate anion by either conventional synthesis or hydrothermal methods. Examples of the former can be found in the discrete $(2\text{–}hepH^+)_2[\{Cu(H_2O)_2(O,N\text{–}2\text{–}hep)\}_2(V_{10}O_{28})].6H_2O$ and $[\{Cu(2\text{–}amp)_2(H_2O)\}_2(H_2V_{10}O_{28})].4H_2O$ molecular pyridyl–derivatives (2–hep = 2–(2–hydroxyethyl)pyridine); amp = 2–(aminomethyl)pyridine, Figure 2.7).[47] The covalent interaction between $\{Cu(en)_2\}^{2+}$ cationic moieties and decavanadate clusters were investigated in the I^0O^0–type $(H_3O)_2[\{Cu(en)_2(H_2O)\}_2(V_{10}O_{28})].3H_2O$[48] and $[\{Cu(en)_2(H_2O)\}_2(H_2V_{10}O_{28})].12H_2O$[46b] decorated compounds (en = ethylendiamine) while $\{Zn(Im)\}^{2+}$ moieties lead to the discrete $[\{Zn(Im)_2(dmf)_2\}_2(H_2V_{10}O_{28})]\cdot Im\cdot dmf$ (Im = imidazole, dmf = dimethylformamide) hybrid.[39a]

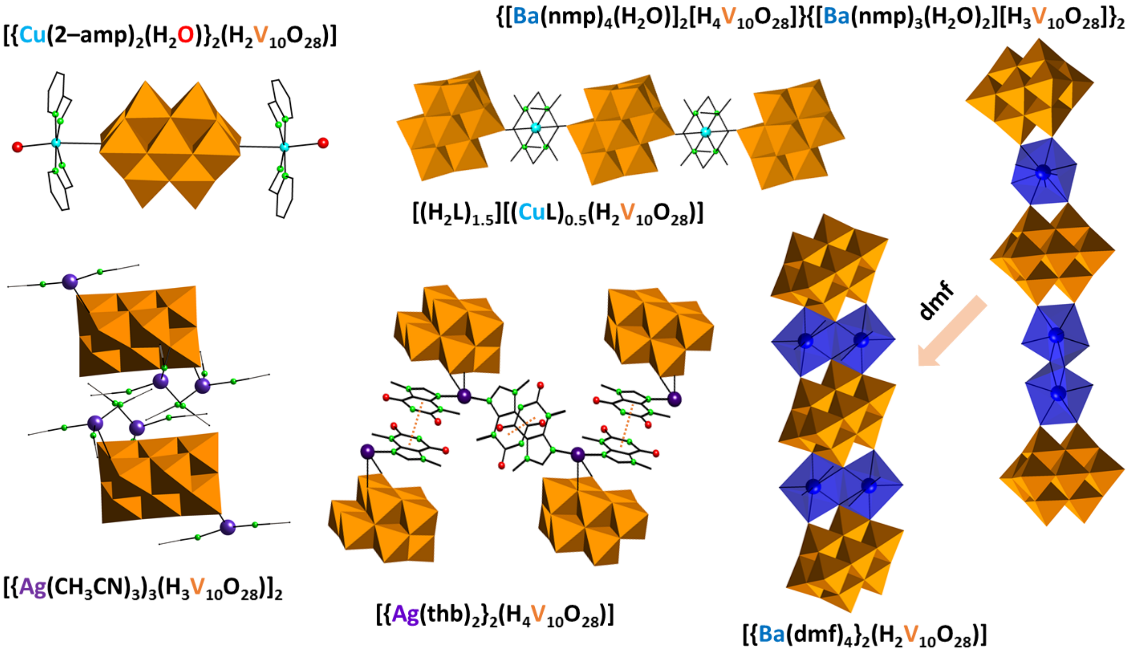

Figure 2.7. Polyhedral representation of some relevant hybrid decavanadates found in the literature. Organic ligands: 2–amp = 2–(aminomethyl)pyridine; nmp = N–methyl–2–pyrrolidone; thb = theobromine; dmf =. N,N–dimethylformamide; nmp and dmf molecules are omitted for clarity.

Regarding decavanadate–based monodimensional assemblies, the use of Zn(II) together with organic ligands such as triazol–derivatives produced the I^1O^1 $\{Zn(H_2O)_6\}[\{Zn(btb)\}_2(H_2O)_6(V_{10}O_{28})].4H_2O$ (btb = 1,4–bis(1,2,4–triazol–1–y1)butane) as well as the I^1O^2–type $[\{Zn(trz)\}_3(H_2O)_4(dmf)_2(V_{10}O_{28})]\cdot 4H_2O\}_n$ (trz = 1,2,4–triazolate) hybrids,[39] respectively. The following monodimensional (I^1O^0) assemblies containing M(II)–ethylendiamine (M = Cu, Zn) moieties can be found in $[Cu(en)_2(H_2O)]_{2.2}[Cu(en)_2(V_{10}O_{28})].2H_3BO_3.2H_2O$;[49] and $[Zn(en)_2]_3[V_{10}O_{28}].5H_2O$ hybrids.[50] The use of copper(II)–complexes of β–alanine[51] also resulted in 1D architectures in $(NH_4)_2[\{Cu(\beta\text{–}Ala)_2\}_2(V_{10}O_{28})].10H_2O$ hybrid, whereas the use of macrocyclic tetraazapolyamines[27] yielded the $[(H_2L)_{1.5}][(CuL)_{0.5}(H_2V_{10}O_{28})].6H_2O$ hybrid chains (L = 5,5,7,12,12,14–hexamethyl–1,4,8,11–tetraazacyclotetradecane, Figure 2.7). Besides 3d–metalorganic moieties, a few other interesting approaches worth mentioning have been applied to prepare novel decavanadate–based molecular as well as monodimensional hybrids in recent years. For example, McGlone et al. succesfully synthetized an unprecedent silver(I)–linked decavanadate dimer with the formula $\{(Ag(CH_3CN)_3)_3[H_3V_{10}O_{28}].CH_3CN\}_2$, prepared from $(TBA)_3[H_3V_{10}O_{28}]$ in acetonitrile (TBA = *tert*–butylammonium), which exhibits a distinctive dimeric configuration entirely supported by cooperative hydrogen bonds[46a] (Figure 2.7).

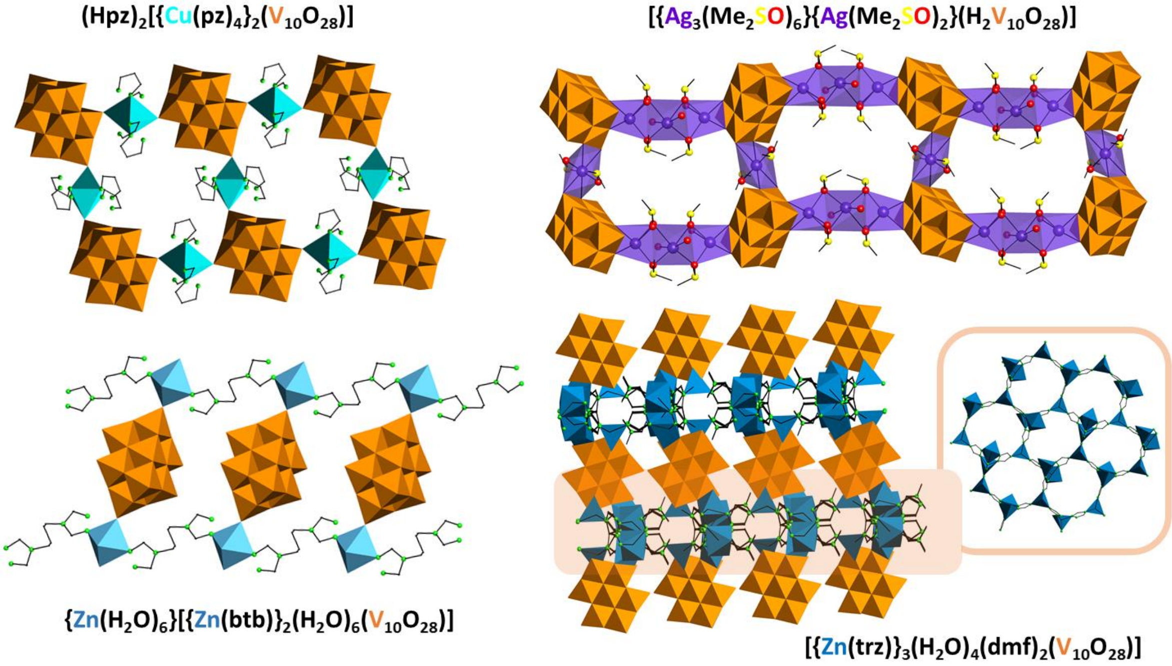
$(Hpz)_2[\{Cu(pz)_4\}_2(V_{10}O_{28})]$

$[\{Ag_3(Me_2SO)_6\}\{Ag(Me_2SO)_2\}(H_2V_{10}O_{28})]$

$\{Zn(H_2O)_6\}[\{Zn(btb)\}_2(H_2O)_6(V_{10}O_{28})]$

$[\{Zn(trz)\}_3(H_2O)_4(dmf)_2(V_{10}O_{28})]$

Figure 2.8. Polyhedral representation of some representative 2D and chain–like hybrid decavanadates found in the literature. Organic ligands: pz = pyrazole ; btb = btb = 1,4–bis(1,2,4–triazol–1–y1)butane; trz = 1,2,4–triazolate; dmf = N,N–dimethylformamide.

Recently, Streb et al. developed a new synthetic route for the assembly of monodimensional Ba(II)–linked decavanadate arrays by using bulky coordinating solvents featuring both a binding site and a blocking site to allow the controlled linkage of the $[V_{10}O_{28}]^{6-}$ clusters by the alkaline earth metal centers. This way, the complex supramolecular $\{[Ba(nmp)_4(H_2O)]_2[H_4V_{10}O_{28}]\}\{[Ba(nmp)_3(H_2O)_2][H_3V_{10}O_{28}]\}_2.2H_2O.10nmp$ compound can be accessed in nmp solvent (nmp = N–methyl–2–pyrrolidone), where alternating mono– and di–nuclear barium subunits coordinate to the triprotonated decavanadates forming a linear covalent hybrid chain (Figure 2.7). Interestingly, replacement of the solvent by dmf results in a less complex 1D architecture, the formula of which is $[\{Ba(dmf)_4\}_2(H_2V_{10}O_{28})]$ and it is formed with just dinuclear barium(II) linkers (dmf = N,N–dimethylformamide).[52] Mat et al. managed to construct a novel monomeric silver(I)–alkynyl cluster encapsulating a decavanadate cluster, $[Ag_{40}(C{\equiv}C^tBu)_{22}(TFA)_{12}(V_{10}O_{28})]\cdot 4CH_3OH$ (TFA = trifluoroacetate) following an acid–induced synthetic approach.[53] The authors described it as a neutral ellipsoidal C*2h* cluster consisting of forty silver(I) ions stabilized by centripetal ethynyl, peripheral trifluoroacetate and methanol ligands along with a $[V_{10}O_{28}]^{6-}$ cluster at its center.

To the best of our knowledge, only two decavanadate/metalorganic hybrid lattices with covalent bidimensional nature (I^2O^0) can be found in the literature,[54] namely $(Hpz)_2[\{Cu(pz)_4\}_2(V_{10}O_{28})]\cdot 2H_2O$ (pz = pyrazole) and $[\{Ag_3(dmso)_6\}\{Ag(dmso)_2\}(H_2V_{10}O_{28})]\cdot 2dmso$ (dmso = dimethylsulfoxide, Figure 2.8). The crystal structure of the former consists on a covalent arrangement of hybrid sheets formed by $[\{Cu(pz)_4\}_2(V_{10}O_{28})]$ in which each decavanadate cluster is linked to four $\{Cu(pz)_4\}$ groups through the V–O–Cu connectivity. All the copper centers are bonded to four equatorial N atoms from the organic ligands with the remaining tow positions occupied by oxygen atoms belonging to two neighboring clusters. Interestingly, charge compensating pyrazolium cations and water molecules fill the hydrophilic pockets that are generated by this connectivity between the $\{Cu–(pyrazol)\}^{2+}$ moieties and the inorganic clusters[54a] (Figure 2.8).The building blocks of the Ag–containing POV however, contain diprotonated decavanadate clusters $[H_2V_{10}O_{28}]^{4-}$ as their main backbone, which are bridged by linear trimeric silver(I)–dmso $[Ag_3(dmso)_6]^{3+}$ subunits coordinated to the cluster through covalent Ag–O–V bonds. In addition, a monomeric silver(I) $[Ag(dmso)_2]^+$ moiety acts as a secondary linker between neighboring clusters resulting in the formation of the layered covalent framework[54b] (Figure 2.8). It is worth highlighting however, that none of these two hybrid compounds show porosity because of an alternate stacking of sheets that renders the cation/solvent–filled voids inaccessible.

In close analogy to vanadates, grafting 3d–transition metal complexes to decavanadate polyanions can result in additional functionalities to the resulting hybrid. For example, Wang et al. recently reported the supramolecular $\{Zn(H_2O)_6\}[\{Zn(btb)\}_2(H_2O)_6(V_{10}O_{28})].4H_2O$ (btb = 1,4–bis(1,2,4–triazol–1–y1)butane) hybrid. In this I^1O^1–type crystal packing, the decavanadate clusters connect two adjacent $\{Zn(btb)\}^{2+}$ metalorganic chains together, resulting in ladder–like chains which interact via weak supramolecular interactions (Figure 2.8). This compound was used as solid modifiers to fabricate three–dimensional bulk–modified carbon paste electrodes and the results of the electrochemical properties indicated a good electrocatalytic activity towards the oxidation of nitrite molecules.[39a] In contrast, the $[\{Zn(trz)\}_3(H_2O)_4(dmf)_2(V_{10}O_{28})]\cdot 4H_2O\}_n$ hybrid (trz = 1,2,4–triazolate, dmf = N,N–dimethylformamide), as it is constructed from cationic $[Zn_3(trz)_3–(H_2O)_4(dmf)]$ layers which are pillared by decavanadate anions[39b] (Figure 2.8). This compound, as well as the ionic $[Zn_3(Htrz)_6(H_2O)_6][V_{10}O_{28}]\cdot 10H_2O\cdot Htrz$ hybrid were reported by Xu and coworkers. These compounds exhibit interesting optical properties in the solid–state at room temperature like intense blue luminescence for the layered hybrid, while the ionic salt possess an infrequent fluorescent property, emitting both blue and yellow luminescences simultaneously, which makes it a good candidate for photoactive materials. This study illustrates how the incorporation of 3d–metal complexes can bestow extra properties to the resulting hybrid and consequently, extend its potential applicability.

2.1.4 SCSC Transformations in Polyoxovanadates

As one of the first examples of a solid–state phase transition involving POM species for which the initial and final stages of the transformation were structurally characterized on the basis of single–crystal X–ray diffraction (XRD), the ring–opening of the cyclic $[V_4O_{12}]^{4-}$ tetravanadate species and subsequent polymerization into a *catena*–form was reported in 1996 for the *tert*–butylammonium salt of this anion.[55] Nucleation and growing of the polymeric metavanadate phase was found to take place within crystals of the *tert*–butylammonium salt of the cyclic anion and the process was monitored by a combination of infrared spectroscopy and powder XRD techniques. Unfortunately, this transformation was of the single–crystal–to–crystalline–powder type which involved the loss of integrity of the single crystals, but the authors were fortunate enough to grow single crystals of the *catena*–form by recrystallization of this powder. This allowed for proposing an irreversible, reconstructive and continuous transition proceeding through a nucleation and growing mechanism on the basis of structural similarities.

As mentioned in chapter 1, single–crystal–to–single–crystal transformations (SCSC), in which crystalline order and integrity is retained along the whole process, are at the forefront of the crystal engineering because they offer an incomparable tool to provide direct insight into the mechanism of such structural changes, to monitor how location of atoms and molecules varies within the crystal packing, and to correlate how a given property of interest can be modified and tuned as a consequence.[56] Regarding SCSC transformations, however, just three examples concerning polyoxovanadate compounds can be found in the literature (disregarding those discussed in this chapter). Two of them are *class II* hybrids consisting on the cyclotetravanadate cluster with grafted cobalt(II) metalorganic complexes, namely, $[Co(Hbpe)_2(V_4O_{12})]$ (bpe = 1,2–di(4–pyridyl)ethane) and $[Co_4(ppca)_4(H_2O)_2(V_4O_{12})]\cdot 3.6H_2O$ (ppca = 4–(pyridin–4–yl)pyridine–2–carboxylate).[57] The former study nicely illustrates a case of temperature–dependent polymorphism promoted by order–disorder crystal phase transitions in POM–based systems. This compound is able to undergo two sequential SCSC transformations into polymorphs of higher symmetry as the temperature increases.[57a] In contrast, the evacuation of guest solvent molecules does not only promote SCSC transformations in robust compounds able to preserve their crystalline architecture nearly unaltered upon phase transition, but they are also known for dynamic compounds in which the transformation proceeds with modifications in the crystal framework and/or the covalent bonding scheme. This is exactly the case for the second polyoxovanadate–based hybrid $[Co_4(ppca)_4(H_2O)_2(V_4O_{12})]\cdot 3.6H_2O$ (ppca = 4–(pyridin–4–yl)pyridine–2–carboxylate) reported by zur Loye et al. back in 2005.[57b] This study represents an illustrative example of such type of dynamic POM–based compounds as it undergoes two sequential SCSC transformations triggered by thermal dehydration to lead to the partially dehydrated intermediate $[Co_4(ppca)_4(H_2O)_2(V_4O_{12})]\cdot 1.1H_2O$ first, and then to the anhydrous $[Co_4(ppca)_4(V_4O_{12})]$ derivative, which resulted in significant changes in the Co^{II} coordination geometry of the metalorganic moieties. Last year, Ou and coworkers prepared the 3D covalent $[\{(Ni(cyclam)\}_3(VO_3)_6]\cdot 5H_2O$ hybrid built from hexanuclear vanadate $[V_6O_{18}]^{6-}$ rings linked to $\{Ni(cyclam)\}^{2+}$ moieties.[58] This compound is able to undergo a reversible thermally triggered

SCSC transformation leading to the anhydrous phase, which is very similar to the hydrated parent structure, confirming the robustness of the initial hybrid framework.

2.1.5 Summary

In the first section of this chapter, the synthesis and crystallochemical characterization of a new porous I^3O^0 hybrid built of metavanadate anions and $\{Cu(cyclam)\}^{2+}$ cationic complexes was carried out, namely $[\{Cu(cyclam)\}(VO_3)_2]\cdot 5H_2O$ (**1–CuV**). This dynamic structure undergoes three sequential and reversible SCSC transformations promoted by gradual dehydration upon heating. The structural modifications induced by the removal of the water molecules resulted in the generation of three new crystalline phases, namely $[\{Cu(cyclam)\}(VO_3)_2]\cdot 3H_2O$ (**2–CuV**), $[\{Cu(cyclam)\}(VO_3)_2]\cdot 1.3H_2O$ (**3–CuV**) and the anhydrous compound $[\{Cu(cyclam)\}(VO_3)_2]$ (**4–CuV**). All of these new phases retain porosity and show channels with different sizes that are determined by the thermally triggered structural modifications. In comparison, the first supramolecular POMOF–like compound assembled from the stacking of covalent layers formed by decavanadate anions and metalorganic linkers, namely $[Cu(cyclam)][\{Cu(cyclam)\}_2(V_{10}O_{28})]\cdot 10H_2O$ (**1–CuV10**) (cyclam = 1,4,8,11–tetraazacyclotetradecane) shows a robust thermostructural behaviour. The robustness and the associated permanent microporosity of its I^2O^0 open–framework has been confirmed by single–crystal X–ray diffraction studies on the thermally generated anhydrous phase **1a–CuV10**, as well as by gas sorption measurements that reveal selective adsorption of CO_2 over N_2. The catalytic activity toward the C–H bond activation of highly stable tricyclic alkanes like adamantane has been assessed in heterogeneous phase as well.

2.2 EXPERIMENTAL SECTION

2.2.1 Materials and Methods

The *tert*–butylammonium metavanadate $[(CH_3)_3CNH_3][VO_3]$ and dihydrogendecavanadate $[(CH_3)_3CNH_3]_4[H_2V_{10}O_{28}]\cdot 8H_2O$ precursors were synthesized according to literature methods and identified by infrared (FT–IR) spectroscopy.[55,59] All other chemicals were obtained from commercial sources and used without further purification. Carbon, hydrogen and nitrogen were determined on a Perkin–Elmer 2400 CHN analyzer. FT–IR spectra were obtained as KBr pellets on a SHIMADZU FTIR–8400S spectrometer. The thermogravimetric (TGA) analyses were carried out from room temperature to 800 °C at a rate of 5 °C min^{-1} on a Mettler Toledo TGA/SDTA851^e thermobalance under a 50 cm^3 min^{-1} flow of synthetic air in the case of **1–CuV10** while the thermal characterization of **1–CuV** and its high–temperature derivatives were performed on a TA Instruments 2960 SDT thermobalance under a 150 cm^3 min^{-1} flow of synthetic air (Figure A2.1 in the Appendix). Powder X–ray diffraction (PXRD) patterns were collected on a Bruker D8 Advance diffractometer operating at 30 kV/20 mA and equipped with Cu K_α radiation (λ = 1.5418 Å), a Vantec–1 PSD detector, an Anton Parr HTK2000 high–temperature furnace, and Pt sample holder (Figures A2.2 in the Appendix). The powder patterns were recorded in 2ϑ steps of 0.033° in the $5 \leq 2\vartheta \leq 35$ range with an exposure time of 0.3 s per step. Data sets were acquired from 30 to 490 °C every 20 °C in the case of **1–**

CuV10. For **1–CuV**, however, the patterns were recorded from 30 to 450 °C every 20 °C (Figures A2.3 in the Appendix). and from 3 to 121 °C every 2 °C.

2.2.2 Synthetic Procedure

[{Cu(cyclam)}(VO$_3$)$_2$]·5H$_2$O (1–CuV). The metavanadate precursor [(CH$_3$)$_3$CNH$_3$][VO$_3$] (0.100 g, 0.60 mmol) was dissolved in distilled water (20 mL) and the pH was adjusted to 9.0 with aqueous 1M NaOH. Then, a solution of CuSO$_4$·5H$_2$O (0.075 g, 0.30 mmol) and cyclam (0.040 g, 0.20 mmol) in distilled water (15 mL) was added dropwise. The mixture was refluxed for 2 h, cooled down to room temperature and the formed dark pink precipitate was filtered. The resulting dark purple solution was left to slowly evaporate at room temperature and purple prismatic crystals suitable for X–ray diffraction were obtained after 3 days. Yield: 49 mg (30% based on V). Anal. Calcd (found) for $C_{10}H_{34}CuN_4O_{11}V_2$: C, 9.74 (9.29); H, 2.48 (2.38); N, 4.26 (3.96). IR (cm^{-1}): 3229 (s), 3165 (s), 2936 (m), 2878 (m), 1638 (m), 1474 (w), 1454 (w), 1442 (w), 1429 (w), 1389 (w), 1358 (w), 1312 (w), 1292 (w), 1253 (w), 1236 (w), 1105 (m), 1091 (w), 1074 (w), 1062 (w), 1016 (m), 1008 (m), 962 (vs), 920 (vs), 895 (m), 883 (s), 854 (s), 758 (s), 544 (w), 521 (w), 499 (m), 440 (m).

[{Cu(cyclam)}(VO$_3$)$_2$]·3H$_2$O (2–CuV). Single crystals of **1–CuV** were heated at 40 °C in an oven for 1 h, which produced a color change from dark purple to light purple.

[{Cu(cyclam)}(VO$_3$)$_2$]·1.3H$_2$O (3–CuV). Single crystals of **1–CuV** were heated in an oven at 60 °C for 1 h, with their color changing to dark pink.

[{Cu(cyclam)}(VO$_3$)$_2$] (4–CuV). Single crystals of **1–CuV** were heated in an oven at 120 °C for 1 h and a slight color change to darker purple was observed.

[Cu(cyclam)][{Cu(cyclam)}$_2$(V$_{10}$O$_{28}$)]·10H$_2$O (1–CuV10). The metavanadate precursor [(CH$_3$)$_3$CNH$_3$][VO$_3$] (0.170 g, 1.00 mmol) was dissolved in aqueous 1M NaCl (20 mL) and the pH was adjusted to 4.6–4.7 with aqueous 0.5M HCl. Then, a solution of CuSO$_4$·5H$_2$O (0.075 g, 0.30 mmol) and cyclam (0.040 g, 0.20 mmol) in aqueous 1M NaCl (15 mL) was added dropwise. The mixture was stirred for 2 h and then filtered to remove a brown solid off. The resulting dark brown solution was left to slowly evaporate in an open container at room temperature and orange block–like crystals suitable for X–ray diffraction were obtained after 6 days. Yield: 44 mg (23% based on V). Anal. Calcd (found) for $C_{30}H_{92}Cu_3N_{12}O_{38}V_{10}$: C, 18.68 (18.51); H, 4.80 (4.69); N, 8.71 (8.60). IR (cm^{-1}): 3186 (vs), 3165 (vs), 2934 (s), 2878 (s), 1627 (s), 1473 (m), 1454 (m), 1427 (m), 1389 (w), 1358 (w), 1300 (w), 1253 (w), 1236 (w), 1138 (m), 1105 (m), 1062 (m), 1009 (m), 960 (vs), 883 (m), 835 (s), 748 (s), 594 (s), 532 (s), 559 (s), 440 (s).

[Cu(cyclam)][{Cu(cyclam)}$_2$(V$_{10}$O$_{28}$)] (1a–CuV10). The anhydrous derivative **1a–CuV10** can be obtained by heating single–crystals of **1–CuV10** at 130 °C in an oven for 1 h. A color change from orange to amber was observed upon dehydration.

2.2.3 Single–Crystal X–Ray Crystallography

Crystallographic data for compounds **1–CuV**, **2–CuV**, **3–CuV** and **4–CuV** as well as **1–CuV10** and **1a–CuV10** are given in Table 2.1. Intensity data were collected on an Agilent

Technologies Super–Nova diffractometer. The diffractometer was equipped with monochromated Cu K*α* radiation (λ = 1.54184 Å) and Atlas CCD detector in the case of **1–CuV10**, whereas the selected radiation and detector for the other compounds were monochromated Mo K*α* (λ = 0.71073 Å) and Eos CCD. The data collection of **1–CuV** and **1–CuV10** were carried out at 100 K. In the case of **2–CuV**, **3–CuV** and **1a–CuV10**, a single crystal was respectively heated in an oven to 313, 333 and 403 K at a rate of 1 K min^{-1} and immediately afterwards covered with Paratone® oil and placed under the N_2 stream of the diffractometer, which was ready to perform a full data collection at 100 K. In the case of **4–CuV**, the crystals were heated to 393 K but cracked upon lowering the temperature to 100 K. Therefore, the full data collection was acquired at high temperature instead. Data frames were processed (unit cell determination, analytical absorption correction with face indexing, intensity data integration and correction for Lorentz and polarization effects) using the CrysAlis Pro software package.[60] The structures were solved using OLEX2[61] and refined by full–matrix least–squares with SHELXL–2014/6.[62] Final geometrical calculations were carried out with PLATON[63] as integrated in WinGX.[64]

Table 2.1. Crystallographic data for **1–CuV1, 2–CuV, 3–CuV, 4–CuV** as well as **1–CuV10** and **1a–CuV10.**

	1–CuV	**2–CuV**	**3–CuV**	**4–CuV**	**1–CuV10**	**1a–CuV10**
Empirical formula	$C_{10}H_{34}Cu N_4O_{11}V_2$	$C_{10}H_{30}Cu N_4O_9V_2$	$C_{10}H_{26.7}N_4 CuO_{7.3}V_2$	$C_{10}H_{24}Cu N_4O_6V_2$	$C_{30}H_{92}Cu_3 N_{12}O_{38}V_{10}$	$C_{30}H_{72}Cu_3 N_{12}O_{28}V_{10}$
FW (g mol⁻¹)	551.83	515.80	485.77	461.75	1929.2	1749.0
Crystal system	triclinic	triclinic	triclinic	triclinic	triclinic	triclinic
Space group	*P–1*	*P–1*	*P–1*	*P–1*	*P–1*	*P–1*
Z	12	3	3	3	1	1
Z'	6	1.5	1.5	1.5	0.5	0.5
T (K)	100(2)	100(2)	100(2)	393(2)	100(2)	100(2)
***a* (Å)**	16.4455(3)	8.0199(2)	8.6253(10)	8.751(2)	10.6665(8)	10.6838(3)
***b* (Å)**	15.0098(5)	13.9524(6)	12.890(2)	13.094(3)	11.9325(9)	11.9275(6)
***c* (Å)**	27.8995(7)	14.2588(5)	13.368(2)	13.364(3)	13.7832(8)	13.7285(7)
***α* (°)**	79.513(2)	102.032(3)	103.208(14)	102.449(18)	95.752(5)	94.433(4)
***β* (°)**	98.024(2)	101.742(3)	106.557(12)	101.653(19)	105.003(6)	104.596(3)
***γ* (°)**	105.156(2)	97.560(3)	95.595(11)	101.148(19)	90.677(6)	92.604(3)
V (Å³)	6505.5(3)	1502.39(10)	1365.7(4)	1418.7(6)	1684.7(2)	1684.08(13)
D_{calcd} (g cm⁻³)	1.690	1.710	1.772	1.621	1.902	1.725
μ (mm⁻¹)	1.873	2.014	2.203	2.111	12.928	2.320
λ (Å)	0.71073	0.71073	0.71073	0.71073	1.54184	0.71073
collected reflns	46122	9271	8867	8399	11577	10744
uniq reflns (R_{int})	22908 (0.036)	5290 (0.017)	4794 (0.067)	4991 (0.097)	5977 (0.046)	5939 (0.027)
obsd reflns [$I > 2\sigma(I)$]	17910	4751	3280	2115	4821	4595
parameters	1558	406	334	316	469	379
$R(F)^a$ [$I > 2\sigma(I)$]	0.046	0.029	0.089	0.108	0.057	0.040
$wR(F^2)^b$ [all data]	0.111	0.074	0.183	0.251	0.166	0.102
GoF	1.038	1.051	1.132	1.058	1.038	1.044

$^a\ R(F)=\Sigma||F_o–F_c||/\Sigma|F_o|$; $^b\ wR(F^2)=\{\Sigma[w(F_o^2–F_c^2)^2]/\Sigma[w(F_o^2)^2]\}^{1/2}$

Thermal vibrations were treated anisotropically for all non–H atoms and hydrogen atoms of the organic ligands were placed in calculated positions and refined using a riding model with standard SHELXL parameters for all six compounds. Thirty–five, ten, two and ten positions suitable for water molecules of hydration were located in the Fourier maps of **1–CuV**, **2–CuV**, **3–CuV** and **1–CuV10**, respectively, and their occupancy was initially refined without restrictions. The resulting total number of 30.5, 4.3, 2.0, and 5.5 water molecules per asymmetric unit was fixed to 30, 4.5, 2 and 5 during the final refinement. The space within the channels occupied by the water molecules of hydration was calculated using HOLLOW[65] and visualized in PyMol.[66]

2.2.4 Gas Sorption Measurements

The porous texture of **1–CuV10** was characterized through the physical adsorption of the following gases: N_2 at –196 °C and CO_2 at 0 °C. The volumetric equipments Autosorb–6B and Autosorb–6 were used respectively. The measurements were performed on crystalline samples that were previously outgassed at 150 °C under vacuum for 4 hours. The Dubinin–Radushkevich (DR) equation[67] was used to calculate the micropore volume. The calculation of pore volumes were carried out as follows: a) the volume of the narrow micropores or ultramicropores (V_{CO2}, pore size < 0.8 nm) was estimated from the CO_2 DR plots at relative P/P_0 pressures lower than 0.015; b) the total volume of micropores (V_{N2}, pore size < 2 nm) was calculated from N_2 DRs plots at relative P/P_0 pressures lower than 0.14.[68]

2.2.5 Catalytic Tests

The oxidation of adamantane was conducted in a glass reactor (27 cm^3 of inner volume) located inside a stainless steel vessel (45 cm^3 of inner volume) coupled to a manometer to monitor the system pressure. The following reactants and solvent were used for the catalytic test: 25 mg of adamantane, 3 cm^3 of hydrogen peroxide (30%), 10 cm^3 of acetonitrile, two drops of concentrated HCl and 100 mg of **1–CuV10** hybrid ($5 \cdot 10^{-5}$ moles). For comparative purposes, V_2O_5 (Aldrich), and two Keggin–type heteropolyacids supported on ZrO_2 ($H_3[PMo_{12}O_{40}]$ and $H_4[PVMo_{11}O_{40}]$, 30 wt.% of POM) were also tested. A small Teflon–coated magnet was added to the mixture and the whole system was immersed in a thermostatic bath of polyethylene glycol at 75 °C while stirring at 800 rpm. A reaction time of 6 h was selected as the optimum value to allow for complete conversion but minimizing hydrogen peroxide decomposition. Both shorter (3 h) and longer (up to 12 h) reaction times were also tested for comparative purposes. The reaction products of the oxidation of adamantane were identified by analyzing an aliquot of the solution (20 µL) taken at the end of the reaction time with an Agilent 6890 gas chromatograph equipped with an HP–1 column of size 30 m x 250 µm x 0.25 µm and coupled to an Agilent 5975 mass spectrometer. Upon identification of all reaction products, the conversion and their evolution were quantitatively estimated using a flame ionization detector coupled to the gas chromatograph above.

2.3 RESULTS AND DISCUSSION

2.3.1 Synthesis

The synthesis of **1–CuV** was carried out by reacting *tert*–butylammonium metavanadate with cyclam and a copper(II) sulfate salt in aqueous medium at pH = 9. Different vanadate sources such as commercial $Na(VO_3)$ and $NH_4(VO_3)$, as well as the preformed

$[(CH_3)_3CNH_3](VO_3)$, were used to determine whether the counterions play any role in the formation of **1–CuV**. Analogously, different copper(II) salts were also tested as the transition metal source (chloride, acetate and nitrate salts). No template effect of the cations was observed and all three metavanadate reagents led to compound **1–CuV**, although slight differences were observed in terms of yield and crystallization speed, being the most optimal reaction that with the alkylammonium salt. While the choice of the transition metal salt did not affect the reaction in any apparent way, the pH of the reaction medium has a key influence in the isolation of **1–CuV** as a pure crystalline phase. When the pH was adjusted to basic values lower than 8.5, mixtures of **1–CuV** with crystals of a second metavanadate–containing hybrid phase (labelled as **2–CuV**) were obtained. Compound **1–CuV** was the major component in all of these mixtures as indicated by the PXRD patterns. Moreover, when the pH was lowered to values below 6.0, crystals of a decavanadate–containing hybrid specie (**1–CuV10**) were isolated instead of the metavanadate hybrid **1–CuV** according to FT–IR spectroscopy (Figure 2.9). These crystals were obtained in trace amounts in mixtures with a yet unidentified powder in the specific pH range 4.0–6.0 whereas no identifiable solid product was obtained at pH values below 4.0.

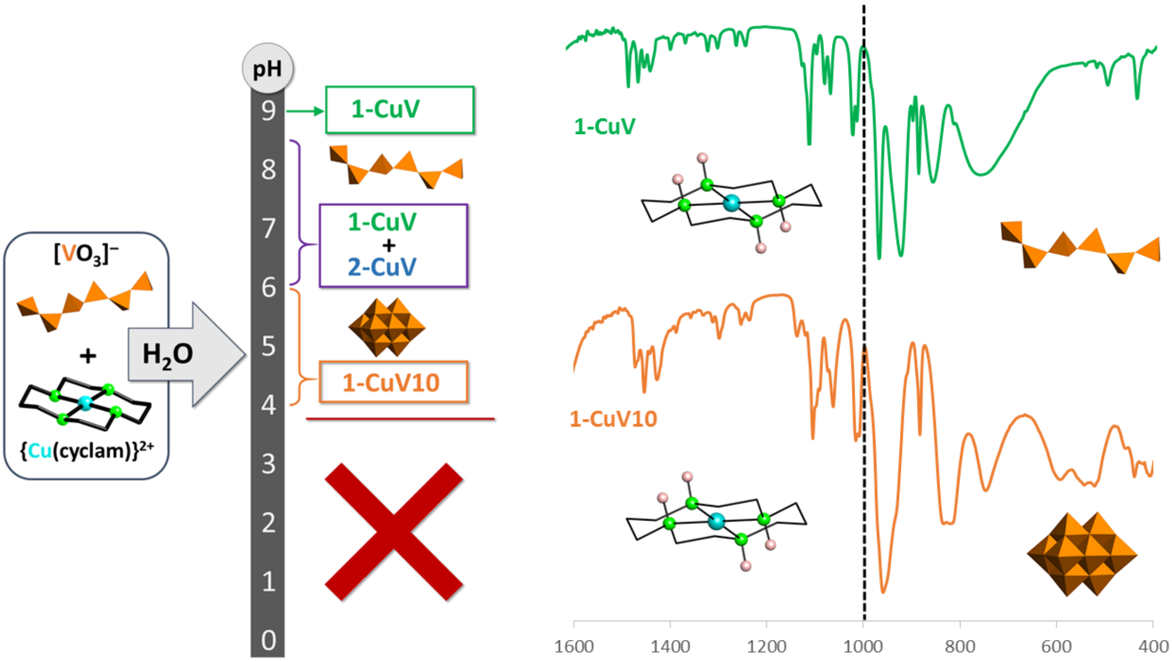

Figure 2.9. Scheme of the synthesis (left) and comparison between the FT–IR spectra for the two different isopolyoxovanadate hybrids highlighting the different regions where the characteristics vibration bands of each building blocks appear (right) for **1–CuV** and **1–CuV10**.

Different reaction temperatures were also investigated (room temperature, 80 °C and reflux conditions). Compound **1–CuV** was obtained in all tested temperatures but we found that the reaction involving $[(CH_3)_3CNH_3](VO_3)$ under reflux conditions (pH = 9) afforded the best yields. Moreover, differences in the crystallization speed were also observed: the reactions at room temperature and 80 °C yielded crystals after approximately two weeks whereas **1–CuV** crystallized in just three days from that performed under refluxing conditions. Therefore, this particular synthetic system, while strongly dependent on the pH of the reaction media, it also appears to be affected by the temperature in a significant way. Although no synthetic conditions led to crystallization of compound **2–CuV** as a single crystalline phase, we found that pure batches of this compound could be prepared just by heating crystals of **1–CuV** at 40 °C for an hour, as it will be commented below. Analogously, compounds **3–CuV** and **4–CuV** could only be obtained by heating samples of **1–CuV** or **2–CuV** (60 °C and 120 °C, respectively), as we could not find any synthetic route to isolate them from solution. This fact nicely illustrates how thermally triggered solid–state reactions can provide access to compounds otherwise impossible to be prepared directly from solution reactions.

Regarding the optimization of the reaction that leads to the above mentioned decavanadate hybrid, we limited our synthetic studies to the pH range 4–6 and conducted several experiments in aqueous media to check the influence of the following parameters on the reaction outcome: pH, temperature, type of precursor (metavanadate vs. decavanadate), and solvent. Neither the temperature nor the precursors appear to have any apparent effect on the final product, as reactions carried out at different temperatures up to reflux conditions or using the preformed $[(CH_3)_3CNH_3]_4[H_2V_{10}O_{28}]\cdot 8H_2O$ resulted in similar mixtures of crystals of **1–CuV10** with the powder as the major component. In close analogy to **1–CuV** hybrid, the pH plays a key role for the isolation of the hybrid decavanadate in a pure manner. We managed to prepare **1–CuV10** as a single, homogeneous crystalline phase at a controlled pH value of 4.6–4.7 as evidenced by the FT–IR spectra and the PXRD patterns, although the yield obtained was still certainly poor (around 1% with cyclam as the limitant). This is due to the formation of large amounts of a brown precipitate as the reaction proceeds, which contains the title compound but in impure bulk form as evidenced by FT–IR and PXRD analyses (Figure A2.5 in the Appendix).

Fortunately, a change in the solvent favored the formation of our hybrid decavanadate by increasing the yield of the crystalline phase and reducing the time for crystallization. When water was replaced with aqueous 1M NaCl and the optimized conditions determined above were applied (metavanadate precursor, room temperature, pH 4.6–4.7), formation of the impure bulk form was minimized and crystallization of **1–CuV10** took place in a few days instead of the several weeks needed in the original attempts. The resulting yield was drastically improved to above 20%, proving that the ionic strength also has a key influence in this particular synthetic system. It is worth mentioning that we also tried to prepare analogues of **1–CuV** and **1–CuV10** but using other divalent transition metals (Mn^{II}, Co^{II}, Ni^{II}, and Zn^{II}) instead of Cu^{II}, but unfortunately, we could not obtain any crystalline material from these experiments. This fact confirms that the plasticity of the coordination sphere of the Cu^{II} centers plays a key role in the formation of both our meta– and decavanadate hybrids, as it will be shown in the structural description below.

2.3.2 Dynamic Metavanadate/Metalorganic Open–Frameworks

Vibrational characterization and thermostructural behavior of 1–CuV

The initial characterization of compound **1–CuV** was performed by FT–IR. The infrared spectrum of **1–CuV** is very similar to that shown by the metavanadate precursor although some notable differences can be observed (Figure 2.10). The bands corresponding to the ν_s(V–

O$_t$) vibration in all hybrid compounds are slightly shifted to lower wavenumbers, compared to the metavanadate precursor while those associated with the ν_{as}(V–O$_t$) vibration split into four weaker signals. In addition, the position of the signal of strong intensity originating from the ν_{as}(V–O$_b$–V) vibration differs greatly from that of the precursor. This signal migrates to lower wavenumbers as the sample is dehydrated in such a way that it appears at 756 cm^{-1} for **1–CuV** while it is centered at 735, 702 and 679 cm^{-1} for **2–**, **3–** and **4–CuV**, respectively. Regarding the metal–organic region of the FT–IR spectra, the peaks associated with the stretching of the –N–H and –C–H bonds are respectively observed at 3200–3150 and 2900–2860 cm^{-1}, whereas several weak to medium signals corresponding to the δ(C–H) and ν(N–C) vibration modes are also present in the 1490–1230 and 1100–1000 cm^{-1} ranges. These signals confirmed the presence of the cyclam ligands in our compounds.

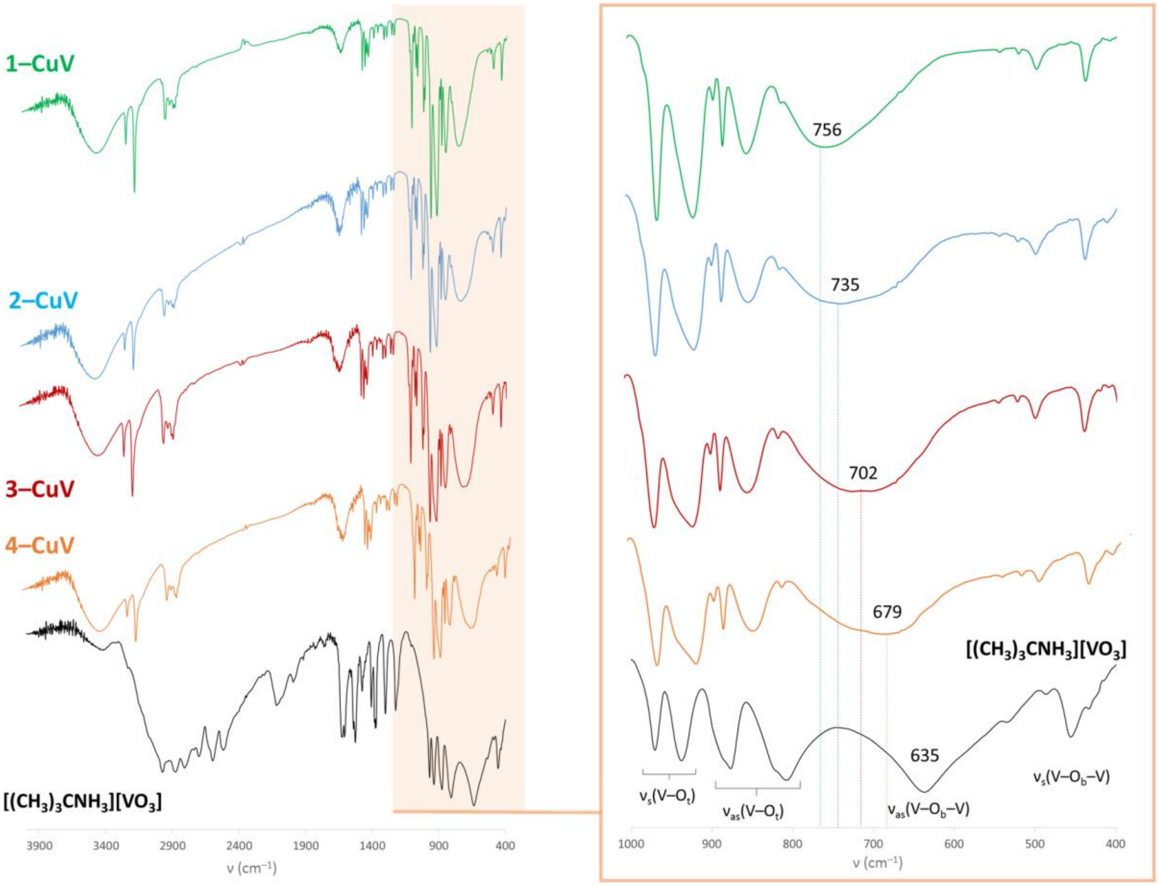

Figure 2.10. FT–IR spectra of **1**–**CuV** and its thermal derivatives compared to that of the [(CH$_3$)$_3$CNH$_3$][VO$_3$] precursor with details of the inorganic region below 1000 cm^{-1}.

The thermal stability of **1–CuV** was investigated by TGA experiments, which show that the title compound decomposes through three mass loss stages with similar profiles (Figure 2.11). The first stage is observed as an endothermic mass loss that extends from room temperature to temperatures around 120 °C and originates from the release of all water molecules of hydration. The mass loss (15.88%) corresponds to 5 water molecules per two vanadium atoms (calc. 16.30%). Dehydration leads to an anhydrous phase (**4–CuV**) that displays a significant range of thermal stability extending up to *ca.* 200 °C. Above this temperature, the anhydrous phase undergoes further decomposition via two overlapping mass loss stages of exothermic nature associated with the combustion of the organic ligands. The overall mass loss for this second stage (37.50%) is in good agreement with one cyclam ligand per two vanadium atoms (calc. 37.17%). The final residue (46.6%) is obtained at temperatures above *ca.* 440 °C (calc for CuV_2O_6: 47.4%).

Variable–temperature powder X–ray diffraction measurements (TPXRD) between 3 and 450 °C show that, as the dehydration proceeds, **1–CuV** transforms into two other crystalline phases before leading to the final anhydrous derivative (**4–CuV**), and hence two different partially hydrated intermediates must exist. The temperatures at which these two solid–state phase transitions take place are 27 and 49 °C (Figure 2.11). The diffraction maxima within this range of temperatures corresponds to those observed for the minor component in the mixtures of crystalline phases obtained when the synthesis of **1–CuV** was carried out at basic values other than 9.0. Therefore, the first partially dehydrated intermediate observed in the TPXRD studies is the same compound **2–CuV** that co–crystallized with **1–CuV** in our systematic investigations on the influence of the pH in the Cu^{2+}:cyclam:VO_3^- synthetic system. The transformation of the second partially hydrated intermediate (**3–CuV**) into the final anhydrous phase **4–CuV** is not as well defined as the two transitions mentioned above. The TPXRD patterns are not substantially modified from 49 to 110 °C (at which all water molecules of hydration are released according to the TGA curve), and only subtle variations can be observed in some of the diffraction maxima of weak intensity that appear at 2θ angles above 10°. For example, the two groups of signals in the $10 < 2\vartheta < 15°$ range undergo a gradual change in their relative intensities that can be traced back to *ca*. 73 °C (Figure 2.11), and this fact suggests that the final form of the hybrid {Cu(cyclam)}/VO_3 framework in the anhydrous phase **4–CuV** is adopted above the latter temperature. This form is able to retain crystallinity upon total dehydration up to temperatures around 190 °C, in such a way that the anhydrous derivative **4–CuV** only becomes amorphous within the temperature range corresponding to the combustion of the organic ligands. The above results are in good agreement with the observations in the TGA curves of compound **1–CuV**. A new crystalline phase corresponding to the final residue starts appearing above 290 °C and reaches full formation at 450 °C. As shown in Figure A2.3 in the Appendix, this final residue has been identified as a mixture of the orthorhombic *Pmn2₁* phase of V_2O_5 (PDF: 01–076–1803)[69] and the monoclinic *C2/c* phase of $Cu_2V_2O_7$ (PDF: 01–073–1032)[70] in similar amounts. Traces of the orthorhombic *Pmn2₁* phase of CuV_2O_6 (PDF: 00–016–0127)[71] have been detected as well.

It is well known that guest solvent molecules located in cavities or channels can often be removed from the open framework host material without causing its collapse, and furthermore, that they can also be reinserted sometimes. In order to explore this possibility, we decided to carry out single–crystal XRD studies in an attempt to determine the structure of the new crystalline phases that are formed during the dehydration process of **1–CuV**: the two partially dehydrated intermediates observed in the 27–49 and 49–73 °C ranges (**2–CuV** and **3–CuV**) and the anhydrous phase (**4–CuV**). A single crystal of **1–CuV** for which full intensity data were initially collected at 100 K was selected, and the temperature was raised from room temperature to 40 °C at a rate of 1 °C min^{-1}. At this point, the temperature was lowered back to 100 K to perform a full data collection. The crystal preserved its integrity and crystallinity during the whole process and this allowed us to determine the structure of **2–CuV**. This process was repeated with a second crystal but the temperature was raised to 60 °C instead, which allowed us to structurally characterize the phase **3–CuV.** As mentioned above, the diffraction patterns do not undergo major changes from 49 to 190 °C (Figure 2.11) and this suggests that the final anhydrous phase **4–CuV** shares a similar packing with the partially dehydrated intermediate **3–CuV**. To verify this observation, we attempted to perform the data collection of **4–CuV** by following an analogous procedure but heating at 120 °C. Unfortunately, the crystal cracked systematically when cooling down to 100 K, leading to datasets of poor quality. Therefore, we decided to skip the cooling stage and carried out the full data collection at 393 K. The diffraction data obtained at this temperature were of sufficient quality to refine the structure of **4–CuV** to acceptable final agreement factors.

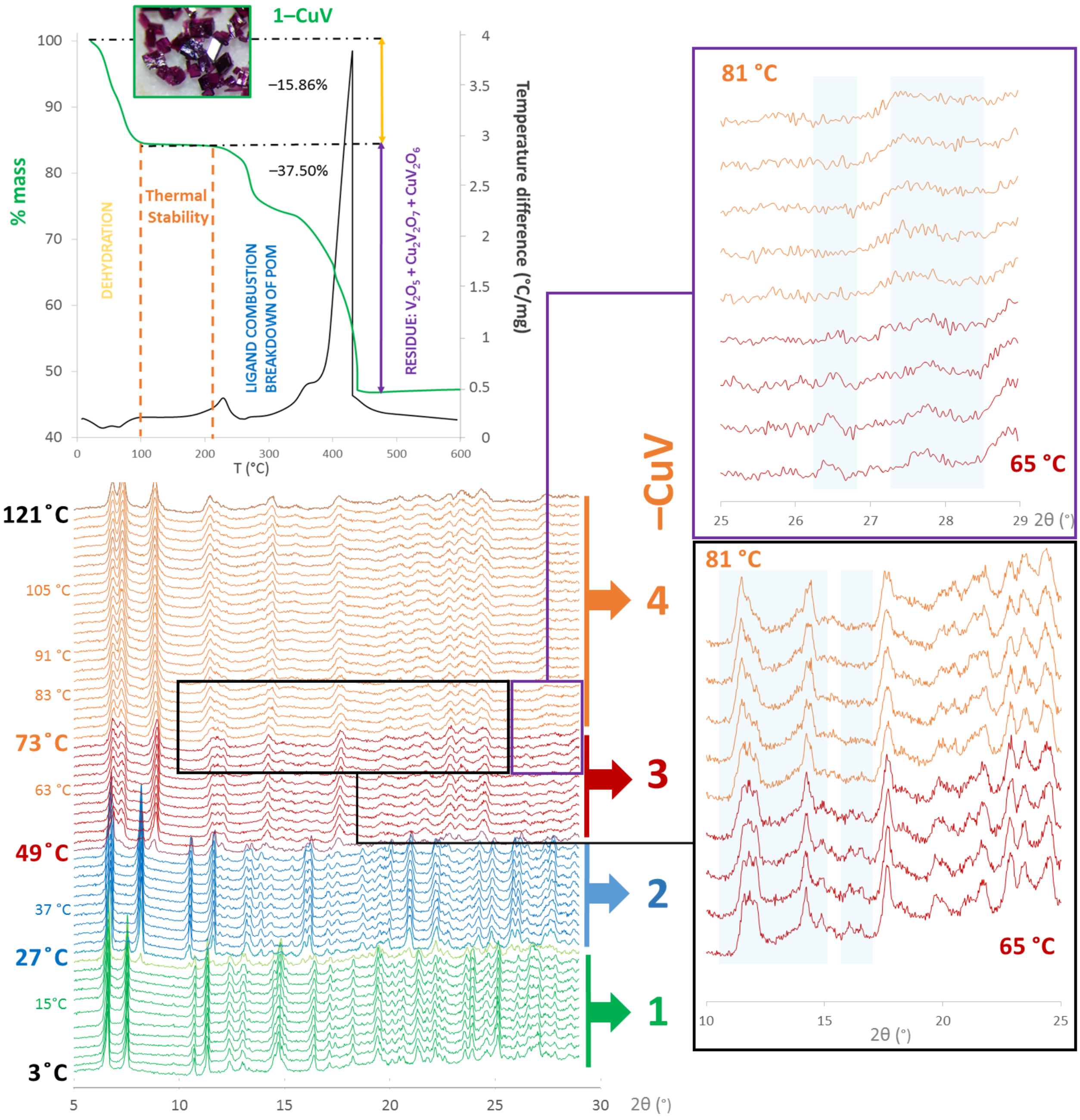

Figure 2.11. Variable–temperature powder X–ray diffraction (TPXRD) studies together with the TGA/DTA curves for **1–CuV.** The range of thermal stability for each crystalline phase and the temperatures at which the transformations take place are highlighted (left). The most relevant changes in the diffraction patterns when going from **3–CuV** to the anhydrous **4–CuV** are also marked (right).

Crystal structure of 1–CuV hybrid

Compound **1–CuV** crystallizes in the triclinic *P–1* space group. The asymmetric unit of **1–CuV** contains two different vanadate fragments. Each fragment corresponds to a crystallographically independent metavanadate polymeric anion (labelled as chain A and chain B) and is built of six corner–sharing {VO_4} tetrahedra. The asymmetric unit is completed with six {Cu(cyclam)} complexes and thirty water molecules of hydration.

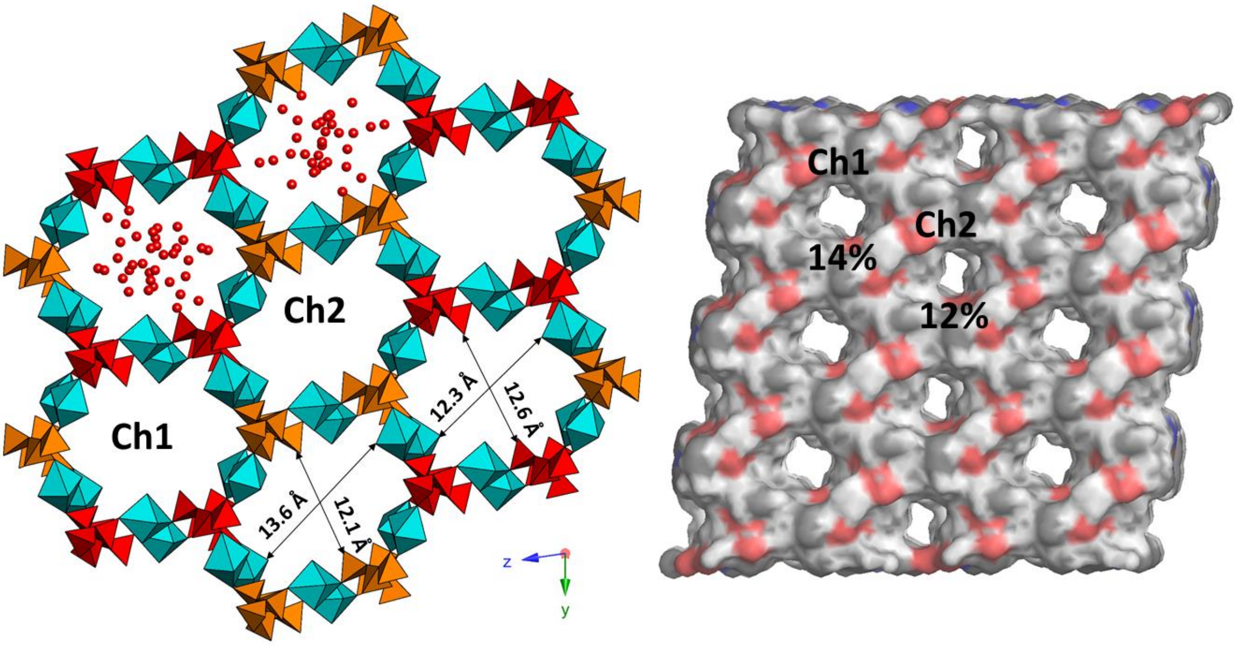

Figure 2.12. Crystal packing of **1–CuV** viewed along the *x* axis (left), showing the two different types of channels (Ch1 and Ch2) and details of the hosted water molecules and their estimated dimensions (cyclam ligands are omitted for clarity); color code: {VO_4} (orange: chain A; dark red: chain B), Cu (blue)). Surface of the hybrid framework showing the shape of the different channels (right).

Table 2.2. Cu–O and Cu–N$_{mean}$ bond lengths (Å) as well as the polyhedral distorsion (CShM) of the {Cu(cyclam)} complexes in **1–CuV** and its thermal derivatives **2–CuV, 3–CuV** and **4–CuV.**

1–CuV				2–CuV		3–CuV		4–CuV
Cu1A–N$_{mean}$	2.015	Cu1D–N$_{mean}$	2.014	Cu1A–N$_{mean}$	2.011	Cu1A–N$_{mean}$	2.007	1.996
Cu1A–O5M	2.431(3)	Cu1D–O8M	2.411(3)	Cu1A–O3M	2.523(3)	Cu1A–O2	2.643(7)	2.636(11)
Cu1A–O2M^{i}	2.524(3)	Cu1D–O11M^{iv}	2.566(3)	Cu1A–O3M^{i}	2.523(3)	Cu1A–O2^{i}	2.643(7)	2.636(11)
OC–6	1.286	OC–6	1.293	OC–6	1.372	OC–6	1.898	1.941
Cu1B–N$_{mean}$	2.013	Cu1E–N$_{mean}$	2.017	Cu1B–N$_{mean}$	2.017	Cu1B–N$_{mean}$	2.013	2.002
Cu1B–O4M	2.335(3)	Cu1E–O1M	2.479(3)	Cu1B–O1M	2.493(3)	Cu1B–O1M	2.587(8)	2.494(10)
Cu1B–O10M^{ii}	2.770(3)	Cu1E–O7M^{v}	2.450(3)	Cu1B–O1M^{ii}	2.493(3)	Cu1B–O1M^{ii}	2.587(8)	2.494(10)
OC–6	1.823	OC–6	1.219	OC–6	1.146	OC–6	1.666	1.194
Cu1C–N$_{mean}$	2.019	Cu1F–N$_{mean}$	2.021	Cu1C–N$_{mean}$	2.020	Cu1C–N$_{mean}$	2.022	2.008
Cu1C–O6M	2.713(3)	Cu1F–O3M	2.398(3)	Cu1C–O2M	2.523(3)	Cu1C–O2M	2.446(8)	2.420(10)
Cu1C–O12M^{iii}	2.457(3)	Cu1F–O9M	2.587(3)	Cu1C–O2M^{iii}	2.523(3)	Cu1C–O2M^{iii}	2.446(8)	2.420(10)
OC–6	1.966	OC–6	1.363	OC–6	1.257	OC–6	1.063	1.057

Symmetry codes: **1–CuV**: i) 1–*x*, 1–*y*, –*z*; ii) 1+*x*, 1+*y*, *z*; iii) 1+*x*, *y*, *z*; iv) –*x*, –*y*, 1–*z*; v) *x*, 1+*y*, *z*. **2–CuV**: i) 1–*x*, 2–*y*, 1–*z*; ii) 1–*x*, 1–*y*, *z*; iii) 1–*x*, 2–*y*, –*z*. **3–CuV**: i) 1–*x*, –1–*y*, 2–*z*; ii) –*x*, –*y*, 1–*z*; iii) 1–*x*, 1–*y*, 1–*z*. **4–CuV**: i) 1–*x*, 1–*y*, 1–*z*; ii) 2–*x*, 2–*y*, 2–*z*; iii) 2–*x*, 1–*y*, 2–*z*. CShM: reference polyhedron OC–6 (octahedron).

All of the six crystallographically independent {Cu(cyclam)} complexes found in **1–CuV** act as bridging metal–organic blocks between metavanadate chains. The coordination spheres of all Cu^{II} centers show distorted octahedral geometries, as indicated by continuous shape measures (CShM),[72] with the four N atoms of the cyclam ligand forming the equatorial plane and the axial positions occupied by terminal O atoms from different vanadate tetrahedra (Figure 2.12 and Table 2.2). While all CuN_4O_2 chromophores show significant Jahn–Teller elongation, it must be noted that this type of distortion is especially remarkable for Cu1B and Cu1C, as shown by one of their respective axial Cu–O bonds that shows lengths near those of semi–coordination as well as their calculated CShM values, which are the highest among all complexes (Table 2.2). All of the complexes found in **1–CuV** display the *trans–III* configuration, that is, two N–H bonds above and the other two below the CuN_4 equatorial plane. This is in perfect agreement with previous reports, which have shown that the most favorable configuration of a {Cu(cyclam)} complex with octahedral geometry is the *trans–III*.[73]

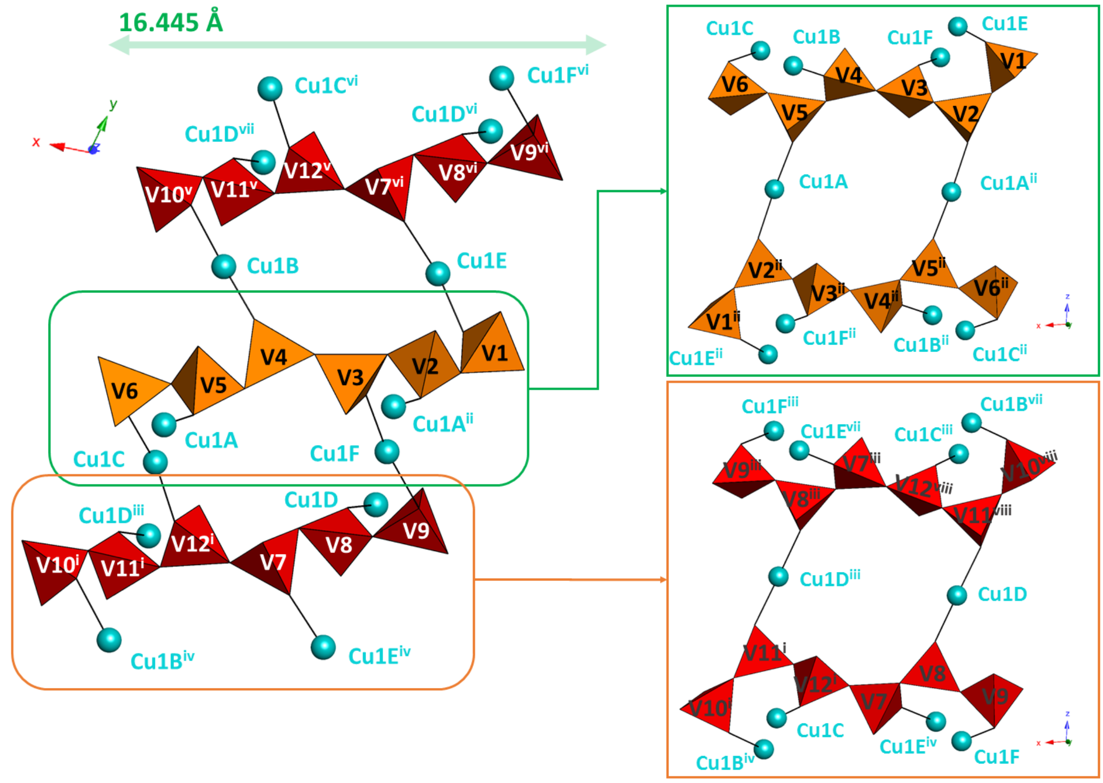

Fig 2.13. Connectivity between metavanadate chains in compound **1–CuV** with atom labeling (cyclam ligands and water molecules of hydration are omitted for clarity). Color code: {VO_4} (orange: chain A; dark red: chain B), Cu (blue). Symmetry codes: i) 1+*x*, *y*, *z*; ii) –1+*x*, *y*, *z*; iii) 1–*x*, –*y*, 1–*z*; iv) *x*, –1+*y*, *z*; v) 1+*x*, 1+*y*, *z*; vi) *x*, 1+*y*, *z*; vii) 1–*x*, 1–*y*, 1–*z*; viii) –*x*, 1–*y*, 1–*z*; ix) –*x*, –*y*, 1–*z*; x) 1–*x*, 1–*y*, –*z*.

The crystal packing of **1–CuV** can be described as a three–dimensional porous structure formed by metavanadate chains that extend along the *x* axis and are covalently linked to neighboring antiparallel chains by {Cu(cyclam)} bridging moieties in such a way that all {VO_4} tetrahedra display one complex anchored to a terminal O atom. This arrangement of polymeric anions and metal–organic complexes results in a hybrid I^3O^0–type open framework with two different types of hexagonal channels parallel to the [100] direction where all the water molecules are located (Figure 2.12). The metavanadate chain A is formed by the six corner–

sharing $\{VO_4\}$ tetrahedra V1 to V6, whereas chain B consists of another six crystallographically independent VO_4 units labelled as V7 to V12. As shown in Figure 2.13, the metal–organic complexes Cu1B, Cu1C, Cu1E and Cu1F link tetrahedra belonging to different chain types along the *y* axis, whereas Cu1A and Cu1D connect equivalent chains (type A and B, respectively) forming pairs along the *z* axis. Each pair of A–type chains is connected to four neighbouring pairs of B–type chains (and vice versa) in such a way that water containing hexagonal channels are generated. This connectivity originates two distinct type of channels, channel 1 (Ch1) and 2 (Ch2). Each channel is delimited by four chains of one type and two chains of the second type (four A–type and two B–type for Ch1 and vice versa), which are connected by copper atoms with approximate cross sections of 12.6 x 13.6 Å^2 for Ch1 (distances O11M···O11M and N8C···N8C) and 12.1 x 12.6 Å^2 for Ch2 (distances O2M···O2M and N1F···N1F). The total solvent accessible volume is 1730 Å^3 which corresponds to a 26% of the unit cell volume of **1–CuV**, as calculated using the PLATON software (Ch1: 922 Å^3, 14% and Ch2: 808 Å^3, 12%). An intrincate network of C–H···O and N–H···O interactions between the cyclam ligands and the oxygen atoms of the metavanadate chains and some of the water molecules further contribute to the structural stability. Distances and angles of such interactions are compiled in Table 2.3.

Table 2.3. Intermolecular N–H···O and C–H···O interactions in **1–CuV** compound.

Donor–H···Acceptor	D···A (Å)	D–H···A (°)	Donor–H···Acceptor	D···A (Å)	D–H···A (°)
N1A–H1A···O2^{i}	3.026(5)	170	N1D–H1D···O8	3.005(5)	164
N4A–H4A···O61	2.934(5)	147	N4D–H4D···O127^{iv}	3.014(5)	138
N11A–H11A···O3^{i}	2.976(5)	146	N8D–H8D···O11^{iv}	3.210(5)	156
C10A–H10B···O30W^{i}	3.474(6)	163	N8D–H8D···O14W^{v}	3.235(6)	126
C9A–H9AA···O3^{i}	3.330(5)	127	N11D–H11D···O9	2.863(5)	151
C5A–H5AB···O12^{iii}	3.467(5)	146	—	—	—
N4B–H4B···O15W	3.046(5)	169	N1E–H1E···O8^{ii}	3.148(5)	161
N8B–H8B···O5	2.984(5)	166	N4E–H4E···O1	2.931(5)	164
N11B–H11B···O10^{vi}	2.903(5)	173	N8E–H8E···O23	3.196(5)	146
C10B–H10E···O56	3.282(6)	169	N11E–H11E···O25W	3.075(5)	145
C14B–H14F···O21W	3.441(7)	139	C13E–H13K···O29W	3.503(6)	150
—	—	—	C3E–H3EB···O89^{viii}	3.352(6)	139
N1C–H1C···O61	2.896(4)	162	N1F–H1F···O3	2.943(5)	163
N4C–H4C···O101^{iii}	3.208(5)	148	N4F–H4F···O89	3.346(5)	167
N8C–H8C···O127^{iii}	3.045(5)	164	N8F–H8F···O9	2.836(5)	170
N11C–H11C···O56	3.185(4)	165	N11F–H11F···O12	3.243(5)	143
C10C–H10J···O4	3.513(6)	164	C12F–H12C···O61^{vii}	3.440(5)	146
C12C–H12J···O7	3.449(5)	148	C13F–H13C···O2M	3.441(6)	163
C13C–H13J···O5M	3.385(5)	158	C3F–H3FA···O7	3.400(6)	173
C14C–H14I···O12M^{iii}	3.113(5)	125	C3E–H3EB···O89^{viii}	3.352(6)	139

Symmetry codes: i) 1–*x*, 1–*y*, –*z*; ii) *x*, 1+*y*, *z*; iii) 1+*x*, *y*, *z*; iv) –*x*, –*y*, 1–*z*; v) 1–*x*, 1–*y*, 1–*z*; vi) 1+*x*, 1+*y*, *z*; vii) –1+*x*, *y*, *z*, viii) *x*, 1+*y*, *z*.

The crystal packing of **1–CuV** is reminiscent of that found by Ou and co–workers in $[\{CuL\}(VO_3)_2]\cdot 0.33H_2O$,[27] where L stands for 5,5,7,12,12,14–hexamethyl–1,4,8,11–tetraazacyclotetradecane (Figure 2.5). However, some noticeable differences can be found between the structures of both compounds. While **1–CuV** shows two distinct types of distorted–hexagonal channels, $[\{CuL\}(VO_3)_2]\cdot 0.33H_2O$ displays only a single type of hexagonal channel with regular shape. This channel is significantly smaller than those found in **1–CuV** (754 Å^3, 14%) due to the strong steric hindrance effects induced by the methyl groups. Moreover, the channels in Ou's metavanadate hybrid constitute highly hydrophobic regions because the methyl groups point to the center of the pores. This fact results in a significantly lower number of water molecules hosted within compared to those found in the hydrophilic pores of compound **1–CuV**.

Thermally induced SCSC transformations: 2–CuV, 3–CuV and 4–CuV hybrids

Compounds **2**–**4–CuV** also crystallize in the triclinic *P–1* space group, but in contrast to **1–CuV**, the asymmetric units of these compounds contain a single metavanadate chain fragment composed of only three corner–sharing $\{VO_4\}$ tetrahedra, together with three halfs of {Cu(cyclam)} complexes located in inversion centers and coordinated to the vanadate polyhedra. Four and a half and two water molecules of hydration complete the asymmetric units of **2–CuV** and **3–CuV**, respectively. As observed for **1–CuV**, all of the {Cu(cyclam)} centrosymmetric complexes present in the structures of **2**–**4–CuV** (Cu1A, Cu1B and Cu1C) also display elongated octahedral CuN_4O_2 coordination geometries with *trans–III* configuration and similar bond lengths in general (Table 2.2). Even though the inorganic building block is common to all four compounds, the comparison between the metavanadate chains reveals significant structural differences that are attributable to the intrinsic flexibility of this polymeric anion, which allows it to modify the orientation of the $\{VO_4\}$ polyhedra as the water molecules of hydration are removed. Thus, although the V–O distances and O–V–O angles do not change significantly when going from the fully hydrated **1–CuV** to the anhydrous **4–CuV**, the torsion angles between consecutive groups of V and O_b atoms along the chains are remarkably modified as shown in Table 2.4.

Table 2.4. Selected V–O_b–V–O_b and O_b–V–O_b–V torsion angles (°) in the vanadate chains of **1**–**4**–**CuV.**

1–CuV				2–CuV		3–CuV	4–CuV
O6–V1–O12–V2	164	O712–V7–O78–V8	114	O13–V1–O12–V2	61	163	162
V1–O12–V2–O23	77	V7–O78–V8–O89	82	V1–O12–V2–O23	61	158	136
O12–V2–O23–V3	86	O78–V8–O89–V9	138	O12–V2–O23–V3	158	110	97
V2–O23–V3–O34	156	V8–O89–V9–O910	94	V2–O23–V3–O13	82	104	121
O23–V3–O34–V4	168	O89–V9–O910–V10	175	V3–O13–V1–O12	171	142	139

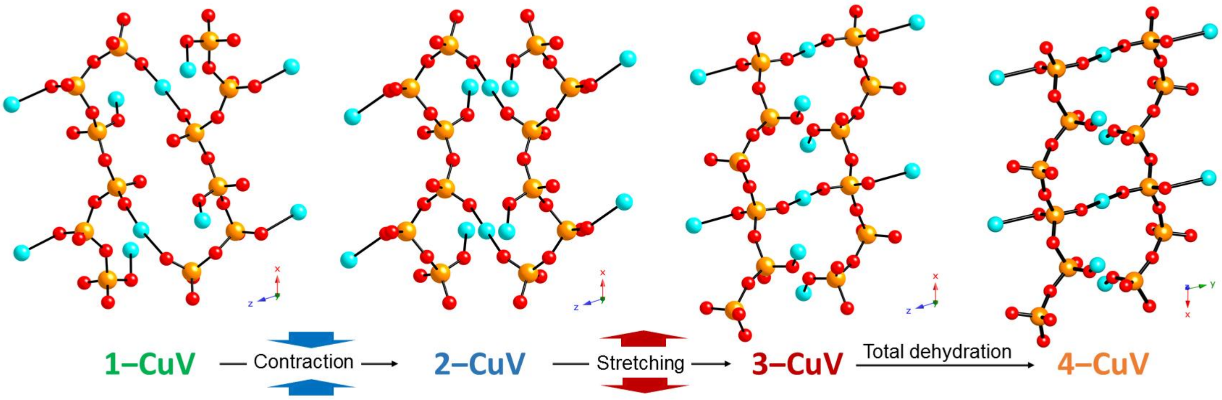

Figure 2.14. Comparison between the metavanadate chains in **1–4–CuV** hybrid compounds.

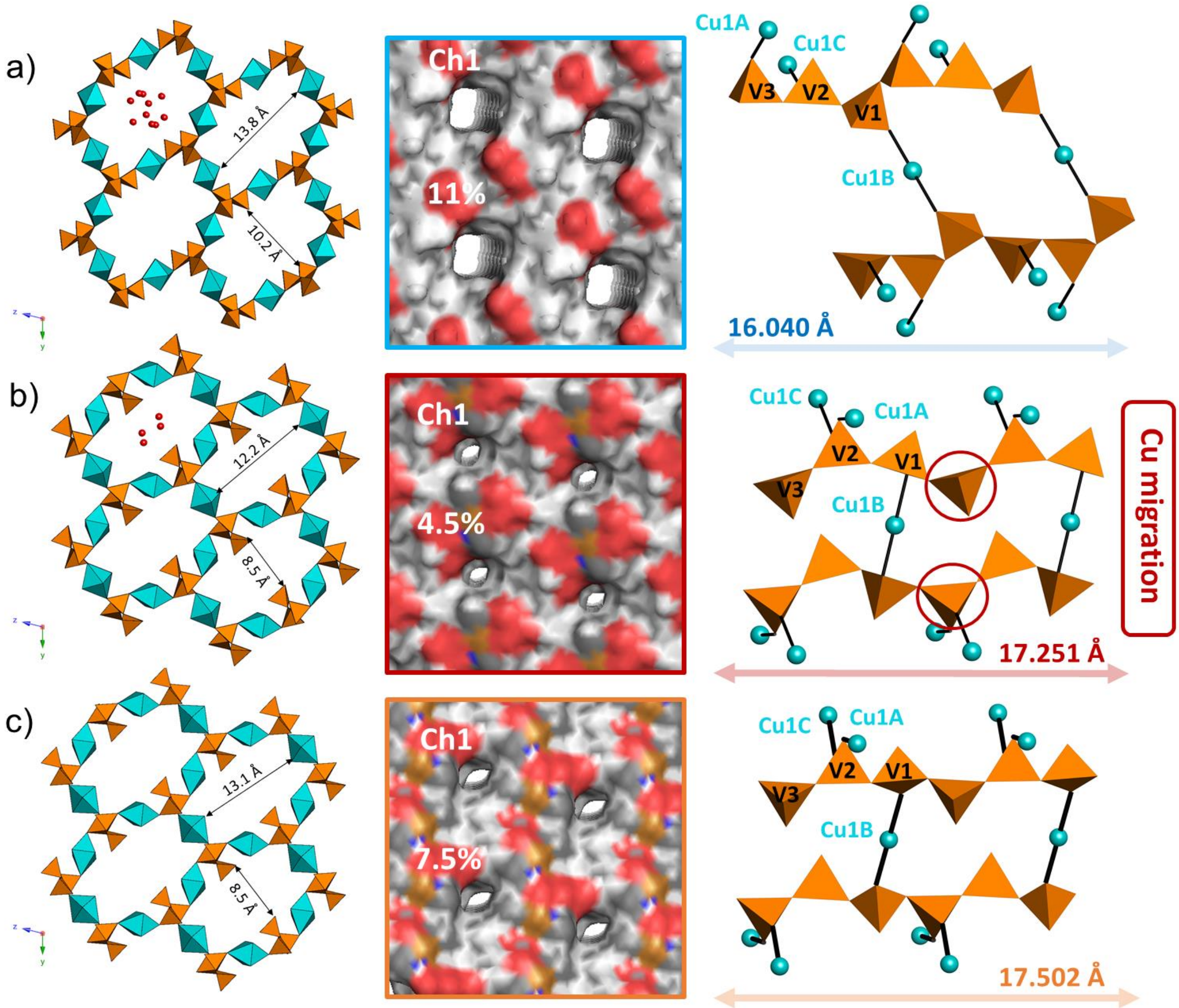

Figure 2.15. Crystal packing of compounds **2–CuV** (a), **3–CuV** (b) and **4–CuV** (c) viewed along the *x* axis with details of the channel dimensions and the hosted water molecules (left); surface of the hybrid frameworks showing the channels (center); and connectivity between the metavanadate chains through different Cu atoms with atom labelling (right) with distances between the nearest equivalent tetrahedral (cyclam ligands are omitted for clarity). Color code: {VO_4} (orange), Cu (blue).

Regarding compound **2–CuV**, significant structural changes take place upon partial dehydration compared to the structure of the parent compound **1–CuV**. Besides the fact that the number of crystallographically independent metavanadate fragments is reduced to one unique chain with a decrease in the periodicity from 6 to 3 {VO_4} units, the transition from **1–CuV** to **2–CuV** also involves drastic changes in some of the cell parameters. While the parameter *b* remains almost invariable, *a* and *c* are halved, and thus the volume of the unit cell is reduced almost four times compared to **1–CuV** (Table 2.1). This is reflected in a contraction of the polymeric anions in the crystal packing with a clear shortening of the distance between consecutive equivalent V atoms in the metavanadate chains (Figure 2.15). For example, the distance between a given V atom and the nearest equivalent in the chain of **1–CuV** with a periodicity of 6 is 16.445 Å, whereas **2–CuV** displays an analogous distance between a V atom and its second nearest equivalent (periodicity 3) of only 16.040 Å. The significant variations in the torsion O_b–V–O_b–V angles along the chains are at the origin of the observed metavanadate contraction when **1–CuV** is transformed into **2–CuV** (Figures 2.14). Due to the crystal rearrangement, the copper atoms in **2–CuV** link equivalent chains arranged in antiparallel fashion as opposed to the assembly determined for **1–CuV**. Therefore, the crystal packing of **2–CuV** shows only one type of hexagonal channel along the *x* axis in which the remaining water molecules of hydration reside (Figure 2.15a).

Table 2.5. Intermolecular N–H···O and C–H···O interactions in **2–CuV, 3–CuV** and **4–CuV.**

2–CuV		**3–CuV**		**4–CuV**	
Donor–H···Acceptor	**D···A (Å)**	**Donor–H···Acceptor**	**D···A (Å)**	**Donor–H···Acceptor**	**D···A (Å)**
N1A–H1A···O3	3.072(3)	N1A–H1A···O3^{i}	2.976(10)	N1A–H1A···O3M^{i}	3.198(17)
N4A–H4A···O2	2.868(3)	N4A–H4A···O12^{ii}	3.035(11)	N1A–H1A···O23^{i}	3.283(17)
C7A–H7AB···O3W	2.885(11)	C2A–H2AA···O1^{vi}	3.245(13)	N4A–H4A···O12	3.077(15)
C7A–H7AB···O5W	3.602(9)	C2A–H2AB···O3^{i}	3.123(13)	C2A–H2AA···O3M^{i}	3.21(2)
—	—	C3A–H3AB···O3^{viii}	3.421(13)	C3A–H3AA···O3M	3.40(2)
—	—	C6A–H6AB···O2W^{vii}	3.364(13)	C3A–H3AA···O13	3.32(2)
N1B–H1B···O1^{i}	2.948(3)	N1B–H1B···O12	3.039(10)	N1B–H1B···O12	3.073(17)
N4B–H4B···O23	3.107(3)	N4B–H4B···O3M^{i}	3.157(10)	N4B–H4B···O3^{ii}	2.831(19)
C3B–H3BA···O12^{iv}	3.439(3)	N4B–H4B···O13^{v}	2.993(10)	C2B–H2BA···O3^{iv}	3.42(2)
C6B–H6BB···O3	3.480(4)	C3B–H3BA···O3M^{i}	3.220(12)	—	—
C6B–H6BA···O9W^{v}	3.442(17)	C5B–H5BB···O1M	3.205(11)	—	—
—	—	C6B–H6BB···O1W	3.328(13)	—	—
N1C–H1C···O2^{ii}	2.931(3)	N1C–H1C···O1^{iv}	2.881(11)	N1C–H1C···O1	2.956(18)
N4C–H4C···O13^{iii}	3.147(3)	N4C–H4C···O2^{iii}	3.135(12)	N4C–H4C···O2^{iii}	3.005(16)
C2C–H2CA···O8W^{vi}	3.101(18)	C2C–H2CB···O1^{iv}	3.028(13)	C2C–H2CA···O2^{v}	3.30(2)
C3C–H3CA···O12^{iii}	3.408(3)	C6C–H6CB···O1W^{v}	3.499(13)	C7C–H7CA···O1^{iv}	3.27(2)
C6C–H6CB···O3M^{iii}	3.448(3)	—	—	—	—

Symmetry codes: **2–CuV:** i) 1–*x*, 1–*y*, –*z*; ii) *x*, *y*, 1+*z*; iii) 1–*x*, 2–*y*, 1–*z*; iv) –1+*x*, *y*, *z*; v) 1–*x*, 1–*y*, 1–*z*; vi) *x*, *y*, –1+*z*. **3–CuV**: i) 1–*x*, –*y*, 1 –*z*; ii) *x*, –1+*y*, –1+*z*; iii) 1–*x*, 1–*y*, 1–*z*; iv) –*x*, 1–*y*, 1–*z*; v) –*x*, –*y*, 1–*z*; vi) *x*, –1+*y*, –1+*z*; vii) 1–*x*, –*y*, –*z*; viii) –1+*x*, –1+*y*, –1+*z*. **4–CuV:** i) 1–*x*, 2–*y*, 2–*z*; ii) 1–*x*, 1–*y*, 1–*z*; iii) 2–*x*, 1–*y*,2 –*z*; iv) 1+*x*, *y*, *z*; v) –*x*, –*y*, –*z*; vi) 1–*x*, 1–*y*, –*z*.

Nevertheless, the overall hybrid framework of **2–CuV** is still highly reminiscent of that described for the parent compound **1–CuV** because each channel is delimited by six metavanadate chains linked to each other through the coordination spheres of six alternating {Cu(cyclam)} moieties. The Cu–O distances in **2–CuV** are in general slightly shorter than those observed in **1–CuV** (Table 2.2), and this fact evidences that the chains approach each other as a result of the removal of two water molecules, which has a noticeable effect in the channel volume of **2–CuV**. The channels show an approximate cross section of 10.2 x 13.8 Å^2 (distances O1···O3 and N1C···N1C) and hence one of the dimensions remarkably shortens compared to those found in either Ch1 or Ch2 in **1–CuV**. Moreover, the solvent accessible volume for **2–CuV** is 339 Å^3, which corresponds to a 22% of the unit cell volume, and this value is somewhat smaller than the 26% found in **1–CuV**. This porous structure is still held together by several C–H···O and N–H···O contacts, the geometrical parameters of which are listed in Table 2.5.

The SCSC transformation of **2–CuV** into **3–CuV** upon further dehydration results in additional relevant changes in the overall hybrid framework. The fluxional metavanadate chains stretch back along the [100] direction (Figures 2.14 and 2.15) and this increases the lattice parameter *a* from 8.02 to 8.60 Å. Consequently, the distance between consecutive equivalent V atoms in the polymeric anion (17.251 Å) is lengthened remarkably compared to that observed for **2–CuV** (16.040 Å) and is even much longer than that found in the parent hybrid **1–CuV** (16.445 Å). This lengthening of the V···V distances is accompanied by a general increase of the torsion O_b–V–O_b–V angles (Table 2.4). The other cell parameters *b* and *c* are slightly reduced when **2–CuV** is transformed into **3–CuV** (Table 2.1), which indicates that the hybrid framework undergoes subtle compression in those directions. This compression translates into a slight decrease of the unit cell volume from 1502 to 1365 Å^3. The solvent accessible channels are still present in **3–CuV** and are still formed through the linkage of six chains by alternating {Cu(cyclam)} complexes in an analogous hexagonal fashion (Figure 2.15b). However, the stretching of the metavanadate anions displaces the Cu1A atom from being coordinated to the V3 tetrahedron to anchor at the V2 neighbor. Thus, the transformation of **2–CuV** into **3–CuV** implies the cleavage and formation of certain Cu–O bonds (Cu1A–O3M and Cu1A–O2M, respectively, see Table 2.2) which appears to be due to a sliding motion between the metavanadate chains as they stretch. This reallocation of the copper atoms leaves the V3 tetrahedron without any grafted complex while both Cu1C and Cu1A moieties become coordinated to V2. The result of this atom migration is a drastic change in the solvent accessible volume of the channels, which occupy only a 9% of the unit cell volume of **3–CuV** (approximately 118 Å^3). This is a substantial decrease when compared to the value of 22% found in **2–CuV**. Indeed, the approximate dimensions of the channels present in the hybrid framework of **3–CuV** decrease to 8.5 x 12.2 Å^2 (distances O3···O3 and N4C···N4C).

When **3–CuV** is heated to 120 °C, all water molecules are removed from the channels and the anhydrous phase **4–CuV** is obtained. As opposed to the previous SCSC transformation, no significant structural modifications were observed in the chains that form **4–CuV** except some minor changes in the overall disposition of the vanadate tetrahedra (Figures 2.14 and 2.15c). It is worth noting however, that these slight structural modifications resulted in a substantial increase of the solvent accessible volume in the channels from the 9% of the unit cell in **3–CuV** to a 15% in **4–CuV** (206 Å^3 approximately). This enlargement is due to the lengthening of only one of the dimensions of the channels, which are approximately 8.5 x 13.1 Å^2 in **4–CuV** (distances O3···O3 and N4C···N4C).

Reversibility of the SCSC transformations

Simple TGA experiments were performed to explore the reversibility of the sequential SCSC transformations observed during the dehydration of **1–CuV**. Crystalline samples of this compound were heated at a rate of 2 °C min^{-1} up to 150 °C, and the so–generated anhydrous samples were kept for a few days in an open container and then heated again at the same rate. The TGA profiles recorded for these anhydrous samples exposed to ambient atmosphere for 1 and 4 days are virtually identical (Figure A2.6 in the Appendix) and differ greatly from the mass loss observed in the initial TGA curve. The initial amount of water is 15.72% but only a 5.30% is recovered upon exposure to air. This value is almost identical to the water content in the intermediate phase **3–CuV**. Indeed, the TGA curves of freshly prepared samples of **2–CuV** and **3–CuV** (see Experimental Section) show mass losses of 10.10 and 5.10% that respectively correspond to 3 (calc. 10.46%) and 1.3 (calc. 4.82%) water molecules per two vanadium atoms. These observations are in good agreement with the water molecules determined by single–

crystal X–ray diffraction data for both compounds. In view of these results, we concluded that the anhydrous phase is not able to undergo full rehydration or needs longer periods to revert to the original hydrated compound **1–CuV** or to the intermediate derivative **2–CuV**.

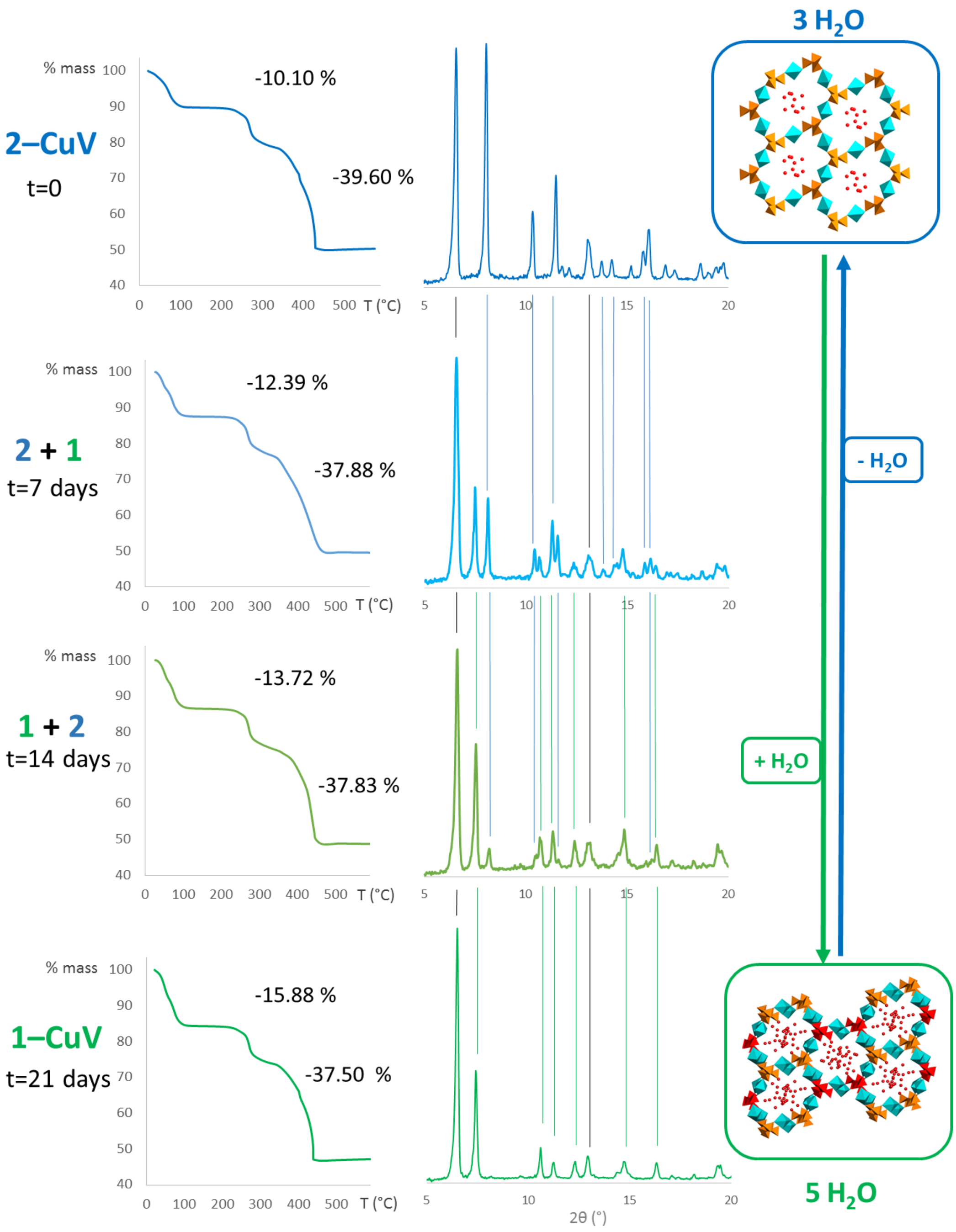

Figure 2.16. Monitoring of the reversibility of the gradual transformation of **2–CuV** into **1–CuV** by TGA and PXRD.

To corroborate the latter hypothesis, we monitored the reversibility of such transformations by combined TGA and PXRD experiments performed once per week during *ca.* one month on samples of compounds **2–4–CuV** that were prepared as described in the Experimental Section and stored in an open container exposed to ambient moisture. Among other modifications, the sequential PXRD patterns of **2–CuV** evidenced a gradual decrease in the intensity of its characteristic diffraction maximum at 8.0° accompanied by the appearance and gradual increase in intensity of a new diffraction maximum at 7.4° that corresponds to the original compound **1–CuV**. After 21 days, the pattern fully corresponded to that expected for the latter compound and traces of **2–CuV** could not be detected any longer (Figure 2.16).

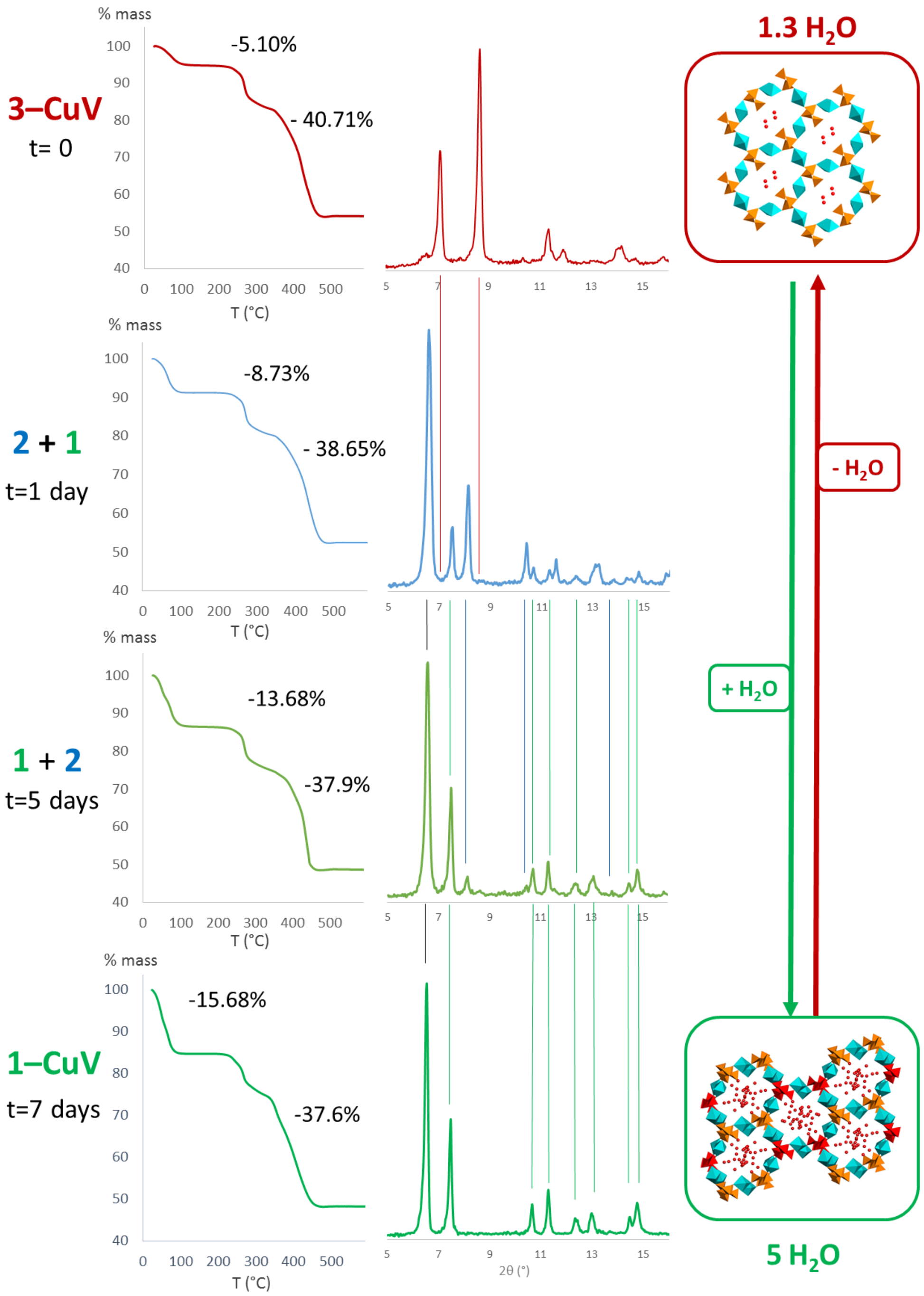

Figure 2.17. Monitoring of the reversibility of the gradual transformation of **3–CuV** into **1–CuV** by TGA and PXRD.

The sequential TGA profiles are in good agreement with the observations above, as they show a gradual increase of the first stage originating from the loss of the water content. While the TGA curve corresponding to the freshly prepared **2–CuV** (*t* = 0) showed a first mass loss of 10.10%, this value was 12.34% for that recorded after 7 days of exposure to air (*t* = 7 days).

After two weeks, the amount of water increased to a 13.72% (*t* = 14 days), and after another week, we were able to record a TGA curve virtually identical to that of pure **1–CuV** with a water content of 15.86% (*t* = 21 days). All these results confirm that the SCSC transformation of compound **1–CuV** into the phase **2–CuV** is fully reversible, in such a way that this partially dehydrated derivative slowly converts back into the original hydrated compound in open air conditions (Figure 2.16).

Analogous experiments were performed on **3–CuV** but no indication of reversibility was found in this case because the PXRD patterns and the TGA curves remained virtually unaltered for at least 37 days. To verify whether the transformation of **1–CuV** into **3–CuV** was indeed permanent, a sample of the latter phase was soaked in water. The PXRD pattern taken after only 1 day did not show any diffraction maxima corresponding to **3–CuV**, but the main signals could only be assigned to a mixture of both **1–CuV** and **2–CuV**, the latter being the major component according to the relative intensities of the maxima. After five days, compound **1–CuV** becomes the major phase in the mixture, and after seven days (*t* = 7 days), no traces of compound **2–CuV** could be detected through PXRD experiments (Figure 2.17). TGA analyses were also carried out on the polycrystalline sample *t* = 7 days and the results unequivocally confirmed that **3–CuV** reverts to the parent **1–CuV** upon being immersed in excess of water for a week. The TGA curve of compound **3–CuV** shows a mass loss associated with dehydration of 5.10% (1.3 H_2O per 2 V atoms), whereas the sample *t* = 7 days (dried in air) displayed a TGA profile nearly identical to that of compound **1–CuV** with a weight loss of 15.68% that corresponds to 5 water molecules per two V atoms (Figure 2.17). In the case of **4–CuV**, this anhydrous phase rapidly rehydrates to **3–CuV** in some hours, as evidenced by the TGA results which are in perfect agreement with those expected for the latter intermediate derivative.

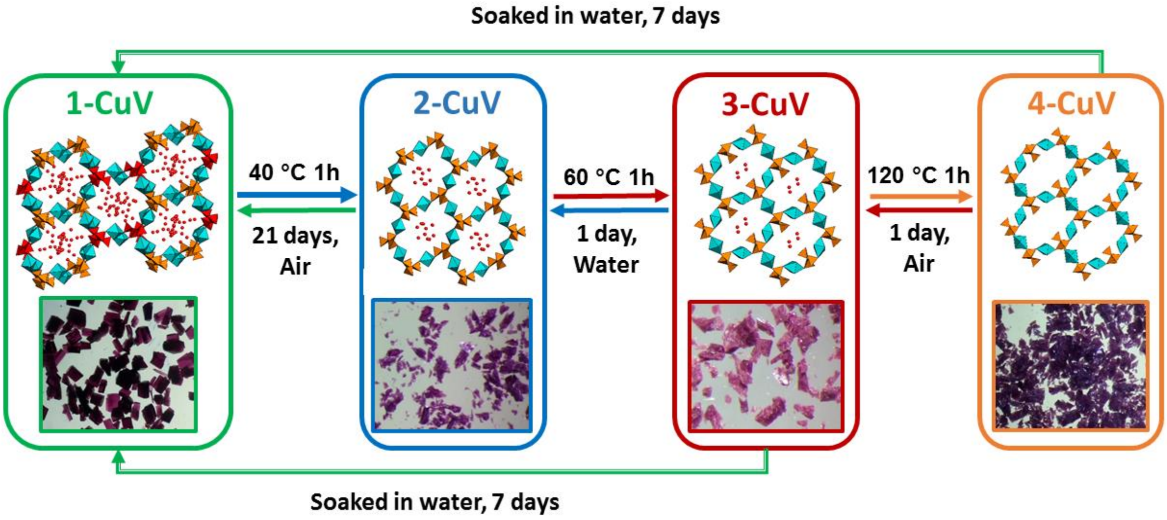

Figure 2.18. Scheme of the reversibility of the SCSC transformations between **1–4–CuV** with digital photographs of the crystals for each of the four compounds.

All in all, the results of these PXRD and TGA combined experiments demonstrate the reversible nature under the appropriate conditions of the three sequential SCSC transformations that the flexible open–framework of **1–CuV** undergoes upon thermal dehydration (Figure 2.18).

2.3.3 Robust Decavanadate/Metalorganic Open–Frameworks

Vibrational characterization and thermostructural behavior of 1–CuV10

The preliminary characterization of compound **1–CuV10** was carried out by means of FT–IR technique. As seen in Figure 2.19, the overall spectrum of the hybrid compound is very similar to that shown by the decavanadate salt and differs significantly from the metavanadate precursor.

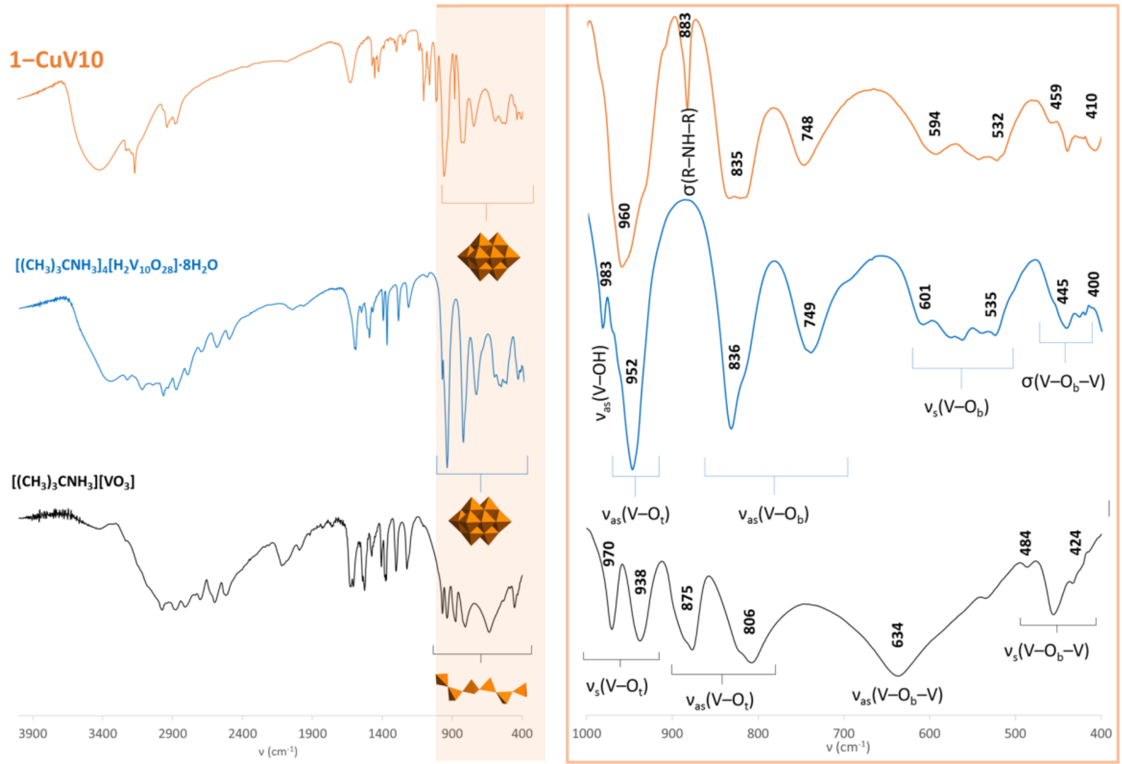

Figure 2.19. FT–IR spectra of **1–CuV10** along with those belonging to the decavanadate and metavanadate precursors with details of the inorganic region.

In this sense, the intense band corresponding to the ν_{as}(V–O$_t$) vibration that appears at 960 cm^{-1} remains virtually unaltered compared to the decavanadate precursor, whereas the signal located at 983 cm^{-1} and associated with the antisymmetric stretching vibration of protonated V–O$_b$ bonds can no longer be found in the spectrum of **1–CuV10**. This fact confirms that no basic oxygen atoms are protonated. The peak of medium intensity observed at 883 cm^{-1} could not be assigned to other than the δ(R–NH–R) vibration originated from the cyclam ligands. The signals at 835 and 748 cm^{-1} are attributable to the ν_{as}(V–O$_b$–V) mode, whereas those spanning from 594 to 532 cm^{-1} correspond to the ν_{as}(V–O$_b$–V) vibration. The poorly defined peaks corresponding to the ν_s(V–O$_b$–V) vibration mode appear in the range 459 and 410 cm^{-1}. Regarding the metal–organic region of the FT–IR spectra, the peaks associated with the stretching of the –N–H and –C–H bonds are respectively observed at 3200–3150 and 2900–2860 cm^{-1}, whereas several weak to medium signals corresponding to the δ(C–H) and ν(N–C) vibration modes are also present in the 1490–1230 and 1100–1000 cm^{-1} ranges. These signals confirmed the presence of the cyclam ligands in our compounds.

The thermal stability of **1–CuV10** was investigated by TGA experiments, which show that the title compound decomposes through three mass loss stages (Figure 2.20). The first stage is observed from room temperature to *ca.* 100 °C and originates from the release of all water molecules of hydration. The experimental mass loss corresponds to 10 water molecules per decavanadate anion (calcd. 9.33%, found 8.94%). Completion of this stage leads to the anhydrous phase **1a–CuV10**, which shows a significant range of thermal stability extending up to *ca.* 150–170 °C. Above this temperature, the anhydrous phase undergoes further decomposition via two overlapping mass loss stages associated with the combustion of the organic ligands and the breakdown of the POM framework. The overall mass loss for these two stages is in good agreement with three cyclam ligands per decavanadate anion (calcd. for $3C_{10}H_{24}N_4$ 31.10%; found 32.11%). The final residue is obtained at temperatures above *ca.* 550 °C (calcd. for $Cu_3O_{28}V_{10}$ 59.50%, found 58.95%).

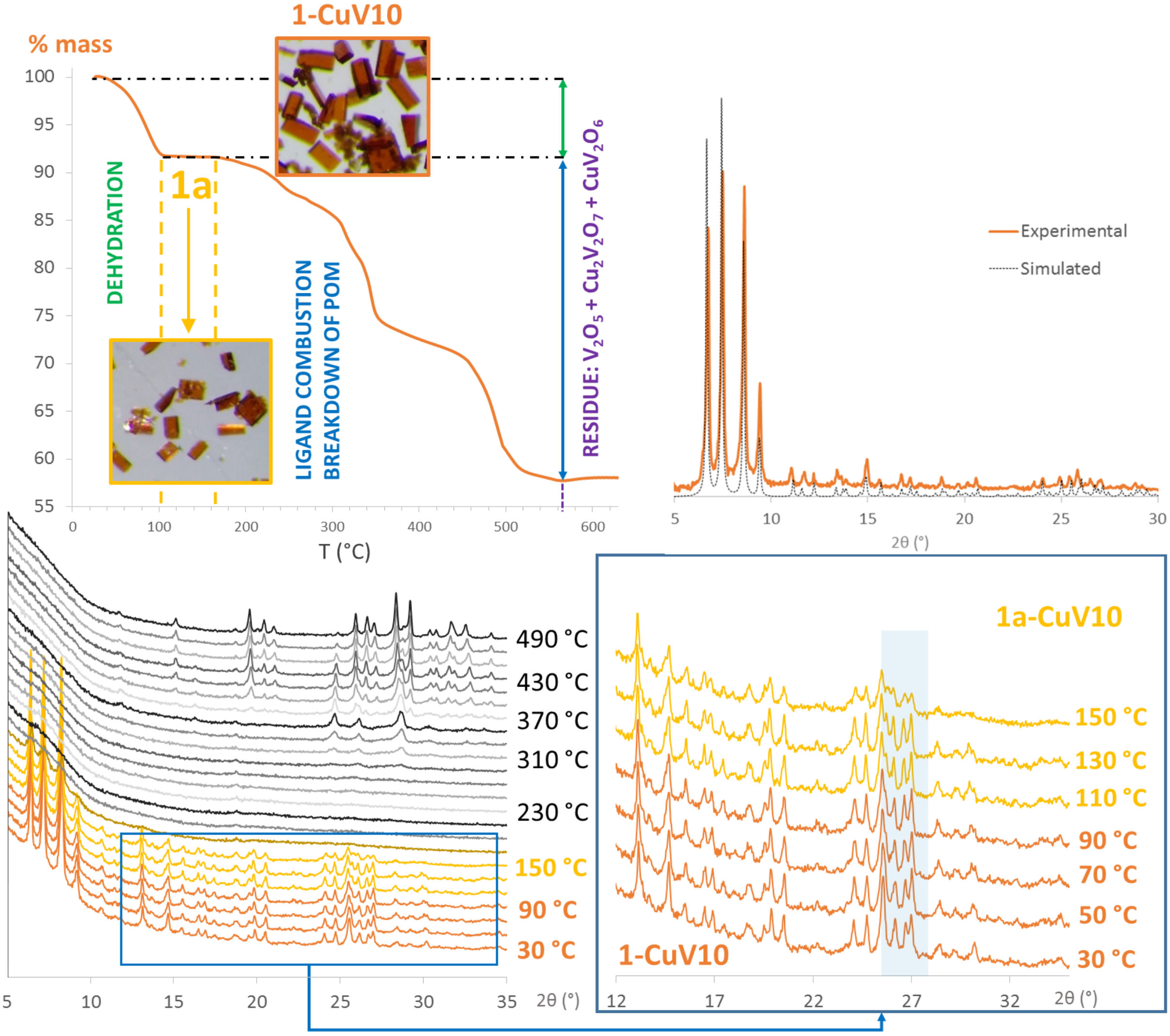

Figure 2.20. TGA curve and TPXRD studies for **1–CuV10** hybrid, along with the comparison of the experimental PXRD pattern and that simulated from the single–crystal XRD data.

Variable–temperature powder X–ray diffraction measurements (TPXRD) between 30 and 490 °C show that compound **1–CuV10** is able to maintain its crystallinity upon dehydration up to temperatures in the 150 to 170 °C range (Figure 2.20). No substantial modifications in neither the positions nor the intensities of the diffraction maxima are observed upon heating, although subtle variations can be noticed when going from 90 °C to 110 °C upon close inspection of the group of maxima in the 2ϑ range 25–27°. This temperature range corresponds to the removal of all water molecules of hydration according to the TGA curve, and hence to the formation of the anhydrous **1a–CuV10** phase, which must display virtually identical crystal packing based on the observations above. The crystalline **1a–CuV10** phase becomes amorphous at temperatures above 150 °C which nearly corresponds to the beginning of the ligand combustion stage in the TGA curve. Signs of new high–temperature phases start appearing at *ca.* 310 °C. At temperatures above 490 °C, these phases forming the final residue of the thermal decomposition are defined enough for being identified as a mixture of orthorhombic $Pmn2_1$ V_2O_5 (PDF: 01–076–1803),[69] monoclinic $C2/c$ $Cu_2V_2O_7$ (PDF: 01–073–1032),[70] and the orthorhombic $Pmn2_1$ phase of CuV_2O_6 (PDF: 00–016–0127)[71] in an approximate ratio 3:1:1 (Figure A2.7 in the Appendix).

Crystal structures of 1–CuV10 and 1a–CuV10

Compound **1–CuV10** crystallizes in the triclinic *P*–1 space group and its asymmetric units contains one half centrosymmetric decavanadate $(V_{10}O_{28})^{6-}$ anion and three crystallographically independent, centrosymmetric {Cu(cyclam)} moieties (Figure 2.21). Five water molecules of hydration disordered over ten positions complete the asymmetric unit. The structure of the decavanadate anion is well established and consists in an arrangement of 10 edge–shared $\{VO_6\}$ octahedra with ideal D_{2h} symmetry. This arrangement can be described as a central $\{V_6O_{12}\}$ core built of six VO_6 octahedra arranged in a 2 × 3 rectangular array and capped with two additional $\{VO_6\}$ units on both sides (Figure 2.21). The V–O bond lengths (1.608–2.318 Å) are consistent with other decavanadate clusters reported in the literature.[74]

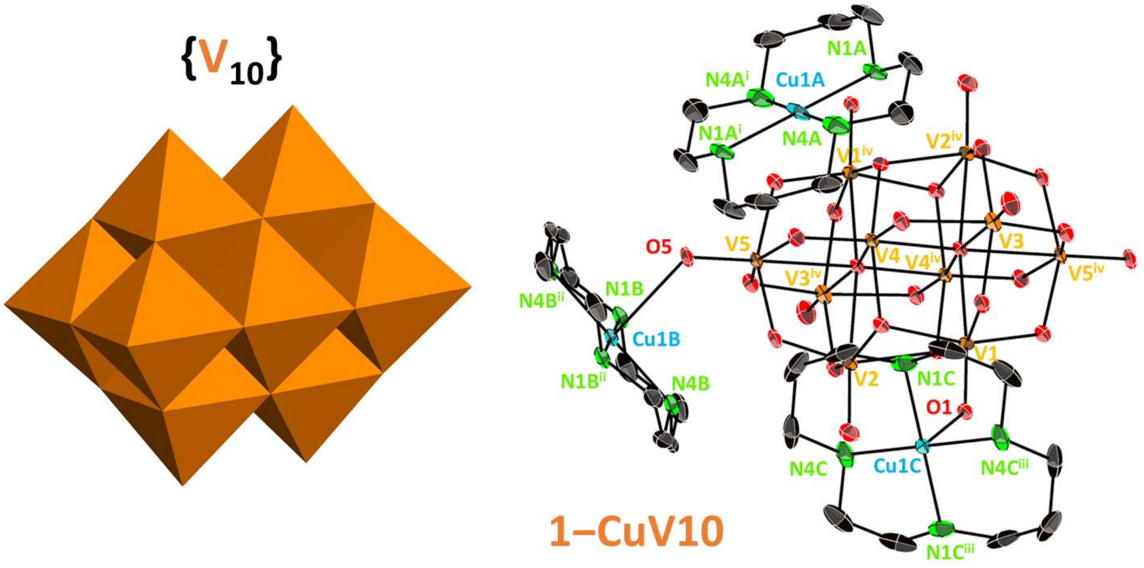

Figure 2.21. Polyhedral representation of the decavanadate cluster and ORTEP view of **1–CuV10** hybrid depicted at 50% probability level with partial atom labelling. Water molecules are ommited for clarity. Symmetry codes: i) 1–*x*, 1–*y*, –*z*; ii) 2–*x*, 1–*y*, 1–*z*; iii) 2–*x*, –*y*, –*z*; iv) 2–*x*, 1–*y*, –*z*.

There are two types of {Cu(cyclam)} units: the complexes Cu1B and Cu1C both play the role of linking moieties, whereas Cu1A is a charge balancing subunit. The coordination spheres of the Cu1B and Cu1C centers show distorted octahedral CuN_4O_2 geometries, as indicated by CShM calculations,[72] with the four N atoms of the cyclam ligand forming the equatorial plane and the axial positions occupied by terminal O atoms from $(V_{10}O_{28})^{6-}$ clusters. In contrast, the Cu1A moiety consist on a square–planar complex (Figure 2.21 and Table 2.6). Both Cu1B and Cu1C display the so–called *trans–III* which is in good agreement with the results reported previously.[73] In regard to square planar complexes, these studies have also demonstrated that the *trans–I* configuration gains stability over the *trans–III* when the coordination number of the metal center is reduced. In our case, however, the configuration of the Cu1A moiety remains the same as that of Cu1B and Cu1C in spite of showing a square–planar geometry.

Table 2.6. Cu–O and Cu–N bond lengths (Å) as well as the polyhedral distorsion (CShM) of the {Cu(cyclam)} complexes in **1–CuV10** and **1a–CuV10**.

1–CuV10		**1a–CuV10**	
Cu1A–N1A	1.995(5)	Cu1A–N1A	1.999(4)
Cu1A–N1A^{i}	1.995(5)	Cu1A–N1A^{i}	1.999(4)
Cu1A–N4A	1.992(7)	Cu1A–N4A	1.997(4)
Cu1A–N4A^{i}	1.992(7)	Cu1A–N4A^{i}	1.997(4)
SP–4	0.130	SP–4	0.135
Cu1B–N1B	2.001(5)	Cu1B–N1B	2.003(4)
Cu1B–N1B^{ii}	2.001(5)	Cu1B–N1B^{ii}	2.003(4)
Cu1B–N4B	2.021(5)	Cu1B–N4B	2.002(4)
Cu1B–N4B^{ii}	2.021(5)	Cu1B–N4B^{ii}	2.002(4)
Cu1B–O5	2.526(3)	Cu1B–O5	2.533(3)
Cu1B–O5^{ii}	2.525(3)	Cu1B–O5^{ii}	2.533(3)
OC–6	1.452	OC–6	1.518
Cu1C–N1C	2.020(5)	Cu1C–N1C	2.003(4)
Cu1C–N1C^{iii}	2.020(5)	Cu1C–N1C^{iii}	2.003(4)
Cu1C–N4C	1.997(5)	Cu1C–N4C	2.005(4)
Cu1C–N4C^{iii}	1.997(5)	Cu1C–N4C^{iii}	2.005(4)
Cu1C–O1	2.604(3)	Cu1C–O1	2.571(3)
Cu1C–O1^{iii}	2.604(3)	Cu1C–O1^{iii}	2.571(3)
OC–6	1.918	OC–6	1.689

Symmetry codes: i) 1–*x*, 1–*y*, –*z*; ii) 2–*x*, 1–*y*, 1–*z*; iii) 2–*x*, –*y*, –*z*. CShM: reference polyhedra SP–4 (square), OC–6 (octahedron).

The crystal packing of **1–CuV10** consists in a supramolecular assembly of covalent hybrid layers in which the decavanadate anions are linked by the Cu1B and Cu1C bridging moieties along the [001] and [010] directions, respectively (Figure 2.22). Thus, each decavanadate anion results connected to four neighboring clusters through four complexes whose grafting sites are VO_6 octahedra belonging to either the central $\{V_6\}$ rectangular core (Cu1B) or to the dimeric caps (Cu1C). This I^2O^0–type arrangement leads to the formation of hybrid grids with water–accessible square–like voids in the *yz* plane. A closely related bidimensional lattice with similar connectivity between building blocks has been reported for the $(Hpz)_2[\{Cu(pz)_4\}_2(V_{10}O_{28})]\cdot 2H_2O$ (pz = pyrazole),[54a] although with the voids filled with Hpz cations in contrast to **1–CuV10**. In our case, the stacking of hybrid grids along the [100] direction is such that the square–like voids result superimposed on each other and this type of supramolecular assembly generates channels parallel to the crystallographic *x* axis in which all of the water molecules are hosted. Thus, the walls of these channels are delimited by rings of four $(V_{10}O_{28})^{6-}$ anions and four $\{Cu(cyclam)\}^{2+}$ complexes in alternate fashion with approximate cross–section of 10.4 × 8.8 Å^2 (distances N4C···N4C and N1B···N1B, Figure 4b). The total solvent accessible volume is 428 Å^3 per unit cell, which corresponds to approximately 25% of the unit cell volume as calculated using PLATON. The surface representation of the channel volume and that of the porous hybrid framework is given in Figure 2.22.

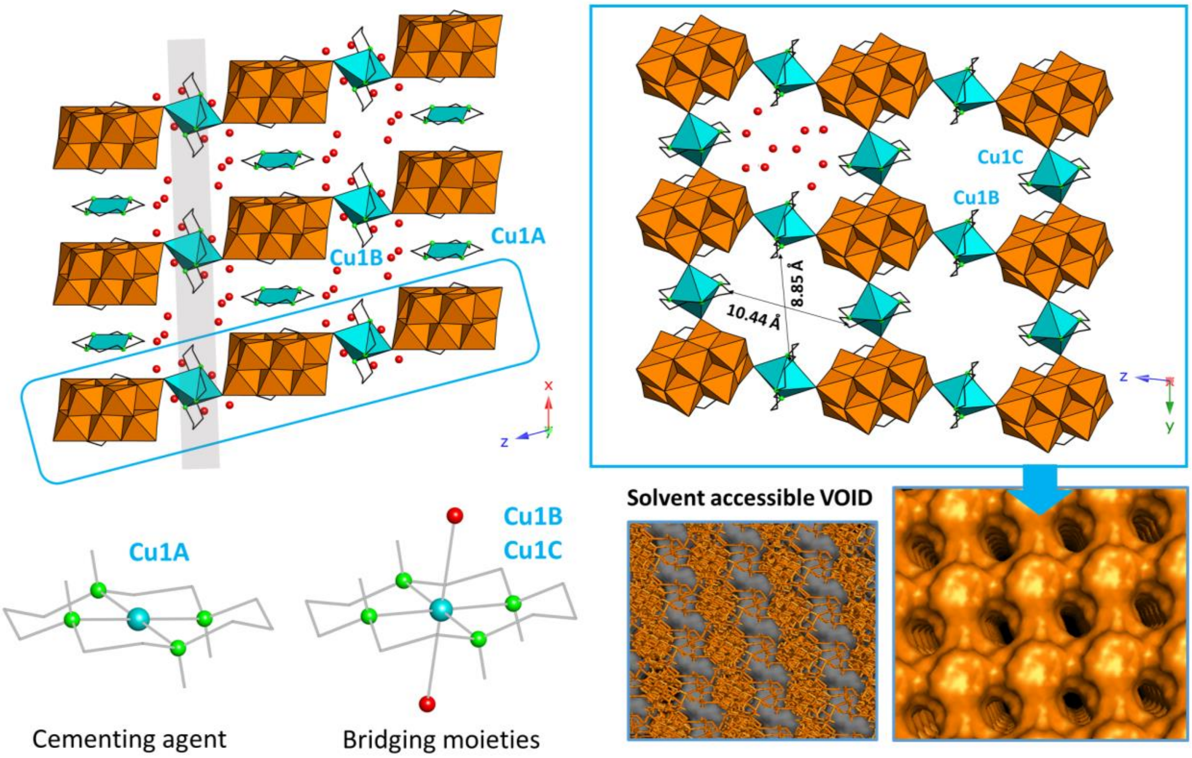

Figure 2.22. Crystal packing of **1–CuV10** viewed along the crystallographic *x* axis (top left) and hybrid layers with details of the hosted water molecules and the estimated dimensions of the channels in the *yz* plane (top right). Different complexes found in **1–CuV10** (bottom left) and surface representations of the channels running along the crystallographic *x* axis and that of the porous metalorganic network (bottom right). H atoms are omitted for clarity. Color code: $\{VO_6\}$ (orange octahedra), Cu (blue polyhedra), N (green), O (red).

The square–planar Cu1A complex cation occupies interlamellar spaces and is sandwiched in between ditriangular faces of two $(V_{10}O_{28})^{6-}$ clusters belonging to different layers (Figure 2.22). Indeed, the Cu1A atom is located at a distance of 3.0730(2) Å from the plane formed by the bridging O atoms of these faces (O12, O15, O24 and O34). Despite the absence of any coordination bond connecting the layers, an extensive network of C–H···O and N–H···O interactions is established between the cyclam ligand of the Cu1A complex and the surfaces of the sandwiching clusters. It should be noted that these interactions are more numerous and more favorable than those established by Cu1B and Cu1C complexes within layers (Table 2.7). As a result, the Cu1A cation acts as an effective cementing agent to reinforce the stacking of the covalent layered lattices into a supramolecular open–framework material.

In comparison, the water molecules of hydration do not appear to have any relevant structural role because they are weakly bound and do not interact with neither the cyclam ligands nor the terminal oxygen atoms of the clusters. In fact, only O7W and O9W appear to slightly contribute to the massive H–bond network amongst hybrid layers and Cu1A cementing complexes (Figure 2.23). It is worth mentioning that another decavanadate–containing hybrid compound sharing similar metalorganic building blocks can be found in the literature: $[(CuL)_{0.5}(H_2L)_{1.5}][H_2V_{10}O_{28}]\cdot 6H_2O$.[27] In this case, the macrocyclic polyamine ligand (L) is the hexamethyl derivative of cyclam and the inorganic cluster is diprotonated (L = 5,5,7,12,12,14–hexamethyl–1,4,8,11–tetraazacyclotetradecane). The structure contains hybrid chains of alternating clusters and complexes, which arrange in supramolecular sheets via hydrogen bonding as opposed to the covalent bi–dimensional lattice of compound **1–CuV10**.

Table 2.7. Comparison of the intermolecular N–H···O and C–H···O Interactions in **1–CuV10** and **1a–CuV10**.

	1–CuV10			**1a–CuV10**		
Donor–H···Acceptor	**H···A (Å)**	**D···A (Å)**	**D–H···A (°)**	**H···A (Å)**	**D···A (Å)**	**D–H···A (°)**
N1A–H1A···O12^{i}	2.36	3.177(6)	140	2.40	3.184(4)	137
N1A–H1A···O16^{ii}	2.24	3.111(6)	148	2.16	3.043(4)	149
N1A–H1A···O34^{ii}	—	—	—	2.57	3.259(4)	128
N4A–H4A···O12^{iii}	2.50	3.266(6)	135	2.44	3.228(4)	137
N4A–H4A···O15^{iii}	2.11	3.015(6)	153	2.14	3.040(4)	151
N4A–H4A···O24	2.56	3.233(7)	126	—	—	—
C2A–H2AA···O5	2.46	3.299(7)	144	2.46	3.298(7)	144
C2A–H2AA···O24	2.51	3.227(7)	131	2.51	3.227(7)	131
C3A–H3AA···O3^{ii}	2.39	3.289(8)	153	2.51	3.306(6)	140
C3A–H3AA···O34^{ii}	2.55	3.280(7)	132	2.44	3.190(5)	134
C3A–H3BA···O7W^{iii}	2.57	3.441(15)	149	—	—	—
C6A–H6AB···O12^{iii}	2.58	3.367(8)	138	2.56	3.339(5)	138
C6A–H6AB···O12^{iii}	2.58	3.367(8)	138	2.56	3.339(5)	138
C6A–H6AA···O2^{iii}	—	—	—	2.51	3.295(6)	138
C6A–H6AB···O1^{iii}	2.52	3.342(8)	142	2.52	3.342(7)	142
N1B–H1B···O35^{iv}	2.15	3.032(5)	149	1.85	2.812(5)	166
N4B–H4B···O25^{v}	1.91	2.846(5)	159	1.87	2.827(5)	165
N1B–H1B···O9W^{iv}	2.58	3.308(13)	131	—	—	—
C2B–H2BB···O9W^{iv}	2.60	3.209(13)	121	—	—	—
C5B–H5BA···O5	2.58	3.185(6)	121	2.57	3.171(6)	120
C6B–H6BB···O35^{iv}	2.55	3.360(7)	141	—	—	—
C6B–H6BA···O16^{iii}	2.45	3.399(6)	167	2.45	3.399(6)	167
N1C–H1C···O13	2.11	2.949(6)	142	1.93	2.813(5)	148
N4C–H4C···O2	2.09	2.976(6)	149	2.18	3.040(5)	146
C3C–H3CA···O13	2.33	3.107(7)	136	2.50	3.211(7)	130
C3C–H3CA···O2	—	—	—	2.59	3.288(5)	129

Symmetry codes: i) –1+*x*, *y*, *z*; ii) 1–*x*, 1–*y*, –*z*; iii) 2–*x*, 1–*y*, –*z*; iv) *x*, *y*, 1+*z*; v) 2–*x*, 1–*y*, 1–*z*; vi) 2–*x*, –*y*, –*z*.

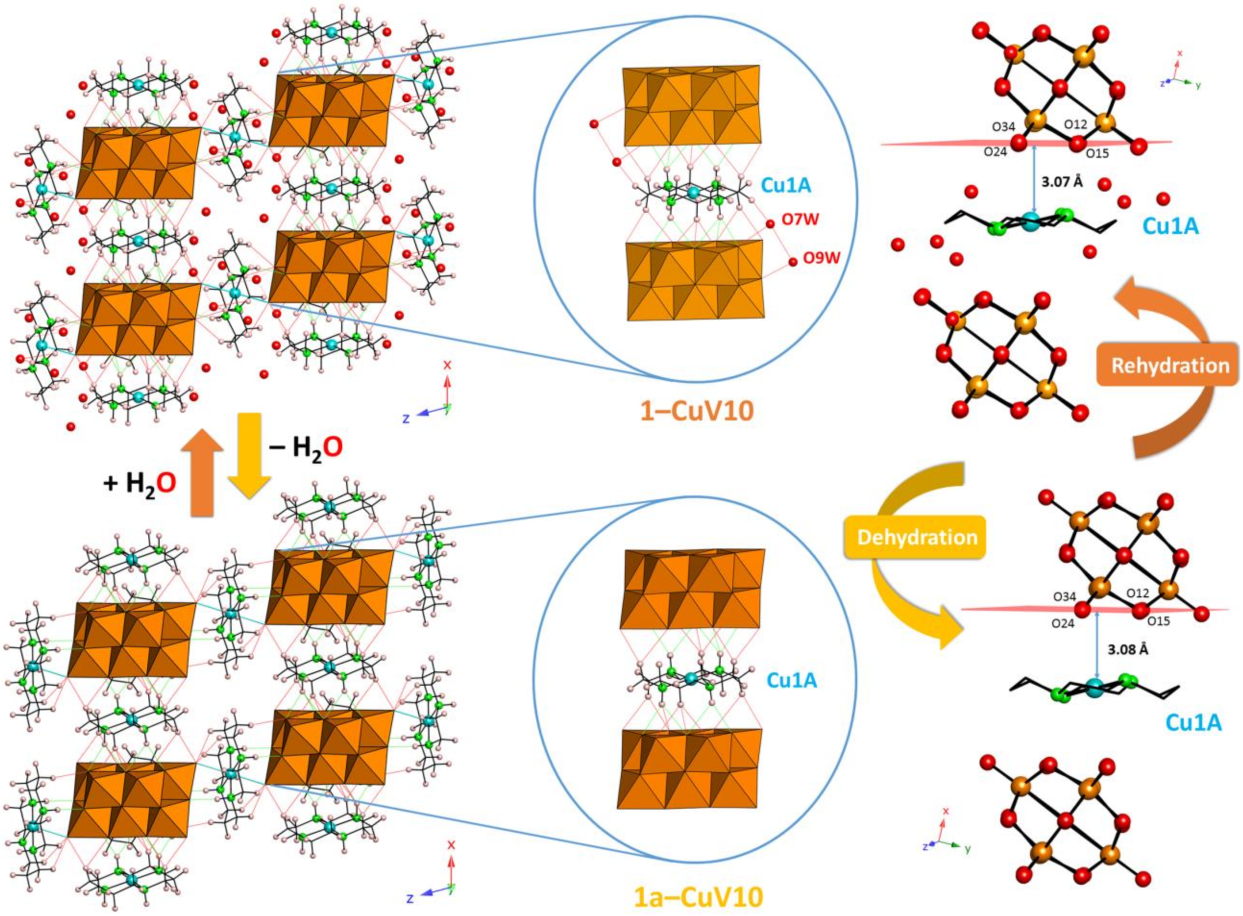

Figure 2.23. Comparison between the supramolecular assembly for **1–CuV10** and **1a–CuV10** showing the massive H–bonding network (green: –N–H···O; red: –C–H···O). The interactions between the sandwiched Cu1A and the clusters are highlighted (left). The distance between the cementing agent and the nearest plane formed by decavanadate oxygen atoms (O12, O15, O24 and O34) is also shown (right).

As mentioned before, guest solvent molecules located in cavities or channels can often be removed from a given host material without causing the crystalline collapse of the porous framework. This should be the case for **1–CuV10** according to the variable–temperature PXRD results. To determine whether the supramolecular three–dimensional assembly of **1–CuV10** is robust enough to effectively maintain its open framework nature upon dehydration and to identify any structural change triggered by the release of the guest solvent, we attempted to perform single–crystal XRD experiments on crystals of **1–CuV10** heated to 130 °C to evacuate all water of hydration in the channels. Fortunately, the crystals maintained their integrity upon thermal treatment, and hence, full data collection on the **1a–CuV10** anhydrous form could be carried out. As expected from the TPXRD analyses, the structure of the anhydrous phase proved to be virtually identical to that of the hydrated **1–CuV10**. The cell parameters including the unit cell volume and the relative arrangement of building blocks in the asymmetric unit, as well as the bond lengths within and among the blocks, remained almost invariable as shown in Tables 2.1 and 2.6. Moreover, the dimensions of the channels did neither undergo significant variations when **1–CuV10** was dehydrated into **1a–CuV10** (Figure 2.24), but for a subtle decrease of *ca.* 30 Å^3 in the total solvent accessible void according to PLATON calculations (397 Å^3, 24% of the unit cell).

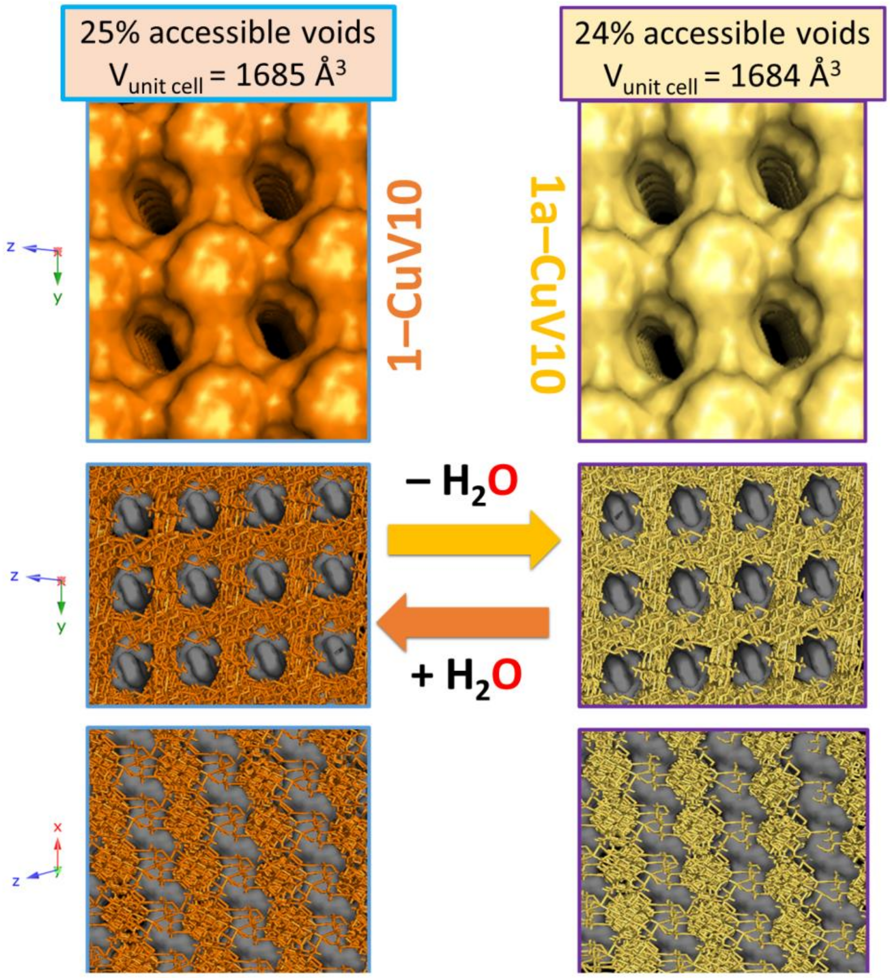

Figure 2.24. Comparison of the porous framework and channels in **1–CuV10** (left) and **1a–CuV10** (right).

This absence of significant modifications in the metal atom positions of the constituent building blocks upon evacuation of guest solvent molecules confirms the robustness of the open hybrid framework, as well as the fact that the water molecules (including O7W and O9W) do not fulfill any key structural role. This fact is consistent with the few intermolecular interactions observed between lattice water molecules and the decavanadate clusters or the cyclam ligands for the hydrated compound **1–CuV10**. Nevertheless, some subtle changes in the extensive hydrogen–bonding network can be observed when transforming **1–CuV10** into **1a–CuV10**. The thermally triggered dehydration produces a rotation of the metal–organic complexes around their axial axes that slightly modifies some of the intermolecular C–H···O and N–H···O interactions between the cyclam ligands and the cluster surfaces (Figure 2.23 and Table 2.7). This relative rotation is notably more accused for the Cu1B moiety (approximately 20°) than for the Cu1A and Cu1C complexes (less than 10°), but the overall number of favorable interactions is maintained nearly constant. Moreover, the interlamellar distance correlated with that of the Cu1A center to the plane formed by the O12, O15, O24 and O34 atoms remains virtually identical (Figure 2.23). These observations show that our hybrid open–framework does not undergo any contraction of the unit cell volume and consequent structural collapse upon dehydration, and hence prove its robustness and permanent microporous nature.

Gas sorption properties

Since the channel dimensions found in the open–framework of **1–CuV10** are larger than those of N_2 and CO_2, we decided to explore whether **1–CuV10** could exhibit gas sorption properties. Our studies revealed that it does not exhibit the capability to adsorb N_2 while CO_2 adsorption does take place. This fact can be explained taking into account the presence of narrow microporosity in **1–CuV10**. Although the kinetic diameter of the CO_2 and N_2 molecules (3.30 Å vs. 3.64 Å) are similar, the higher adsorption temperature for CO_2 confers the gas molecules a larger kinetic energy that favors their access into the narrow porosity, whereas N_2 molecules are kinetically restricted due to the low temperatures at which the adsorption of this gas is performed.[67,68,75],

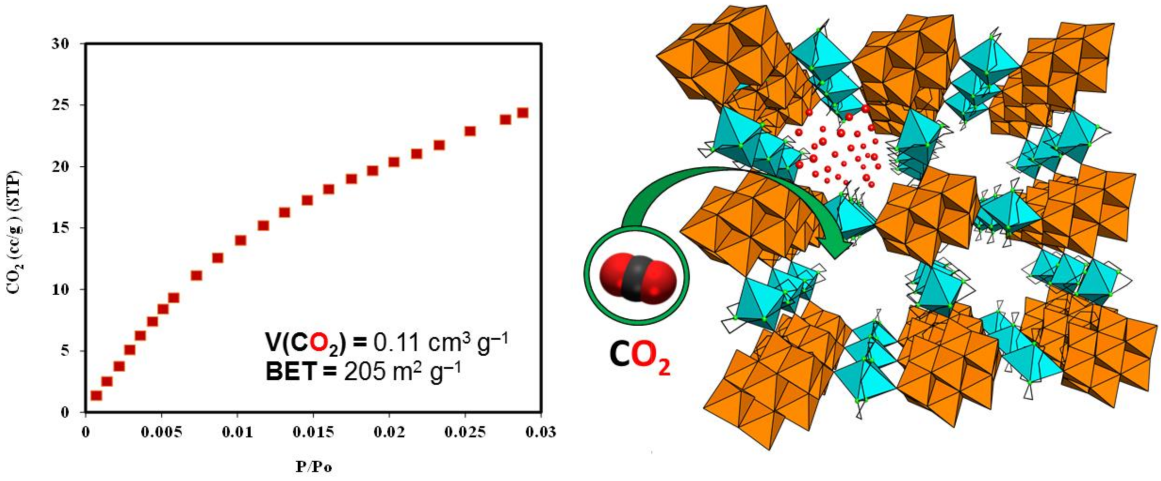

Figure 2.25. Sorption properties of the activated **1–CuV10** compound, showing the type I isotherm for CO_2 adsorption at 273 K.

Compound **1–CuV10** displays a type I isotherm for CO_2 adsorption, which is indeed characteristic of a microporous material (Figure 2.25). In regard to the characterization of its porous texture, it is first worth noticing that while the total micropore volume obtained from the N_2 adsorption corresponds to the whole range of microporosity (pore size up to 2 nm), the CO_2 adsorption (V_{CO2}) only provides specific information about narrow microporosity only (pore size < 0.8 nm). The volume of the micropores in **1–CuV10** is 0.11 cm^3 g^{-1}, while the BET (Brunauer–Emmett–Teller) surface area is 205 m^2 g^{-1}, as calculated from the CO_2 sorption isotherm at 273 K. These experimental data confirm that the micropores with approximate cross–sections of 10.4 × 8.8 $Å^2$ observed from single–crystal XRD studies (Figure 2.22) are accessible and fully operative, which endows the hybrid open–framework of **1–CuV10** with functionality in CO_2 capturing.

Reports on BET data for POM–based crystalline open–framework materials are scarce.[76] A limited number of microporous hybrid compounds with CO_2 adsorption capability can be found in the literature. Mizuno's $K_2[Cr_3O(OOCH)_6(4\text{–ethylpyridine})_3]_2[\alpha\text{–}SiW_{12}O_{40}]$ is a representative example as it shows a high CO_2/C_2H_2 sorption selectivity.[77] The closely related $[Cr_3O(OOCCH{=}CH_2)_6(H_2O)_3]_3[\alpha\text{–}PW_{12}O_{40}]$ ionic crystal displays shape–selective adsorption of CO_2 and C_2H_2 over the larger N_2 and methane molecules, due to the kinetic diameters of the former being comparable to the minimum pore aperture.[78] Compared to our compound, both examples show lower BET surface areas (75 and 50 m^2 g^{-1}, respectively) and this can be explained attending to their smaller channel apertures (3.5 Å and 3.3 Å, respectively). Some fully inorganic POM–based microporous materials have also displayed CO_2 sorption properties. For example, Ueda et al reported two inorganic microporous materials based on ε–Keggin–type clusters,[79] but both the BET surface areas and micropore volumes are approximately three to four times lower than those estimated for our compound. Wang et al. recently prepared the $(TBA)_2[Cu^{II}(BBTZ)_2(\alpha\text{–}Mo_8O_{26})]$ POMOF (BBTZ = 1,4–bis(1,2,4–triazol–1–ylmethyl)–benzene), which exhibits the highest adsorption capacity reported for a POM–based hybrid.[80] The CO_2 uptake capacity at saturation of 165 cm^3 g^{-1} at 195 K and 87.7 cm^3 g^{-1} at 273 K is comparable to the best performing zeolite–like MOFs.[81] These results together with a remarkable BET surface area of 773 m^2 g^{-1} derived from the presence of a three–directional system of intersecting channels, as opposed to the system of parallel channels found in **1–CuV10**. In fact, the total solvent accessible volume is approximately 50% of the unit cell volume which is roughly twice the empty volume observed for our compound **1–CuV10** upon thermal activation. To our knowledge, compound **1–CuV10** is the first decavanadate–based crystalline material that exhibits CO_2 sorption capability as a straightforward consequence of i) the robust nature of its supramolecular open–framework structure and ii) the appropriate dimensions and accessibility of the channels.

Catalytic activity tests

The POM–catalyzed oxidation of hydrocarbons has been thoroughly studied over the past decades owing to its importance from industrial and synthetic viewpoints.[82] In this context, much attention has been paid to the oxidation of the tricyclic saturated hydrocarbon adamantane because this particular reaction is used as a probe to measure the C–H bond activation ability of a given catalyst. Thus, several compounds have been tested in both homogeneous and heterogeneous phase with different oxidizing agents (e.g. PhI, NaOCl, H_2O_2, O_2, alkyl hydroperoxides, percarboxylic acids), affording a great variety of results in terms of conversion and selectivity.[83]

The catalytic activity of **1–CuV10** toward the oxidation of adamantane has been explored in heterogeneous phase using hot acetonitrile as solvent and an environmentally friendly oxidant such as H_2O_2. Some other archetypal POM catalysts ($H_3[PMo_{12}O_{40}]$ and $H_4[PVMo_{11}O_{40}]$), as well as V_2O_5, have also been tested in the same experimental conditions for comparative purposes (Table 2.8). As expected, the reaction does not take place in the absence of any catalyst under the selected experimental conditions due to the high stability of the tricyclic alkane. It is also remarkable that the $H_3[PMo_{12}O_{40}]$ heteropolyacid, which is a well–established oxidation catalyst for a range of organic substrates,[82] is in fact inactive in our conditions. The replacement of molybdenum centers with vanadium atoms in the framework of Keggin–type anions has proven to be beneficial for redox catalysis as it enhances the redox character of the cluster.[84] The higher catalytic activity observed for the mono–substituted $H_4[PVMo_{11}O_{40}]$ species in this reaction (90% conversion after 6 h) is in good agreement with the comment above. In comparison, the catalytic activity of V_2O_5 is lower than that of the vanadium–containing Keggin type heteropolyacid (50% conversion after 6 h) despite the higher content of V atoms. These results are consistent with those reported by other authors, which suggests that vanadium constitutes the catalytic center for this reaction while the Keggin–type framework serves as scaffold to enhance its activity.[85]

Compound **1–CuV10** displays the highest activity among all catalysts tested in this study, reaching a conversion of 99% after just 6 h of reaction (Table 2.8). The good stability of our hybrid during the catalytic oxidation was confirmed by the absence of any modifications in both FT–IR spectrum and PXRD patterns compared to those of a freshly prepared sample of **1–CuV10** (Figure 2.26). The distribution of the reaction products shows low–to–moderate selectivity toward 1–Adamantanol (1–AdOH) over other products from oxidation at secondary C–H bonds (2–AdOH, 2–Adamantanone). Selectivity toward 1–AdOH reaches a maximum of 45% after 3 h of reaction and decreases to 36% after 6 h due to the formation of other overoxidized side–products (Table 2.8 and Figure 2.26). To our knowledge, no reports on the catalytic activity of decavanadate–containing compounds toward the H_2O_2–based oxidation of cycloalkanes can be found in the literature.

Table 2.8. Conversion of adamantane and selectivity after 6 h of reaction in different cycles.

Catalyst	Time (h)	Conv. (% mol)	Selectivity (%)[a]			
			P1[b]	P2	P3	P
None	24	0	—	—	—	—
$H_3[PMo_{12}O_{40}]$	6	0	—	—	—	—
$H_4[PVMo_{11}O_{40}]$	6	90	45	30	11	13
1–CuV10	3	38	45	26	28	1
	6	99	36	20	31	13
V_2O_5	6	50	22	23	8	47

[a]based on the initial moles of adamantane; [b]P1: 1–Adamantanol (1–AdOH), P2: 2–Adamantanone (2–AdO), P3: 2–Adamantanol (2–AdOH), P: Other products (1,3–Adamantanediol, 5–hydroxy–2–adamantanone, 1,3,5–Adamantanetriol). Experimental conditions: 75 °C, $4{\cdot}10^{-5}$ moles of catalyst; 25 mg adamantane; 3 cm^3 of hydrogen peroxide (30%); 10 cm^3 of solvent (acetonitrile).

The fact that compound **1–CuV10** affords the highest conversion in the shorter reaction time among all selected catalysts is worth remarking because vanadium substituted Keggin–type species like the $H_4[PVMo_{11}O_{40}]$ comparative model have been identified as catalysts with the highest activity among POMs and certainly higher than those of transition–metal complexes such as $VO(acac)_2$ (acac = acethylacetonate).[82] As an illustrative comparison of the higher activity of **1–CuV10**, 12 h of reaction were needed to reach conversions in the 49–65% range when vanadium–substituted phosphomolybdate acids heterogeneized in SBA15 mesoporous silica were used with butyronitrile as solvent.[85a] When turning to homogeneous phase, several other POMs have been found to catalyze the oxidation of adamantane with H_2O_2 in acetonitrile, such as the divanadium–substituted phosphotungstate $[\gamma\text{–}PW_{10}O_{38}V_2(\mu\text{–}OH)(\mu\text{–}O)]^{4-}$, hybrid species consisting of a metallosalen moiety covalently linked to a Keggin–type silicotungstate $[SiW_{11}O_{39}]^{8-}$, or the $[\gamma\text{–}SiW_{10}\{Fe(OH_2)\}_2O_{38}]^{6-}$ cluster.[86] These species yield conversions from 42 up to 98%, but the selectivity is much improved to values in the 74–94% range toward 1–AdOH except for the iron–containing catalyst, which affords a selectivity of 71% toward the 2–AdOH derivative.[86d]

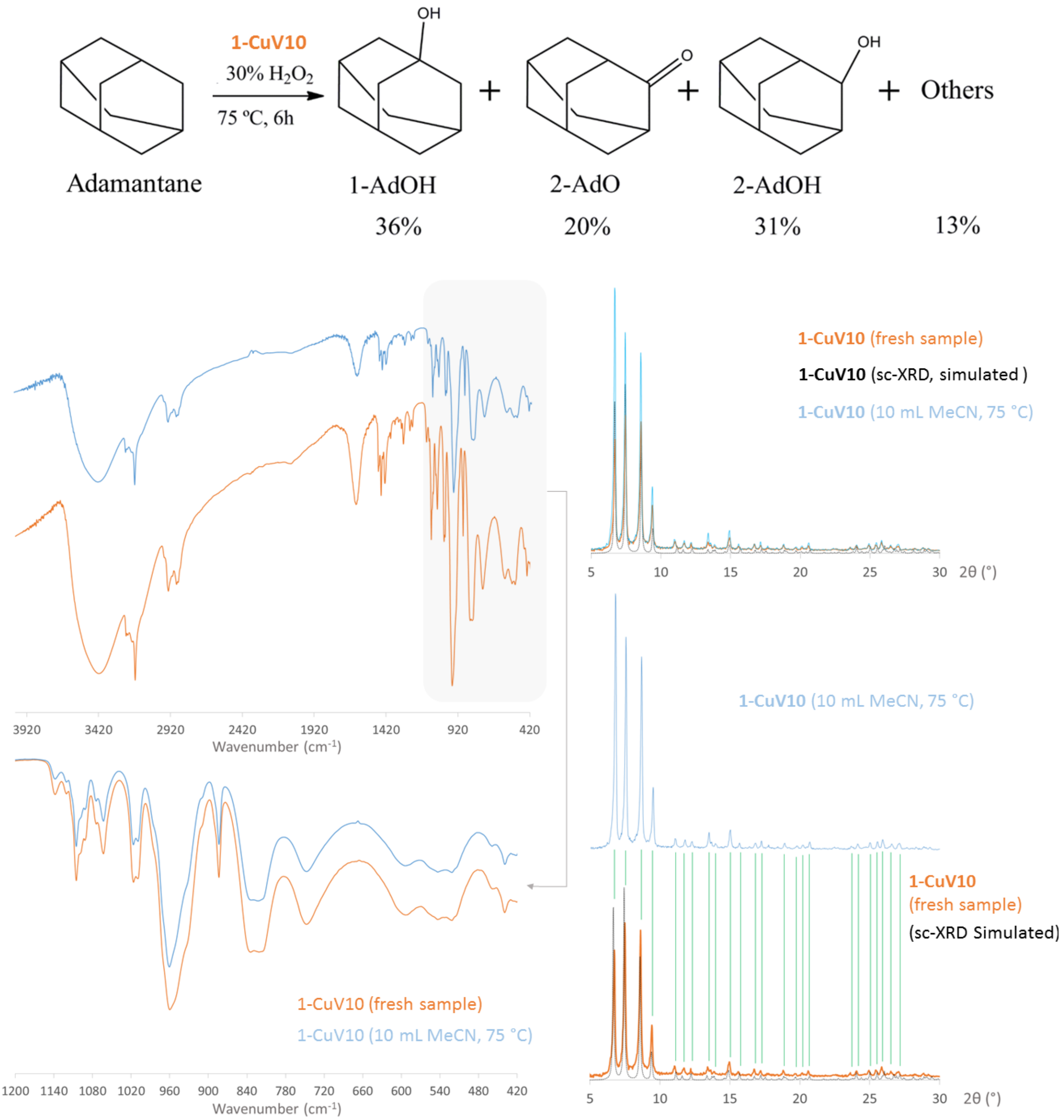

Figure 2.26. Scheme of the catalytic oxidation as well as the confirmation of the good stability during the catalytic oxidation of our hybrid by FT–IR and PXRD measurements on a **1–CuV10** sample under the same conditions of the catalytic tests compared to those obtained for a freshly prepared sample.

The high catalytic activity displayed by **1–CuV10** could originate from its larger atomic proportion of vanadium per mole of catalyst. However, the tested V_2O_5 does show a significantly lower conversion, and hence other effects must also be influencing the catalytic performance of **1–CuV10**. The {Cu(cyclam)} metalorganic moieties coordinated to the $\{V_{10}O_{28}\}$ clusters could very well be responsible for enhancing the catalytic activity of the V centers, in close analogy with the role of the Keggin scaffold in the vanadium–substituted phosphomolybdates. Moreover, the permanent porosity of the hybrid supramolecular open–

framework, as well as the dimensions of the channels in **1–CuV10**, may also have a key enhancing effect.

2.4 CONCLUSIONS

In this chapter, two porous extended polyoxovanadate–based hybrid open–frameworks with Cu(II) complexes of macrocyclic polyamines that show very different thermostructural behavior were prepared and fully characterized: a dynamic open–framework constructed by metavanadate flexible chains and a robust one constituted by decavanadate clusters. The former represents the first reported metavanadate hybrid that undergoes thermally activated single–crystal–to–single–crystal (SCSC) transformations upon evacuation of solvent molecules while the latter constitutes the first decavanadate–based covalent microporous framework with genuine sorption properties.

The flexible three–dimensional covalent metavanadate hybrid $[\{Cu(cyclam)\}(VO_3)_2]\cdot 5H_2O$ (**1–CuV**) undergoes a series of sequential and reversible SCSC structural transformations upon gradual dehydration that can be followed by single–crystal X–ray diffraction and take place at 40, 60 and 120 °C. These transformations result in the formation of three new porous crystalline phases with channels of different sizes, which are $[\{Cu(cyclam)\}(VO_3)_2]\cdot 3H_2O$ (**2–CuV**), $[\{Cu(cyclam)\}(VO_3)_2]\cdot 1.3H_2O$ (**3–CuV**) and $[\{Cu(cyclam)\}(VO_3)_2]$ (**4–CuV**). While the hybrid open frameworks of **1–CuV** and the partially dehydrated **2–CuV** are structurally highly reminiscent, the transformation of **2–CuV** into **3–CuV** involves the migration of Cu^{II} centers, which drastically decreases the size of the channel. In contrast, the total dehydration did not produce significant structural modifications in the metavanadate chains but for a slight reorientation of the vanadate tetrahedra, which was accompanied by a substantial increase of the solvent accessible volume in the channels. In terms of stability, **1–CuV** and **3–CuV** are stable in ambient conditions, whereas **2–CuV** constitutes a metastable state that slowly transforms back into **1–CuV** upon exposure to air. The anhydrous phase rapidly adsorbs ambient moisture and reverts to **3–CuV** after some hours, whereas the latter can only be converted back into the original fully hydrated compound when immersed in water.

Compared to the flexible hybrid metavanadate–based network, the first supramolecular POMOF–like microporous hybrid open–framework based on decavanadate clusters, namely $[Cu(cyclam)][\{Cu(cyclam)\}_2(V_{10}O_{28})]\cdot 10H_2O$ (**1–CuV10**), displays a robust open–framework. This supramolecular architecture contains covalent decavanadate/{Cu(cyclam)} grids with square–like voids the stacking of which is driven by a massive network of intermolecular N–H···O and C–H···O interactions established with interlamellar cementing complexes. This way, the structure is able to remain virtually unaltered upon thermal evacuation of guest solvent molecules located in the system of parallel channels generated by the stacking of the hybrid layers, as evidenced by a single crystal X–ray diffraction studies on the anhydrous **1a–CuV10** derivative. The permanent microporous nature of **1–CuV10** results in functional properties such as selective adsorption of CO_2 gas over N_2 and remarkable catalytic activity toward the oxidation of the highly–stable organic substrate adamantane in heterogeneous phase. To our knowledge, this is the first decavanadate–based compound, as well as one of the few POM–containing covalent hybrid materials, that shows both CO_2 sorption capability and catalytic activity in the oxidation of cycloalkanes owing to its microporous nature, accessibility of channels and robustness of the framework.

2.5 REFERENCES

---

[1] (a) Miras, H. N.; Long, D.-L.; Cronin, L. *Chem. Soc. Rev.* **2012**, *41*, 7403. (b) Long, D.-L.; Burkholder, E.; Cronin, L. *Chem. Soc. Rev.* **2007**, *36*, 105. (c) Basler, R.; Chaboussant, G.; Sieber, A.; Andres, H.; Murrie, M.; Kögerler, P.; Bögge, H.; Crans, D. C.; Krickemeyer, E.; Janssen, S.; Mutka, H.; Müller, A. *Inorg. Chem*. **2002**, *41*, 5675. (d) Li, S.; Sun, W.-L.; Wang, K.; Ma, H.-Y.; Pang, H.-J.; Liu, H.; Zhang, J.-X. *Inorg. Chem.* **2014**, *53*, 4541. (e) Zhou, J.; Zhao, J.-W.; Wei, Q.; Zhang, J.; Yang, G.-Y. *J. Am. Chem. Soc.* **2014**, *136*, 5065. (f) Kögerler, P.; Tsukerblat, B.; Müller, A. *Dalton Trans.* **2010**, *39*, 21.

[2] Cruywagen J. J.; Heyns, J. B. B.; Westra, A. N. *Inorg. Chem*. **1996**, *35*, 1556.

[3] Elvingson, K.; Gonzalez-Baro, A.; Petterson, L. *Inorg. Chem*. **1996**, *35*, 3388.

[4] (a) Heath, E.; Howarth, O. W. *J. Chem. Soc., Dalton Trans.* **1981**, 1105. (b) Livage, J. *Chem. Matter*. **1991**, *3*, 578. (c) McCann, N.; Wagner, M.; Hasse, H. *Dalton trans.* **2013**, *42,* 2622.

[5] (a) Bensch, W.; Hug, P.; Reller, A.; Oswald, H. R. *Mater. Res. Bull*. **1989**, *24*, 403. (b) Hamilton, E. E.; Fanwick, P. E.; Wilker, J. J. *J. Am. Chem. Soc*. **2002**, *124*, 78. (c) Roman, P.; Luque, A.; Gutierrez-Zorrilla, J. M. *Inorg. Chem.* **1993**, *32*, 775. (d) Day, V. W.; Klemperer, W. G.; Yaghi, O. M. *J. Am. Chem. Soc.* **1989**, *111*, 4518. (e) Day, V. W.; Klemperer, W. G.; Maltbie, D. J. *J. Am. Chem. Soc.* **1987**, *109*, 2991. (f) Day, V. W.; Klemperer, W. G.; Yaghi, O. M. *J. Am. Chem. Soc.* **1989**, *111*, 5959. (g) Hou, D.; Hagen, K. S.; Hill, C. L. *J. Am. Chem. Soc.,* **1992**, *114*, 5864. (h) Hou, D.; Hagen, K. S.; Craig, H. L. *J. Chem. Soc., Chem. Commun.* **1993**, 426. (i) Marrot, J.; Barthelet, K.; Simmonet, Corine; Riou, D. *C. R. Chim*. **2005**, *8*, 971.

[6] (a) Hayashi, Y.; Miyakoshi, T.; Singuchi, T.; Uehara, A. *Chem. Lett*. **2001**, 170. (b) Müller, A.; Krickemeyer, E.; Penk, M.; Walberg, H.-J.; Bögge, H. *Angew. Chem., Int. Ed.* ***1987,*** *26*, 1045. (c) Chen, Y.-H.; Gu, X.-J.; Peng, J.; Shi, Z.-Y.; Yu, H.-Q.; Wang, E.-B.; Hu, N.-H. *Inorg. Chem. Commun*. **2004**, *7*, 705. (d) Khan, M. I.; Ayesh, S.; Doedens, R. J.; Yu, M.-H.; O'Connor, C. J. *Chem. Commun*. **2005**, 4658. e) Müller, A.; Krickemeyer, Penk, M.; Rohlfing, R.; Armatage, A.; Bögge, H. *Angew. Chem., Int. Ed. Engl*., **1991**, *30*, 1674. (f) Suber, L.; Bonamico, M.; Fares, V. *Inorg. Chem*. **1997**, *36*, 2030. (g) Müller, A.; Rohlfing, R.; Döring, J.; Penk, M. *Angew. Chem., Int. Ed. Engl.,* **1991**, *30*, 588.

[7] (a) Aronica, C.; Chastanet, G.; Zueva, E.; Borshch, S. A.; Clemente-Juan, J. M.; Luneau, D. *J. Am. Chem. Soc.* **2008**, *130*, 2365. (b) Fry, F. H.; Dougan, B. A.; Ziegler, C. J., Brasch, N. E. *Inorg. Chem.* **2005**, *44*, 5197.

[8] Johnson, G. K.; Schlemper, E. O. *J. Am. Chem. Soc.* **1978**, *100*, 3645.

[9] Hayashi, Y. *Coord. Chem. Rev.* **2011**, *255*, 2270.

[10] (a) Kato, R.; Kobayashi, A.; Sasaki, Y. *J. Am. Chem. Soc.* **1980**, *102,* 6571. (b) Kato, R.; Kobayashi, A., Yukiyoshi, S. *Inorg. Chem*. **1982**, *21*, 240. (c) Ichida, H.; Nagai, K.; Sasaki, Y. *J. Am. Chem. Soc.* **1989**, *111*, 586. (d) Liu, S.; Li, D.-H.; Xie, L.-H.; Zhao, X.-Y.; Su, Z.-M. *Inorg. Chem.* **2006**, *45*, 8036.

[11] Kurata, T.; Uehara, A.; Hayashi, Y.; Isobe, K. *Inorg. Chem.* **2005**, *44*, 2524.

[12] Müller, A.; Sessoli, R.; Krickemeyer, E.; Bögge, H.; Meyer, J.; Gatteschi, D.; Pardi, L.; Westphal, J.; Hovermeier, K.; Rohlfing, R.; DOring, J.; Hellweg, F.; Beugholt, C.; Schmidtmann, M. *Inorg. Chem*., **1997**, *36*, 5239.

[13] Okaya, K.; Kobayashi, T.; Koyama, Y.; Hayashi, Y.;Isobe, K. *Eur. J. Inorg. Chem.* **2009**, 5156.

[14] Müller, A.; Penk, M.; Rohlfing, R.; Krickmeyer, E.; Döring, J. *Angew. Chem. Int. Ed. Engl*. **1987**, *26*, 1045.

[15] (a) Khan, M. I.; Yohanes, E.; Doedens, R. J. *Angew. Chem., Int. Ed.* **1999**, 38, 1292. (b) Khan, M. I.; Yohanes, E.; Powell, D. *Chem. Commun.* **1999**, 23. (c) Khan, M. I.; Yohanes, E.; Doedens, R. J. *Inorg. Chem.* **2003**, 42, 3125.

[16] Monakhov, K. Y.; Bensch, W.; Kögerler, P. *Chem. Soc. Rev.* **2015**, *44*, 8443 and references therein.

[17] Fernández de Luís, R.; Orive, J.; Larrea, E. S.; Urtiaga, M. K.; Arriortua, M. I. *CrystEngComm* **2014**, *16*, 10332 and references therein.

[18] Hartman, P. J.; Finn, R. C.; Zubieta, J. *Solid State Sci.* **2001**, *3*, 745.

---

[19] (a) Ulicka, L. *Chem. Pap.* **1988**, *42*, 11.

[20] Zavalij, P. Y.; Whittingham, S. *Acta Crystallogr.* **1999**, *B55*, 627.

[21] (a) Cheetham, A. K.; Rao, C. N. R.; Feller, R. K. *Chem. Commun*., **2006**, 4780. (b). Rao, C. N. R.; Cheetham, A. K.; Thirumurugan, A. *J. Phys.: Condens. Matter,* **2008**, *20*, 83.

[22] (a) Yi, Z.-H.; Cui, X.-B.; Zhang, X.; Yu, J.-H.; Lu, J.; Xu, J.-Q.; Yang, G.-D.; Wang, T.-G.; Yu, H.-H.; Duan, W.-J., *Dalton Trans*. **2007**, 2115. (b) Finn, R. C.; Sims, J.; O'Connor, C. J.; Zubieta, J. *J. Chem. Soc., Dalton Trans.* **2002**, 159. (c) Liu, C. M.; Hou, Y.-L.; Zhang, J.; Gao, S. *Inorg. Chem.* **2002**, *41*, 140. (d) Devi, R. N.; Zubieta, J. *Inorg. Chim. Acta* **2003**, *343*, 313. (e) Hartman, P. J.; Zubieta, J. *Inorg. Chem*. **2001**, *40*, 2800. (f) Liu, C.-M.; Gao, S.; Hu, H.-M.; Wang, Z.-M. *Chem. Commun*., **2001**, 1636.

[23] (a) Maggard, P. A.; Boyle, P. D. *Inorg. Chem.* **2003**, *42*, 4250. (b) Larrea, E. S.; Mesa, J. L.; Pizarro, J. L.; Fernández de Luis, R.; Rodriguez-Fernandez, J.; Rojo, T.; Arriortua, M. I. *Dalton Trans.* **2012**, *41*, 14170. (c) Yang, L.; Hu, C.; Naruke, H.; Yamase, T. *Acta Crystallogr.* **2001**, *C57*, 799. (d) Fernández de Luís, R.; Urtiaga, M. K.; Mesa, J. L.; Vidal, K.; Lezama, L.; Rojo, T.; Arriortua, M. I. *Chem. Mater.* **2010**, *22*, 5543. (e) Fernández de Luís, R.; Orive, J.; Larrea, E. S.; Urtiaga, M. K.; Arriortua, M. I. *Cryst. Growth Des*. **2014**, *14*, 658. (f) Lan, Y.-Q.; Li, S.-L.; Wang, X.-L.; Shao, K.-Z.; Du, D.-Y.; Su, Z.-M.; Wang, E.-B. *Chem. Eur. J.* **2008**, *14*, 9999. (g) Hu, Y.; Luo, F.; Dong, F.-F. *Chem. Commun*., **2011**, *47*, 761. (h) Qi, Y.-F.; Lv, C.-P.; Li, Y.-G.; Wang, E.-B.; Li, J.; Song, X.-L. *Inorg. Chem. Commun*., **2010**, *13*, 384.

[24] (a) Ouellette, W.; Zubieta, J. *Solid State Sci.* **2007**, *9*,658. (b) Rarig, R. S. Jr.; Zubieta, J. *Dalton Trans*. **2003**, 1861. (c) Li, J.-R.; Yu, Q.; Sañudo, E. C.; Tao, Y.; Song, W.-C.; Bu, X.-H. *Chem. Mater.* **2008**, *20*, 1218. (d) Hartman, P. J.; Bridges, C.; Greedan, J. E.; Zubieta, J. *J. Chem. Soc., Dalton Trans*. **1999**, 2901. E) Ouellette, W.; Burkholder, E.; Manzar, S.; Beweley, L.; Rarig, R. S.; Zubieta, J. *Solid State Sci*. **2004**, *6*, 77.

[25] (a) Tao, J.; Zhang, X.-M.; Tong, L.-M.; Chen, X.-M. *J.* Chem. *Soc., Dalton Trans.* **2001**, 700. (b) Li, G.; Shi, Z.; Xu, Y.-H.; Feng, S.-H. *Inorg. Chem*. **2003**, *42*, 1170.

[26] Zheng, L.-M.; Whitfield, T.; Wang, X.; Jacobson, A. J. *Angew. Chem., Int. Ed.* **2000**, *39*, 4528. B) Ellsworth, J. M.; Smith, M. D.; zur Loye, H.-C. *Solid State Sci*. **2008**, *10*, 1822.

[27] Ou, G.-C.; Jiang, L.; Feng, X.-L.; Lu, T.-B. *Dalton Trans*. **2009**, 71.

[28] Devi, R. N.; Rabu, P.; Golub, V. O.; O' Connor, C. J.; *Zubieta*, J. *Solid State Sci*. **2002**, *4*, 1095.

[29] (a) Li, G.; Shi, Z.; Xu, Y.-H.; Feng, S.-H. *Inorg. Chem.* **2003**, *42*, 1170. (b) Law, T. S.-C.; Sung, H. H.-Y.; Williams, I. D. *Inorg. Chem. Commun.* **2000**, *3*, 420.

[30] (a) Do, J.; Jacobson, A. J. *Inorg. Chem.* **2001**, *40*, 2468. (b) Lin, B.-Z.; Liu, S.-X. *Polyhedron* **2000**, *19*, 2521. (c) Lin, B.-Z.; Liu, S.-X., *J. Chem. Soc., Dalton Trans.* **2002**, 865. (d) Zavalij, P. Y.; Zhang, F.; Whittingham, M. S. *Acta Crystallogr..* **1999**, *B55*, 953. (e) Shi, Z.; Zhang, L.-R.; Zhu, G.-S.; Yang, G.-Y, Hua, J.; Ding, H.; Feng, S.-H. *Chem. Mater*. **1999**, *11*, 3565.

[31] (a) Yang, L.; C. Hu; Naruke, H.; Yamase, T. *Acta Crystallogr.* **2001**, C*57*, 799. (b) Khan, M. I.; Yohannes, E.; Nome, R. C.; Ayesh, S.; Golub, V. O.; O'Connor, C. J.; Doedens, R. Jr. *Chem. Mater.* **2004**, *16*, 5273.

[32] Fernández de Luís, R.; Urtiaga,.M. K.; Mesa, J. L.; Aguayo, A. T.; Rojo, T.; Arriortua, M. I. *CrystEngComm*, **2010**, *10*, 1880.

[33] See for example: (a) Li, J.; Huang, X.-Q.; Song, Y.; Xu, Y.-Q.; Hu, C.-W. *Cryst. Growth Des.,* **2015**, *15*, 1907. (b) Zhang, H. M.; Yang, J.; Kan, W.-Q.; Liu, Y.-Y.; Ma, J.-F. *Cryst. Growth Des.* **2016**, *16*, 265.

[34] (a) Aureliano, M. *Dalton Trans.,* **2009**, 9093. (b) Aureliano, M.; Crans, D. C. *J. Inorg. Biochem*. **2009**, *103*, 536. (c) Fraqueza, G.; Batista de Carvalho, L. A. E.; Marques, M. P. M.; Maia, L.; Ohlin, C. A.; Casey, W. H.; Aureliano, M. *Dalton Trans.* **2012**, *41*, 12749.

[35] Hou, W., Guo, J.-Y.; Wang, Z.-X.; Xu, Yan *J. Coord. Chem.* **2013**, *66*, 2434.

[36] Pavliuk, M. V.; Makhankova, V. G.; Kokozay, V. N.; Omelchenko, I. V.; Jezierska, J.; Thapper, A.; Styring, S. *Polyhedron* **2015***,* 88, 81.

[37] Klištincová, L.; Rakovský, E.; Schwendt, P., *Transition Met. Chem.* **2010,** *35*, 229.

[38] Lin, S. W.; Wu, Q.; Tan, H. Q.; Wang, E. B. *J. Coord. Chem.* **2011**, *64*, 3661.

---

[39] (a) Wang, M.; Sun, W.-L.; Pang, H.-J.; Ma, H.-Y.; Yu, J.; Zhang, Z.-F.; Niu, Y.; Yin, M.-M. *J. Solid State Chem*. **2016**, *235*, 175. (b) Xu, W. M.; Jiang, F.-L.; Zhou, Y.-F.; Xiong, K.; Chen, L.; Yang, M.; Feng, R.; Hong, M. C. *Dalton Trans.* **2012**, *41*, 7737.

[40] Zhang, X.-M.; Chen, X.-M. *Inorg. Chem. Comm.* **2003**, *6*, 206.

[41] (a) Abishek, K. I.; Soumyabrata, R.; Remesh, H.; Sebastian, C. P. *Dalton Trans.* **2014**, *43*, 2153. (b) Liu, H.-X.; Wang, J.; Li, Y.-F.; Jian, F.-F. *J. Chem. Crystallogr.* **2011**, *41*, 1254.

[42] Wang, L.; Sun. X.-P.; Liu, D.; Qi, Y.-F.; Wang, E. B. *J Clust. Sci.* **2008**, *19*, 531.

[43] Schulz-Dobrick, M.; Jansen M. *Inorg. Chem.* **2007***, 46, 4380.*

[44] Kulikov, V.; Meyer, G. *Cryst. Growth Des.* **2013**, *13*, 2916.

[45] Li, T.; Lü, J.; Gao, S.-Y.; Feng, L.; Cao, R. *Chem. Lett.* **2007**, *36*, 356.

[46] (a) McGlone, T.; Thiel, J.; Streb, C.; Long, D.-L.; Cronin, L. *Chem. Commun.* **2012**, *48*, 359. (b) Ma, H.; Meng, X.; Sha, J.-Q.; Pang, H.-J.; Wu, L. H. *Solid State Sci.* **2011**, *13*, 850.

[47] Bartošová, L. *Polyhedron* **2012**, *31*, 565.

[48] Pavliuk, M. V.; Makhankova, V. G.; Khavryuchenko, O. V.; Kokozay, V. N.; Omelchenko, I. V.; Shishkin, O. V.; Jezierska, J. *Polyhedron* **2014**, *81*, 597.

[49] An, L.; Liu, X.; Zhou, J.; Hu, F.-L.; Zhu, L.-L. *Z. Naturforsch.* ***2012**, 67b, 860.*

[50] Pang, H.-Y.; Meng, X.; Zhou, J.; Hu, F.-L.; Zhu, L.-L. *Z. Naturforsch.* **2012**, *67b*, 855.

[51] Klištincová, L.; Rakovský, E.; Schwendt, P. *Inorg. Chem. Comm.* **2008**, *11*, 1140.

[52] Kastner, K.; Streb, C. *CrystEngComm* **2013**, *15*, 4948.

[53] Gao, G.-G.; Cheng, P. S.; Mak, T. C. W. *J. Am. Chem. Soc.* **2009**, *131*, 18257.

[54] (a) Thomas, J.; Agarwal, M.; Ramanan, A.; Chernova, N.; Whittingham, M. S. *CrystEngComm* **2009**, *11*, 625. (b) Streb, C.; Tsunashima, R.; MacLaren, R. A.; McGlone, T.; Akutagawa, T.; Nakamura, T.; Scandurra, A.; Pignataro, B.; Gadegaard, N.; Cronin, L. *Angew. Chem. Int. Ed.* **2009**, *48*, 6490.

[55] (a) Wéry, A. S. J.; Gutiérrez-Zorrilla, J. M.; Luque, A.; Ugalde, M.; Román, P. *Chem. Mater*. **1996**, *8*, 408−413.

[56] (a) Halasz, I. *Cryst. Growth Des*. **2010**, *10*, 2817 and references therein. (b) Friscic, T.; McGillivray, L. R. *Z. Kristallogr*., **2005**, *220*, 351. (c) Hao, Z.-M.; Zhang, X.-M. *Dalton Trans*. **2011**, *40*, 2092. (d) Coronado, E. Espallargas, G. M. *Chem. Soc. Rev*. **2013**, 42, 1525. (e) Ke, S.-Y.; Wang, C.-C. *CrystEngComm* **2015**, *17*, 8776.

[57] (a) Fernández de Luís, R.; Urtiaga, M. K.; Orive, J.; Rojo, T.; Arriortua, M. I. *CrystEngComm* **2011**, 13, 6488. (b) Chen, C. L.; Goforth, A. M.; Smith, M. D.; Su, C.-Y.; zur Loye, H.-C. *Angew. Chem. Int. Ed.* **2005**, 44, 6673.

[58] Ou, G.-C.; Yuan, X.-Y.; Li, Z.-Z.; Li, W.-Y.; Zeng, F.; Deng, J.-H.; Zhong, D.-C. *Eur. J. Inorg. Chem.* **2016**, 3500.

[59] Wéry, A. S. J.; Gutiérrez-Zorrilla, J. M.; Luque, A.; Román, P. *Polyhedron* **1996**, *15*, 4555.

[60] *CrysAlisPro Software System,* Version *171.37.34*; Agilent Technologies UK Ltd.: Oxford, U. K., **2012**.

[61] Dolomanov, O. V.; Bourhis, L. J.; Gildea, R. J.; Howard, J. A.; Puschmann, H. J. *J. Appl. Crystallogr.* **2009**, *42*, 339.

[62] Sheldrick, G. M. *Acta Crystallogr.* **2008**, *A64*, 112.

[63] Spek, A. L. *Acta Crystallogr*. **2009**, *D65*, 148.

[64] Farrugia, L. J. *J. Appl. Crystallogr*. **1999**, *32*, 837.

[65] K. H. Bosco and F. Gruswitz, *BMC Struct. Biol.,* 2008, **8**, 49.

[66] DeLano, W. L. *The PyMOL Molecular Graphics System*; DeLano Scientific: San Carlos, CA, **2002**.

[67] Polyakov, N. S.; Dubinin, M. M.; Kataeva, L. I.; Petuhova, G. A. *Pure Appl. Chem*. **1993**, *65*, 2189.

[68] Cazorla-Amorós, D.; Alcañiz-Monge, J.; Linares-Solano, A. *Langmuir* 1996, *12*, 2820.

[69] Ketelaar, J. A. A. *Chem. Weekbl*. **1936**, *33*, 51.

---

[70] Mercurio-Lavaud, D.; Frit, B. *C. R. Seances Acad. Sci., Ser. C* **1973**, *277*, 1101.

[71] Brisi, C. et al., *Ann. Chim. Rome* **1958**, *48*, 263.

[72] D. Casanova, M. Llunell, P. Alemany, S. Alvarez, *Chem. Eur. J.* **2005**, *11*, 1479.

[73] Bakaj, M.; Zimmer, M. *J. Mol. Struct.* **1999**, *508*, 59.

[74] Román, P.; Aranzabe, A.; Luque, A; Gutiérrez-Zorrilla, J. M.; Martínez-Ripoll, M. *J. Chem. Soc., Dalton Trans.* **1995**, *13*, 2225.

[75] (a) Rodríguez-Reinoso, F.; Linares-Solano, A. *Microporous Structure of Activated Carbons as Revealed by Adsorption Methods*, *Vol. 2*; Dekker: New York, 1988. (b) Cazorla-Amorós, D.; Alcañiz-Monge, J.; de la Casa-Lillo, M. A.; Linares-Solano, A. *Langmuir* **1998**, *14*, 4589.

[76] Du, D.-Y.; Qin, J.-S.; Li, S.-L.; Su, Z.-M.; Lan, Y.-Q. *Chem. Soc. Rev*. **2014**, *43*, 4615.

[77] Eguchi, R.; Uchida, S.; Mizuno, N. *Angew. Chem., Int. Ed.* **2012**, *51*, 1635.

[78] Kawahara, R.; Uchida, S.; Mizuno, N. *Inorg. Chem.* **2014**, *53*, 3655.

[79] (a) Zhang, Z.; Sadakane, M.; Murayama, T.; Izumi, S.; Yasuda, N.; Sakaguchi, N.; Ueda, W. *Inorg. Chem.* **2014**, *53*, 903. (b) Zhang, Z.; Sadakane, M.; Noro, S.; Murayama, T.; Kamachi, T.; Yoshizawa, K.; Ueda, W. *J. Mater. Chem. A*, **2015**, *3*, 746.

[80] Fu, H.; Qin, C.; Lu, Y.; Zhang, Z.-M.; Li, Y.-G.; Su, Z.-M.; Li, W.-L.; Wang, E.-B. *Angew. Chem. Int. Ed.* **2012**, *51*, 7985.

[81] Qin, J.-S.; Du, D.-Y.; Li, W.-L.; Zhang, J.-P.; Li, S.-L.; Su, Z.-M.; Wang, X.-L.; Xu, Q.; Shao, K.-Z.; Lan, Y.-Q. *Chem. Sci*. **2012**, *3*, 2114.

[82] (a) Mizuno, N.; Kamata, K. *Coor. Chem. Rev.* **2011**, *255*, 2358. (b) Kozhevnikov, I. V. *Catalysts for Fine Chemical Synthesis, Vol 2*; John Wiley & Sons: Chichester, U. K., 2002. (c) Kozhevnikov, I. V. *Catalysis by Polyoxometalates*; John Wiley & Sons: Chichester, U. K., 2000. (d) Mizuno, N.; Misono, M. *Chem. Rev.* **1998**, *98*, 199.

[83] See for example: (a) Joseph, T.; Hartmann, M.; Ernst, S.; Halligudi, S. B. *J. Mol. Catal. A* **2004**, *207*, 131. (b) Ishito, N.; Kobayashi, H.; Nakajima, K.; Maegawa, Y.; Inagaki, S.; Hara, K.; Fukuoka, A. *Chem. Eur. J.* **2015**, *21*, 15564. (c) Bonchio, M.; Scorrano, G.; Toniolo, P.; Proust, A.; Artero, V.; Conte, V. *Adv. Synth. Catal.* **2002**, *344*, 841. (d) Farzaneh, F.; Moghzi, F. *React. Kinet., Mech. Catal.* **2015**, *115*, 175.

[84] Molinari, J. E.; Nakka, L.; Kim, T.; Wachs, I. E. *ACS Catal*. **2011**, *1*, 1536.

[85] (a) Bordoloi, A.; Vinu, A.; Halligudi, S. B. *Appl. Catal. A: Gen.* **2007**, *333*, 143. (b) Shinachi, S.; Matsushita, M.; Yamaguchi, K.; Mizuno, N. *J. Catal.* **2005**, *233*, 81.

[86] (a) Kamata, K.; Yonehara, K.; Nakagawa, Y.; Uehara, K.; Mizuno, N. *Nat. Chem.* **2010**, *2*, 478. (b) Mirkhani, V.; Moghadam, M.; Tangestaninejad, S.; Mohammadpoor-Baltork; I., Rasouli, N. *Catal. Commun.* **2008**, *9*, 2171. (c) Mizuno, N. *Catal. Surv. Jpn* **2000**, *4*, 149. (d) Mirkhani, V.; Moghadan, M.; Tangestaninejad, S.; Mohammadpoor-Baltork, I.; Rasouli, N. *Catal. Commun.* **2008**, *9*, 2411.

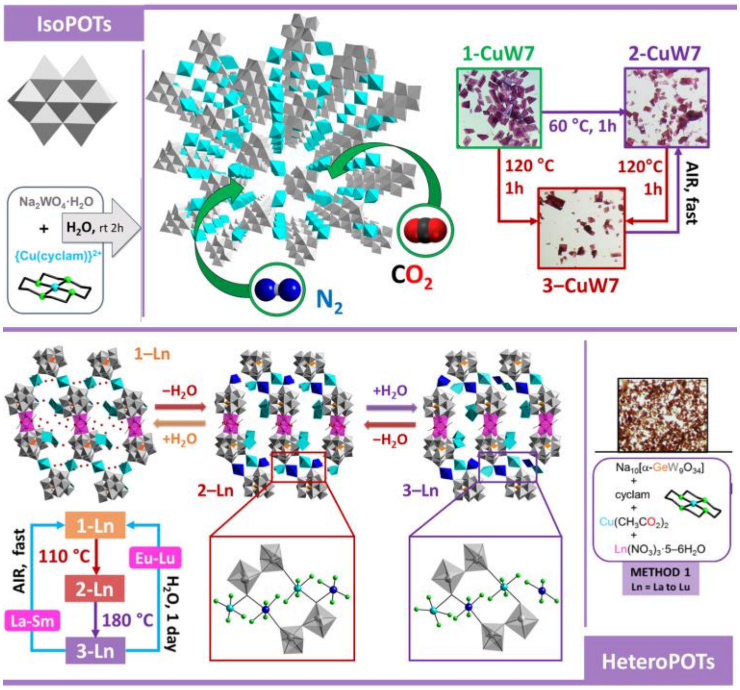

THERMALLY TRIGGERED SCSC TRANSFORMATIONS UPON GRADUAL DEHYDRATION IN ISO– AND LANTHANIDE SUBSTITUTED HETERO–POLYOXOTUNGSTATES

Chapter 3

*In this chapter, two extended dynamic systems based on polyoxotungstate clusters were prepared and fully characterized. The first one consist on isopolyoxotungstates, specifically the heptatungstate $[W_7O_{24}]^{6-}$ cluster, which upon combination with {Cu(cyclam)} affords a functional 3D covalent porous hybrid framework, namely $[\{Cu(cyclam)\}_3(W_7O_{24})]\cdot 15.5\ H_2O$ (**1–CuW7**). Interestingly, this extended structure undergoes two SCSC transformation upon thermal evacuation of solvent molecules resulting in important structural modifications in the resulting partially hydrated intermediate (**2–CuW7)** and anhydrous phases (**3–CuW7)**. The permanent porosity of the latter was confirmed by gas sorption measurements, which revealed that the anhydrous phase is capable of adsorbing moderate amounts of both N_2 and CO_2 gases. In the second part, the entire family of {Cu(cyclam)} coordinated lanthanide–substituted acetate–bridged germanotungstate family was prepared and characterized, the formula of which is $[Cu(cyclam)]_2[\{Cu(cyclam)\}_4\{(\alpha\text{–}GeW_{11}O_{39})Ln(H_2O)(\mu\text{–}CH_3COO)\}_2]\cdot 17\text{–}19H_2O$ (**1–Ln,** Ln = La to Lu). These covalent 2D dimeric hybrid systems undergo two SCSC transformations upon heating leading to new 1D crystalline phases (**2–Ln**, Ln = Eu, Er and **3–Ln**, Ln = Ce, Eu) which exhibit drastic structural modifications in their architectures. Single–crystal XRD, together with simultaneous PXRD and TGA analyses revealed that rehydration kinetics depends strongly on the Ln analogue for the **2–Ln** to **1–Ln** phase transition while the second transformation is totally reversible upon exposure to ambient moisture.*

THERMALLY TRIGGERED SCSC TRANSFORMATIONS UPON GRADUAL DEHYDRATION IN ISO– AND LANTHANIDE SUBSTITUTED HETERO–POLYOXOTUNGSTATES

3.1 INTRODUCTION

3.1.1 Polyoxotungstates: A Brief Introduction

Hystorically, polyoxotungstates (POWs) have been the most studied family among POMs (Figure 3.1), owing to their well–defined pH–dependent thermodynamic and kinetic stability ranges as well as their higher resistance to reduction compared to their polyoxomolybdate counterparts.[1] They are considered one of the most attractive POM subfamilies due to the availability of a huge number of stable and easy–to–prepare lacunary species susceptible of incorporating 3d or 4f metals and also undergoing further organic functionalization. As a result, POWs have found important applications in a wide variety of fields including but not limited to optics, biomedicine and materials science.[2]

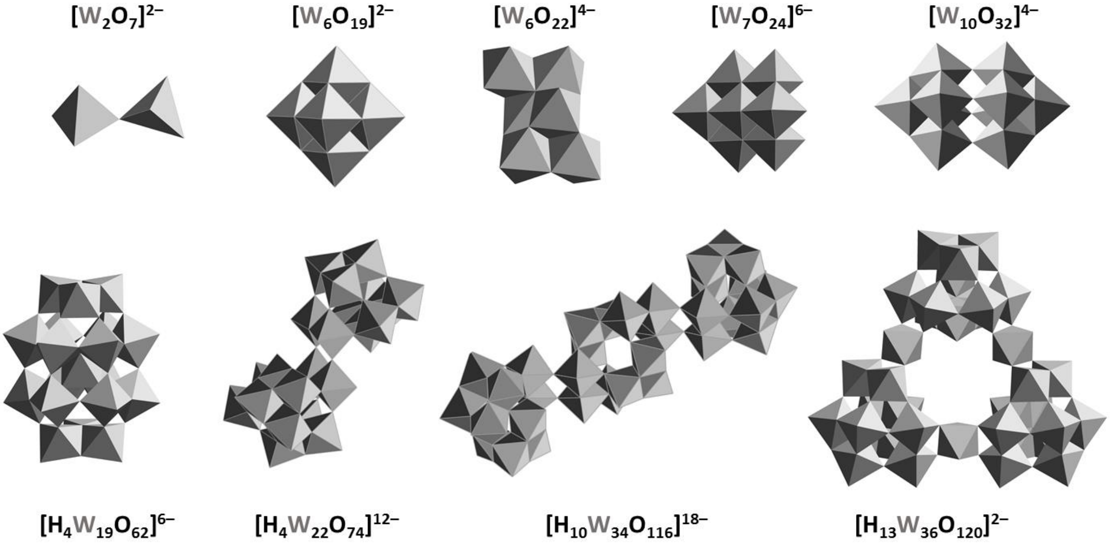

Figure 3.1. Structural diversity in typical isoPOWs of different nuclearity.

In close analogy to the monovanadate anion, in the high alkaline region over pH > 8 only the tungstate $[WO_4]^{2-}$ specie exists in aqueous solution. Upon acidification to nearly neutral pH values (pH = 5–6) however, the heptatungstate or paratungstate A $[W_7O_{24}]^{6-}$ polyanion is rapidly formed, which is then converted thermodynamically to the paratungstate B $[W_{12}O_{36}(OH)_{10}]^{10-}$ ion establishing a slow equilibrium that is shifted toward the latter.[3] The paratungstate B anion constitutes the predominant isoPOW specie in solution at high tungstate concentrations in this pH zone, as evidenced by spectroscopic and scattering investigations[4] whereas the heptatungstate is the main specie for diluted solutions.[5] Decreasing the pH to values around 3–4 results in the formation of the so–called Ψ–$[W_{24}O_{72}(OH)_{12}]^{12-}$ and α–$[H_2W_{12}O_{40}]^{6-}$ Keggin–metatungstate species whereas further acidification leads to the formation of the decatungstate $[W_{10}O_{32}]^{4-}$ specie, which is known as tungstate–ϒ (Figure 3.2). At low tungstate concentrations, however, the formation of any isopolyoxotugstates is avoided as only the highly insoluble tungstic acid H_2WO_4 precipitates by direct protonation upon acidification.[4]

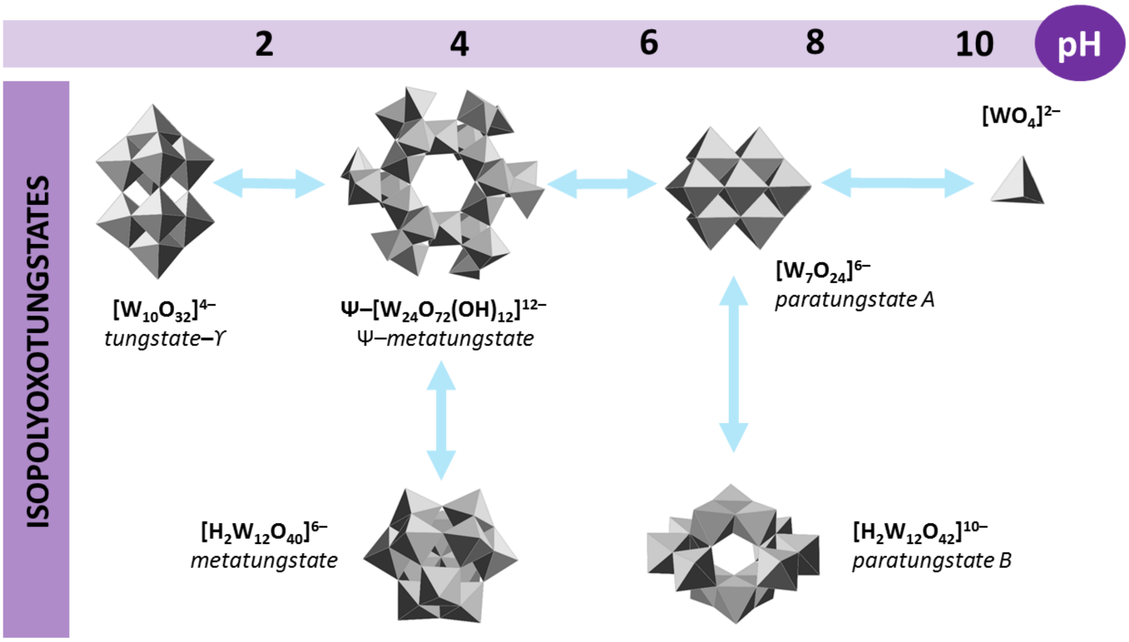

Figure 3.2. General scheme showing the stability range of the predominant isoPOW species of different nuclearity in aqueous solution as a function of the pH.

Even though an enormous amount of compounds based on POWs have been reported so far, most of them consist on heteroPOWs.[6] In comparison, reports on isoPOWs, which only contain W and O atoms in their inorganic skeletons, are far less common. In this context, only a handful of examples involving these types of compounds can be found across the crystallographic databases. These include the following species which are mainly present as alkali metal or organic ammonium salts (*class I* hybrids): $[W_2O_7]^{2-}$,[7] $[HW_5O_{19}]^{7-}$,[8] $[W_6O_{19}]^{2-}$,[9] $[H_3W_6O_{22}]^{5-}$,[10] $[W_6O_{22}]^{8-}$,[11] $[W_7O_{24}]^{6-}$,[12] $[W_{10}O_{32}]^{4-}$,[13] $[H_4W_{11}O_{38}]^{6-}$,[14] $[H_2W_{12}O_{40}]^{6-}$,[15] $[H_2W_{12}O_{42}]^{10-}$,[16] $[H_4W_{19}O_{62}]^{6-}$,[17] $[H_4W_{22}O_{74}]^{12-}$,[18] $[W_{24}O_{84}]^{24-}$,[7] $[H_{10}W_{34}O_{116}]^{18-}$,[18] and $[H_{12}W_{36}O_{120}]^{12-}$,[19] the latter being the largest known isoPOW present in solution under non–reducing conditions (Figure 3.1). This evident far less attention paid to isopolyoxotungstates can be explained attending to the fact that some of them are present as metastable intermediates or low concentration fragments in solution, which cannot be stabilized and/or isolated easily. Thus, the preparation of hybrid assemblies containing isoPOWs have remained mostly unexplored during the last two decades in comparison with other types of POMs. This fact could very well represent a great opportunity to explore the possibility of using them as transferable building blocks for the preparation of new extended multifunctional materials upon combination with transition metal complexes of macrocyclic polyamines such as M(cyclam) moieties.

Compared to isoPOWs, the Keggin–type heteroPOWs, with the general formula $[XW_{12}O_{40}]^{3/4-}$ (X = P^V, As^V, Si^{IV}, Ge^{IV}) have been extensively studied and their several lacunary derivatives can be prepared in high yields, such as the monolacunary $[XW_{11}O_{39}]^{7/8-}$, dilacunary $[XW_{10}O_{38}]^{11/12-}$, and trilacunary $[XW_9O_{34}]^{9/10-}$[20] species (X = P^V, As^V, Si^{IV}, Ge^{IV}).These vacant clusters, as well as the Dawson–Wells lacunary analogues, possess higher negative charge and stronger coordination ability by exposing active coordination sites to metal centers and hence, can act as multidentate inorganic ligands toward transition metal (3d) and lanthanide (4f) cations which had led to a rich and diverse class of 3d[21]– or 4f–[22]substituted heteroPOW families, disregarding the less reported heterometallic 3d–4f POWs which contain both transition metals and lanthanide centers in their cluster frameworks. The main reason for the lower number of reports concerning this heterometallic complexes is due to the inevitable coordination competition that arise between the highly reactive oxophilic 4f cations compared to that of the relatively less active 3d–metal centers.[23] Besides 3d–4f POWs, another kind of heterometallic hybrid systems has recently become a great focus in synthetic POM chemistry. In comparison, this type of hybrids are assembled from either 4f or 3d–substituted POMs connected by transition metal or lanthanide centers belonging to metalorganic complexes that act as bridging moieties between the substituted clusters (*class II* hybrids), respectively.[24] As seen in Chapter 2, this approach constitutes a valid method for the preparation of novel high dimensional isoPOVs. We attempted to investigate the possibility of obtaining such type of hybrids using both iso– and heteroPOWs building blocks, since the resulting extended polyoxotungstate–based hybrids could afford interesting architectures and topologies as well as new or enhanced properties compared to those of the individual constituents.[25]

3.1.2 Heptatungstate–based Hybrids

The lower number of reports on isopolyoxotungstates is even more accused for compounds containing the heptatungstate $[W_7O_{24}]^{6-}$ cluster. Indeed, up to date only five crystal structures based on this fragment have been reported to our knowledge, four of them consisting in salts with counterions such as Na^+, simple bulky organic ammonium cations and cobalt–ethylendiamine metalorganic complexes, namely $Na_6[W_7O_{24}]\cdot 21H_2O$, $[(C_5H_{10}NH_3)]_6[W_7O_{24}]$, $[(t\text{–}C_4H_9)NH_3]_6[W_7O_{24}]\cdot 2H_2O$, and $[Co(en)_3]_2[H_2W_7O_{24}]\cdot 8H_2O$, respectively.[12] The remaining crystal containing $\{W_7\}$ fragments, namely $Na[\{Cu(en)_2\}_2(HW_7O_{24})]\cdot 5H_2O$, constitutes the first high–dimensional coordination polymer constructed by covalent layers of $\{Cu(en)\}^{2+}$ cationic complexes and monoprotonated $\{W_7\}$ units where sodium cations act as bridges between the layers resulting in the first *class II* $\{W_7\}$–hybrid with a I^3O^0 architecture[26] (Figure 3.3). This obvious lack of $\{W_7\}$–based compounds is a direct consequence of the inherent difficulty to obtain pure solid or crystals of $[W_7O_{24}]^{6-}$ due to the simultaneous formation of paratungstate B $[H_2W_{12}O_{42}]^{10-}$ (Figure 3.2). In this sense, it has been proven that during the acidification of a solution of $[WO_4]^{2-}$ at pH 6–8 both paratungstates A and B are formed at the same time, stablishing an equilibrium as demonstrated by ^{183}W–NMR and Raman spectroscopies as well as electrospray ionization mass spectrometry.[3,5] Furthermore, these spectroscopic techniques confirmed $[W_7O_{24}]^{6-}$ to be the predominant species in the equilibrating mixtures at pH below 7. Nevertheless, in these cases generally the salt of the paratungstate B crystallizes, which is less soluble and thermodynamically more stable than the former $\{W_7\}$ specie,[5,16a] unless specific synthetic measures such as the use of organic amines or transition metal–complex cations are taken,[27] as the latter are known to not only provide buffer media for the self–assembly processes but also promote the crystallization of the metastable POM species. Another synthetic approach extensively used over the last few decades is the use of hydrothermal methods, which may be considered a new strategy for the design and synthesis of isoPOW–based hybrid compounds.[28] Generally, the hydrothermal environment can change the equilibrium phases of the POM reaction system from the thermodynamically stable compounds to the kinetically stable species. As a result, the structurally more complicated metastable phases and various intermediate species difficult or even impossible to isolate under bench conditions could be crystallized under hydrothermal conditions.[29]

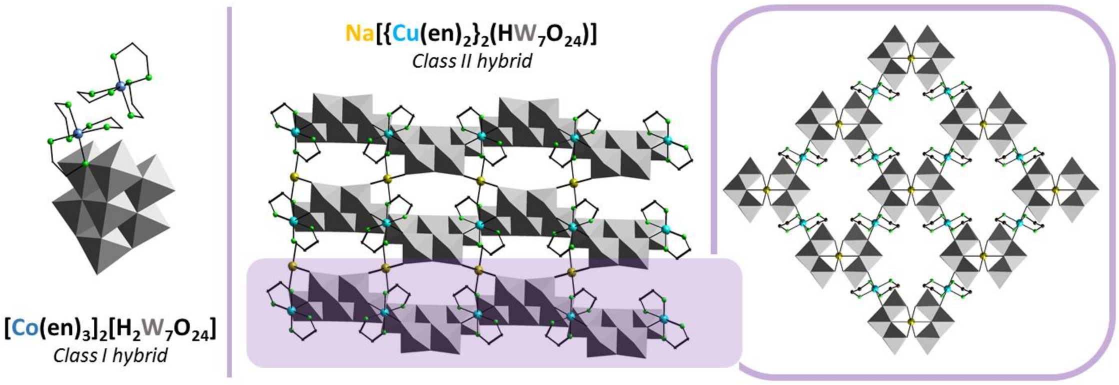

Figure 3.3 Molecular structure of an heptatungstate hybrid belonging to class I (left); crystal packing of the only 3D covalent framework constructed from heptatungstate clusters and transition metal complexes.

The inherent complexity of the chemical equilibrium involving the paratungstate clusters together with the few reports on $\{W_7\}$ compounds prove that the isolation of crystals based on this cluster is still a notable challenge in current synthetic POM chemistry. Consequently, this fact greatly limits the potential applicability of the heptatungstate cluster[30] which is known to have interesting photocatalytic properties.[31] As a representative example, Hu's group demonstrated that an *in situ* prepared solution containing $[W_7O_{24}]^{6-}$as the predominant specie could be used as a photocatalyst for water purification purposes, as it was able to efficiently photodegrade up to 22 different organochlorine compounds.[31a] Similarly, the layered double hydroxide pillared by $\{W_7\}$ ion, namely $Mg_{12}–Al_6(OH)_{36}(W_7O_{24})·4H_2O$, was prepared by Guo et al via an anion–exchange reaction and was evaluated as a heterogeneous photocatalyst in water. By irradiating the heptatungstate–containing compound in the near UV area, they managed to totally degrade trace aqueous organochlorine pesticides such as hexachlorocyclohexane.[31b] Recently, Li's group showed that the $[Co(en)_3]_2[H_2W_7O_{24}]·8H_2O$ hybrid can also act as an effective photocatalyst for the aqueous degradation of rhodamine–B under UV irradiation in heterogeneous phase.[12d]

3.1.3 Lanthanide–substituted Polyoxotungstates

Combination of lacunary POMs with 4f–metals represents a powerful strategy to prepare novel complex structures that range from dimeric entities to giant macroassemblies, including those among the largest POMs known to date. In this sense, the characteristic features of 4f centers such as their large size, oxophilic nature and high coordination numbers makes them ideal linkers to connect POM fragments into a large variety of architectures. The chemistry of such 4f–substituted POMs is largely dominated by POWs, the vast majority of them being heteroPOWs, as it is the subfamily with the most number of available lacunary species susceptible of incorporating 4f centers. The interactions between 4f–metal and lacunary POWs clusters have been extensively investigated over the past few decades because of the interesting structural and physicochemical properties (e.g. photoluminescence, magnetism or increased catalytic activity) that the resulting POWs might exhibit due to the incorporation of the 4f–centers to the polyanionic framework.[32]

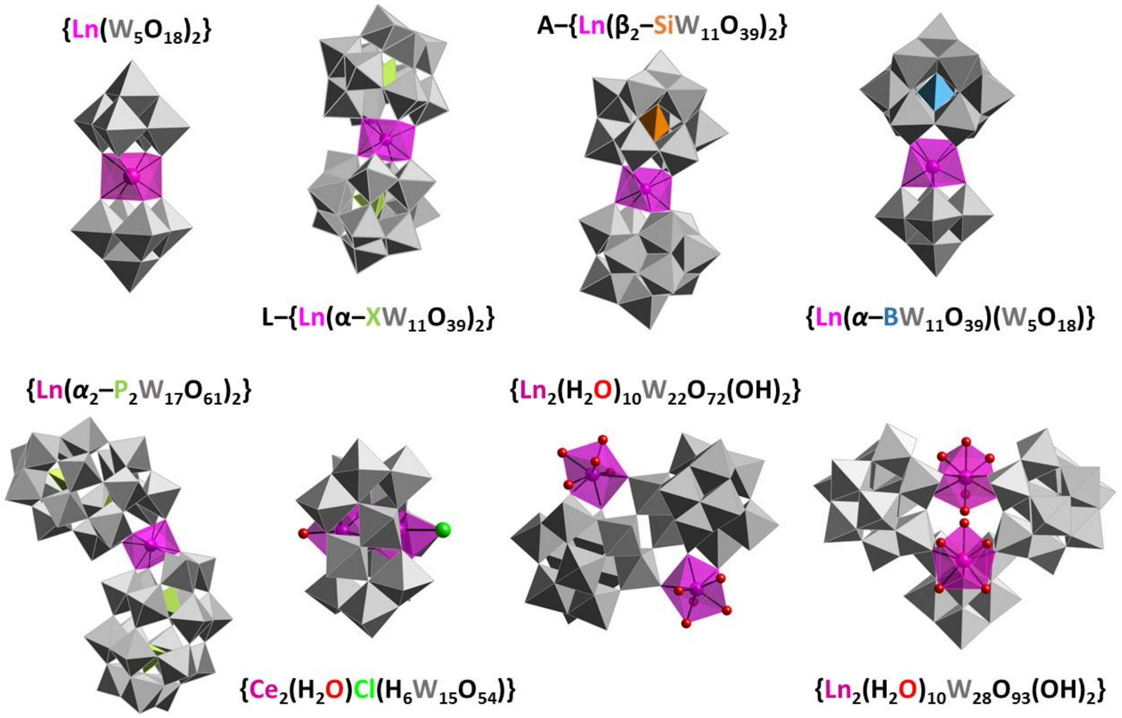

Figure 3.4. Molecular structures of representative Peacock–Weakley type POWs along with the three known 4f–substituted isoPOWs: the $[Ce_2(H_2O)Cl(H_6W_{15}O_{54})]^{7–}$ anion; the $[Ln_2(H_2O)_{10}W_{22}O_{72}(OH)_2]^{8–}$ framework and the $[Ln_2(H_2O)_{10}W_{28}O_{93}(OH)_2\}]^{14–}$ polyanion.

Historically, the first family of lanthanide–containing POMs was reported by Peacock and Weakley in 1971, namely $[Ln(W_5O_{18})_2]^{9–}$ (Ln^{III} = La–Sm, Ho, Yb) along with the $[Ce^{IV}(W_5O_{18})_2]^{8–}$ cluster.[33] These decatungstate species consist on two monolacunary Lindqvist–type pentatungstates sandwiching an eight–coordinated square–antiprismatic 4f–metal center (Figure 3.4). After the pioneering work of Peacock and Weakly, the subsequent "sandwich"–type clusters formed by two monolacunary fragments trapping a 4f–metal reported later on have been named after them.[34] Besides the 4f–decatungstate, only another three Peacock–Weakley type POWs have been reported so far. Li et al. reported the $[Ce_2(H_2O)Cl(H_6W_{15}O_{54})]^{7–}$ cluster, in which a dimeric Ce^{III} fragment is encapsulated by a cyclic $\{H_6W_{15}O_{54}\}$ structure composed of three $\{W_3O_{14}\}$ units linked to each other by corner sharing with three $\{W_2O_{10}\}$ moieties. This way, the coordination sphere of each Ce atom is completed by either one H_2O molecule or Cl atom.[35] Kortz's group prepared the remaining two 4f–isoPOWs which are $[Ln_2(H_2O)_{10}W_{22}O_{72}(OH)_2]^{8–}$ dimer (Ln = La, Ce, Tb–Lu) [36] and the V–shaped $[Ln_2(H_2O)_{10}W_{28}O_{93}(OH)_2\}]^{14–}$ trimer (Ln = La –Eu),[37] both based on the undecatungstate monolacunary cluster.[38] While the former structure is built from two corner sharing undecatungstate fragments stabilized by two 4f–metal atoms, the latter is formed by two undecatungstate units in addition to one hexatungstate fragment which are linked by two nonacoordinated lanthanide cations (figure 3.4). Regarding heteroPOWs, several Peacock–

Weakly type POWs constructed from different Keggin as well as Wells–Dawson monolacunary isomers have been reported so far, including $\{Ln(\alpha–XW_{11}O_{39})_2\}$ (X = Si^{IV}, P^{V}, As^{V}),[39] $\{Ln(\beta_2–SiW_{11}O_{39})_2\}$[40] or $\{Ln(\alpha–P_2W_{17}O_{61})_2\}$ ($\alpha = \alpha_1, \alpha_2$)[41] families (Figure 3.4). Furthermore, the mixed iso/hetero Peacock–Weakley type $\{Ln(\alpha–BW_{11}O_{39})(W_5O_{18})\}$ mixed–assembly was also prepared by Yamase.[42] Although lanthanide substituted monomeric species were identified in solution by Peacock and Weakley in their pioneering studies, self–assembled derivatives forming chains[43] or dimers[41] with accessible coordination water molecules, have only been isolated in the solid state so far. While Keggin subunits usually lead to 1D architectures or dimeric assemblies, a variety of dimers showing *cap–to–cap*, *belt–to–belt* and *cap–to–belt* coordination modes have been observed for Wells–Dawson fragments depending on the size of the employed lanthanide.

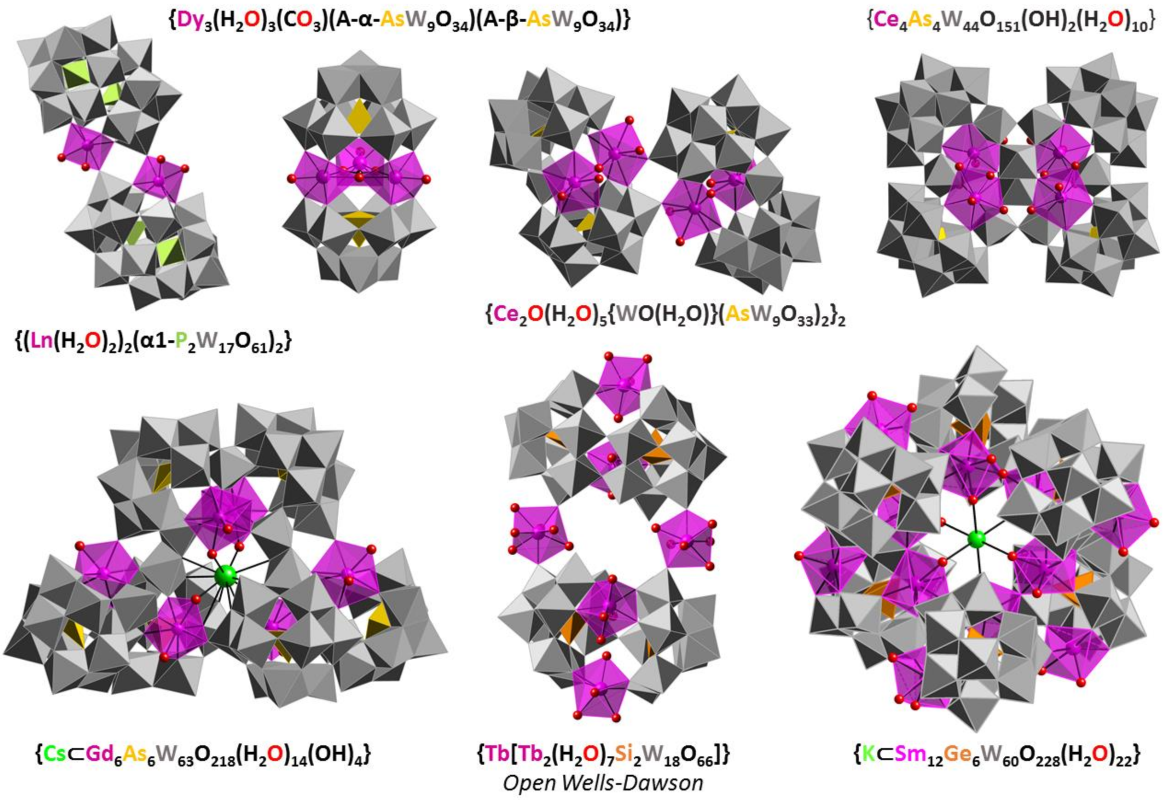

Figure 3.5. Structural diversity of some representative 4f–substituted polylacunary POWs of different composition and nuclearity.

Besides Peacock–Weakley species, some other lanthanide containing dimeric POMs are known, which are based on trilacunary Keggin units. These include Krebs and Knoth –type POWs incorporating 4f–metals, the so–called open Wells–Dawson polyanions, or 4f–substituted $[As_2W_{19}O_{67}]^{14–}$ clusters formed by two $[B–\alpha–AsW_9O_{33}]^{9–}$ fragments linked through one $\{WO_6\}$ octahedron.[44] Alternatively, polylacunary Wells–Dawson fragments encapsulating a central rhomblike cerium cluster as well as a $\{Yb_6O_6\}$ hexamer have been prepared, and even more complex lanthanide–containing architectures based on the Preyssler–type $[P_5W_{30}O_{110}]^{15–}$ or the wheel–shaped $[P_8W_{48}O_{184}]^{40–}$ polyanions have been isolated.[45] While just a handful of examples of trimeric lanthanopolyoxotungstates have been reported, the analogous tetrameric species represent a huge subfamily where almost all of them are built from dilacunary Keggin–type POMs or trilacunary units with lone–pair containing heteroatoms such as As^{III} or Sb^{III}. The $[Ce^{IV}_2(PW_{10}O_{38})(PW_{11}O_{39})_2]^{17-}$ 4f–polyoxotungstate prepared by Nogueira, which contains dilacunary *α*–Keggin type phosphotungstate units in its structure, represents an illustrating example of the former group.[46] Alternatively, Yamase's $[Ln_3(\alpha\text{–}SbW_9O_{33})(W_5O_{18})_3]^{18-}$, the $[Ce_3(H_2O)_8\{Sb_4O_4\}\{WO_2(H_2O)\}_2(\alpha\text{–}SbW_9O_{33})_4]^{19-}$ anion trapping the rare $\{Sb_4O_4\}$ moiety, the $[(BiW_9O_{33})_4(WO_3)\{Bi_6(\mu^3\text{–}O)_4(\mu^2\text{–}OH)_3\}(Ln_3(H_2O)_6CO_3)]^{22-}$ assembly showing the central $\{Bi_6(\mu^3\text{–}O)_4(\mu^2\text{–}OH)_3\}$ cluster, Francesconi's $[(Eu_2PW_{10}O_{38})_4(W_3O_{14})]^{30-}$ anions and some other compounds prepared from the tetrameric $\{As_4W_{40}O_{140}\}$ POW cryptate could also be considered as relevant examples within the second group.[47] Furthermore, lanthanide–substituted POWs showing higher nuclearity have also been observed in crown–shaped $\{M\subset\{Eu(H_2O)_2(\alpha\text{–}AsW_9O_{33}\}_n\}$ tetra–or hexameric assemblies (where M = K, n= 6; M = Cs, n= 4) or the hexameric $[Cs\subset\{Ln_6As_6W_{63}O_{218}(H_2O)_{14}(OH)_4\}]^{25-}$ and $[Ho_5(H_2O)_{16}(OH)_2As_6W_{64}O_{220}]^{25-}$macroanions.[48] Very recently, Artetxe et al. prepared a series of giant POMs by one–pot reaction of lanthanide(III) ions, GeO_2 and Na_2WO_4 in sodium acetate buffer resulting in a library of $[Ln_2(GeW_{10}O_{38})]^{6-}$ clusters which consist of dilacunary Keggin fragments stabilized by the coordination of 4 f–metal atoms to the vacant sites which show the ability to undergo cation–directed association processes (Figure 3.5). Interestingly, some of these 4f–substituted macroPOMs exhibit the ability to self–assemble into spherical, hollow, and single–layered vesicle–like *blackberry*–type structures in solution, as monitored by dynamic (DLS) and static (SLS) light scattering techniques and confirmed by transmission electron microscopy (TEM).[49]

3.1.4 Hybrid 4f–substituted heteropolyoxotungstates

Lanthanide centers belonging to lacunary POM cluster usually have several accesible water molecules in their coordination sphere susceptible of being replaced with organic fragments, except for Peacock–Weakley type isoPOMs. However, direct organic derivatization on those 4f–metal centers can be a challenging task to carry out. Even though the highly oxophilic character of the lanthanide centers makes carboxylic acids suitable organic ligands to achieve such functionalization, the electrostatic repulsion originated by the overall negative charge of the 4f–substituted polyanion often prevents the coordination from suceeding. In addition, a bulky POM cluster can also show a significant steric hindrance effect preventing the ligands from getting closer to the 4f centers. These two drawbacks have been overcome by using small ligands in a large excess, chelating ligands or even positively charged POMs, as well as resorting to hydrothermal methods. For instance, the use of carboxylate ligands such as oxalate bridging ligand can lead to the oligomerization of late–lanthanide monosubstituted Wells–Dawson or Keggin anions.[50] Similar reaction results in the monodimensional hybrid $[Yb_2(H_2O)_2(C_2O_4)\{\alpha\text{–}PW_{10}O_{38}\}]_n^{3-}$when Yb^{III} is used as lanthanide source. The use of N,O–chelating ligands such as picolinic acid allowed Boskovic et al. to prepare some organically functionalized Tb and Eu derivatives of the $[As_2W_{19}O_{67}(H_2O)]^{14-}$ lacunary polyanion, which show interesting photoluminescent properties.[51] Recently, Xu et al. reported a Dy^{III}–disubstituted Keggin POW, namely $[Dy_2\{Hcit\}_2AsW_{10}O_{38}]^{11-}$ (cit = citrate), where a citrate ligand is tri–coordinated to each dysprosium centers through two carboxylate oxygen atoms and one OH group[52] (Figure 3.6).

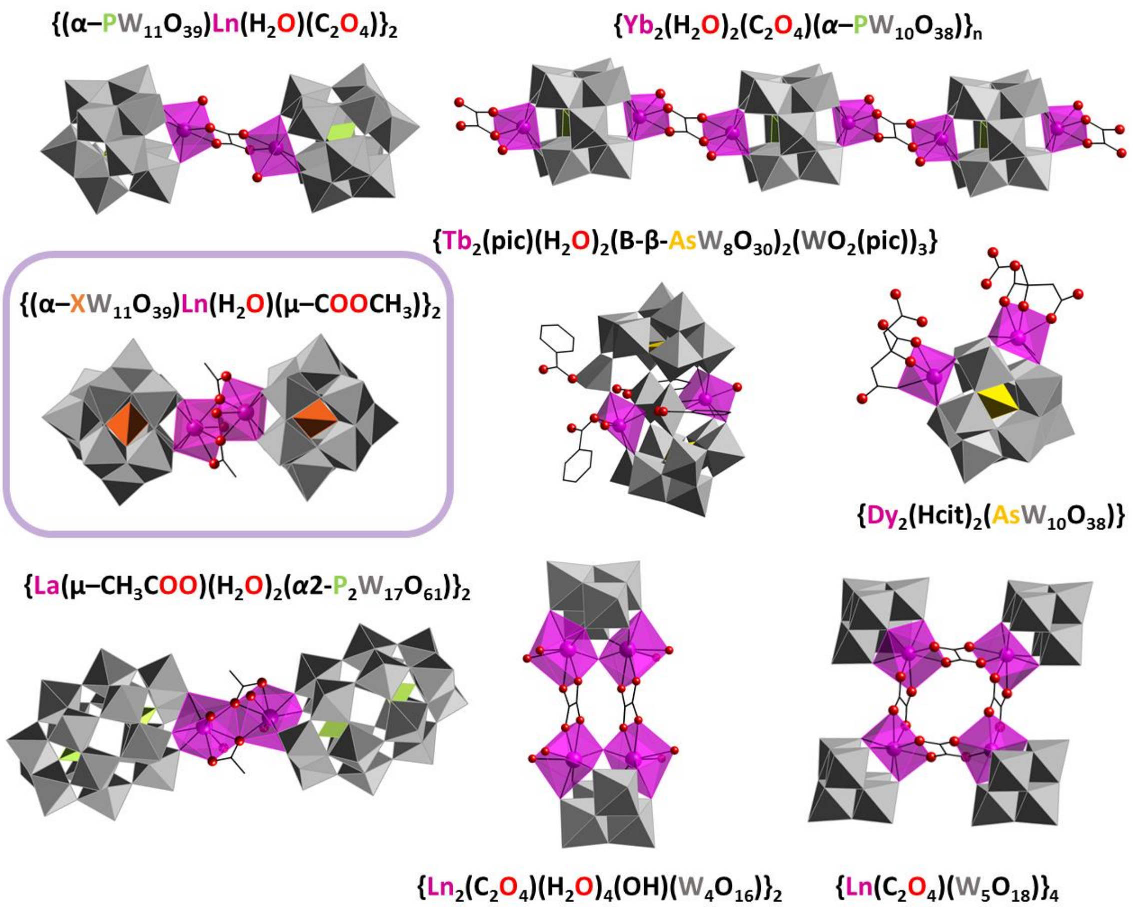

Figure 3.6. Some representative carboxylate–bridged Ln–substituted POWs (acetate or oxalate) highlighting the $\{(\alpha\text{–}XW_{11}O_{39})Ln(H_2O)(\mu\text{–}COOCH_3)\}_2$ fragment, along with citrate or picolinate–coordinated Ln–heteroPOWs. Organic ligands: pic = 2–picolinate; cit = citrate.

A representative example of the growing Ln–substituted heteroPOW family consists on Keggin–type 4f–monosubstituted anions that form dimeric entities through acetate ligands bridging the lanthanide centers (Figure 3.6), the general formula of which is $[\{(\alpha\text{–}XW_{11}O_{39})Ln(H_2O)(\mu\text{–}COOCH_3)\}_2]^{10/12-}$ (X = P^V, Si^{IV}, Ge^{IV}). The first two examples containing such fragment were isolated by Mialane et al. (X = Si, Ln = Gd, Yb).[53] After that, a few analogues belonging to the germanotungstate (Ln = Eu–Yb)[54] and phosphotungstate (Ln = Sm–Er)[55] families were obtained and recently, more 4f–derivatives of the silico– and phosphotungstate systems were obtained by Hussain and coworkers (Ln = Eu–Tb)[56] and Niu's group (Ln = Dy, Lu),[57] respectively. It is worth remarking that analogous salts containing early 4f–metals have not been isolated yet. The grafting of metalorganic moieties to these 2:2 type acetate–bridged POMs have met limited success, as heterometallic hybrids constructed from these dimmers are scarce. In this sense, only Cu(II) complexes of simple ligands (en) have been grafted so far on the surface of such clusters which required the use of hydrothermal methods in all cases (en = ethylendiamine). The former hybrids are limited to just five crystal structures belonging to {SiW} (Ln = Ce, Nd, Sm),[58] {PW} (Ln = Sm), and {GeW} (Ln = Tb)[59] Keggin. Interestingly, among these hybrids only the Ce–containing silicotungstate shows a ladder–like mono–dimensional arrangement, whereas the others consist on discrete heterometallic complexes (Figure 3.7). Some closely related compounds with similar {XW}–Ln–organic ligand–Ln–{XW} connection motif can also be found in the literature. For instance, replacement of the bridging acetate ligands for the tetradentate oxalate resulted in various molecular ox–bridged polyoxotungstates like $\{[(\alpha\text{–}PW_{11}O_{39})Ln(H_2O)]_2(C_2O_4)\}^{10-}$ (Ln = Dy–Er)[50b] or the series of di–substituted Lindqvist–type isopolyoxotungstates such as the dimeric $[\{Ln_2(C_2O_4)(H_2O)_4(OH)W_4O_{16}\}_2]^{10-}$ and tetrameric $[\{Ln(C_2O_4)W_5O_{18}\}_4]^{20-}$ (Ln = Eu–Tb) polyanions reported by Chen's group,[60] as well as Kortz's acetate–bridged Dawson–type $[\{La(\alpha_2\text{–}P_2W_{17}O_{61})(H_2O)_2(\mu\text{–}CH_3COO)\}_2]^{16-}$ salt[61] (Figure 3.6). Yang et al. prepared a monodimensional 3d–4f hybrid based on $[\{Cu(en)_2\}_2[(\alpha\text{–}PW_{11}O_{39})Tb(H_2O)_2]_2(C_2O_4)]_2^{6-}$ dimeric units where ox acts as bridge and the POM units are linked by dinuclear $[Cu_2(en)_2(C_2O_4)]^{2+}$ complexes,[62] while Sun's group reported similar monodimensional ox–bridged silicotungstate hybrids with Cu(II)–en complexes (Ln = Dy, Er).[63] The latter hybrid compounds were identified as excellent adsorbents for the selective separation for cationic dyes such as methylene blue in aqueous solution. It is worth mentioning the series of heterometallic hybrids with mixed ligands prepared by Wang's group that contain bridging Cu(II)–pzda (pzda = pyrazine–2,3–dicarboxylate) moieties and grafted Cu(II)–en complexes, which show both discrete (Ln = Dy, Yb, Lu) and 1D assemblies (Ln = Ce)[64] (Figure 3.7).

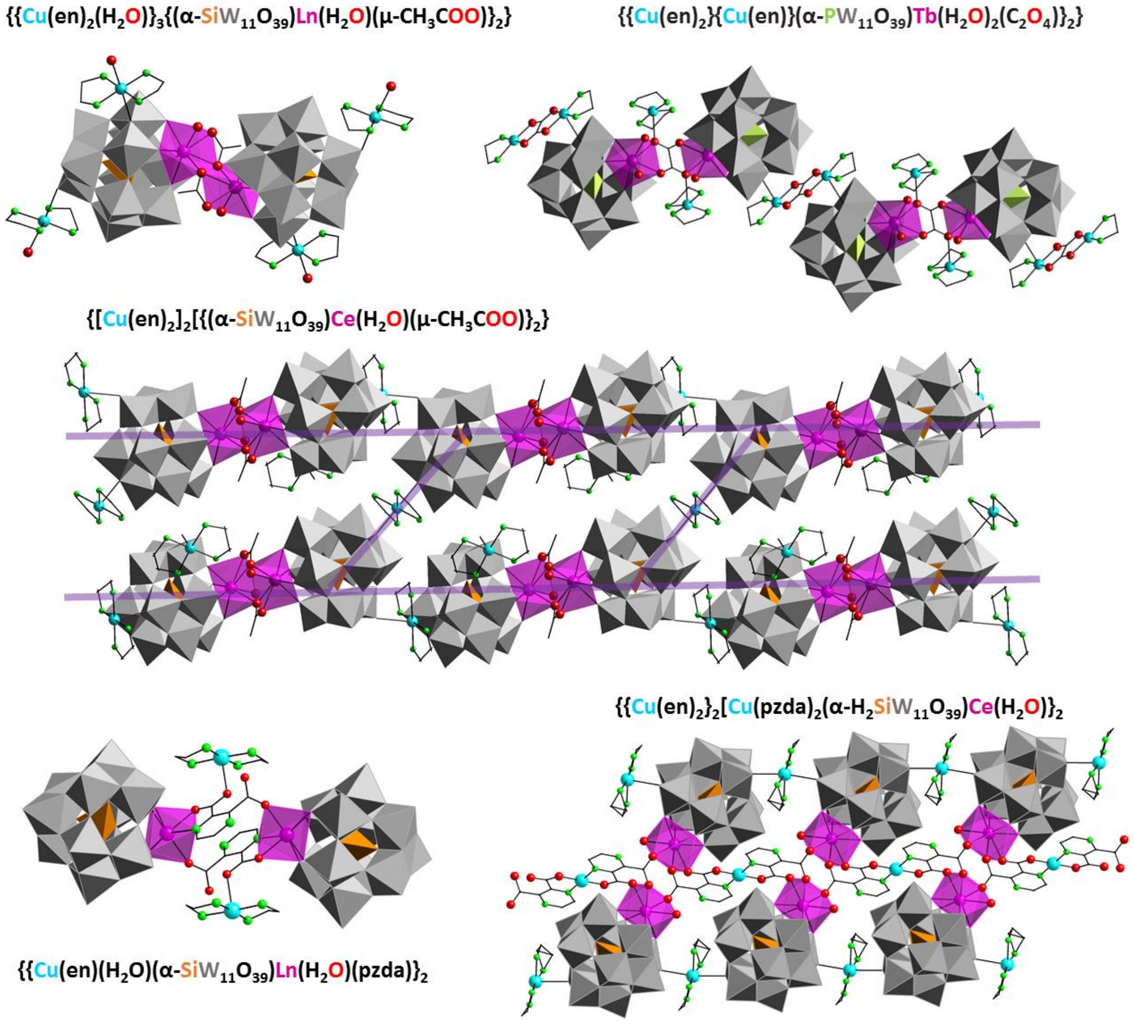

Figure 3.7. Some representative carboxylate–bridged Ln–substituted heteroPOWs, showing both discrete and monodimensional assemblies. Organic ligands: pzda = pyrazine–2,3–dicarboxylate; ox = oxalate.

3.1.5 SCSC Transformations in Polyoxotungstates

Solid–state transformations have been long known in POW chemistry as exemplified by the isomerization of the trilacunary [A, α–PW_9O_{34}]$^{9-}$ Keggin–type heteroPOW cluster into the B,α–form upon thermal treatment reported back in 1987.[65] In addition, among the 28 reports on stimuli–responsive POM–based compounds able to undergo SCSC transformations that have been reported to date, the vast majority of them consist in polyoxotungstates (19 reports), exclusively those belonging to the heteroPOW subfamily, as no reports on isoPOW–based compounds undergoing such type of phase transitions have been reported as of yet. The reported heteroPOWs are formed exclusively by either Keggin–type structure or some of its derivatives, comprising examples of nearly all types of inductive processes observed in SCSC transformations so far (light, redox, removal of solvent/guest molecules and post–synthetic functionalization).

The four compounds belonging to a family of $(Hmorph)_n[H_mM_{12}X_7W_{72}O_{268}]$ (morph = morpholine; M = Mn, Co; X = Si, Ge; {m, n} = {12, 40} for Mn and {6, 46} for Co, respectively) covalent hybrid frameworks reported by Cronin et al. constitute the single example in the literature of POM–based compounds able to undergo redox–induced SCSC transformations. In these studies, the Mn–containing silico–[66] and germanotungstate[67] derivatives undergo selective reduction of the Mn^{III} centers to the oxidation state Mn^{II} with retention of the 3D covalent framework of polysubstituted Keggin clusters, whereas the analogous Co derivatives suffer a selective oxidation of the Co^{II} to Co^{III} with similar results in the overall packing.[68] SCSC transformations upon irradiation of crystals with light are also scarce in comparison with the number of processes promoted by the absorption/desorption of guest molecules. In fact, a single example of a POM–based compound able to undergo a photoinduced SCSC transformation can be found in the literature, namely $[Gd_2(nmp)_{12}(PW_{12}O_{40})][PW_{12}O_{40}]$ (nmp = N–methyl–2–pyrrolidone). This hybrid compound was prepared by Zhang and coworkers and is able to undergo sunlight induced photopolymerization of discrete cationic and anionic clusters into a 1–dimensional hybrid polymeric assembly.[69]

In the past few years, Mizuno's group reported a large collection of microporous crystalline materials with tunable gas sorption properties.[70] These ionic solids are composed of POM clusters (mostly α–Keggin frameworks) and (μ^3–O)–centered trinuclear $[M^{III}_3O(OOCR)_6(L)_3]^+$ macrocations with triangular shape, in which the trivalent transition metals (M^{III} = Cr, Fe) are linked by six carboxylate anions (OOCR) in bridging μ^2–(κ^2–O:O') fashion showing one terminal ligand each (L = H_2O, pyridines, etc.). The complementary topologies of anions and cations favor the formation of ionic crystal packings with open framework nature that show voids and/or channels filled with guest solvent molecules. According to powder XRD studies, the latter can be evacuated without collapse of the micropores and with retention of the crystallinity for several of these compounds,[71] but only in a few cases the structure of the resulting guest–free phase has been determined by single–crystal XRD. The pair formed by compound $Cs_5[Cr_3O(OOCH)_6(H_2O)_3][CoW_{12}O_{40}]\cdot7.5H_2O$ and its partially dehydrated derivative $Cs_5[Cr_3O(OOCH)_6(H_2O)_3][CoW_{12}O_{40}]\cdot3.5H_2O$ are one amongst these rare examples, but worth being remarked as they constitute the first reported SCSC transformation study involving a POM–based compound.[72] Compounds

$K_2[Cr_3O(OOCC_2H_5)_6(H_2O)_3]_2[SiW_{12}O_{40}]\cdot3H_2O$ and $Rb_2[Cr_3O(OOCC_2H_5)_6(H_2O)_3]_2[SiW_{12}O_{40}]\cdot4H_2O$ represent additional examples of microporous ionic frameworks based on α–Keggin anions and $[M^{III}_3O(OOCR)_6(L)_3]^+$ macrocations for which the structures of their anhydrous phases, namely $K_2[Cr_3O(OOCC_2H_5)_6(H_2O)_3]_2[SiW_{12}O_{40}]$ and $Rb_2[Cr_3O(OOCC_2H_5)_6(H_2O)_3]_2[SiW_{12}O_{40}]$, have been determined by single–crystal XRD.[73]

Ionic POM–based compounds can also show dynamic behavior and undergo crystal phase transitions triggered by the evacuation of solvent molecules that involve rupture and formation of covalent bonds. The SCSC transformations of the α–Keggin type silicotungstate[74] $[Cu(bpmen)(H_2O)][SiW_{12}O_{40}\{Cu(bpmen)\}]$ and its related germanotungstate derivative[75] $[Cu(bpmen)(H_2O)][GeW_{12}O_{40}\{Cu(bpmen)\}]\cdot3.5H_2O$ into their corresponding anhydrous phases $[XW_{12}O_{40}\{Cu(bpmen)\}_2]$ (X = Si; X = Ge) are illustrative examples of this phenomenon (bpmen = N,N′–dimethyl–N,N′–bis–(pyridin–2–ylmethyl)–1,2–diaminoethane). Dynamic behavior associated with the rupture and formation of coordinative bonds triggered by the thermal evacuation of solvent molecules has also been observed for neutral, molecular hybrid species based on POM clusters and metalorganic moieties, such as those in the isostructural compounds $[XW_{12}O_{40}\{Cu(bpmpn)(H_2O)\}_2]\cdot3.5H_2O$ (X = Si; X = Ge; bpmpn = N,N′–dimethyl–N,N′–bis(pyridin–2–ylmethyl)–1,3–diaminopropane).[74] An additional example of bonding disruption within a crystal framework that is essentially preserved upon evacuation of solvent molecules can be found for the isostructural compounds $[C(NH_2)_3]_4[\{XW_{12}O_{40}\}\{Cu_2(pic)_4\}]_2[Cu_2(pic)_4(H_2O)]\cdot6H_2O$ (X = Si, Ge; pic = 2–picolinate), which transforms into the $[C(NH_2)_3]_4[\{XW_{12}O_{40}\}\{Cu_2(pic)_4\}]_4[Cu(pic)_2]_2$ phases upon full dehydration.[76]

A representative example of postsynthetic functionalization that occurs through a SCSC transformation triggered by concomitant exchange of cations and lattice solvent molecules is illustrated by compound $[H_3O]_4[Mn_4(H_2O)_{18}][WZnMn_2(H_2O)_2(ZnW_9O_{34})_2]\cdot18H_2O$ reported by Wu and coworkers.[77] Crystals of the title compound are able to incorporate divalent transition metal ions into architectural interstices as shown by the postfunctionalized phases $[M_2(H_2O)_6][Mn_4(H_2O)_{16}][WZnMn_2(H_2O)_2(ZnW_9O_{34})_2]\cdot10H_2O$ (M = Co, Cu) obtained through a cationic exchange process. In 2011, Uehara and Mizuno prepared the $[SiV_2W_{10}O_{39}]^{4-}$ heterocluster[78] which was isolated as the $(TBA)_4[SiV_2W_{10}O_{39}]\cdot2DCE$ salt (TBA = tetra–*n*–butylammonium, DCE = 1,2–dichloroethane). The authors provided crystallographic confirmation of the $[H_2SiV_2W_{10}O_{40}]^{4-}$ POM precursor being a γ–Keggin type polyoxotungstate cluster with two bis(hydroxo)–bridged vanadium (V) atoms occupying the addenda metal positions 1 and 2 according to the IUPAC nomenclature.[79] Mizuno also used single–crystal XRD technique to determine the structural changes promoted by ligand/cation sequential exchange processes in two of his macrocations–containing potassium salts, namely $K_2[Cr_3O(OOCH)_6(etpy)_3]_2[SiW_{12}O_{40}]\cdot8H_2O$ and $K_2[Cr_3O(OOCH)_6(mepy)_3]_2[SiW_{12}O_{40}]\cdot8H_2O$ (etpy = 4–ethylpyridine; mepy = 4–methylpyridine). These SCSC transformations proceed in both cases with retention of the initial robust ionic open–frameworks.[80]

Very recently, Zhan and coworkers reported what they call the first “flexi–crystal”, namely $Li_9K_7W_1Co_{10}[H_2P_8W_{48}O_{186}]\cdot132\ H_2O$, the denomination of which stands for a flexible crystalline transition metal oxide compound that is dynamically switchable between many phases and capable of performing numerous SCSC transformations.[81] This compound consist on a one–dimensional chain–like structure in which adjacent $\{P_8W_{48}\}$ rings are bridged together by Co^{II} ions. This compound, was synthesized under relatively mild conditions, using a two–step approach involving the reaction of the preformed $\{P_8W_{48}\}$ building block with $Co(ClO_4)_2 \cdot 6H_2O$ in aqueous media and exhibits at least 8 crystal–to–crystal states connected at 11 different routes. These SCSC transformations can be induced by various environmental stimuli and they range in the relative topology and/or connectivity of the rings spanning the full range of dimensionalities, from zero to three–dimensional architectures, with fully isolated 0D, 1D, 2D and 3D systems.

3.1.6 Summary

In the first section of this chapter, we report the first 3D covalent structure with permanent porosity constructed from the relatively uncommon $\{W_7\}$ cluster and {Cu(cyclam)} metalorganic bridging complexes. Interestingly, compound **1–CuW7** undergoes two sequential SCSC transformations upon gradual dehydration leading to the partially hydrated **2–CuW7** and the anhydrous **3–CuW7**, which constitutes the first example of a heptatungstate–based isoPOM that exhibit such type of thermally activated transformations. The permanent porosity of these hybrids has been assessed by gas sorption experiments which revealed that our compounds are one of the few POM–based hybrids with both N_2 and CO_2 gas sorption functionality. Meanwhile, the preparation and crystallochemical characterization of the first covalent bidimensional 2:2 type acetate–bridged Ln–substituted germanotungstate hybrids with {Cu(cyclam)} moieties for all Ln derivatives (Ln = La to Lu), namely $[Cu(cyclam)]_2[\{Cu(cyclam)\}_4\{(\alpha\text{–}GeW_{11}O_{39})Ln(H_2O)(\mu\text{–}CH_3COO)_2]\cdot 17\text{–}19H_2O$ (**1–Ln**, Ln =La to Lu) is described in the second section of the chapter. These dimeric hybrids undergo reversible SCSC transformations promoted by dehydration upon heating to give new 1D crystalline phases (**2–Ln**, Ln = Eu, Er and **3–Ln**, Ln = Ce, Eu). Single–crystal XRD, together with simultaneous PXRD and TGA analyses revealed that rehydration kinetics depends strongly on the Ln analogue for the **2–Ln** to **1–Ln** phase transition. This is the first time that such interesting thermally triggered transformations have been reported in these type of acetate–bridged heterometallic hybrids.

3.2 ISOPOLYOXOTUNGSTATES

3.2.1 Experimental Section

Materials and methods

All chemicals were obtained from commercial sources and used without further purification. Carbon, hydrogen and nitrogen contents were determined on a Perkin–Elmer 2400 CHN analyzer. FT–IR spectra were obtained as KBr pellets on a SHIMADZU FTIR–8400S spectrometer. Thermogravimetric (TGA) analysis was carried out from room temperature to 650 °C at a rate of 5 °C min^{-1} on a Mettler Toledo TGA/SDTA 851^e thermobalance under a 50 cm^3 min^{-1} flow of synthetic air. Powder X–ray diffraction (PXRD) patterns were collected on a Bruker D8 Advance diffractometer operating at 30 kV/20 mA and equipped with Cu Kα

radiation (λ = 1.5418 Å), a Vantec–1 PSD detector, an Anton Parr HTK2000 high–temperature furnace, and Pt sample holder (Figure A3.1 in the Appendix). The powder patterns were recorded in 2θ steps of 0.033° in the $5 \leq 2\vartheta \leq 35$ range, counting for 0.3 s per step. Data sets were acquired from 30 to 530 °C with a 0.16 °C s^{-1} heating rate between temperatures.

Synthetic procedure

[{Cu(cyclam)}$_3$(W$_7$O$_{24}$)]·15.5 H$_2$O (1–CuW7). $Na_2WO_4 \cdot 2H_2O$ (0.230 g, 0.70 mmol) was dissolved in 20 mL of water at room temperature, and the pH was adjusted with 0.5 M NaOH to 8.3. Then, a solution composed of $CuSO_4$ (0.075 g, 0.30 mmol) and cyclam ligand (0.060 g, 0.30 mmol) in 15 mL of water was added dropwise to the tungstate solution. Afterwards, the resulting dark purple solution was stirred at room temperature for 2 h and then filtered off. Finally, the solution was left to slowly evaporate at room temperature and purple block crystals suitable for XRD diffraction were obtained after 4 days. Yield: 36 mg (13% based on $Na_2WO_4 \cdot 2H_2O$). Anal. Calcd (found) for $C_{30}H_{103}Cu_3N_{12}O_{39.5}W_7$: C, 13.14 (12.75); H, 3.83 (3.79); N, 6.13 (5.88). IR (cm^{-1}): 3228 (vs), 3163 (vs), 2935 (s), 2865 (s), 1630 (m), 1474 (w), 1454 (w), 1443 (w), 1430 (w), 1387 (w), 1358 (w), 1314 (w), 1292 (w), 1254 (w), 1234 (w), 1105 (m), 1065 (m), 1063 (m), 1016 (m), 1014 (m), 962 (vs) 883 (vs), 843 (s), 812 (s), 669 (s), 577 (sh), 486 (m), 436 cm^{-1} (m).

[{Cu(cyclam)}$_3$(W$_7$O$_{24}$)]·12H$_2$O (2–CuW7). Single crystals of **1–CuW7** were heated at 60 °C in an oven for 1 h, which produced a slight colour change from dark pink to brighter pink.

[Cu(cyclam)]$_{0.5}$[{Cu(cyclam)}$_{2.5}$(W$_7$O$_{24}$)] (3–CuW7). Single crystals of **1–CuW7** were heated in an oven at 120 °C for 1 h, with their colour changing to maroon.

Single–crystal X–ray crystallography

Crystallographic data for **1–CuW7, 2–CuW7** and **3–CuW7** isopolyoxotungstate hybrids are given in Table 3.1. Intensity data were collected on an Agilent Technologies Super–Nova diffractometer, which was equipped with monochromated Mo Kα radiation (λ = 0.71073 Å) and Eos CCD detector with the exception of **1–CuW7**. For the latter, the selected radiation and detector were monochromated Cu Kα radiation (λ = 1.54184 Å) and Atlas CCD, respectively. The data collection temperature was 100 K for all compounds.

In the cases of the partially dehydrated **2–CuW7** and the anhydrous phase **3–CuW7**, single crystals of each compound were respectively heated to 333 and 393 K at a rate of 1 K min^{-1} in an oven, mounted on the diffractometer which was at 333 (**2–CuW7**) and 393 K (**3–CuW7**) and then cooled down to 100 K to perform the full data collection. Data frames were processed (unit cell information, analytical absorption correction with face indexing, intensity data integration and correction for Lorentz and polarization effects) using the CrysAlis Pro software package.[82] The structures were solved using OLEX2[83] and refined by full–matrix least–squares with SHELXL–2014/6.[84] Final geometrical calculations were carried out with PLATON[85] as integrated in WinGX.[86] Thermal vibrations were treated anisotropically for heavy atoms (W and Cu). Hydrogen atoms of the organic ligands were placed in calculated positions and refined using a riding model with standard SHELXL parameters. Twenty positions suitable for water molecules of hydration were located in the Fourier map of **1–CuW7** and their occupancy was initially refined without restrictions. The resulting total number of 15.4 water molecules per heptatungstate cluster was fixed to 15.5 during the final refinement. For **2–CuW7** however, 24 positions per two hepatungstate fragment with whole occupancy were located and fixed as that. The space within the channels occupied by the water molecules of hydration was visualized by PyMol.[87]

Table 3.1. Crystallographic data for **1–CuW7**, **2–CuW7** and **3–CuW7** isopolyoxotungstates.

	1–CuW7	2–CuW7	3–CuW7
empirical formula	$C_{30}H_{103}Cu_3N_{12}O_{39.5}W_7$	$C_{30}H_{96}Cu_3N_{12}O_{36}W_7$	$C_{30}H_{72}Cu_3N_{12}O_{24}W_7$
fw (g mol^{-1})	2741.81	2678.75	2462.56
Z	2	4	8
crystal system	triclinic	triclinic	monoclinic
space group	*P–1*	*P–1*	$P2_1/a$
temperature (K)	100(2)	100(2)	100(2)
***a* (Å)**	15.8305(5)	16.0175(2)	24.3100(3)
***b* (Å)**	11.6366(4)	20.1960(3)	20.4530(2)
***c* (Å)**	20.8710(6)	20.5149(3)	26.8571(2)
α (°)	74.229(3)	89.9080(10)	90
β (°)	95.933(2)	96.2760(10)	82.4570(10)
γ (°)	106.308(3)	84.7810(10)	90
V (Å^3)	3549.6(2)	6568.79(16)	13238.1(2)
K_α (Å)	1.54184	0.71073	0.71073
ρ_{calc} (g cm^{-3})	2.565	2.709	2.471
μ (mm^{-1})	22.107	13.248	13.122
collected rflns	26669	42612	94635
unique rflns (R_{int})	12624 (0.037)	23105 (0.026)	24638 (0.044)
observed rflns [$I > 2\sigma(I)$]	11309	20330	18419
parameters	441	817	715
$R(F)^a$ [$I > 2\sigma(I)$]	0.038	0.031	0.050
$wR(F^2)^b$ [all data]	0.101	0.078	0.102
GoF	1.028	1.081	1.150

^{a} $R(F)=\Sigma||F_o–F_c||/\Sigma|F_o|$; ^{b} $wR(F^2)=\{\Sigma[w(F_o^2–F_c^2)^2]/\Sigma[w(F_o^2)^2]\}^{1/2}$

Gas sorption measurements

The gas physisorption measurements were performed on a Quantachrome Autosorb–iQ–MP. All samples were activated in vacuum at 120 °C for 24 h prior to gas adsorption measurements. Lower or higher activation temperatures did not result in samples with larger gas uptake capacity. The PXRD patterns of the outgassed samples showed that the structure remains stable without any loss of crystallinity. Nitrogen isotherms were acquired at 77 K, while carbon dioxide physisorption data were recorded at 273, 293 and 298 K. The specific surface area was calculated from the N_2 adsorption branch using the Brunauer–Emmett–Teller (BET) method.[88]

3.2.2. RESULTS AND DISCUSSION

Synthesis

The synthesis of the heptatungstate hybrid **1–CuW7** was carried out by reacting $Na_2WO_4 \cdot 2H_2O$ in aqueous media at pH = 8.3 with cyclam ligand and copper sulfate salt. Different salts were used as transition metal source like chloride, acetate and nitrate in an attempt to figure out if they could have a decisive role in the formation of the product **1–CuW7**. The results indicated that no effect took place as the same compound **1–CuW7** was obtained when NO_3^-, Cl^- and CH_3COO^- anions were present in the reaction medium. We also screened a wide range of pH values to determine the pH values in which **1–CuW7** was stable enough to isolate it. In this sense, our results indicated that pure crystals of **1–CuW7** can only be obtained when the tungstate solution was adjusted to pH values in the specific range of 6.0–9.5 with a highly variable yield depending on the final pH. At pH values between 6.0–7.3 only a few single crystals of **1–CuW7** (yield below 1%) were obtained whereas a significant increase in the reaction yield was observed when the reaction was adjusted to higher pH values in the range 7.5–9.5 with the highest observed at 8.3 (yield 13%). When the reaction medium was adjusted to values above 9.5 however, a new crystalline hybrid phase constituted by tungstate $[WO_4]^{2-}$anions and $\{Cu(cyclam)\}^{2+}$ complexes was obtained as evidenced by single–crystal XRD, which will not be covered in this dissertation. In contrast, no identifiable solid formation was observed below pH = 6.0. (Figure 3.8).

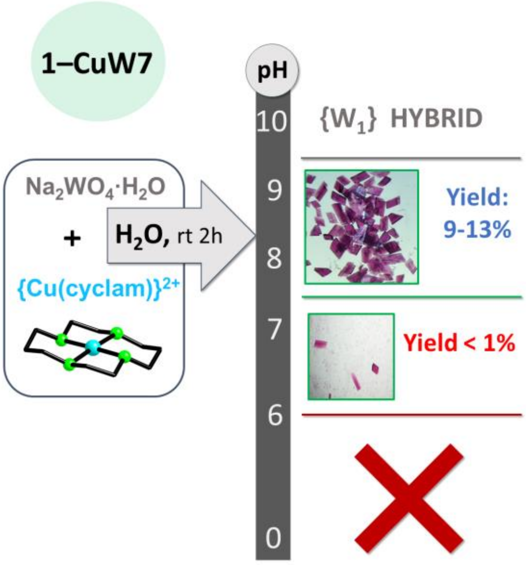

Figure 3.8. Influence of the pH in the Cu^{2+}:cyclam:WO_4^{2-} synthetic system.

Apart from that, similar reactions were performed at 50 °C, 90 °C and under refluxing conditions at pH = 7.5–9.5 in order to verify the influence of the temperature in the reaction that led to the hybrid **1–CuW7**. Interestingly enough, while purple block crystals were obtained at 50 °C as well as at room temperature in comparable yields, when the reaction temperature was raised above mild heating no product formation was observed for weeks. After three weeks however, the formation of a light purple polycrystalline powder was observed (yield < 10%), which was identified as the same **1–CuW7** phase, as evidenced by FT–IR and PXRD patterns. In view of this, we determined that the temperature has an important effect since it affected not only the crystallinity grade and the crystallization speed, but also the yield of the resulting $\{W_7\}$ hybrid in a significant way. Finally, isolation of compound **1–CuW7** also depends heavily on the nature of the transition metal. We tried to prepare analogous compounds with similar reactions at room temperature and 50 °C but using Co^{II}, Ni^{II} and Zn^{II} instead of Cu^{II}. The resulting amorphous brownish, greenish and white precipitates could not be further characterized on the basis of IR spectroscopy, confirming that the plasticity that Cu^{II} centres display seems to play a key role in the stabilization of the heptatungstate clusters and thus, the formation of the heptatungstate hybrid **1–CuW7**.

Vibrational characterization and thermostructural behaviour of 1–CuW7

The preliminary characterization of **1–CuW7** was carried out by means of FT–IR spectroscopy (Figure 3.9). The FT–IR spectrum of **1–CuW7** shows the characteristic peaks at around 962, 883–843 and 669 cm^{-1} which have been attributed to $\nu_{as}(W–O_t)$, $\nu_{as}(W–O_b–W)$ and $\nu_s(W–O_b–W)$ bands arising from the $[W_7O_{24}]^{6-}$ cluster, respectively (O_t: terminal oxygen atom; O_b: bridging oxygen atom). At lower wavenumber values weaker bands attributable to $\delta(W–O_b–W)$ vibration can be found as well. Regarding the metal–organic region of the FT–IR spectrum, the peaks associated with the stretching of the –N–H and –C–H bonds are respectively observed at 3228–3163 and 2935–2865 cm^{-1}, whereas several weak to medium signals corresponding to the δ(C–H) and ν(N–C) vibration modes are also present in the 1474–1234 and 1105–1014 cm^{-1} ranges. These signals confirm the presence of the cyclam ligand while the strong signal at 3420 cm^{-1} is associated with the characteristic vibration of H_2O.

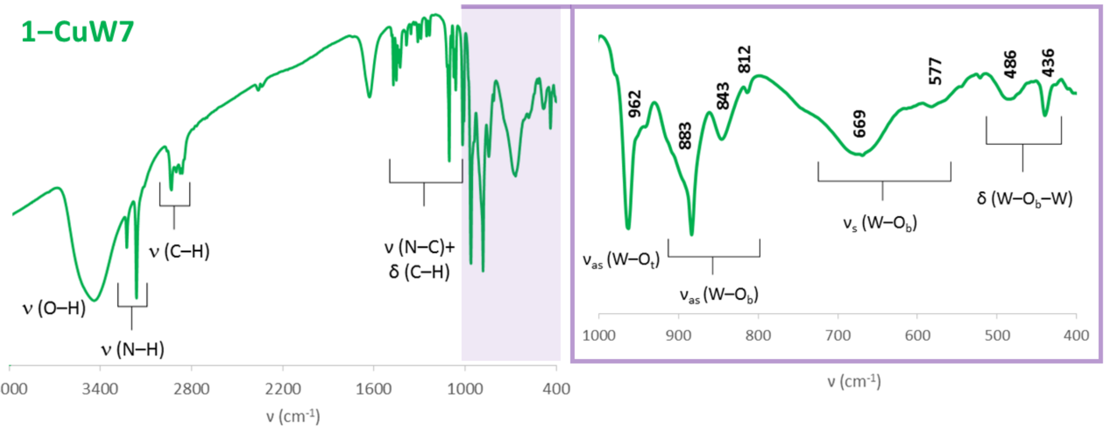

Figure 3.9. FT–IR spectrum of **1–CuW7** hybrid heptatungstate with details of the inorganic region.

Thermal stability of compound **1–CuW7** was investigated by thermogravimetric measurements (Figure 3.10). The first stage is observed as a mass loss that extends from room temperature to *ca*. 80 °C, which corresponds to the release of all free water molecules. The initial mass loss of 10.25% corresponds to 31 water molecules per two cluster (calcd 10.18%). Total dehydration leads to the anhydrous phase (**3–CuW7**), which shows a significant interval of thermal stability until its degradation at *ca.* 220 °C. The anhydrous phase then undergoes further decomposition via various overlapping mass loss stages of due to the crumbling of the POM framework and the combustion of the organic ligands. The overall mass loss for this second stage is 22.21%, which is in good agreement with six cyclam ligands per two cluster (calcd 21.88%). The final residue is obtained at temperatures above *ca.* 450 °C (calcd. for $Cu_3O_{24}W_7$ 67.89%, found 67.95%).

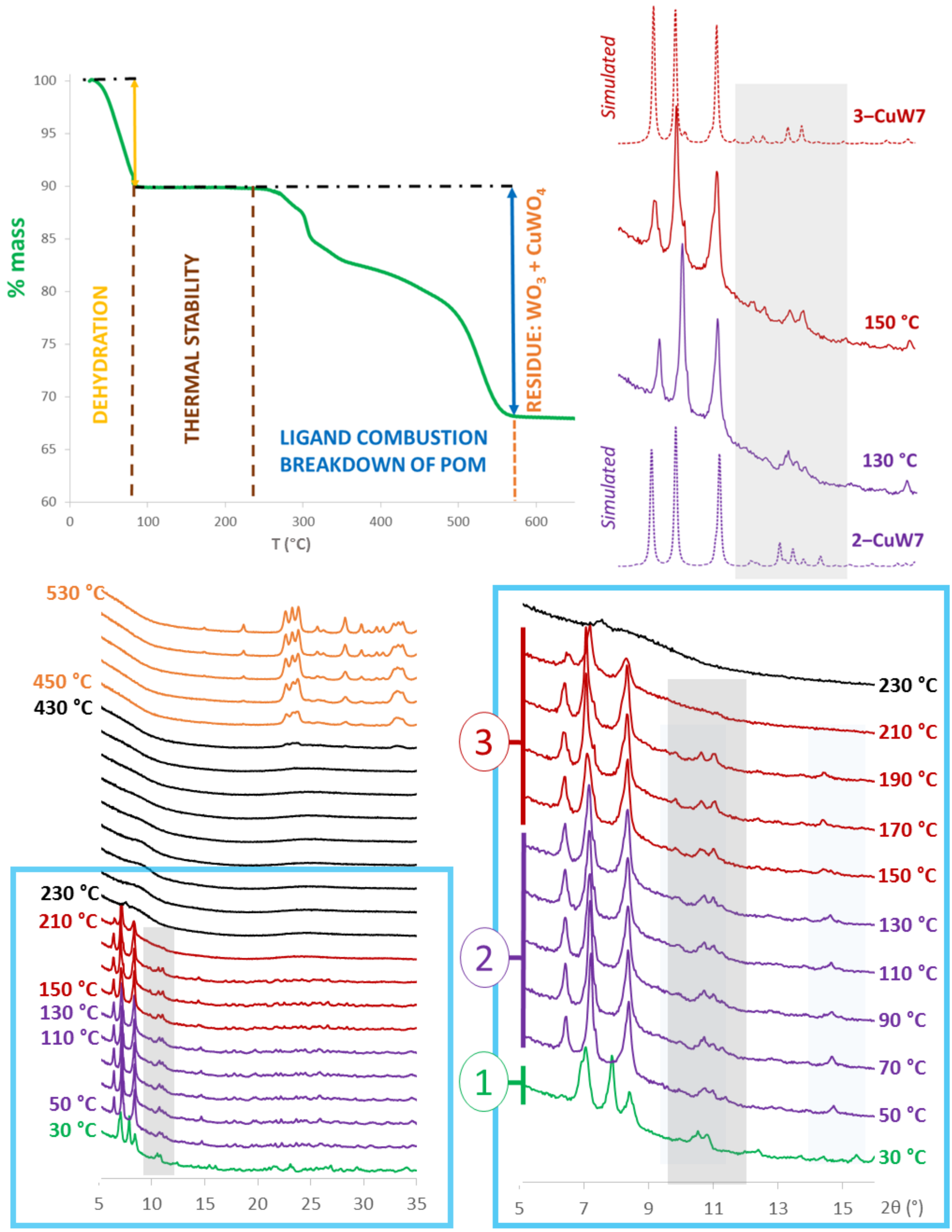

Figure 3.10. Thermostructural studies for **1–CuW7** hybrid. TGA curve (top left) and TPXRD measurements (bottom) highlighting the different thermal derivatives (**1–**,**2–** and **3–CuW7**) and the most notable changes when going from **2–** to **3–CuW7**, in both experimental (bottom right) and simulated from sc–XRD data diffractograms (top right).

Taking into account the thermal stability range that **1–CuW7** displays and encouraged by our previous results in vanadium–based hybrid frameworks with temperature dependent crystal transitions (See chapter 2), we decided to study this kind of structural transformations in **1–CuW7** as well. In order to analyze its thermostructural behavior, variable–temperature powder X–ray diffraction (TPXRD) measurements were carried out. TPXRD experiments between 30 and 530 °C showed that **1–CuW7** transforms into another partially hydrated phase (**2–CuW7**) at the early temperature of 50 °C as demonstrated by notable modifications in the positions of the most intense diffraction maxima in the low 2ϑ region (Figure 3.10). In particular, the maximum at 7.9° disappears at 50 °C whereas a new one appears at 2ϑ values around 6.6°. Furthermore, subtle variations can be observed in several diffraction maxima of weak intensity that appear at 2ϑ angles in the $9 < 2\vartheta < 15°$ range. Regarding the patterns collected above 50 °C, no relevant modification is observed in the positions of the most intense diffraction maxima until complete amorphization at 230 °C, which is in good agreement with the results observed in the TGA analyses that show a thermal stability range for the anhydrous phase that extends up to this temperature. Nevertheless, close inspection of the weak intensity diffraction maxima in the 9–12° range reveals the presence of two different phases in the crystalline region. (Figure 3.10). The partially hydrated **2–CuW7** undergoes a gradual change to exclusively lead to the anhydrous **3–CuW7** above 150 °C. This transformation can be traced by the presence of three overlapped maxima centered at 2ϑ = 11° in **2–CuW7** that evolves into two peaks in **3–CuW7**. In addition, the relatively broad maximum at 10° is divided into two well defined peaks when going from **2–CuW7** to **3–CuW7.** Several diffraction maxima belonging to new high–temperature crystalline phases start appearing above *ca.* 450 °C. At 550 °C, these phases forming the final residue of the thermal decomposition are defined enough for being identified as a mixture of orthorhombic *Pmnb* WO_3 (PDF: 01–071–0131)[89] and triclinic *P–1* $CuWO_4$ (PDF: 01–088–0269),[90] with Scheelite–type structure in an approximate ratio 55:45 (Figure A3.2 in the Appendix).

We decided to carry out single–crystal XRD studies in an attempt to determine the structure of the new partially dehydrated intermediate observed at temperatures above 50 °C (**2–CuW7**). For that end, a single crystal of **1–CuW7** for which full intensity data were initially collected at 100 K was heated to 60 °C, after which the temperature was lowered back to 100 K to perform a full data collection. The crystal preserved its integrity and crystallinity during the whole process and this allowed us to determine the structure of **2–CuW7**. Similarly, the previous process was repeated with a second crystal but the temperature was raised to 120 °C instead to ensured total dehydration of the sample and thus, we were able to structurally characterize the thermally stable anhydrous phase (**3–CuW7**).

Crystal structure of 1–CuW7

Compound **1–CuW7** crystallizes in the triclinic *P–1* space group. The asymmetric unit of **1–CuW7** consists of an heptatungstate $\{W_7\}$ fragment, five {Cu(cyclam)} complexes, which four of them are centrosymmetric, and several lattice water molecules. The heptatungstate polyoxoanion is formed by the connection of six $\{WO_6\}$ octahedra that share edges and corners forming a ring, where at its center another $\{WO_6\}$ unit is connected through its edges (Figure 3.11). Compared to other planar clusters like the Anderson–type POM, the heptatungstate cluster displays a non–planar structural feature that results in its characteristic V shape. The W–O bond lengths are in the range of 1.729(6)–2.419(5) Å, which are comparable to those reported in the literature.[12]

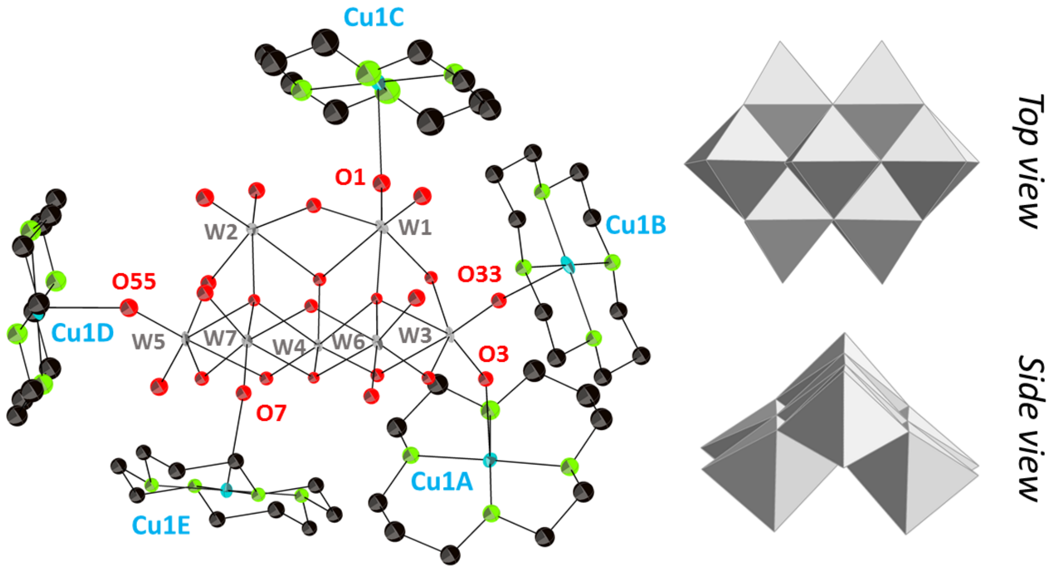

Figure 3.11. ORTEP view depicted at 50% of the hybrid POM of **1–CuW7** with partial atom labelling (left) along with the polyhedral representation of the top and side views of the heptatungstate cluster (right).

Table 3.2. Cu–O bond lengths and Cu···O distances as well as the polyhedral distorsion (CShM) of the {Cu(cyclam)} complexes in **1–CuW7** and its thermal derivatives **2–CuW7** and **3–CuW7**.

1–CuW7		**2–CuW7**				**3–CuW7**			
Cu1A–N$_{mean}$	2.012	Cu1A–N$_{mean}$	2.009	Cu2A–N$_{mean}$	2.006	Cu1A–N$_{mean}$	1.997	Cu2A–N$_{mean}$	2.001
Cu1A–O3	2.597(6)	Cu1A–O22A	2.624(4)	Cu2A–O77B	2.664(4)	Cu1A···O22A	2.898(10)	Cu2A–O11B	2.549(10)
Cu1A–O77^{i}	2.731(6)								
OC–6	3.017	SPY–5	1.612	SPY–5	1.403	SP–4	0.172	SPY–5	1.595
Cu1B–N$_{mean}$	2.024	Cu1B–N$_{mean}$	2.024	Cu2B–N$_{mean}$	2.021	Cu1B–N$_{mean}$	2.033	Cu2B–N$_{mean}$	2.027
Cu1B–O33	2.348(6)	Cu1B–O33A	2.316(4)	Cu2B–O33B	2.347(4)	Cu1B–O33A	2.292(9)	Cu2B–O33B	2.578(8)
Cu1B–O33^{ii}	2.348(6)	Cu1B–O33A^{i}	2.316(4)	Cu2B–O33B^{vi}	2.347(4)	Cu1B–O33A^{i}	2.292(9)	Cu2B–O33B^{iii}	2.578(8)
OC–6	0.634	OC–6	0.527	OC–6	0.739	OC–6	0.449	OC–6	1.812
Cu1C–N$_{mean}$	2.015	Cu1C–N$_{mean}$	2.026	Cu2C–N$_{mean}$	2.017	Cu1C–N$_{mean}$	2.013	—	—
Cu1C–O1	2.572(6)	Cu1C–O1A^{ii}	2.458(5)	Cu2C–O1B	2.478(5)	Cu1C–O1A	2.403(10)	—	—
Cu1C–O1^{iii}	2.572(6)	Cu1C–O1A^{iii}	2.458(5)	Cu2C–O1B^{iii}	2.478(5)	Cu1C–O1B	2.654(10)	—	—
OC–6	1.631	OC–6	0.958	OC–6	1.174	OC–6	1.411	—	—
Cu1D–N$_{mean}$	2.026	Cu1D–N$_{mean}$	2.019	Cu2D–N$_{mean}$	2.021	Cu1D–N$_{mean}$	2.019	Cu2D–N$_{mean}$	2.004
Cu1D–O55	2.456(6)	Cu1D–O55A^{iv}	2.457(4)	Cu2D–O55B	2.419(5)	Cu1D–O55B	2.328(10)	Cu2D–O55A	2.515(8)
Cu1D–O55^{iv}	2.456(6)	Cu1D–O55A^{ii}	2.457(4)	Cu2D–O55B^{vii}	2.419(5)	Cu1D–O55B^{ii}	2.328(10)	Cu2D–O55A^{iv}	2.515(8)
OC–6	1.038	OC–6	1.187	OC–6	1.160	OC–6	0.593	OC–6	1.595
Cu1E–N$_{mean}$	2.018	Cu1E–N$_{mean}$	2.032	Cu2E–N$_{mean}$	2.019	Cu1E–N$_{mean}$	2.019	—	—
Cu1E–O7	2.492(6)	Cu1E–O7A	2.452(4)	Cu2E–O7B	2.492(4)	Cu1E–O7A	2.374(10)	—	—
Cu1E–O7^{v}	2.492(6)	Cu1E–O7A^{v}	2.452(4)	Cu2E–O7B^{viii}	2.492(4)	Cu1E–O7B^{v}	2.656(10)	—	—
OC–6	1.283	OC–6	1.675	OC–6	1.285	OC–6	1.722	—	—

Symmetry codes: **1–CuW7:** i) *x*, 1+*y*, *z*; ii) –*x*, 2–*y*, 2–*z*; iii) 1–*x*, 2–*y*, 2–*z*; iv) 1–*x*, 2–*y*, 1–*z*; v) 1–*x*, 2–*y*, 1–*z*. **2–CuW7:** i) 1–*x*, 2–*y*, 1–*z*; ii) *x*, 1+*y*, *z*; iii) –*x*, 3–*y*, 1–*z*; iv) –*x*, 3–*y*, 2–*z*; v) 1–*x*, 2–*y*, 2–*z*; vi) 1–*x*, 3–*y*, 1–*z*; vii) –*x*, 3–*y*, 2–*z*; viii) 1–*x*, 3–*y*, 2–*z*. **3–CuW7:** i) 1–*x*, 2–*y*, 1–*z*; ii) 1–*x*, –3–*y*, 1–*z*; iii) 1–*x*, 3–*y*, –*z*; iv) 1–*x*, 2–*y*, –*z*; v) –1/2+*x*, 5/2–*y*, *z*. CShM: reference polyhedra SP–4 (square), SPY–5 (square pyramid) and OC–6 (octahedron).

All of the {Cu(cyclam)} cationic complexes found in **1–CuW7** are grafted to terminal O atoms of the cluster and thus, they act as bridging metal–organic blocks between the POMs, showing the typical *trans–III* configuration. The coordination spheres of all Cu^{II} centers show distorted octahedral geometries as indicated by continuous shape measures (CShM),[91] with the four N atoms of the cyclam ligand forming the equatorial plane and the axial positions occupied by terminal O atoms from different tungstate octahedra. While all CuN_4O_2 chromophores show significant Jahn–Teller elongation, it must be noted that this type of distortion is especially remarkable for Cu1A, as one of its axial Cu–O bonds shows a length near that of semi–coordination as well as the highest CShM value (Table 3.2).

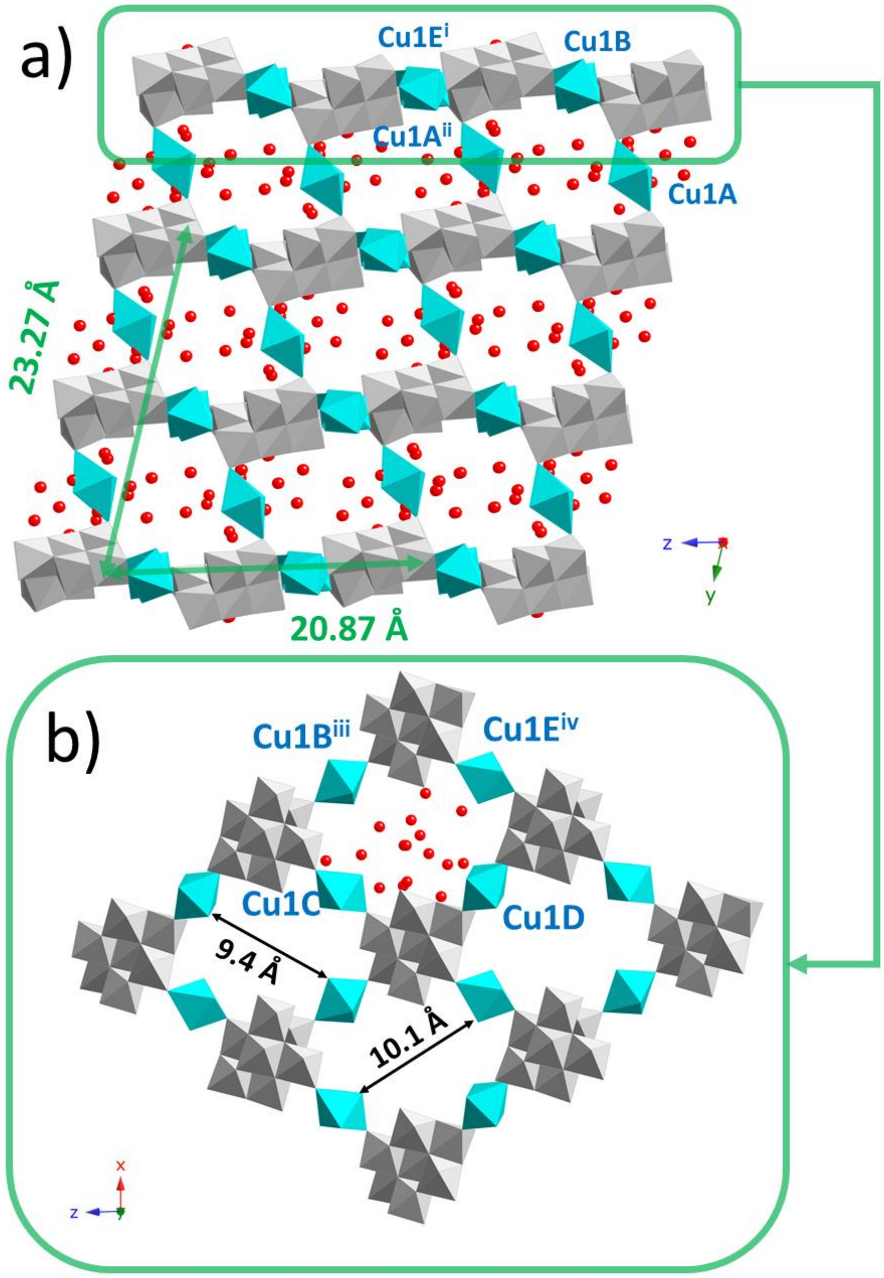

Figure 3.12. a) View of the crystal packing of **1–CuW7** along the y axis showing W1···W1 distances. b) Hybrid layers with approximate dimensions of the channels in the *xz* plane. Cyclam ligands are omitted for clarity. Color code: W (grey), Cu (blue), O (red). Symmetry codes: i) –*x*, 2–*y*, 2–*z*; ii) –*x*, 3–*y*, 2–*z*; iii) 1–*x*, 2–*y*, 2–*z*; iv) –*x*, 2–*y*, 1–*z*.

The crystal packing of **1–CuW7** can be described as an extended covalent open–framework constructed by hybrid layers of {W_7} clusters and {Cu(cyclam)} complexes in the xz plane, which are connected through the metalorganic moieties generating a 3D covalent arrangement with water–containing rhombic–like channels along the *y* axis (Figures 3.12). Thus, each heptatungstate anion is linked to six neighboring clusters, four of them through four centrosymmetric complexes (Cu1B, Cu1C, Cu1D and Cu1E) forming the layers (*xz* plane) and the other two acting as bridges between adjacent layers (Cu1A) along the y axis, the grafting site of which are exclusively terminal O atoms of the clusters. This arrangement results in the generation of hybrid grids with water–filled rhombic–like voids in the *xz* plane. The hybrid grids in **1–CuW7** are covalently linked to each other along the [010] direction by means of the non–centrosymmetric Cu1A moiety in such a way that the rhombic–like voids result superimposed on each other generating channels parallel to the crystallographic *y* axis in which the H_2O molecules are hosted (Figure 3.12a). Thus, the walls of these channels are delimited by four {W_7O_{24}}$^{6-}$ anions and four {Cu(cyclam)}$^{2+}$ cationic moieties in alternate fashion with approximate cross–section of 10.1 × 9.4 Å^2 (distances N1D···N4B and N4C···N4E, Figure 3.12b). It is worth mentioning that contiguous clusters within the same layer display an alternate disposition in such a way that the long edge of the cluster contained in the mirror plane of the V–shaped anion is pointing at either above or below the layer plane.

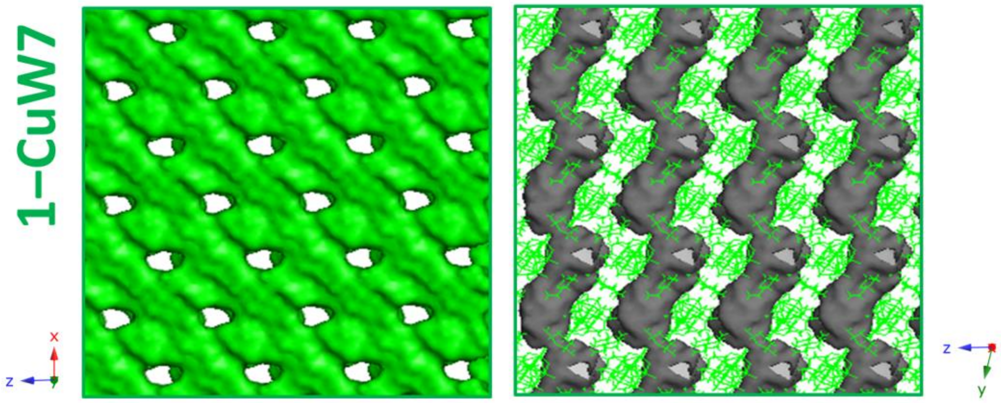

Figure 3.13. Visual representations of the porous framework (left) and that of the total accessible solvent volume showing the 2D interconnected system of the channels (right) in **1–CuW7** with the PyMol software.

The total solvent accessible volume is 1070 Å^3 which corresponds to roughly 30% of the unit cell volume of **1–CuW7**, as calculated using the PLATON software. These cavities show a strong bidimensional characters because adjacent channels in the same layer are interconnected as seen in the surface representation of the total accessible solvent voids with PyMol software (Figure 3.13). Apart from that, a substantial network of C–H···O and N–H···O interactions between the metal–organic blocks and the oxygen atoms of the inorganic clusters contribute to the overall structural stability of the title compound (Table 3.3). The water molecules of hydration also partake in the H–bonding network as some solvent molecules also (O12W, O13W and O15W) display a few favorable intermolecular interactions towards the organic ligands.

Table 3.3. Intermolecular N–H···O and C–H···O interactions (Å) in **1–CuW7**.

Donor–H···Acceptor	D–H	H···A	D···A	D–H···A
N1A–H1A···O22^{i}	0.98	2.41	3.239(9)	142
N4A–H4A···O34	0.98	1.77	2.729(8)	164
N8A–H8A···O13W	0.98	2.01	2.926(10)	156
N11A–H11A···O67^{i}	0.98	1.89	2.814(9)	156
C7A–H7AB···O12W	0.97	2.55	3.37(3)	143
C10A–H10A···O15W^{i}	0.97	2.55	3.394(13)	145
C13A–H13A···O12	0.97	2.55	3.376(12)	142
N1B–H1B···O66^{ii}	0.98	1.87	2.819(8)	164
N4B–H4B···O11	0.98	2.20	3.149(8)	162
N4C–H4C···O2^{iii}	0.98	1.86	2.817(10)	165
C3C–H3CA···O11	0.97	2.34	3.236(12)	153
C5C–H5CB···O18W^{ii}	0.97	2.55	3.463(13)	157
N1D–H1D···O9W	0.98	2.06	2.87(2)	139
N1D–H1D··· O10W	0.98	2.26	3.070(13)	139
N4D–H4D···O5^{iv}	0.98	2.03	2.962(9)	159
C3D–H3DA···O17W^{v}	0.97	2.36	3.26(2)	154
N1E–H1E···O6	0.98	2.37	3.153(8)	136
N1E–H1E··· O467	0.98	2.52	3.422(8)	152
N4E–H4E···O57^{vi}	0.98	1.82	2.789(8)	172
C3E–H3EA···O6	0.97	2.37	3.115(9)	134

Symmetry codes: i) x, $1+y$, z; ii) $-x$, $2-y$, $2-z$; iii) $1-x$, $2-y$, $2-z$; iv) $1-x$, $2-y$, $1-z$; v) $1+x$, y, z; vi) $-x$, $2-y$, $1-z$.

SCSC transformations induced by thermal evacuation of solvent molecules

Even though compound **2–CuW7** also crystallized in the triclinic *P–1* space group, significant structural modifications were observed as a result of the partial dehydration. The SCSC transformation forced contiguous layers to slightly slide in the opposite direction with the consequent reduction in the overall symmetry of the crystal, which resulted in the duplication of the unit cell content generating a crystallographically independent {WO_6} polyhedron and a {Cu(cyclam)}$^{2+}$ moiety for each one found in the parent **1–CuW7**. In this sense, the asymmetric unit of **2–CuW7** is composed of two heptatungstate fragments (labelled as A and B) with twelve {Cu(cyclam)} complexes (Cu1A–Cu1E and Cu2A–Cu2E), eight of them located in inversion centers, along with 24 water molecules of hydration.

Similar to **1–CuW7**, the eight bridging {Cu(cyclam)} centrosymmetric moieties present in **2–CuW7** also display elongated octahedral CuN_4O_2 coordination geometries with *trans–III* configuration of the ligand and similar bond lengths in general (Table 3.2). However, the non–centrosymmetric Cu1A and Cu2A moieties became antenna ligands as opposed to their bridging role between layers displayed by their related Cu1A in the hydrated phase **1–CuW7,** as one of their axial position became free after the sliding of the layers, and thus, the dimensionality of **2–CuW7** is reduced to a layered covalent arrangement (Figure 3.14). These two moieties generate from the Cu1A complex in **1–CuW7** as a result of the migration of half Cu1A atoms from W3 to the adjacent W2A octahedron (Cu1A in **2–CuW7**) while the other half remained linked to the same W7B grafting site (Cu2A in **2–CuW7**) as in **1–CuW7**. Even though their coordination number has been reduced to five, both Cu1A and Cu2A antenna moieties also show the *trans–III* configuration of the cyclam ligand. All these structural changes resulted in the rearrangement of the clusters in such a way that two nearly identical but crystallographically independent layers (A and B) that stack alternatively along the *y* axis are generated. In this sense, layer A is composed by A clusters in conjunction with Cu1A–Cu1E moieties while layer B contains B cluster and the remaining Cu2A–Cu2E complexes (Figure 3.14b). Interestingly, the heptatungstate anions in layer A rotated about 40° along the [10–1] direction, whereas those in B remained unaltered compared to the parent structure **1–CuW7** (Figure 3.14a).

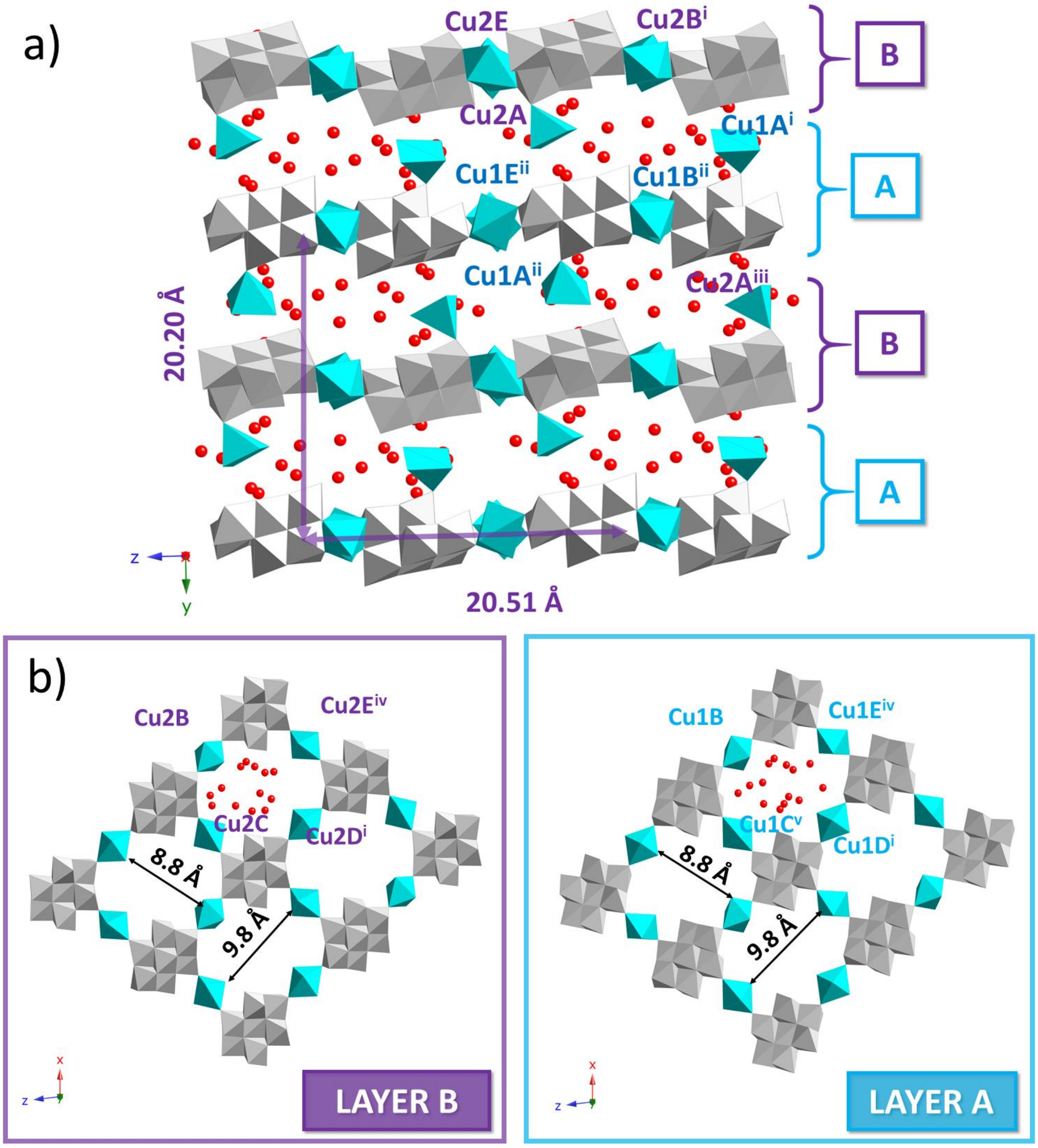

Figure 3.14. a) View of the crystal packing of the partially hydrated **2–CuW7** showing W1A···W1A distances and the two distinct layers. b) Hybrid layers showing the approximate dimensions of the channels for layer A and layer B. Cyclam ligands are omitted for clarity. Color code: W (grey), Cu (blue), O (red). Symmetry codes: i) –*x*, 3–*y*, 1–*z*; ii) –1+*x*, 1+*y*, *z*; iii) –*x*, 4–*y*, 1–*z*; iv) *x*, *y*, –1+*z*; v) *x*, –1+*y*, *z*; vi) –*x*, 2–*y*, 1–*z*.

Despite the obvious structural changes promoted by the SCSC transformation in the metalorganic complexes, the overall hybrid framework of **2–CuW7** is still highly reminiscent of that described for the parent compound **1–CuW7** because each rhombic–like channel is delimited by four $\{W_7\}$ clusters (A or B) and the corresponding centrosymmetric bridging moieties, Cu1B–Cu1E for A and Cu2B–Cu2E for B clusters, respectively. Even though they are crystallographically different, both channels found in **2–CuW7** are virtually identical in size and shape and they show an approximate cross section of 9.8 x 8.8 Å^2 (distances N1C···N1E and N1B···N1D in layer A and distances N21E···N21C and N21B···N21D in layer B; Figure 3.14b). This fact leads to channels that do not form an interconnected system anymore running along the crystallographic *y* axis (Figure 3.15). Compared to **1–CuW7**, the partially hydrated phase displays a slightly smaller total solvent accessible volume which accounts for the 22% of the total volume of the unit cell (1500 Å^3).

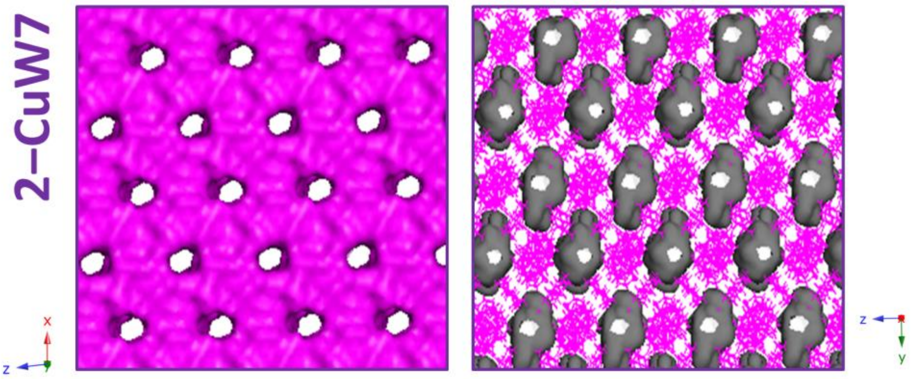

Figure 3.15. Visual representations of the porous framework (left) and that of the total accessible solvent volume showing the monodimensional nature of the channels (right) in **2–CuW7** with the PyMol software.

The transition from **1–CuW7** to **2–CuW7** also resulted in relevant changes in the cell parameters as expected. While the parameters *a* and *c* remained nearly constant, *b* almost doubled and consequently the volume of the unit cell doubled as well compared to that of **1–CuW7** (Table 3.1). Indeed, distances between equivalent W1 atoms in the same layer along the z axis remain practically unchanged (W1···W1 = 20.9 and W1B···W1B = 20.5 Å) while a significant reduction of *ca.* 3 Å in the distance between equivalent W1 atoms belonging to different layers along the y axis was observed (W1···W1 = 23.3 and W1B···W1B = 20.2 Å), indicating that the layers have approached to each other after the partial dehydration (Figures 3.12–3.14). This porous structure is still held together by several C–H···O and N–H···O contacts, the geometrical parameters of which are listed in Table 3.4. Interestingly, the transition from bridging units to antenna ligands of the non–centrosymetric Cu1A and Cu2A moieties resulted in a significant increase in the overall number of favorable intermolecular contacts compared to those observed in the structure of **1–CuW7** and for the other complexes in **2–CuW7**.

When **1–CuW7** is heated to 120 °C, all water molecules of hydration are removed and the anhydrous phase **3–CuW7** is obtained which crystallized in the monoclinic $P2_1/a$ space group, as opposed to the previous triclinic hydrated phases. The asymmetric unit of **3–CuW7** is composed of two crystallographically independent clusters (A and B) and six {Cu(cyclam)} complexes, four of them centrosymmetric (Cu1A, Cu2A, Cu1C and Cu1E) together with the remaining non–centrosymmetric (Cu1B, Cu2B, Cu1D and Cu2D) moieties. Despite what the TPDX analyses initially suggested, total dehydration brought for drastic changes in the overall packing compared to that of **2–CuW7** (Figure 3.16).

Table 3.4. Intermolecular N–H···O and C–H···O interactions (Å) in **2–CuW7.**

Donor–H···Acceptor	D···A	D–H···A	Donor–H···Acceptor	D···A	D–H···A
N1A–H1A···O5B	3.270(7)	133	N1D–H1D···O23W^{iv}	3.009(7)	147
N1A–H1A···O25B	3.364(7)	153	N4D–H4D···O5A^{ii}	2.877(7)	146
N1A–H1A···O45B	3.121(8)	127	C6D–H6DB···O5A^{v}	3.287(9)	137
N4A–H4A···O77A	2.954(8)	154	N1E–H1E···O6A	2.951(7)	155
N8A–H8A···O12A	2.803(8)	153	N4E–H4E···O77A	3.317(8)	139
N11A–H11A···O421	3.067(8)	163	C2E–H2EA···O77A^{vi}	3.272(8)	148
C3A–H3AA···O5B	3.299(9)	128	N21A–H21A···O467^{ii}	3.152(7)	162
C3A–H3AA···O45B	3.202(9)	129	N24A–H24A···O67B	2.768(7)	160
C6A–H6AA···O67B	3.161(9)	173	N28A–H28A···O22B	3.110(7)	153
C7A–H7AA···O34B	3.100(9)	139	N31A–H31A···O5A^{ii}	2.890(7)	150
C9A–H9AB···O13B	3.372(9)	153	N31A–H31A···O45A^{ii}	3.104(7)	126
C9A–H9AB···O34B	3.341(9)	135	C23A–H23E···O34A^{ii}	3.243(9)	141
C10A–H10D···O12A	3.303(9)	127	C25A–H25F···O34A^{ii}	3.092(9)	145
C13A–H13D···O2B	3.442(9)	143	C26A–H26A···O12B	3.192(9)	172
C13A–H13D···O25B	3.381(9)	152	C32A–H32A···O77B	3.139(9)	124
C14A–H14D···O22A	3.048(9)	127	C33A–H33B···O57A^{ii}	3.286(9)	167
N1B–H1B···O66A^{i}	2.990(8)	160	N21B–H21B···O66B^{vii}	2.872(8)	162
N4B–H4B···O11A	2.998(8)	159	N24B–H24B···O11B	3.396(8)	171
C6B–H6BA···O11A	3.389(9)	138	N21C–H21C···O2B	2.876(7)	160
C7B–H7BA···O6W^{i}	3.260(9)	146	C22C–H22G···O11B^{iii}	3.231(9)	153
C7B–H7BB···O3A	3.459(9)	168	N21D–H21D···O5B	2.926(8)	158
N1C–H1C···O2A^{ii}	2.939(8)	148	C21D–H21D···O20W^{v}	3.338(9)	129
N4C–H4C···O13A^{ii}	3.067(8)	146	C25D–H25D··O18W^{v}	3.384(10)	141
C2C–H2CB···O13A^{iii}	3.244(9)	137	N21E–H21E···O6B	2.979(7)	142
C3C–H3CB···O2A^{ii}	3.331(9)	127	N24E–H24E···O57B	2.830(8)	154
C6C–H6CA···O412^{ii}	3.434(9)	155	C22E–H22J···O57B^{viii}	3.260(9)	132
C6C–H6CB···O21W	3.416(10)	136	C23E–H23I···O6B^{viii}	3.267(8)	126

Symmetry codes: i) 1–*x*, 2–*y*, 1–*z*; ii) *x*, 1+*y*, *z*; iii) –*x*, 3–*y*, 1–*z*; iv) –*x*, 4–*y*, 2–*z*; v) –*x*, 3–*y*, 2–*z*; vi) 1–*x*, 2–*y*, 2–*z*; vii) 1–*x*, 3–*y*, 1–*z*; viii) 1–*x*, 3–*y*, 2–*z*.

Thermal evacuation of all solvent molecules triggered a slight rearrangement of the POM clusters and Cu(Cyclam) bridging units within each layer in such a way that the straight rows of POMs observed in the previous hydrated phases became distorted and thus, adopted a laddered disposition along the *z* axis (Figure 3.16). As opposed to the crystal packing of **2–CuW7**, there are no longer two types of crystallographically independent layers but a single one composed of both crystallographically independent A and B clusters. This way, each type of cluster is aligned in a zig–zag fashion along the *z* axis through alternated Cu1B and Cu2D complexes in the case of A while Cu2B and Cu1D moieties bridge B clusters. These rows of equivalent clusters connect to adjacent rows of the other type by the non–centrosymmetric Cu1C and Cu1E bridging moieties and thus, the hybrid covalent grids are formed. This connectivity generates two different types of channels with slightly different sizes in the *xz* plane (Figures 3.16b and 3.17), the walls of which are still delimited through the linkage of four $\{W_7\}$ clusters (two A and two B clusters) by alternated four {Cu(cyclam)} complexes. Specifically, the link between Cu2B, Cu1C, Cu2D and Cu1E moieties generates channel 1 (Ch1) while channel 2 (Ch2) is composed by Cu1B, Cu1C, Cu1D and Cu1E complexes, with approximate cross sections of 10.0 x 9.1 Å^2 for Ch1 (distances N11C···N11E and N21B···N21D) and 9.2 X 8.6 Å^2 for Ch2 (distances N4C···N4E and N1D···N1B), respectively (Figure 3.16b).

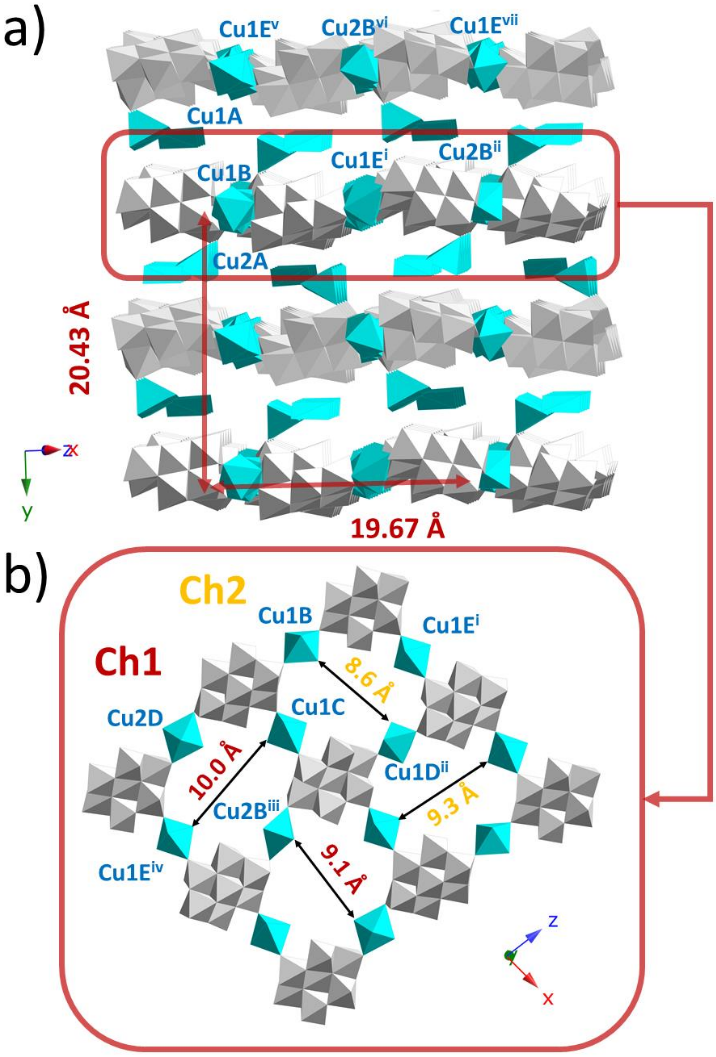

Figure 3.16. a) View of the crystal packing of **3–CuW7** along the *y* axis showing W1B···W1B distances. b) Hybrid layers with approximate dimensions of the channels in the *xz* plane. Cyclam ligands are omitted for clarity. Color code: W (grey), Cu (blue), O (red). Symmetry codes: i) 1–*x*, 2–*y*, 1–*z*; ii) 3/2–*x*, –1/2+*y*, 1–*z*; iii) 1/2+*x*, 5/2–*y*, z; iv) 1–*x*, 2–*y*, –*z*; v) *x*, –1+*y*, *z*; vi) 1–*x*, 2–*y*, 1–*z*; vii) 3/2–*x*, –1/2+*y*, 1–*z*.

The cell parameters also suffered changes as both *a* and *c* lattice parameters have significantly increased although *b* remained almost unaltered compared to the unit cell of **2–CuW7** (Table 3.1). Total rehydration also produced significant differences in the Cu(II) bonding of the different complexes compared to those shown by their equivalent moieties **2–CuW7** compound (Table 3.2). In close analogy to the previous SCSC transformation, half the antenna Cu1A and Cu2A moieties found in **2–CuW7** became non–coordinated after separating from their grafting sites (W2A and W7B, respectively) adopting a square planar geometry and situating in the intralamellar space (Cu1A in **3–CuW7**). Similarly, the other half Cu1A and Cu2A in **2–CuW7** migrated from their grafting sites (W2A and W7B) to the adjacent W1B octahedron and remained as antenna ligands (Cu2A in **3–CuW7**) as can be seen in Figures 3.18 and 3.19.

Even though Cu1A changed its geometry to a square planar geometry, the ligand still shows the *trans–III* configuration. In spite of these structural changes, the distance between equivalent octahedra belonging to adjacent layers remain virtually identical to that found in **2–CuW7** (W1B···W1B = 20.4 Å) as well as the distance of equivalent octahedra within the layers (W1B···W1B = 19.7 Å, Figure 3.16).

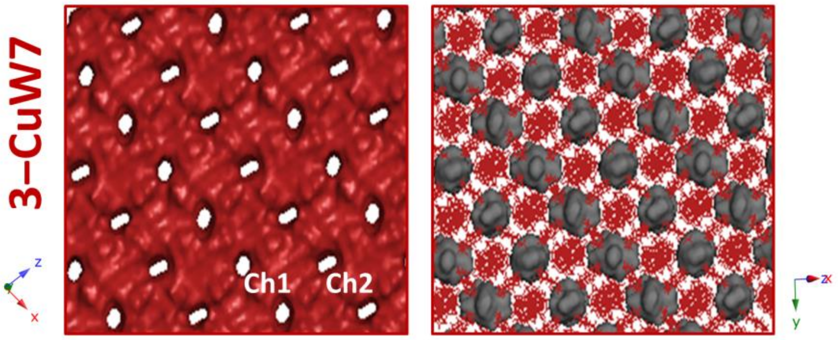

Figure 3.17. Visual representation of the porous structure (left) and the total accessible solvent volume (right) in the *xz* plane showing the two different pores in **3–CuW7** with the PyMol software.

Table 3.5. Intermolecular N–H···O and C–H···O interactions (Å) in **3–CuW7.**

Donor–H···Acceptor	D···A	D–H···A	Donor–H···Acceptor	D···A	D–H···A
N1A–H1A···O12A	2.81(2)	158	N21A–H21A···O5A	2.961(18)	140
N4A–H4A···O476^{i}	3.150(19)	154	N21A–H21A···O45A	2.940(17)	139
N8A–H8A···O34B^{i}	2.944(18)	140	N24A–H24A···O66A	3.280(18)	139
N8A–H8A···O36B^{i}	3.430(18)	146	N28A–H28A···O12B	2.727(19)	163
N11A–H11A···O77A	3.126(19)	141	N31A–H31A···O467	3.160(18	155
C2A–H2AB···O57B^{i}	3.25(3)	169	C27A–H27A···O3A	3.31(3)	146
C6A–H6AB···O6B^{i}	3.38(2)	151	C27A–H34A···O34A	3.15(3)	142
C6A–H6AB···O36B^{i}	3.38(2)	145	C27A–H27B···O2B	3.29(3)	133
C7A–H7AA···O22A	3.18(2)	131	C29A–H29A···O36A	3.34(3)	168
C10A–H10F···O34B^{i}	3.17(3)	132	C33A–H33A···O57A	3.28(3)	167
C13A–H13E···O67A	3.30(3)	145	N21B–H21B···O33B	3.139(19)	159
C14A–H14E···O5B^{i}	3.21(3)	148	N24B–H24B···O36B	3.077(18)	161
C14A–H14E···O45B^{i}	3.26(3)	138	C22B–H24B···O3B	3.31(3)	152
N1B–H1B···O6A	2.891(18)	165	C26B–H26D···O6B	3.48(3)	156
N4B–H4B···O11A^{ii}	3.032(18)	168	C26B–H26D···O66B	3.46(3)	141
N1C–H1C···O2A	3.028(18)	148	C27B–H27D···O3B^{iii}	3.47(3)	145
N4C–H4C···O13B^{iv}	3.222(17)	138	N1D–H1D···O77B^{v}	3.396(18)	166
N4C–H4C···O421^{iv}	3.314(17)	144	N4D–H4D···O2B	2.844(17)	165
N8C–H8C···O22B^{iv}	2.765(18)	149	N1E–H1E···O67B^{vii}	3.43(2)	151
N11C–H11C···O13A	2.854(17)	153	N4E–H4E···O66A	2.923(19)	153
C2C–H2CB···O13B^{iv}	3.16(2)	143	N8E–H8E···O77A	3.121(18)	147
C6C–H6CB···O421^{iv}	3.37(3)	148	N11E–H11E···O6B^{vii}	2.822(18)	157
C9C–H9CA···O13A	3.20(2)	132	C3E–H3EA···O77B^{vii}	3.18(3)	150
C13C–H13B···O412	3.46(3)	155	C7E–H7EA···O7B^{vii}	3.19(3)	125
N24D–H24D···O25A^{vi}	2.922(19)	173	C10E–H10C···O77A	3.28(2)	139

Symmetry codes: i) *x*, −1+*y*, *z*; ii) 1−*x*, 2−*y*, 1−*z*; iii) 1−*x*, 3−*y*, −*z*; iv) 1/2+*x*, 5/2−*y*, *z*; v) 1−*x*, 3−*y*, 1−*z*; vi) 1−*x*,2−*y*, −*z*; vii) −1/2+*x*, 5/2−*y*, *z*.

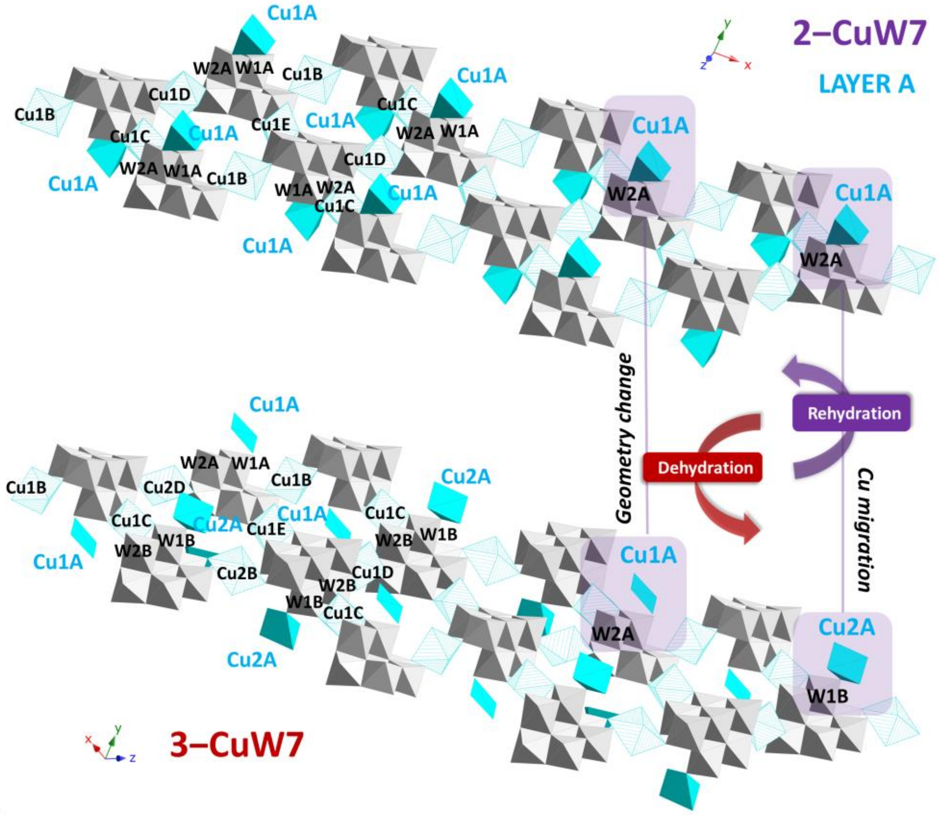

Figure 3.18. Comparison between the antenna Cu1A in **2–CuW7** (layer A) and the equivalent Cu1A/Cu2A complexes in **3–CuW7**: half Cu1A in **2–CuW7** separated from W2A becoming a square planar fragment (Cu1A in **3–CuW7**) while the other half migrated to an adjacent {WO$_6$} octahedron (from W2A in **2–CuW7** to W1B in **3–CuW7**, Cu2A).

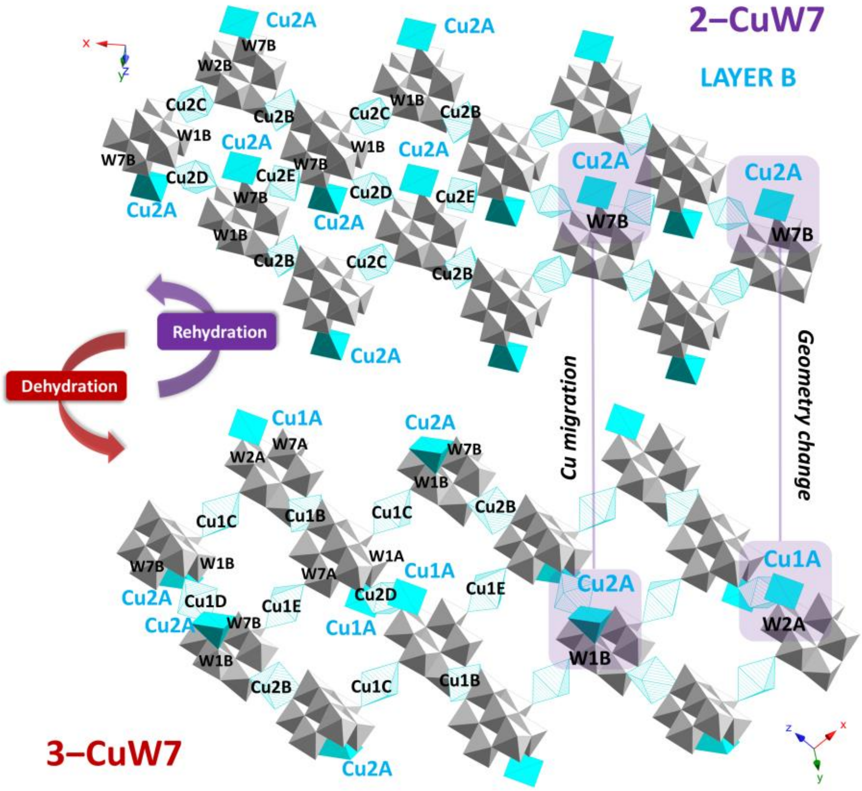

Figure 3.19. Comparison between the antenna Cu2A in **2–CuW7** (layer B) and the equivalent Cu1A/Cu2A complexes in **3–CuW7**: half Cu2A in **2–CuW7** separated from W7B becoming a square planar fragment (Cu1A in **3–CuW7**) while the other half migrated to an adjacent {WO$_6$} octahedron (from W7B in **2–CuW7** to W1B in **3–CuW7**, Cu2A).

The anhydrous phase shows a total solvent accessible volume of 2982 Å^3 which corresponds to a combined value of 22% of the unit cell volume of **3**, as calculated using the PLATON software (Ch1: 775x2 Å^3, 12% and Ch2: 716x2 Å^3, 10%), which is the same as that observed for **2–CuW7**. As opposed to the interconnected channel system found in **1–CuW7**, the channels in **3–CuW7** remain unconnected just like those seen in the partially hydrated intermediate **2–CuW7** (Figure 3.20). The overall number of favorable intermolecular C–H···O and N–H···O interactions found in the anhydrous structure of **3–CuW7** has been slightly reduced compared to those shown by **2–CuW7** and they are grouped in Table 3.5.

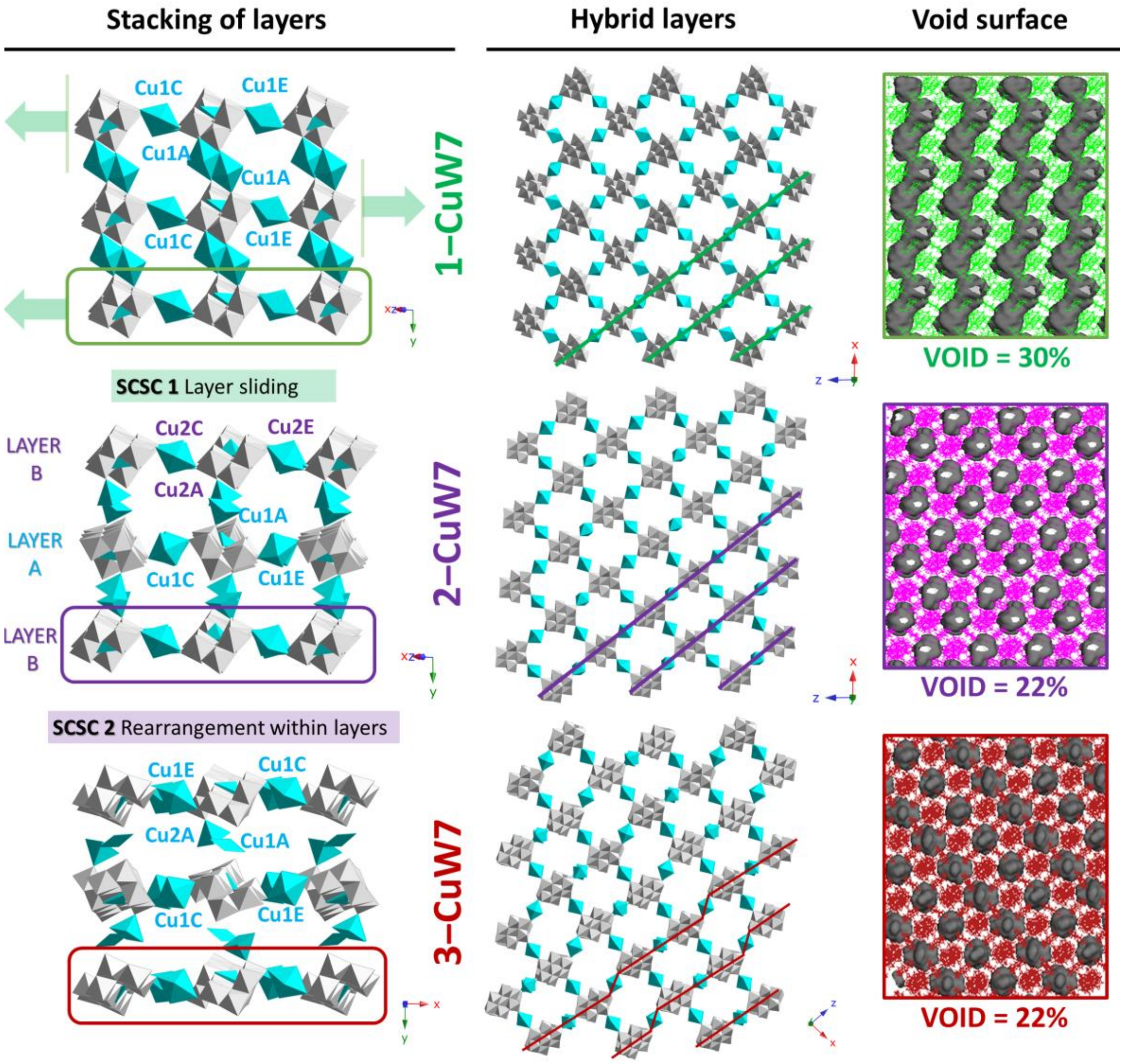

Figure 3.20. Comparison between the crystal packing along the *y* axis and the hybrid covalent layers in the *xz* plane (left), visual representation of the total accessible solvent volume showing the different type of channels with the PyMol software (right) of compounds **1–**, **2–** and **3–CuW7**. Colour code: W (grey), Cu (blue).

Reversibility of the SCSC transformations

Regarding the reversibility of the SCSC transformations, **3–CuW7** rapidly reverts back to the partially hydrated phase **2–CuW7** in air exposure within one day in open air conditions, as confirmed by simultaneous PDX and TGA analyses. Crystalline samples of a freshly prepared compound **1–CuW7** were heated at a rate of 2 °C min^{-1} up to 180 °C, and the so–generated anhydrous samples were kept for 1 day in an open container and then heated again at the same rate. The TGA profiles recorded for these anhydrous samples exposed to ambient atmosphere for 1 and 30 days are virtually identical and differ significantly from the mass loss observed in the initial TGA curve of a freshly prepared batch of **1–CuW7** (Figure 3.21). The initial amount of water is 10.29% whereas only a 7.81% is recovered upon exposure to air. This value corresponds to 24 water molecules per two clusters (calc. 8.06%), which is in perfect agreement with the water molecules determined by single–crystal X–ray diffraction data for the intermediate phase. In addition, PXRD measurements carried out after the heating confirm that **2–CuW7** does not transform back to **1–CuW7** since the patterns taken at 1 day and 30 days are virtually the same and coincide with the corresponding simulated patterns of **2–CuW7**. Furthermore, the transition from **2–CuW7** to the parent fully hydrated phase does not take place even when crystals of the former are immersed in water for one week. In view of these results, we concluded that the anhydrous phase is not able to undergo full rehydration but rapidly transforms back to the stable intermediate phase instead, as evidenced by the simultaneous PXRD and TGA measurements discussed above, proving that the first SCSC transformation is indeed of irreversible nature. Finally, it is worth mentioning that these transformations can be followed visually due to the different colors of the crystals which are a direct result of the modifications of the coordination sphere of the Cu atoms belonging to the complexes for **1–CuW7** and its thermal derivatives (Figure 3.21).

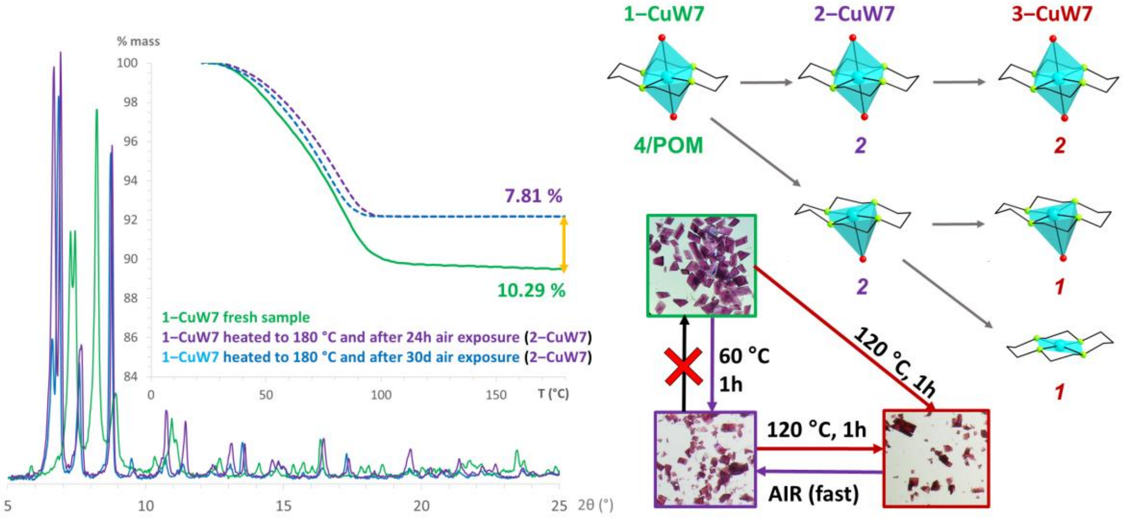

Figure 3.21. Comparison of TGA curves and PXRD patterns on a freshly prepared sample of **1–CuW7** (green) as well as dehydrated samples heated to 180 °C and exposed to air moisture for 24 h (purple) and 30 days (blue), indicating that the second SCSC is reversible while the the first one is irreversible.

Gas sorption properties

Since single–crystal XRD and variable temperature PXRD studies confirmed that our hybrid open–framework is indeed a permanent porous compound with channels larger than N_2 and CO_2 molecules, we decided to check if it could exhibit gas sorption capacity. The N_2 and CO_2 sorption experiments were carried out on a crystalline sample activated under vacuum at 120 °C to promote the evacuation of all the water molecules. The sample was identified as phase **3–CuW7** on the basis of powder X–ray diffraction (Figure A3.3 in the Appendix). These studies indicate that the uptake of both gases takes place, confirming that channels are accessible and fully operatives, which makes our hybrid one of the few POM–based compounds to show genuine functions derived from its permanent porosity.[92]

The isotherm for the N_2 sorption/desorption process at 77.5 K shows a characteristic curve for a mesoporous material (Figure 3.22). This behavior can be explained attending to the fact that when the adsorbate molecules manage to leave the channels they can accommodate in the voids between different grains of the crystalline material, which results in a slight increase of the N_2 uptake by the host framework. The BET (Brunauer–Emmett–Teller) surface area is 62.6 $m^2\ g^{-1}$, as calculated from the low pressure region of the N_2 sorption isotherm at 77.5 K. Furthermore, a hysteresis loop is observed upon desorption (starting at $P/P_0 = 0.60$) suggesting that N_2 molecules do not have enough time to leave the channels because their kinetic restrictions arising from the low working temperatures prevent the pressure from decreasing.

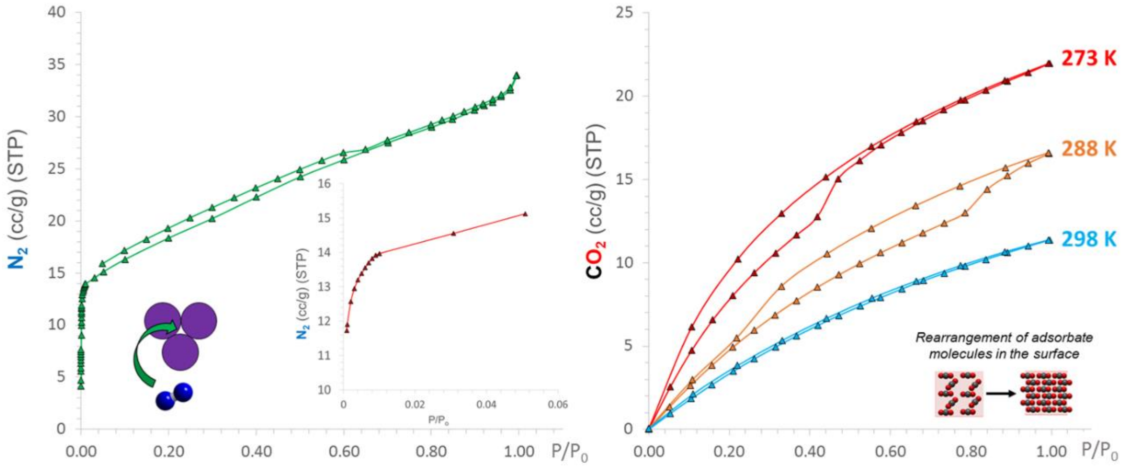

Figure 3.22. Isotherm for N_2 sorption/desorption at 77.5 K along with the fitting of the low pressure region where the BET surface area was calculated, as well as type I isotherms for CO_2 sorption/desorption at 298, 288 and 273 K.

Regarding the CO_2 sorption properties, gas sorption experiments show a characteristic type I isotherms, indicating that our compound is indeed a microporous material (Figure 3.22). In this sense, a sudden CO_2 uptake can be observed at high relative pressure values ($P/P_0 = 0.40$) accompanied by a hysteresis loop in the sorption−desorption isotherms at 273 K. Compared to the hysteresis observed in N_2 isotherms, the loop in the CO_2 data was larger, suggesting a stronger interaction of CO_2 with the components of the hybrid host material. We repeated the adsorption experiment at a higher temperature of 288 K and the same sudden uptake increase was observed but at much higher values of P/P_0 (around 0.80). When the isotherm was carried out at 298 K, however, both the increase of the adsorbate volume and the consequent hysteresis cycle disappeared. These results can be explained considering the rearrangement of the adsorbate molecules at the surface of the host material and the relative kinetic energy of the gas molecules due to the different temperatures at which the isotherms were recorded. During the adsorption process, some CO_2 molecules are randomly deposited into the surface of **1–CuW7** until they reach a certain value. At this point, the adsorbate molecules rearrange themselves in such a way that they leave free space for other molecules to incorporate into the surface and thus, a sudden increase in the adsorbed CO_2 volume takes place. This occurs when the adsorbate uptake reaches *ca.* 13 cc g^{-1}, as can be observed in both isotherms at 273 and 288 K. The difference in the P/P_0 can be explained taking into account the higher adsorption temperature for CO_2 in the isotherm measured at 288 K, which confers the gas molecules a larger kinetic energy favoring their departure from the pores, and hence, a higher pressure is needed to observe the rearrangement of the molecules and the consequent increase in their adsorbed volume. This is in complete agreement with the absence of the increase in CO_2 volume and the hysteresis loop in the isotherms carried out at 298 K.

Reports on BET data for POM–based crystalline open–framework materials are infrequent.[92a] Searching through the literature only yields a limited number of studies involving microporous polyanions which can exhibit functionality in CO_2 capture functionality. A representative example of one of such compounds could be the $[Cr_3O(OOCCH{=}CH_2)_6(H_2O)_3]_3[\alpha\text{–}PW_{12}O_{40}]$ hybrid salt prepared by Mizuno's group which displays shape–selective sorption of CO_2 and acetylene over the larger methane and N_2 molecules, because the minimum pore aperture is comparable to the kinetic diameters of the adsorbate gas molecules.[93] Compared to our compound, the ionic crystal above shows a slightly lower BET surface area of 50 $m^2\ g^{-1}$ which can be attributed to its smaller channel apertures (approximately 3.3 Å). Various fully inorganic microporous polyoxoanions have also shown CO_2 sorption capabilities. For example, inorganic microporous lattices based on ε–Keggin–type V–substituted[94] and Zn–substituted[95] molybdate species were reported by Ueda et al. with estimated BET surface areas of 60 and 68 $m^2\ g^{-1}$ respectively, which are comparable to that calculated for our $\{W_7\}$ hybrid. In the previous chapter, the microporous decavanadate hybrid **1–CuV10** also exhibited CO_2 sorption properties, and compared to our heptatungstate hybrid, a significant higher BET surface area of 205 $m^2\ g^{-1}$ together with a slightly higher CO_2 uptake capacity at saturation (25 cc g^{-1}) were observed for the polyoxovanadate. The overall higher capacity to adsorb CO_2 could be because the open–framework of **1–CuV10** is robust enough to maintain its structure upon total removal of guest solvent molecules, as opposed to the dynamic one observed for **1–CuW7** which undergoes two SCSC transformations upon dehydration instead, reducing the total solvent accessible voids significantly (a decrease of around 8% of the total unit cell volume). Nevertheless, this results pale in comparison to those recently reported by Wang's group in the extended $(TBA)_2[Cu^{II}(BBTZ)_2(\alpha\text{–}Mo_8O_{26})]$ (BBTZ = 1,4–bis(1,2,4–triazol–1–ylmethyl)–benzene) hybrid, which exhibits the highest adsorption capacity reported for a POM–based hybrid.[96] In fact, the CO_2 uptake capacity at saturation is comparable to the best performing zeolite–like MOFs.[97] This octamolybdate open–framework possess a three–directional system of intersecting channels, as opposed to the bidimensional system found in **1–CuW7** or the parallel channels observed in **2–CuW7** and **3–CuW7**. This structural feature combined with a total solvent accessible volume of 50% of the total unit cell volume (which roughly twice the accessible solvent volume for our compounds), results in a remarkable BET surface area of 773 $m^2\ g^{-1}$.

To the best our knowledge, our hybrid compound is the first heptatungstate–based crystalline material that undergoes SCSC transformations triggered upon heating. These transformations lead to the formation of two new crystalline porous phases upon gradual dehydration which exhibit interesting properties like both N_2 and CO_2 sorption capacities derived from the permanent porosity of the hybrid open–framework.

3.3 HETEROPOLYOXOTUNGSTATES

3.3.1 Experimental Section

Materials and methods

The trilacunary Keggin salt $Na_{10}[\alpha–GeW_9O_{34}]\cdot14H_2O$ and the preformed $Na_4K_8[\{(GeW_{11}O_{39})Ln(H_2O)(\mu–CH_3COO)\}_2]\cdot20H_2O$ (Ln = Eu–Er) precursors were synthesized following literature methods and identified by FT–IR spectroscopy.[98] All other chemicals were obtained from commercial sources and used without further purification. Carbon, hydrogen and nitrogen contents were determined on a Perkin–Elmer 2400 CHN analyzer. FT–IR spectra were obtained as KBr pellets on a SHIMADZU FTIR–8400S spectrometer (Figure A3.4 in the Appendix). Thermogravimetric and differential thermal analyses (TGA/DTA) were carried out from room temperature to 780 °C at a rate of 5 °C min^{-1} on a SHIMADZU DTG–60 thermobalance under a 50 cm^3 min^{-1} flow of synthetic air (Figure A3.5 in the Appendix). Powder X–ray diffraction (PXRD) patterns were collected on a Bruker D8 Advance diffractometer operating at 30 kV/20 mA and equipped with Cu Kα radiation (λ = 1.5418 Å), a Vantec–1 PSD detector, an Anton Parr HTK2000 high–temperature furnace, and Pt sample holder (Figures A3.6 in the Appendix). The powder patterns were recorded in 2ϑ steps of 0.033° in the $5 \leq 2\vartheta \leq 35$ range, counting for 0.3 s per step. Data sets were acquired from 30 to 810 °C every 20 °C with a 0.16 °C s^{-1} heating rate between temperatures for **1–Ln** (Figures A3.7–A3.12 in the Appendix).

Synthetic procedure

Two different synthetics methods were evaluated:

Method 1: a mixture of $Na_{10}[\alpha–GeW_9O_{34}]\cdot14H_2O$ (0.550 g, 0.20 mmol), $Ln(NO_3)_3\cdot XH_2O$ (0.10 mmol, Ln = La to Tb, X = 5 or 6) or $LnCl_3\cdot XH_2O$ (0.10 mmol, Ln = Dy to Lu, x = 5 or 6), $Cu(CH_3COO)_2$ (0.078 g, 0.40 mmol), cyclam (0.080 g, 0.40 mmol) in 1M CH_3COOK/CH_3COOH buffer solution (15 mL) was stirred for 1 h, transferred to a 50 mL Teflon–lined autoclave, and kept at 160 °C for 72 h. After cooling the reaction mixture to room temperature for 48 h, a mixture of orange polycrystalline powder (Ln = La to Lu) and plates suitable for XRD diffraction (except for Ln = Eu–Er derivatives) were isolated. Crystals were separated for structure determination and powder X–ray diffraction experiments together with FT–IR measurements confirmed that the polycrystalline fraction was the same phase as that of the corresponding crystals in all cases.

Method 2: this method is similar to method 1 except that 0.10 mmol of the following preformed precursors were employed, namely $Na_4K_8[\{(GeW_{11}O_{39})Ln(H_2O)(CH_3COO\}_2].16–20 H_2O$ (Ln = Eu–Er), instead of $Na_{10}[\alpha–GeW_9O_{34}]\cdot14H_2O$ and the lanthanide source. Single crystals suitable for XRD which method 1 could not afford were obtained for mid–to–late **1–Ln** derivatives (Ln = Eu–Er) in comparable yields as large orange plates.

$[Cu(cyclam)]_2[\{Cu(cyclam)\}_4\{(\alpha–GeW_{11}O_{39})La(H_2O)(\mu–CH_3COO)\}_2]\cdot18H_2O$ (1–La). Method 1: $La(NO_3)_3\cdot6H_2O$ (0.043 mg, 0.10 mmol) was used as lanthanide source and a mixture of orange plates and polycrystalline powder was obtained. Yield: 113 mg (29% based on $La(NO_3)_3\cdot 6H_2O$). Anal. Calcd (found) for $C_{64}H_{190}Cu_6Ge_2N_{24}La_2O_{102}W_{22}$: C, 9.88 (10.03); H, 2.46 (2.35); N, 4.32 (4.27). IR (cm^{-1}): 3188 (m), 3138 (m), 2935 (m), 2921 (m), 1636 (s), 1547 (m), 1458 (m), 1429 (m), 1344 (w), 1298 (w), 1247 (w), 1134 (w), 1097 (m), 1068 (m), 1020 (m), 939 (s), 868 (s), 810 (vs), 779 (sh), 698 (s), 520(m), 462 (m).

$[Cu(cyclam)]_2[\{Cu(cyclam)\}_4\{(\alpha{-}GeW_{11}O_{39})Ce(H_2O)(\mu{-}CH_3COO)\}_2]\cdot 18H_2O$ (1–Ce). Method 1: $Ce(NO_3)_3\cdot 6H_2O$ (0.043 g, 0.10 mmol) was used instead of $La(NO_3)_3\cdot 6H_2O$ and a mixture of orange plates and polycrystalline powder was obtained. Yield: 114 mg (29% based on $Ce(NO_3)_3\cdot 6H_2O$). Anal. Calcd (found) for $C_{64}H_{190}Ce_2Cu_6Ge_2N_{24}O_{102}W_{22}$: C, 9.88 (9.90); H, 2.46 (2.31); N, 4.32 (4.22). IR (cm^{-1}): 3184 (m), 3134 (m), 2931 (m), 2872 (m), 1632 (s), 1549 (m), 1456 (m), 1429 (m), 1344 (w), 1298 (w), 1248 (w), 1136 (w), 1097 (m), 1069 (m), 1022 (m), 937 (s), 868 (s), 808 (vs), 779 (sh), 698 (s), 519 (m), 463 (m).

$[Cu(cyclam)]_2[\{Cu(cyclam)\}_4\{(\alpha{-}GeW_{11}O_{39})Pr(H_2O)(\mu{-}CH_3COO)\}_2]\cdot 17H_2O$ (1–Pr). Method 1: $Pr(NO_3)_3\cdot 6H_2O$ (0.044 g, 0.10 mmol) was used and a mixture of orange plates and polycrystalline powder was obtained. Yield: 122 mg (31% based on $Pr(NO_3)_3\cdot 6H_2O$). Anal. Calcd (found) for $C_{64}H_{188}Ge_2Cu_6N_{24}O_{101}Pr_2W_{22}$: C, 9.90 (10.00); H, 2.44 (2.26); N, 4.33 (4.26). IR (cm^{-1}): 3185 (m), 3134 (m), 2932 (m), 2872 (m), 1636 (s), 1547 (m), 1458 (m), 1429 (m), 1344 (w), 1298 (w), 1248 (w), 1136 (w), 1098 (m), 1069 (m), 1022 (m), 937 (s), 868 (s), 808 (vs), 779 (sh), 694 (s), 519 (m), 463 (m).

$[Cu(cyclam)]_2[\{Cu(cyclam)\}_4\{(\alpha{-}GeW_{11}O_{39})Nd(H_2O)(\mu{-}CH_3COO)\}_2]\cdot 18H_2O$ (1–Nd). Method 1: $Nd(NO_3)_3\cdot 6H_2O$ (0.044 g, 0.10 mmol) was used and a mixture of orange plates and polycrystalline powder was obtained. Yield: 110 mg (28% based on $Nd(NO_3)_3\cdot 6H_2O$). Anal. Calcd (found) for $C_{64}H_{190}Ge_2Cu_6N_{24}Nd_2O_{102}W_{22}$: C, 9.87 (10.01); H, 2.46 (2.32); N, 4.32 (4.31). IR (cm^{-1}): 3185 (m), 3134 (m), 2932 (m), 2872 (m), 1630 (s), 1547 (m), 1458 (m), 1429 (m), 1344 (w), 1298 (w), 1248 (w), 1138 (w), 1097 (m), 1069 (m), 1022 (m), 937 (s), 868 (s), 808 (vs), 779 (sh), 694 (s), 519 (m), 463 (m).

$[Cu(cyclam)]_2[\{Cu(cyclam)\}_4\{(\alpha{-}GeW_{11}O_{39})Sm(H_2O)(\mu{-}CH_3COO)\}_2]\cdot 19H_2O$ (1–Sm). Method 1: $Sm(NO_3)_3\cdot 6H_2O$ (0.044 g, 0.10 mmol) was used and a mixture of orange plates and polycrystalline powder was obtained. Yield: 111 mg (28% based on $Sm(NO_3)_3\cdot 6H_2O$). Anal. Calcd (found) for $C_{64}H_{192}Cu_6Ge_2N_{24}O_{103}Sm_2W_{22}$: C, 9.83 (9.98); H, 2.47 (2.49); N, 4.30 (4.28). IR (cm–1): 3186 (m), 3134 (m), 2933 (m), 2874 (m), 1638 (s), 1545 (m), 1458 (m), 1431 (m), 1346 (w), 1298 (w), 1248 (w), 1138 (w), 1097 (m), 1069 (m), 1022 (m), 939 (s), 868 (s), 810 (vs), 779 (sh), 698 (s), 520 (m), 461 (m).

$[Cu(cyclam)]_2[\{Cu(cyclam)\}_4\{(\alpha{-}GeW_{11}O_{39})Eu(H_2O)(\mu{-}CH_3COO)\}_2]\cdot 17H_2O$ (1–Eu). Method 1: $Eu(NO_3)_3\cdot 5H_2O$ (0.43 g, 0.10 mmol) was used and a mixture of orange plates and polycrystalline powder was obtained. Yield: 115 mg (30% based on $Eu(NO_3)_3\cdot 5H_2O$). Method 2: $Na_4K_8[\{(GeW_{11}O_{39})Eu(H_2O)(\mu{-}CH_3COO)\}_2]$ $20H_2O$ (0.800 g, 0.10 mmol) was used and **1–Eu** was obtained as large orange plates. Yield: 60 mg (8% based on precursor). Anal. Calcd (found) for $C_{64}H_{188}Cu_6Eu_2Ge_2N_{24}O_{101}W_{22}$: C, 9.87 (9.90); H, 2.43 (2.31); N, 4.31 (4.22). IR (cm–1): 3185 (m), 3134 (m), 2924 (m), 2872 (m), 1630 (s), 1545 (m), 1458 (m), 1426 (m), 1342 (w), 1298 (w), 1248 (w), 1138 (w), 1097 (m), 1069 (m), 1022 (m), 937 (s), 866 (s), 810 (vs), 779 (sh), 692 (s), 519 (m), 463 (m).

$[Cu(cyclam)]_2[\{Cu(cyclam)\}_4\{(\alpha\text{–}GeW_{11}O_{39})Gd(H_2O)(\mu\text{–}CH_3COO)\}_2]\cdot 18H_2O$ (1–Gd). Method 1: $Gd(NO_3)_3\cdot 6H_2O$ (0.045 g, 0.10 mmol) was used and a mixture of orange plates and polycrystalline powder was obtained. Yield: 112 mg (29% based on $Gd(NO_3)_3\cdot 6H_2O$). Method 2: $Na_4K_8[\{(GeW_{11}O_{39})Gd(H_2O)(\mu\text{–}CH_3COO)\}_2]$ $20H_2O$ (0.800 g, 0.10 mmol) was used and **1–Gd** was obtained as large orange plates. Yield: 54 mg (7% based on precursor). Anal. Calcd (found) for $C_{64}H_{190}Cu_6Gd_2Ge_2N_{24}O_{102}W_{22}$: C, 9.84 (9.74); H, 2.45 (2.33); N, 4.30 (4.17). IR (cm–1): 3185 (m), 3134 (m), 2932 (m), 2872 (m), 1636 (s), 1552 (m), 1456 (m), 1429 (m), 1346 (w), 1298 (w), 1248 (w), 1138 (w), 1097 (m), 1068 (m), 1022 (m), 939 (s), 868 (s), 810 (vs), 781 (sh), 698 (s), 519 (m), 465 (m).

$[Cu(cyclam)]_2[\{Cu(cyclam)\}_4\{(\alpha\text{–}GeW_{11}O_{39})Tb(H_2O)\ (H_2O)(\mu\text{–}CH_3COO)\}_2]\cdot 18H_2O$ (1–Tb). Method 1: $Tb(NO_3)_3\cdot 5H_2O$ (0.044 g, 0.10 mmol) was used and a mixture of orange plates and polycrystalline powder was obtained. Yield: 102 mg (26% based on $Tb(NO_3)_3\cdot 6H_2O$). Method 2: $Na_4K_8[\{(GeW_{11}O_{39})Tb(H_2O)(\mu\text{–}CH_3COO)\}_2]$ $18H_2O$ (0.800 g, 0.10 mmol) was used and **1–Tb** was obtained as large orange plates. Yield: 50 mg (6% based on precursor) Anal. Calcd (found) for $C_{64}H_{190}Cu_6Ge_2N_{24}O_{102}Tb_2W_{22}$: C, 9.83 (9.63); H, 2.45 (2.30); N, 4.30 (4.15). IR (cm–1): 3185 (m), 3134 (m), 2929 (m), 2872 (m), 1630 (s), 1555 (m), 1458 (m), 1431 (m), 1341 (w), 1298 (w), 1248 (w), 1138 (w), 1098 (m), 1069 (m), 1022 (m), 940 (s), 868 (s), 812 (vs), 781 (sh), 698 (s), 519 (m), 465 (m).

$[Cu(cyclam)]_2[\{Cu(cyclam)\}_4\{(\alpha\text{–}GeW_{11}O_{39})Dy(H_2O)(\mu\text{–}CH_3COO)\}_2]\cdot 18H_2O$ (1–Dy). Method 1: $DyCl_3\cdot 6H_2O$ (0.038 g, 0.10 mmol) was used and a mixture of orange plates and polycrystalline powder was obtained. Yield: 108 mg (28% based on $DyCl_3\cdot 6H_2O$). Method 2: $Na_4K_8[\{(GeW_{11}O_{39})Dy(H_2O)(\mu\text{–}CH_3COO)\}_2]$ $16H_2O$ (0.800 g, 0.10 mmol) was used and **1–Dy** was obtained as large orange plates. Yield: 48 mg (6% based on precursor). Anal. Calcd (found) for $C_{64}H_{190}Cu_6Dy_2Ge_2N_{24}O_{102}W_{22}$: C, 9.82 (9.54); H, 2.45 (2.30); N, 4.30 (4.17). IR (cm–1): 3185 (m), 3136 (m), 2933 (m), 2874 (m), 1630 (s), 1555 (m), 1458 (m), 1431 (m), 1346 (w), 1298 (w), 1263 (w), 1248 (w), 1097 (m), 1069 (m), 1022 (m), 939 (s), 868 (s), 812 (vs), 781 (sh), 700 (s), 519 (m), 465 (m).

$[Cu(cyclam)]_2[\{Cu(cyclam)\}_4\{(\alpha\text{–}GeW_{11}O_{39})Ho(H_2O)(\mu\text{–}CH_3COO)\}_2]\cdot 19H_2O$ (1–Ho). Method 1: $HoCl_3\cdot 6H_2O$ (0.038 g, 0.10 mmol) was used and polycrystalline powder was obtained. Yield: 102 mg (26% based on $HoCl_3\cdot 6H_2O$). Method 2: $Na_4K_8[\{(GeW_{11}O_{39})Ho(H_2O)(\mu\text{–}CH_3COO)\}_2]$ $18H_2O$ (0.800 g, 0.10 mmol) was used and **1–Ho** was obtained as large orange plates. Yield: 46 mg (6% based on precursor). Anal. Calcd (found) for $C_{64}H_{192}Cu_6Ge_2Ho_2N_{24}O_{103}W_{22}$: C, 9.82 (9.72); H, 2.45 (2.50); N, 4.29 (4.17). IR (cm–1): 3185 (m), 3136 (m), 2932 (m), 2874 (m), 1636 (s), 1555 (m), 1458 (m), 1431 (m), 1346 (w), 1298 (w), 1248 (w), 1138 (w), 1097 (m), 1069 (m), 1022 (m), 939 (s), 868 (s), 814 (vs), 781 (sh), 698 (s), 520 (m), 465 (m).

$[Cu(cyclam)]_2[\{Cu(cyclam)\}_4\{(\alpha\text{–}GeW_{11}O_{39})Er(H_2O)(\mu\text{–}CH_3COO)\}_2]\cdot 18H_2O$ (1–Er). Method 1: $ErCl_3.5H_2O$ (0.038 g, 0.10 mmol) was used and a polycrystalline powder was obtained. Yield: 117 mg (30% based on $ErCl_3.5H_2O$). Method 2: $Na_4K_8[\{(GeW_{11}O_{39})Er(H_2O)(\mu\text{–}CH_3COO)\}_2]$ $18H_2O$

(0.800 g, 0.10 mmol) was used and **1–Er** was obtained as large orange plates. Yield: 45 mg (6% based on precursor). Anal. Calcd (found) for $C_{64}H_{190}Cu_6Er_2Ge_2N_{24}O_{102}W_{22}$: C, 9.79 (9.76); H, 2.47 (2.34); N, 4.28 (4.18). IR (cm–1): 3185 (m), 3134 (m), 2934 (m), 2874 (m), 1630 (s), 1555 (m), 1466 (m), 1431 (m), 1346 (w), 1298 (w), 1248 (w), 1138 (w), 1097 (m), 1069 (m), 1022 (m), 939 (s), 868 (s), 813 (vs), 781 (sh), 700 (s), 519 (m), 467 (m).

$[Cu(cyclam)]_2[\{Cu(cyclam)\}_4\{(\alpha–GeW_{11}O_{39})Tm(H_2O)(\mu–CH_3COO)\}_2]\cdot18H_2O$ (1–Tm). Method 1: $TmCl_3.6H_2O$ (0.038 g, 0.10 mmol) was used and a mixture of orange plates and polycrystalline powder was obtained. Yield: 111 mg (28% based on $TmCl_3.6H_2O$). Anal. Calcd (found) for $C_{64}H_{190}Cu_6Ge_2N_{24}O_{102}Tm_2W_{22}$: C, 9.80 (9.86); H, 2.44 (2.32); N, 4.29 (4.18). IR (cm–1): 3183 (m), 3134 (m), 2931 (m), 2872 (m), 1636 (s), 1558 (m), 1456 (m), 1429 (m), 1346 (w), 1298 (w), 1248 (w), 1136 (w), 1098 (m), 1069 (m), 1022 (m), 939 (s), 868 (s), 812 (vs), 781 (sh), 698 (s), 519 (m), 459 (m).

$[Cu(cyclam)]_2[\{Cu(cyclam)\}_4\{(\alpha–GeW_{11}O_{39})Yb(H_2O)(\mu–CH_3COO)\}_2]\cdot18H_2O$ (1–Yb). Method 1: $YbCl_3.6H_2O$ (0.039 g, 0.10 mmol) was used and a mixture of orange plates and polycrystalline powder was obtained. Yield: 114 mg (29% based on $TmCl_3.6H_2O$). Anal. Calcd (found) for $C_{64}H_{190}Cu_6Ge_2N_{24}O_{102}W_{22}Yb_2$: C, 9.80 (9.88); H, 2.44 (2.38); N, 4.28 (4.19). IR (cm–1): 3183 (m), 3134 (m), 2932 (m), 2872 (m), 1636 (s), 1558 (m), 1456 (m), 1429 (m), 1346 (w), 1298 (w), 1250 (w), 1138 (w), 1098 (m), 1069 (m), 1024 (m), 939 (s), 868 (s), 814 (s), 783 (sh), 698 (s), 519 (m), 453 (m).

$[Cu(cyclam)]_2[\{Cu(cyclam)\}_4\{(\alpha–GeW_{11}O_{39})Lu(H_2O)(\mu–CH_3COO)\}_2]\cdot17H_2O$ (1–Lu). Method 1: $LuCl_3.6H_2O$ (0.039 g, 0.10 mmol) was used and a mixture of orange plates and polycrystalline powder was obtained. Yield: 101 mg (26% based on $LuCl_3.6H_2O$) Anal. Calcd (found) for $C_{64}H_{188}Cu_6Ge_2Lu_2N_{24}O_{101}W_{22}$: C, 9.82 (9.96); H, 2.42 (2.27); N, 4.29 (4.30). IR (cm^{-1}): 3183 (m), 3132 (m), 2930 (m), 2872 (m), 1636 (s), 1558 (m), 1456 (m), 1429 (m), 1346 (w), 1298 (w), 1250 (w), 1138 (w), 1098 (m), 1068 (m), 1023 (m), 938 (s), 866 (s), 815 (s), 770 (sh), 696 (s), 519 (m), 457 (m).

$[\{Cu(cyclam)\}_6\{(\alpha–GeW_{11}O_{39})Ln(H_2O)(\mu–CH_3COO)\}_2]\cdot4H_2O$ (2–Ln, Ln = Eu, Er): Single crystals of **1–Ln** were heated at 110 °C in an oven for one hour.

$[Cu(cyclam)]_{0.5}[\{Cu(cyclam)\}_{5.5}\{(\alpha–GeW_{11}O_{39})Ln(\mu–CH_3COO)\}_2]$ (3–Ln, Ln = Ce, Eu): Single crystals of **1–Ln** were heated at 180 °C in an oven for one hour.

Single–crystal X–ray crystallography

Crystallographic data for the initial compounds **1–Ln** (Ln = La to Lu), the partially dehydrated intermediates **2–Ln** (Ln = Eu, Er) and the anhydrous phases **3–Ln** (Ln = Ce, Eu) are given in Tables 3.6–3.8 whereas those regarding the fully rehydrated phases **1R–Ln** (Ln = Ce, Eu, Er) can be found in Table A3.1 in the Appendix. Intensity data were collected on an Agilent Technologies Super–Nova diffractometer, which was equipped with monochromated Cu K_α radiation (λ = 1.54184 Å) and Atlas CCD detector in all cases with the exception of **1–Eu** and **1–Tb**. For the latter, the partially dehydrated **2–Er** and **2–Eu** as well as the anhydrous **3–Ce** and **3–Eu** and the rehydrated phases **1R–Eu** and **1R–Er,** the selected radiation and detector were monochromated Mo K_α radiation (λ = 0.71073 Å) and Eos CCD, respectively. The data collection temperature was 100 K for all **1–Ln** and **1R–Ln**. In the case of **2–Eu**, a single crystal was heated in an oven to 383 K at a rate of 1 K min^{-1}, and immediately afterwards covered with Paratone® oil and placed under the N_2 stream of the diffractometer, which was ready to perform a full data collection at 100 K. For the anhydrous **3–Ln** (Ln = Ce, Eu) as well as **2–Er** the same procedure was applied but they were heated to 433 K instead. For the rehydrated samples (**1R–Ln**), the same heating process to 433 K was employed but we waited a full day before performing the data acquisition to assure full rehydration. Thermal vibrations were treated anisotropically for heavy atoms (W, Ln, Cu, Ge) in all structures. Hydrogen atoms of the organic ligands were placed in calculated positions and refined using a riding model with standard SHELXL parameters. Several positions suitable for water molecules of hydration were located in the Fourier maps of **1–Ln**, **2–Ln** and **1R–Ln** compounds and their occupancy was initially refined without restrictions. The resulting total number of 8.3–9.5 (**1–Ln**), 7.7–8.0 (**1R–Ln**) and 4.0 (**2–Ln**) water molecules of hydration per Keggin subunit was fixed to 8.5–9.5, 8.0 and 4.0 respectively, during the final refinements. Data acquisition, structure solving and geometrical calculations were performed using the same software mentioned in the first section for the isopolyoxotungstate derivatives.

Table 3.6. Crystallographic data for **1–Ln** hybrid heteropolyoxotungstates (Ln = La–Eu).

	1–La	**1–Ce**	**1–Pr**	**1–Nd**	**1–Sm**	**1–Eu**
Empirical formula	$C_{64}H_{190}Cu_6Ge_2La_2N_{24}O_{102}W_{22}$	$C_{64}H_{190}Cu_6Ce_2Ge_2N_{24}O_{102}W_{22}$	$C_{64}H_{188}Cu_6Ge_2N_{24}O_{101}Pr_2W_{22}$	$C_{64}H_{190}Cu_6Ge_2N_{24}Nd_2O_{102}W_{22}$	$C_{64}H_{192}Cu_6Ge_2N_{24}O_{103}Sm_2W_{22}$	$C_{64}H_{188}Cu_6Eu_2Ge_2N_{24}O_{101}W_{22}$
fw (g mol^{-1})	7777.34	7779.76	7763.32	7787.99	7818.22	7785.42
crystal system	triclinic	triclinic	triclinic	triclinic	Triclinic	triclinic
space group	*P–1*	*P–1*	*P–1*	*P–1*	*P–1*	*P–1*
***T* (K)**	100(2)	100(2)	100(2)	100(2)	100(2)	100(2)
***a* (Å)**	13.5867(3)	13.5968(3)	13.5947(2)	13.6064(3)	13.6266(7)	13.5580(3)
***b* (Å)**	13.8341(3)	13.8641(3)	13.8564(2)	13.8468(3)	13.8921(6)	13.8266(3)
***c* (Å)**	23.2032(5)	23.1308(4)	23.0964(4)	23.0559(5)	22.9645(10)	22.9904(6)
α (°)	92.3404(17)	92.4830(16)	92.5406(13)	92.5406(16)	92.476(3)	92.667(2)
β (°)	99.5031(17)	99.6151(18)	99.6878(15)	99.8360(16)	100.153(4)	99.921(2)
γ (°)	110.1147(19)	110.184(2)	110.1352(15)	110.0390(17)	109.931(4)	110.057(2)
V (Å^3)	4016.58(14)	4010.96(14)	4001.93(11)	3995.96(14)	3997.7(3)	3961.79(17)
ρ_{calc} (g cm^{-3})	3.215	3.221	3.221	3.236	3.247	3.263
K_α (Å)	1.54184	1.54184	1.54184	1.54184	1.54184	0.71073
μ (mm^{-1})	34.344	34.661	35.006	35.347	35.899	17.932
collected reflns	31563	31190	30174	30436	27547	27080
unique reflns (R_{int})	14315 (0.056)	14298 (0.059)	14256 (0.047)	14248 (0.033)	14237 (0.066)	13965 (0.034)
obsd reflns [$I > 2\sigma(I)$]	12960	12415	12903	13553	12288	11766
parameters	537	541	526	532	549	530
$R(F)^a$ [$I > 2\sigma(I)$]	0.057	0.048	0.049	0.036	0.055	0.039
$wR(F^2)^b$ [all data]	0.158	0.129	0.135	0.093	0.151	0.090
GoF	1.061	1.029	1.049	1.042	1.030	1.059

^{a} $R(F)=\Sigma||F_o-F_c||/\Sigma|F_o|$; ^{b} $wR(F^2)=\{\Sigma[w(F_o^2-F_c^2)^2]/\Sigma[w(F_o^2)^2]\}^{1/2}$

Regarding the partially hydrated structures (**2–Eu** and **2–Er**), the occupation of all C, N, and Cu atoms belonging to the two disordered Cu1B and Cu1C complex moieties were initially refined with free occupancy resulting in virtually identical occupancy and thus, all of them were fixed to 0.50. No H atoms were placed in any of the disordered ligands (B and C). Numerous restriction had to be applied involving Cu–N and N–C distances as well as N–Cu–N angles in order to modelize the strong B–C disorder. A few distance and angle restrictions were also necessary in the Cu1D complex for the ligand to show the appropriate connectivity, and as a result, we could not place any H atoms in the C2D and C14D carbon atoms of the organic ligand. It is worth mentioning that while the B–C disorder in **2–Eu** could be modelized well, the Cu1C complex in **2–Er** could not despite our efforts. In close analogy to the **2–Ln**, the occupation of all C, N, and Cu atoms belonging to the four disordered Cu1B, Cu1C, Cu2B and Cu2C moieties in the anhydrous **3–Ln** (Ln = Ce, Eu) were initially refined with free occupancy resulting in virtually identical occupancy and thus, all of them were fixed to 0.50.

Table 3.7. Crystallographic data for **1–Ln** hybrid heteropolyoxotungstates (Ln = Gd–Tm).

	1–Gd	**1–Tb**	**1–Dy**	**1–Ho**	**1–Er**	**1–Tm**
Empirical formula	$C_{64}H_{190}Cu_6Gd_2Ge_2N_{24}O_{102}W_{22}$	$C_{64}H_{190}Cu_6Ge_2N_{24}O_{102}Tb_2W_{22}$	$C_{64}H_{190}Cu_6Dy_2Ge_2N_{24}O_{102}W_{22}$	$C_{64}H_{192}Cu_6Ge_2Ho_2N_{24}O_{103}W_{22}$	$C_{64}H_{190}Cu_6Er_2Ge_2N_{24}O_{102}W_{22}$	$C_{64}H_{190}Cu_6Ge_2N_{24}O_{102}Tm_2W_{22}$
fw (g mol^{-1})	7814.01	7817.35	7824.51	7847.40	7834.03	7837.37
crystal system	triclinic	triclinic	triclinic	triclinic	Triclinic	triclinic
space group	*P–1*	*P–1*	*P–1*	*P–1*	*P–1*	*P–1*
***T* (K)**	100(2)	100(2)	100(2)	100(2)	100(2)	100(2)
***a* (Å)**	13.6058(3)	13.5799(4)	13.5812(2)	13.6372(4)	13.6108(4)	13.6150(3)
***b* (Å)**	13.8465(3)	13.8263(4)	13.82489(16)	13.8817(4)	13.8628(3)	13.8513(3)
***c* (Å)**	22.9325(5)	22.9456(7)	22.9028(3)	22.9016(6)	22.8601(5)	22.8390(4)
α (°)	92.6299(18)	92.643(2)	92.6518(11)	92.556(2)	92.7378(19)	92.7860(15)
β (°)	99.9501(17)	100.113(2)	100.0425(13)	100.143(2)	100.061(2)	100.1276(16)
γ (°)	110.011(2)	109.968(3)	109.9715(13)	109.958(3)	110.005(2)	110.0238(17)
V (Å^3)	3972.62(16)	3960.1(2)	3953.56(10)	3985.66(19)	3963.69(18)	3956.02(14)
ρ_{calc} (g cm^{-3})	3.266	3.278	3.286	3.269	3.282	3.290
K_α (Å)	1.54184	0.71073	1.54184	1.54184	1.54184	1.54184
μ (mm^{-1})	35.967	18.042	35.771	32.330	32.602	32.797
collected reflns	31164	26922	33678	34858	30567	30197
unique reflns (R_{int})	14156 (0.065)	13956 (0.038)	16237 (0.070)	16365 (0.070)	14114 (0.040)	14104 (0.051)
obsd reflns [$I > 2\sigma(I)$]	12484	11394	14172	13473	12701	12587
parameters	537	533	525	539	540	532
$R(F)^a$ [$I > 2\sigma(I)$]	0.062	0.038	0.070	0.061	0.041	0.032
$wR(F^2)^b$ [all data]	0.185	0.088	0.215	0.175	0.103	0.078
GoF	1.039	1.053	1.039	1.039	1.103	1.023

^{a} $R(F)=\Sigma||F_o–F_c||/\Sigma|F_o|$; ^{b} $wR(F^2)=\{\Sigma[w(F_o^2–F_c^2)^2]/\Sigma[w(F_o^2)^2]\}^{1/2}$

Similar to the previous structures, the collected data for the rehydrated samples (**1R–Ce**, **1R–Eu** and **1R–Er**) was not of enough quality for all the ligands to show the correct connectivity and thus, their refinements required several restriction regarding Cu–N and N–C distances as well as N–Cu–N angles. These measures allowed us to solve the structures of **1R–Eu** and **1R–Er** correctly. Unfortunately, this was not the case for **1R–Ce** due to the significantly inferior quality of the collected data for the latter compared to the formers. This fact prevented us from placing all H atoms belonging to the Cu1D ligand and hence, C12D and C13D atoms do not carry any H atoms. In addition, the structures of **1R–Ln** are one (**1R–Eu**) and two (**1R–Ce**, **1R–Er**) water molecules short compared to the corresponding **1–Ln** structures, but TGA analyses demonstrated that they have the same amount of water. It is worth mentioning that the largest residual peaks are located close to the *addenda* atoms in the final difference maps of all the structures. In some compounds however, we have experienced notable difficulties with absorption effects and high residual peaks in some compounds. This can be explained attending to the fact that large residual peaks in the final difference maps are a common problem encountered in the solution and refinement of POWs structures due to the higher adsorption of W *addenda* centers compared to V and Mo analogues.[99]

Table 3.8. Crystallographic data for **1–Ln**, **2–Ln** and **3–Ln** hybrid heteropolyoxotungstates.

	1–Yb	**1–Lu**	**2–Eu**	**2–Er**	**3–Ce**	**3–Eu**
Empirical formula	$C_{64}H_{190}Cu_6Ge_2N_{24}O_{102}W_{22}Yb_2$	$C_{64}H_{188}Cu_6Ge_2Lu_2N_{24}O_{101}W_{22}$	$C_{64}H_{162}Cu_6Eu_2Ge_2N_{24}O_{88}W_{22}$	$C_{64}H_{162}Cu_6Er_2Ge_2N_{24}O_{88}W_{22}$	$C_{64}H_{150}Ce_2Cu_6Ge_2N_{24}O_{82}W_{22}$	$C_{64}H_{150}Cu_6Eu_2Ge_2N_{24}O_{82}W_{22}$
fw (g mol^{-1})	7845.6	7831.4	7551.21	7581.81	7419.44	7442.95
crystal system	triclinic	triclinic	triclinic	triclinic	triclinic	triclinic
space group	*P–1*	*P–1*	*P–1*	*P–1*	*P–1*	*P–1*
***T* (K)**	100(2)	100(2)	100(2)	100(2)	100(2)	100(2)
***a* (Å)**	13.6180(3)	13.5580(2)	12.9784(4)	12.9188(3)	12.9244(3)	12.9511(3)
***b* (Å)**	13.8455(3)	13.8181(2)	13.7387(6)	13.7285(4)	25.1300(3)	25.2030(6)
***c* (Å)**	22.8414(5)	22.8696(4)	23.4443(6)	23.3071(7)	23.8354(5)	23.7355(6)
α (°)	92.8040(18)	92.6585(15)	94.068(3)	94.426(3)	70.522(2)	70.616(2)
β (°)	100.0329(16)	99.9826(14)	103.968(2)	104.146(2)	85.939(2)	85.658(2)
γ (°)	110.0315(19)	109.8052(15)	112.939(4)	112.862(3)	87.5180(10)	87.387(2)
V (Å^3)	3956.75(14)	3944.43(12)	3671.6(2)	3624.25(19)	7278.5(2)	7285.6(3)
ρ_{calc} (g cm^{-3})	3.293	3.281	3.415	3.474	3.385	3.393
K_α (Å)	1.54184	1.54184	0.71073	0.71073	0.71073	0.71073
μ (mm^{-1})	32.876	33.174	19.338	19.883	19.268	19.485
collected reflns	30174	30522	26508	24265	69823	68558
unique reflns (R_{int})	14090 (0.041)	14066 (0.042)	12931 (0.061)	12756 (0.038)	28576 (0.066)	28536 (0.058)
obsd reflns [$I > 2\sigma(I)$]	12394	12960	10241	10112	20552	21196
parameters	532	526	548	544	1101	1101
$R(F)^a$ [$I > 2\sigma(I)$]	0.039	0.051	0.065	0.062	0.072	0.058
$wR(F^2)^b$ [all data]	0.100	0.135	0.167	0.152	0.202	0.125
GoF	1.037	1.025	1.018	1.050	1.031	1.076

[a] $R(F)=\Sigma||F_o-F_c||/\Sigma|F_o|$; [b] $wR(F^2)=\{\Sigma[w(F_o^2-F_c^2)^2]/\Sigma[w(F_o^2)^2]\}^{1/2}$

3.3.2. RESULTS AND DISCUSSION

Synthesis

Transition metal (TM) and lanthanide (Ln) containing species have attracted an increasing attention over the years owing to their potential applications in catalysis, molecular adsorption, and magnetism, as well as their intriguing architectures and topologies and hence, the preparation of such compounds has become an important research focus in POM chemistry.[100,101] Compared to the relatively weak activity of TM centers, the higher oxophilic reactivity of the Ln cations towards the POM clusters tend to lead to amorphous precipitates in synthetic systems involving the three TM–Ln–{XW} components. One valid approach to overcome this challenge is the hydrothermal method, since it has proven to be an extraordinary synthetic technique for the preparation of several POM–based hybrids.[100] Indeed, the high temperatures and pressures increase the solubility of the reactants, facilitate the incorporation of various organic components into inorganic frameworks and also favors the formation of metastable phases that can be then captured and stabilized by TM or Ln cations. These features make possible the preparation of hybrids otherwise difficult or even impossible to obtain with traditional synthetic methods. In this chapter, the entire series of Cu–Ln {GeW}–based heterometallic hybrids (La to Lu) were synthesized using two different methods under hydrothermal conditions (Figure 3.23). Method 1 involves the use of the trilacunary $Na_{10}[\alpha–GeW_9O_{34}]$ precursor with Ln(III) cations and the *in situ* prepared {Cu(cyclam)} complex in 1M KOAc/HAc medium. With this first method, we conveniently accessed the entire compound series (Ln = La to Lu) with a common synthetic protocol. Unfortunately, this method did not yield XRD–quality single crystals for some mid–to–late **1–Ln** (Ln = Eu to Er) derivatives. This problem was solved by using the preformed precursor (method 2), $Na_4K_8[\{(\alpha–GeW_{11}O_{39})Ln(\mu–CH_3COO)(H_2O)\}_2]\cdot16–20H_2O$ (Ln = Eu–Er), although the observed yields were *ca.* 4 times lower than those observed following method 1.

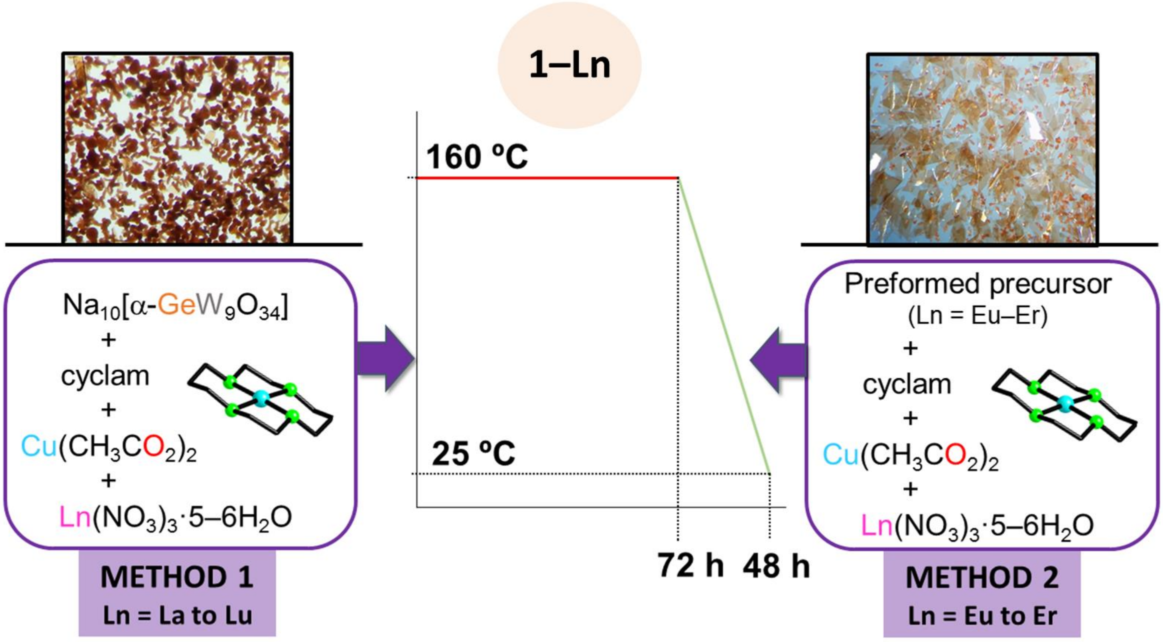

Figure 3.23. Schematic representation of the synthetic hydrothermal approach for the preparation of **1–Ln** hybrids.

Since **1–Ln** compounds contain two monolacunary fragments instead of the starting trilacunary $[\alpha–GeW_9O_{34}]^{10–}$ precursor, we attempted to prepare **1–Ln** compounds under similar hydrothermal conditions, but using $K_8[\alpha–GeW_{11}O_{39}]$ synthetized as reported.[98a] These reactions only lead to brownish precipitates that did not correspond to pure **1–Ln**, as shown in their respective PXRD patterns and FT–IR spectra. Likewise, similar results were obtained starting with both GeO_2 and Na_2WO_4 or the plenary $[GeW_{12}O_{40}]^{4–}$ precursor. These facts suggested that the transformation from {α–GeW$_9$} to {α–GeW$_{11}$} plays an important role in the formation of **1–Ln**. Besides, it is worth mentioning that the reaction does not take place if 1M or 0.5M NaOAc/HAc buffer or water is used instead of the potassium buffer under the same hydrothermal conditions, proving that even if they are absent from the structure, K$^+$ cations must play a key role in the formation of **1–Ln** compounds. This conclusion is further reinforced by the fact that **1–Ln** compounds could not be isolated in more diluted 0.5M KOAC/HAc medium starting with neither of the precursors. Isolation of these compounds also depends heavily on the nature of the transition metal. We tried to prepare analogous compounds with similar hydrothermal reactions following both methods but using Co^{II}, Ni^{II} and Zn^{II} instead of Cu^{II}. The resulting amorphous red–brownish, greenish and white precipitates could not be further characterized confirming that the plasticity of the Cu^{II} centers seems to play a key role in the formation of **1–Ln**. In addition, we also try to verify if **1–Ln** compounds could be isolated under bench conditions. Similar reactions following both methods were performed from room temperature up to reflux conditions but they only led to mixtures of some Peacock–Weakley 1:2 type hybrids {Ln(α–GeW$_{11}$O$_{39}$)$_2$} instead, which will be reported elsewhere and will not be covered in this dissertation.

Finally, we also attempted to explore the effect of the heteroatom X in our products by replacing the {α–GeW$_9$} with {α–SiW$_9$} and {α–PW$_9$} analogous precursors. Similar hydrothermal syntheses following method 1 were carried out using the silico– and phosphotungstate trilacunary precursors, prepared as described in the literature.[98a] Interestingly enough, while the reactions involving Cu–Ln–{PW} synthetic system only yielded amorphous precipitates that could not be further characterized, single crystals of some derivatives of the Cu–Ln–{SiW} were obtained, which were revealed to be isostructural to **1–Ln** compounds. The latter will not be covered within this dissertion.

Vibrational characterization and thermostructural behaviour of 1–Ln

Compounds **1–Ln** (Ln = La to Lu) were preliminary characterized using FT–IR spectroscopy. The FT–IR spectra are clearly divided into two regions, the metalorganic one above 1000 cm^{-1} and the inorganic region below this wavenumber, all of them displaying characteristic vibration patterns derived from the Keggin framework (Figure A3.4 in the Appendix). Regarding the metal–organic region of the FT–IR spectra, the peaks associated with the stretching of the –N–H and –C–H bonds are respectively observed at 3229–3165 and 2936–2878 cm^{-1}, whereas several weak to medium signals corresponding to the δ(C–H) and ν(N–C) vibration modes are also present in the 1474–1236 and 1105–1008 cm^{-1} ranges (Figure 3.24). These signals confirm the presence of the cyclam ligands in our compounds. Besides, various distinct stretching frequencies can be observed in the spectral range of 1429–1550 cm^{-1} which were assigned to ν$_{as}$(C=O) and ν$_{as}$(C–O) vibrations of the acetate bridging ligands in the (η^2–μ–1,1) coordination mode. Four distinct vibration bands attributable to ν(W–O$_t$), ν(Ge–O$_c$), ν(W–O$_v$) and ν(W–O$_e$) (t= terminal, c= central, v= vertex–sharing and e= edge sharing) can be observed in the low–wavenumber region at around 938, 868, 808 and 694 cm^{-1}, respectively. The last signals correspond to δ(W–O$_e$–W) as well as δ(W–O$_v$–W) and δ(Ge–O–Ge) vibration modes at ca. 520 and 463 cm^{-1}, respectively. The FT–IR spectra of **1–Ln** closely resembles that of the {α–GeW$_{11}$O$_{39}$} cluster, indicating that they contain the monovacant Keggin type fragments in their skeletons. Compared to the FT–IR spectrum of {α–$GeW_{11}O_{39}$}, the ν(W–O_t) vibration bands are almost not shifted whereas the ν(W–O_e) and ν(W–O_v) bands shift to slightly lower wavenumber values, the possible mayor reason for which could be the distortion of the {$GeW_{11}O_{39}$} fragments due to the incorporation of the Ln^{III} atom to the vacant site. As expected, the inorganic region of the spectra of the precursors used in method 2 are virtually identical to those seen for the **1–Ln** compounds (Figure 3.25).

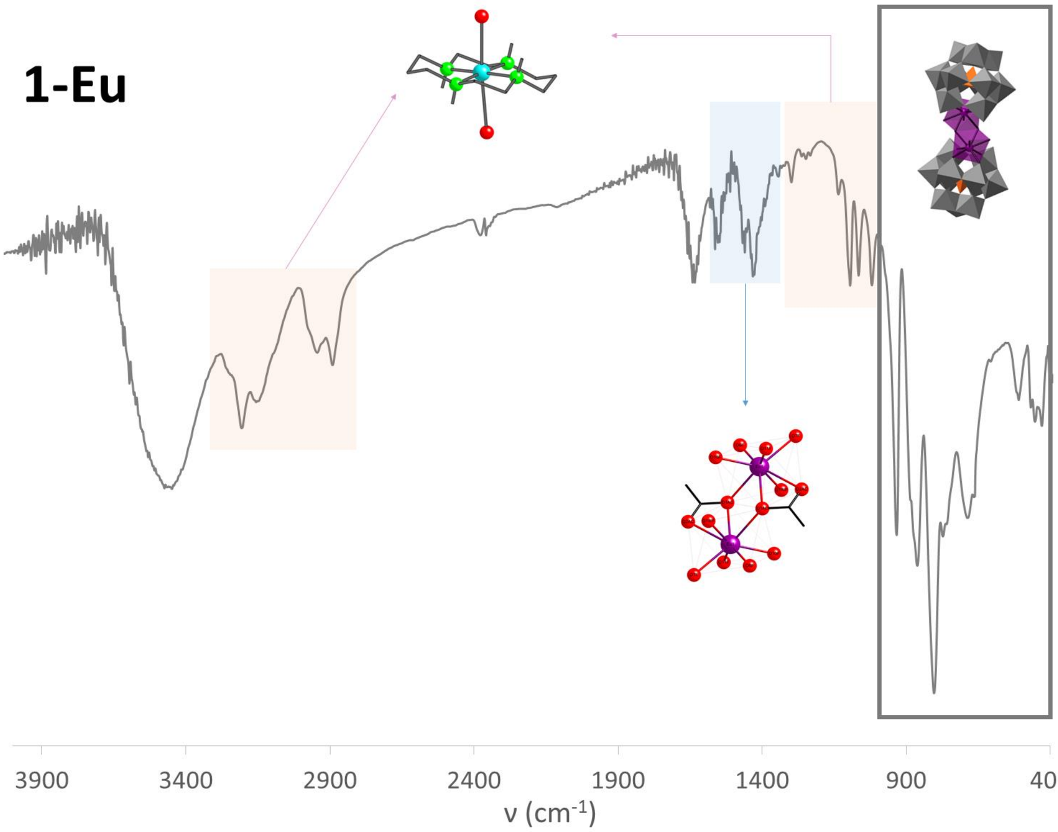

Figure 3.24. FT–IR spectra of **1–Eu** derivative highlighting the bands originating from each subunit.

Thermal stability of compounds **1–Ln** (Ln = La to Lu) was investigated by TGA/DTA experiments. In all cases, thermal decomposition occurred in three stages which show nearly identical profiles (Figures 3.26 and A3.5 in the Appendix). The first stage is observed as an endothermic mass loss that extends from room temperature to temperatures around 150–160 °C, which originates from the release of all hydration/coordination water molecules. The mass loss corresponds to 19–21 water molecules (calcd. 4.38 to 4.85%; found 4.28 to 4.65%) along the series. Dehydration leads to the corresponding anhydrous phases, which show a significant range of thermal stability up to *ca.* 250–270 °C. Above this temperature, the anhydrous phases undergo further decomposition via various overlapping mass loss stages of exothermic nature due to the combination of the organic ligands combustion and crumbling of the dimeric Keggin frameworks. The overall mass loss for this stage is in good agreement with six cyclam and two acetate ligands (calcd. for $3C_{10}H_{24}N_4 + 2C_2H_3O_2$ 16.80 to 16.95%; found 16.52 to 16.69%) in all cases. The final residue (calcd. for $Cu_6Ge_2Ln_2O_{78}W_{22}$ 78.13 to 78.73%; found 78.76 to 79.25%) is obtained at temperatures above *ca*. 610–630 °C.

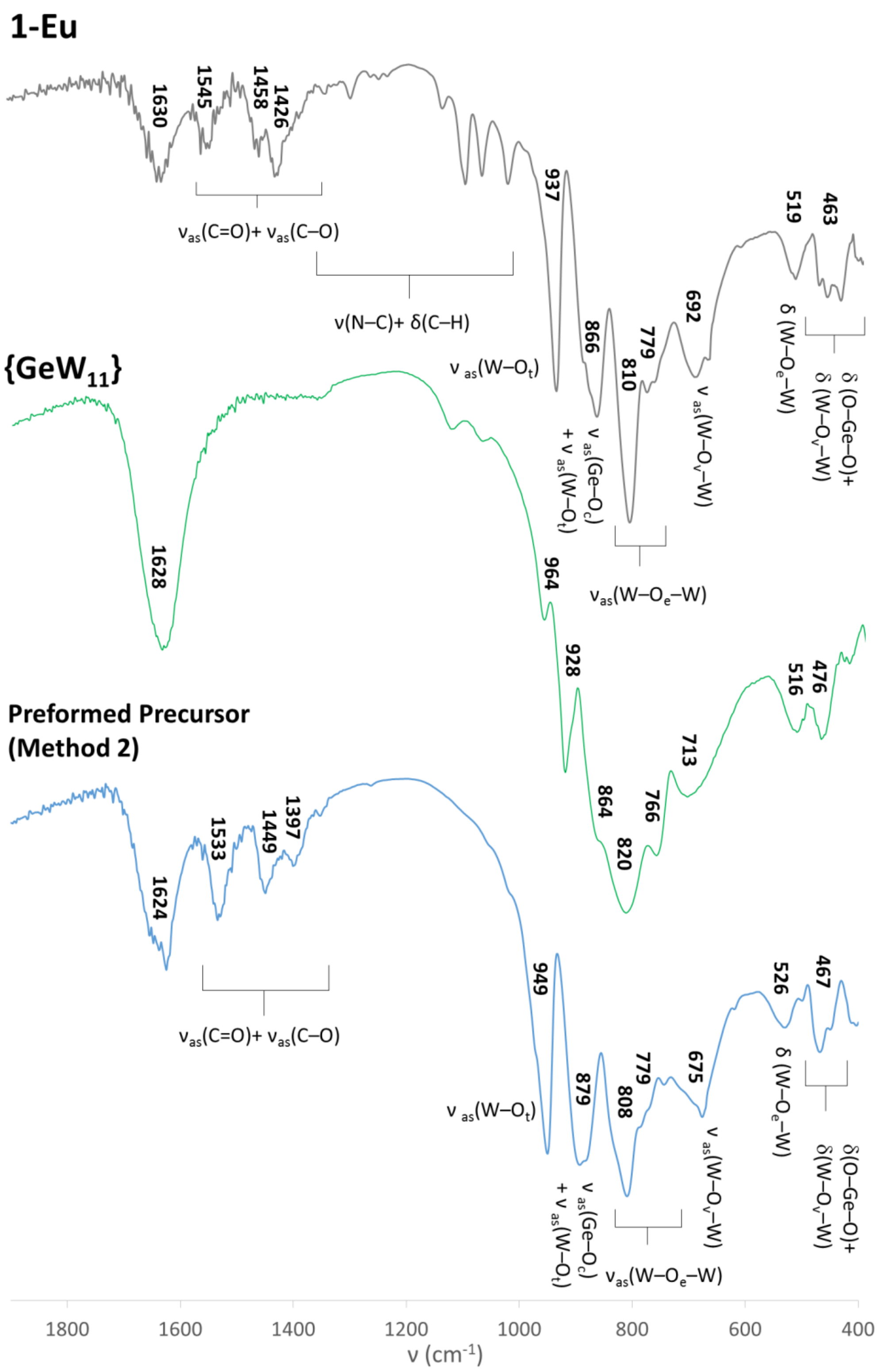

Figure 3.25. Details of the low–wavenumber region of the FT–IR spectra of **1–Eu** compared to those of the monolacunary {GeW$_{11}$} and the preformed precursor used in method 2.

The experimental PXRD patterns of **1–Ln** are in good agreement with the corresponding simulated ones from the single crystal XRD data suggesting a good phase purity (Figures 3.26 and A3.5 in the Appendix). The slight differences in intensity between them could be a result of a variation in preferred orientation of the powder sample during the measurements. TPXRD experiments between room temperature and 630 °C show that **1–Ln** retain crystallinity upon dehydration up to *ca.* 270–300 °C approximately (Figures 3.26 and A3.7–A3.12 in the Appendix), which is consistent with the above observations on the corresponding TGA curves. Notable variations in the positions of some diffraction maxima can be found in some less intense peaks at around 2ϑ values in the range 8–10° and 23–27° starting at *ca.* 70–90 °C, which suggest that the gradual dehydration process is accompanied by a thermally activated phase transition (**2–Ln**). Similarly, the TPXRD patterns are substantially modified from 130–150 to 250–290 °C (at which all water molecules of hydration are released according to the TGA curves) indicating that yet another phase transformations occurs (**3**–**Ln**), as can be seen in some of the diffraction maxima highlighted in Figure 3.26.

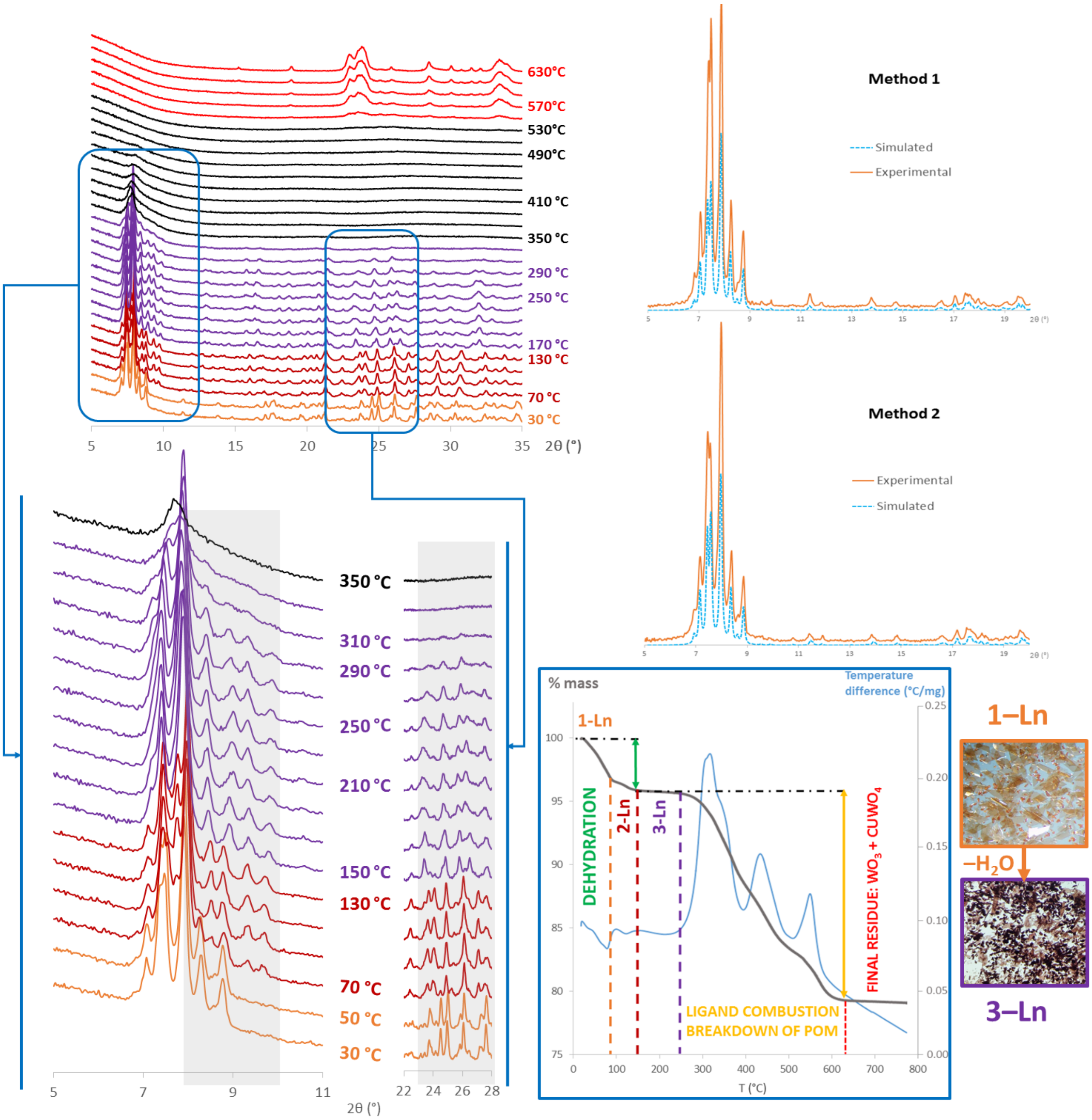

Figure 3.26. Variable–temperature PXRD patterns (TPXRD) from room temperature to 630 °C of **1–Er** derivative with details along with the TGA curve and digital photographs of the hydrated and anhydrous phase. Comparison between the experimental (Method 1 and 2) and simulated PXRD patterns for **1–Er** are also shown.

After that, the crystalline anhydrous phase (**3–Ln**) transforms into an amorphous solid in the temperature range corresponding to the combustion of organic ligands and the crumbling of the POM structure and new high–temperature crystalline phases start appearing at temperatures around 490–530 °C reaching complete formation at *ca.* 610 °C, which is in good agreement with the observations in the above TGA curve. At 550 °C these phases forming the final residue of the thermal decomposition are defined enough for being identified as a mixture of tetragonal *P4/nmm* WO_3 (PDF: 01–085–0807),[102] and triclinic *P*–1 $CuWO_4$ (PDF: 01–080–1918, PDF: 01–088–0269, PDF: 01–070–1732),[90,103] with an approximate WO_3:$CuWO_4$ ratio of 2:3 for all **1**–**Ce**, **1–Eu** and **1–Er** (Figures A3.13–A3.15 in the Appendix), no crystal phases containing any Ln could be found in the diffraction patterns of neither of them. This fact could be explained considering the low content of Ln compared to the other components in our compounds (W: Cu: Ln ratio is approximately 11: 3: 1) that prevents the diffraction peaks associated with any Ln–containing phases from being detected in the diffraction patterns. Encouraged by the TGA/DTA and TPXRD results over polycrystalline samples, we decided to carry out analogous single–crystal XRD studies to determine the structural changes promoted by the dehydration processes. We selected for this purpose **1–Ce, 1–Eu** and **1–Er** compounds because of their higher crystal quality compared to that of other derivatives and so the results could be representative for at least one early, mid and late–lanthanide derivative. Fortunately, single crystals of all **1–Ce, 1–Eu** and **1–Er** were able to maintain their integrity after heating to 383 and 433 K and thus, it allowed us to determine the structures of the isostructural intermediates **2–Ln** (Ln = Eu, Er) as well as the anhydrous phases **3–Ln** (Ln = Ce, Eu). On the other hand, due to the rapid rehydration of **1–Er** derivative, we could not determine the anhydrous phase but the partially hydrated one instead, even when the crystals were heated to 433 K. In view of these results, we tried to measure the anhydrous derivatives of Tm, Yb and Lu late–Ln analogues and even though the collected data was of poor quality, it allowed us to confirm that all three unit cells were isostructural to that of the measured intermediate phases **2–Ln**. The following Table 3.9 summarizes the sc–XRD measurements carried out for these hybrids compounds.

Table 3.9. Summary of sc–XRD results for **1–Ln** hybrid compounds and their thermal derivatives.

	La	Ce	Pr	Nd	Sm	Eu	Gd	Tb	Dy	Ho	Er	Tm	Yb	Lu
1–Ln	sc	sc	sc	sc	sc	sc	sc	sc	sc	sc	sc	sc	sc	sc
2–Ln	–	PQ	–	–	–	sc	–	–	–	–	sc	PQ	PQ	PQ
3–Ln	–	sc	–	–	–	sc	–	–	–	–	X	X	X	X
1R–Ln	–	sc	–	–	–	sc	–	–	–	–	sc	–	–	–

sc = single–crystal; PQ = poor quality sc–XRD data, X= unit cell of **2–Ln**.

Crystal structures of 1–Ln

Isostructural compounds **1–Ln** crystallize in the triclinic space group *P–1*, the unit cell of which contains a hybrid dimeric core $[\{(\alpha\text{–}GeW_{11}O_{39})Ln(H_2O)(\mu\text{–}CH_3COO)\}_2]^{12-}$, six {Cu(cyclam)} cationic moieties (Cu1A, Cu1B, Cu1C and Cu1D) and several water molecules of hydration (17–19 H_2O), some of which are disordered. The 2:2 type dimeric core is composed of two identical symmetrically related mono–substituted $\{(\alpha\text{–}GeW_{11}O_{39})Ln(H_2O)(\mu\text{–}CH_3COO)\}^{6-}$ fragments, where two monolacunary $\{\alpha\text{–}GeW_{11}O_{39}\}$ Keggin units are linked together by two Ln atoms, each one coordinated to a bridging acetate chelating ligand in the (η^2–μ–1,1) coordination mode. Each Keggin cluster is decorated by three crystallographically independent {Cu(cyclam)} moieties (Cu1A–Cu1C) through terminal oxygen atoms of the mono–substituted units whereas the non–supported Cu1D {Cu(cyclam)} complexes act as a charge compensation units (Figure 3.27).

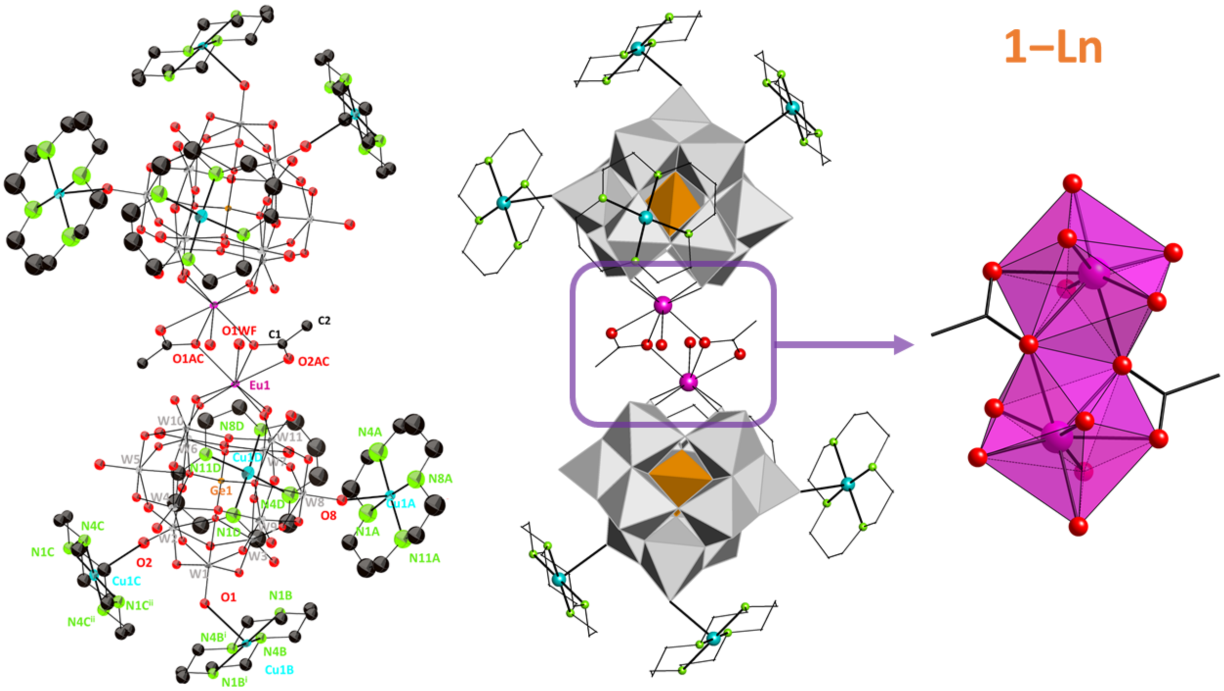

Figure 3.27. ORTEP view of **1–Eu** depicted at the 50% probability level, with partial atom labelling and polyhedral representation of the dimeric hybrid, showing the coordination sphere of the Ln atom (water molecules and H atoms are omitted for clarity). Color code: Symmetry codes: i) –*x*, –1–*y*, 1–*z*; ii) 1–*x*, –*y*, 1–*z*.

In these **1–Ln** dimeric structures, the Ln atoms are accomodated in the vacant site of the defect $[\alpha\text{–}GeW_{11}O_{39}]^{8-}$ Keggin subunit and exhibit a distorted eight–coordinate square antiprism (SAPR) or biaugmented trigonal prism (BTPR) geometry depending on the Ln, as confirmed by CShM calculations[91] (Table 3.10). Each lanthanide atom is coordinated to four oxygen atoms that delimit the vacant site of the lacunary cluster (O6F, O7F, O10F and O11F), two oxygen atoms belonging to the carboxylate group of one acetate ligand (O1Ac and O2Ac) and another carboxyl atom from the other centrosymmetric one (O1Ac^i where i: 1–*x*, –*y*, 2–*z*; Figure 3.27). The remaining position is occupied by one water molecule (O1WF) with Ln–O1WF bond lengths in the range of 2.32–2.56 Å across the series. The distances between Ln and O atoms belonging to the POM vary from 2.26 to 2.46 Å whereas distances to the carboxylic O atoms are slightly longer and can be found in the range 2.35–2.60 Å along the series (Table 3.10). These distances demonstrate the influence of the Ln radii on the local environment as Ln–O bond lengths decrease with the radius of the trivalent Ln center. Moreover, distances between adjacent Ln···Ln atoms also follow this trend varying from 4.00 to 4.27 Å which is consistent with the lanthanide contraction as well (Figure 3.28), except for that of **1–Ho** derivative, which could be explained attending to the type of distortion calculated by CShM

(BTPR < SAPR, Table 3.10). This way, the coordination polyhedron of **1–Ho** resembles more those found for the early–Ln derivatives (BTPR) compared to the late–Ln analogues (SAPR), resulting in slightly longer Ln···Ln and Ln-O$_{average}$ distances.

Table 3.10. Ln–O bonds lengths (Å) and the polyhedral distorsion (CShM) in **1–Ln** compounds.

Ln–O	**1–La**	**1–Ce**	**1–Pr**	**1–Nd**	**1–Sm**	**1–Eu**	**1–Gd**
Ln–O6F	2.456(8)	2.424(8)	2.424(8)	2.409(6)	2.398(8)	2.387(7)	2.365(9)
Ln–O7F	2.442(8)	2.433(8)	2.416(7)	2.393(6)	2.368(8)	2.375(7)	2.334(9)
Ln–O10F	2.440(7)	2.435(7)	2.402(7)	2.393(5)	2.359(8)	2.357(7)	2.356(9)
Ln–O11F	2.415(8)	2.394(8)	2.378(7)	2.366(6)	2.361(8)	2.333(7)	2.345(10)
Ln–O1AC	2.590(8)	2.592(7)	2.491(7)	2.566(6)	2.448(8)	2.435(8)	2.435(9)
Ln–O2AC	2.599(9)	2.593(8)	2.568(8)	2.555(6)	2.513(8)	2.511(8)	2.469(10)
Ln–O1AC^{i}	2.538(8)	2.492(8)	2.578(7)	2.480(6)	2.543(8)	2.540(8)	2.514(9)
Ln–O1WF	2.559(9)	2.521(8)	2.481(8)	2.477(6)	2.452(8)	2.423(8)	2.418(10)
Ln–O$_{average}$	2.505	2.486	2.467	2.455	2.430	2.420	2.405
BTPR–8	1.534	1.548	1.483	1.551	1.502	1.508	1.563
SAPR–8	2.327	2.114	1.989	1.867	1.693	1.688	1.617
Ln–O	**1–Tb**	**1–Dy**	**1–Ho**	**1–Er**	**1–Tm**	**1–Yb**	**1–Lu**
Ln–O6F	2.342(7)	2.325(9)	2.340(9)	2.301(7)	2.299(5)	2.312(6)	2.271(8)
Ln–O7F	2.357(8)	2.324(9)	2.329(9)	2.320(6)	2.297(5)	2.295(6)	2.264(8)
Ln–O10F	2.335(8)	2.313(8)	2.322(8)	2.315(7)	2.292(5)	2.287(6)	2.272(7)
Ln–O11F	2.308(7)	2.296(9)	2.302(8)	2.287(7)	2.278(5)	2.261(6)	2.268(7)
Ln–O1AC	2.405(7)	2.403(9)	2.406(9)	2.392(7)	2.368(5)	2.353(7)	2.372(7)
Ln–O2AC	2.456(8)	2.452(9)	2.460(9)	2.432(7)	2.413(5)	2.409(7)	2.410(8)
Ln–O1AC^{i}	2.525(7)	2.482(9)	2.487(8)	2.473(7)	2.496(5)	2.491(6)	2.417(7)
Ln–O1WF	2.404(8)	2.385(10)	2.391(9)	2.368(8)	2.338(5)	2.331(7)	2.321(8)
Ln–O$_{average}$	2.392	2.373	2.380	2.360	2.348	2.342	2.324
BTPR–8	1.588	1.527	1.556	1.607	1.659	1.614	1.710
SAPR–8	1.571	1.515	1.611	1.498	1.401	1.451	1.384

Symmetry codes: i) 1–*x*, –*y*, 2–*z*; ii) 1–*x*, 1–*y*, 2–*z*. CShM: reference polyhedra BTPR–8 (biaugmented trigonal prism) and SAPR–8 (square antiprism).

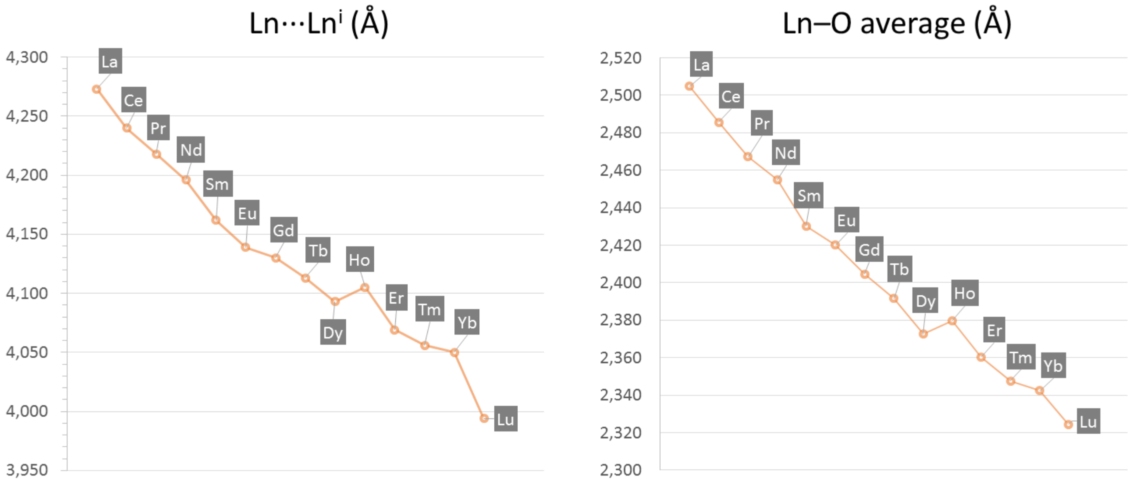

Figure 3.28. Variation of Ln···Ln shortest distances and average Ln–O bond lengths for all **1–Ln** derivatives. Symmetry code: i) 1–*x*, –*y*, 1–*z*.

Four different *trans–III* {Cu(cyclam)} complexes can be found in **1–Ln** structures. Three of them consist on a metal–organic block grafted to the Keggin surface (Cu1A, Cu1B and Cu1C) whereas the other one is a non–supported square planar cationic complex (Cu1D). The coordination sphere of Cu1A adopts a tetragonally elongated CuN_4O square pyramidal geometry, where the four N atoms of the ligand form the basal plane and the apical position is occupied by one terminal O atom from the cluster (O8). The distance Cu1A–O8 does not vary in a significant way as it ranges from 2.35 to 2.41 Å along the series. In contrast, the coordination spheres of both centrosymmetric Cu1B and Cu1C moieties show distorted octahedral geometries with the four N atoms of the cyclam ligand forming the equatorial plane and the axial positions occupied by terminal O atoms from different Keggin clusters (O1 and O2 for Cu1B and Cu1C, respectively, Figure 3.27). While these two CuN_4O_2 chromophores show a Jahn–Teller elongation, thedistortion is especially remarkable for Cu1C as indicated by the highest CShM values and its respective axial Cu–O bonds showing lengths near those of semi–coordination (Cu1C–O2 distances slightly vary from 2.64–2.69 Å, Table 3.11).

Table 3.11. Cu–O and Cu–N$_{mean}$ bond lengths (Å) as well as the polyhedral distorsion (CShM) in **1–Ln** compounds.

	1–La	**1–Ce**	**1–Pr**	**1–Nd**	**1–Sm**	**1–Eu**	**1–Gd**
Cu1A–N$_{mean}$	2.036	2.030	2.021	2.026	2.020	2.016	2.024
Cu1A–O8	2.379(10)	2.389(9)	2.390(8)	2.388(6)	2.403(9)	2.388(8)	2.381(10)
vOC–5	0.727	0.653	0.861	0.743	0.713	0.803	0.709
SPY–5	0.887	0.965	0.901	0.893	0.972	0.911	0.968
Cu1B–N$_{mean}$	2.011	2.030	2.022	2.023	2.027	2.022	2.024
Cu1B–O1	2.439(9)	2.462(8)	2.444(8)	2.445(6)	2.424(8)	2.440(8)	2.428(9)
Cu1B–O1^{i}	2.439(9)	2.462(8)	2.444(8)	2.445(6)	2.424(8)	2.440(8)	2.428(9)
OC–6	1.197	1.127	1.157	1.142	1.123	1.143	1.043
Cu1C–N$_{mean}$	2.018	2.032	2.022	2.026	2.000	2.023	2.033
Cu1C–O2	2.647(10)	2.657(9)	2.665(9)	2.660(7)	2.652(9)	2.666(9)	2.676(10)
Cu1C–O2^{ii}	2.647(10)	2.657(9)	2.665(9)	2.660(7)	2.652(9)	2.666(9)	2.676(10)
OC–6	1.997	2.047	2.106	2.010	2.058	2.073	2.063
Cu1D–N$_{mean}$	2.003	2.002	2.000	2.007	2.005	2.010	1.999
SP–4	0.320	0.339	0.291	0.242	0.166	0.232	0.210

	1–Tb	**1–Dy**	**1–Ho**	**1–Er**	**1–Tm**	**1–Yb**	**1–Lu**
Cu1A–N$_{mean}$	2.026	2.019	2.025	2.015	2.018	2.017	2.028
Cu1A–O8	2.378(8)	2.374(9)	2.412(9)	2.399(7)	2.382(5)	2.390(7)	2.386(9)
vOC–5	0.695	0.757	0.746	0.779	0.703	0.734	0.711
SPY–5	0.905	0.945	0.954	0.916	0.923	0.913	0.869
Cu1B–N$_{mean}$	2.026	2.041	2.033	2.026	2.024	2.021	2.026
Cu1B–O1	2.441(10)	2.435(9)	2.440(9)	2.438(7)	2.440(5)	2.435(7)	2.432(9)
Cu1B–O1^{i}	2.441(10)	2.435(9)	2.440(9)	2.438(7)	2.440(5)	2.435(7)	2.432(9)
OC–6	1.088	1.028	1.073	1.078	1.094	1.075	1.082
Cu1C–N$_{mean}$	2.028	2.024	2.019	2.021	2.022	2.019	2.016
Cu1C–O2	2.677(9)	2.664(9)	2.680(9)	2.653(10)	2.660(8)	2.682(7)	2.677(9)
Cu1C–O2^{ii}	2.677(9)	2.664(9)	2.680(9)	2.653(10)	2.660(8)	2.682(7)	2.677(9)
OC–6	2.062	2.055	2.135	1.989	2.062	2.152	2.139
Cu1D–N$_{mean}$	2.001	2.007	2.011	2.004	2.009	2.007	2.007
SP–4	0.226	0.223	0.221	0.167	0.181	0.182	0.209

Symmetry codes: i) −*x*, −1−*y*, 1−*z*; ii) 1−*x*, −*y*, 1−*z*. CShM: reference polyhedra SP–4 (square), vOC–5–(vacant octahedron), SPY–5 (square pyramid) and OC–6 (octahedron).

The crystal packing of the **1–Ln** compounds can be described as a covalent bidimensional arrangement formed through the coordination of contiguous hybrid dimers through the {Cu(cyclam)} moieties generating a staggered brickwork assembly parallel to the (1–10) plane (Figure 3.28). This way, each monosubstituted Keggin subunit results connected to two neighboring clusters through the Cu1B and Cu1C bridging moieties which leads to the formation of the hybrid layers (Figure 3.28b). In contrast, the Cu1A antenna moiety is slightly oriented toward the intralamellar space where the square–planar Cu1D complex is located. The covalent layers stack alongside the [1–10] direction (Figure 3.28a) by means of an extensive supramolecular network of N–H···O and C–H···O intermolecular interactions between these two Cu1A and Cu1D moieties and the O atoms belonging to Keggin anions of adjacent layers, as well as some of the water molecules of hydration (O1W, O4W, O5W, O7W and O9W) and the carboxylic O atoms of the acetate bridging ligands (Tables 3.12 and 3.13). These intermolecular interactions also take place within the layers, as the bridging Cu1B and Cu1C complexes display numerous favorable N–H···O and C–H···O interactions toward contiguous Keggin subunits. This disposition of the ligands creates an hexagonal metalorganic framework along the [111] direction where the polyanions are located generating a massive H–bonding network (Figure 3.28c) which further contribute to the overall stability of the bi–dimensional hybrid assembly.

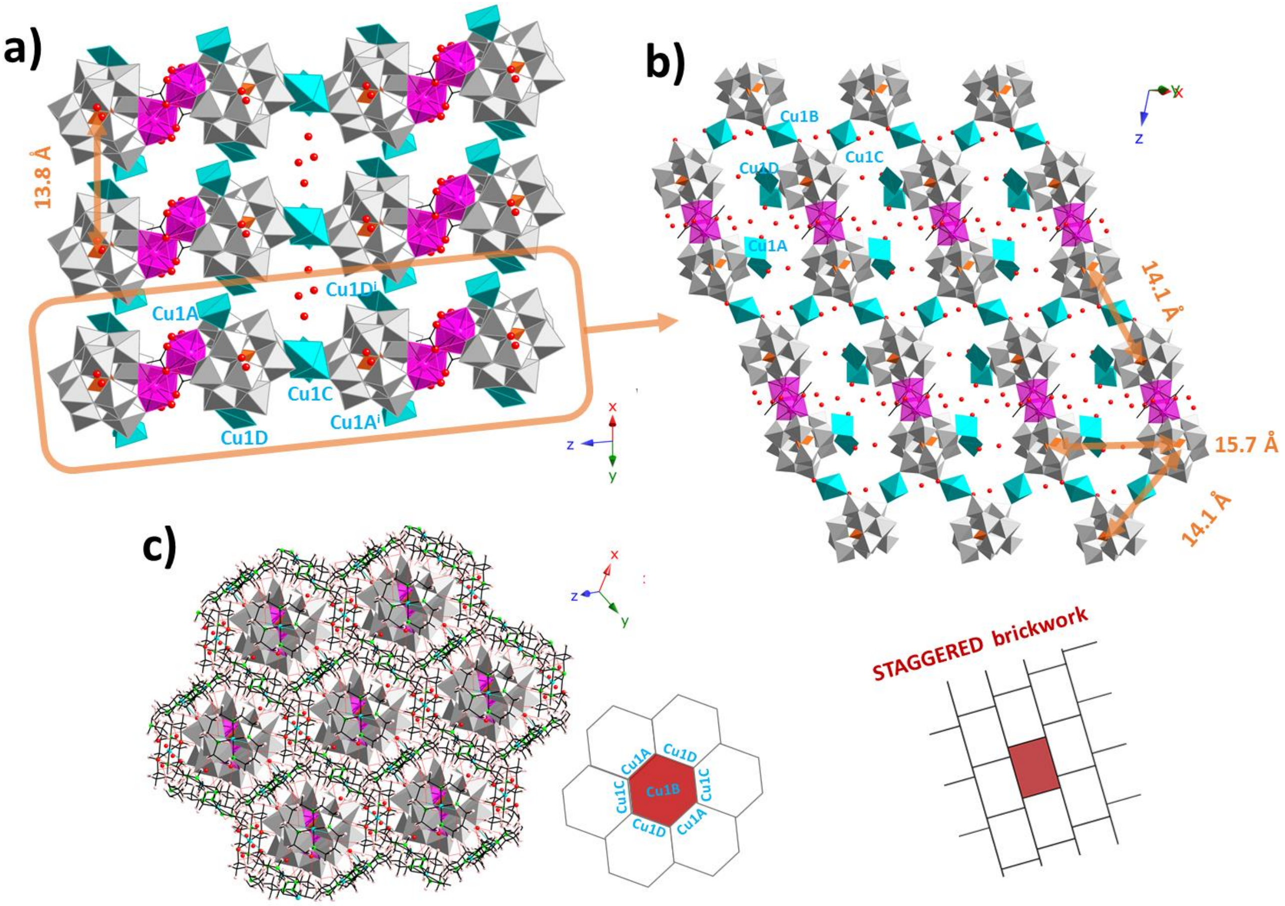

Figure 3.28. a) Crystal packing of **1–Ln** (Ln = Eu) hybrids along the [110] direction and b) hybrid covalent layers in the (1–10) plane. Cyclam ligands are omitted for clarity. c) Hexagonal metalorganic framework showing the massive H–bond network. Color code: W (grey), Ge (orange), Cu (blue), Ln (pink), N (green), O (red), C (black), H (pale pink). Symmetry codes: i) 1–*x*, –*y*, 1–*z*; (ii) –*x*, –1–*y*, 1–*z*.

Table 3.12. Intermolecular N···O and C···O interactions (Å) in **1–Ln** compounds (Ln = La–Gd).

Donor···Acceptor	1–La	1–Ce	1–Pr	1–Nd	1–Sm	1–Eu	1–Gd
N1A···O510[i]	2.91(2)	2.927(19)	2.929(16)	2.908(12)	2.919(14)	2.939(18)	2.921(19)
N4A···O7W	3.12(3)	3.10(2)	3.16(2)	3.176(15)	3.212(16)	3.19(2)	3.16(2)
N8A···O4W	3.01(4)	2.98(3)	3.01(2)	2.99(2)	3.009(19)	2.97(2)	2.99(2)
N11A···O410[i]	2.974(19)	3.011(19)	2.977(17)	2.981(12)	2.981(15)	2.974(17)	3.00(2)
C3A···O2AC[ii]	3.41(3)	3.43(2)	3.11(2)	3.406(14)	3.436(16)	3.422(18)	3.45(2)
C5A···O2AC[ii]	3.36(3)	3.33(2)	3.43(2)	3.267(13)	3.261(19)	3.318(19)	3.28(3)
C13A···O45[i]	3.28(4)	3.28(2)	3.21(2)	3.193(16)	3.215(17)	3.23(2)	3.21(2)
N1B···O19	3.094(14)	3.062(13)	3.32(2)	3.070(9)	3.081(13)	3.087(12)	3.080(16)
N4B···O13	2.904(14)	2.887(13)	3.063(13)	2.895(9)	2.882(12)	2.913(13)	2.896(15)
C2B···O9	3.253(19)	3.238(17)	2.897(12)	3.252(13)	3.229(15)	3.293(17)	3.240(19)
C7B···O5W	3.44(2)	3.46(2)	3.225(16)	3.439(16)	3.43(2)	3.48(2)	3.44(2)
N1C···O12[iii]	2.886(14)	2.915(14)	3.055(13)	2.892(11)	2.923(14)	2.913(13)	2.906(19)
N4C···O25	3.052(14)	3.062(14)	3.45(2)	3.046(10)	3.030(12)	3.038(14)	3.12(2)
C3C···O5	3.223(2)	3.229(19)	2.912(13)	3.209(13)	3.211(17)	3.200(16)	3.21(2)
C3C···O1W[iii]	3.48(2)	3.454(18)	3.215(18)	3.449(13)	3.442(17)	3.469(16)	3.43(3)
C7C···O2	3.235(19)	3.23(2)	3.444(18)	3.228(15)	3.238(17)	3.213(17)	3.22(2)
N1D···O37	3.31(2)	3.297(18)	3.24(3)	3.295(13)	3.343(18)	3.305(17)	3.31(2)
N4D···O9[iv]	3.067(19)	3.099(19)	2.881(18)	3.072(12)	2.903(17)	3.096(15)	3.05(2)
N4D···O5W[iv]	3.01(3)	3.01(3)	3.074(18)	3.021(17)	3.027(16)	3.03(2)	3.04(3)
N8D···O911[iv]	2.765(19)	2.771(18)	3.290(19)	2.770(12)	3.313(18)	2.778(15)	2.76(2)
N11D···O6	3.303(19)	3.3011(19)	2.777(16)	3.296(12)	2.781(17)	3.285(14)	3.29(2)
N11D···O67	2.91(2)	2.88(2)	3.316(17)	2.884(10)	3.201(16)	2.876(15)	2.89(2)
C2D···O3	3.28(3)	3.26(3)	3.40(3)	3.258(17)	3.41(2)	3.24(2)	3.25(3)
C5D···O7	3.31(3)	3.30(3)	3.02(2)	3.350(14)	3.08(2)	3.36(2)	3.34(3)
C6D···O9W[ii]	2.92(4)	3.05(4)	3.35(2)	3.38(3)	3.29(2)	3.44(4)	3.32(5)
C12D···O49[iv]	3.36(3)	3.39(3)	3.36(5)	3.379(17)	3.32(3)	3.387(19)	3.40(3)
C13D···O26	3.36(3)	3.38(3)	3.38(2)	3.378(18)	3.41(2)	3.39(2)	3.37(3)

Symmetry codes: i) x, $-1+y$, z; ii) $1-x$, $-1-y$, $2-z$; iii) $1-x$, $-y$, $1-z$; iv) $1+x$, y, z.

PLATON analyses reveal slight residual solvent accessible microvoids in all **1–Ln** derivatives. These empty volumes sum up to *ca.* 112–122 Å^3, which corresponds to 4% of the total volume of the unit cell, could suggest that these microvoids are a direct consequence of the highly disordered lattice water molecules. In contrast, the total solvent accessible volume ranges from 697 to 734 Å^3 (*ca*. 18% of the unit cell volume) across the series.

A structural comparison between the different **1–Ln** derivatives reveals an overall decrease of the cell parameter *c* with Ln radius whereas the other directions display a less regular trend (Figure 3.29). This was expected since the Ln atoms are aligned along the *z* axis and thus, this variation is a direct result of the lanthanide contraction. In a similar way, the variation of the cell volume *V* as a function of the Ln radius shows a similar profile which can be explained in the same way, although from Eu to Ho derivatives a more irregular trend can be observed. As mentioned above, Cu1C–O distances are significantly longer than those displayed by Cu1B complex indicating a weaker coordination bond for the former. Cu1C–O distance generally increases with the atomic number until **1–Dy**, after which it follows a fluctuating trend for the late lanthanide derivatives in such a way that **1–La** and **1–Pr** show the shortest while **1–Ho** and **1–Yb** display the weakest bond. The remaining bridging moiety Cu1B as well as Cu1A antenna complexes show distances to terminal O1 and O8 atoms that oscillate across the entire Ln derivatives.

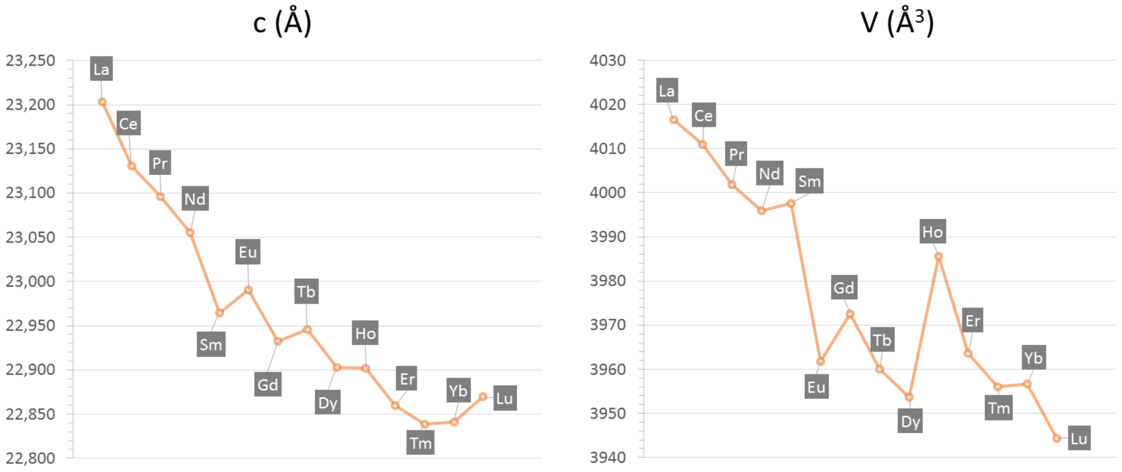

Figure 3.29. Variation of cell parameters *c* and unit cell volume (*V*) in the series of **1–Ln** derivatives.

Table 3.13. Intermolecular N···O and C···O interactions (Å) in **1–Ln** compounds (Ln = Tb–Lu).

Donor···Acceptor	**1–Tb**	**1–Dy**	**1–Ho**	**1–Er**	**1–Tm**	**1–Yb**	**1–Lu**
N1A···O510^{i}	2.901(14)	2.90(2)	2.948(14)	2.936(12)	2.921(10)	2.920(11)	2.918(16)
N4A···O7W	3.151(15)	3.14(2)	3.174(16)	3.190(13)	3.189(10)	3.185(14)	3.242(19)
N8A···O4W	2.994(17)	2.99(3)	3.02(2)	3.014(15)	3.012(11)	3.016(16)	3.04(2)
N11A···O410^{i}	2.970(14)	2.973(18)	2.949(14)	2.988(12)	2.979(8)	2.973(12)	2.961(15)
C3A···O2AC^{ii}	3.449(17)	3.46(2)	3.100(18)	3.444(14)	3.479(10)	3.119(15)	3.445(19)
C5A···O2AC^{ii}	3.275(16)	3.27(2)	3.467(17)	3.264(15)	3.272(10)	3.467(14)	3.274(18)
C13A···O45^{i}	3.205(17)	3.21(2)	3.219(16)	3.192(14)	3.192(10)	3.177(14)	3.17(2)
N1B···O19	3.059(11)	3.058(15)	3.255(16)	3.076(11)	3.065(8)	3.276(13)	3.054(13)
N4B···O13	2.889(11)	2.902(15)	3.052(14)	2.901(11)	2.903(9)	3.075(11)	2.898(13)
C2B···O9	3.236(14)	3.256(18)	2.905(13)	3.250(14)	3.260(10)	2.904(10)	3.267(16)
C7B···O5W	3.437(16)	3.47(2)	3.233(15)	3.426(16)	3.428(12)	3.281(13)	3.44(2)
N1C···O12^{iii}	2.891(14)	2.889(16)	3.041(14)	2.897(13)	2.903(9)	3.024(13)	2.908(14)
N4C···O25	3.045(13)	3.058(15)	3.46(4)	3.039(11)	3.030(9)	3.421(16)	3.021(14)
C3C···O5	3.234(16)	3.203(19)	2.908(15)	3.188(14)	3.186(11)	2.893(13)	3.197(17)
C3C···O1W^{iii}	3.434(17)	3.42(2)	3.196(17)	3.426(14)	3.444(11)	3.179(15)	3.426(19)
C7C···O2	3.239(15)	3.26(2)	3.45(2)	3.218(16)	3.228(11)	3.433(16)	3.223(18)
N1D···O37	3.297(13)	3.37(2)	3.245(19)	3.363(13)	3.382(9)	3.237(17)	3.279(14)
N4D···O9^{iv}	2.901(13)	2.87(2)	3.212(16)	2.890(13)	2.907(9)	3.319(12)	3.042(18)
N4D···O5W^{iv}	3.074(13)	3.030(18)	2.907(16)	3.045(15)	3.050(10)	2.892(12)	3.04(2)
N8D···O911^{iv}	3.366(14)	3.30(2)	3.324(15)	3.287(13)	3.287(9)	3.399(11)	2.783(14)
N11D···O6	2.766(12)	2.744(19)	3.324(16)	2.777(12)	2.754(8)	3.292(12)	3.280(16)
N11D···O67	3.302(14)	3.301(18)	2.746(15)	3.287(13)	3.327(9)	2.759(11)	2.917(15)
C2D···O3	3.385(17)	3.37(2)	3.400(16)	3.372(17)	3.371(12)	3.402(14)	3.264(18)
C5D···O7	3.039(15)	3.00(3)	3.034(16)	3.035(17)	3.021(11)	3.058(14)	3.37(2)
C6D···O9W^{ii}	3.359(16)	3.36(2)	3.04(4)	3.368(17)	3.375(12)	3.066(16)	3.30(4)
C12D···O49^{iv}	3.34(3)	3.17(7)	3.332(18)	3.24(2)	3.24(2)	3.371(15)	3.345(19)
C13D···O26	3.397(16)	3.37(3)	3.27(3)	3.441(16)	3.413(11)	3.23(3)	3.36(2)

Symmetry codes: i) *x*, –1+*y*, *z*; ii) 1–*x*, –1–*y*, 2–*z*; iii) 1–*x*, –*y*, 1–*z*; iv) 1+*x*, *y*, *z*.

In contrast, the square–planar Cu1D moiety located in the interlamellar space shows a distance to the nearest Keggin O atom (O9^{i} where i: 1+*x, y, z*) that vary from 2.79 to 2.89 Å as opposed to the significantly shorter Cu1B–O and Cu1A–O distances. In this sense, **1–Dy** shows the shortest Cu1D···O9 distance as opposed to the longest distance displayed by **1–Sm** derivative. These distances are related with the intralamellar distance and they do not display a regular trend along the series suggesting that the separation between layers and thus, the compaction of the crystal packing is not strongly affected by the lanthanide contraction effect.

SCSC transformation: 2–Ln structures

When single crystals of **1–Ln** were heated to 110 °C, several water molecules of hydration were removed and the partially hydrated intermediates were formed (**2–Ln**), as suggested from the TPXRD measurements. Similar to **1–Ln**, the unit cell of **2–Ln** intermediates contain a $[\{(\alpha\text{–GeW}_{11}\text{O}_{39})\text{Ln}(\text{H}_2\text{O})(\mu\text{–CH}_3\text{COO})\}_2]^{12-}$ dimeric fragment, six {Cu(cyclam)] cationic moieties (two of them centrosymmetric, Cu1B and Cu1C) and four water molecules of hydration. The partial dehydration brought forth drastic changes in the overall packing of **2–Ln** compared to that found in the hydrated phases, as important modifications in the Cu(II) bonding, and consequently in the dimensionality of the hybrid framework took place as a result of the thermally activated SCSC transformation (Figures 3.30 and 3.31).

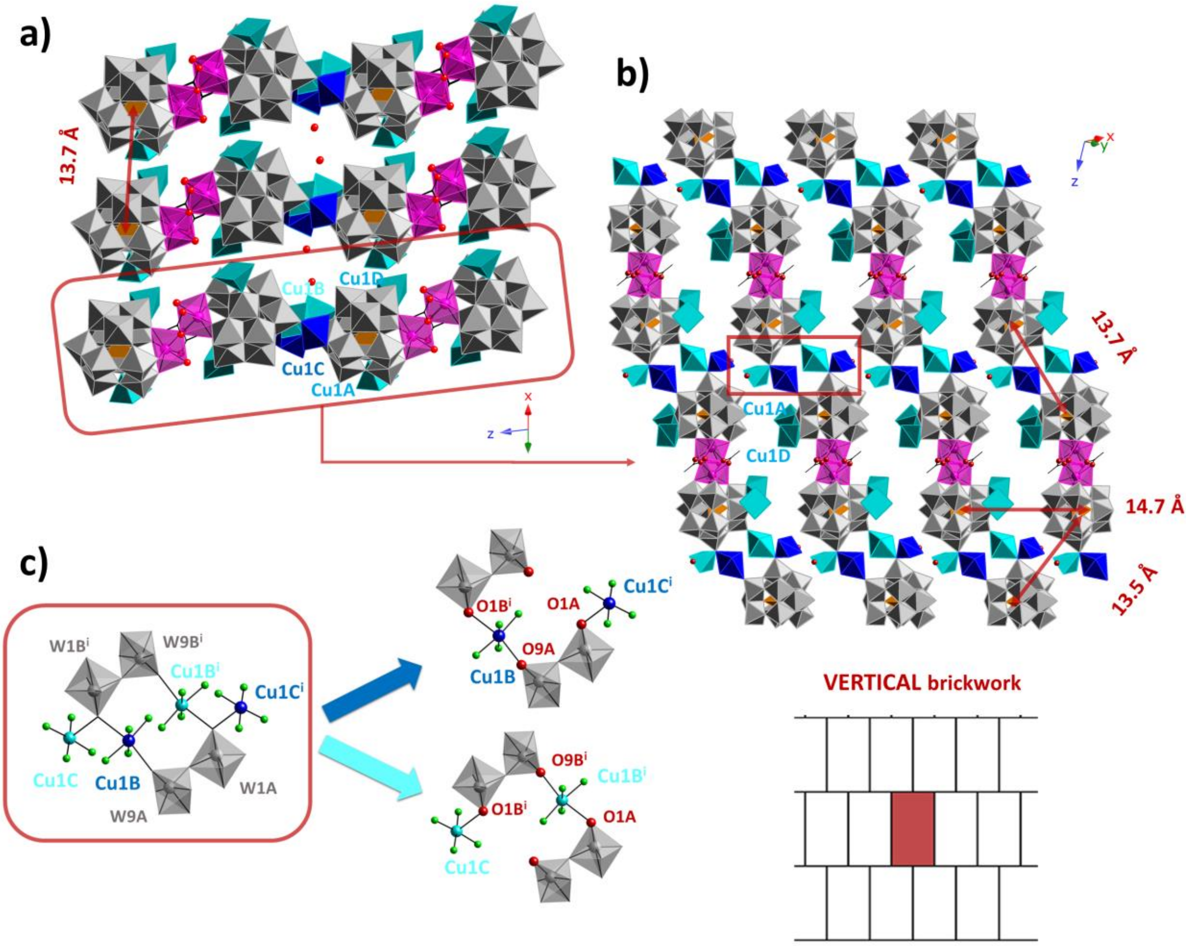

Figure 3.30. a) Crystal packing of **2–Ln** along [110] and b) in the (1–10) plane with partial atom labelling. c) Details of the crystallographic disorder showing the two equivalent forms. C and H atoms of the ligands are omitted for clarity. Color code: W (grey), Ge (orange), Cu (blue), Ln (pink), O (red), N (green). Symmetry code: i) –*x*, –*y*, 1–*z*.

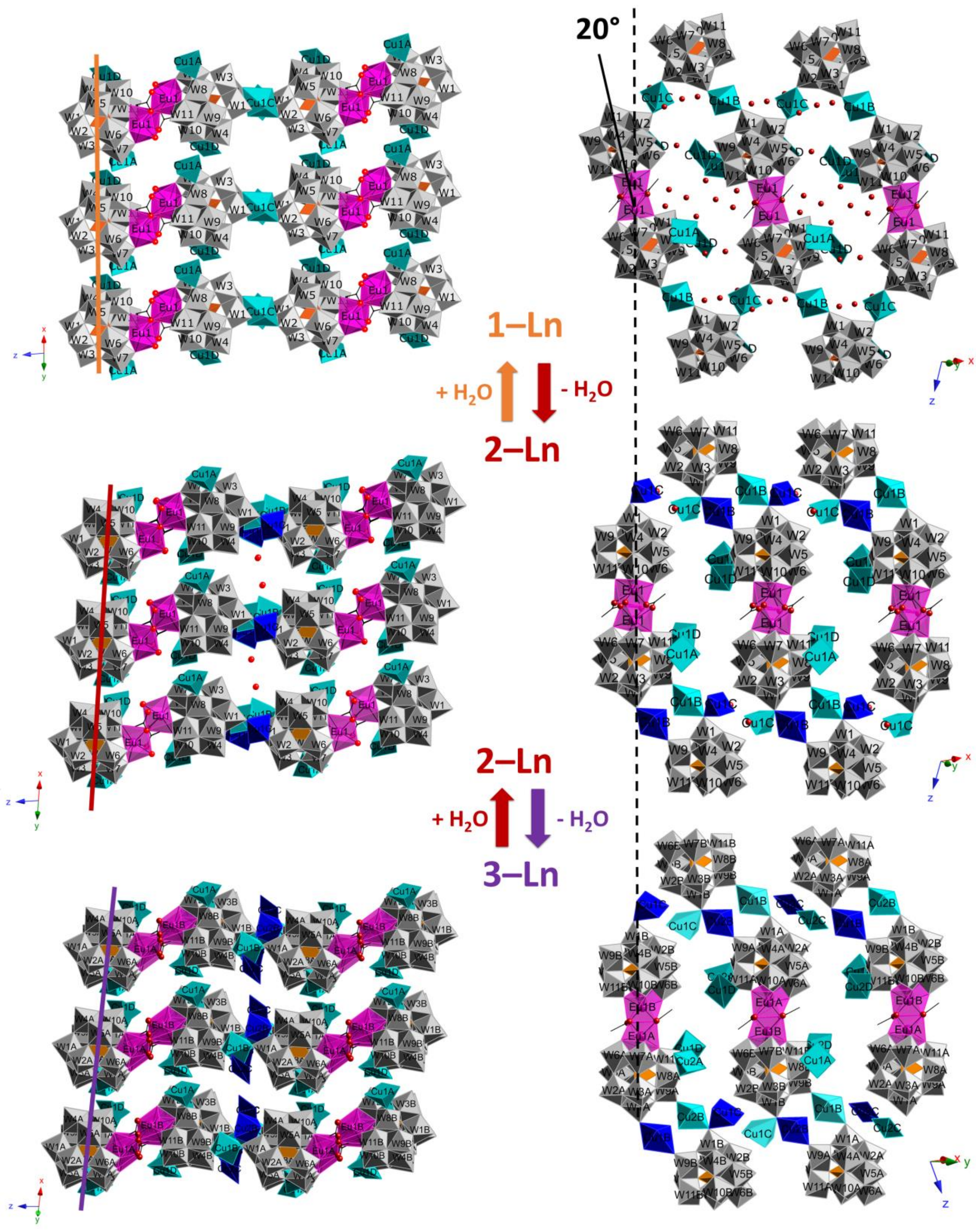

Figure 3.31. Structural comparison between the crystal packing of **1–Eu, 2–Eu** and **3–Eu** with atom labeling.

First, a slight shortening of the *a* parameter as well as a slight increase in *c* can be observed while the *b* parameter remained almost constant, which resulted in a smaller unit cell volume and hence, a more compacted crystal architecture (Tables 3.6–3.8). The most notable change, however, is the generation of a crystallographic disorder involving Cu1B and Cu1C moieties. This way, two crystallographically equivalent forms can be distinguished which are represented in Figure 3.30. While in **1–Ln** compounds each Keggin subunit results connected to two neighboring clusters through the Cu1B and Cu1C bridging moieties forming the hybrid layers, each polyanion in **2–Ln** connects a single adjacent Keggin by one Cu1B linking complex forming a chain–like hybrid assembly (Figures 3.30). Compared to Cu1B in **1–Ln** which bridged two W1 octahedra, even though it remains as an hexacoordinated bridging complex, Cu1C in **2–Ln** migrated from W1 to the adjacent W9 octahedron upon the gradual dehydration process resulting with a slightly longer Cu–O bond. In contrast, the former bridging complex Cu1C which connected two adjacent W2 in **1–Ln** migrated from one W2 to the neighboring W1 octahedron becoming an antenna ligand in **2–Ln** showing a slightly shorter Cu1C–O1 bond. Because of this, the dimensionality of **2–Ln** diminishes which changed from a covalent bi–dimensional packing in the (1–10) plane to a monodimensional one constituted by corrugated hybrid chains by means of Cu1B moieties along the *z* axis showing a vertical brickwork arrangement (Figures 3.30). This disposition originates from the approximately 20° rotation of each dimeric entity along the *z* axis compared to the hydrated phases that took place upon partial dehydration (Figure 3.31). The SCSC transformation also forced the countercation Cu1D which was located near W9 (Cu1D···O9 = 2.791(9) Å) in **1–Ln** to migrate to the neighboring W11 octahedron and thus, to coordinate to O11 terminal atoms becoming yet another antenna ligand in **2–Ln**. In comparison, Cu1A antenna complex remained largely the same as in **1–Ln** hydrated compounds, although with a notably stronger Cu1A–O8 bond than that shown in the parent phases (Table 3.14.)

Table 3.14. Cu–O bond and selected Cu···O distances (Å) as well as the polyhedral distorsion (CShM) of the {Cu(cyclam)} complexes observed in some **1–Ln**, **2–Ln** and **3–Ln** (Ln = Eu, Er) derivatives.

1–Ln			**2–Ln**			**3–Ln**			
	1–Eu	**1–Er**		**2–Eu**	**2–Er**	**3–Eu**			
Cu1A–O8	2.388(8)	2.399(7)	Cu1A–O8	2.264(14)	2.261(14)	Cu1A–O8B	2.212(12)	Cu2A–O8A	2.233(12)
vOC–5	0.803	0.779	vOC–5	0.617	0.660	vOC–5	0.395	vOC–5	0.444
SPY–5	0.911	0.916	SPY–5	1.144	1.167	SPY–5	1.019	SPY–5	1.047
Cu1B–O1	2.440(8)	2.438(7)	Cu1B–O9	2.410(18)	2.429(16)	Cu1B–O9B^{v}	2.574(12)	Cu2B–O9A	2.258(13)
Cu1B–O1^{i}	2.440(8)	2.438(7)	Cu1B–O1^{iv}	2.549(20)	2.537(11)	Cu1B–O1A	2.527(11)	Cu2B–O1B^{v}	2.408(12)
OC–6	1.143	1.078	OC–6	1.633	1.286	OC–6	1.459	OC–6	1.198
Cu1C–O2	2.666(9)	2.653(10)	Cu1C–O1^{iv}	2.561(18)	2.718(13)	Cu1C–O1B^{v}	2.757(13)	Cu2C···O1A	3.488(13)
Cu1C–O2^{ii}	2.666(9)	2.653(10)							
OC–6	2.073	1.989	SPY–5	1.854	5.938*	SPY–5	3.558*	SP–4	0.152
Cu1D···O9^{iii}	2.791(9)	2.820(9)	Cu1D–O11	2.268(13)	2.256(14)	Cu1D–O11A	2.294(12)	Cu2D–O11B	2.296(13)
SP–4	0.232	0.167	vOC–5	0.938	0.681	vOC–5	1.007	vOC–5	0.874
—	—	—	SPY–5	1.245	1.108	SPY–5	1.380	SPY–5	0.912

Symmetry codes: i) –*x*, –1–*y*, 1–*z*; ii) 1–*x*, –*y*, 1–*z*; iii) 1+*x*, *y*, *z*; iv) –*x*, –*y*, 1–*z*; v) *x*, *y*, 1+*z*. CShM: reference polyhedra SP–4 (square), SPY–5 (square pyramid), vOC-5-(vacant octahedron) and OC–6 (octahedron). * Expected high CShM values due to strong crystallographic disorder.

Partial dehydration also resulted in a significant contraction along the *z* axis leading to a more compacted crystal packing along the direction where the hybrid chains extend (Tables 3.6–3.8). Taking the Eu derivative as an example, this is clearly reflected in the Ge···Ge distances between contiguous Keggin anions belonging to the same row which are significantly longer in the hydrated phases (**1–Eu**, Ge···Ge = 15.7 Å, Figure 3.28) compared to the equivalent distance found in **2–Eu** compound (Ge···Ge = 14.7 Å; Figure 3.30). Similarly, the distance between consecutive dimers along the direction where the hybrid chains meander in **2–Ln** (Ge···Ge = 13.7 Å and 13.5 Å) is notably reduced compared to the equivalent one observed in **1–Ln** (Ge···Ge = 14.1 Å). In contrast, the Ge···Ge distances between the nearest Keggin units belonging to different layers, remained nearly constant along the *x* axis (**1–Eu**, Ge···Ge = 13.8 Å) compared to those found in **2–Eu** between adjacent Keggin polyanions belonging to different hybrid chains (Ge···Ge = 13.7 Å). PLATON analyses reveal small residual solvent accessible microvoids that sum up to 6% of the total volume of the unit cell, which amounts to *ca.* 183 Å^3 in **2–Eu** derivative and corresponds to approximately six water molecules of hydration per dimeric entity. The total solvent accessible volume, however, sum up to *ca.* 300 Å^3 (8% of the unit cell volume) which drastically decreased compared to the parent hydrated phases (18%), further evidencing the compaction that took place upon the SCSC process.

SCSC transformation: 3–Ln structures

When single crystals of **1–Ln** or **2–Ln** were heated to 180 °C, total removal of all water molecules was achieved resulting in the anhydrous **3–Ln** structures. The measured dehydrated phases (Ln = Ce, Eu) show isomorphism just like the parent hydrated and intermediate analogues between them, as well as an identical crystallographic disorder in which two {Cu(cyclam)} moieties are disordered over four positions with identical occupancy (Cu1B, Cu1C, Cu2B and Cu2C), evidencing an absence of dependence with the Ln atoms. Even though the space group remained unchanged, some notable structural modifications could be observed compared to the previous partially hydrated phases.

The second SCSC transformation almost doubled the lattice parameter *b* and consequently, the content and volume of the unit cell (Tables 3.6–3.8). The unit cell of **3–Ln** contains two hybrid dimeric entities $[\{(\alpha\text{–}GeW_{11}O_{39})Ln(\mu\text{–}CH_3COO)\}_2]^{12-}$ (labelled as A and B) and twelve {Cu(cyclam)} cationic moieties, four of them (Cu1B, Cu1C, Cu2B and Cu2C) involved in the strong crystallographic disorder mentioned above and in the experimental section (Figure 3.32). These changes in the unit cell resulted in the generation of four new crystallographically independent {Cu(cyclam)} complexes (Cu2A–Cu2D) for each of the four crystallographically independent moieties found in **1–Ln** and **2–Ln** compounds (Cu1A–Cu1D). Despite this, the overall crystal structure of the anhydrous **3–Ln** is highly reminiscent of that described for the **2–Ln** intermediates as it still consist on hybrid chains that extend along the *z* axis in a zig–zag manner, although notable changes were observed in some of the metallocyclam complexes. Regarding the latter, Cu1A and Cu1D as well as the related Cu2A and Cu2D moieties did not undergo major modifications as both the geometry and grafting point of the 3d–metal and their Cu–O bond lengths remained comparable to those found in **2–Ln** (Table 3.14). In contrast, the metallocyclam complexes involved in the crystallographic disorder, that is Cu1B, Cu1C and their related Cu2B, Cu2C moieties, did suffer significant changes in their coordination distances after total dehydration.

The mentioned crystallographic disorder is stronger than that observed for **2–Ln**, which is identical for both **3–Ce** and **3–Eu** and it is represented in Figures 3.32c. In this sense, two {Cu(cyclam)} moieties are disordered over four positions (Cu1B, Cu1C, Cu2B and Cu2C). Since the organic ligands of Cu1C–Cu2B and Cu1B–Cu2C pairs overlap with each other and the Cu1C–

Cu2B pair share the terminal O atom at which they are grafted, only one pair of complexes can exist at a given time, (Cu1B–Cu1C and Cu2B–Cu2C). As opposed to the disorder observed in **2–Ln** structures, these two forms are not equivalent, although the overall monodimensional packing showed by each form does not change in a significant way. This fact is corroborated attending to the virtually identical occupation for each form observed during the free structural refinement, as indicated above. The form composed of Cu1B and Cu1C is virtually identical to that observed in the previous **2–Ln**, although a significant increase in the Cu1B–O9B bond distance can be observed, indicating a weaker coordination between dimers that form the hybrid zig–zag chains (Table 3.14). In contrast, the increase in the bond distance is particularly notable in Cu1C–O1B, as the distorted antenna moiety is grafted to the POM with a bond length near semicoordination. Alternatively, the second form is not crystallographically equivalent to the former and hence, it differs from those observed in **2–Ln** (Figure 3.33). In this sense, Cu2B bridges O1B and O9B atoms belonging to adjacent polyanions forming the chains with comparable bond lengths to those observed in **2–Ln**. However, the remaining metalorganic moiety Cu2C is not connected to any terminal O atoms and hence, acts as a square–planar tetracoordinated complex instead of the antenna role that its related Cu1C fulfilled in the alternate form (Figure 3.33).

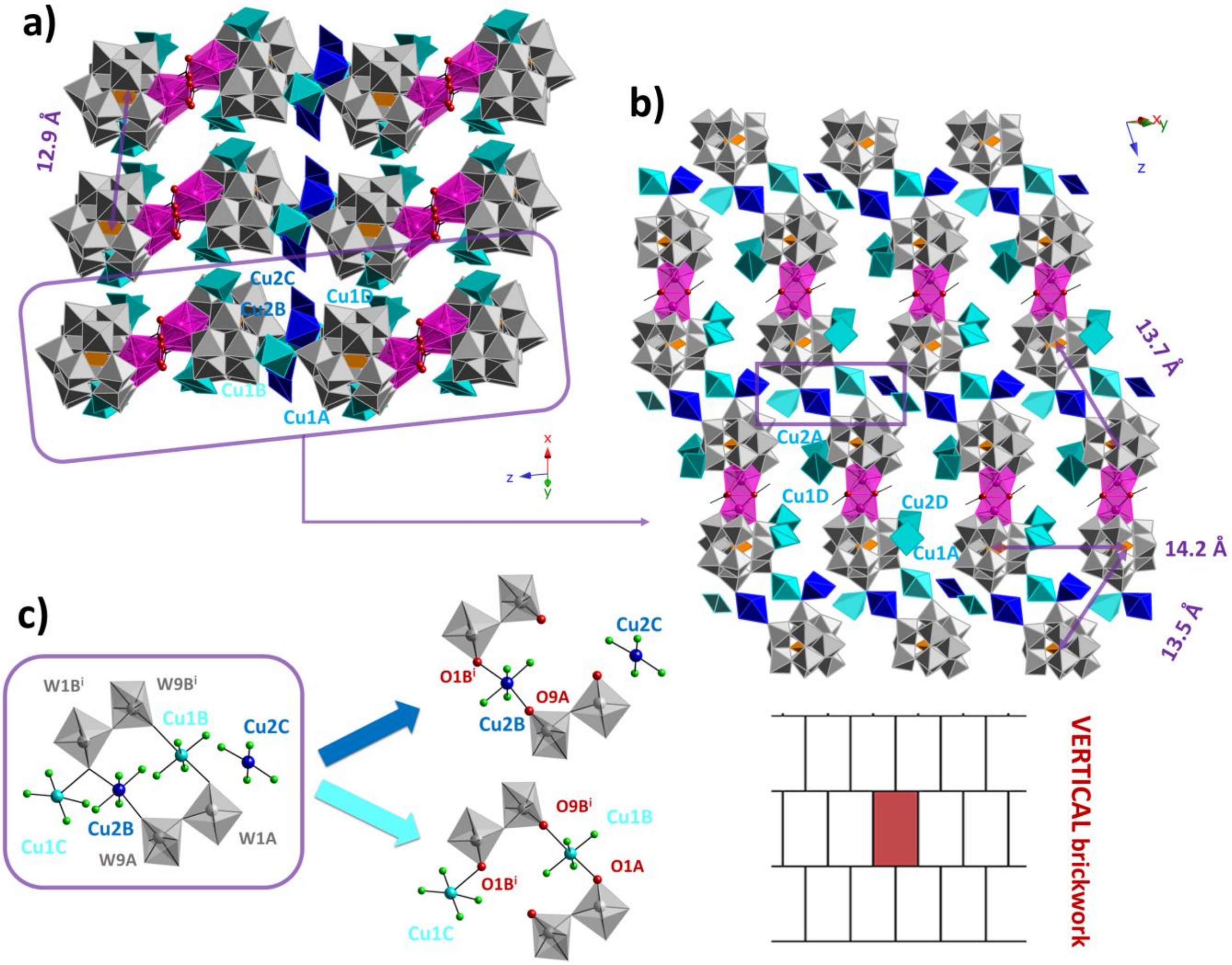

Figure 3.32. a) Crystal packing of **3–Ln** along [110] and b) in the (1–10) with partial atom labelling. c) Details of the crystallographic disorder showing the two non–equivalent forms. C and H atoms of the ligands are omitted for clarity. Color code: W (grey), Ge (orange), Cu (blue), Ln (pink), O (red), N (green). Symmetry code: i) 1–*x*, 2–*y*, –*z*.

Table 3.15. Comparison between the Ln–O bonds lengths (Å) as well as the polyhedral distorsion (CShM) of the Ln polyhedra in **1–Ln**, **2–Ln** and **3–Ln** (Ln = Eu).

1–Eu		2–Eu		3–Eu			
Eu1–O6F	2.387(7)	Eu1–O6F	2.329(12)	Eu1A–O6FA	2.316(11)	Eu1B–O6FB	2.344(11)
Eu1–O7F	2.375(7)	Eu1–O7F	2.359(11)	Eu1A–O7FA	2.326(10)	Eu1B–O7FB	2.338(11)
Eu1–O10F	2.357(7)	Eu1–O10F	2.360(13)	Eu1A–O0FA	2.270(11)	Eu1B–O0FB	2.278(12)
Eu1–O11F	2.333(7)	Eu1–O11F	2.303(14)	Eu1A–O1FA	2.285(11)	Eu1B–O1FB	2.257(11)
Eu1–O1AC	2.435(8)	Eu1–O1AC	2.491(13)	Eu1A–O1AC	2.682(11)	Eu1B–O3AC	2.584(11)
Eu1–O2AC	2.511(8)	Eu1–O2AC	2.536(13))	Eu1A–O2AC	2.411(13)	Eu1B–O4AC	2.426(12)
Eu1–O1AC^{i}	2.540(8)	Eu1–O1AC^{ii}	2.547(12)	Eu1A–O3AC	2.399(11)	Eu1B–O1AC	2.465(11)
Eu1–O1WF	2.423(8)	Eu1–O1WF	2.462(17)	—	—	—	—
Eu1–O$_{\text{average}}$	2.420	Eu–O$_{\text{average}}$	2.423	Eu1A–O$_{\text{average}}$	2.384	Eu1B–O$_{\text{average}}$	2.384
BTPR–8	1.508	BTPR–8	1.172	CTPR–7	2.690	CTPR–7	2.386
SAPR–8	1.688	SAPR–8	1.831	COC–7	3.952	COC–7	4.101

Symmetry codes: i) 1–*x*, –*y*, 2–*z*; ii) 1–*x*, 1–*y*, 2–*z*. CShM: reference polyhedra COC–7 (capped octahedron), CTPR–7 (capped trigonal prism), BTPR–8 (biaugmented trigonal prism) and SAPR–8 (square antiprism).

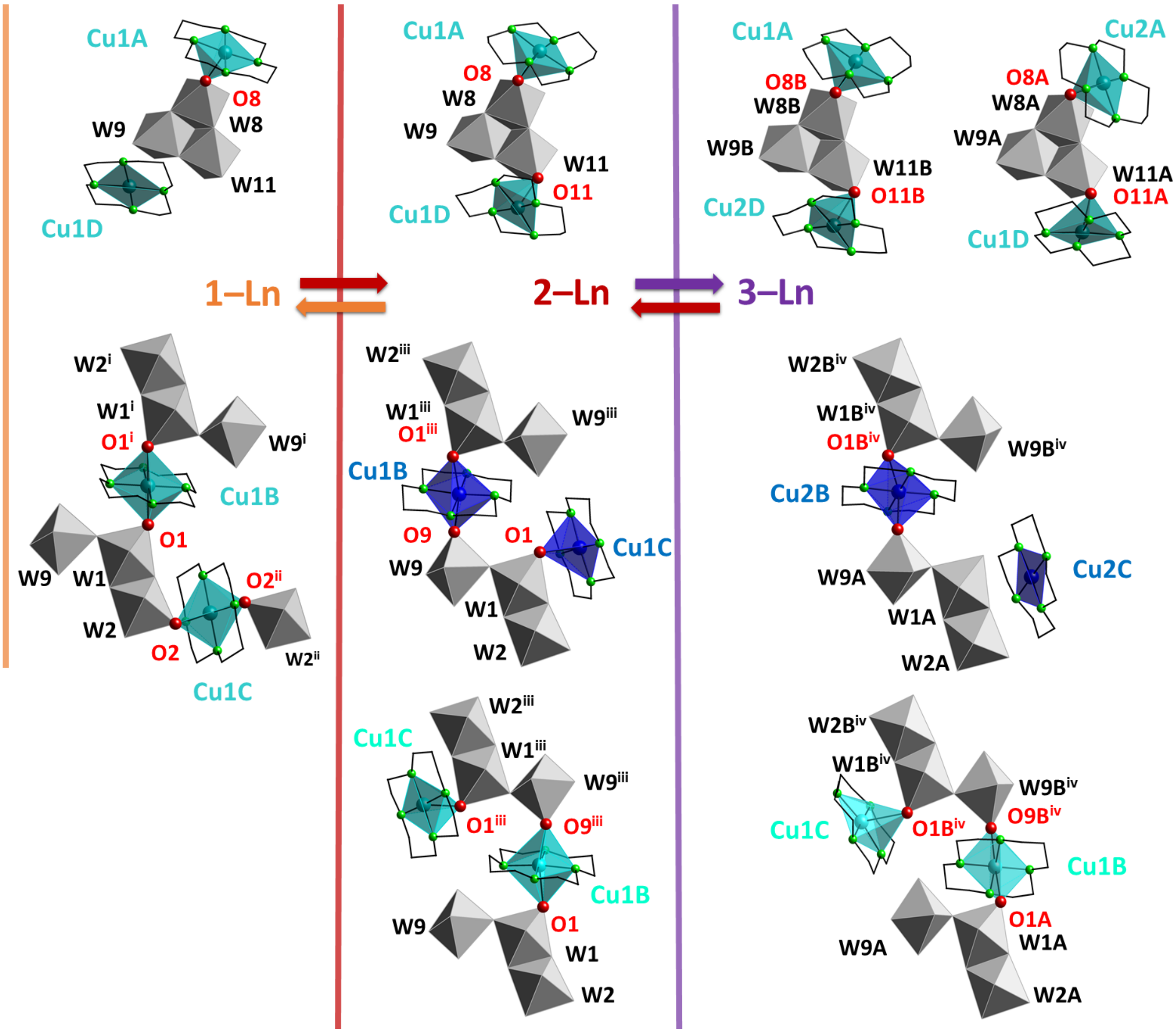

Figure 3.33. Evolution of the connectivity and geometry of the different Cu(cyclam) complexes found in **1–Ln** through the sequential SCSC transformations with atom labelling. Cu atoms belonging to the different forms of the crystallographic disorders in **2–Ln** and **3–Ln** are colored differently. H atoms are omitted for clarity. Color code: W (grey), Cu (blue), O (red), N (Green). Symmetry codes: i) –*x*, –1–*y*, 1–*z*; ii) 1–*x*, –*y*, 1–*z*, iii) –*x*, –*y*, 1–*z*, iv) *x*, *y*, 1+*z*.

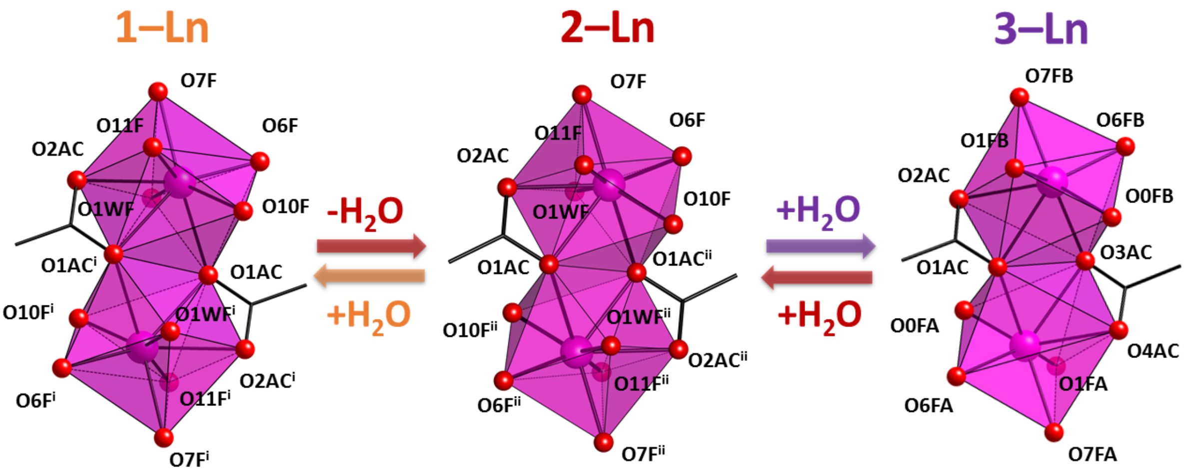

Figure 3.34. Comparison of the coordination sphere of Ln upon dehydration in **1–Ln**, **2–Ln** and **3–Ln** with atom labelling (Ln = Eu). Symmetry codes: i) 1–*x*, –*y*, 2–*z*; ii) 1–*x*, 1–*y*, 2–*z*.

PLATON calculations indicate several solvent accessible voids that sum up to a total of 400 Å^3 (6% of the total volume of the unit cell) which is comparable to the value of 8% found in the intermediate phases. Total dehydration induced the removal of the coordination water O1WF linked to the Ln centers changing their geometry from a highly distorted octacoordinated biaugmented trigonal prims (BTPR) to a less common seven–coordinated distorted capped trigonal prism (CTPR) geometry (Figures 3.34), showing significant modifications in the Ln–O bond lengths of their coordination spheres (Table 3.15).

Continuos Shape Measures (CShM)

Lanthanide atoms in each $\{(\alpha\text{–GeW}_{11}\text{O}_{39})\text{Ln(H}_2\text{O)}(\mu\text{–CH}_3\text{COO})\}_2$ anion belonging to non–anhydrous phases (**1–Ln** and **2–Ln**) display highly distorted eight–coordinated geometries that have been analyzed through Continuous Shape Measures (CShM).[91] For the lanthanide atoms in fully hydrated phases, CShM values in the 1.48–1.71 range have been obtained with the biaugmented trigonal prism (BTPR) as the reference shape, whereas close CShM values (1.50–1.69) relative to the square antiprism (SAPR) can also be observed, with the exception of early lanthanides (La to Pr) that show considerably higher values (2.00–2.33, Table 3.10). Comparison with any other eight–coordinated reference polyhedron results in significantly higher values for all derivatives (above 2.50).

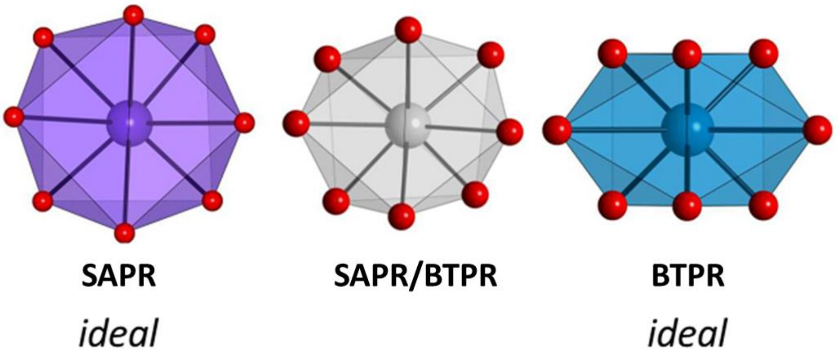

Figure 3.35. Reference ideal polyhedra for CShM calculations along with the distorted SAPR/BTPR polyhedra that best describe the octacoordinated Ln centers in both **1–Ln** and **2–Ln** compounds.

Nevertheless, the SAPR versus BTPR shape map shows that the 4f scatter from the ideal SAPR geometry toward the BTPR one, but lying outside the trend marked by the minimal distortion pathway between the two reference polyhedra with path deviation values in the 0.58–0.84 range (far away from the upper limit of 0.3 established by Casanova et al.). In comparison, the values obtained for **2–Ln** structures are slightly lower for both SAPR and BTPR reference geometries (Table 3.15), indicating that the partial dehydration resulted in a less distorted Ln polyhedra. These results confirm the best description of the lanthanide centers as highly distorted eight coordination polyhedra in intermediate stages between BTPR and SAPR ideal geometries (Figure 3.35). In contrast, the uncommon heptacoordinated lanthanide centers found in the anhydrous **3–Ln** phases consist in a strongly distorted capped trigonal prism shape showing high CShM values ranging from 2.39–3.34 (Table 3.15), whereas calculations with any other reference heptacoordinated shapes resulted in values above 4.

Reversibility of the SCSC transformations

The anhydrous phases rapidly adsorbs water from ambient moisture within a day in open air conditions at room temperature (Ln = La to Lu), as evidenced by thermogravimetric measurements carried out one day after dehydrating the samples by heating freshly prepared samples to 180 °C (Figures 3.36 and A3.16–A3.20 in the Appendix). Given the speed of the rehydration process, the use of a desiccant was required to prevent the anhydrous phases from adsorbing water and thus, determine both the partially hydrated **2–Ln** (Ln = Eu, Er) and the anhydrous **3–Ln** (Ln = Ce, Eu) structures. However, a significant difference in the rehydration speed was observed because late–lanthanides derivatives seemed to rehydrate faster, as evidenced by the fact that we were unable to measure the anhydrous phases of Er, Yb and Lu–derivatives even with the use of the desiccant. Instead, the partially rehydrated phases **2–Ln** were measured (Ln = Er, Yb, Lu).

While the rehydration process is fully reversible and occurs rapidly within one day for all derivatives, the SCSC transformations are not in all cases, as evidenced by both single–crystal and powder XRD measurements on the same dehydrated/rehydrated samples used in the TGA analyses above. Interestingly, the early–lanthanide derivatives (Ln = La to Sm) revert back to the original phase **1–Ln** upon rehydration within a day in air exposure while mid–to–late derivatives (Ln = Eu to Lu) are unable to return completely to their initial phases under these conditions, as the PXRD patterns of the samples heated for the TGA analyses suggest (Figures 3.30 and A3.16–A3.20 in the Appendix). However, single–crystal XRD measurements on samples of Ce, Eu and Er, which were heated to 180 °C to assure total dehydration one day prior to the full data acquisition, resulted in the **1R–Ln** structures (Ln = Ce, Eu, Er) with the same unit cell as the corresponding parent **1–Ce**, **1–Eu** and **1–Er** phases (Table A3.1 in the Appendix). The PXRD patterns of mid–to–late Ln–analogues (Ln = Eu to Lu) indicate that, even though they fully rehydrate in one day just like the early Ln derivatives as seen in the TGAs above, the transformation to their corresponding parent **1–Ln** structure is far slower. In fact, the PXRD patterns exhibit diffraction maxima belonging to both **1–Ln** and **2–Ln** phases (Figures 3.30 and A3.16–A3.20 in the Appendix). Moreover, these diffraction patterns do not undergo any significant changes after 1 and 2 weeks in air exposure. In view of these contradictory results, we soaked the dehydrated samples of mid–to–late Ln derivatives (Ln = Eu to Lu) in water for 24 hours, after which new diffractograms were recorded. The obtained patterns coincide perfectly with the simulated ones obtained from the single crystal data of the parent hydrated **1–Ln** compounds (Figures 3.30 and A3.17–A3.20 in the Appendix), confirming both the reversibility as well as the difference in the kinetics governing the SCSC from **2–Ln** to **1–Ln**.

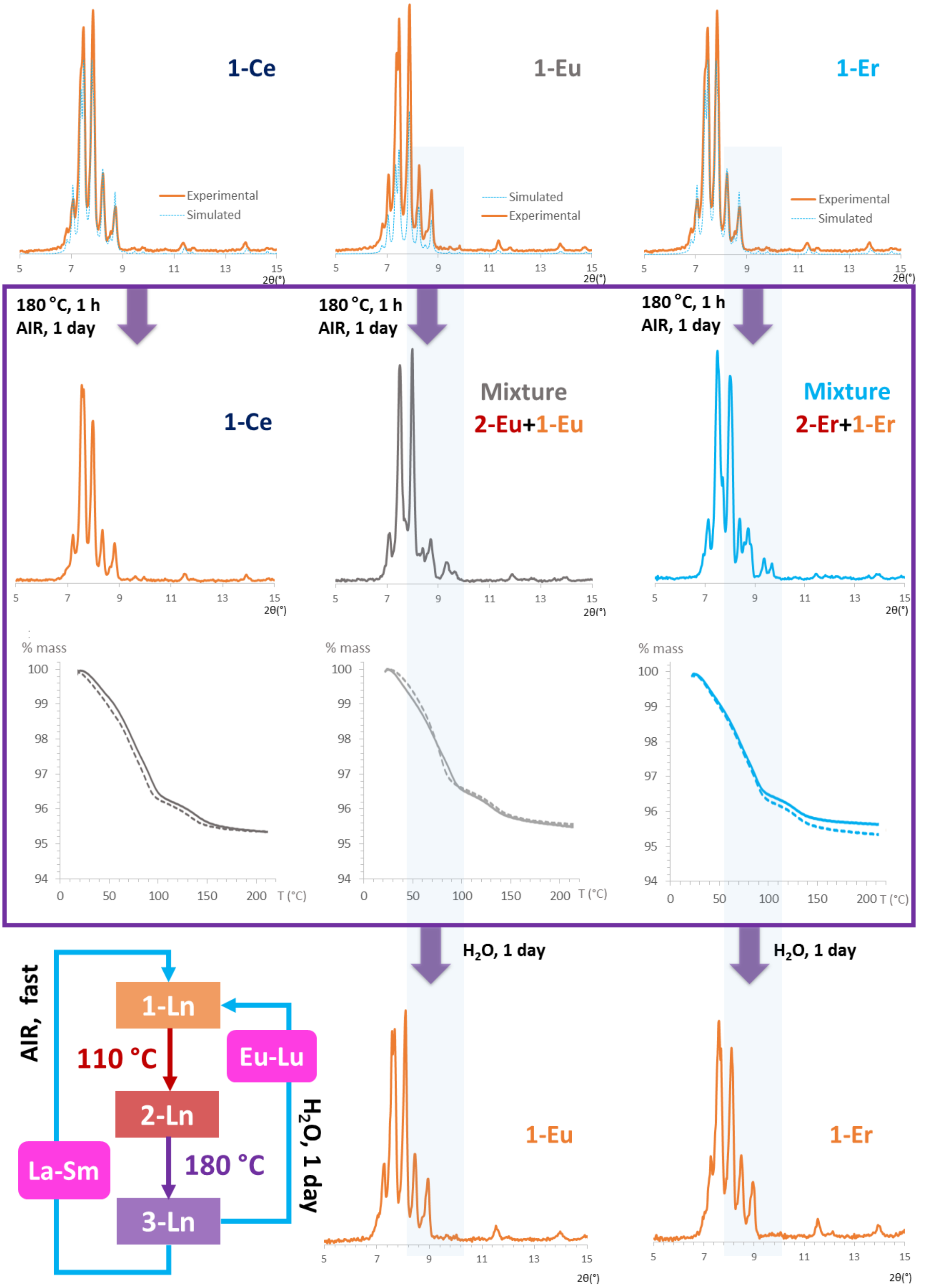

Figure 3.36. Study of the reversibility of the SCSC transformations for Ce, Eu and Er derivatives by TGA and PXRD techniques along with a scheme of the reversibility of the SCSC transformations for the different Ln derivatives.

In summary, the combined results from both single–crystal and powder–XRD together with the TGA curves from the dehydrated samples confirms that the SCSC transformations are totally reversible in air within 24 h for La–Sm derivatives while Er to Lu analogues required to be immersed in water for at least 24 h to fully revert back to their initial phase.

3.4 CONCLUSIONS

This chapter is divided into two well–differentiated sections: the first one consist on the study of SCCS transformations in heptatungstate–based hybrids whereas the second one involves lanthanide–substituted heteropolyoxotungstates.

In the first section, the preparation and full characterization of a porous three–dimensional covalent isoPOW hybrid, namely $[\{Cu(cyclam)\}_3(W_7O_{24})]\cdot 15.5H_2O$ (**1–CuW7**) (cyclam= 1,4,8,11–tetraazacyclotetradecane) has been carried out, in which gradual loss of water molecules of hydration upon heating triggers a series of sequential single–crystal–to–single–crystal structural transformations. These phase transitions result in the formation of two new supramolecular covalently layered porous structures as a straightforward consequence of modifications in the Cu(II) bonding of the complexes, layer sliding and cluster rearrangement within the hybrid layers upon dehydration, which are $[\{Cu(cyclam)\}_3(W_7O_{24})]\cdot 12H_2O$ (**2–CuW7**) and $[Cu(cyclam)]_{0.5}[\{Cu(cyclam)\}_{2.5}(W_7O_{24})]$ (**3–CuW7**), respectively. Interestingly, **1–CuW7** displays an interconnected systems of channels while **2–CuW7** show cavities of monodimensional nature with a significant lesser total solvent accessible volume. Unlike the hydrated phases, the anhydrous **3–CuW7** possess two types of crystallographically independent channels with slight different cross–sections. In terms of stability, **1–CuW7** and **2–CuW7** are chemically stable at ambient conditions while **3–CuW7** rapidly transform back to the partially hydrated **2–CuW7** phase under ambient conditions. The permanent porosity was confirmed by gas sorption measurements, which revealed that our hybrid heptatungstate is able to adsorb moderate amounts of both N_2 and CO_2 gases.

In the second section, the entire family of heterometallic polyoxotungstate–based dimeric hybrids (Ln = La to Lu), namely, $[Cu(cyclam)]_2[\{Cu(cyclam)\}_4\{(\alpha–GeW_{11}O_{39})Ln(H_2O)(\mu–CH_3COO)\}_2]\cdot 17–19\ H_2O$ (**1–Ln**) have been prepared and characterized. Among the few crystal structures based on acetate–bridged Ln–substituted POMs with grafted metalorganic complexes reported so far, **1–Ln** hybid compounds constitute the first example of an extended covalent bidimensional assembly. It must be noted that this is also the first synthetic method that provides the whole family of lanthanide derivatives for a particular TM–Ln–{XW} synthetic system. These compounds undergo thermally induced single–crystal–to–single–crystal transformations upon gradual dehydration which lead to new monodimensional crystalline phases: the partially hydrated intermediate $[\{Cu(cyclam)\}_6\{(\alpha–GeW_{11}O_{39})Ln(H_2O)(\mu–CH_3COO)\}_2]\cdot 4H_2O\cdot$(**2–Ln**, Ln = Eu, Er;**)** and the anhydrous $[Cu(cyclam)]_{0.5}[\{Cu(cyclam)\}_{5.5}\{(\alpha–GeW_{11}O_{39})Ln(\mu–CH_3COO)\}_2]$ (**3–Ln**, Ln = Ce, Eu), that resulted in major structural modifications in both Cu^{II} and Ln^{III} coordination spheres and consequently in the corresponding hybrid frameworks. Continuous Shape Measures (CShM) were also performed to determine the distortion of the Ln centers upon the gradual dehydration process. The reversibility of such transformations was found to be strongly dependent on the Ln–derivative, as early Ln–derivatives return to the parent **1–Ln** upon air exposure but mid–to–late require to be immersed in water to do so. To the best of our knowledge, this is the first time that such interesting thermally triggered transformations are observed upon dehydration in these type of 2:2 acetate–bridged heterometallic Keggin hybrids.

3.5 REFERENCES

---

[1] (a) Contant, R.; Hervé, G. Rev. *Inorg. Chem.* **2002**, *22*, 63. (b) *Polyoxometalate Molecular Science*; Borrás-Almenar, J. J., Coronado, E., Müller, A., Pope, M. T., Eds.; Kluwer: Dordrecht, The Netherlands, **2003**, pp. 33–54. (c) Müller,A.; Pierre G. *Chem. Soc. Rev.* **2012**, *41*, 7431.

[2] a) Murai, S.; Ryu, I.; Sonoda, N. *J. Organomet. Chem.* **1983**, *250*, 121. b) Kuwajima, I.; Nakamura, E. *Top. Curr. Chem.* **1990**, *155*, 1. c) Pope, M. T.; Müller, A. *Angew. Chem.* **1991**, *103*, 56. *Angew. Chem. Int. Ed. Engl.* **1991**, *30*, 34. d) Hill, C. L. *Chem. Rev.* **1998**, *98*, 1. e) Yamase, T. *Chem. Rev.* **1998**, *98*, 307. f) Mizuno, N.; Misono, M. *Chem. Rev.* **1998**, *98*, 199. g) Kozhevnikov*,* I. V. *Chem. Rev.* **1998**, *98*, 171.

[3] (a) Duncan, J. F.; Kepert, D. L. *J. Chem. Soc.* **1961**, 5317. (b) Duncan, J. F.; Kepert, D. L. *J. Chem Soc.* **1962**, 205.

[4] Simon, K.-Y.; Gulari, E. *Polyhedron* **1984**, *3*, 1001.

[5] Fan, L.-Y.; Cao, J.; Hu, C.-W. *RSC Adv.* **2015**, *5*, 83377.

[6] See for example: a) Lin, J.-X.; Lü, J.; Yang, H.-X.; Cao, R. *Cryst. Growth Des.* **2010**, *10*, 1966. b) Yan, J.; Long, D. L.; Miras, H. N.; Cronin, L. *Inorg. Chem*. **2010**, *49*, 1819.

[7] (a) Brudgam, I.; Fuchs, J.; Hartl, H.; Palm, R. *Angew. Chem.* **1998**, *110*, 2814. (b) Brudgam, I.; Fuchs, J.; Hartl, H.; Palm, R. *Angew. Chem. Int. Ed.* **1998**, *37*, 2668.

[8] Fuchs, J.; Palm, R.; Hartl, H. *Angew. Chem.* **1996**, *108*, 2820. (b) Fuchs, J.; Palm, R.; Hartl, H. *Angew. Chem. Int. Ed. Engl.* **1996**, *35*, 2651.

[9] LaRue, W. A.; Liu, A. T.; San Filippo Jr, J. *Inorg. Chem.* **1980**, *19*, 315.

[10] (a) Hartl, H.; Palm, R.; Fuchs, J. *Angew. Chem.* **1993**, *105*, 1545. (b) Hartl, H.; Palm, R.; Fuchs, J. *Angew. Chem. Int. Ed. Engl.* **1993**, *32*, 1492.

[11] Reinoso, S.; Dickman, M. H.; Kortz, U. *Inorg. Chem.* **2006**, *45*, 10422.

[12] a) Burtseva, K. G.; Chernaya, T. S.; Sirota, M. I. *Dokl. Akad. Nauk* **1978**, *243*, 104. b) Fuchs, J.; Flindt, E. P.; *Z. Naturforsch.* **1979**, *34B*, 412. c) Ikenoue, S.; Mikuriya, M.; Miyauchi, O.; Nukada, R.; Yagasaki, A. *Bull. Chem. Soc. Jpn* **1994**, *67*, 25902. d) Yan, G.; Wang, X.; Ma, Y.; Cheng, X.; Wang, Y.; Li, Y. *Solid State Sci.* **2013**, *17*,146.

[13] Sasaki, Y.; Yamase, T.; Ohashi, Y.; Sasada, Y. *Bull. Chem. Soc. Jpn.* **1987**, *60*, 4285.

[14] Lehmann, T.; Fuchs, J. *Z. Naturforsch.* **1988**, *43B*, 89.

[15] Singer, R.; Gross, H. *Helv. Chim. Acta* **1934**, *17*, 1076.

[16] a) Allmann, R. *Acta Crystallogr.* **1971**, *B27*, 1393. b) Chrissafidou, A. Fuchs, J.; Hartl, H.; Palm, R. *Z. Naturforsch.* **1995**, *50B*, 217.

[17] (a) Long, D.-L.; Kögerler, P.; Parenty, A. D. C.; Fielden, J.; Cronin, L. *Angew. Chem.* **2006**, *118*, 4916. (b) Long, D. L.; Kögerler, P.; Parenty, A. D. C.; Fielden, J.; Cronin, L. *Angew. Chem. Int. Ed.* **2006**, *45*, 4798.

[18] Miras, H. N.; Yan, J.; Long, D.-L.; Cronin, L. *Angew. Chem. Int. Ed.* **2008**, *47*, 8420.

[19] Long, D.-L.; Abbas, H.; Kögerler, P.; Cronin, L. *J. Am. Chem. Soc.* **2004**, *126*, 13880.

[20] Ginsberg, A. P. *Inorganic Synthesis*, John Wiley & Sons, New York, United States, **1990**.

[21] (a) Ma, X.; Li, H.; Chen, L.; Zhao, *J. Dalton Trans.* **2016**, *45*, 4935 and references therein. (b) Oms, O.; Dolbecq, A.; Mialane, P. *Chem. Soc. Rev.* **2012**, *41*, 7497. See for example: (c) Quanten, T.; Shestakova, P.; Van Den Bulck, D.;

Kirschhock, C.; Parac-Vogt, T. N. *Chem. Eur. J.* **2016**, *22*, 1. (d) Sap, A.; Absillis, G.; Parac-Vogt, T. N. *Dalton Trans.* **2015**, *44*, 1539.

[22] (a) Bassil, B. S.; Kortz, U. *Z. Anorg. Allg. Chem.* **2010**, *636*, 222 and references therein. See for example: (b) Li, L.-L.; Han, H.-Y.; Wang, Y.-H.; Tan, H.-Q.; Zang, H.-Y.; Li, Y.-G. *Dalton Trans.* **2015**, *44*, 11429. (c) Suzuki, K.; Sugawa, M.; Kikukawa, Y.; Kamata, K.; Yamaguchi, K.; Mizuno, N. *Inorg. Chem.* **2012**, *51*, 6953. (d) Reinoso, S.; Giménez-Marqués, M.; Galán-Mascarós, J. R.; Vitoria, P.; Gutiérrez-Zorrilla, J. M. *Angew. Chem., Int. Ed.* **2010**, *49*, 8384.

[23] (a) Reinoso, S. *Dalton Trans.* **2011**, *40*, 6610–6615 and references therein. See for example: (b) Ibrahim, M.; Mereacre, V.; Leblanc, N.; Wernsdorfer, W.; Anson, C. E.; Powell, A. K. *Angew. Chem., Int. Ed.* **2015**, *54*, 15574–15578. (c) Yu, T.-T.; Ma, H.-Y.; Zhang, C.-J.; Pang, H.-J.; Li, S.-B.; Liu, H. *Dalton Trans.* **2013**, *42*, 16328. (d) Reinoso, S.; Galán-Mascarós, J. R. *Inorg. Chem.* **2010**, *49*, 377.

[24] (a) Zhao, J.-W.; Li, Y.-Z.; Chen, L.-J.; Yang, G.-Y. *ChemComm* **2016**, *52*, 4418. See for example: (b) Xu, L.-J.; Zhou, W.-Z.; Zhang, L.-Y.; Li, B.; Zang, H.-Y.; Wang, Y.-H.; Li, Y.-G. *CrystEngComm*, **2015**, *17*, 3708. (c) Zhao, H.-Y.; Zhao, J.-W.; Yang, B.-F.; He, Huan, Yang, G.-Y. *Cryst. Growth Des.* **2013**, *13*, 5169.

[25] (a) Dolbecq, A.; Dumas, E.; Mayer, C. R.; Mialane, P. *Chem. Rev.* **2010**, *110*, 6009. (b) Santoni, M.-P.; Hanan, G. S.; Hasenknopf, B. *Coord. Chem. Rev.* **2014**, *281*, 64. See for example: (c) Niu, J.-Y.; Zhang, S.-W.; Chen, H.; Zhao, J.-W.; Ma, P.-T.; Wang, J.-P. *Cryst. Growth Des*. **2011**, *11*, 3769.

[26] Wang, X.-F.; Cao, J.; Huang, K.-L.; Xu, Y.-Q.; Chi, Y.-N.; Hu, C.-W. *Eur. J. Inorg. Chem.* **2013**, 1788.

[27] (a) Long, D.-L.; Kögerler, P.; Parenty, A. D. C.; Fielden, J.; Cronin, L. *Angew. Chem., Int. Ed.* **2006**, *45*, 4798. (b) Long, D.-L.; Abbas, H.; Kögerler, P.; Cronin, L. *J. Am. Chem. Soc.* **2004**, *126*, 13880. (c) Shen, L.: Li, C.-H.; Chi, Y.-N.; Hu, C.-W. *Inorg. Chem. Commun.* **2008**, *11*, 992. (d) Cui, F.-Y.; Huang, K.-L.; Ma, X.-Y.; Li, C.; Han, Z.-G.; Gao, Y.-Z.; Liu, X.; Chi, Y.-N.; Hu, C.-W. *Dalton Trans*. **2010**, *39*, 5080. (e) G. L. Guo, Y. Q. Xu, J. Cao and C. W. Hu, *Chem. Commun*., **2011**, *47*, 9411.

[28] Cui, F.-Y.; Huang, K.-L.; Ma, X.-Y.; Li, C.; Han, Z.-G.; Gao, Y.-Z.; Liu, X.; Chi, Y.-N.; Hu, C.-W. *Dalton Trans.* **2010**, *39*, 5080.

[29] (a) Yu, K.; Li, Y.-G.; Zhou, B.-B.; Su, Z.-H.; Zhao, Z.-F.; Zhang, Y.-N. *Eur. J. Inorg. Chem.* **2007,** 5662. (b) Zhang, Y.-N.; Zhou, B.-B.; Li, Y.-G.; Sua, Z.-H.; Zhao, Z.-F. *Dalton Trans.* **2009**, *43*, 9446. (c) Zhao, J.-W.; Jia, H.-P.; Zhang, J.; Zheng, S.-T.; Yang, G.-Y. *Chem. Eur. J.* **2007**, *13*, 10030.

[30] Hastings, J. J.; Howarth, O. W. *J. Chem. Soc., Dalton Trans.* **1992**, 209.

[31] (a) Hu, C.-W.; Yue, B.; Yamase, T. *Appl. Catal., A* **2000**, *194–195*, 99. (b) Guo, Y.-H.; Li, D.-F.; Hu, C.-W.; Wang, Y.-H.; Wang, E.-B.; Zhou, Y.-C.; Feng, S.-H. *Appl.Catal., B: Environ.* **2001**, *30*, 337.

[32] (a) Pope, M. T. *Handb. Phys. Chem. Rare Earths*, **2007**, *38*, 337. (b) Bassil, B. S.; Kortz, U. *Z. Anorg. Allg. Chem*. **2010**, *636*, 2222. (c) Granadeiro, C. M.; de Castro, B.; Balula, S. S.; Cunha-Silva, L. *Polyhedron* **2013**, *52*, 10.

[33] (a) Peacock, R. D.; Weakley, T. J. R. *J. Chem. Soc. A* **1971**, 1836. (b) Iball, J.; Low, J. N.; Weakley, T. J. R. *J. Chem Soc., Dalton Trans.* **1974**, 2021.

[34] (a) Ozeki, T.; Takahashi, M.; Yamase, T. *Acta Crystallogr*. **1992**, *C48*, 1370. (b) Yamase, T.; Ozeki, T. *Acta Crystallogr.* **1993**, *C49*, 1577. (c) Ozeki, T.; Yamase, T. *Acta Crystallogr.* **1994**, *B50*, 128. (d) Yamase, T.; Ozeki, T.; Tosaka, M. *Acta Crystallogr.* **1994**, *C50*, 1849.

[35] Li, T.; Li, F.; Jian, L.; Lü, J; Guo, Z.; Gao, S.; Cao, R. *Inorg. Chem.* **2008**, *47*, 5612.

[36] Ismail, A. H.; Dickman, M. H.; Kortz, U. *Inorg. Chem*. **2009**, *48*, 1559.

[37] Ismail, A. H.; Bassil, B. S.; Suchopar, A.; Kortz, U. *Eur. J. Inorg. Chem.* **2009**, 5247.

[38] Lehmann, T.; Fuchs, J. *Z. Naturforsch.* **1988**, *43B*, 89.

[39] (a) Shan, Y. K.; Liu, Z. X. *Sci. China Ser. B* **1991**, *34*, 313; *Acta Chim. Sin.* **1992**, 364. (b) Niu, J.; Wang, Z.; Wang, J. *J. Coord. Chem.* **2003**, *56*, 895. (c) Chen, W.; Chen, B.; Li, Y.; Wang, Y.; Wang, E. *Inorg. Chim. Acta* **2009**, *362*, 5043. (d) Iijima, J.; Ishikawa, E.; Nakamura, Y.; Naruke, H. *Inorg. Chim. Acta* **2010**, *363*, 1500.

[40] (a) Bassil, B. S.; Dickman, M. H.; von der Kammer, B.; Kortz, U. *Inorg. Chem.* **2007**, *46*, 2452. (b) AlDamen, M. A.; Cardona-Serra, S.; Clemente-Juan, J. M.; Coronado, E.; Gaita-Ariño, A.; Martí-Gastaldo, C.; Luis, F.; Montero, O. *Inorg. Chem.* **2009**, *48*, 3467.

---

[41] (a) Luo, Q.; Howell, R. C.; Dankova, M.; Bartis, J.; Williams, C. W.; DeW. Horrocks, W., Jr.; Young, V. G., Jr.; Rheingold, A. L.; Francesconi, L. C.; Antonio, M. R. *Inorg. Chem.* **2001**, *40*, 1894. (b) Luo, Q.; Howell, R. C.; Dankova, M.; Bartis, J.; Williams, C. W.; DeW. Horrocks, W., Jr.; Rheingold, A. L.; Francesconi, L. C. *Inorg. Chem.* **2002**, *41*, 6112. (c) Belai, N.; Dickman, M. H.; Pope, M. T.; Contant, R.; Keita, B.; Mbomekalle, I. M.; Nadjo, L. *Inorg. Chem.* **2005**, *44*, 169. (d) Jing, J.; Burton-Pye, B. P.; Francesconi, L. C.; Antonio, M. R. *Inorg. Chem.* **2008**, *47*, 6889. (e) Burton-Pye, B. P.; Francesconi, L. C. *Dalton Trans.* **2011**, *40*, 4421.

[42] Naruke, H.; Yamase, T. Bull. Chem. Soc. Jpn. 2000, 73, 375.

[43] (a) Sadakane, M.; Dickman, M. H.; Pope, M. T. *Angew. Chem. Int. Ed.* **2000**, *39*, 2914. (b) Mialane, P.; Lisnard, L.; Mallard, A.; Marrot, J.; Antic-Fidancev, E.; Aschehoug, P.; Vivien, D.; Sécheresse, F. *Inorg. Chem*. **2003**, *42*, 2102. (c) Wang, J.; Duan, X.; Du, X.; Niu, J. *Cryst. Growth Des.* **2006**, *6*, 2266. (d) Lu, Y.; Xu, Y.; Li, Y.; Wang, E.; Xu, X.; Ma, Y. *Inorg. Chem.* **2006**, *45*, 2055.

[44] (a) Knoth, W. H.; Domaille, P. J.; Harlow, R. L. *Inorg. Chem.* **1986**, *25*, 1577. (b) Chen, W.; Li, Y.; Wang, Y.; Wang, E.; Su, Z. *Dalton Trans.* **2007**, 4293. (c) Ismail, A. H.; Bassil, B. S.; Römer, I.; Redeker, N. C. Kortz, U. *Z. Naturforsch.* **2010**, *65B*, 383. (d) Ni, L.; Hussain, F.; Spingler, B.; Weyeneth, W.; Patzke, G. R. *Inorg. Chem.* **2011**, *50*, 4944. (e) Ismail, A. H.; Bassil, B. S.; Römer, I.; Kortz, U. *Z. Anorg. Allg. Chem.* **2013**, *639*, 2510.

[45] (a) Creaser, I.; Heckel, M. C.; Neitz, R. J.; Pope, M. T. *Inorg. Chem.* **1993**, *32*, 1573. (b) Ostuni, A.; Pope, M. T. *C. R. Acad. Sci. Paris, Sér. IIc*. **2000**, 3, 199. (c) Fang, X.; Anderson, T. M.; Benelli, C.; Hill, C. L. *Chem. Eur. J.* **2005**, *11*, 712. (d) Zimmermann, M.; Belai, N.; Butcher, R. J.; Pope, M. T.; Chubarova, E. V.; Dickman, M. H.; Kortz, U. *Inorg. Chem.* **2007**, *46*, 1737.

[46] (a) Sousa, F. L.; Almeida Paz, F. A.; Cavaleiro, A. M. V.; Klinowski, J.; Nogueira, H. I. S. *Chem.Commun.* **2004**, 2656.

[47] (a) Yamase, T.; Naruke, H.; Sasaki, Y. *J. Chem. Soc., Dalton Trans.* **1990**, 1687. (b) Naruke, H.; Yamase, T. *Bull. Chem. Soc. Jpn.* **2001**, *74*, 1289. (c) Wassermann, K.; Pope, M. T. *Inorg. Chem.* **2001**, *40*, 2766. (d) Howell, R. C.; Perez, F. G.; Jain, S.; DeW. Horrocks, W., Jr.; Rheingold, A. L.; Francesconi, L. C. *Angew. Chem. Int. Ed.* **2001**, *40*, 4031. (e) Xuie, G.; Vaissermann, J.; Gouzerh, P. *J. Cluster Sci.* **2002**, *13*, 409. (f) Cui, K.; Li, F.; Xu, L.; Xu, B.; Jiang, N.; Wang, Y.; Zhang, *J. Dalton Trans.* **2012**, *41*, 4871.

[48] (a) Fukaya, K.; Yamase, T. *Angew. Chem. Int. Ed.* **2003**, *42*, 654. (b) Drewes, D.; Piepenbrink, M.; Krebs, B. *Z. Anorg. Allg. Chem.* **2006**, *632*, 534. (c) Hussain, F.; Spingler, B.; Conrad, F.; Speldrich, M.; Kögerler, P.; Boskovic, C.; Patzke, G. R. *Dalton Trans.* **2009**, 4423.

[49] Artetxe, B. *ChemistryOpen* **2016**, *5*, 261.

[50] (a) Mialane, P.; Dolbecq, A.; Marrot, J.; Sécheresse, F. *Inorg. Chem. Commun.* **2005**, 3477. (b) Zhang, S.; Wang, Y.; Zhao, J.; Ma, P.; Wang, J; Niu, J. *Dalton Trans.* **2012**, *41*, 3764.

[51] (a) Ritchie, C.; Moore, E. G.; Speldrich, M.; Kögerler, P.; Boskovic, C. *Angew. Chem. Int. Ed.* **2010**, *49*, 7702. (b) Ritchie, C.; Baslon, V.; Moore, E. G.; Reber, C.; Boskovic, C. *Inorg. Chem.* **2012**, *51*, 1142.

[52] Li, F.; Guo, W.; Xu, L.; Ma, L.; Wang, Y. *Dalton Trans.* **2012**, *41*, 9220.

[53] Mialane, P.; Dolbecq, A.; Rivière, E.; Marrot, J.; Sècheresse, F. *Eur. J. Inorg. Chem.* **2004**, 33.

[54] Hussain, F.; Sandriesser, S.; Speldrich, M.; Patzke, G. R. *J. Solid State Chem.* **2011**, *184*, 214.

[55] Niu, J.-G.; Wang, K.-H.; Chen, H.; Zhao, J.-W.; Ma, P.-T.; Wang, J.-P.; Li, M.-X.; Bai, Y.; Dang, D.-B. *Cryst. Growth Des.* **2009**, *9*, 4362.

[56] Saini, M. K.; Gupta, R.; Parbhakar, S.; Mishra, A. K.; Mathur, R.; Hussain, F. *RSC adv.* **2014**, *4*, 25357.

[57] Zhang, D.; Zhang, C.; Chen, H.; Ma, P.-T.; Wang, J.-P.; Niu, *Inorg. Chim. Acta* **2012**, *391*, 218.

[58] Du, D.-Y.; Qin, J.-S.; Li, S.-L.; Lan, Y.-Q.; Wang, X.-L.; Su, Z.-M. *Aust. J. Chem.* **2010**, *63*, 1389.

[59] Zhao, H.-Y.; Zhao, J.-W.; Yang, B.-F.; He, H.; Yang, G.-Y. *CrystEngComm* **2013**, *15*, 8186.

[60] Zhao, J.-W.; Li, H.; Li, Y.-Z.; Li, C.-Y.; Wang, Z.-L.; Chen, L.-J. *Cryst. Growth Des.* **2014**, *14*, 5495.

[61] Kortz, U. *J. Cluster Sci*. **2003**, *14*, 205.

[62] Zhao, H.-Y.; Zhao, J.-W.; Yang, B.-F.; He, H.; Yang, G.-Y. *CrystEngComm* **2013**, *15*, 5209.

[63] Yi, F.-Y.; Zhu, W.; Dang, S.; Li, J.-P.; Wu, D.; Li, Y.-h.; Sun, Z.-M. *Chem. Commun*. **2015**, *51*, 3336.

---

[64] Zhang, S.-W.; Zhao, J.-W.; Ma, P.-T.; Niu, J.-Y.; Wang, J.-P. *Chem. Asian J.* **2012**, *7*, 966.

[65] Finke, R. G; Droege, M. W; Domaille, P. *Inorg. Chem.* **1987**, *26*, 3886.

[66] Ritchie, C.; Streb, C.; Thiel, J.; Mitchell, S. G. ; Miras, H. N.; Long, D.-L.; Boyd, T.; Peacock, R. D.; McGlone, T.; Cronin, L. *Angew. Chem. Int. Ed.* **2008**, *47*, 6881.

[67] Thiel, J.; Ritchie, C.; Streb, C.; Long, D.-L.; Cronin, L. *J. Am. Chem. Soc.* **2009**, *131*, 4180.

[68] Thiel, J.; Ritchie, C.; Miras, H. N.; Streb, C.; Mitchell, S. G.; Boyd, T.; Corella Ochoa, M. N.; Rosnes, M. H.; McIver, J.; Long, D. L.; Cronin, L. *Angew. Chem Int. Ed*. **2010**, *49*, 6984.

[69] Zhang, L.-Z; Gu, W.; Liu, X.; Dong, Z.; Li, B. *CrystEngComm* **2008**, *10*, 652.

[70] (a) Uchida, S.; Mizuno, N. *Coord. Chem. Rev.* **2007**, *251*, 2537. (b) Mizuno, N.; Uchida, S.; Uehara, K. *Pure Appl. Chem.* **2009**, *81*, 2369.

[71] (a) Uchida, S.; Kawamoto, R.; Akatsuka, T.; Hikichi, S.; Mizuno, N. *Chem. Mater.* **2005**, *17*, 1367. (b) Tagami, H.; Uchida, S.; Mizuno, N. *Angew. Chem. Int. Ed.* **2009**, *48*, 6160. (c) Uchida, S.; Eguchi, R.; Nakamura, S.; Ogasawara, Y.; Kurosawa, N.; Mizuno, N. *Chem. Mater.* **2012**, *24*, 325. (d) Uchida, S.; Kawahara, R.; Ogasawara, Y.; Mizuno, N. *Dalton Trans.* **2013**, *42*, 16209. (e) Kawahara, R.; Uchida, S.; Mizuno, N. *Inorg. Chem*. **2014**, *53*, 3655.

[72] (a) Uchida, S.; Mizuno, N. *J. Am. Chem. Soc.* **2004**, *126*, 1602. (b) Uchida, S.; Kawamoto, R.; Mizuno, N. *Inorg. Chem.* **2006**, *45*, 5136.

[73] (a) Kawamoto, R.; Uchida, S.; Mizuno, N. *J. Am. Chem. Soc.* **2005**, *127*, 10560. (b) Lesbani, A.; Kawamoto, R.; Uchida, S.; Mizuno, N. *Inorg. Chem*. **2008**, *47*, 3349.

[74] Iturrospe, A.; Artetxe, B.; Reinoso, S.; San Felices, L.; Vitoria, P.; Lezama, L.; Gutiérrez-Zorrilla, J. M. *Inorg. Chem*. **2013**, *52*, 3084.

[75] Iturrospe, A.; San Felices, L.; Reinoso, S.; Artetxe, B.; Lezama, L.; Gutiérrez-Zorrilla, J. M. *Cryst. Growth Des.* **2014**, *14*, 2318.

[76] Pache, A.; Reinoso, S.; San Felices, L.; Iturrospe, A.; Lezama, L.; Gutiérrez-Zorrilla, J. M. *Inorganics* **2015**, *3*, 194.

[77] Shi, L.-X.; Zhao, W.-F.; Xu, X.; Tang, J.; Wu, C.-D. *Inorg. Chem*. **2011**, *50*, 12387.

[78] Uehara, K.; Mizuno, N. *J. Am. Chem. Soc.* **2011**, *133*, 1622.

[79] Jeannin, Y.-P. *Chem. Rev.* **1998**, *98*, 51.

[80] (a) Eguchi, R.; Uchida, S.; Mizuno, N. *Angew. Chem. Int. Ed.* **2012**, *51*, 1635. (b) Eguchi, R.; Uchida, S.; Mizuno, N. *J. Phys. Chem. C* **2012**, *116*, 16105. (c) Uchida, S.; Takahashi, E.; Mizuno, N. *Inorg. Chem.* **2013**, *52*, 9320. (d) Uchida, S.; Eguchi, R.; Mizuno, N. *Angew. Chem. Int. Ed.* **2010**, *49*, 9930. (e) Uchida, S.; Mizuno, K.; Kawahara, R.; Takahashi, E.; Mizuno, N. *Chem. Lett.* **2014**, *43*, 1192.

[81] Zhan, C.; Cameron, J. M.; Thomas-Boyd, D.-G.; Winter, R. S.; Vilá-Nadal, L.; Mitchell, S. G.; Glatzel, S.; Breternitz, J.; Gregory, D. H.M; Long, D.-L.; Macdonell, A.; Cronin, L. *Nat. Commun.* **2017**, *8*, 14185.

[82] *CrysAlisPro Software System*, Version 171.37.34; Agilent Technologies UK Ltd.: Oxford, U. K., **2012.**

[83] Dolomanov, O. V.; Bourhis, L. J.; Gildea, R. J.; Howard, J. A.; Puschmann, H. J. *J. Appl. Crystallogr.* **2009**, *42*, 339.

[84] Sheldrick, G. M. *Acta Crystallogr.* **2008**, *A64*, 112.

[85] Spek, A. L. *Acta Crystallogr.* **2009**, *D65*, 148.

[86] Farrugia, L. J. *J. Appl. Crystallogr.* **1999**, *32*, 837.

[87] W. L. DeLano, *The PyMOL Molecular Graphics System*; DeLano Scientific: San Carlos, CA, **2002**.

[88] Brunauer, S.; Emmett, P. H.; Teller, E. *J. Am. Chem. Soc.* **1938**, *60*, 309.

[89] Salje, E. *Acta Crystallogr*. **1977**, *B33*, 574.

[90] Schofield, P. F.; Knight, K. S.; Redfern, S. A. T.; Cressey, G. *Acta Crystallogr*. **1997**, *B53*, 102.

[91] D. Casanova, M. Llunell, P. Alemany, S. Alvarez, *Chem. Eur. J.* **2005**, *11*, 1479.

---

[92] a) D.-Y Du, J.-S. Qin, S.-L. Li, Z.-M. Su, Y.-Q Lan, *Chem. Soc. Rev.* **2014**, *43*, 4615−4632. (b) H. N. Miras, L. Vilà-Nadal, L. Cronin, Chem. Soc. Rev. **2014**, *43*, 5679.

[93] R. Kawahara, S. Uchida, N. Mizuno, *Inorg. Chem*. **2014**, *53*, 3655.

[94] Z. Zhang, M. Sadakane, T. Murayama, S. Izumi, N. Yasuda, N. Sakaguchi, W. Ueda, *Inorg. Chem.* **2014**, *53*, 903.

[95] Z. Zhang, M. Sadakane, S. Noro, T. Murayama, T. Kamachi, K. Yoshizawa, W. Ueda, *J. Mater. Chem. A* **2015**, *3*, 746.

[96] H. Fu, C. Qin, Y. Lu, Z.-M. Zhang, Y.-G. Li, Z.-M. Su, W.-L Li, E.-B. Wang, *Angew. Chem. Int. Ed.* **2012**, *51*, 7985.

[97] J.-S. Qin, D.-Y. Du, W.-L. Li, J.-P. Zhang, S.-L. Li, Z.-M. Su, X.-L. Wang, Q. Xu, K.-Z. Shao, Y.-Q. Lan, *Chem. Sci.* **2012**, *3*, 2114.

[98] (a) Ginsberg, A. P. *Inorganic Synthesis*, John Wiley & Sons, New York, United States, 1990. (b) Hussain, F.; Sandriesser, S.; Speldrich, M.; Patzke, G. R. *J. Solid State Chem.* **2011**, *184*, 214.

[99] (a) *Casan*-Pastor, N.; Gomez-Romero, P.; Jameson, G. B.; Baker, L. C. W. *J. Am. Chem. Soc.* **1991**, *113*, 5658. (b) Sazani, G.; Dickman, M. H.; Pope, M. T. *Inorg. Chem.* **2000**, *39*, 939. (c) Ortega, F.; Pope, M. T.; Evans, H. T., Jr. *Inorg. Chem.* **1997**, *36*, 2166. (d) Xin, F.; Pope, M. T. *Inorg. Chem*. **1996**, *35*, 5693. (e) Zhang, X. Y.; O'Connor, C. J.; Jameson, G. B.; Pope, M. T. *Inorg. Chem.* **1996**, *35*, 30. (f) Jeannin, Y.; Launay, J. P.; Seid Sedjadi, M. A *Inorg. Chem*. **1980**, *19*, 2933.

[100] a) Zhao, J.-W.; Li, Y.-Z.; Chen, L.-J.; Yang, G.-Y. *ChemComm* **2016**, *52*, 4418. See for example: (b) Xu, L.-J.; Zhou, W.-Z.; Zhang, L.-Y.; Li, B.; Zang, H.-Y.; Wang, Y.-H.; Li, Y.-G. *CrystEngComm*, **2015**, *17*, 3708. (c) Zhao, H.-Y.; Zhao, J.-W.; Yang, B.-F.; He, Huan, Yang, G.-Y. *Cryst. Growth Des.* **2013**, *13*, 5169.

[101] (a) Dolbecq, A.; Dumas, E.; Mayer, C. R.; Mialane, P. *Chem. Rev.* **2010**, *110*, 6009. (b) Santoni, M.-P.; Hanan, G. S.; Hasenknopf, B. *Coord. Chem. Rev.* **2014**, *281*, 64. See for example: (c) Niu, J.-Y.; Zhang, S.-W.; Chen, H.; Zhao, J.-W.; Ma, P.-T.; Wang, J.-P. *Cryst. Growth Des.* **2011**, *11*, 3769.

[102] Kehl, W. L. *J. Appl. Phys.* **1952**, *23*, 212.

[103] a) Forsyth, J. B. *J. Phys.: Condens. Matter* **1991**, *3*, 8433–8440. (b) Klein, S.; Weitzel, H. *J. Appl. Crystallogr.* **1975,** *8*, 54.

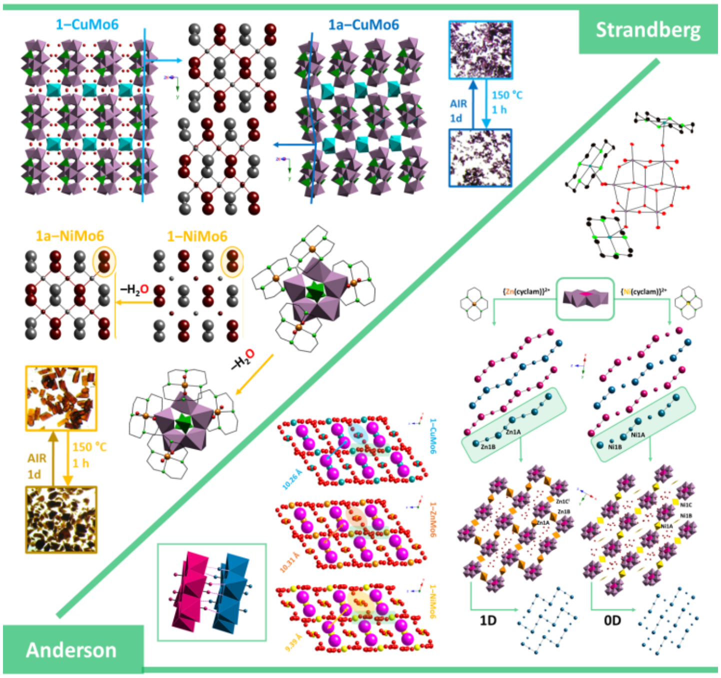

THERMOSTRUCTURAL STUDIES IN MULTIDIMENSIONAL STRANDBERG AND ANDERSON–EVANS TYPE HYBRID HETEROPOLYOXOMOLYBDATES

Chapter 4

In the first section of this chapter, the synthesis and thermostructural characterization of two Strandberg–type hybrids built from 3d–cyclam complexes have been carried out, namely $[\{Cu(cyclam)\}_2(H_2P_2Mo_5O_{23})].4.5H_2O$ ***(1–CuMo5)*** *and* $[\{H_2(cyclam)\}_{0.3}\{Ni(cyclam)\}_{0.7}][\{Ni(cyclam)\}(H_2P_2Mo_5O_{23})].5H_2O$ ***(1–NiMo5)****. Even though they are isostructural,* ***1–CuMo5*** *analogue exhibits an interesting 2–fold interpenetrated diamond–like network while* ***1–NiMo5*** *consist on a 1D covalent assembly, as a consequence of the different plasticity of the 3d centers. In the case of* ***1a–NiMo5****, a rare thermally activated 1D to 3D SCSC is observed resulting in a similar interpenetrated diamond–like framework shown by the hydrated* ***1–CuMo5,*** *whereas the latter is able to maintain its 2–fold complex architecture upon total dehydration, albeit with significant distortion of the initial entangled complex network (****1a–CuMo5****). In the second section, a series of Anderson–type hybrids were prepared and characterized, the formula of which are* $[\{Cu(cyclam)\}_3(H_6CrMo_6O_{24})_2].18H_2O$ ***(1–CuMo6),*** $[\{H_2(cyclam)\}_{1.3}\{Zn(cyclam)\}_{0.3}]$ $[\{Zn(cyclam)\}_{1.4}(H_6CrMo_6O_{24})_2].18H_2O$ ***(1–ZnMo6)*** *and* $[\{Ni(cyclam)\}_2][\{Ni(cyclam)\}(H_6CrMo_6O_{24})_2].18H_2O$ *(****1–NiMo6****). Similar to the Strandberg hybrids, despite being isostructural, the difference in coordination ability of each 3d–metal results in covalent multidimensional architectures comprising 2D, 1D and 0D topologies, respectively. While the cell parameters and the relative arrangement of building blocks in the asymmetric unit are virtually identical in Cu and Zn derivatives, significant structural differences in the geometry of the complexes and the distribution of water molecules were observed for the* ***1–NiMo6*** *analogue, which led to a slightly different and more compacted crystal assembly.*

THERMOSTRUCTURAL STUDIES IN MULTIDIMENSIONAL STRANDBERG AND ANDERSON–EVANS TYPE HYBRID HETEROPOLYOXOMOLYBDATES

4.1 INTRODUCTION

4.1.1 Polyoxomolybdates: A Brief Introduction

While polyoxotungstates (POWs) have well–defined pH–dependent stability ranges, most of the polyoxomolybdates (POMos) are usually in equilibrium due to their low kinetic but comparable thermodynamic stability.[1–3] Differences between POMos and POWs are especially remarkable when the reduced species are considered, as the former are more easily reduced than the latter. In this sense, partial reduction of acidified molybdate solutions allows the generation of a variety of building blocks that can be linked together to create very complex and large molecular systems via stepwise self–assembly processes.[2] Such a considerable structural and chemical diversity arises from a combination of favorable kinetic, thermodynamic and structural factors, which makes the polyoxomolybdate family unique in chemistry.[3] As a result, Müller's group extensively investigated and synthetized numerous giant species with sizes comparable to those shown by some proteins as well as unique molecular multifunctional architectures and like giant wheel–[4] sphere–[5] and hedgehog–shaped[6] POMos, providing the basis for a new era of inorganic– and nanochemistry leading to promising applications in materials science.[7]

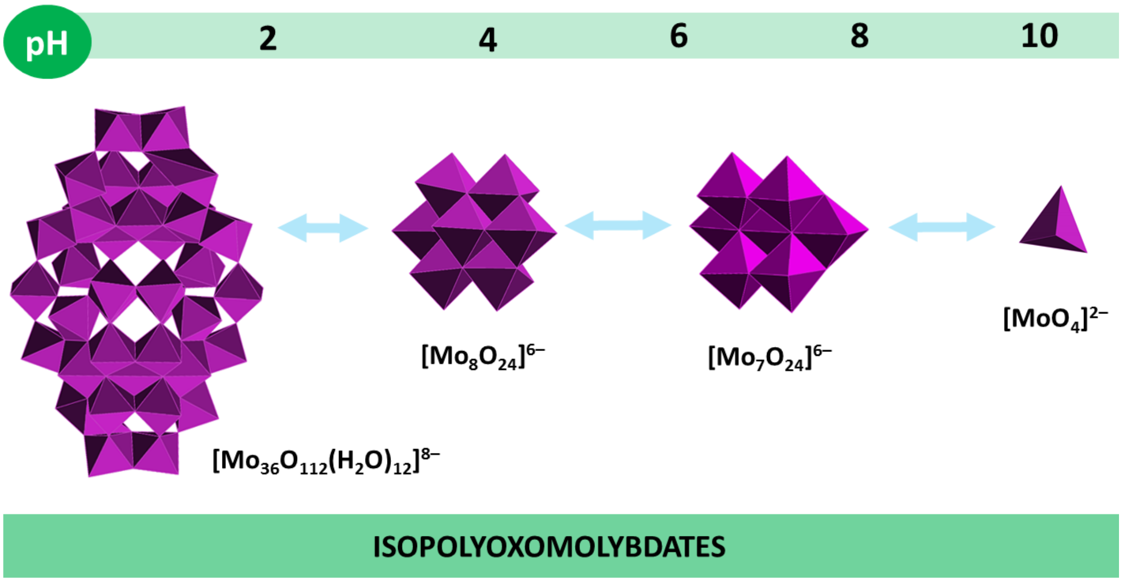

Figure 4.1. Predominant species of IsoPOMos in aqueous solution as a function of the pH.

POMos can form a wide variety of structures, due to the flexibility in the Mo–O–Mo links, the easy redox changes particularly involving Mo^V and Mo^{VI}, the different Mo coordination numbers possible (particularly 6 and less frequently 7) and the strong hydration stabilization. In the majority of POMos structures molybdenum atoms are octahedrally coordinated to six oxygen atoms, although coordination polyhedra with four (tetrahedral) and five (square pyramidal and trigonal bipyramidal) oxygen atoms have been also reported. The formation of polyoxomolybdates via condensation processes upon acidification of alkaline solutions containing the monomeric $[MoO_4]^{2-}$ oxoanions is well documented.[8] In aqueous solution, the molybdate $[MoO_4]^{2-}$ ion is the only stable specie above pH 6.5, whereas in the slightly acidic region between 4.5 < pH < 6.5 the heptamolybdate or paramolybdate $(Mo_7O_{24})^{6-}$ specie exists in equilibrium with $[MoO_4]^{2-}$ ions. Further acidification leads to the formation of the well–known octamolybdate $[Mo_8O_{26}]^{4-}$ polyanion which is stable between pH = 3.0–1.5, although larger aggregates like $[Mo_{36}O_{112}]^{8-}$ can be formed when acidified to values below pH < 2 (Figure 4.1), which represents the largest known isoPOMos present in solution under non–reducing conditions.[9] In the acidic region pH < 1 however, the molybdic acid $[H_2MoO_4]$ precipitates which redissolves with further increase in the hydrogen ion concentration.

Currently, organic derivatives of polyoxomolybdates are considered an active field within the POM chemistry. As a result, several POMo–based organic–inorganic hybrid materials (both *class I* and *II*) comprising different architectures, compositions and topologies have been prepared in the last decades via both solvothermal methods and under mild conditions.[10,12–18] The inclusion of different heteroatoms into acidic molybdate solutions under appropriate synthetic conditions results in the generation of archetypal POM clusters like Keggin, Wells–Dawson and Anderson–Evans structures similar to those observed in polyoxotungstate analogues,[1] as well as some structures that are almost exclusive to the POMo family like the Strandberg–type diphosphopentametalate anion. However, comparing to the latter analogues, reports on organic–inorganic hybrids based on heteroPOMos building blocks and 3d–metalorganic complexes are more limited,[10] which is mainly due to the lower chemical stability of POMos and their lacunary species than that shown by the polyoxotungstate family, particularly in aqueous solutions.[11] Similarly, IsoPOMo–based hybrids are almost limited to $\{Mo_3O_{10}\}$ and $\{Mo_4O_{18}\}$ low–nuclearity clusters, Lindqvist–type $\{Mo_6O_{19}\}$ hexamolybdates and the $\{Mo_8O_{26}\}$ octamolybdates (and their related α, β and γ structures),[12] as well as some scarce reports involving the heptamolybdate $\{Mo_7O_{24}\}$ anion.[13] In order to overcome this limitations, various authors designed different synthetic approaches have been applied to construct such hybrids.[14–18] For instance: a) the incorporation of tris–alkoxo ligands into the POM framework resulting in a family of polyoxoalkoxometalates,[14] b) reacting $[MoO_4]^{2-}$ ions in conjunction with organophosphonate and organoarsonate ligands resulting in cyclic architectures[15] but also Keggin–type derivatives[16] c) functionalization of some HeteroPOMos with amino acids[17] or phosphonocarboxylates[18], among others.

Seen in previous chapters that the grafting of metallocyclam moieties to different types of POM precursors, namely both polyoxovanadate and –tungstate, afforded interesting hybrid structures, we attempted to investigate the possibility of obtaining similar hybrids using heteroPOMos building blocks, since the resulting extended polyoxomolybdate–based hybrids could potentially result in novel architectures and topologies or even enhanced properties due to synergistic relationships between the different building blocks. To achieve that goal, we made use of the well–known Strandberg–type diphosphopentamolybdate clusters as well as Anderson–Evans chromiumhexamolybdate polyanions.

4.1.2 Hybrid Strandberg–type POMos

Among the versatile polyoxomolybdate catalogue, the diphosphopentamolybdate polyanion, $[H_xP_2Mo_5O_{23}]^{(6-x)-}$ (x = 0–2), which was first observed as a sodium salt by Strandberg back in 1973,[19] , namely $Na_6[P_2Mo_5O_{23}]$ $13H_2O$, can be regarded as a valuable building unit due to its ability to link transition–metal complexes through diverse coordination modes,[20] that is, by terminal O atoms belonging to either the capping phosphate groups or molybdate polyhedra and even both, as well as their chemical versatility, since they can be modified easily by substitution of the capping phosphate groups by organophosphate and similar pendant groups.[20a,21] Regarding the latter, many organoderivatives of the Strandberg anion have been reported in the last decades, for instance, organophosphonate derivatives ($[(RPO_3)_2Mo_5O_{15}]^{4-}$, R = CH_3 , C_2H_5, Ph, $NH_2C_2H_4$, $CH_3CH(NH_2)$, $CH_3CH(CH_3)CH(NH_2)$, $CH_2C_6H_4NH_2$, S–$(CH_2CH_2)_2NHCH_2$, crown ether) and phosphite derivative ($[(HPO_3)_2Mo_5O_{15}]^{4-}$),[22] phosphonocarboxylate derivatives ($[(O_2CCH_2PO_3)_2Mo_5O_{15}]^{6-}$,’[20b,23] organodiphosphonates derivatives ($\{(O_3PRPO_3)–Mo_5O_{15}\}_n^{4n-}$; R = $(CH_2)_x$ where x = 2−5, C_6H_4, Ph−Ph)[24]. In addition, the Strandberg–type clusters have a relatively smaller size and hence, higher charge densities compared to other archetypal POMs such as Keggin or Wells–Dawson anions, which could induce more metalorganic cationic fragments to coordinate to it favoring the construction of high dimensional hybrid architectures when appropriate metalorganic linkers are used. The structure of the Strandberg–type polyanion consists in a chiral $\{Mo_5O_{21}\}$ core formed by five edge– and corner–sharing $\{MoO_6\}$ octahedra, which is capped with one $\{PO_3(OH)\}$ tetrahedron on both sides of it through corner sharing with ideal *C*2 symmetry (Figure 4.2). Compositional variations of the Strandberg core has met limited success over the years, as only $\{P_2W_5\}$ and $\{Se_2Mo_5\}$ isostructural anions have been reported till date. Reports on the former consist in fully inorganic compounds as well as alkylammonium–containing *class I* hybrids[25] while the latter can be found as inorganic salts and also as ionic compounds stabilized by ligands such as ethylendiamine, 4,4’–bipyridine, piperazine and 2–aminopiridyne.[26]

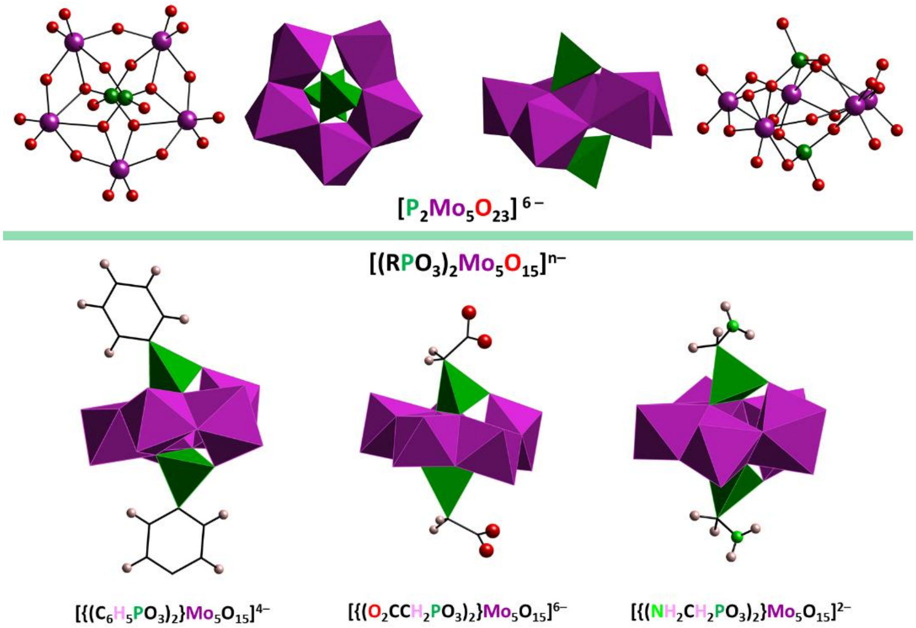

Figure 4.2. Polyhedral and ball&sticks representations of the Strandberg–type structure along with some of its representative organoderivatives.

Although reports on organic–inorganic materials based on these heteropolyoxomolybdates and covalently linked transition metal–complexes are still limited compared to those involving typical Keggin[27] and Anderson–type[28] POM analogues, several hybrids containing Strandberg–type clusters and diverse 3d–metalorganic moieties showing different grafting sites of the complexes and varied dimensionalities have been reported in the past decades.[20,21,29–37] In such compounds, the terminal oxygen atoms belonging to the capping phosphate groups can be either non–protonated ($[P_2Mo_5O_{23}]^{6-}$) or protonated, one ($[HP_2Mo_5O_{23}]^{5-}$) or both of them ($[H_2P_2Mo_5O_{23}]^{4-}$), respectively. In the former cases, the non–protonated oxygen atoms can partake in the coordination sphere of 3d–metal atoms. In contrast, in the organoderivatives ($[(RPO_3)_2Mo_5O_{15}]^{4-}$, the pending R group does not usually participate in coordination towards the transition metal center.[20a,22] Regarding the metalorganic blocks, the most common 3d metals that can be found in studies involving Strandberg–type hybrid structures is Cu^{II} by far, followed up by Ni^{II} and Co^{II}, and there are a few reports involving Zn^{II} and Mn^{II} complexes as well. A vast number of different N– or O–donor organic ligands showing diverse chemical nature, composition and sizes have been employed in the construction of such hybrids, including but not limited to bidentate chelating bipyridine, imidazole, pyrazine and some of their respective derivatives as well as some macrocyclic polyamines and dicarboxylic acids. It must be noted however that the vast majority of such hybrids were prepared using hydrothermal methods, as compounds obtained via mild traditional methods are quite limited in comparison.

For instance, Zubieta's group prepared numerous organophosphonate–modified $\{(RPO_3)_2Mo_5O_{15}\}^{4-}$ hybrids using bridging binuclear copper(II) complexes of tetra–2–pyridylpyrazine (tpypyz) under hydrothermal conditions resulting in both 2D and 3D covalent[29] assemblies (Figure 4.3). Similarly, Finn and coworkers prepared closely related mono– and bidimensional organophosphonate–substituted hybrids using 2,2'–bipyridine or terpyridine organoimines with different Cu(II) sources[30] (Figure 4.3). Grafting of bidentate Cu(bpy) moieties yielded the extended three–dimensional $[H_2bpy]_2[\{Cu(bpy)_2\}(P_2Mo_5O_{23})]\cdot 4H_2O$ hybrid framework (bpy = 4,4–bipyridine) reported by Lu et al. which is formed by metallorganic sheets pillared by Strandberg clusters[31] (Figure 4.3). In 2008, Wang's group reported the first enantiomeric chiral 3D frameworks using Ni^{II} complexes of an N–heterocyclic achiral ligand and $\{HP_2Mo_5O_{23}\}$ as building blocks, which exhibited an unusual triflexural helical motifs.[32] In the same year, Ramanan's group reported the use of Cu(II)–pyrazole complex as templating agent to prepare a series of hybrids comprising various dimensional architectures and coordination modes for the 3d centers[33] (Figure 4.3). Armatas and coworkers prepared an extensive multidimensional copper(II)–molybdophosphonate family using binuclear $\{Cu_2(bpyr)\}^{4+}$ as building blocks to connect $\{(RPO_3)_2Mo_5O_{15}\}^{4-}$ clusters[34] (bpyr = bipyrimidine) whereas Su's group reported a 2D supramolecular ionic compound containing mixed copper(II)–complexes of both ethylendiamine and 4,4'–bipyridine ligands, namely $[\{Cu^{I}(4,4'\text{–bipy})\}_2\{Cu^{II}(en)_2\}][HP_2Mo_5O_{19}]\ 6H_2O$.[35] In 2010, DeBurgomaster and coworkers reported a series of low dimensional compounds sharing the same cluster in conjunction with Co^{II}, Ni^{II} and Cu^{II} complexes of diverse ligands such as o–phenanthroline, terpyridine and 2,2'–bipiridine which resulted in 1D hybrid chains for the Cu derivative whereas the other metals yielded discrete decorated clusters.[36] Recently, Ou et al. prepared two hybrid using transition metal macrocyclic $[ML]^{2+}$ complexes closely related to the cyclam ligand (L = 5,5,7,12,12,14–hexamethyl–1,4,8,11–tetraazacyclotetradecane, M= Cu, Ni).[37] While the Cu derivative consist on a simple 1D covalent arrangement, the Ni derivative exhibits an interesting 3D open–framework with hydrophobic channels along the *z* axis where the water molecules reside (Figure 4.3).

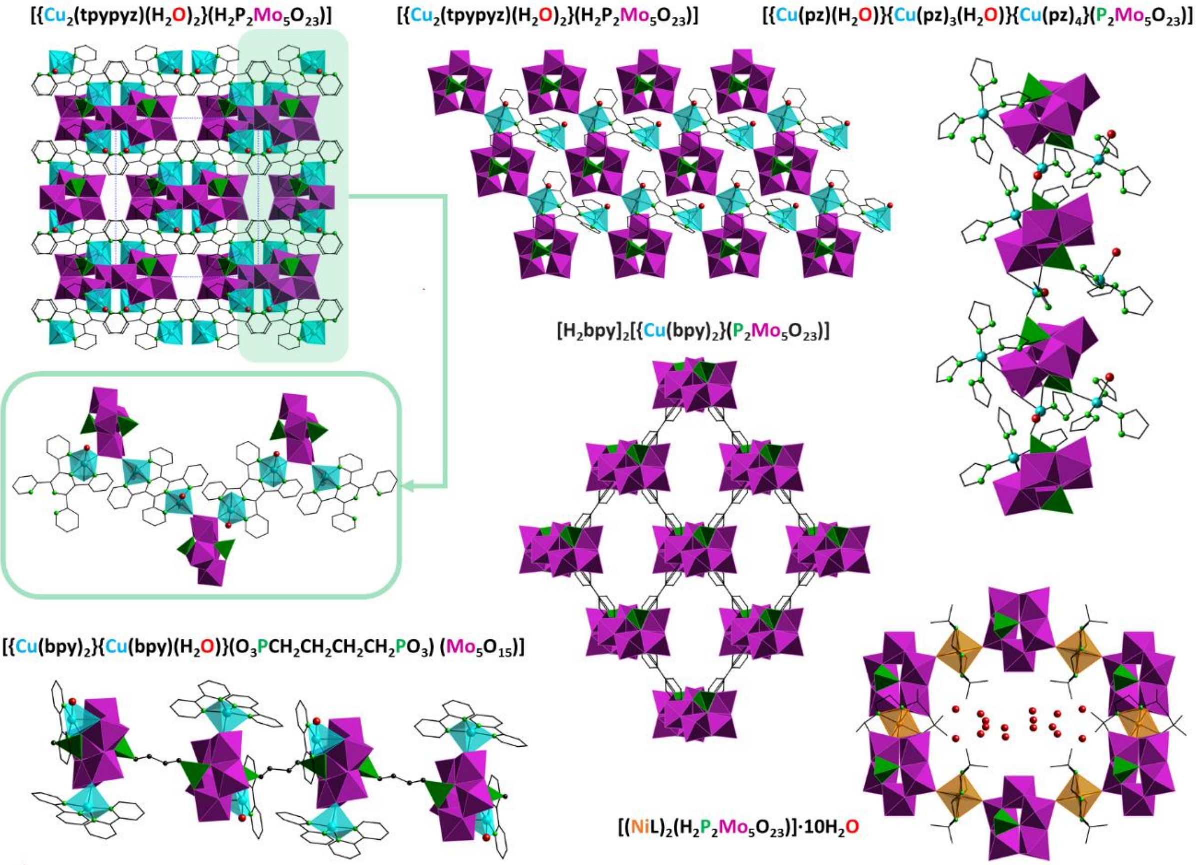

Figure 4.3. Polyhedral representation of representative Strandberg–type hybrids showing different dimensionalities as well as coordination modes of the transition metal centers belonging to the metallorganic moieties. Organic ligands: tpypyz = tetra–2–pyridylpyrazine, pz = pyrazole, bpy = 4,4–bipyridine, L = 5,5,7,12,12,14–hexamethyl–1,4,8,11–tetraazacyclotetradecane.

Recently, some notable properties for these kind of hybrids are being gradually recognized which has attracted significant attention towards this interesting heteroPOMo.[39–43] In 2012, Banerjee et al. first reported the proton conductivity of a Cu–phen tricoordinated Strandberg–type monodimensional hybrid[38] (phen = 1,10–phenanthroline, Figure 4.4). In 2014, Song et al reported a series of 3D supramolecular type I hybrids using Ni(II)–bim and –phen complexes (bim = 2,2′–biimidazole, phen = 1,10–phenanthroline) displaying good electrocatalytic activity in the reduction of H_2O_2 and strong fluorescent emission in solution.[39] Later, Zhu synthesized three Zn–H_2bim–supported $\{HP_2Mo_5O_{23}\}$ hybrids (H_2bim = 2,2′–biimidazole), where the N–donor ligand exhibits three different coordination modes (Figure 4.4) and evaluated their potential catalytic activity towards the protection of carbonyl compounds like cyclohexanona with glycol.[40] Similar catalytic studies were conducted in two Cu–bipy grafted 3D organophosphomolybdate hybrids (bipy = 4,4′–bipyridyl) which also exhibited solid–state photoluminiscent properties[41] (Figure 4.4). In 2015, Xu and coworkers reported the third–order nonlinear optical properties of the hybrid Strandberg $[Ni(ntb)(H_2O)]_2[(H_2P_2Mo_5O_{23})]\cdot 9.25H_2O$ (ntb = tris(2–benzimidazylmethyl)amine),[42] the covalent 3D framework of which is reinforced by π–π stacking interactions (Figure 4.4). Very recently, Wang's group reported the synthesis of the hybrid $[H_2pybim]_2\{[Zn(pybim)_2(H_2O)(P_2Mo_5O_{23})]$ $5H_2O_5$ (pybim = 2–(3–pyridyl)benzimidazole) which consist on a chain–like arrangement[43] (Figure 4.4). The authors managed to fabricate a hybrid composite material by the combination of nanorod of the former POM and polypyrrole via a facile in situ chemical oxidation polymerization process under the initiation of ammonium persulfate. Interestingly, the resulting composite exhibited considerably higher photocatalytic efficiency compared to that observed for the individual components towards the degradation of rhodamine B under the irradiation of visible light.

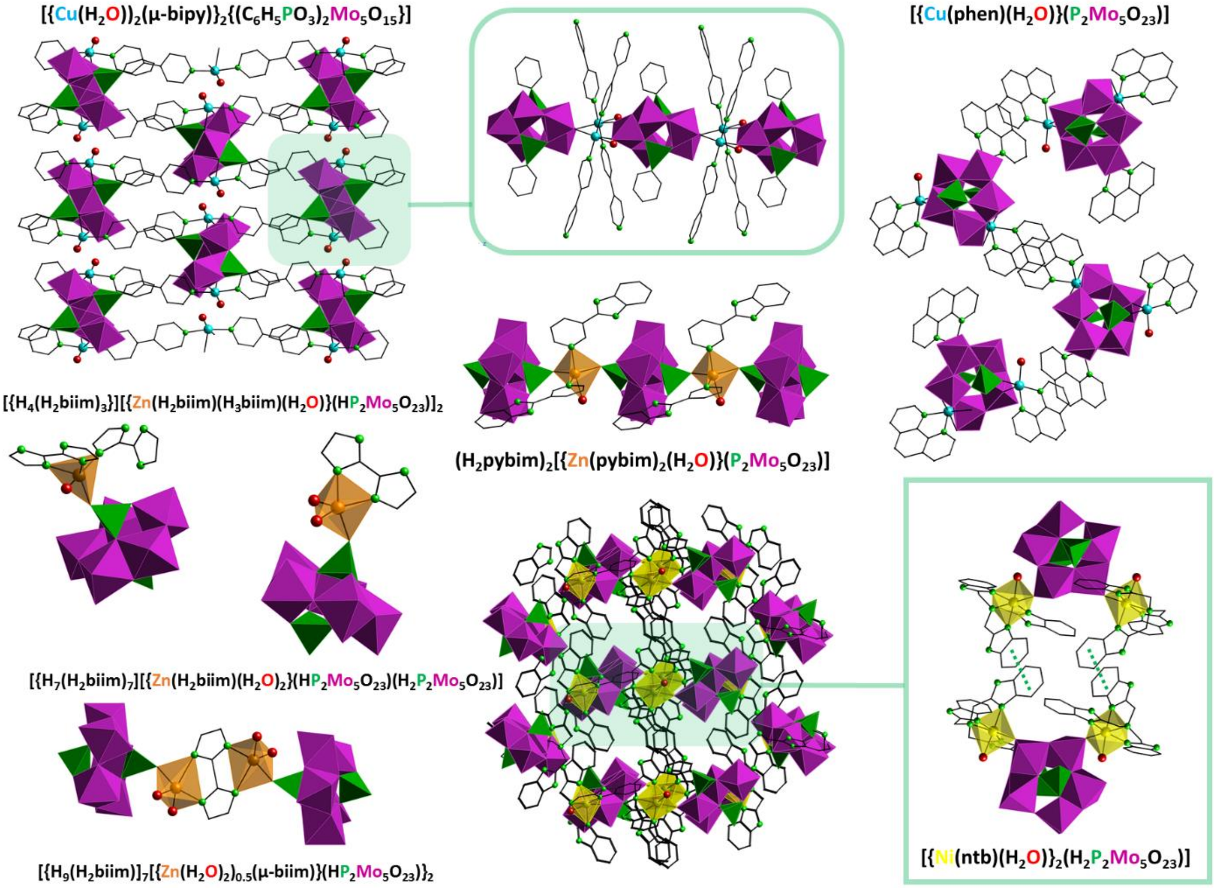

Figure 4.4. Polyhedral representation of some recent functional Strandberg–type covalent hybrids. Organic ligands: bipy = 4,4'–bipyridyl, bim = 2,2'–biimidazole, pybim = 2–(3–pyridyl)benzimidazole, phen = 1,10–phenanthroline, ntb = tris(2–benzimidazylmethyl)amine).

These studies as well as our previous results obtained in prior chapters motivated us to make use of the Strandberg–type cluster as inorganic building block to construct extended hybrid systems upon combination with metallocyclam complexes, which will be discussed in the first section of this chapter.

4.1.3 Hybrid Anderson–Evans type POMos

One of the most common polyoxometalates is the Anderson–Evans cluster with the general formula $[H_yXM_6O_{24}]^{n-}$ (y = 0–6, n = 2–8, M = Mo^{VI} or W^{VI} and X = central heteroatom), although heptaprotonated species have also been reported.[44] The structure of this archetypal POM was first proposed by Anderson back in 1937 for the $[Te^{VI}Mo_6O_{24}]^{6-}$ cluster[45] and was confirmed with X–ray diffraction experiments by Evans nearly ten years later.[46] The Anderson–Evans polyoxoanion is composed of six edge–sharing $\{MO_6\}$ octahedra surrounding a central, edge–sharing heteroatom of octahedral geometry (XO_6) leading to a planar arrangement with an approximate *D3d* symmetry.[46] Three different coordination modes of oxygen atoms are found in the structure: six triple–shared oxygen atoms (μ_3–O) connect the heteroatom and two addenda atoms, whereas six double–bridged oxygen atoms (μ_2–O) connect two addenda atoms and two terminal oxygen atoms (O_t) are connected to each of the six addenda atoms (Figure 4.5). These POMs can be roughly divided into two main types:[47] the non–protonated A–type with central heteroatoms in high oxidation states with the general formula $[X^{n+}M_6O_{24}]^{(12-n)-}$ (X = e.g., Te^{VI},[48] I^{VII} [49]) and the hexaprotonated B–type with heteroatoms in low oxidation states and the general formula $[X^{n+}(OH)_6M_6O_{18}]^{(6-n)-}$(X = e.g., Cr^{III},[50] Fe^{III}[51]), with the six protons usually being located on the six μ_3–O atoms surrounding the heteroatom.[47] Anderson–Evans–type structures have also been elucidated with the octahedral heteroatom being replaced by trigonal pyramidal or tetrahedral atoms such as V^V,[52] As^V [53] and Te^{IV} [54]) on each side of the planar structure keeping the hexameric ring intact.

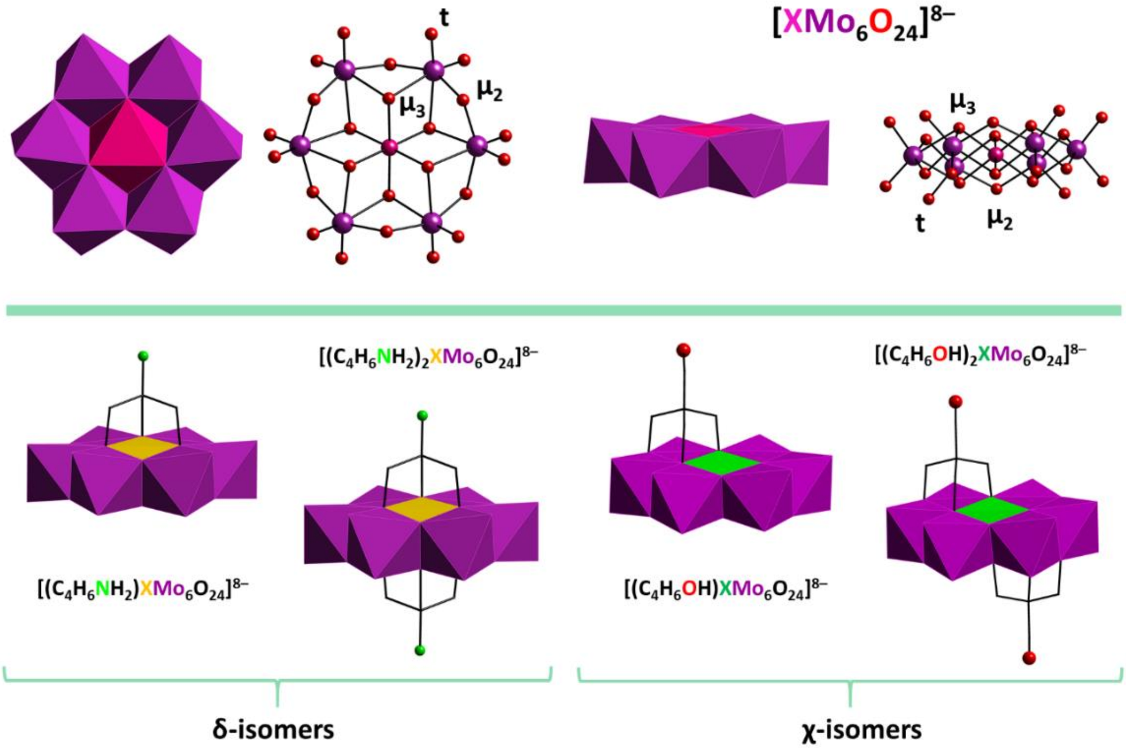

Figure 4.5. Polyhedral and ball&sticks representation of the Anderson–Evans cluster highlighting the three distinct O atoms along with the types of single– and double–sided tris–functionalized hybrids.

From the compositional point of view, the $\{XMo_6\}$ system incorporates a greater variety of heteroatoms than the analogue $\{XW_6\}$ system. All first–row transition metals except for Sc, Ti and V have been described in the literature to act as a heteroatom in the former system. In contrast, $\{XW_6\}$ system exist with $Mn^{II/IV}$[55] and Ni^{II}[56] forming the B–type Anderson–Evans POM, incorporating six hydrogen atoms which is rather unusual when W act as addenda atoms. Interestingly, given the large number of hybrid structures containing Mn^{III} as heteroatom, no inorganic crystal structure exist till date even though synthesis and spectroscopic evidence has been obtained.[57] Out of the heavier transition metal centers, only noble metals have been reported to be able to enter so far into the addenda ring of both {XMo$_6$} and {XW$_6$} systems. Post–transition metals and metalloids are also represented with Al^{III}, Ga^{III}, Sb^{V}, Te^{VI} and I^{VII} within the {XMo$_6$} system as well as Sb^{V} and Te^{VI} in the {XW$_6$} system. In contrast, noble metals like Ru$^{II/III}$ and Rh^{II} are not represented in either system and several of the first–row transition metals are missing in the case of {XW$_6$} system such as Cr, Fe, Co and Cu. The majority of the alkali and alkaline–earth metals as well as the entire lanthanide series, however, have been employed as countercations as well.[44]

Regarding Anderson–based organic–inorganic hybrids, one extensively studied yet elegant method consist on the replacement of shell oxygen atoms of the clusters by O– or N–donor ligands, which is exemplified by the used of trisalkoxoligands. The six protons attached to μ_3–O atoms (Figure 4.5) of the B–type cluster can be replaced with a wide variety of trisalkoxo–ligands ($RC(CH_2OH)_3$, R = e.g., NH_2, OH, CH_2OH, and further derivatization with imine and amide bonds either before or after attachment to the POM.[58] The tris–ligands can be synthesized first and then grafted onto the POM (pre–functionalization) or tris–ligands can further be modified by organic reactions after attachment onto the POM (post–functionalization).[59] They may cap either a tetrahedral cavity by connecting to two μ_3–O atoms and one μ_2–O atom (χ–isomer, Figure 4.5) or cap the heteroatom connecting to three μ_3–O atoms (δ–isomer, Figure 4.5).[60] Due to the high symmetry of the inorganic Anderson–Evans cluster and the presence of protonated μ_3–O atoms on both sides of the planar structure, functionalization with tris–ligands naturally results in double–sided products but both isomers can be synthesized single–sided too (Figure 4.5). All known tris–functionalized systems belong to the {XMo$_6$} system with the majority of them containing Mn^{III} or Cr^{III} heteroatoms. Compared to the pure inorganic structures, this field is mostly unexplored in terms of heteroatoms but the variety in ligands attached onto has seen far more variety and is still increasing in a fast pace.

On the other hand, grafting of metalorganic moieties results in decoration through terminal O atoms of the clusters and several of such multidimensional hybrids have been reported along the past two decades. In particular, a wide variety of neutral N–donor ligands including pyridine–, pyrazine, imidazole–, triazole–, and tetrazole–based ligands have been succesfully introduced into the Anderson cluster family.[61] However, reports on the combination between Anderson–type POMs and 3d–metalorganic moieties based on N–donor and N/O–donor ligands are relatively limited, especially those showing high dimensional architectures.[62] In regards to the {CrMo$_6$} cluster, the vast majority of such hybrids were prepared using Cu^{II} as the 3d–coordination metal in conjunction with a wide variety of ligands including 2,2'–bipyridine[63] pyrazole,[64] as well as phenantroline–,[65] piperazine–[66] and nicotine–derivatives[67] and also some aminoacids like glycine,[68] alanine[69] and histidine[70]. Some examples using Co, Ni and Zn divalent atoms can be found in the literature as well, although these compounds consist exclusively in pyrazine (Co, Ni, Zn),[71] piridyl– and pyrazine–carboxylate derivatives (Co, Ni)[72] as well as asparagine aminoacid (Zn).[73] A few hybrids containing Mn have been also published, these compounds being limited to pyridylacrylic acid ligands [74] and metal–Schiff–base complexes.[76,77] Incorporation of Fe centers as ferrocinium derivatives into this cluster was also reported by Golhen et al almost two decades ago.[75]

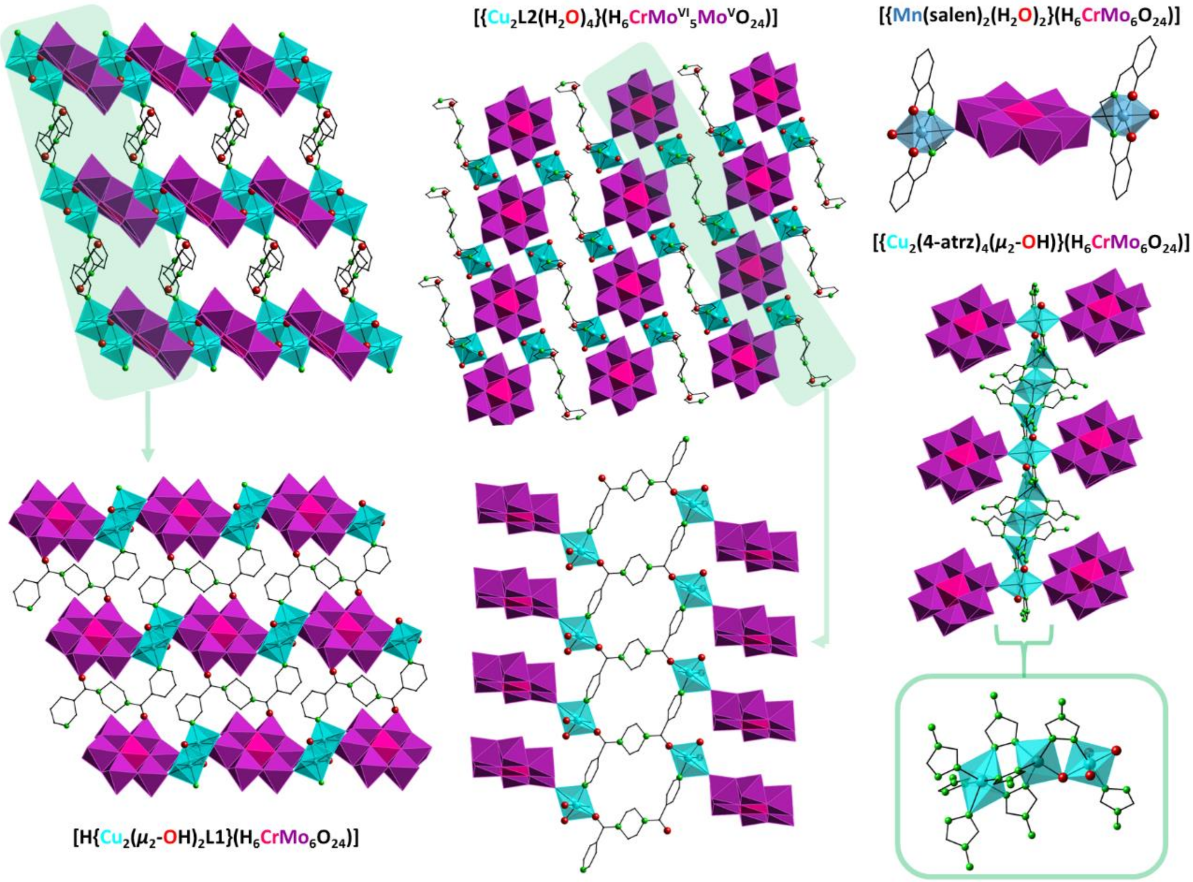

Figure 4.6. Polyhedral representation of some recent functional hybrids containing the Anderson–type {$CrMo_6$} building blocks. Organic ligands: L1 = N, N'–bis(3–pyridinecarboxamide)–piperazine, L2 = N,N'–bis(4–pyridinecarboxamide)–piperazine, salen = *N*,*N'*–ethylene–bis(salicylideneiminate, 4–atrz = 4–amino–1,2,4–triazole.

Recently, various studies showing the applicability of hybrids constructed from {$CrMo_6$} inorganic building blocks have been carried out, which have attracted our interest towards this cluster. In 2009, Wu et al. achieved the incorporation of $[Mn(salen)(H_2O)]_2(ClO_4)_2(H_2O)]$ metalorganic moieties (salen = *N*,*N'*–ethylene–bis(salicylideneiminate), into this chromiumhexamolybdate systems leading to the isolation of a discrete Anderson–type hybrid material with single–molecule magnetic behavior.[76] In 2011, the same authors reported yet another similar combination of heteropolyoxomolybdates and metal–Schiff–base complexes in the hybrid dicoordinated $[\{Mn(salen)_2(H_2O)\}_2(H_6CrMo_6O_{24})](arg)\cdot 11H_2O$ (arg = L–arginine) compound (Figure 4.6) which exhibited high catalytic activity towards the photodegradation of rhodamine B with UV irradiation.[77] Later, Zhang's group reported the hydrothermal synthesis of two 3D {$CrMo_6$}–based metal–organic frameworks built by isomeric bis(pyridilformyl)piperazine ligands, namely, $[H\{Cu_2(\mu_2–OH)_2L1\}(H_6CrMo_6O_{24})]\cdot 4H_2O$ and $[\{Cu_2L2(H_2O)_4\}(H_6CrMo^{VI}_5Mo^{V}O_{18})]\cdot 4H_2O$ (L1 = N, N'–bis(3–pyridinecarboxamide)–piperazine, L2 = N,N'–bis(4–pyridinecarboxamide)–piperazine). In the former structure, the hexadentate polyoxoanion bridges the Cu^{II} centers to generate a 2D Cu–POM inorganic layer, which is further extended by the μ_2–bridging L1 ligands via ligation of pyridyl nitrogen atoms (Figure 4.6). In contrast, the latter is constructed from the quatridentate mixed–valence polyoxoanions and μ_4–bridging L2 ligands via ligation of both pyridyl nitrogen and carbonyl oxygen atoms (Figure 4.6). Both compounds show remarkable photocatalytic activities for the degradation of methylene blue organic dye under UV, visible and sunlight irradiation.[78] Similar photocatalytic studies were conducted by the same group in the ladder–like chains observed in $H\{CuL3_{0.5}[H_6CrMo_6O_{24}](H_2O)\}\cdot 0.5L3$ as well as in the extended network $[\{Cu_2(L4)\}_2(H_5CrMo_6O_{24})(H_2O)_2\}\cdot 2H_2O$ (L3 = N,N'–bis(3–pyridinecarboxamide)–1,2–ethane, L4 = N,N'–bis(3–pyridinecarboxamide)–1.3–propane), which exhibited remarkable activity in the photodegradation some organic dyes like methylene blue and rhodamine B under UV and visible light irradiation.[79]

Grafting of Cu(II) complexes of the multidentate 4–amino–1,2,4–triazole (4–atrz) ligand resulted in an interesting 1D linear arrangement where the $[H_6CrMo_6O_{24}]^{3-}$ anions hang on two sides of the chains constituted by trinuclear $[Cu_3(4\text{–}atrz)_6]^{6+}$ cationic moieties (Figure 4.6).[80] Systematic studies carried out by Wang et al. on the effect of different types of polyoxoanions and pH values of the reaction medium on the self–assembly process resulted in the preparation of two Anderson–type hybrids with different dimensionality using a semi–rigid bis–pyridil–bis–amide ligand.[81] While $\{[Cu^{II}{}_2L5_2(\mu_2\text{–}OH)[H_6CrMo_6O_{18}]\cdot 4H_2O\}\cdot 4H_2O$ compound (L5 = 1,4–bis(3–pyridinecarboxamido)benzene), shows a 2D network constructed from inorganic Cu_2–$CrMo_6$ chains and bidentate L5 ligands (pH = 4.1). When the pH was adjusted to 4.8, the 3D framework of $\{Cu^{I}{}_2Cu^{II}{}_2L5(\mu_3\text{–}OH)_2[H_5CrMo_6O_{24}]\cdot 6H_2O\}\cdot 4H_2O$ was obtained, where $\{CrMo_6\}$ clusters are connected by adjacent $[Cu^{I}{}_2Cu^{II}{}_2(\mu_3\text{–}OH)_2(H_2O)_6]^{4+}$ subunits to form a Cu_4–$\{CrMo_6\}$ inorganic chains that are further connected to L5 ligands giving rise to the 3D network. Both compounds also showed remarkable photocatalytic activity for the degradation of methylene blue under sunlight and UV irradiation. In 2016, two hybrids based on pyridincarboxamide–derivatives were hydrothermally prepared by Wang's group, namely, $\{Cu_5(\mu_2\text{–}OH)_2(4\text{–}dpye)_2\}[H_5CrMo_6O_{19}]_2(H_2O)_{10}$ and $\{Cu(4\text{–}Hdpye)\}[(H_6CrMo_6O_{24})(H_2O)_2]\cdot 2H_2O$ (4–dpye= N,N'–bis(4–pyridinecarboxamide)–1,2–ethane). Their electrochemical behavior and electrocatalytic activity towards the reduction of bromate and hydrogen peroxide were evaluated, as well as the selective photocatalytic properties and adsorption of organic dyes (congo red and methylene blue).[82] Very recently, Gong et al. prepared an organic–inorganic hybrid material consisting on a flexible organic amine modified, namely tris[(2–pyridyl)methyl]amine, in conjunction with Anderson–type $\{CrMo_6\}$ heteroPOMo with excellent activity towards the degradation of pararosaniline hydrochloride organic dye.[83] These studies further confirms the excellent photocatalytic activities of Anderson–type POMo–based hybrids.

Taking all this into account, it can be summarize that the Anderson–Evans archetype is a highly flexible POM cluster that allows modification from several point–of–views; (a) it can incorporate a large number of different heteroatoms differing in size and oxidation state, (b) it can incorporate inorganic and organic cations and molecules demonstrating different coordination motifs, and (c) covalent attachment with tris(hydroxymethyl)methane ligands allows it to be combined with specific organic functionalities. Recent studies regarding 3d–complexes combined with $\{CrMo_6\}$ clusters results in interesting photocatalytic as well as electrochemical properties for the latter. Because all of this, we decided to use this interesting building block in conjuction with metallocyclam moieties to construct similar novel extended hybrid architectures that could display such interesting properties and/or architectures.

4.1.4 SCSC transformations in POMos

As mentioned in previous chapters, the occurrence of SCSC transformations in POM–based compounds is dominated by heteropolyoxotungstate–based compounds. In regards to stimuli–responsive POMos, just a handful reports can be found in the actual literature involving such type of polyoxoanions. Interestingly, all of them show polymorphism phenomenon at low temperature.

The first reported study on a SCSC transformation phenomenon associated with temperature–dependent polymorphism in POM–based compounds dates back to 2008, when Zhang and coworkers reported the structures of the room– and low– temperature polymorphs of a Tm–containing Anderson–Evans type $[Tm_2(H_2O)_{14}H_6CrMo_6O_{24}][H_6CrMo_6O_{24}]\cdot16H_2O$ heteroPOMo.[84] The room temperature *P–1* triclinic polymorph undergoes a thermally triggered SCSC transformation upon cooling at 113 K with retention of the space group which also is accompanied by important changes in the lattice parameters of the resulting low–temperature polymorph. The drastic modification below 113 K of the unit cell dimensions is due to subtle variations in the atomic sites of the constituents, which break the centrosymmetry on anionic clusters and polyoxocations upon cooling. The authors demonstrate that the interconversion between both polymorphs is fast and reversible as the lattice parameters of the low–temperature polymorph can be recovered just by heating above 113 K. When Kortz et al. prepared the previously reported the monoclinic *C2/c* $[C(NH_2)_3]_6[Mo_7O_{24}]\cdot H_2O$ heptamolybdate phase [85] in an attempt to synthetize a guanidinium salt of a dimethyltin–containing phosphotungstate, a monoclinic $P2_1/c$ polymorph was found on cooling a single crystal of the former to 173 K to perform a full data collection.[86] The crystal packing is essentially preserved upon the crystalline phase transition, but the disordered species in the room–temperature polymorph become located in fixed positions at 173 K, which produced the breakage of the symmetry from the parent *C2/c* in the room–temperature structure to the final $P2_1/c$ in the low–temperature polymorph. As a result, this SCSC transformation is accompanied by subtle changes in the supramolecular network of intermolecular N–H···O hydrogen bonds for the low–temperature polymorph compared to the initial *C2/c* structure.

Temperature–driven polymorphic behavior was also observed by Banerjee et al. who first reported the proton conductivity of a Cu–phen tricoordinated Strandberg–type hybrid (phen = 1,10–phenanthroline), namely $[\{Cu(phen)(H_2O)\}_3(P_2Mo_5O_{23})]\cdot5H_2O$,[38] that undergo a totally reversible thermally activated phase transition upon dehydration. Unfortunately, even though the authors studied the reversibility of such transformation by PXRD and optical images, they did not structurally characterized the anhydrous phase. In contrast, Neumann and coworkers conducted thermostructural studies for the V–disubstituted $H_5PV_2Mo_{10}O_{40}\cdot8H_2O$ Keggin–type phosphomolybdic acid, which undergoes a SCSC transition between two different triclinic *P–1* phases upon cooling to 120 K.[87] The octahydrate form of the $H_5PV_2Mo_{10}O_{40}$ heteropolyacid was prepared by partial removal of the solvent molecules of the parent compound $H_5PV_2Mo_{10}O_{40}\cdot36H_2O$ by slightly heating to 40 °C. This compound was obtained by recrystallization of the well–known acidic species[88] from aqueous solution and its dehydration into the octahydrate form proceeded via two sequential SCSC transformations promoted by gradual dehydration into the partially hydrated intermediates $[H_5PV_2Mo_{10}O_{40}]\cdot14H_2O$ and

$[H_5PV_2Mo_{10}O_{40}]\cdot 8H_2O$ with sequential contraction of the crystal packing. Full dehydration of the latter takes place at temperatures around 100 °C and results in the formation of an amorphous powder as shown by variable–temperature powder XRD studies. The authors showed that this process is fully reversible toward the parent fully hydrated form and that rehydration proceeds with recovery of the crystallinity, although they do not provide any indication about the reversibility of the crystal phase transition concerning the temperature–dependent polymorphic phase.

4.1.5 Summary

In the first section of this chapter, the synthesis and thermostructural characterization of two Strandberg–type hybrids built from 3d–cyclam complexes (cyclam = 1,4,8,11–tetraazacyclotetradecane) have been carried out, namely $[\{Cu(cyclam)\}_2(H_2P_2Mo_5O_{23})].4.5H_2O$ (**1–CuMo5**) and $[\{H_2(cyclam)\}0._3\{Ni(cyclam)\}_{0.7}][\{Ni(cyclam)\}(H_2P_2Mo_5O_{23})].5H_2O$ (**1–NiMo5**). Even though they are isostructural, **1–CuMo5** analogue exhibits an interesting 2–fold interpenetrated diamond–like network while **1–NiMo5** consist on a 1D covalent assembly, as a consequence of the different plasticity of the 3d centers. Both hybrids undergo reversible thermally triggered single–crystal–to–single–crystal (SCSC) transformations upon dehydration (**1a–MMo5**) with drastically different outcomes. In the case of **1a–NiMo5**, a rare 1D to 3D SCSC is observed resulting in a similar interpenetrated diamond–like framework shown by the hydrated **1–CuMo5,** whereas the latter is able to maintain its 2–fold complex architecture upon total dehydration, albeit with significant distortion of the initial entangled complex network. In the second section a series of Anderson–type chromohexamolybdate hybrids have been isolated from aqueous solution upon coordination to 3d–metallocyclam complexes, namely $[\{Cu(cyclam)\}_3(H_6CrMo_6O_{24})_2].18H_2O$ **(1–CuMo6),** $[\{H_2(cyclam)\}_{1.3}\{Zn(cyclam)\}_{0.3}][\{Zn(cyclam)\}_{1.4}(H_6CrMo_6O_{24})_2].18H_2O$ **(1–ZnMo6)** and $[\{Ni(cyclam)\}_2][\{Ni(cyclam)\}(H_6CrMo_6O_{24})_2].18H_2O$ (**1–NiMo6**). Despite being isostructural, the difference in the chemical nature and coordination ability of each transition metal results in covalent multidimensional architectures including “bow–tie” bi–dimensional arrangements, 1D chain–like assemblies and 0D discrete topologies, respectively. While the cell parameters and the relative arrangement of building blocks in the asymmetric unit, are virtually identical in Cu and Zn derivatives, significant structural differences in the geometry of the metalorganic complexes as well as the distribution of water molecules were observed for the **1–NiMo6** analogue, which led to a slightly different and more compacted crystal assembly.

4.2 STRANDBERG–TYPE HYBRIDS

4.2.1 Experimental Section

Materials and methods

The *t*–butylammonium diphosphopentamolybdate salt precursor, namely $[(CH_3)_3CNH_3]_4[H_2P_2Mo_5O_{23}]\cdot 5H_2O$, was synthesized according to literature methods and identified by infrared (FT–IR) spectroscopy. [89] All other chemicals were obtained from commercial sources and used without further purification. Carbon, hydrogen and nitrogen were determined on a Perkin–Elmer 2400 CHN analyzer. FT–IR spectra were obtained as KBr pellets on a SHIMADZU FTIR–8400S spectrometer (Figure A4.1 in the Appendix). Thermogravimetric (TGA) analyses were carried out from room temperature to 700 °C at a rate of 5 °C min^{-1} on a Mettler Toledo TGA/SDTA851^e thermobalance under a 50 cm^3 min^{-1} flow of synthetic air. Powder X–ray diffraction (PXRD) patterns were collected on a Bruker D8 Advance diffractometer operating at 30 kV/20 mA and equipped with Cu K_α radiation (λ = 1.5418 Å), a Vantec–1 PSD detector, an Anton Parr HTK2000 high–temperature furnace, and Pt sample holder (Figure A4.2 in the Appendix). The powder patterns (PXRD) were recorded in 2ϑ steps of 0.033° in the $5 \leq 2\vartheta \leq 35$ range with an exposure time of 0.3 s per step. Data sets were acquired from 30 to 570 °C every 20 °C, with a heating rate of a 0.16 °C s^{-1}

Synthetic procedure

[{Cu(cyclam)}$_2$($H_2P_2Mo_5O_{23}$)].4.5H_2O (1–CuMo5). A solution of $CuSO_4\cdot5H_2O$ (0.050 g, 0.20 mmol) and cyclam (0.040 g, 0.20 mmol) in aqueous 1M NaCl (10 mL) was added dropwise to an aqueous 1M NaCl (15 mL) solution containing the $[(CH_3)_3CNH_3]_4[H_2P_2Mo_5O_{23}]\cdot5H_2O$ (0.130 g, 0.10 mmol) preformed precursor. The mixture was stirred for 1 h at room temperature and then filtered to remove a purple solid. The resulting dark purple solution was left to slowly evaporate in an open container at room temperature and purple block–like crystals suitable for X–ray diffraction were obtained after 2 days. The filtered purple solid was later confirmed to be pure **1–CuMo5**. Total combined yield: 44 mg (29% based on the precursor). Anal. Calcd (found) for $C_{20}H_{59}Cu_2Mo_5N_8O_{27.5}P_2$: C, 15.80 (16.03); H, 3.91 (4.01); N, 7.37 (7.47). IR (cm^{-1}): 3254(s), 3215(s), 2926(m), 2870(m), 1647(m), 1458(m), 1430(m), 1327(w), 1296(w), 1248(w), 1119(s), 1096(m), 1065(m), 1047(s), 1010(s), 920(s), 885(s), 673(s), 577(m), 544(m), 502(m), 447(m), 428(m).

[{Cu(cyclam)}$_2$($H_2P_2Mo_5O_{23}$)]·(1a–CuMo5). The anhydrous derivative was obtained by heating single–crystals of **1–CuMo5** at 150 °C in an oven for 1 h, which resulted in a slight color change of the crystals.

[{H_2(cyclam)}$_{0.3}${Ni(cyclam)}$_{0.7}$][{Ni(cyclam)}($H_2P_2Mo_5O_{23}$)].5H_2O (1–NiMo5). The synthesis method is similar to that of **1–CuMo5** except that $Ni(NO_3)_3\cdot5H_2O$ (0.070 g, 0.20 mmol) was used instead of the copper salt. The mixture was stirred for 1 h and then filtered to remove a yellowish solid which was later confirmed to be a **1–NiMo5** in impure bulk form. The resulting dark orange solution was left to slowly evaporate in an open container at room temperature and orange block–like crystals suitable for X–ray diffraction were obtained the next day. Yield: 24 mg (17% based on the precursor). Anal. Calcd (found) for $C_{20}H_{60.6}Mo_5N_8Ni_{1.70}O_{28}P_2$: C, 15.98 (16.19); H, 4.06 (4.31); N, 7.46 (7.60). IR (cm^{-1}): 3283(s), 3252(s), 2922(m), 2864(m), 1628(m), 1458(m), 1429(m), 1337(w), 1294(w), 1249(w), 1124(s), 1097(s), 1009(s), 1065(sh), 1047(s), 916(s), 889(m), 677(m), 575(m), 534(m), 500(m), 443(m), 419(m), 407(m).

[H_2(cyclam)]$_{0.3}$[{Ni(cyclam)}$_{1.7}$($H_2P_2Mo_5O_{23}$)] (1a–NiMo5). The anhydrous derivative was obtained by heating single–crystals of **1a–NiMo5** at 150 °C in an oven for 1 h.

Single–crystal X–ray crystallography

Crystallographic data for Strandberg–type hybrids **1–MMo5** and **1a–MMo5** (M = Cu, Ni) are given in Table 4.1. Intensity data were collected on an Agilent Technologies Super–Nova diffractometer which was equipped with monochromated Mo K_α (λ = 0.71073 Å) and Eos CCD detector. The data collection of **1–CuMo5** and **1–NiMo5** compounds was carried out at 100 K. In the case of the anhydrous Strandberg–type hybrids, **1a–CuMo5** and **1a–NiMo5**, a single crystal of each phase was heated in an oven to 403 K at a rate of 1 K min^{-1} to achieve full dehydration, and immediately afterwards covered with mineral oil and placed under the N_2 stream of the diffractometer, which was ready to perform a full data collection at 100 K. Data frames were processed (unit cell determination, analytical absorption correction with face indexing, intensity data integration and correction for Lorentz and polarization effects) using the CrysAlis Pro software package.[90] The structures were solved using OLEX2[91] and refined by full–matrix least–squares with SHELXL–2014/6.[92] Final geometrical calculations were carried out with PLATON[93] as integrated in WinGX.[94]

Table 4.1. Crystallographic data for **1–MMo5** and **1a–MMo5** (M = Cu, Ni) Strandberg–type hybrids.

	1–CuMo5	**1a–CuMo5**	**1–NiMo5**	**1a–NiMo5**
empirical formula	$C_{20}H_{59}Cu_2Mo_5N_8O_{27.5}P_2$	$C_{20}H_{50}Cu_2Mo_5N_8O_{23}P_2$	$C_{20}H_{60.6}Mo_5N_8Ni_{1.7}O_{27.5}P_2$	$C_{20}H_{50.6}Mo_5N_8Ni_{1.7}O_{23}P_2$
fw (g mol^{-1})	1520.5	1439.4	1502.81	1412.73
crystal system	monoclinic	monoclinic	monoclinic	monoclinic
space group	*P2/n*	*P2$_1$/n*	*P2/n*	*P2/n*
temperature (K)	100(2)	100(2)	100(2)	100(2)
***a* (Å)**	13.6609(5)	13.8438(5)	13.815(2)	14.9096(11)
***b* (Å)**	12.4151(3)	24.9486(7)	12.294(2)	10.9800(9)
***c* (Å)**	14.0678(5)	13.2666(5)	13.839(2)	12.8916(11)
α (°)	90.	90	90	90.00
β (°)	104.786(4)	109.791(4)	103.656(16)	104.128(9)
γ (°)	90	90	90	90.00
***V* (Å^3)**	2306.90(14)	4311.4(3)	2283.9(7)	2046.6(3)
ρ_{calc} (g cm^{-3})	2.189	2.218	2.185	2.292
μ (mm^{-1})	2.384	2.537	2.183	2.419
λ(Å)	0.71073	0.71073	0.71073	0.71073
collected reflns	15395	29701	16686	14143
unique reflns (R_{int})	4056 (0.0259)	7600 (0.0597)	4019 (0.1038)	3589 (0.0893)
obsd reflns [$I > 2\sigma(I)$]	3756	6195	3323	2810
parameters	367	546	431	271
$R(F)$a [$I > 2\sigma(I)$]	0.0373	0.0404	0.0587	0.0584
$wR(F^2)^b$ [all data]	0.0894	0.0925	0.1470	0.1479
GoF	1.057	1.102	1.062	1.043

$^aR(F) = \Sigma||F_o - F_c||/\Sigma|F_o|$; $^bwR(F^2) = \{\Sigma[w(F_o^2 - F_c^2)^2]/\Sigma[w(F_o^2)^2]\}^{1/2}$

Thermal vibrations were treated anisotropically for all non–H atoms in all compounds. Hydrogen atoms of the organic ligands were placed in calculated positions and refined using a riding model with standard SHELXL parameters. Three positions suitable for water molecules of hydration were located in the Fourier maps of both **1–CuMo5** and **1–NiMo5** and their occupancy was initially refined without restrictions. The resulting total number of 2.63 and 2.27 water molecules per half Strandberg cluster was fixed to 2.50 and 2.25 during the final refinement for **1–CuMo5** and **1–NiMo5** respectively, as indicated by the TGA experiments. For **1–CuMo5**, **1–NiMo5** and **1a–NiMo5** some organic ligands were disordered into two positions (labelled A and B or C and D) and refined with variable occupation (**1–CuMo5**: A 0.65, B 0.35; **1–Ni**: A 0.50, B 0.50 and C 0.68, D: 0.32; **1a–NiMo5**: C 0.51 and 0.49 and then fixed at those values.

4.2.2. Results and Discussion

Synthesis

As commented above, the vast majority of hybrid Strandberg were prepared following hydrothermal methods. This synthetic protocol has some advantages (i.e. increasing solubility of reactants and reactivity) but special apparatus and high energy consumption are necessary, and so aqueous synthesis is always preferred as it is more consistent with eco–friendly philosophy. Taking this into account, we carried out the initial synthesis of **1–CuMo5** by reacting the preformed *tert*–butylammonium dihidrogendiphosphopentamolybdate $[(CH_3)_3CNH_3]_4[H_2P_2Mo_5O_{23}]\cdot 5H_2O$ precursor with cyclam and a copper(II) sulfate salt in aqueous medium at room temperature. This way, a few single crystals of **1–CuMo5** were obtained after 3 weeks upon slow solvent evaporation. It must be noted that the reaction yield was really low in these synthetic conditions (less than 5% based on the precursor) which is due to the formation of large amounts of a purple precipitate as the reaction proceeds. Fortunately, this precipitate was later identified as the title compound in pure bulk form as evidenced by both FT–IR and PXRD analyses which together with the crystals resulted in a total combined yield of 10% based on the precursor (Figures A4.1 and A4.2 in the Appendix). Similar results were observed when using different Cu(II) salts (acetate, nitrate and chloride) evidencing an absence of any potential template effect in this particular reaction.

In order to raise the overall reaction yield, we increased the ionic strength of the medium by performing similar reactions in 1M NaCl medium, as this proved to be a viable way to rise the reaction yield as well as crystallization speed in our previous work.[30] Fortunately, the change in solvent favoured both the crystallization speed and the reaction yield as we initially intended and pure block crystals of **1–CuMo5** were isolated after just 2 days with a drastic increase in the overall yield (13% yield based on the precursor). The purple precipitate formed during this reaction was also analysed by FT–IR and PXRD techniques and fortunately, those measurements revealed that it was indeed pure **1–CuMo5** which together with the crystalline fraction summed up to a total yield of 29%. In contrast, the temperature did not affect the reaction in any apparent way as evidenced by analogous reactions carried out from 50 °C to refluxing conditions, which led to our compound in comparable yields. The influence of the pH in this particular $H_2P_2Mo_5O_{23}$: Cu: cyclam synthetic system, however, did have a notable influence in the reaction outcome. The initial pH of the reaction was 3.5 and it led to **1–CuMo5** as a single, homogeneous crystalline phase with a significantly higher yield (13% based on the precursor) than that observed in the absence of NaCl (less than 5%). When the pH was adjusted with NaOH 0.1 M in the range 4.0–6.0, however, **1–CuMo5** was also isolated but as both crystals and as polycrystalline powder after 1 week. Even though the overall yield remained comparable in this specific pH range it is worth mentioning that as the medium became less acidic the polycrystalline powder became the major fraction. Above this pH value up to 12.0 no identifiable solid product could be obtained upon total solvent evaporation whereas when the pH was acidified with 0.1 M HCl to values below 3.0 only block crystals of NaCl were isolated from the mother liquors. The purple precipitate formed when the pH was adjusted in the range 3.0–6.0 corresponded to pure **1–CuMo5** in all cases whereas reactions where the pH was higher or lower resulted in precipitates which could not be further characterized.

We also tried to prepare analogous hybrids using other divalent transition metals (Mn^{II}, Co^{II}, Ni^{II}, and Zn^{II}) instead of Cu^{II}, but unfortunately, only the reaction where Ni was used resulted in a crystalline material upon solvent evaporation (**1–NiMo5**). In this case, significantly less precipitate was formed during the reaction and thus, the yield of the crystals of **1–NiMo5** was higher compared to that of **1–CuMo5** (17% and 13%, respectively). However, the PXRD patterns of that precipitate did not correspond to that of the simulated pattern from the single crystal data of **1–NiMo5**, as opposed to the case when Cu was used as metal source and hence, the total yield is higher for the Cu derivative. Moreover, when Mn and Co were used as 3d–metal source, the PXRD patterns of the formed precipitates did not correspond to the simulated ones of **1–CuMo5** or **1–NiMo5** in the case of Mn while the analogous precipitate of Co showed almost no crystallinity. For the reaction involving Zn, however, the resulting precipitate could be identified as a mixture of an isostructural phase but in impure bulk form on the basis of PXRD and its FT–IR spectrum further corroborates it (Figures A4.1 and A4.2 in the Appendix). Unfortunately, single–crystals of neither the isostructural Zn–containing phase nor the Mn–phase could not be obtained despite our efforts.

Vibrational and thermostructural characterization of 1–CuMo5 and 1–NiMo5

The initial characterization of compounds **1–CuMo5** and **1–NiMo5** was performed by FT–IR analyses. Even though some differences can be observed, the inorganic region of the infrared spectra of **1–MMo5** compounds is highly reminiscent of that of the dihydrogendiphosphopentamolybdate precursor (Figure 4.8). In this sense, the wide strong band arising from the "breathing modes" of the POM shifted to slightly lower wavenumbers in the hybrids while the absorption bands originating from the $\nu(Mo–O_t)$ and $\nu(Mo–O_t)$ vibrations remained almost invariable. The same behavior was observed in the $\delta(P–O_b)$ and $\delta(Mo–O_t)$ flexion modes in the low wavenumber area. However, some of the $\nu(P–O_b)$ bands split into weaker signals at around 1050 cm^{-1}. Regarding the metal–organic region of the FT–IR spectra, the peaks associated with the stretching of the –N–H and –C–H bonds of the cyclam ligand are respectively observed at around 3150 and 2860 cm^{-1}, whereas several weak to medium signals corresponding to the $\delta(C–H)$ and $\nu(N–C)$ vibration modes are also present in the 1490–1230 and 1100–1000 cm^{-1} ranges.

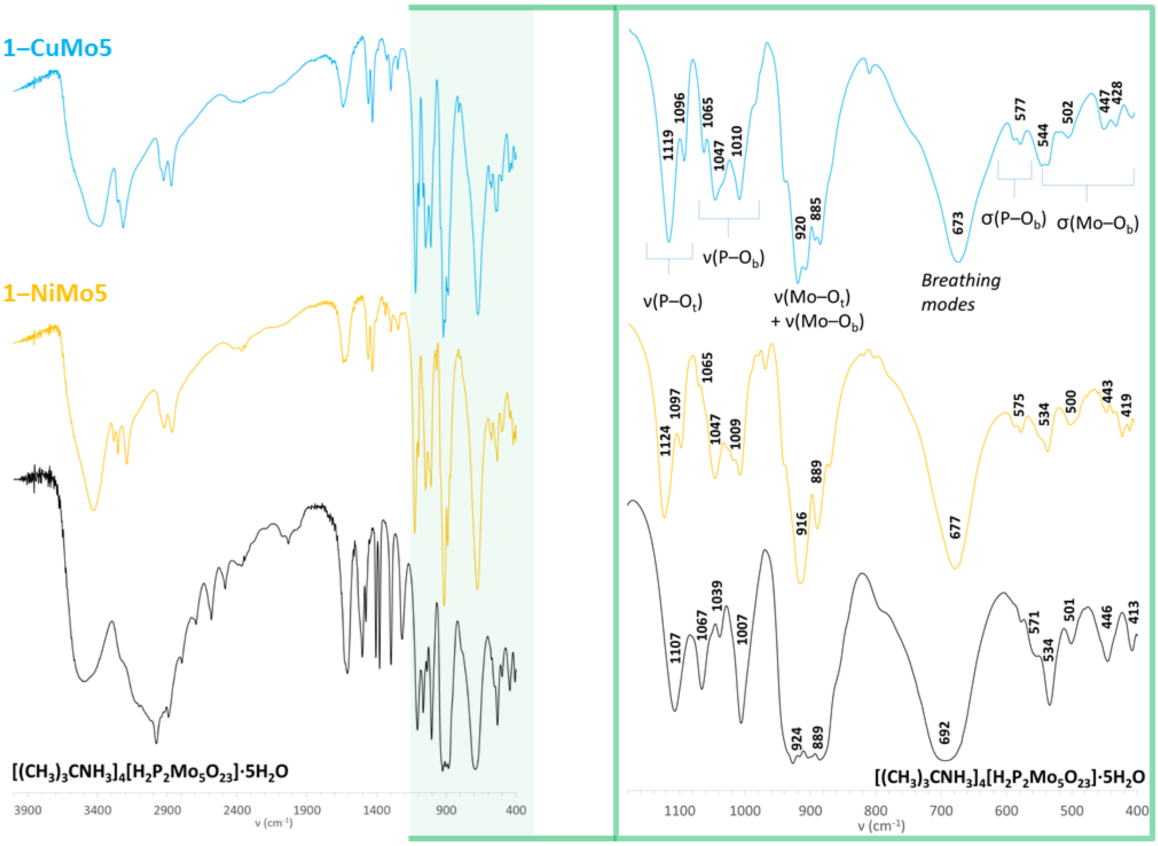

Figure 4.8. FT–IR spectra of **1–CuMo5** and **1–NiMo5** hybrids along with that of the precursor highlighting the inorganic region.

Thermal stability of **1–CuMo5** and **1–NiMo5** hybrids was studied by TGA experiments, which show that both hybrids decompose in a similar manner through three mass loss stages (Figure 4.9). The first stage starts from room temperature to *ca.* 110 °C and corresponds to the evacuation of all water molecules of hydration. The experimental mass loss corresponds to 4.5 and 5 water molecules per Strandberg cluster (calcd. 5.26% and 5.98%, found 5.27% and 5.51% for **1–CuMo5** and **1–NiMo5**, respectively). After this stage a notable range of thermal stability can be observed for the anhydrous phases **1a–CuMo5** and **1a–NiMo5**, which extends up to *ca.* 260 °C. After that, the anhydrous phases undergo further decomposition through two overlapping mass loss stages which are associated with the combustion of the cyclam ligands and the consequent breakdown of the inorganic framework. The overall mass loss for these two stages is in good agreement with two cyclam ligands per Strandberg anion (calcd. for $2C_{10}H_{24}N_4$ 26.83% and 26.75%; found 27.20% and 27.73% for **1–CuMo5** and **1–NiMo5**, respectively). The final residue is obtained at temperatures above 580 °C for both compounds (calcd. for $Cu_2Mo_5O_{23}P_2$ 68.00%, found 67.51%; calcd. for $Mo_5Ni_{1.7}O_{23}P_2$ 67.50%, found 66.80%). Variable–temperature powder X–ray diffraction measurements (TPXRD) between 30 and 570 °C show that both hybrids **1–CuMo5** and **1–NiMo5** maintain their crystallinity upon total dehydration up to temperatures in the 230 to 250 °C range (Figure 4.9). Important modifications in the positions and intensities of several diffraction maxima are observed at temperatures above 70 and 90 °C for **1–CuMo5** and **1–NiMo5**, respectively, indicating that a phase transition took place while heating. This modified diffraction pattern is conserved until the amorphization of the samples suggesting that the anhydrous phases **1a–CuMo5** and **1a–NiMo5** share a virtually identical crystal packing to that of the partially dehydrated samples at 70–90 °C.

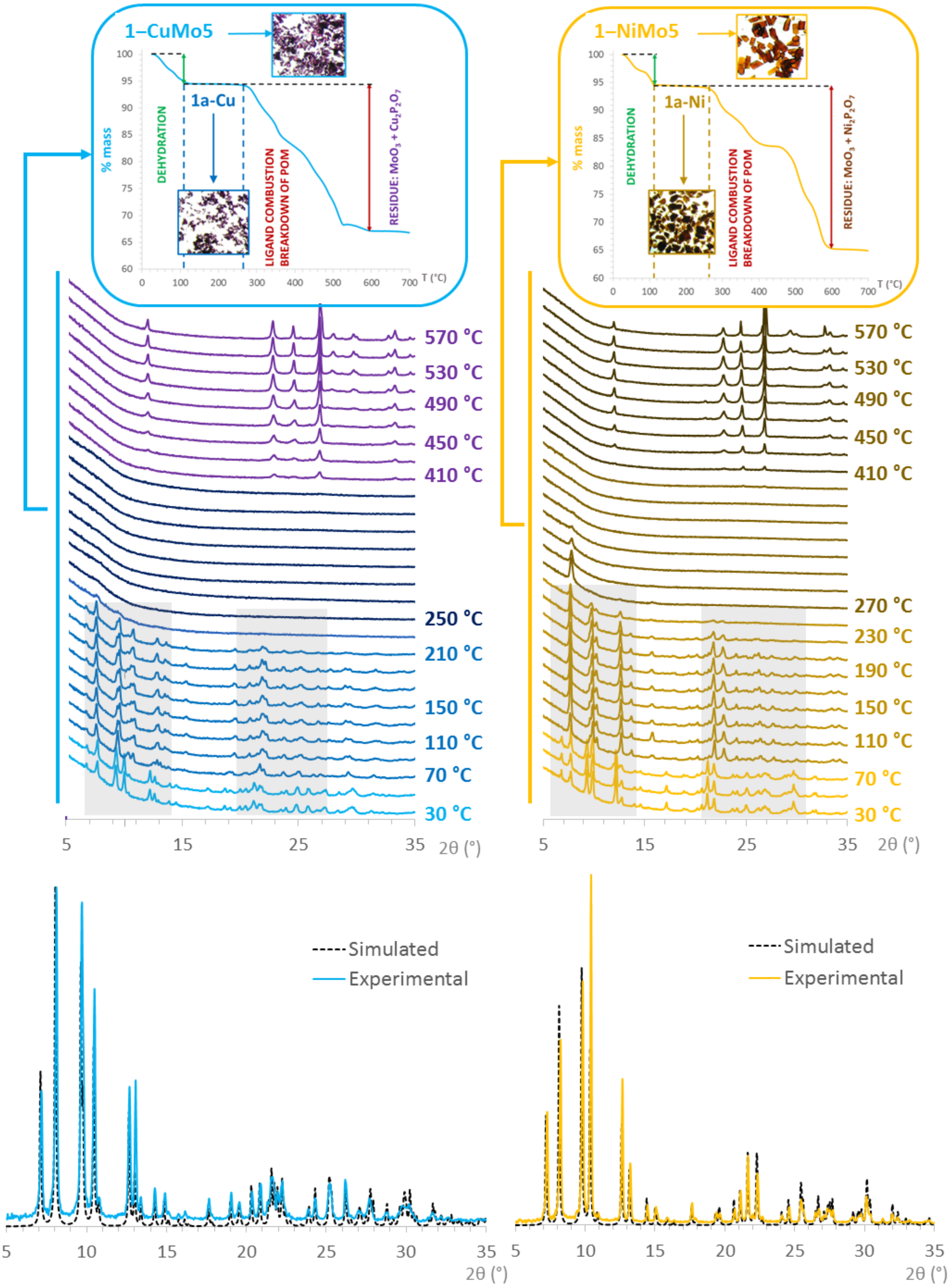

Figure 4.9. TPXRD measurements for **1–CuMo5** and **1–NiMo5** highlighting the two distinct patterns along with the corresponding TGA curves and digital photographs of each phase as well as the comparison between the experimental PXRD patterns and those simulated from the single–crystal XRD data.

Above the dehydration temperature of *ca.* 120 °C, the crystalline **1a–CuMo5** and **1a–NiMo5** phases become amorphous at temperatures above 230 and 250 °C respectively, which nearly corresponds to the beginning of the ligand combustion stage in the TGA curves above. Signs of new high–temperature phases start appearing at *ca.* 410 °C and are defined enough at 550 °C for being identified as a mixture of orthorhombic *Pbnm* MoO_3 (PDF: 00–035–0609)[95] and the corresponding metallic phosphate, that is, the monoclinic *C2/c* $Cu_2P_2O_7$ (PDF: 00–044–0182),[96] in the case of **1–CuMo5** and the monoclinic $B2_1/c$ phase of $Ni_2P_2O_7$ (PDF: 01–074–1604)[97] for **1**–**NiMo5**, in an approximate 2:3 ratio (Figures A4.3 and A4.4 in the Appendix).

Crystal structures of 1–CuMo5 and 1–NiMo5

The isostructural **1–CuMo5** and **1–NiMo5** hybrids crystallize in the orthorhombic *P2/n* space group. The asymmetric unit of **1–CuMo5** contains one half two–fold symmetric Strandberg–type $\{H_2P_2Mo_5O_{23}\}^{4-}$ cluster, two half {Cu(cyclam)} grafted moieties and 4.5 water molecules of hydration that are disordered over six positions. The crystallographic disorder involving one of the tetraazaligands occupies two positions (A and B) which are related by a *ca.* 18 ° rotation (N4A–Cu1A–N1B) around their axial axes with a significant difference in the occupancy (A: 65 and B: 0.35). In comparison, the asymmetric unit of **1–NiMo5** is composed of one half Strandberg cluster, one unsupported half {Ni(cyclam)} complex (Ni1A with a occupation of 0.69) and another half coordinated metalorganic moiety (Ni1C), both of them disordered over two positions, and five disordered water molecules of hydration. The disordered ligands are related by a *ca.* 15° and 31° rotation (N4A–Ni1A–N4B and N1C–Cu1C–N1D, respectively) around their axial axes with a significant difference in the occupancy for the latter (A: 0.50, B: 0.50; and C: 0.68, D:0.32).

The structure of the Strandberg–type polyanion has been described for a long time and it consists in a chiral $\{Mo_5O_{21}\}$ core formed by five edge– and corner–sharing $\{MoO_6\}$ octahedra, which is capped with one $\{PO_3(OH)\}$ tetrahedron on both sides of it through corner sharing, as can be seen in Figure 4.10. The pendant oxygen atom of each phosphorus tetrahedron is protonated, as indicated by charge balance considerations. The Mo–O and P–O bond lengths of both compounds **1–CuMo5** and **1–NiMo5** are in the range 1.70–2.33 Å and 1.50–1.57 Å respectively, which are consistent with other Strandberg–type polyanions found in crystallographic databases.[89]

As seen in Figure 4.10, there are two crystallographically independent {Cu(cyclam)} complexes in **1–MMo5** hybrids (M = Cu, Ni) and both of them display the *trans–III* configuration of the macrocyclic polyamine ligand. Regarding **1–CuMo5** compound, the coordination sphere of both Cu1A and Cu1C metal centers display distorted octahedral CuN_4O_2 geometries, as confirmed by Continuous Shape Measures (CShM),[98] (which are shown in Table 4.2) with the four N atoms of the tetraazaligand forming the equatorial plane and the axial positions occupied by terminal oxygen atoms belonging to the $\{H_2P_2Mo_5O_{23}\}^{4-}$ clusters (O1 and O22).

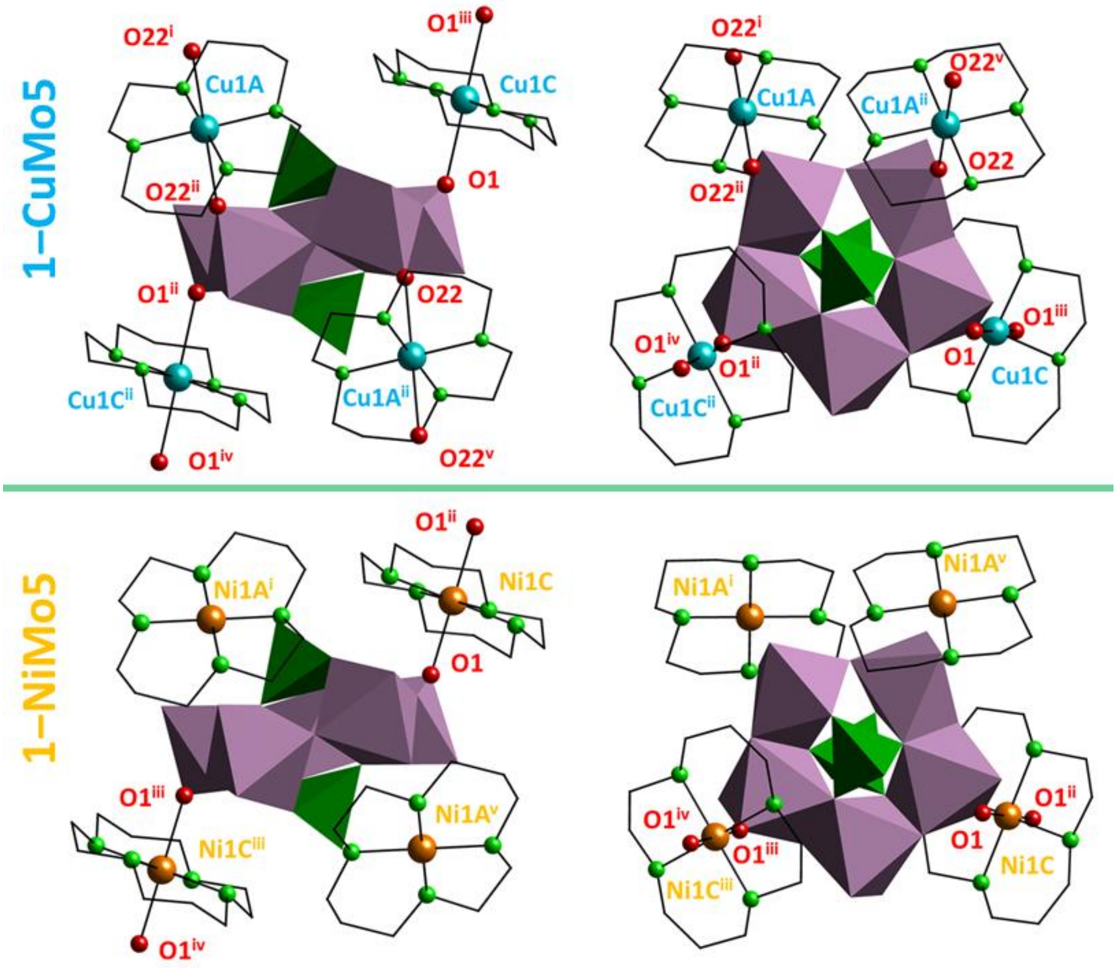

Figure 4.10 Polyhedral representations of the hybrid POMs in **1–MMo5** (M = Cu, Ni) with partial atom labelling. H atoms and water molecules are omitted for clarity. H atoms are omitted for clarity. Color code: blue (Cu), orange (Ni), violet (Mo), dark green (P), bright green (N), red (O). Symmetry codes: **1–CuMo5:** i) –1/2+*x*, –*y*, –1/2+*z*; ii) 3/2–*x*, *y*, 3/2–*z;* iii) 2–*x*, 1–*y*, 1–*z*; iv) –1/2+*x*, 1–*y*, 1/2+*z*; v) 2–*x*, –*y*, 2–*z*. **1–NiMo5**: i) *x*, 1+*y*, *z*; ii) 1–*x*, –*y*, –*z*; iii) 1/2–*x*, *y*, 1/2–*z*; iv) –1/2+*x*, –*y*, 1/2+*z;* v) 1/2–*x*, 1+*y*, 1/2–*z*.

The crystal packing of **1–CuMo5** consist on an three–dimensional covalent hybrid network constructed from the connection of Strandberg–type $[H_2P_2Mo_5O_{23}]^{4-}$ clusters and bridging $\{Cu(cyclam)\}^{2+}$ cationic complexes which lead to the formation of a complex 2–fold interpenetrated diamond–like structure (Figure 4.11). In this structure, each polyanion is linked to another four clusters via four metalorganic moieties (two Cu1A and two Cu1C) which act as pseudotetrahedral 4–connecting nodes and thus, the geometry of the coordination sites (Figure 4.10) are responsible for the generation of the diamondoid topology. The hybrid 3D framework can be described as follows: POM–{Cu(cyclam)}–POM hybrid chains that are formed exclusively by Cu1C moieties run along the [10–1] direction in a zig–zag fashion (Figure 4.11a). These hybrid chains connect to adjacent chains by one of the two Cu1A bridging moieties resulting in the formation of hybrid layers with hexagonal large cavities parallel to the (1–11) plane. The hybrid layers are constituted by the linkage between one cluster to three adjacent polyanions by means of three complexes (one Cu1A and two Cu1C) in such a way that each hexagonal cavity is delimited by six metalorganic moieties (four Cu1C that form the chains and two Cu1A bridging moieties) bonding six clusters (Figure 4.11b).

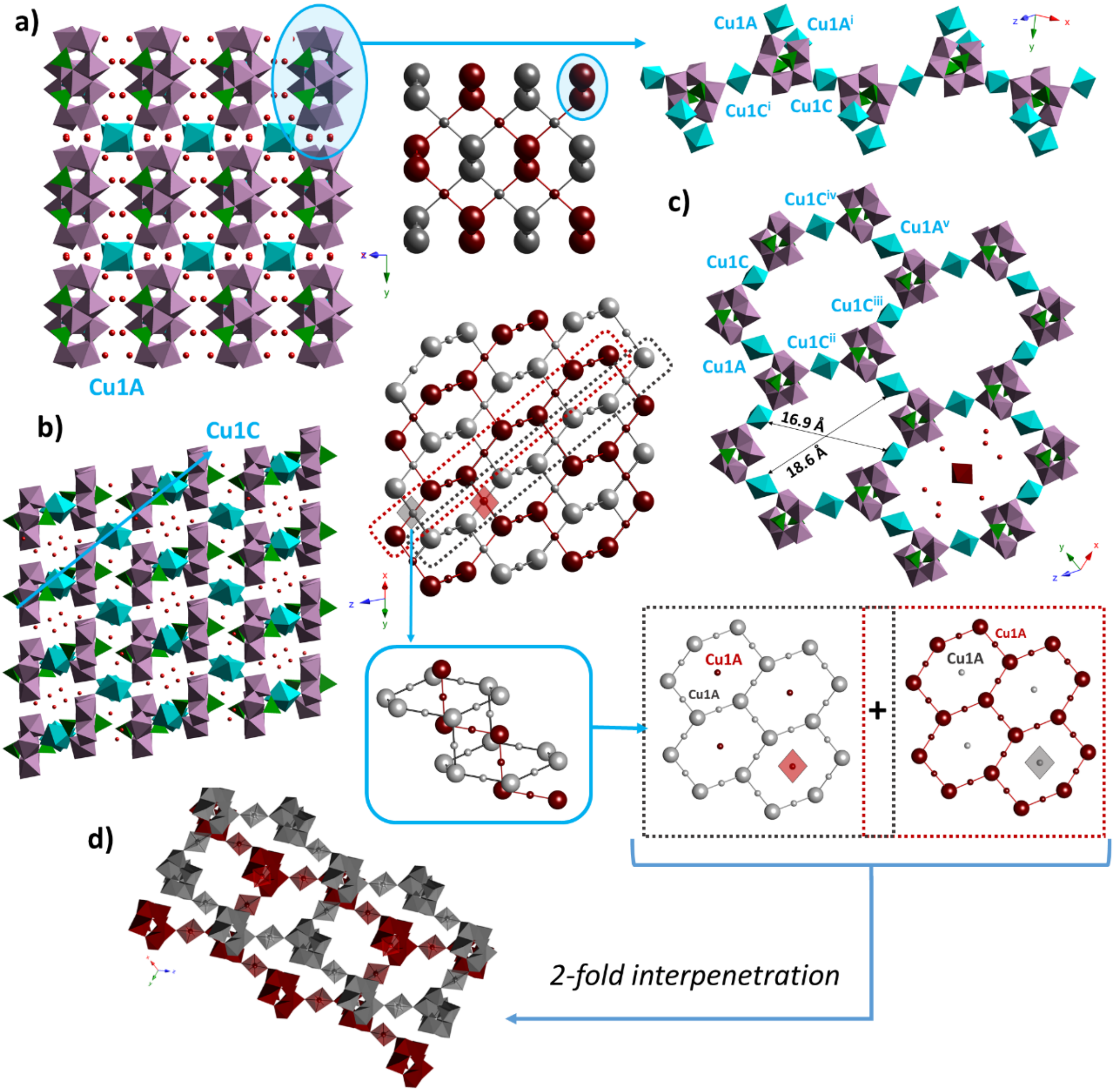

Figure 4.11. a) Polyhedral representation of the crystal packing along the [10–1] direction and Cu1C–POM chains along with a schematic representation of the 2–fold interpenetrated diamond–like hybrid network of **1–CuMo5**. b) Polyhedral representation of the crystal packing along the [110] direction with an schematic representation of the 2–fold hybrid framework showing the interpenetration phenomenon. c) Hybrid layers with partial atom labelling and estimated dimensions of the hexagonal cavities. d) Polyhedral representation of the two interpenetrated hybrid frameworks with different colors. H atoms and cyclam ligands are omitted for clarity. Color code: blue (Cu), violet (Mo), dark green (P), red (O). Bigger balls stand for the clusters whereas the small ones represent Cu atoms. Symmetry codes: i) 3/2–*x*, *y*, 3/2–*z*; ii) 2–*x*, –*y*, –*z*; iii) 3/2–*x*, –1+*y*, 1/2–*z*; iv) 5/2–*x*, y, 1/2–*z*; v) 1+*x*, *y*, –1+*z*.

The connection between neighboring layers by the remaining Cu1A bridging complex along the [1–11] direction results in the generation of the above mentioned 3D diamond–like hybrid framework that show microchannels along both [010] and [001] directions where the water molecules of hydration are located (Figure 4.12). Regarding the hexagonal cavities, the approximate cross–section of which are 18.6 × 16.9 $Å^2$ (distances N4A···N4A and N1C···N1C, Figure 4.11c), are large enough to allow further nucleation in the void space and a second diamond–like network is generated within the first framework. This way, the Cu1A complex responsible for connecting two contiguous layers from the second network penetrates the hexagonal cavities of the layers belonging to the first net resulting in a 2–fold interpenetrated hybrid arrangement (Figure 4.11b). As a result, consecutive layers of one framework result superimposed to each other in such a way that the cavities of each layer are blocked on both sides by clusters bridged by Cu1A moieties belonging to adjacent layers of the other interpenetrated network (Figure 4.11d). This fact explains the low value calculated for the total solvent accessible voids (190 Å^3, 8% of the total volume of the unit cell) using the Platon software. In regards to the metallocyclam complexes, the distances between the building blocks are significantly shorter for the Cu1C moiety that forms the above mentioned chains whereas Cu1A moiety displays a bond length near that of semi–coordination (2.393(4) and 2.565(4) Å, respectively), indicating a weaker coordination between different chains (Table 4.2).

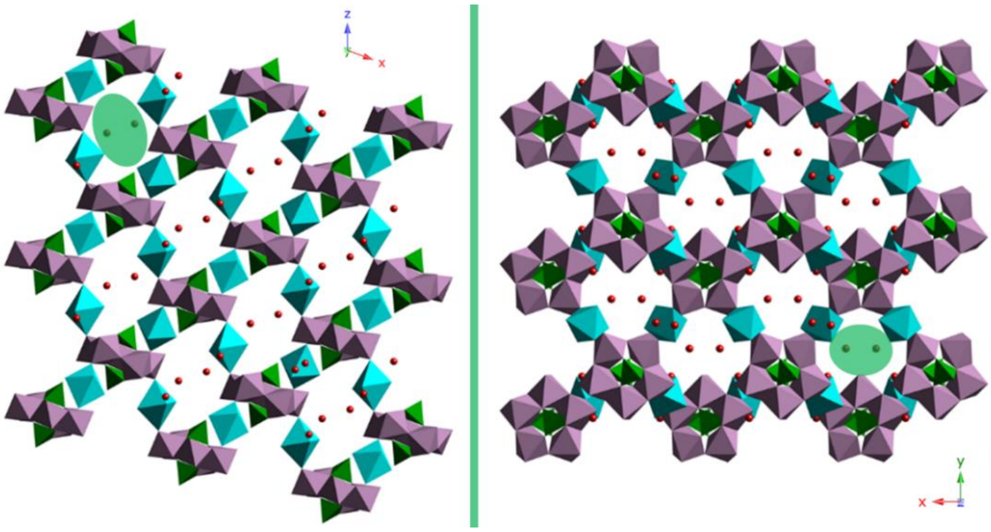

Figure 4.12. a) Polyhedral representation of the crystal packing of **1–CuMo5** along [010] and [001] directions highlighting the microchannels where the water molecules of hydration are hosted. H atoms and cyclam ligands are omitted for clarity. Color code: blue (Cu), violet (Mo), dark green (P), red (O).

Table 4.2. Cu–O and Cu–N bond lengths (Å) as well as the polyhedral distorsion (CShM) of the {M(cyclam)} complexes in **1–MMo5** and **1a–MMo5** (M = Cu, Ni).

1–CuMo5		**1a–CuMo5**		**1–NiMo5**		**1a–NiMo5**	
Cu1A–N$_{mean}$	2.021	Cu1A–N$_{mean}$	2.015	Ni1A–N$_{mean}$	1.977	Ni1A–N$_{mean}$	2.055
Cu1A–O22^{ii}	2.565(4)	Cu1A–O22	2.298(4)	Ni1A···O22^{ii}	2.726(7)	Ni1A–O22	2.194(7)
Cu1A–O22^{iii}	2.565(4)	Cu1A–O5^{i}	2.449(4)	Ni1A···O22^{iii}	2.726(7)	Ni1A–O22^{i}	2.194(7)
OC–6	1.463	OC–6	0.752	SP–4	0.020	OC–6	0.110
Cu1C–N$_{mean}$	2.023	Cu1C–N$_{mean}$	2.016	Ni1C–N$_{mean}$	2.062	Ni1C–N$_{mean}$	2.069
Cu1C–O1	2.393(4)	Cu1C–O1	2.478(4)	Ni1C–O1	2.124(5)	Ni1C–O1	2.122(6)
Cu1C–O1^{iv}	2.393(4)	Cu1C–O1^{ii}	2.478(4)	Ni1C–O1^{iv}	2.124(5)	Ni1C–O1^{ii}	2.122(6)
OC–6	1.008	OC–6	1.225	OC–6	0.172	OC–6	0.083
—	—	Cu21C–N$_{mean}$	2.016	—	—	—	—
—	—	Cu2C–O4	2.513(5)	—	—	—	—
—	—	Cu2C–O4^{iii}	2.514(5)	—	—	—	—
—	—	OC–6	1.210	—	—	—	—

Symmetry codes: **1–CuMo5:** ii) −1/2+*x*, −*y*, −1/2+*z*; iii) 3/2−*x*, *y*, 3/2−*z*; iv) 2−*x*, 1−*y*, 1−*z*. v) −1/2+*x*, 1−*y*, 1/2+*z*. **1a–CuMo5:** i) 1/2+*x*, 1/2−*y*, 1/2+*z*; ii) 2−*x*, 1−*y*, 1−*z*; iii) 1−*x*, 1−*y*, 2−*z*. **1–NiMo5**: ii) 1/2−*x*, −1+*y*, 1/2−*z*; iii) −1/2+*x*, −*y*, −1/2+*z*; iv) 1−*x*, −*y*, −*z*. **1a–NiMo5**: i) 1−*x*, 1 −*y*, 2−*z*; ii) 1−*x*, −*y*, 1−*z*. CShM: reference polyhedra SP–4 (square) and OC–6 (octahedron).

The 2–fold crystal hybrid lattice is further reinforced by a significant H–bond network that results from the interactions between the different metalorganic complexes and terminal O atoms of the POM clusters, as well as some crystallization water molecules (Table 4.3).

Table 4.3. Intermolecular N–H···O and C–H···O interactions (Å) in **1–CuMo5** and the anhydrous **1a–CuMo5.**

1–CuMo5				**1a–CuMo5**	
Donor–H···Acceptor	**D···A**	**Donor–H···Acceptor**	**D···A**	**Donor–H···Acceptor**	**D···A**
O1P–H1P···O1W^{v}	2.544(5)	—	—	O1P–H1P···O13^{ii}	3.073(5)
—	—	—	—	O2P–H2P···O44^{iii}	2.775(5)
N1A–H1A···O1W^{i}	2.976(8)	N1B–H1B···O20^{vi}	3.511(18)	N1A–H1A···O1P	3.473(6)
—	—	N1B–H1B···O2P^{iv}	3.415(17)	—	—
N4A–H4A···O2P^{ii}	3.324(8)	N4B–H4B···O1W^{vii}	3.051(18)	N4A–H4A···O21^{i}	3.470(6)
—	—	—	—	N4A–H4A···O25^{i}	3.347(6)
C2A–H2AA···O3^{iii}	3.236(10)	—	—	C2A–H2AB···O33^{ii}	3.092(8)
C2A–H2AB··O20	3.437(11)	—	—	C2A–H2AB··O3^{ii}	3.481(8)
C3A–H3AA···O2	3.319(11)	C3B–H3BA···O3^{viii}	3.239(15)	C3A–H3AB···O2^{i}	3.313(9)
C6A–H6AB···O1P^{ii}	3.477(11)	C6B–H6BA···O2P^{ii}	3.45(2)	C6A–H6AB···O21^{i}	3.274(8)
C7A–H7AB···O2^{iv}	3.523(10)	C7BC–H7BB···O3W^{ix}	3.53(2)	—	—
		—	—	C13A–H13A···O54	3.289(9)
N1C–H1C···O12^{x}	3.374(8)	—	—	N1C–H1C···O3^{ii}	3.160(6)
N4C–H4C···O31^{ii}	3.444(7)	—	—	N4C–H4C···O31	3.166(6)
N4C–H4C···O1P^{ii}	3.283(7)	—	—	N4C–H4C···O2P	3.165(7)
C2C–H2CA···O3	3.280(9)	—	—	C2C–H2CA···O12	3.401(7)
C2C–H2CB···O2W^{x}	3.367(12)	—	—	—	—
C3C–H3CA···O11^{vii}	3.239(8)	—	—	—	—
C6C–H6CA···O3W^{ix}	3.282(15)	—	—	C6C–H6CA···O3	3.269(8)
—	—	—	—	N24C–H24C···O54	3.404(6)
—	—	—	—	N24C–H24C···O45	2.974(6)
—	—	—	—	C22C–H22A···O43	3.308(7)
—	—	—	—	C26C–H26A···O45^{iv}	3.366(8)
—	—	—	—	C27C–H27A···O11^{ii}	3.282(8)

Symmetry codes: **1–CuMo5:** i) 3/2–*x*, –1+*y*, 3/2–*z*; ii) 3/2–*x*, *y*, 3/2–*z*; iii) *x*, –1+*y*, –*z*; iv) –1/2+*x*, –*y*, –1/2+*z*; v) 2–*x*, 1–*y*, 2–*z*; vi) 1–*x*, –*y*, 1–*z*; vii) –1/2+*x*, 1–*y*, –1/2+*z*; viii) 1–*x*, 1–*y*, 1–*z*; ix) 2–*x*, –*y*, 1–*z*; x) 2–*x*, 1–*y*, 1–*z*. **1a–CuMo5:** i) 1/2+x, 1/2–y, 1/2+z; ii) 2–x, 1–y, 2–z; iii) 1–x, 1–y, 1–z; iv) 1–x, 1–y, 2–z.

Even though **1–NiMo5** is isostructural to **1–CuMo5** (Table 4.1), the difference in the plasticity of the coordination sphere of the metals results in a different connectivity between the different building blocks. As a result and opposed to **1–CuMo5**, Ni1A complex is not coordinated to the clusters (Ni1A···O22 = 2.726(7) Å) and adopts a square planar geometry (Figures 4.10 and table 4.2), which also shows a *trans–III* configuration of the ligand. The other complex Ni1C however, remains coordinated to the polyoxoanions with a distorted octahedral geometry just like the equivalent one observed in **1–CuMo5** (Ni1C–O1 = 2.124(5) Å) and hence, similar zig–zag chains can be observed along the [10–1] direction (Figure 4.13).

As a consequence of the differences in the Ni(II) bonding in Ni1A, the chains are no longer connected and consequently, no covalent layers can be found in the structure, which reduces the overall dimensionality to a monodimensional assembly compared to the 3D covalent arrangement observed in **1–CuMo5**. This way, a system of hybrid zig–zag chains are observed along the [10–1] direction which interact with each other via H–bond intermolecular interactions (Figure 4.13a.) and these interactions are responsible for the formation of supramolecular hybrid grids which are highly reminiscent of the covalent layers found in **1–CuMo5**, as expected (Table 4.4). The approximate cross–section of these cavities are 18.9 x 16.6 Å^2 (distances N1A···N1A and N4C···N4C) the stacking of which is similar to those found in the Cu derivative (Figure 4.13b), resulting in an identical value of 8% for the total solvent accessible volume as well (Platon software). Interestingly, the occupation of the square planar Ni1A center is incomplete (0.68) which means that nearly one third of that position in the crystal (Ni1A) is occupied by a protonated {H$_2$cyclam}$^{2+}$ fragment instead of a metallorganic complex. In order to check if this feature was indeed inherent to this particular crystal structure and not an artifact of some sort, we repeated the synthesis of **1–NiMo5** with a significant excess of the Ni source (2.0 mmols instead of 0.20 mmols) and measured a single crystal obtained from it, which resulted in the exact structure as **1–NiMo5** with the same value for the occupancy of the defect metal center Ni1A.

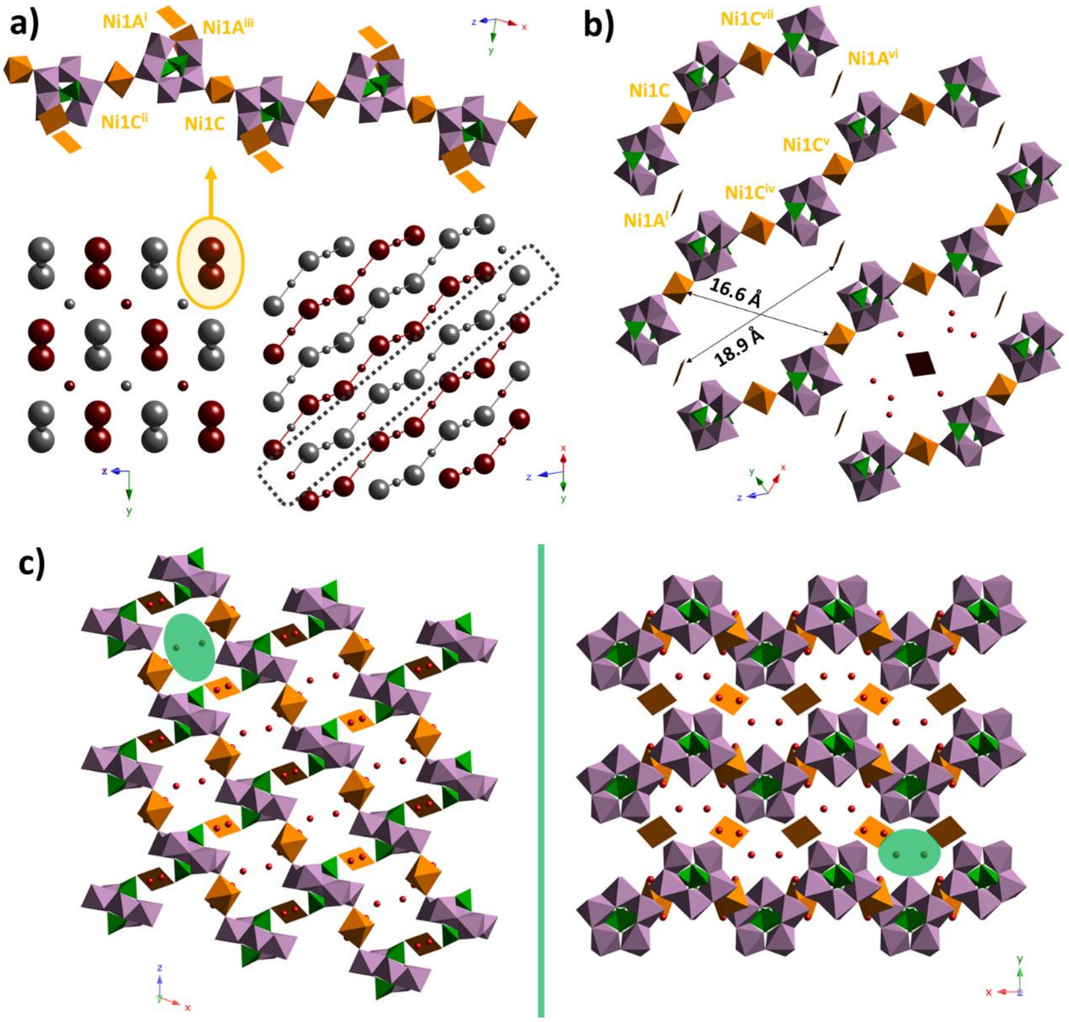

Figure 4.13. a) Polyhedral representation of the hybrid Ni1C–POM chains with schematic representations of the framework along [10–1] and [110] directions in **1–NiMo5**. b) Supramolecular layers with partial atom labelling and estimated dimensions of the cavities. c) Crystal packing along [010] and [001] directions highlighting the microchannels where the water molecules of hydration are hosted. H atoms and cyclam ligands are omitted for clarity. Color code: orange (Ni), violet (Mo), dark green (P), red (O). Bigger balls stand for the clusters whereas the small ones represent Ni atoms. Symmetry codes: i) *x*, 1+*y*, *z*; ii) 1/2–*x*, *y*, 1/2–*z*; iii) 1/2–*x*, 1+*y*, 1/2–*z*; iv) –1/2+*x*, 1–*y*, –1/2+*z*; v) *x*, 1+*y*, –1/2+*z*, –1+*z*; vi) 1–*x*, –*y*, –1–*z*; vii) 3/2–*x*, *y*, –1/2–*z*.

Table 4.4. Intermolecular N–H···O and C–H···O interactions (Å) in **1–NiMo5** and the anhydrous **1a–NiMo5.**

1–NiMo5				**1a–NiMo5**			
O1P–H1P···O1W^{ii}	2.571(8)	—	—	—	—	—	—
N1A–H1A···O2P^{i}	3.373(18)	N1B–H1B···O2P^{i}	3.311(18)	N1A–H1A···O2P^{i}	3.398(10)	—	—
—	—	—	—	N1A–H1A···O1P^{i}	3.242(11)	—	—
N4A–H4A···O1W	3.041(17)	N4B–H4B···O1W	2.951(17)	—	—	—	—
C2A–H2AB···O2^{i}	3.312(18)	C2B–H2BB···O2^{i}	3.36(2)	—	—	—	—
C3A–H3AB··O3	3.140(19)	C3B–H3BA···O20^{i}	3.410(19)	C3A–H3AB···O3^{ii}	3.213(13)	—	—
—	—	C3B–H3BA···O23	3.195(19)	C3A–H3AB··O13^{iii}	2.994(12)	—	—
N1C–H1C···O31	3.412(13)	N1D–H1D···O31	3.32(2)	N1C–H1C···O31	3.489(17)	N1D–H1D···O12	2.984(17)
—	—	—	—	N1C–H1C···O2P	3.383(17)	—	—
N4C–H4C···O12^{iii}	3.199(14)	N4D–H4D···O12^{iii}	3.03(3)	N4C–H4C···O12	3.206(18)	N4D–H4D···O31	3.356(16)
N4C–H4C···O3W	3.359(18)	—	—	—	—	N4D–H4D···O1P	3.359(15)
C2C–H2CA···O11^{iv}	3.350(17)	C2D–H2DB···O3W	3.06(3)	C2C–H2C2···O19	3.30(2)	—	—
C3C–H3CB···O3	3.22(2)	C3D–H3DB···O3	3.13(3)	—	—	—	—
C6C–H6CB···O2W^{v}	3.18(3)	C6D–H6DA···O1P	3.37(3)	C6C–H6CB···O12	3.42(2)	C6D–H6DB···O2P	3.22(2)
—	—	—	—	C6C–H6CB···O2	3.45(3)	C6D–H2D2···O3^{iv}	3.35(2)

Symmetry codes: **1–NiMo5:** i) *x*, –1+*y*, *z*; ii) –*x*, –*y*, –*z*; iii) 1–*x*, –*y*, –*z*; iv) –1/2+*x*, –*y*, –1/2+*z*; v) 1–*x*, –*y*, –*z*. **1a–NiMo5:** i) 1/2–*x*, *y*, 3/2–*z*; ii) x, *1*+y, *z*; iii) 1/2–*x*, 1+*y*, 3/2–*z*; iv) 1/2–*x*, –*y*, –1/2+*z*.

Two Strandberg hybrids built from Cu^{II} and Ni^{II} complexes of a closely related macrocyclic ligand, namely 5,5,7,12,12,14–hexamethyl–1,4,8,11– tetraazacyclotetradecane, can be found in the literature.[37] While the Cu derivative consist on a simple 1D covalent arrangement, the Ni derivative exhibits an interesting 3D open–framework with hydrophobic channels along the *z* axis where the water molecules reside, the approximate dimensions of which are 10.7 x 10.9 Å^2 (C···C distances of the single methyl groups, Figure A4.5 in the Appendix). As opposed to our compounds, there is no interpenetration phenomenon and thus, the total solvent accessible volume is quite high (46% which corresponds to 3951 Å^3 of the total volume of the unit cell). In contrast, Ramanan et al. reported a water–mediated extended interpenetrated framework based on Cu(pz) moieties,[13] the formula of which is $[\{Cu(pz)_4\}_2(H_2P_2Mo_5O_{23})]\cdot H_2O$ (pz = pyrazole).

SCSC transformations: 1a–CuMo5 and 1a–NiMo5 structures

Total removal of water molecules was achieved by heating single crystals of both compounds to 150 °C for an hour, which resulted in the transformation to their respective anhydrous **1a–CuMo5** and **1a–NiMo5** phases, the structures of which were determined owing to their capacity to maintain their crystallinity throughout the heating process. The anhydrous **1a–CuMo5** hybrid crystallizes in the monoclinic $P2_1/n$ space group. The modification of the space group resulted in a slight decrease of the cell parameter *c* accompanied by the duplication of the *b* parameter (Table 4.1) which led to a different asymmetric unit content resulting in the generation of a third crystallographically independent Cu complex (Cu2C). Thus, the asymmetric unit of **1a–CuMo5** is formed by one full Strandberg–type cluster and three half {Cu(cyclam)} moieties (Cu1A, Cu1C and Cu2C), all of them grafted at the same coordination site at the surface of the POM as in the hydrated phase (Figure 4.14). As opposed to **1–CuMo5**, no crystallographic disorder was observed for the anhydrous derivative.

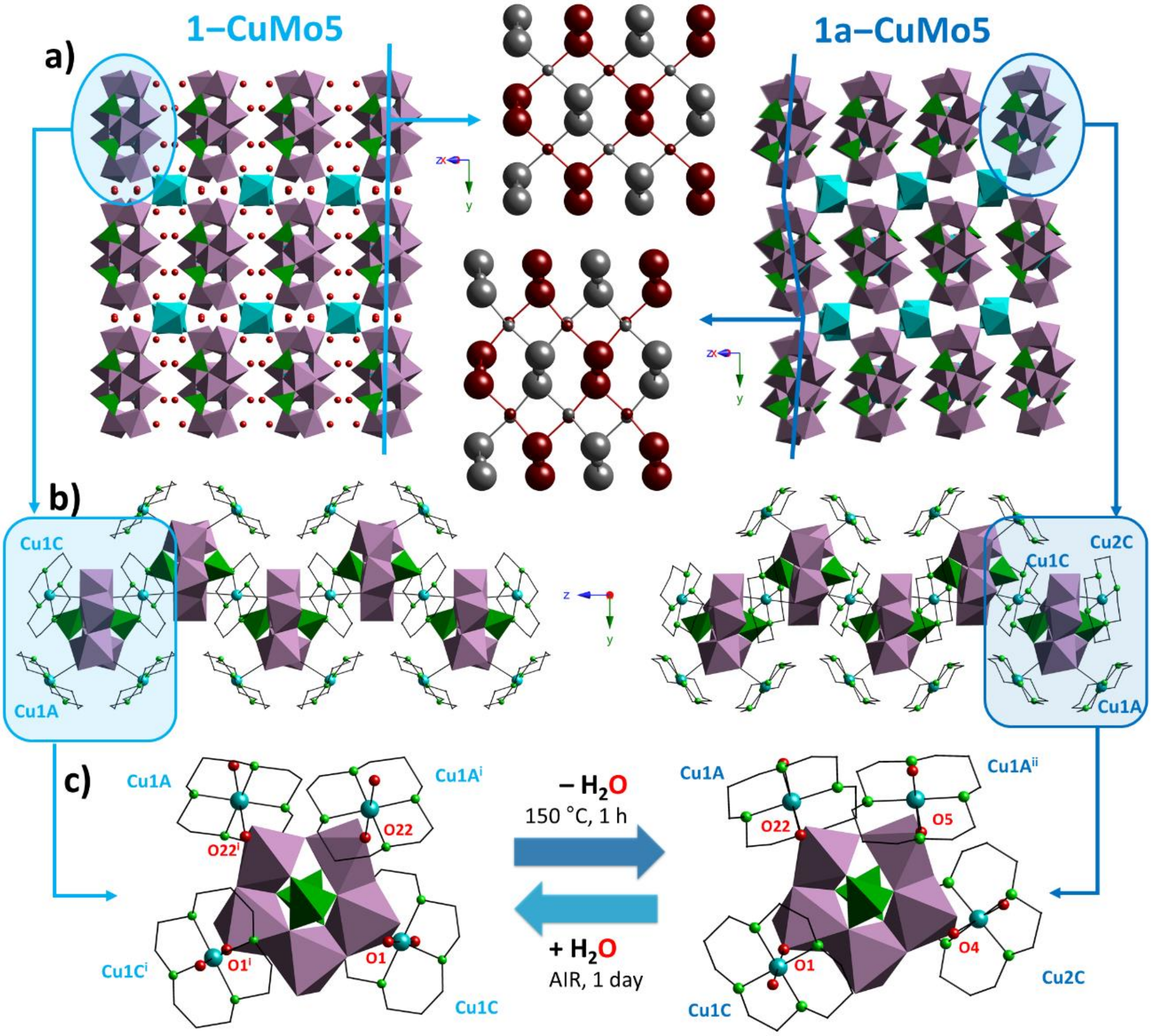

Figure 4.14. a) Polyhedral representation of the crystal packing together with schematic representations along the [10–1] direction of the 2–fold interpenetrated structure for both **1–CuMo5** and **1a–CuMo5** showing the distortion of the network triggered by the SCSC process. b) Comparison between the hybrid Cu1C–POM hybrid chains in both thermal derivatives. c) Hybrid polyanions with partial atom labelling showing the geometrical modifications of the complexes triggered by the SCSC transformation upon dehydration. H atoms are omitted for clarity. Color code: blue (Cu), violet (Mo), dark green (P), bright green (N), red (O). Bigger balls stands for the clusters whereas the small ones represent Cu atoms. Symmetry codes: i) 3/2–*x*, *y*, 3/2–*z;* ii) –1/2+*x*, 1/2–*y*, –1/2–*z*.

The crystal packing of **1a–CuMo5** remained largely the same as the hydrated analogue (Figures 4.14a), although some notable structural modifications took place after the dehydration. First, slight differences in the Cu–O bond lengths between the different building blocks can be observed after the SCSC transformation. While Cu1C and Cu2C complexes undergo a slight lengthening of their respective Cu–O bonds evidencing a weaker coordination between clusters belonging to the same chain, dehydration also resulted in a significant shortening of the bond lengths shown by the Cu1A complexes, which in turn indicated that the chains drew near to each other (Table 4.7). The hybrid layers remained also virtually unaltered as confirmed by the similar dimensions of the hexagonal cavities as seen in Figure 4.15b (19.3 × 16.6 Å^2, distances N4A···N11A and N1C···N1D), as well as the reinforcing H–bond network (Table 4.8).

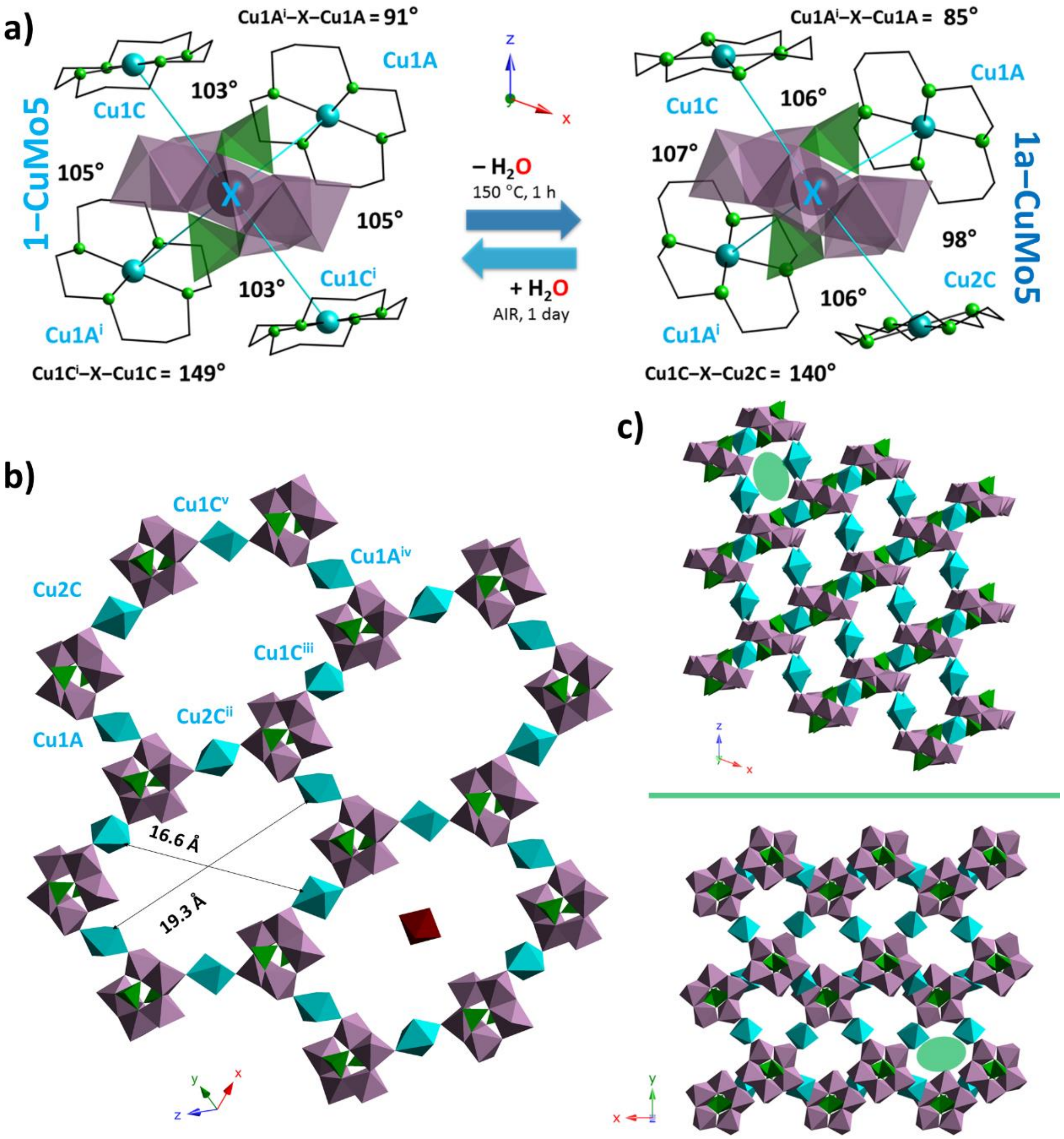

Figure 4.15. a) Pseudotetrahedral geometry of the coordination sites showing M–X–M angles (°) where X is the calculated centroid between the two P atoms of the Strandberg clusters before and after the SCSC transformations (P1–P1 for **1–CuMo5**; P1–P2 for **1a–CuMo5**). b) Hybrid layers with partial atom labelling and estimated dimensions of the hexagonal cavities. c) Crystal packing along [010] and [001] directions highlighting the microchannels in the anhydrous **1a–CuMo5**. Color code: blue (Cu), violet (Mo), dark green (P), bright green (N), red (O). Symmetry codes: **1–CuMo5:** i) 3/2–*x*, *y*, 3/2–*z*. **1a–CuMo5**: i) –1/2+*x*, 1/2–*y*, –1/2–*z*. ii) 2–*x*, –*y*, –*z*; iii) 3/2–*x*, –1+*y*, 1/2–*z*; iv) 5/2–*x*, y, 1/2–*z*; v) 1+*x*, *y*, –1+*z*.

However, the most notable structural change is associated with the Cu1C and Cu2C ligands that form the hybrid chains. Compared to Cu1C in **1–CuMo5**, the equivalent ligands found in **1a–CuMo5** suffered a remarkable *ca*. 90° rotation around their axial axes as can be seen in Figure 4.14b whereas an approximate 20 ° rotation was also observed for the Cu1A ligands. Angles between the different Cu centers and the centroid calculated from the two P atoms show almost no variations when going from **1–CuMo5** to **1a–CuMo5** as well, except Cu1A–X–Cu1A that exhibits a decrease of almost 6° (Figure 4.15a). As a result, even though the overall structure is maintained (Figure 4.15c), a slight distortion of the 2–fold diamantoid framework can be observed compared to that found in the hydrated analogue (Figure 4.14a). This distortion results in a total accessible solvent volume of 271 Å^3 which corresponds to roughly 12 % of the total volume of the unit cell of **1a–CuMo5**, as opposed to the significantly lower value of 8% found for the more regular framework of the hydrated **1–CuMo5** derivative.

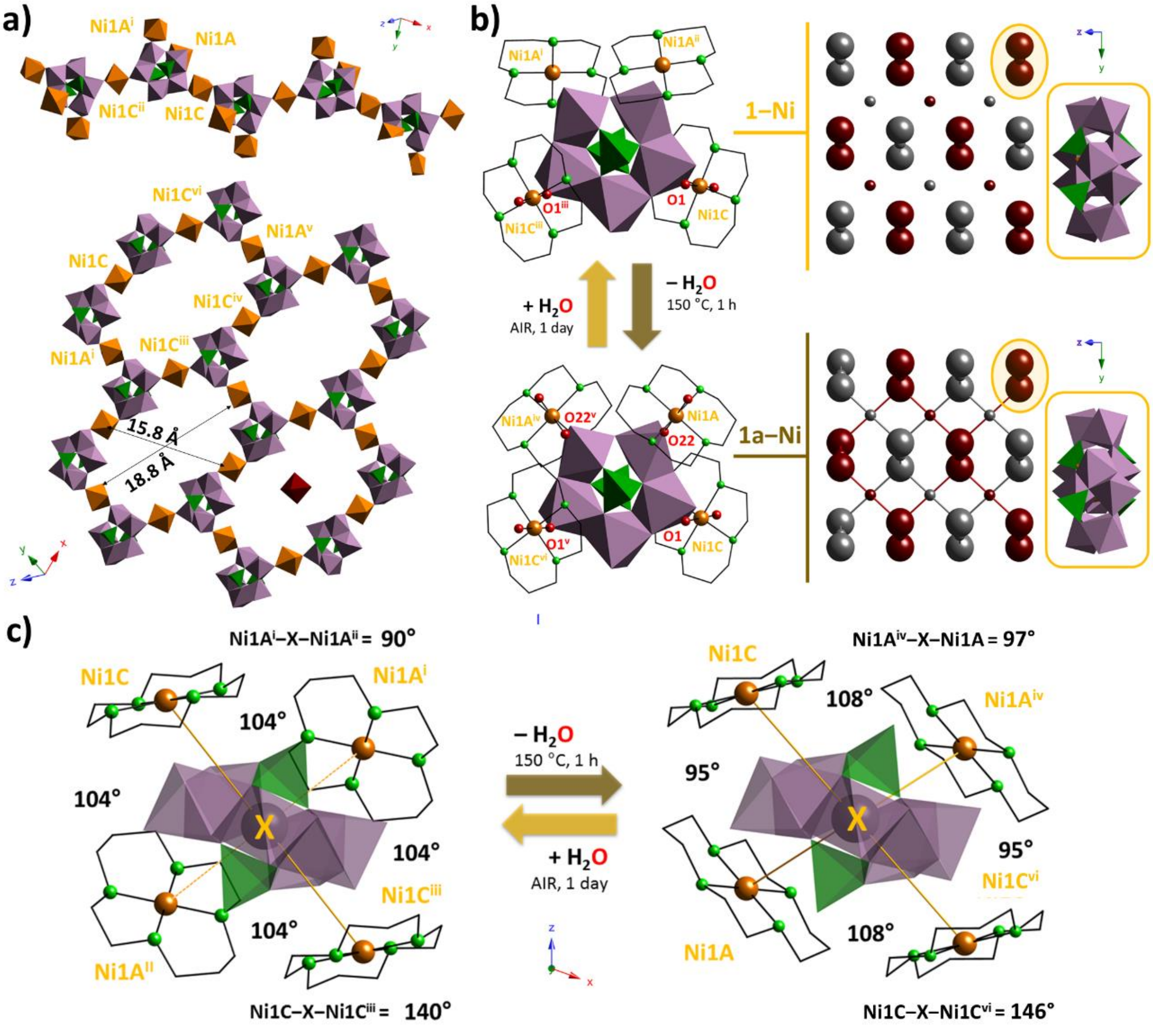

Figure 4.16. a) Polyhedral representation of the hybrid Ni1C–POM chains a well as the hybrid layers with partial atom labelling and estimated dimensions of the hexagonal cavities. b) Hybrid POMs in **1–NiMo5** and **1a–NiMo5** with partial atom labelling showing the geometrical modifications of the complexes induced by the 0D to 3D SCSC transformation together with schematic representations of the hybrid networks along the [10–1] direction. c) Pseudotetrahedral geometry of the coordination sites showing M–X–M angles (°) where X is the calculated centroid between the two P1 atoms of the Strandberg clusters before and after the SCSC transformations. H atoms and water molecules are omitted for clarity. Color code: orange (Ni), violet (Mo), dark green (P), bright green (N), red (O). Bigger balls stands for the clusters whereas small ones represent Ni atoms. Symmetry codes in a): i) –1/2+*x*, 1–*y*, –1/2+*z*; ii) –1/2+*x*, –*y*, 1/2+*z*, iii) 1/2+*x*, 1–*y*, –1/2+*z*; iv) *x*, 1+*y*, –1+*z*; v) 1/2+*x*, 1–*y*, –3/2+*z*; vi) 1/2+*x*, –*y*, –1/2+*z*. Symmetry codes in b) and c): i) *x*, 1+*y*, *z*; ii) 1/2–*x*, 1+*y*, 1/2–*z*; iii) 1/2–*x*, *y*, 1/2–*z*; iv) –1/2+*x*, 1–*y*, –1/2+*z*; v) 1/2–*x*, *y*, 3/2–*z*; vi) –1/2+*x*, –*y*, 1/2+*z*.

Regarding the Ni derivative, the anhydrous **1a–NiMo5** hybrid maintains the P*2/n* space group observed in the hydrated **1–NiMo5** and **1–CuMo5** hybrid lattices. As a result, the asymmetric unit of **1a–NiMo5** is similar to that of the hydrated phases (Figure 4.16), which is formed by one half cluster and two half coordinated metalorganic moieties (Ni1A and Ni1C) with the exact same occupancy for the defect Ni1A (0.68) metal center observed in **1–NiMo5**. In close analogy to **1–CuMo5** however, one of the {Ni(cyclam)} moieties (Ni1C) is disordered over two positions which are related by a *ca.* 18° rotation (N4C–Cu1C–N1D) around their axial axes showing nearly identical occupancies (C: 0.51 and D: 0.49), as opposed to the disorder observed around Ni1C in the hydrated **1–NiMo5**, where the difference in the occupancy is significantly higher (C: 0.68, D:0.32). Even though the parameter *a* increased, both *b* and *c* decreased significantly compared to the cell unit of the hydrated **1–NiMo5** (Table 4.1) indicating that a compression of the crystal lattice took place, which resulted in an approximately reduction in the unit cell volume of *ca.* 400 Å^3 leading to the anhydrous **1a–NiMo5.**

Compared to the transition from **1–CuMo5** into **1a–CuMo5** where the overall structure did not undergo major changes, the transformation from **1–NiMo5** into **1a–NiMo5** constitutes a rare case of a SCSC involving a 1D to 3D transition. After removal of the solvent molecules, the resulting compaction forced adjacent clusters to approach each other and thus, the square planar Ni1A cations seen in **1–NiMo5** became grafted to Mo2 octahedron belonging to different chains (Ni1A–O22 = 2.194(7)) becoming octahedral bridging complexes in the process (See Table 4.2). Since the coordination sites are identical to those observed in the Cu derivatives, dehydration resulted in the generation of a virtually identical 2–fold interpenetrated diamond–like structure to that of the hydrated **1–CuMo5** derivative (Figure 4.16), although a more compacted one due to the shorter Ni–O bonds and the absence of the flexibility of the Cu coordination sphere. Compared to Cu derivatives, the occurrence of the SCSC transformation left Ni1C moieties practically unaltered with virtually identical bond lengths (Table 4.2) while the Ni1A complexes rotated *ca*. 30° around their axial axes (Figure 4.16b). Angles between the Ni metals and the centroid calculated from the two P atoms show subtle variations as well upon dehydration (Figure 4.16c). The hexagonal cavities found in **1a–NiMo5** show approximate dimensions slightly smaller (18.8 x 15.8 Å^2, distances N1A···N1A and N4C···N4C) compared to those seen **1–NiMo5** which further confirms that a compression took place after removing the solvent molecules ((Figure 4.16a). As a result and because of the shorter Ni–O bonds, no potential solvent accessible volume was found for **1a–NiMo5**, as opposed to the results obtained for **1a–CuMo5** and the hydrated derivatives**.** Similar to the previous structures, the anhydrous Ni derivative is still held by a significant number of favorable H–bond interactions (Table 4.4).

Finally, the reversibility of the thermally triggered SCSC transformations discussed above were investigated by simultaneous TGA and PXRD experiments carried out on dehydrated samples of **1–CuMo5** and **1–NiMo5** (Figure 4.17). Freshly prepared samples of both derivatives were heated to 150 °C in an oven for an hour to ensure the removal of all water molecules and then they were left in contact with air for approximately 24 h. After that, both TGA and PXRD patterns were recorded. As seen in the TGA curve, the rehydration is total with similar profiles compared to the TGA of a freshly prepared sample **1–MMo5** (M= Cu, Ni). Analogously, no modifications in either the positions or the intensities of any reflection maxima could be observed in the PXRD patterns obtained after the dehydration of any of the samples. In view of these results, we concluded that the SCSC transformations for both **1–CuMo5** and **1–NiMo5** hybrid derivatives are totally reversible within a day in open air conditions. To the best of our knowledge, this is the first time that such thermostructural studies involving thermally induced single–crystal–to–single–crystal transformations promoted by dehydration processes have been reported for Strandberg–type diphosphopentamolybdate hybrids.

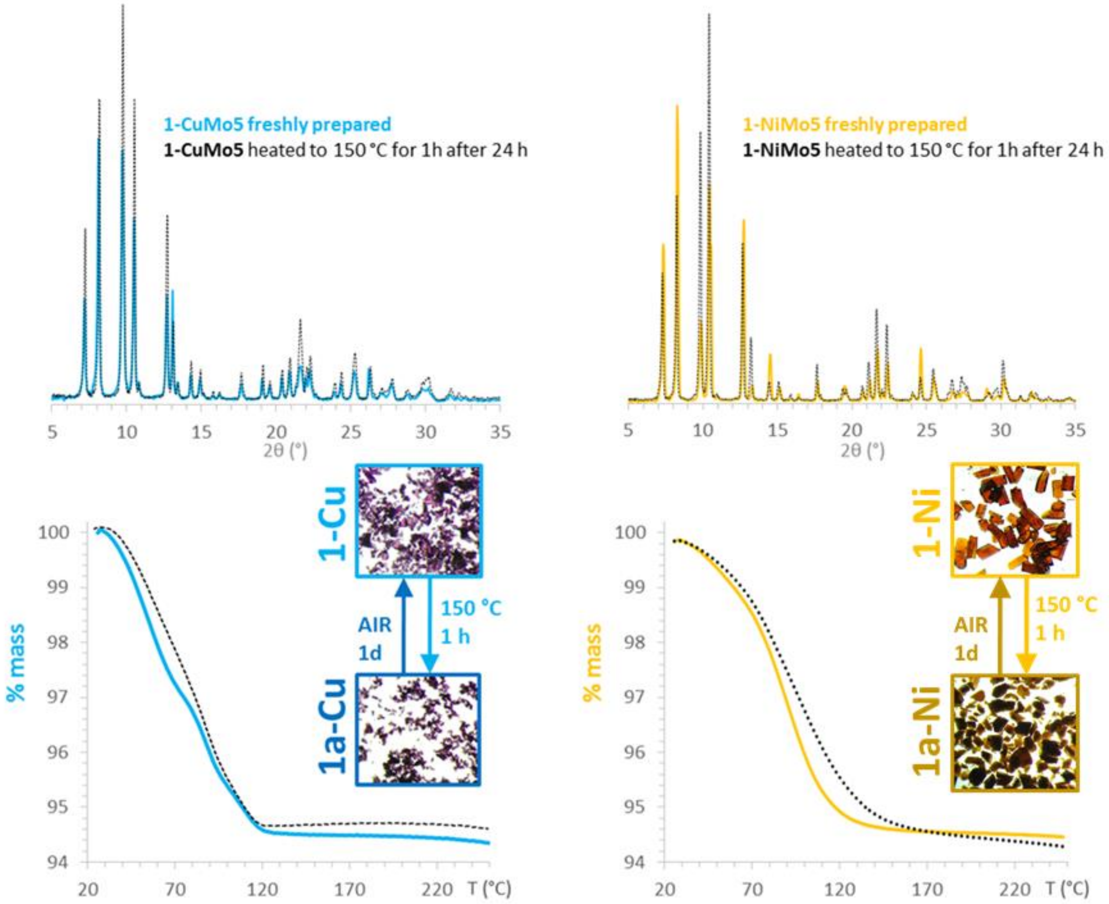

Figure 4.17. Reversibility studies of the SCSC transformations of **1–CuMo5** and **1–NiMo5** showing PDX and TGA mesurements of a freshly prepared sample and those of the dehydrated sample obtained after 24 h of air exposure.

4.3 ANDERSON–TYPE HYBRIDS

4.3.1 Experimental Section

Materials and methods

The *tert*–butylammonium chromiumhexamolybdate salt precursor, namely $[(CH_3)_3CNH_3]_3[H_6CrMo_6O_{24}]\cdot 8H_2O$, was synthesized according to literature methods and identified by infrared (FT–IR) spectroscopy.[99] All other chemicals were obtained from commercial sources and used without further purification. Carbon, hydrogen and nitrogen were determined on a Perkin–Elmer 2400 CHN analyzer. FT–IR spectra were obtained as KBr pellets on a SHIMADZU FTIR–8400S spectrometer (Figure A4.6 in the Appendix). Thermogravimetric (TGA) analyses were carried out from room temperature to 700 °C at a rate of 5 °C min^{-1} on a

Mettler Toledo TGA/SDTA851^e thermobalance under a 50 cm^3 min^{-1} flow of synthetic air. Powder X–ray diffraction (PXRD) patterns were collected on a Bruker D8 Advance diffractometer operating at 30 kV/20 mA and equipped with Cu K_α radiation (λ = 1.5418 Å), a Vantec–1 PSD detector, an Anton Parr HTK2000 high–temperature furnace, and Pt sample holder (Figure A4.7 in the Appendix). The powder patterns (PXRD) were recorded in 2ϑ steps of 0.033° in the $5 \leq 2\vartheta \leq 35$ range with an exposure time of 0.3 s per step. Data sets were acquired from 30 to 470°C every 20 °C, with a heating rate of a 0.16 °C s^{-1}.

Synthetic procedure

[{Cu(cyclam)}$_3$(H$_6$CrMo$_6$O$_{24}$)$_2$].18H$_2$O (1–CuMo6). A solution containing $CuSO_4\cdot5H_2O$ (0.50 g, 0.20 mmol) and cyclam (0.040 g, 0.20 mmol) in aqueous 1M NaCl (10 mL) was added dropwise to an aqueous 1M NaCl (15 mL) solution containing the $[(CH_3)_3CNH_3]_3[H_6CrMo_6O_{24}]\cdot8H_2O$ (0.150 g, 0.1 mmol) preformed precursor. The mixture was stirred for 2 h at room temperature and then filtered to remove a purple solid. The resulting dark purple solution was left to slowly evaporate at room temperature and purple block–like crystals suitable for X–ray diffraction were obtained after 2 days. Yield: 34 mg (22% based on the precursor). Anal. Calcd (found) for $C_{30}H_{120}Cr_2Cu_3Mo_{12}N_{12}O_{66}$: C, 11.43 (11.23); H, 3.84 (4.01); N, 5.33 (5.47). IR (cm^{-1}): 3238(s), 3167(s), 2953(m), 2879(m), 1638(m), 1468(m), 1425(m), 1384(m), 1319(w), 1263(w), 1248(w), 1234(w), 1097(m), 1067(m), 1037(m), 1011(m), 997(s), 935(s), 912(vs), 889(s), 652(vs), 575(s), 544(sh), 445(s), 415(s).

[{Ni(cyclam)}$_2$][{Ni(cyclam)}(H$_6$CrMo$_6$O$_{24}$)$_2$].18H$_2$O (1–NiMo6). The synthesis is similar to that of **1–CuMo6** except that $Ni(NO_3)_3\cdot5H_2O$ (0.070 g, 0.20 mmol) was used as metal source. The resulting dark orange solution was left to slowly evaporate at room temperature and purple block–like crystals suitable for X–ray diffraction were obtained after 2 days. Similar to **1–ZnMo6**, the filtered orange solid was later confirmed to be pure **1–NiMo6**. Total combined yield: 52 mg (36% based on the precursor). Anal. Calcd (found) for $C_{30}H_{120}Cr_2Mo_{12}N_{12}Ni_3O_{66}$: C, 11.49 (11.13); H, 3.86 (3.71); N, 5.36 (5.27). IR (cm^{-1}): 3236(s), 3162(s), 2938(m), 2880(m), 1637(m), 1468(m), 1425(m), 1385(m), 1320(w), 1263(w), 1248(w), 1235(w), 1098(m), 1067(m), 1038(m), 1009(m), 997(s), 936(s), 913(vs), 887(s), 652(vs), 574(s), 553(sh), 445(s), 417(s).

[{H$_2$(cyclam)}$_{1.3}${Zn(cyclam)}$_{0.3}$][{Zn(cyclam)}$_{1.4}$(H$_6$CrMo$_6$O$_{24}$)$_2$].18H$_2$O (1–ZnMo6). The synthesis is similar to that of **1–CuMo6** except that $Zn(NO_3)_2\cdot6H_2O$ (0.060 g, 0.20 mmol) was used as Zn(II) source. The mixture was stirred for 2 h at room temperature and then filtered to remove a purple solid. The resulting grey solution was left to slowly evaporate at room temperature and purple block–like crystals suitable for X–ray diffraction were obtained after 2 days. The filtered orange solid was later confirmed to be pure **1–ZnMo6** as well. Total combined yield: 56 mg (37% based on the precursor). Anal. Calcd (found) for $C_{30}H_{122.6}Cr_2Mo_{12}N_{12}O_{66}Zn_{1.70}$: C, 11.89 (11.51); H, 4.06 (3.82); N, 5.54 (5.31). IR (cm^{-1}): 3236(s), 3167(s), 2954(m), 2879(m), 1637(m), 1466(m), 1426(m), 1386(m), 1321(w), 1264(w), 1247(w), 1236(w), 1095(m), 1068(m), 1038(m), 1010(m), 998(s), 937(s), 912(vs), 885(s), 651(vs), 575(s), 543(s), 444(s), 416(s).

Single–crystal X–ray crystallography

Crystallographic data for Anderson–type **1–MMo6** compounds (M = Ni, Cu, Zn) is shown in Table 4.5. Intensity data were collected on an Agilent Technologies Super–Nova diffractometer which was equipped with monochromated Mo K_α (λ = 0.71073 Å) and Eos CCD detector. Intensity data were collected on an Agilent Technologies Super–Nova diffractometer which was equipped with monochromated Mo K_α (λ = 0.71073 Å) and Eos CCD detector. The data collection of **1–MMo6** compounds (M = Ni, Cu, Zn) was carried out at 100 K in all cases. Data frames were processed (unit cell determination, analytical absorption correction with face indexing, intensity data integration and correction for Lorentz and polarization effects) using the CrysAlis Pro software package.[90] The structures were solved using OLEX2[91] and refined by full–matrix least–squares with SHELXL–2014/6.[92] Final geometrical calculations were carried out with PLATON[93] as integrated in WinGX.[94]

Table 4.5. Crystallographic data for **1–MMo6** (M = Cu, Ni) Anderson–type hybrids.

	1–NiMo6	**1–CuMo6**	**1–ZnMo6**
Empirical formula	$C_{30}H_{120}Cr_2Mo_{12}N_{12}Ni_3O_{66}$	$C_{30}H_{120}Cr_2Cu_3Mo_{12}N_{12}O_{66}$	$C_{30}H_{122.6}Cr_2Mo_{12}N_{12}O_{66}Zn_{1.70}$
fw (g mol^{-1})	3136.78	3151.27	3074.4
crystal system	*triclinic*	*triclinic*	*triclinic*
space group	*P–1*	*P–1*	*P–1*
T (K)	100(2)	100(2)	100(2)
a (Å)	12.5047(6)	13.5514(7)	13.4964(6)
b (Å)	13.7291(4)	13.9338(8)	13.8933(7)
c (Å)	14.2942(6)	14.1177(6)	14.1568(6)
α (°)	102.028(3)	99.913(4)	99.952(4)
β (°)	108.152(4)	108.429(4)	108.027(4)
γ (°)	100.666(3)	106.640(5)	107.313(4)
V (Å^3)	2196.61(16)	2319.7(2)	2305.0(2)
ρ_{calc} (g cm^{-3})	2.371	2.256	2.213
K_α (Å)	0.71073	0.71073	0.71073
μ (mm^{-1})	2.625	2.565	2.339
collected reflns	18237	15106	16701
unique reflns (R_{int})	7685 (0.0208)	8171 (0.0308)	8107 (0.0186)
obsd reflns [$I > 2\sigma(I)$]	6767	6838	6840
parameters	551	599	564
$R(F)^a$ [$I > 2\sigma(I)$]	0.0769	0.0316	0.0373
$wR(F^2)^b$ [all data]	0.2206	0.0758	0.0931
GoF	1.031	1.036	1.059

$^aR(F) = \Sigma||F_o - F_c||/\Sigma|F_o|$; $^bwR(F^2) = \{\Sigma[w(F_o^2 - F_c^2)^2]/\Sigma[w(F_o^2)^2]\}^{1/2}$

Thermal vibrations were treated anisotropically for all non–H atoms in all compounds. Hydrogen atoms of the organic ligands were placed in calculated positions and refined using a riding model with standard SHELXL parameters, except for H65 in **1–CuMo6** and **1–NiMo6** structures, which was assigned manually and given half occupancy. Twelve and ten positions suitable for water molecules of hydration were located in the Fourier maps of **1–CuMo6** and **1–NiMo6,** respectively, and their occupancy was initially refined without restrictions. The resulting total number of 9.1 water molecules per Anderson cluster was fixed to 9.0 in during the final refinement in both cases. For **1–ZnMo6** hybrid**,** however, nine positions for water molecules were found and refined with full occupancy.

4.3.2. RESULTS AND DISCUSSION

Synthesis

We reacted the preformed *tert*–butylammonium chromiumhexamolybdate $[(CH_3)_3CNH_3]_3[H_6CrMo_6O_{24}]\cdot 8H_2O$ precursor with metallocyclam moieties under similar synthetic conditions to those described earlier for the Strandberg–type hybrids (i.e. room temperature, NaCl 1 M medium) starting with copper(II) as the 3d–metal source. Fortunately, purple block single crystals of sufficient quality were obtained in just two days with an acceptable 22% yield based on the precursor. The formation of large amounts of a purple precipitate upon addition of the metalorganic building block was observed and preliminary characterization was carried out by FT–IR spectroscopy (Figure A4.6 in the Appendix). Even though the precipitate displayed a virtually identical FT–IR spectrum to that of single–crystals of **1–CuMo6**, PXRD analyses confirmed that the powder was in fact the title compound in impure bulk form as evidenced by additional maxima found in the diffractogram (Figure A4.7 in the Appendix). Different copper(II) salts were also tested as the transition metal source (chloride, acetate and nitrate salts) but no template effect of any kind was observed whatsoever, as all of them led to the formation of **1–CuMo6** in comparable yields as well as similar crystallization speeds.

With the goal of increasing the overall reaction yield as well as finding out if the temperature could influence the outcome of this synthetic system, we performed similar reactions from 50 °C to refluxing conditions. These experiments yielded similar results and block crystals of **1–CuMo6** were obtained in comparable yields in all tested temperatures. However, it must be noted that the crystallization speed was significantly inferior as crystals of **1–CuMo6** appeared almost one week later compared to the reactions carried out at room temperature. The influence of the pH in this synthetic system was also evaluated and it did have a considerable effect in the reaction outcome. The initial pH of the reaction was 2.9 and it led to **1–CuMo6** as a single, homogeneous crystalline phase with a yield of 22% based on the precursor. Upon basification of the reaction medium to slightly higher pH values using NaOH 0.1 M, a significant decrease in the overall yield was observed (pH = 3.0–4.0, yield = 12–16% based on the precursor). Above this pH value no identifiable solid product could be obtained upon total solvent evaporation whereas when the pH was acidified with 0.1 M HCl to values below 2.5 only big block crystals of sodium chloride could be isolated. In close analogy to the initial synthesis, the purple precipitates formed during the reactions where the pH was adjusted in the range 3.0–4.0 could be also identified as **1–CuMo6** in impure bulk form.

We attempted to synthetize analogous hybrids using other divalent transition metals (Mn^{II}, Co^{II}, Ni^{II} and Zn^{II}) following similar reactions at room temperature in NaCl 1 M media. Upon solvent evaporation, single–crystals of Ni (**1–NiMo6**) and Zn (**1–ZnMo6**) derivatives were obtained although with a significantly lower yield than that obtained for **1–CuMo6**. In contrast and as opposed to **1–CuMo6**, the orange and greyish precipitates that formed during the respective reactions could be identified as pure **1–NiMo6 and 1–ZnMo6** compounds as evidenced by both FT–IR and PDX measurements (Figures A4.6 and A4.7 in the Appendix), which resulted in a higher total combined yield of *ca.* 36% for the latter. Similarly to the Cu analogue, the choice of the transition metal salt did not affect the reaction in any apparent way as different Ni(II) and Zn(II) reactants (chloride and nitrate salts) resulted in both comparable yields and crystallization speeds. Regarding Co and Mn–containing precipitates, no crystalline materials could be obtained at all, although both pale green precipitates showed nearly identical FT–IR spectra to those seen for the structurally characterized phases, evidencing that the pale green solids are also constituted by both metallocyclam units and {$CrMo_6$} clusters. Interestingly, various intense reflexion maxima in the low–angle region, in particular for the Mn–containing precipitate, also coincide with those observed for the measured derivatives, suggesting that the solids could be constituted by the corresponding isostructural phase although in impure form (Figures A4.6 and A4.7 in the Appendix). Unfortunately, no single crystals of Mn– and Co–containing phases could be obtained in any cases despite our efforts.

Vibrational and thermostructural characterization of 1–MMo6 (M = Cu, Zn, Ni)

The preliminary characterization of **1–NiMo6**, **1–CuMo6** and **1–ZnMo6** hybrids was carried out by FT–IR spectroscopy. As expected, the inorganic region of the infrared spectra of **1–MMo6** compounds is highly reminiscent of that of the type–B Anderson precursor (Figure 4.18). In this sense, the strong bands corresponding to the symmetric and asymmetric ν(Mo–O_t) vibrations found in the range 950–850 cm^{-1} did not undergo significant changes upon combination with the metalorganic complexes. While the strong absorption band attributed to ν(Mo–O_b) vibration appears at the same spectral position as that of the precursor, it seems to slightly widen in the hybrids. The signals arising from the ν(Cr–O_b–H) vibration remained mostly invariable as can be seen in the low wavernumber area (575–540 cm^{-1}) while the same behavior was observed for the δ(Mo–O_t) flexion modes in 445–415 cm^{-1} range. In regards to the metal–organic region of the FT–IR spectra, the peaks associated with the stretching of the –N–H and –C–H bonds of the organic ligands are respectively observed at around 3200 and 2880 cm^{-1}, whereas several weak to medium signals corresponding to the δ(C–H) and ν(N–C) vibration modes can also be found in the 1480–1230 and 1100–1000 cm^{-1} ranges.

The thermal stability of **1–MMo6** compounds (M = Ni, Cu and Zn) was studied by TGA experiments, which confirm that all three hybrids decompose in a similar manner through three mass loss stages (Figures 4.19). The first stage starts from room temperature to *ca.* 110 °C and corresponds to the evacuation of all water molecules of hydration. The experimental mass loss corresponds to 9 water molecules per Anderson cluster (calcd. 10.32, 10.28 and 10.55%, found 9.80, 9.67 and 9.68% for **1–NiMo6, 1–CuMo6 and 1–ZnMo6**, respectively). Afterwards, a small range of thermal stability can be observed for the anhydrous phases, which extends up to *ca.* 170–180 °C. Afterwards, the anhydrous phases undergo further decomposition through two overlapping mass loss stages which are associated with the combustion of the cyclam ligands and the consequent breakdown of the inorganic clusters. The overall mass loss for these two stages is consistent with three cyclam ligands per Anderson cluster (calcd. for $3C_{10}H_{24}N_4$ 19.63, 19.14 and 19.22%; found 20.90, 20.80 and 21.32% for **1–NiMo6, 1–CuMo6 and 1–ZnMo6**, respectively). The final residue is obtained at temperatures above *ca.* 500 °C for all compounds (calcd. for $Cr_2Mo_{12}O_{48}Ni_2$, 68.25; $Cr_2Cu_2Mo_{12}O_{48}$, 70.23; and $Cr_2Mo_{12}O_{48}Zn_{1.7}$, 67.97 and found 69.30, 69.53 and 69.00% for **1–NiMo6, 1–CuMo6 and 1–ZnMo6**, respectively).

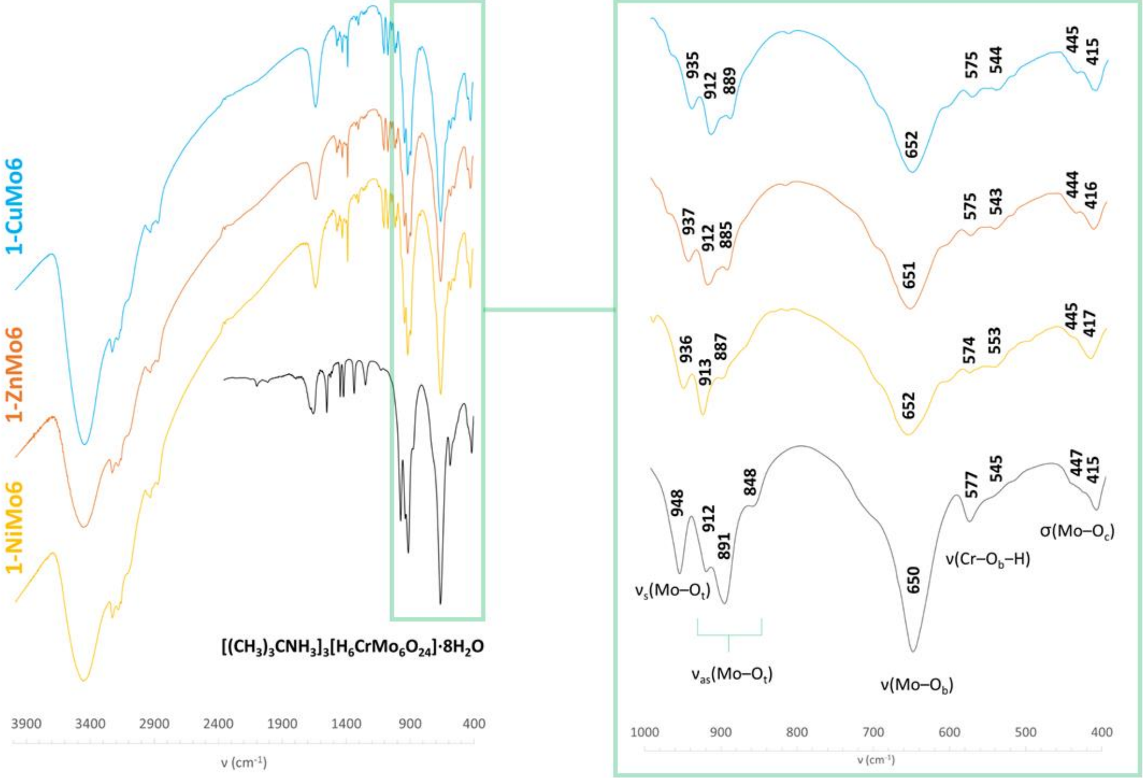

Figure 4.18. FT–IR spectra of **1–NiMo6, 1–CuMo6** and **1–ZnMo6** hybrids along with that of the precursor highlighting the inorganic region.

Variable–temperature powder X–ray diffraction measurements (TPXRD) between 30 and 470 °C show that these compounds are able to maintain their crystallinity up to temperatures in the range of 210–230 °C (Figures 4.19). Important modifications in both the positions and intensities of numerous diffraction maxima are observed at temperatures above 50°C, confirming that a thermally activated phase transition must take place upon heating. These modified diffraction patterns are conserved until the loss of crystallinity for all three derivatives, suggesting that the anhydrous phases may share a virtually identical crystal packing to that of the partially dehydrated samples at 50 °C. After that, the crystalline anhydrous phases become amorphous at temperatures above 210–230 °C, which is consistent with the results observed in the TGA curve above.

Signs of new high–temperature phases start appearing at *ca.* 370–390 °C, which are defined enough at 470 °C for being identified (Figures A4.8–A4.10 in the Appendix). These final residues are mainly formed by the orthorhombic *Pbnm* MoO_3 as the major phase (PDF: 00–035–0609, 01–076–1003)[100] together with various other molybdate oxides such as the monoclinic *P2₁/a* Mo_4O_{11} (**1–NiMo6**, PDF: 01–072–0447),[101] or *P2/a* Mo_9O_{25} phases (**1–ZnMo6**, PDF: 01–081–1263).[102] The corresponding metallic molybdates were also found in these residues, those being the monoclinic *C2/m* $NiMoO_4$, the triclinic *P-1* $CuMoO_4$ and the monoclinic *P2/c* $ZnMoO_4$ (PDF: 00–032–0692; 00–022–0242; 00–016–0310),[103] as well as an orthorhombic $Zn(OH)_2$ phase

(PDF: 00–020–1437),[104] and a Cr–containing phase (orthorhombic and monoclinic phases of $Cr_2Mo_3O_{12}$ in the case of the formers and the rhombohedral *R3m* CrO(OH) for **1–ZnMo6**, PDF: 00–020–0310; 01–078–1654 for the oxide; PDF: 01–085–1373 for the hydroxide).[105]

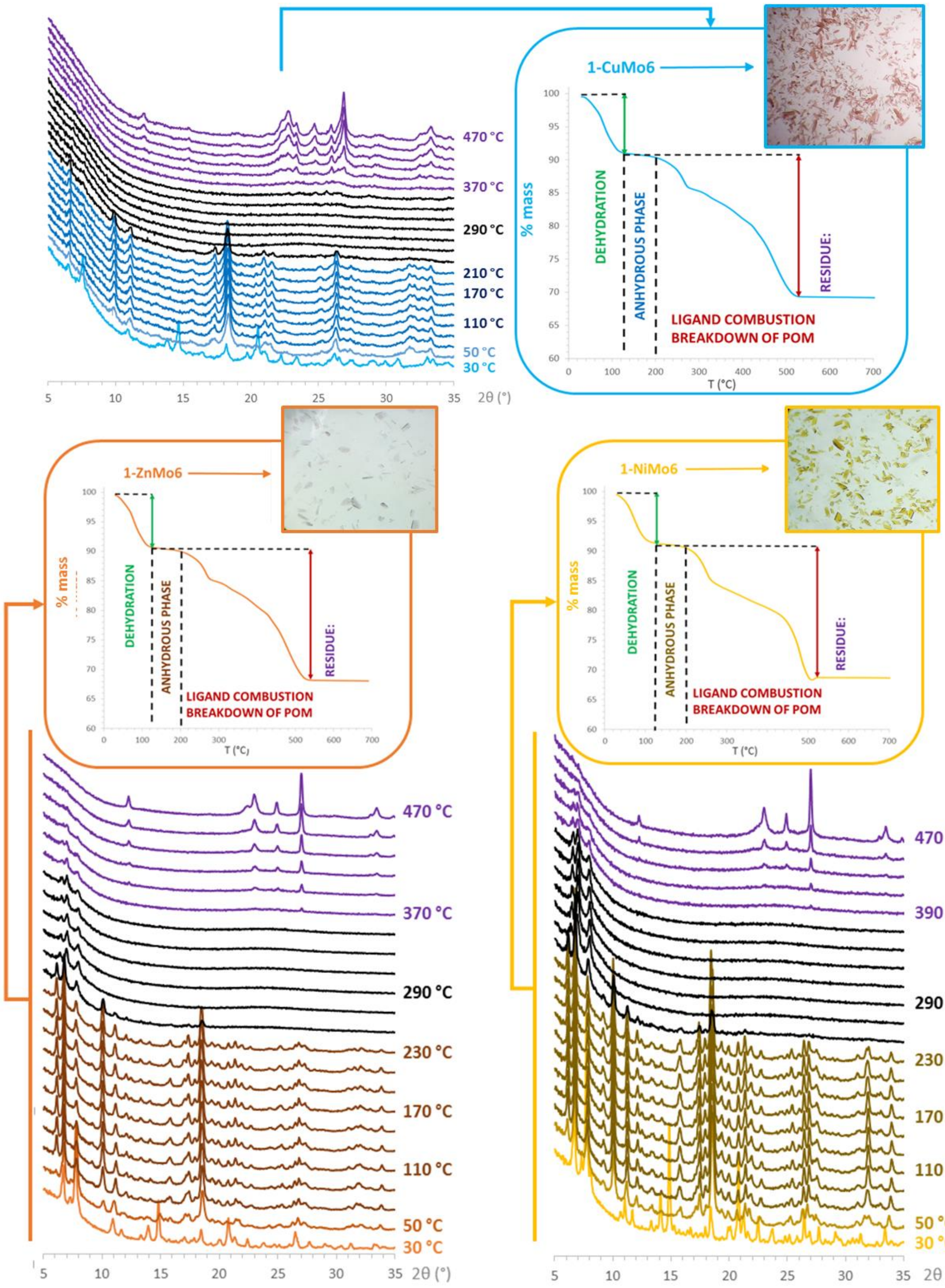

Figure 4.19. TPXRD studies for **1–NiMo6, 1–CuMo6** and **1–ZnMo6** hybrid derivatives, highlighting the thermally activated phase transition along with the TGA curve and digital photographs of the crystals.

Crystal structures of 1–MMo6 (M = Ni, Cu, Zn)

Three novel Anderson–Evans type polyoxomolybdate hybrids have been prepared under mild conditions in aqueous medium using different 3d–metal sources (**1–NiMo6**, **1–CuMo6** and

1–ZnMo6), which crystallize in the triclinic *P–1* space group. Even though they are isostructural, the different coordination ability of their corresponding 3d–metal centres results in multidimensional covalent crystal packings, that is 2D, 1D and discrete assemblies for Cu, Zn and Ni derivatives respectively.

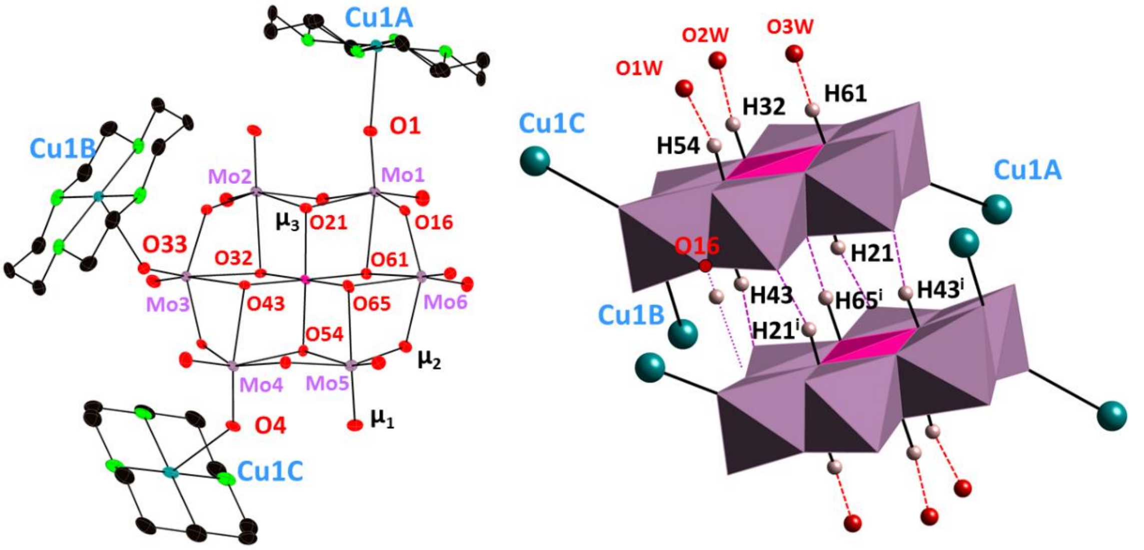

Figure 4.20. ORTEP view depicted at 50% for **1–CuMo6** with partial atom labelling along with the polyhedral representation of the Anderson dimers highlighting the H–bonds (dashed line) and the most probable remaining protonation site in μ_2–O16 (dotted line). Symmetry codes: i) –*x*, 1–*y*, 1–*z*.

The asymmetric unit of all three compounds consist on one Anderson–Evans cluster $[H_6CrMo_6O_{24}]^{3-}$, three half metallocyclam moieties and nine water molecules of hydration some of which are disordered (**1–CuMo6** and **1–NiMo6**). The structure of this archetypal POM is well–known and is composed of six edge–sharing $\{MO_6\}$ octahedra surrounding a central, edge–sharing heteroatom of octahedral geometry $\{XO_6\}$ leading to a planar arrangement with an approximate *D3d* symmetry (Figure 4.20). Charge balance considerations indicate that the cluster must be a B–type Anderson POM, that is, a six–protonated cluster. The six hydrogen atoms in the B–type are usually located on the six μ_3–O atoms surrounding the heteroatom, although some structures with protons located in other positions such as bridging μ_2–O atoms have been also reported.[99,106] Bond–valence sum (BVS) calculations[107] were carried out to locate the protonation sites confirming that the six μ_3–O atoms belonging to the $\{CrO_6\}$ octahedron are indeed protonated in all three compounds (O21, O32, O43, O54, O61, O65; bond orders: 0.70–0.86). However, one of such μ_3–O atom (O65) cannot possess a full hydrogen atom because it overlaps with its centrosymmetric partner, so it must have half occupancy instead. As a result, the remaining half hydrogen must be joined to another O atom or delocalized between various oxygen atoms to achieve electroneutrality, but BVS results were inconclusive in this regard. In view of this, an analysis of the H–bonding network between Anderson dimmers was carried out and interestingly only one O atom (O16) of the cluster did not show any N–H···O or C–H···O interactions toward adjacent ligands or even with water molecules of hydration in any of the three hybrids. Because of that, we believe this bridging μ_2–O atom to be the most probable site to be protonated at 50% just like the μ_3–O65 atom (Figure 4.20) leading to the neutral crystal assembly. The Mo–O and Cr–O bond lengths of all three **1–MMo6** compounds (M = Ni, Cu, Zn) are in the range 1.70–2.30 Å and 1.96–1.98 Å respectively, which are in good agreement with other Anderson–type POMs found in crystallographic databases.[99]

Three crystallographically independent centrosymmetric {Cu(cyclam)} complexes can be found in **1–CuMo6**, all of them showing the typical *trans–III* configuration of the ligand. They consist on a metal–organic block grafted to the polyanion surface showing distorted octahedral geometries with the four N atoms of the cyclam ligand forming the equatorial plane and the axial positions occupied by terminal O atoms from different Anderson clusters (O1, O33 and O4 for Cu1A, Cu1B and Cu1C, respectively; Figure 4.20). While these CuN_4O_2 chromophores show Jahn–Teller elongation, this type of distortion is especially remarkable for Cu1C, as confirmed by CShM calculations[98] and its respective axial Cu–O bonds that shows lengths near those of semi–coordination (Cu1C–O4 2.636(4) Å), as can be seen in Table 4.6.

Table 4.6. M–O, M–N bond lengths (Å) and M···O distances as well as the polyhedral distorsion (CShM) of the {M(cyclam)} complexes in **1–MMo6** compounds (Ni, Cu, Zn).

1–NiMo6		**1–CuMo6**		**1–ZnMo6**	
Ni1A–N$_{\mathrm{mean}}$	2.054	Cu1A–N$_{\mathrm{mean}}$	2.019	Zn1A–N$_{\mathrm{mean}}$	2.083
Ni1A–O1	2.121(7)	Cu1A–O1	2.373(3)	Zn1A–O1	2.241(3)
Ni1A–O1$^{\mathrm{i}}$	2.121(7)	Cu1A–O1$^{\mathrm{i}}$	2.373(3)	Zn1A–O1$^{\mathrm{i}}$	2.241(3)
OC–6	0.122	OC–6	0.695	OC–6	0.226
Ni1B–N$_{\mathrm{mean}}$	1.945	Cu1B–N$_{\mathrm{mean}}$	2.019	Zn1B–N$_{\mathrm{mean}}$	2.043
Ni1B···O33	2.856(12)	Cu1B–O33	2.495(4)	Zn1B–O33	2.473(4)
Ni1B···O33$^{\mathrm{ii}}$	2.856(12)	Cu1B–O33$^{\mathrm{ii}}$	2.495(4)	Zn1B–O33$^{\mathrm{ii}}$	2.473(4)
SP–4	0.206	OC–6	1.369	OC–6	1.394
Ni1C–N$_{\mathrm{mean}}$	1.960	Cu1C–N$_{\mathrm{mean}}$	2.012	Zn1C–N$_{\mathrm{mean}}$	2.022
Ni1C···O4	2.951(10)	Cu1C–O4	2.636(4)	Zn1C···O4$^{\mathrm{iii}}$	2.668(5)
Ni1C···O4$^{\mathrm{iii}}$	2.951(10)	Cu1C–O4$^{\mathrm{iii}}$	2.636(4)	Zn1C···O4$^{\mathrm{iv}}$	2.668(5)
SP–4	0.110	OC–6	2.123	SP–4	0.007

Symmetry codes: **1–NiMo6:** i) −*x*, −*y*, 6−*z*; ii) −*x*, 1−*y*, 2−*z*; iii) 1−*x*, 2−*y*, 2−*z*. **1–CuMo6**: i) −*x*, −*y*, 1−*z*; ii) −*x*, 1−*y*, 2−*z*; iii) 1−*x*, 2−*y*, 2−*z*. **1–ZnMo6**: i) −*x*, −1−*y*, −*z*; ii) −*x*, −*y*, 1−*z*; iii) x, −1+y, z; iv) 1−x, −y, 1−z. CShM: reference polyhedra SP–4 (square) and OC–6 (octahedron).

The crystal packing of **1–CuMo6** consist on covalent "bow tie"–like layers built from Anderson clusters and bridging Cu(cyclam) complexes, where consecutive clusters form strongly H–bonded dimers with clusters belonging to adjacent layers giving rise to a 3D supramolecular network (Figure 4.21). This structure can be described as follows: each Anderson cluster is linked to three metallocyclam moieties forming hybrid chains that run along the [0–1–1] direction in a zig–zag fashion through Cu1A and Cu1B complexes. These chains link contiguous chains through the coordination sphere of the Cu1C moiety in such a way that covalent layers showing a "bow tie"–like motif are generated in the (101) plane where the numerous water molecules are hosted. Moreover, clusters belonging to one layer are further linked with the nearest cluster of an adjacent layer to form very stable dimeric units through six pairs of hydrogen bonds between the bridging oxo ligands. The donor–acceptor distances of these hydrogen contacts are less than 2.9 Å (Table 4.7) indicating that these interactions are strong enough to stabilize such dimeric subunits, and thus, a 3D supramolecular architecture is generated. PLATON calculations confirms a total solvent accesible volume of 577 Å^3 (25% of the unit cell volume) which is consistent with the number of cristalization water molecules seen in single–crystal XRD analysis.

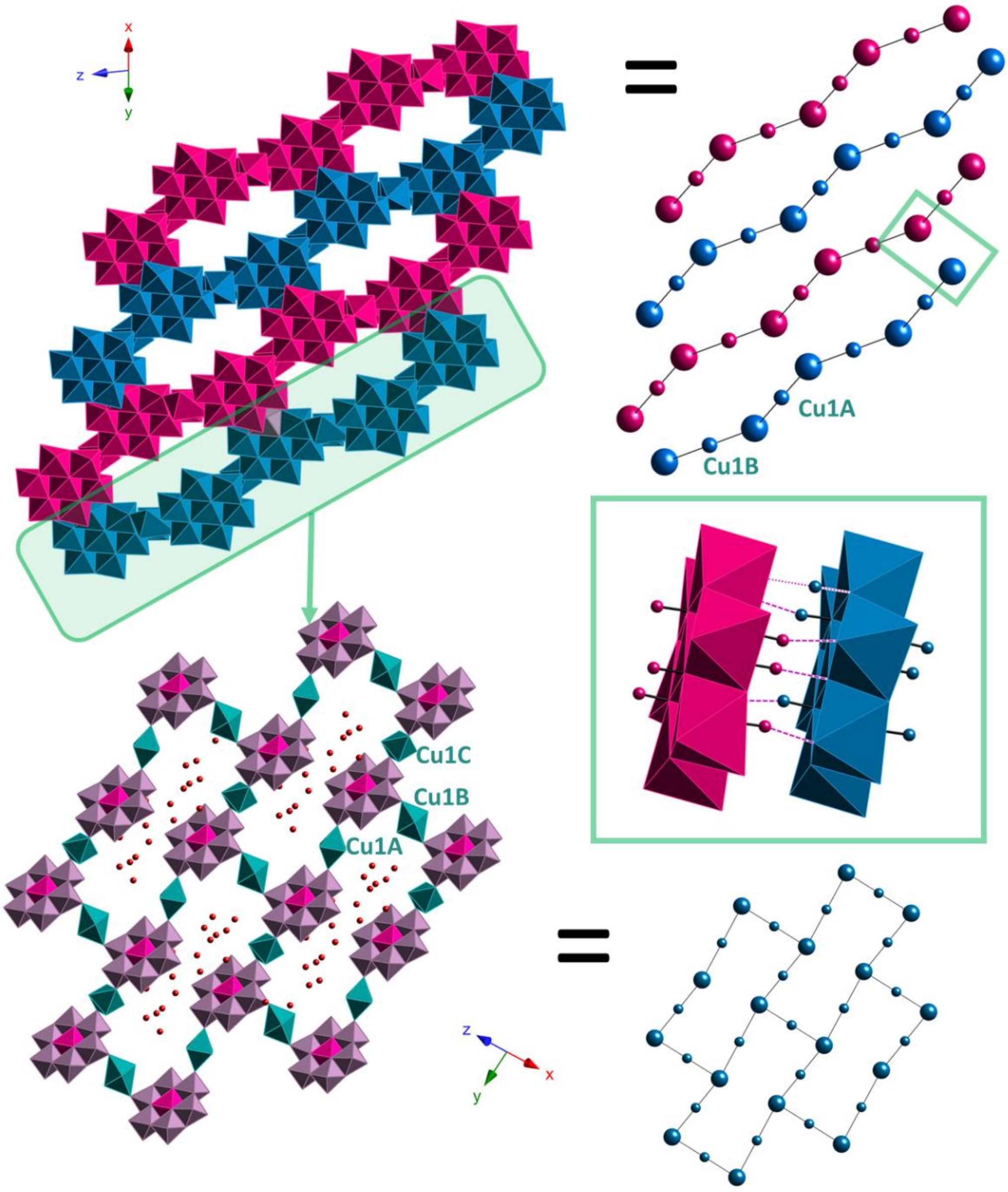

Figure 4.21. Crystal packing of **1–CuMo6** with partial atom labelling showing the zig–zag Cu1B–POM–Cu1A chains that extend to “bow tie”–like layers through the Cu1C moiety and the dimeric H–bonded units. Cyclam ligands are omitted for clarity. Color code: violet (Mo), pink (Cr), red (O). Small balls represent Cu atoms while the bigger ones stand for the POM cluster.

The structure of **1–ZnMo6** is highly reminiscent to that of **1–CuMo6** although it shows notable differences, which are a direct result of the different 3d–centers of the metalorganic building blocks (Figure 4.22). While Zn1A and Zn1B remained coordinated to O1 and O33 respectively, the Zn1C complex no longer acts as a bridging unit (Zn1C···O4 = 2.668(5) Å) but as a countercation instead, adopting a square planar geometry (Table 4.6), which also shows a *trans–III* configuration of the ligand. As a result and opposed to **1–CuMo6,** even though similar zig–zag Zn1A–POM–Zn1B chains can be observed along the [0–1–1] direction the covalent layers cannot be formed and thus, the overall dimensionality of the crystal is reduced to a covalent 1D hybrid arrangement (Figure 4.22a). In contrast, **1–ZnMo6** displays a virtually identical H–bond network to that of the Cu analogue (Table 4.7). Interestingly, the occupation of the octahedral Zn1B as well as the square planar Zn1C metal center is incomplete (0.40 and 0.30 respectively) which means that approximately one third of those positions in the crystal is occupied by a protonated {H_2cyclam}$^{2+}$ fragment instead of a metallorganic complex. In order to check if this feature was indeed inherent to this particular crystal structure and not an artifact of some sort, we repeated the synthesis of **1–ZnMo6** with a significant excess of the Zn source (1.2 mmols instead of 0.10 mmols) and measured a single crystal obtained from it, which resulted in the exact structure as **1–ZnMo6** with the same value for the occupancy of the defect metal centers Zn1B and Zn1C. Apart from the that, the organic ligands remained virtually unaltered compared to those shown in **1–CuMo6** (Figure 422a). In close analogy to **1–CuMo6**, a total solvent accessible volume corresponding to 26% of the unit cell volume (592 Å^3) was calculated using PLATON for this structure.

Table 4.7. Comparison of the Intermolecular N–H···O and C–H···O interactions (Å) in **1–MMo6** (M= Ni, Cu, Zn).

1–NiMo6		**1–CuMo6**		**1–ZnMo6**	
Donor–H···Acceptor	**D···A**	**Donor–H···Acceptor**	**D···A**	**Donor–H···Acceptor**	**D···A**
O54–H54···O1W	2.613(6)	O54–H54···O1W	2.673(4)	O54–H54···O1W	2.689(10)
O32–H32···O2W	2.702(5)	O32–H32···O2W	2.722(4)	O32–H32···O2W	2.627(10)
O61–H61···O3W	2.708(7)	O61–H61···O3W^{i}	2.738(4)	O61–H61···O3W	2.726(10)
O21–H21··O55	2.706(5)	O21–H21··O55^{i}	2.738(4)	O21–H21··O55^{i}	2.678(10)
O43–H43···O6	2.630(5)	O43–H43···O6^{i}	2.652(4)	O43–H43···O6^{i}	2.607(9)
O65–H65···O65	2.870(7)	O65–H65···O65^{i}	2.922(6)	O65–H65···O65^{i}	2.859(15)
N1A–H1A···O2	2.935(6)	N1A–H1A···O55^{ii}	3.366(4)	N1A–H1A···O45^{ii}	3.349(13)
N4A–H4A···O55^{i}	3.397(5)	N4A–H4A···O2	2.915(4)	N4A–H4A···O2	2.918(12)
C2A–H2AA···O45^{i}	3.255(6)	C2A–H2AB···O5^{ii}	3.331(5)	—	—
C3A–H3AB···O4^{i}	3.429(7)	C3A–H3AA···O45^{ii}	3.273(5)	—	—
C3A–H3AB···O5^{i}	3.369(7)	—	—	—	—
C5A–H5AB···O5^{i}	3.374(6)	—	—	C5A–H5AA···O11^{iii}	3.416(17)
—	—	—	—	C5A–H5AA···O11^{iii}	3.416(17)
—	—	—	—	C6A–H6AA···O10W	3.39(3)
—	—	C7A–H7AA···O5^{ii}	3.286(5)	C7A–H7AB···O5^{ii}	3.205(18)
—	—	—	—	C7A–H7AA···O11	3.415(18)
N1B–H1B···O23	3.030(6)	N1B–H1B···O23	2.832(5)	N1B–H1B···O23	2.796(17)
N4B–H4B···O6	2.787(6)	N4B–H4B···O6^{i}	2.939(5)	N4B–H4B···O6^{i}	3.064(17)
C3B–H3BB···O66	3.378(7)	C3B–H3BB···O66^{i}	3.439(6	—	—
—	—	C6B–H6BB···O55^{i}	3.382(6)	C6B–H6BB···O55^{i}	3.247(19)
N1C–H1C···O34^{ii}	2.762(6)	N1C–H1C···O34^{iii}	2.806(4)	N1C–H1C···O34^{iv}	2.887(13
N4C–H4C···O1W^{ii}	3.132(7)	N4C–H4C···O1W^{iii}	3.037(5)	N4C–H4C···O4^{iv}	2.994(15)
—	—	—	—	N4C–H4C···O5W	3.068(17)
—	—	—	—	C2C–H2CA···O34^{iv}	3.282(17)
C5C–H5CA···O8W^{ii}	3.461(7)	C5C–H5CA···O8W^{iv}	3.274(12)	C5C–H5CA···O9W	3.36(4)
—	—	—	—	C6C–H6CA···O22^{v}	3.311(15)
C7C–H7CA···O4^{ii}	3.387(8)	C7C–H7CA···O4	3.248(5)	—	—

Symmetry codes: **1–NiMo6:** i) –x, 1–y, 1–z; ii) x, –1+y, +z; iii) –x, –y,1–z; iv) 1–x, 2–y, 2–z; v) x, 1+y, z. **1–CuMo6**: i) –x, 1–y, 1–z; ii) x, –1+y, +z; iii) –x, –y,1–z; iv) 1–x, 2–y, 2–z; v) x, 1+y, z. **1–ZnMo6**: i) x, –1+y, z; ii) 1–x, –y, 1–z.

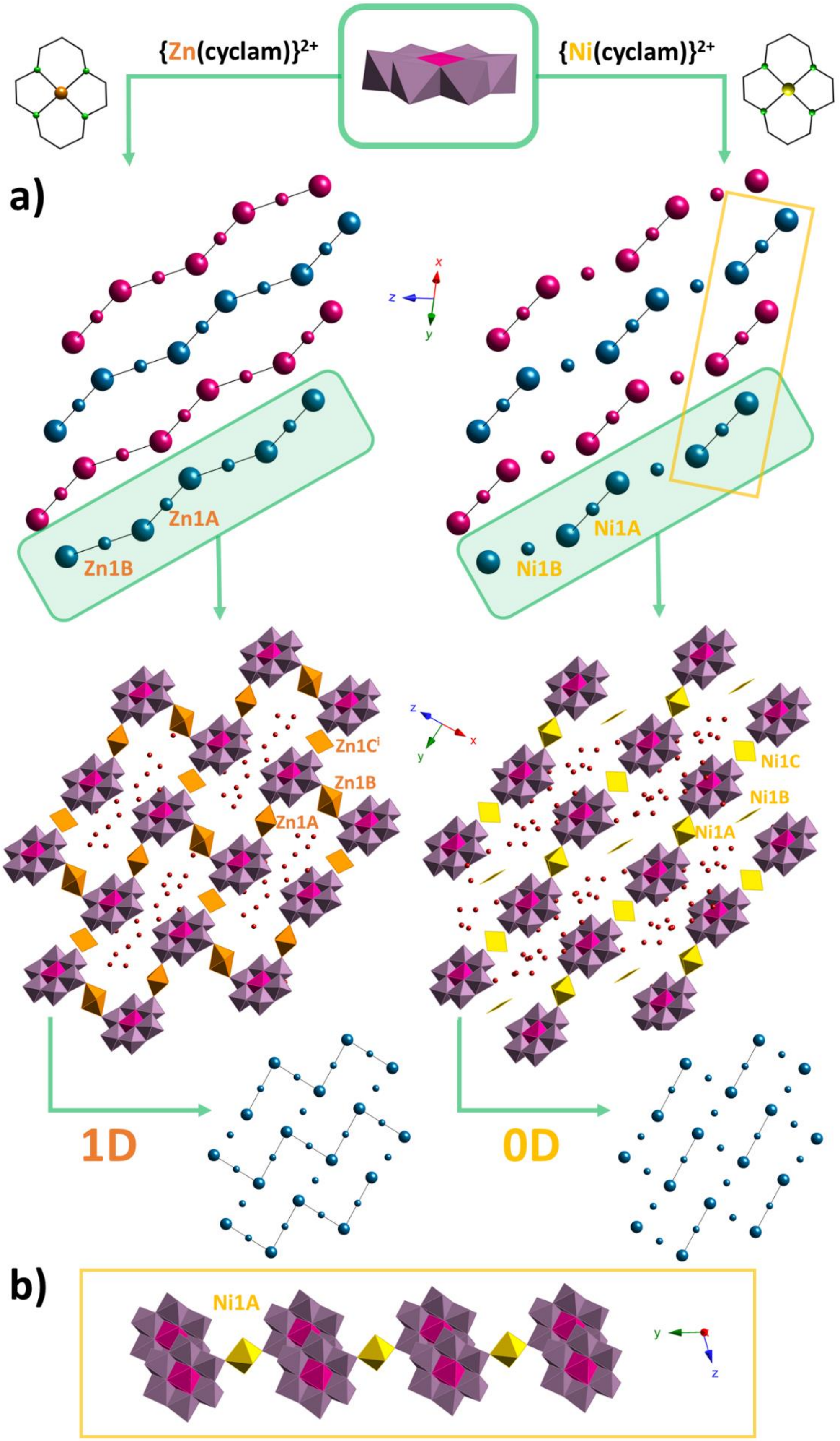

Figure 4.22. a) Comparison between the crystal packing of **1–ZnMo6** and **1–NiMo6** compounds with partial atom labelling showing the different dimensionalities. b) Hybrid supramolecular chains in **1–NiMo6** showing the Ni1A linked H–bonded Anderson dimers. H atoms and cyclam ligands are omitted for clarity. Color code: violet (Mo), pink (Cr), red (O). Smaller balls represent M atoms (Ni, Zn) while the bigger ones stand for the POM clusters. Symmetry codes: i) *x*, 1+*y*, *z*.

Further structural changes can be observed in the **1–NiMo6** analogue, compared to the previous Cu and Zn derivatives. In this structure, Ni1A is the only complex moiety that coordinates to the terminal O atoms of the inorganic clusters, as both Ni1B and Ni1C adopt square planar NiN_4 geometries showing the typical *trans–III* configuration of the ligand (Figure 4.22). This connectivity is clearly reflected in the long distances Ni···O of the latter complexes compared to the other two derivatives (Table 4.6), resulting in a covalent 0D crystal assembly. Because of this change in the bonding of the 3d–metal, the structure can be view as H–bonded dimers that are linked through Ni1A to another cluster belonging to an adjacent dimmer, the connection of which results in supramolecular zig–zag chains along the *y* axis (Figure 4.22b).

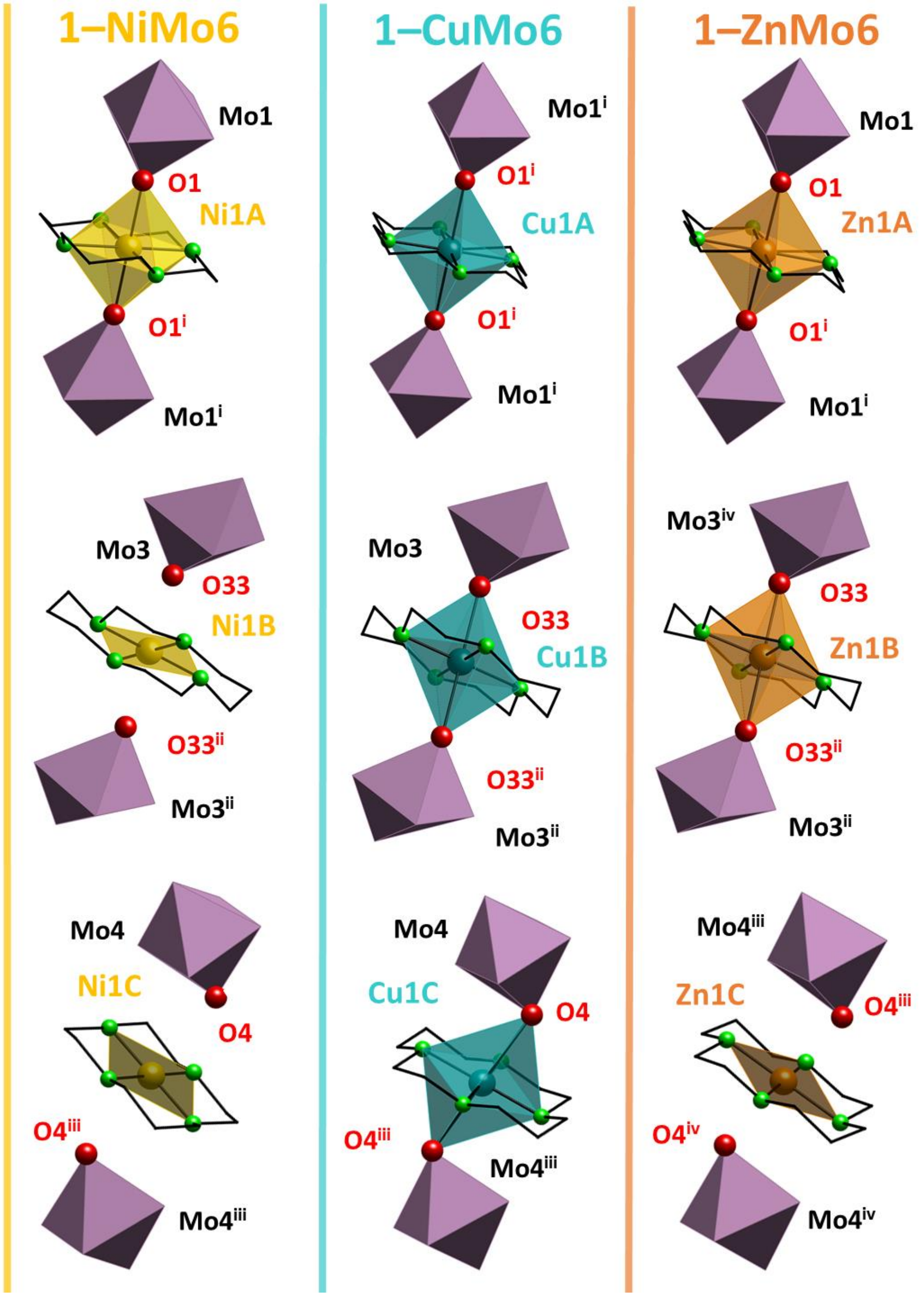

Figure 4.23. Connectivity and geometry of the different M(cyclam) complexes found in **1–MMo6** hybrids with atom labelling (M = Ni, Cu, Zn). Color code: Mo (violet), Cu (blue), Zn (orange), Ni (yellow), O (red), N (Green), C (black). Symmetry codes: **1–NiMo6:** i) –*x*, –*y*, 6–*z*; ii) –*x*, 1–*y*, 2–*z*; iii) 1–*x*, 2–*y*, 2–*z*. **1–CuMo6**: i) –*x*, –*y*, 1–*z*; ii) –*x*, 1–*y*, 2–*z*; iii) 1–*x*, 2–*y*, 2–*z*. **1–ZnMo6**: i) –*x*, –1–*y*, –*z*; ii) –*x*, –*y*, 1–*z*; iii) x, –1+y, z; iv) 1–x, –*y*, 1–*z*.

Despite the low–dimensional packing of **1–NiMo6**, this structure display slightly higher number of favorable intermolecular contacts than those seen in the previous derivatives, in particular those N–H···O and C–H···O interactions originating from the Ni1C square–planar complex (Table 4.7). This is a direct result of the disposition of the ligands, which differs from the equivalent ones observed in Cu and Zn analogues as can be seen in Figure 4.23. Compared to Cu1A and Zn1A in previous structures, the equivalent ligands found in **1–NiMo6** exhibits a *ca*. 11° rotation around their axial axes, whereas a more subtle 6° rotation is observed in the Zn1B moiety. The most important change however reside in the Zn1C complex, as it is rotated around its axial axes more significantly than the other two moieties (*ca.* 25°) which results in the generation of two more favorable H–bond contacts than the Cu and Zn derivatives (Table 4.7).

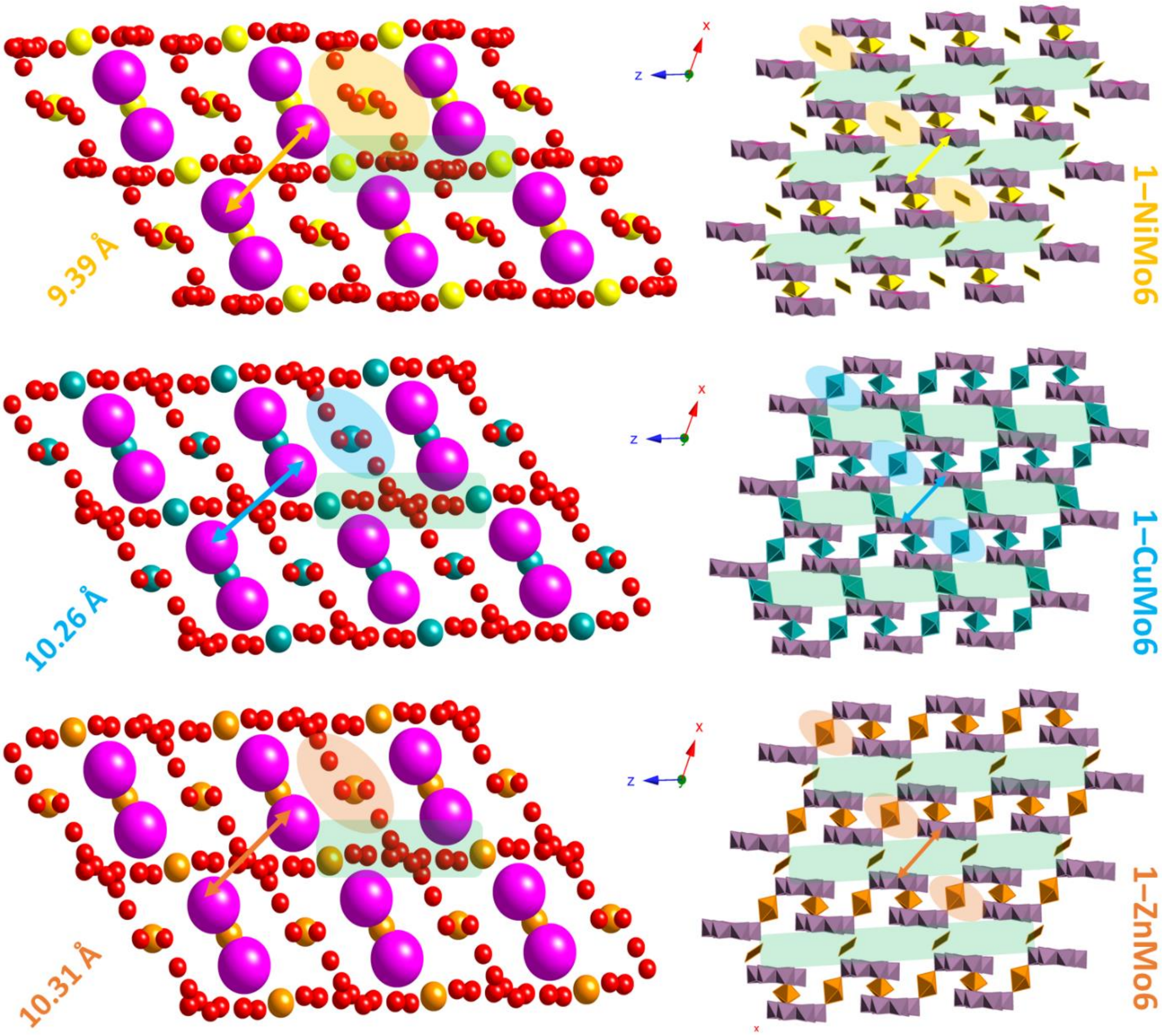

Figure 4.24. Comparison of the distribution of water molecules of hydration and the effect in the highlighted Cr···Cr distance between two clusters of adjacent H–bonded dimers along the *x* axis. Color code: pink (Cr), blue (Cu), orange (Zn), yellow (Ni), red (O), Mo (violet).

All in all, the crystal packing of **1–NiMo6** is more compacted as only 368 Å^3 corresponds to the total solvent accessible volume (16% of the unit cell volume), which is a substantial decrease compared to the 25–26% calculated for the **1–CuMo6** and **1–ZnMo6** hybrids. This compaction is also evident in the cell parameter *a* which decreased nearly 0.9 Å compared to the other two cells (Table 4.5), as well as the shorter Cr···Cr distances in the H–bonded dimers (6.1 vs 5.8 Å). As a result of the latter, the H–bond system between the two clusters in the dimers interact stronger in **1–NiMo6** (Table 4.7). Interestingly, the slightly different distribution of the water molecules seem to be responsible for the contraction of the *a* parameter. Even though all Cr···Cr distances of contiguous clusters are comparable in all three compounds, the distance Cr···Cr between adjacent H–bonded dimers within the same supramolecular "layer" along the *x* axis is reduced considerably for **1–NiMo6**, from *ca.* 10.3 to 9.4 Å. The reason for this is that, even though they possess the same crystallization water content, the solvent molecules are slightly more localized along the *x* axis in both **1–CuMo6** and **1–ZnMo6**, whereas solvent molecules in **1–ZnMo6** appear to be more distributed along the z axis as well, allowing the clusters to get slightly closer in that direction (Figure 4.24).

Finally, it is worth mentioning that we tried to measure the high–temperature phases observed in the variable temperature powder XRD analyses (i.e. single–crystal–to–single–crystal transformations). To do so, a single crystal was heated in an oven to 333 K at a rate of 1 K min^{-1}, and immediately afterwards covered with Paratone® oil and placed under the N_2 stream of the diffractometer, which was ready to perform a full data collection at 100 K. Unfortunately the crystals were not able to maintain their integrity. Alternatively, we directly mounted a single crystal into the diffractometer which was at 333 K and afterwards cool down to 100 K to perform the data acquisition but same results were observed, preventing us from determining any structure. As future work, we will try to evacuate the solvent molecules by applying vacuum to a single crystal instead of heating and check if we can determine the solvent–free phases this way. Due to the high total solvent accessible volume of these hybrid framework the study of the sorption properties of these compounds could be interesting as well, in particular for the Cu analogue.

4.4 CONCLUSIONS

In this chapter two different heteropolyoxomolybdate systems were studied, the first one consisting on Strandberg–type hybrids and the second one involving Anderson–Evans type clusters.

In the first section, two novel Strandberg–type hybrids have been prepared under mild conditions and isolated from aqueous solution, namely $[\{Cu(cyclam)\}_2(H_2P_2Mo_5O_{23})].4.5H_2O$ (**1–CuMo5**) and $[\{H_2(cyclam)\}_{0.3}\{Ni(cyclam)\}_{0.7}][\{Ni(cyclam)\}(H_2P_2Mo_5O_{23})].5H_2O$ (**1–NiMo5**). Despite being isostructural, **1–CuMo5** exhibits an interesting 2–fold interpenetrated diamond–like network whereas **1–NiMo5** exhibits a 1D hybrid covalent arrangement, as a consequence of the difference in the plasticity of the metal centers. Both hybrids undergo thermally induced single–crystal–to–single–crystal (SCSC) transformations upon removal of solvent molecules with drastically different outcomes (**1a–MMo5,** M = Cu, Ni). While an uncommon 1D to 3D SCSC transformation is observed for **1a–NiMo5** resulting in a similar interpenetrated diamond–like hybrid network seen in the hydrated **1–CuMo5,** the latter is able to maintain its 2–fold complex architecture upon transforming into the anhydrous **1a–CuMo5**, albeit with significant distortion of the initial entangled complex network. Simultaneous TGA and PXRD measurements revealed that the thermally triggered SCSC transformations are fully reversible for both analogues in open–air conditions within a day. To our knowledge, this is the first report describing Strandberg–type POMs undergoing such interesting thermally activated phase transitions.

Regarding the second section, three novel Anderson–type hybrids have been isolated from aqueous solution under mild conditions by grafting different 3d–metallocyclam complexes, namely $[\{Cu(cyclam)\}_3(H_6CrMo_6O_{24})_2].18H_2O$ **(1–CuMo6),** $[\{H_2(cyclam)\}_{1.3}\{Zn(cyclam)\}_{0.3}][\{Zn(cyclam)\}_{1.4}(H_6CrMo_6O_{24})_2].18H_2O$ **(1–ZnMo6)** and $[\{Ni(cyclam)\}_2][\{Ni(cyclam)\}(H_6CrMo_6O_{24})_2].18H_2O$ (**1–NiMo6**). Despite being isostructural, these hybrid compounds exhibit covalent multidimensional architectures comprising covalent 2D, 1D and 0D topologies respectively, due to the different nature of the 3d–metal and their coordination ability. While the cell parameters and the relative arrangement and disposition of the building blocks in the asymmetric unit, are virtually identical in **1–CuMo6** and **1–ZnMo6** derivatives, notable structural differences in the geometry of the metalorganic moieties and distribution of water molecules were observed for the **1–NiMo6** analogue, which led to a more compacted 0D crystal packing for the latter. Thermostructural studies indicate that at least one high temperature phase must exist for each derivative above 50 °C but we could not structurally characterized any of them because of the brittleness of the crystals upon heating.

4.5 REFERENCES

---

[1] (a) Contant, R.; Hervé, G. *Rev. Inorg. Chem.* **2002**, *22*, 63–111; (b) Hervé, G.; Tézé, A.; Contant, R. *Polyoxometalate Molecular Science*; Borrás-Almenar, J. J.; Coronado, E.; Müller, A.; Pope, M. T.; Eds.; Kluwer, Dordrecht, 2003, pp. 33–54.

[2] Schäffer, C.; Todea, A. M.; Gouzerh, P.; Müller, A. *Chem. Commun*. **2012**, *48*, 350.

[3] Müller, A.; Gouzerh, P. *Chem. Soc. Rev.* **2012**, *41*, 7431.

[4] (a) Müller, A.; Krickemeyer, E.; Meyer, J.; Bögge, H.; Peters, F.; Plass, W.; Diemann, E.; Dillinger, S.; Nonnenbruch, F.; Randerath, M.; Menke, *C. Angew. Chem., Int. Ed. Engl.* **1995**, *34*, 2122. (b) Müller, A.; Serain, C. *Acc. Chem. Res.* **2000**, *33*, 2.

[5] Müller, A.; Krickemeyer, E.; Bögge, H.; Schmidtmann, M.; Peters, F. *Angew. Chem., Int. Ed.* **1998**, *37*, 3360.

[6] (a) Müller, A.; Beckmann, E.; Bögge, H.; Schmidtmann, M.; Dress, A. *Angew. Chem., Int. Ed*. **2002**, *41*, 1162. (b) Müller, A.; Botar, B.; Das, S. K.; Bögge, H.; Schmidtmann, M.; Merca, A. *Polyhedron* **2004**, *23*, 2381. (c) H.-E. Schaefer, *Nanoscience: The Science of the Small in Physics, Engineering, Chemistry, Biology and Medicine*; World Scientific, New Jersey, 2012, pp. 109–179.

[7] (a) Müller, A.; Roy, S. *The Chemistry of Nanomaterials: Synthesis, Properties and Applications*; Rao, C. N. R.; Müller, A.; Cheetham, A. K.; Eds.; Wiley-VCH, Weinheim, 2004, pp. 452–475. (b) Long, D.-L.; Burkholder, E.; Cronin, L. *Chem. Soc. Rev.* **2007**, *36*, 105. (c) Long, D.-L.; Cronin, L. *Chem. Eur. J.* **2006**, *12*, 3698. (d) Cronin, L. *Comprehensive Coordination Chemistry II: From Biology to Nanotechnology;* McCleverty, J. A.; Meyer, T. J.; Eds.; Elsevier, Amsterdam, 2004, vol. 7, pp. 1–56. (e) Long, D.-L.; Tsunashima, R.; Cronin, L. *Angew. Chem., Int. Ed.* **2010**, *49*, 1736. (f) Pope, M. T. *Comprehensive Coordination Chemistry II: From Biology To Nanotechnology;* McCleverty, J. A.; Meyer, T. J.; Eds.; Elsevier, Amsterdam, 2004, vol. 4, pp. 635–678; see also related papers in the following books; (g) *Polyoxometalates: From Platonic Solids to Anti–Retroviral Activity;* Pope, M. T., Müller, A., Eds.; Kluwer: Dordrecht, The Netherlands, 1994. (c) *Polyoxometalate Chemistry: from Topology via Self–Assembly to Applications;* Pope, M. T., Müller, A., Eds.; Kluwer: Dordrecht, The Netherlands, 2001.

[8] Pope, M. T.; Müller, A. *Angew. Chem., Int. Ed. Engl.* **1991**, *30*, 34.

[9] Long, D.-L.; Abbas, H.; Kögerler, P.; Cronin, L. *J. Am. Chem. Soc.* **2004**, *126*, 13880.

[10] (a) Yu, H.-H.; Cui, X.-B.; Cui, J.-W.; Kong, L.; Duan, W.-J.; Xu, J.-Q.; Wang, T.-G. *Dalton Trans.* **2008**, 195. (b) Han, Q. X.; Ma, P. T.; Zhao, J. W.; Wang, Z. L.; Yang, W. H.; Guo, P. H.; Wang, J. P.; Niu, J. Y. *Cryst. Growth Des.* **2011**, *11*, 436.

(c) Liu, C.-M.; Zhang, D.-Q.; Zhu, D.-B. *Cryst. Growth Des.* **2006**, *6*, 524. (d) Lei, C.; Mao, J.-G.; Sun, Y.-Q.; Song, J.-L. *Inorg. Chem.* **2004**, *43*, 1964. (e) Walsh, J.; Zhu, J.; Zeng, Q.; Forster, R. J.; Keyes, T. E. *Dalton Trans.* **2012**, *41*, 9928. (f) Jin, H.-J.; Zhou, B.-B.; Yu, Y.; Zhao, Z.-F.; Su, Z.-H. *CrystEngComm* **2011**, *13*, 585. (g) Zang, H.-Y.; Tan, K.; Guan, W.; Li, S.-L.; Yang, G.-S.; Shao, K.-Z.; Yan, L.-K.; Su, Z.-M. *CrystEngComm* **2010**, *12*, 3684. (h) Sun, C.-Y.; Li, Y.-G.; Wang, E.-B.; Xiao, D.-R.; An, H. Y.; Xu, L. *Inorg. Chem.* **2007**, *46*, 1563. (i) Niu, J.-Y.; Hua, J.-H.; Ma, X.; Wang, J.-P. *CrystEngComm* **2012**, *14*, 4060. (j) Shivaiah, V.; Nagaraju, M.; Das, S. K. *Inorg. Chem.* **2003**, 42, 6604.

[11] (a) Combs-Walker, L. A.; Hill, C. L. *Inorg. Chem.* **1991**, *30*, 4016. (b) Rusu, M.; Muresan, L.; Tomsab, A. R.; Rusuc, D.; Marcua, G. *Synth. React. Inorg. Met.-Org. Chem.* **2000**, *30*, 499. (c) Neumann, R.; Dahan, M. *Polyhedron* **1998**, *17*, 3557. (d) Fernandes, D. M.; Cunha-Silva, L.; Ferreira, R. A. S.; Balula, S. S.; Carlos, L. D.; de Castro, B.; Freire, C. *RSC Adv.* **2013**, *3*, 16697.

[12] Cindric, M.; Veksli, Z.; Kamenar, B. *Croat. Chem. Acta* **2009**, *82*, 345.

[13] Li, T.; Lu, J.; Gao, S.; Cao, R. *Inorg. Chem. Commun.* **2007**, *10*, 1342.

[14] (a) Hasenknopf, B.; Delmont, R.; Herson, P.; Gouzerh, P. *Eur. J. Inorg. Chem*. **2002**, 1081. (b) Marcoux, P. R.; Hasenknopf, B.; Vaissermann, J.; Gouzerh, P. *Eur. J. Inorg. Chem.* **2003**, 2406.

[15] Dolbecq, A.; Sécheresse, F. *Adv. Inorg. Chem.* **2002**, *53*, 1.

[16] (a) Barkigia, K. M.; Rajkovic-Blazer, L. M.; Pope, M. T.; Quicksall, C. O. *Inorg. Chem.* **1981**, *20*, 3318. b) Johnson, B. S. J.; Schroden, R. C.; Zhu, C.; Stein, A. *Inorg. Chem.* **2001**, *40*, 5972.

[17] a) Kortz, U.; Savelieff, M. G.; Abou-Gali, F. Y.; Khalil, L. M.; Maalouf, S. A.; Sinno, D. I. *Angew. Chem.* **2002**, *114*, 4246; *Angew. Chem Int. Ed.* **2002**, *41*, 4070. b) Kortz, U.; Vaissermann, J.; Thouvenot, R.; Gouzerh, P. *Inorg. Chem.* **2003**, *42*, 1135.

[18] Kortz, U.; Marquer, C.; Thouvenot, R.; Nierlich, M. *Inorg. Chem.* **2003**, *42*, 1158.

[19] Strandberg, R. *Acta Chem. Scand.* **1973,** *27*, 1004.

[20] a) Jones, S.; Zubieta, J. *Metal Phosphonate Chemistry: From Synthesis to Applications*; Clearfield, A.; Demadis, K.; Eds.; Royal Society of Chemistry: Cambridge, **2012**, pp 192−234. (b) Burkholder, E.; Golub, V.; O'Connor, C. J.; Zubieta, J. *Inorg. Chem.* **2003**, *42*, 6729.

[21] (a) Li, X-M.; Chen, Y.-G.; Su, C.-N.; Zhou, S.; Tang, Q.; Shi, T. *Inorg. Chem.* **2013**, *52*, 11422.

[22](a) Hedman, B. *Acta Chem. Scand.* **1973**, *27*, 3335. (b) Kwak, W.; Pope, M. T.; Scully, T. F. *J. Am. Chem. Soc.* **1975**, *97*, 5753. (c) Stalick, J. K.; Quicksall, C. O. *Inorg. Chem.* **1976**, *15*, 1577. (d) Hedman, B.; Strandberg, R. *Acta Crystallogr.* **1979**, *B35*, 278. (e) Pettersson, L.; Andersson, I.; Öhman, L.-O. *Acta Chem. Scand.* **1985**, *A39*, 53. (f) Pettersson, L.; Andersson, I.; Öhman, L.-O. *Inorg. Chem.* **1986**, *25*, 4726. (g) Yagasaki, A.; Andersson, I.; Pettersson, L. *Inorg. Chem.* **1987**, *26*, 3926. (h) Ozeki, T.; Ichida, H.; Miyamae, H.; Sasaki, Y. *Bull. Chem. Soc. Jpn.* **1988**, *61*, 4455. (i) Lyxell, D.-G.; Strandberg, R. *Acta Crystallogr.* **1988**, *C44*, 1535. (j) Lyxell, D.-G.; Strandberg, R.; Boström, D.; Pettersson, L. *Acta Chem. Scand.* **1991**, *45*, 681. (k) Lowe, M. P.; Lockhart, J. C.; Clegg, W. P.; Fraser, K. A. *Angew. Chem., Int. Ed.* **1994**, *33*, 451. (l) Lowe, M. P.; Lockhart, J. C; Forsyth, G. A.; Clegg, W.; Fraser, K. A. *J. Chem. Soc., Dalton Trans.* **1995**, 145. (m) Inoue, M.; Yamase, T. *Bull. Chem. Soc. Jpn.* **1996**, *69*, 2863. (n) Harrison, W. T. A.; Dussack, L. L.; Jacobson, A. J. Acta *Crystallogr.* **1997**, *C53*, 856. (o) Lyxell, D.-G.; Boström, D.; Hashimoto, M.; Pettersson, L. *Acta Chem. Scand.* **1998**, *52*, 425. (p) Mayer, C. R.; Marrot, J.; Sécheresse, F. *J. Mol. Struct.* **2004**, *704*, 59. (q) Carraro, M.; Sartorel, A.; Scorrano, G.; Maccato, C.; Dickman, M. H.; Kortz, U.; Bonchio, M. *Angew. Chem., Int. Ed.* **2008**, *47*, 7275.

[23] (a) Kortz, U.; Marquer, C.; Thouvenot, R.; Nierlich, M. *Inorg. Chem.* **2003**, *42*, 1158. (b) Chubarova, E. V.; Klöck, C.; Dickman, M. H.; Kortz, U. *J. Cluster Sci.* **2007**, *18*, 698.

[24] (a) Finn, R. C.; Burkholder, E.; Zubieta, J. *Chem. Commun.* **2001**, 1852. (b) Finn, R. C.; Zubieta, J. *Inorg. Chem.* **2001**, *40*, 2466. (c) Burkholder, E.; Zubieta, J. *Inorg. Chim. Acta* **2004**, *357*, 1229. (d) Burkholder, E.; Golub, V.; O'Connor, C. J.; Zubieta, J. *Inorg. Chem.* **2004**, *43*, 7014. (e) Zhang, H.-S.; Fu, R.-B.; Zhang, J.-J.; Wu, X.-T.; Li, Y.-M.; Wang, L.-S.; Huang, X.-H. J. *Solid State Chem.* **2005**, *178*, 1349. (f) Fu, R.-B.; Wu, X.-T.; Hu, S.- M.; Zhang, J.-J.; Fu, Z.-Y.; Du, W.–X.; Xia, S.-Q. *Eur. J. Inorg. Chem.* **2003**, 1798. (g) Burkholder, E.; Golub, V.; O'Connor, C. J.; Zubieta, J. *Chem. Commun.* **2003**, 2128. (h) Armatas, N. G.; Allis, D. G.; Prosvirin, A.; Carnutu, G.; O'Connor, C. J.; Dunbar, K.; Zubieta, J. *Inorg. Chem.* **2008**, *47*, 832. (i) Bartholomä, M.; Chueng, H.; Pellizzeri, S.; Ellis-Guardiola, K.; Jones, S.; Zubieta, J. *Inorg. Chim. Acta* **2012**, *389*, 90.

[25] (a) Knoth, W. H.; Harlow, R. L. *J. Am. Chem. Soc.* **1981**, *103*, 1865. (b) Lin, B.-Z.; Li, Z.; Xu, B.-H.; He, L.-W.; Liu, X.-Z.; Ding, C. *J. Mol. Struct.* **2006**, *825*, 87. (c) Cao, X.-G.; He, L.-W.; Lin, B.-Z.; Xiao, Z.-J. *J. Chem. Cryst.* **2010**, *40*, 443.

---

[26] (a) Nagazi, I.; Haddad, A. *Mater. Res. Bull.* **2012**, *47*, 356. (b) Kong, F.; Hu, C.-L.; Xu, X.; Zhou, T.-H.; Mao, J.-G. *Dalton Trans.* **2012**, *41*, 5687. (c) Lian, Z.-X.; Huang, C.-C.; Zhang, H.-H.; Huang, X.-H.; Yang H.-F. *Chinese. J. Struct. Chem.* **2004**, *23*, 705. (d) Feng, M.-L.; Mao, J.-G. *Eur. J. Inorg. Chem.* **2004**, *18*, 3712. (e) Ayed, M.; Nagazi, I.; Ayed, B.; Haddad, A. *J. Cluster Sci.* **2012**, *23*, 1133. (f) Nagazi, I.; Haddad, A. *J. Clust. Sci.* **2013**, *24*, 145.

[27] (a) Coronado, E.; Curreli, S.; Gimenez-Saiz, C.; Gomez-Garcia, C. J.; Alberola, A.; Canadell, E. *Inorg. Chem.* **2009**, *48*, 11314. (b) Bu, W.; Uchida, S.; Mizuno, N. *Angew. Chem., Int. Ed.* **2009**, *48*, 8281. (c) Granadeiro, C. M.; Ferreira, R. A. S.; Soares-Santos, P. C. R.; Carlos, L. D.; Nogueira, H. I. S. *Eur. J. Inorg. Chem.* **2009**, 5088.

[28] (a) Ito, T.; Yashiro, H.; Yamase, T. *Langmuir*, **2006**, *22*, 2806. (b) Cao, R.; Liu, S.; Xie, L.; Pan, Y.; Cao, J.; Ren, Y.; Xu, L. *Inorg. Chem*. **2007**, *46*, 3541. (c) Honda, D.; Ozeki, T.; Yagasaki, A. *Inorg. Chem*. **2005**, *44*, 9616.

[29] Burkholder, E.; Zubieta, J. *Chem. Commun.* **2001**, 2056.

[30] Finn, R. C.; Rarig, R. S. Jr; Zubieta, J. *Inorg.Chem*. **2002**, *41*, 2109.

[31] Jin, H.-J.; Zhou, B.-B.; Yu, Y.; Zhao, Z.-Z.; Su, Z.-H. *Eur. J. Inorg. Chem.* **2005**, 1239.

[32] Qin, C.; Wang, X.-L.; Yuan, L.; Wang, E.-B. *Cryst. Growth Des*. **2008**, *8*, 2093.

[33] Thomas, J.; Ramanan, A. *Cryst. Growth Des*. **2008**, *8*, 3390.

[34] Armatas, N. G.; Oulelette, W.; Whitenack, K.; Pelchert, J.; Liu, H.-X.; Romaine, E.; O'Connor, C. J.; Zubieta, J. *Inorg. Chem.* **2009**, *48*, 8897.

[35] Su, Z.-H.; Zhao, Z.-F.; Zhou, B.-B.; Cai, Q.-H.; Wang, Q. *Solid State Sci.* **2011**, *13*, 417.

[36] DeBurgomaster, P.; Aldous, A.; Liu, H.-X.; O'Connor, C. J.; Zubieta, J. *Cryst. Growth Des.* **2010**, *10*, 2209.

[37] Ou, G.-C.; Yuan, X.-Y.; Li, Z.-Z.; Ding, M.-H. *J. Coord. Chem* **2013**, *66*, 2065.

[38] Dey, C.; Kundu, T.; Banerjee, R. *Chem. Commun*. **2012**, *48*, 266.

[39] Song, L.; Su, Z.-H.; Wang, C.-X.; Wang, C.-M.; Zhou, B.-B. *J. Coord. Chem.* **2014** *67*, 522.

[40] Li, Z.-L.; Wang, Y.; Zhang, L.-C.; Wang, J.-P.; You, W.-S.; Zhu, Z.-M. *Dalton Trans*. **2014**, *43*, 5840.

[41] Wang, J.-P.; Ma, H.-X.; Zhang, L.-C.; You, W.-S.; Zhu, Z.-M. *Dalton Trans.* **2014**, *43*, 17172.

[42] Dong, Y.; Xu, X.; Zhou, G.-P.; Miao, H.; Hu, G.-H.; Xu, Y. *Dalton Trans.* **2015**, *44*, 18347.

[43] Xu, X.-X.; Gao, X.; Lu, T.-T.; Liu, X.-X.; Wang, X.-L. *J. Mater. Chem. A* **2015**, *3*, 198.

[44] Blazevic, A.; Rompel, A. *Coord. Chem. Rev.* **2016**, *307*, 42 and references therein.

[45] Anderson, J. S. *Nature* **1937**, *140*, 850.

[46] Evans, H. T. Jr. *J. Am. Chem. Soc.* **1948**, *70*, 1291.

[47] Pope, M. T. *Heteropoly and Isopoly Oxometalates,* Springer-Verlag, Berlin, 1983.

[48] Schmidt, K. J.; Schrobilgen, G. J.; Sawyer, J. F. *Acta Crystallogr.* 1986, *C42*, 1115.

[49] Kondo, H.; Kobayashi, A.; Sasaki, Y. *Acta Crystallogr.* **1980**, *B36*, 661.

[50] Perloff, A. *Inorg. Chem.* **1970**, *9*, 2228.

[51] Wu, C.; Lin, X.; Yu, R.; Yang, W.; Lu, C.; Zhuang, H. *Sci. China, Ser. B: Chem.* **2001**, *44*, 49.

[52] (a) Björnberg, A. *Acta Crystallogr.* **1979**, *B35*, 1995. (b) Nenner, A.-M. *Acta Crystallogr*. **1985**, *C41*, 1703.

[53] Livage, C.; Dumas, E.; Marchal-Roch, C.; Hervé, G. *C.R. Acad. Sci., Ser. IIc: Chim.* **2000**, *3*, 95.

[54] (a) Vidyavathy, B.; Vidyasagar, K. *Inorg. Chem.* **1999**, *38*, 1394; (b) *Inorg. Chem.* **1998**, *37*, 4764.

[55] Oreshkina, A. V.; Kaziev, G. Z.; Holguin-Quinones, S.; Stash, A. I.; Shipilova, P. A. *Russ. J. Coord. Chem.* **2011**, 37, 845.

[56] (a) Rozantsev, G. M. Radio, S. V.; Gumerova, N. I; Baumer, V. N.; Shishkin, O. B. *J. Struct.Chem.* **2009**, *50*, 296. (b) Sun, C.-Y.; Liu, S.-X.; Xie, L.-H.; Wang, C.-L.; Gao, B.; Zhang, C.-D.; Su, Z.-M. *J. Solid State Chem.* **2006**, *179*, 2093. (c) Moroz, Y. A.; Gruba, A. I.; Zayats, M. N.; Danileiko, L. A.; Dumanova, E. V. *Zh. Neorg. Khim.* **1987**, *32*, 927. (d) Polyakov, E. V.; Denisova, T. A.; Maksimova, L. G.; Gyrdasova, O. I.; Manakova, L. I. *Inorg. Mater.* **2002**, 38, 956.

[57] Nomiya, K.; Takahashi, T.; Shirai, T.; Miwa, M. *Polyhedron* **1987**, *6*, 213.

---

[58] (a) Marcoux, P. R.; Hasenknopf, B.; Vaissermann, J.; Gouzerh, P. *Eur. J. Inorg. Chem*. **2003**, 2406. (b) Song, Y.-F.; Long, D.-L.; Kelly, S. E.; Cronin, L. *Inorg. Chem*. **2008**, *47*, 9137.

[59] Yvon, C.; Macdonell, A.; Buchwald, S.; Surman, A. J.; Follet, N.; Alex, J.; Long, D.-L.; Cronin, L. *Chem. Sci.* **2013**, *4*, 3810.

[60] Hasenknopf, B.; Delmont, R.; Herson, P.; Gouzerh, P. *Eur. J. Inorg. Chem*. **2002**, 1081.

[61] (a) Tripuramallu, B. K.; Das, S. K. *Cryst. Growth. Des*. **2013**, *13*, 2426. (b) Lan, Y.-Q.; Li, S.-L.; Wang, X.-L.; Shao, K.-Z.; Du, D.-Y.; Zang, H.-Y.; Su, Z.-M. *Inorg. Chem*. **2008**, *47*, 8179. (c) Dong, B.-X.; Xu, Q. *Cryst. Growth. Des*. **2009**, *9*, 2776. (d) Liu, M.-G.; Zhang, P.-P.; Peng, J.; Meng, H.-X.; Wang, X.; Zhu, M.; Wang, D.-D.; Meng, C.-L.; Alimaje, K. *Cryst. Growth. Des*. **2012**, *12*, 1273.

[62] (a) Wang, Y.; Xiao, D.-R.; Qi, Y.-F.; Wang, E.-B.; Liu, J. *J. Clust. Sci.* **2008**, *19*, 367; (b) An, H.-Y.; Xiao, D.-R.; Wang, E.-B.; Li, Y.-G.; Wang, X.-L.; Xu, L. *Eur. J. Inorg. Chem*. **2005**, *44*, 854; (c) Li, S.-Z.; Ma, P.-T.; Wang, J.-P.; Guo, Y.-Y.; Niu, H.-Z.; Zhao, J.-W.; Niu, J.-Y. *CrystEngComm* **2010**, *12*, 1718.

[63] (a) Cao, R.-G.; Liu, S.-X.; Xie, L.-H.; Pan, Y.-B.; Cao, J.-F.; Ren, Y.-H.; Xu, L. *Inorg. Chem.* **2007**, *46*, 3541. (b) Cao, R.-G.; Liu, S.-X.; Liu, Y.; Tang, Q.; Wang, L.; Xie, L.-H.; Su, Z.-M. *J. Solid State Chem*. **2009**, *182*, 49.

[64] Pavani, K.; Singh, M.; Ramanan, A. *Aust. J. Chem.* **2011**, *64*, 68.

[65] (a) Ran, R.; Pang, H.-J.; Yu, Z.-G.; Ma, H.-Y. *J. Coord. Chem*. **2011**, *64*, 2388. (b) Zhang, S.-W.; Li, Y.-X.; Liu, Y.; Cao, R.-G.; Sun, C.-Y.; Ji, H.-M.; Liu, S.-X. *J. Mol. Struct*. **2009**, *920*, 284. (c) Tan, R.-K.; Liu, S.-X.; Zhang, W.; Li, S.-J.; Zhang, Y.-Y. *Inorg. Chem. Commun.* **2011**, *14*, 384. (d) Ma, H.-Y.; Wu, L.-Z.; Pang, H.-J.; Meng, X.; Peng, J. *J. Mol. Struct*. **2010**, *967*, 15. (e) Shivaiah, V.; Das, S. K. *Inorg. Chem.* **2005**, *44*, 8846.

[66] (a) Wang, X.-L.; Chang, Z.-H.; Lin, H.-Y.; Tian, A.-X.; Liu, G.-C.; Zhang, J.-W. *Dalton Trans.* **2014**, *43*, 12272.

[67] Wang, X.-L.; Xu, N.; Zhao, X.-Z.; Zhang, J.-W.; Gong, C.-H.; Li,. T.-J. *CrystEngComm* ***2015***, *17*, 7038.

[68] (a) An, H.-Y.; Guo, Y.-Q.; Li, Y.-G.; Wang, E.-B.; Lu, J.; Hu, C.-W. *Inorg. Chem. Commun.* **2004**, *7*, 521. (b) Wang, Y.; Xiao, D.-R.; Qi, Y.-F.; Wang, E.-B. Liu, J. *J. Clust. Sci.* **2008**, *19*, 367.

[69] An, H.-Y.; Xu, T.-Q.; Wang, E.-B.; Meng, C.-G. *Inorg. Chem. Commun.* **2007**, *10*, 1453.

[70] Zhang, P.-P.; Peng, J.; Tian, A.-X.; Sha, J.-Q.; Pang, H.-J.; Chen, Y.; Zhu, M.; Wang, Y.-H. *J. Mol. Struct.* **2009**, *931*, 50.

[71] Singh, M.; Lofland, S. E.; Ramanujachary, K. V.; Ramanan, A. *Cryst. Growth Des.* **2010**, *10*, 5105.

[72] Singh, M.; Ramanan, A. *Cryst. Growth Des.* **2011**, *11*, 3381.

[73] An, H.-Y.; Han, Z.-B.; Xu, T.-Q.; Meng, C.-G.; Wang, E.-B. *Inorg. Chem. Commun.* **2008**, *11*, 914.

[74] An, H.; Liu, X.; Chen, H.; Han, Z.-B.; Zhang, H.; Chen, Z.-F.*CrystEngComm* **2011**, *13*, 5384.

[75] Golhen, S.; Ouahab, L.; Grandjean, D.; Molinié, P. *Inorg. Chem.* **1998**, *37,* 1499.

[76] Wu, Q.; Li, Y.-G.; Wang, Y.-H.; Clérac, R.; Lu, Y.; Wang, E.-B. *Chem. Commun*. **2009**, 5743.

[77] Wu, Q.; Chen, W.-L.; Liu, D.; Liang, C.; Li, Y.-G.; Lin, S.-W.; Wang, E.-B. *Dalton Trans*. **2011**, *40*, 56.

[78] Wang, Y.; Chang, Z.-H.; Lin, H.-Y.; Tian, A.-X.; Liu, G.-C.; Zhang, J.-W. *Dalton Trans.* **2014**, *43*, 12272.

[79] Wang, X.-L.; Chang, Z.-H.; Lin, H.-G.; Tian, A.-X.; Liu, G.-C.; Zhang, J.-W.; Liu, D. RSC Adv. **2015**, *5*, 14020.

[80] Wang, X.-L.; Gong, C.-H.; Zhang, J.-W.; Liu, G.-C.; Kan, X.-M.; Xu, N. *CrystEngComm* **2015**, *17*, 4179.

[81] Wang, X.-L.; Xu, N.; Zhao, X.-Z.; Zhang, J.-W.; Gong, C.-H.; Li, T.-J. *CrystEngComm* **2015**, *17*, 7038.

[82] Wang, X.-L.; Sun, J.-J.; Lin, H.-Y.; Chang, Z.-H.; Liu, G.-C.; Wang, X. *RSC Adv.* **2016**, *6*, 110583.

[83] Gong, C.-H.; Zeng, X.-H.; Zhu, C.-F.; Shu, J.-H.; Xiao, P.-X.; Xu, H.; Liu, L.-C.; Zhang, J.-Y.; Zheng, Q.-D.; Xie, J.-L. *RSC Adv.* **2016**, *6*, 106248.

[84] Zhang, L.-Z.; Gu, W.; Dong, Z.; Liu, X.; Li, B. *CrystEngComm* **2008**, *10*, 1318.

[85] Don, A.; Weakley, T. J. R. *Acta Crystallogr.* **1981**, *B37*, 451.

[86] Reinoso, S.; Dickman, M. H.; Praetorius, A.; Kortz, U. *Acta Crystallogr.* **2008**, *E64*, 614.

[87] Barats-Damatov, D.; Shimon, L. J. V.; Feldman, Y.; Bendikov, T.; Neumann, R. *Inorg. Chem*. **2015**, *54*, 628.

---

[88] Tsigdinos, G. A.; Hallada, C. J. *Inorg. Chem*. **1968**, *7*, 437.

[89] Aranzabe, A.; Wéry, A. S. J.; Martín, S.; Gutiérrez-Zorrilla, J. M.; Luque, A.; Martínez-Ripoll, M.; Román P. *Inorg. Chim. Acta* **1997**, *255*, 35–45.

[90] *CrysAlisPro Software System*, Version 171.37.34; Agilent Technologies UK Ltd.: Oxford, U. K., **2012.**

[91] Dolomanov, O. V.; Bourhis, L. J.; Gildea, R. J.; Howard, J. A.; Puschmann, H. J. *J. Appl. Crystallogr.* **2009**, *42*, 339–342.

[92] Sheldrick, G. M. *Acta Crystallogr.* **2008**, *A64*, 112–122.

[93] Spek, A. L. *Acta Crystallogr.* **2009**, *D65*, 148–155.

[94] Farrugia, L. J. *J. Appl. Crystallogr.* **1999**, *32*, 837–838.

[95] *Nat. Bur. of Stand. (US), Monogr.* **1984**, 25, 20, 118.

[96] Robertson, B., Calvo, C., *Acta Crystallogr*. **1967**, *22*, 665–672.

[97] Lukaszewicz, K. *Bull. Acad. Pol. Sci., Ser. Sci. Chim.,* **1967**, *15*, 47–51.

[98] D. Casanova, M. Llunell, P. Alemany, S. Alvarez, *Chem. Eur. J.* **2005**, *11*, 1479.

[99] Wery, A. S. J.; Gutiérrez-Zorrilla, J. M.; Luque, A.; Ugalde, M.; Román P.; Lezama, L.; Rojo, T. *Acta Chem. Scand.* **1998**, *52*, 1194.

[100] (a) *Natl. Bur. Stand (U.S.) Monogr.* **1984**, *25*, 118. (b) Kihlborg, L. *Ark. Kemi,* **1963**, *21*, 357.

[101] Kihlborg, L. *Ark. Kemi,* **1963**, *21*, 365.

[102] Portemer, F.; Sundberg, M.; Kihlborg, L.; Figlarz, M. *J. Solid State Chem.* **1993**, *103*, 403.

[103] (a) Erdos, E.; Sulzer Brothers Ltd., Winthertur, Switzerland. (b) Nassau, A. *J. Cryst. Growth* **1968**, *2*, 136. (c) Schwartz, Y. *Science* **1963**, *141*, 348.

[104] Giovanoli, R.; Oswald, H. R.; Feitknecht, W. *Helv. Chim. Acta* **1966**, *49*, 1971.

[105] (a) Trunov, K. *Inorg. Mater. (Engl. Transl.)* **1966**, *2*, 127.; (b) Battle, P. D.; Cheetam, A. K.; Harrison, W. T. A.; Faber, Jr. J. *J. Solid State Chem.* **1985**, *58*, 221. (c) Christensen, A. N.; Hansen, P.; Lehman, M. S. *J. Solid State Chem.* **1977**, *21*, 325.

[106] Wu, P.-F.; Yin, P.-C.; Zhang, J.; Hao, J.; Xiao, Z.-C.; Wei, Y.-G. *Chem. Eur. J.* **2011**, *17*, 12002–12005.

[107] Brese, N. E.; Keeffe, M. O. *Acta. Cryst.* **1991**, B*47*, 192–197.

*POMs, as nanometric inorganic components with intrinsic multifunctionality, are considered well–defined platforms for the development of new materials. By reducing the structural dimensions of the POMs from bulk solids to low–dimensional structures (i.e. at the surface of nanoparticles or interphases of films), these nanoclusters can be used as components for functional devices such as electrodes, electronic circuits, as well as heterogeneous catalyst and soft materials, among others. In this final chapter, the preliminary work in a new research line within our group involving the immobilization of hybrid POMs onto functional polymeric surfaces is exposed and discussed. Thus, various hybrid polymer–inorganic films were prepared by anchoring selected hybrid POMs into tailored polymeric surfaces that consist on "breath figures" made of polystyrene–b–poly(acrylic acid)/polystyrene (PS–b–PAA/PS) blends (**BF**). The functionalization of the **BF** films was performed by interfacial migration of the amphiphilic block copolymer toward the pores located at the interface to expose the anchoring/coordination sites. These carboxylic acid functional groups contained within the PAA blocks were then employed to anchor **1–CuV1**, **1–CuV10**, **1–CuW7** and **1–CuMo5** hybrid POMs by immersing the films into aqueous solutions of the in situ formed hybrid clusters. Alternatively, various hybrid gel composites were also synthetized by direct mixing of the carboxylic block PAA and solutions containing the hybrid POMs, from which different hybrid surfaces were prepared (**HS**). The superficial analysis of these polymeric films was carried out by sophisticated ion beam–based techniques such as Low–Energy Ion Scattering (LEIS, for **HS** samples) and Time–of–Flight Secondary Ion Mass Spectrometry (ToF–SIMS, for **BF** films), the fundamentals of which are also briefly discussed here in the introduction.*

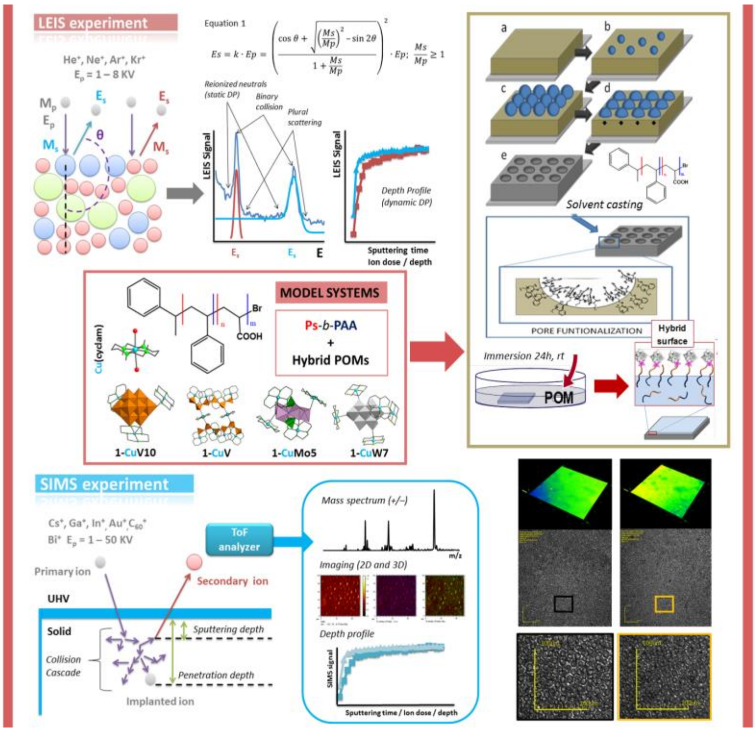

INCORPORATION OF HYBRID POMs ONTO TAILORED POLYMERIC SURFACES

Chapter 5

INCORPORATION OF HYBRID POMs ONTO TAILORED POLYMERIC SURFACES

5.1 INTRODUCTION

5.1.1 POM–based Organic–Inorganic Composites

Organic–inorganic composites represent one of the current hot topics in materials science due to the possibility of combining the specific characteristics of two different components in a single material to obtain unusual properties that may result in novel applications. Recently, the association of inorganic and organic species in hybrid composites has made available a vast scientific area around the development of multifunctional materials. Because of their outstanding features[1] and consequent applicability in current issues of interest related to technology, health, energy, and environment,[2] these anionic clusters are widely recognized as one of the most interesting types of inorganic components suitable for being incorporated into multifunctional materials.[3] In recent years, POMs have been combined as inorganic components with amphiphilic molecules or cationic surfactants to construct several discrete architectures (micelles, capsules, vesicles), monodimensional arrangements such as fibers, wires and tubes, or highly ordered bidimensional arrays like self–assembled monolayers, Langmuir and Langmuir–Blodgett films as well as Layer–by–Layer structures for diverse applications including catalytic, photoluminescent and photo– or electrochromic devices[4] (Figure 5.1). POMs have also been incorporated to several types of organic materials, like carbon nanotubes, graphene, metal–organic frameworks, and diverse polymeric matrices either by adsorption or by co–polymerization when derivatized with suitable functionalities.[5]

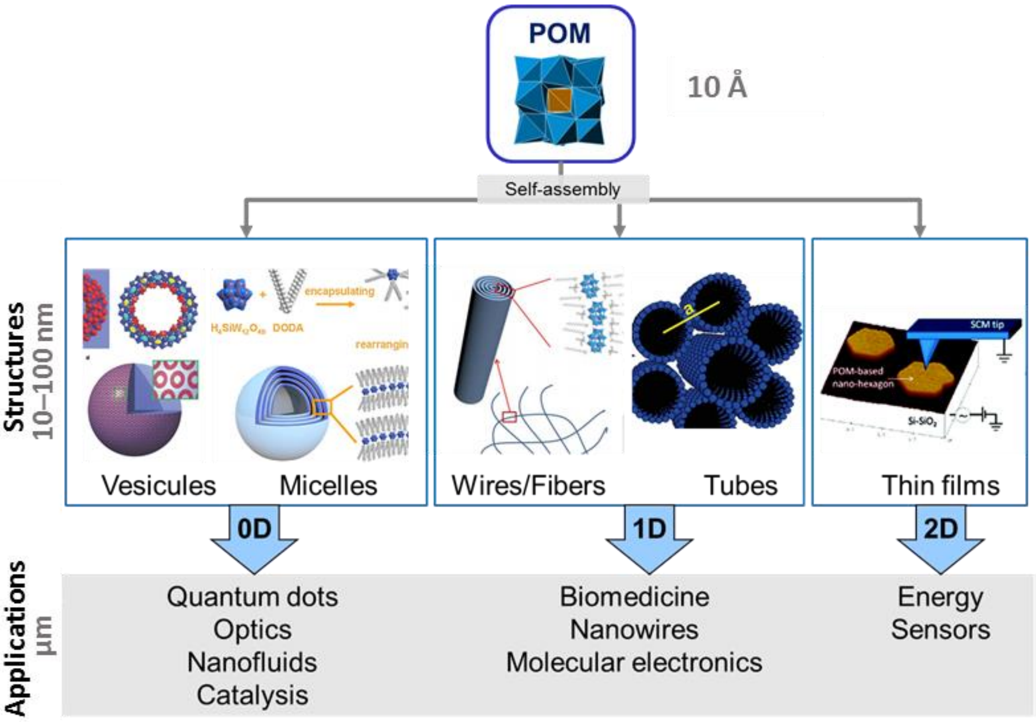

Figure 5.1. Structural and dimensional diversity in polyoxometalate–based organic–inorganic composites for a variety of different potential applications.

Immobilization of POMs onto solid surfaces represents a key step toward processing these nanoclusters into functional and practical devices.[6] For instance, the anchorage of a given POM to a solid substrate can lead to the combination of its inherent catalytic activity in homogeneous phase with the ease of recovery and recycling characteristic of heterogeneous catalysts, which represents a clear demand for actual industrial purposes.[7] Different solid substrates have been employed as POM supports, such as oxides (alumina, silica), metals (silicon and gold) or highly oriented pyrolytic graphite.[8] Since POMs are negatively charged, their immobilization usually relies on electrostatic interactions, which might lead to partial leaching of these clusters from the target surfaces. Usually, surfaces are functionalized with positively charged residues and/or H–donor groups to enhance the electrostatic interactions and/or to generate a reinforcing network of intermolecular hydrogen bonds, although this does not ensure that the leaching phenomenon is completely avoided. Thus, different strategies based on the covalent linkage of POMs have been applied to overcome this,[9] like using organically derivatized POMs and substrates bearing complementary functionalities to induce the formation of a covalent bond (e.g. amino and carboxylic groups)[10] or grafting N–donor groups on the solid surface to coordinate 3d–metal substituted–POMs with terminal aqua ligands.[11] However, the former approach limits the catalogue of suitable POMs mainly to lacunary derivatives of the Keggin and Wells–Dawson type anions. To our knowledge, only one example of hybrid film composite involving POMs and diblock copolymers has been described in the literature up to now, in which the formation of aggregates in solution is employed to direct the self–assembly of highly ordered films with inverse hexagonal topology.[12]

Up to date the most common route to the integration of POMs into functional architectures and devices relies on inorganic/organic hybrids. However, the direct preparation of functional POM–based materials has been rather scarce because POMs usually are crystalline solids that are hard to process. Overcoming this hindrance could result in the design and fabrication of novel functional materials that combine the unique properties of POMs and counterpartners (e.g., magnetism, conductivity or optical properties, sensing and so on), which are expected to be the focus of future developments within this field. Instead of using 3d–centers incorporated into the POM, (i.e. metal–substituted POMs) we decided to try a similar coordinative approach mentioned above but employing a transition–metal belonging to a metalorganic complex covalently linked at the POM surface (i.e. a *class II* hybrid POM) as the anchorage point instead (Figure 5.2). For this purpose, we selected hybrid POMs containing copper(II) complexes of cyclam because of the plasticity of the coordination sphere of the Cu^{II} centers and the Jahn–Teller elongation they undergo when involved in octahedral environments to act as potential flexible anchoring point toward carboxylate–terminated polymeric blends. This way, the cyclam macrocyclic ligand should allow the axial positions of the coordination sphere of the metal to be readily available to coordinate to the carboxylic functions of the poly(acrylic acid) block. In order to test the reactivity of the macrocyclic copper complex toward the PAA, we reacted an *in situ* prepared solution of the macrocyclic complex with commercial hydrophylic poly(acrylic acid), which led to the formation of a purple homogeneous gel. Similar gels were obtained when reacting solutions of Cu(cyclam) containing POMs with solid PAA under the same conditions (Figure 5.2).

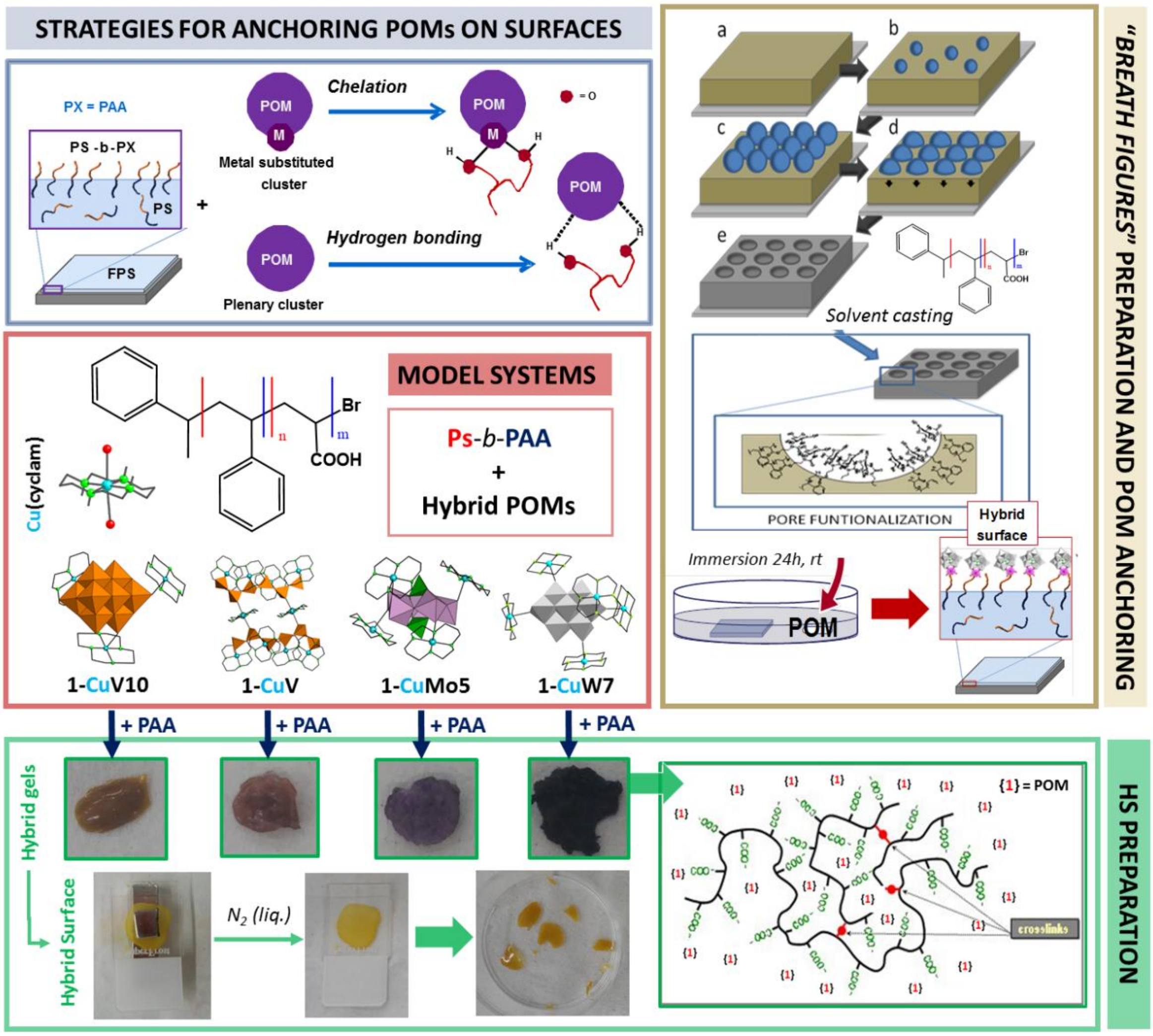

Figure 5.2. Different strategies for the inmobilization of POMs onto polymeric surfaces along the model systems used in this work (top left), as well as an schematic representation of the static breath figure preparation method (**BF**, top right) and hybrid surfaces (**HS**, bottom). PS = polystyrene; PAA = poly(acrylic acid).

In this chapter, we describe the preparation of functionalized "breath figures" films (**BF**) composed of polystyrene–*b*–poly(acrylic acid)/polystyrene blends (PS–*b*–PAA/PS). As will be depicted, the surface segregation of the poly(acrylic acid) block allows the immobilization of POMs via their flexible polystyrene branches terminated with O–donor polycarboxylic residues which are located primarily in the cavities of the surface. The static procedure for breath figure patterning method used in this work is schematized in Figure 5.2: a) a diblock amphiphilic copolymer solution in a high volatile solvent is cast onto a substrate under adequate relative humidity, b) The fast evaporation of the solvent temporally cool down the solvent/air interface and water droplets begin to deposit by condensation of H_2O from the humid air; c) these droplets grow over time while d) the hydrophilic block is oriented towards the water droplets; and finally e) the solvent droplets evaporate leaving pores functionalized with the hydrophilic block of the copolymer. The hybrid POMs selected as initial models to test the anchoring capability of these films were the **1–CuV** and **1–CuV10** polyoxovanadates, the Strandberg–type polyoxomolybdate **1–CuMo5** and the heptatungstate **1–CuW7** hybrids, which were studied in chapters 2, 3 and 4, respectively. Alternatively, a series of different surfaces labelled as **HS** were made from the colored gels obtained by reaction of each POM with PAA following a simple procedure as previously mentioned. These gels were soaked in water, press between two sample holders with the aid of a Nd–based magnet and freeze with liquid nitrogen in order to flatten the samples. After cooling down to room temperature, the composite gel were detached form the glass yielding moderately flat surfaces, labelled as **HS** samples (Figure 5.2).

Among the wide range of available surface analysis techniques, ion beam–based techniques, such as Time–of–Flight Secondary Ion Mass Spectrometry (ToF–SIMS) and Low–Energy Ion Scattering (LEIS), are recently being considered as very powerful characterization tools for materials research and development due to their analytical capabilities for the determination of the chemical and isotopic composition at the surface and near–surface regions.[13] These hybrid POM–polymer surfaces were characterized during a stay at *I^{2}CNER* at *Kyushu University* (Fukuoka, Japan) using LEIS and ToF–SIMS surface analysis techniques, the fundamentals of which will be briefly described in the following pages.

5.1.2 Low Energy Ion Scattering (LEIS)

Low–Energy Ion Scattering (LEIS) has existed as an analytical technique since the late 1960's, but important advances in instrumentation have dramatically improved its capabilities and applicability in recent years.[14] Unlike X–Ray Photoelectron Spectroscopy (XPS), which analyze the first few nanometers of a given material, the greatest strength and unique feature of LEIS is that it is sensitive to the outermost atomic layer of a material.[14,15] Because these final atoms of a surface often govern the chemical interaction with other materials, LEIS is a powerful tool for understanding the relationship between surface composition and important phenomena including but not limited to catalysis, wetting, diffusion, adhesion, and contamination issues.[14d,16]

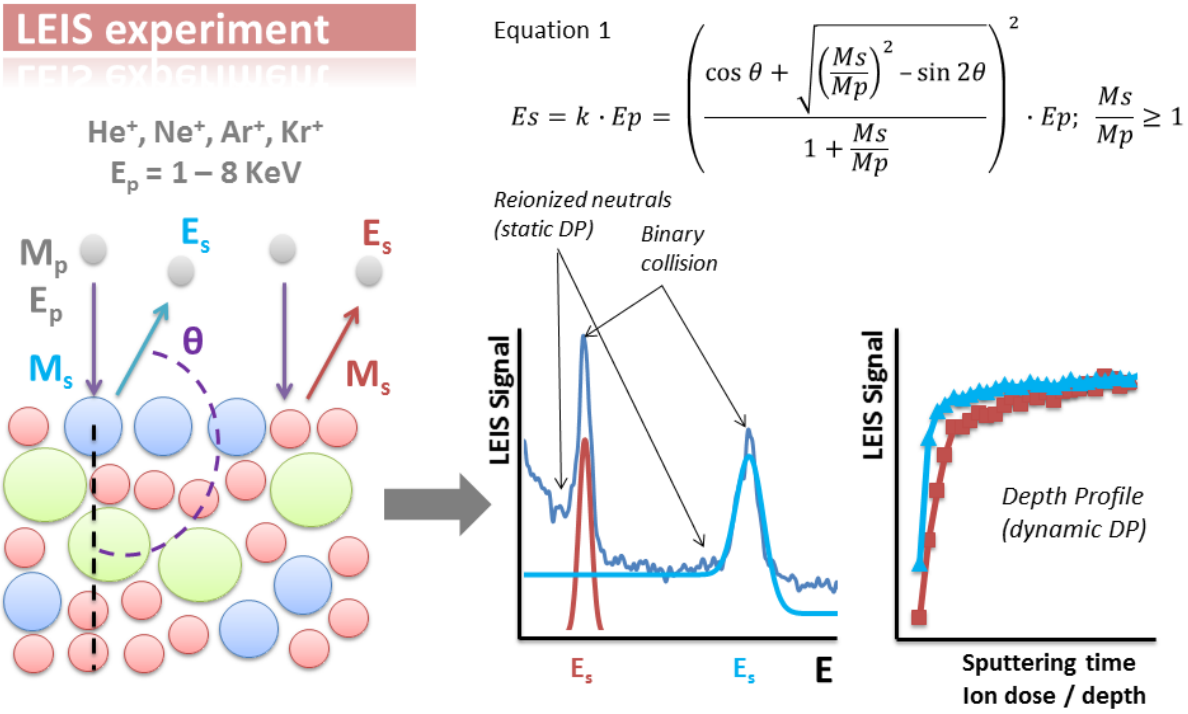

Equation 1

$$Es = k \cdot Ep = \left(\frac{\cos\theta + \sqrt{\left(\frac{Ms}{Mp}\right)^{2} - \sin 2\theta}}{1 + \frac{Ms}{Mp}}\right)^{2} \cdot Ep; \quad \frac{Ms}{Mp} \geq 1$$

Figure 5.3. Fundamentals of Low–Energy Ion Scattering (LEIS) surface analysis technique.

In a conventional LEIS experiment, a low energy beam of noble gas ions (typically He^+, Ne^+ or Ar^+ and, less frequently, Kr^+) in the range of 1–8 KeV is directed onto a sample surface under ultra–high vacuum (UHV) conditions. When these primary ions backscatter as a result of collisions with the surface atoms, they lose energy and this energy loss is a function of the masses of both the projectile ion and the analyte atom at the surface (Figure 5.3). Ions backscattered through an angle of 145° with respect to the incident direction are able to enter the double toroidal kinetic energy analyzer and can be detected by the position sensitive detector. The energy of the backscattered ions is then measured, and the change in kinetic energy between the initial energy and that of the backscattered ion is used to identify the analyte atom by mass. One of the main strengths of LEIS is its very high surface specificity, as primary ions penetrating deeper than the first atomic surface layer are very effectively neutralized by the atoms underneath, and hence, are unlikely to be detected since only ionic species can be detected in LEIS. Figure 5.3 shows the fundamental concepts of the experiment along with the governing equation of LEIS.[14a] The variables in this equation are the energy of the primary ion (E_P), the energy it has after scattering (E_S), the mass of the primary ion (M_P), the mass of the particle it scatters off of (M_S) and the angle (θ) through which the scattering takes place. A condition for Equation 1 shown in Figure 5.3 is that $M_S/M_P \geq 1$, that is, the surface atom from which scattering occurs must be heavier than the ion striking it. If this condition is not fulfilled (for instance, He^+ strikes a hydrogen atom), no backscattering takes place, only forward scattering, and no LEIS signal will be observed. Thus, LEIS can be used to detect all elements in the periodic table except for H and ^2He.

In a typical LEIS experiment E_P, M_P, θ, and E_S are known or defined by the apparatus, and thus, M_S can be determined. The LEIS equation can be derived entirely from classical physics using the principles of conservation of energy and momentum. In practice, however, there are inelastic contributions to the scattering process, which shift the measured scattering energies to slightly lower energies than those calculated using Equation 1 and give the peaks in LEIS spectra a Gaussian shape,[14d] which are directly related to the surface coverage of a certain element/isotope at the sample. LEIS identifies elements by their masses, and successful identification of an element depends on optimizing the analysis parameters so that one nuclear mass can be distinguished from another similar mass based on the energies of their backscattered particles (i.e. mass resolution).[14c,d] The most important parameters that the user can control to optimize mass resolution in LEIS are the type and energy of the ions used to probe a surface. Indeed, different noble gas ions show different sensitivities to surface atoms with different masses. For example, He^+ projectiles are very discriminating to the lighter elements up to M_s = 40 u, while Ne^+ shows a higher resolution power for elements with M_s = 41–105 u. In contrast, Ar^+ is typically used for heavy analytes in the range M_s =106–199 u while Kr^+ is best employed for the heaviest of elements for M_s > 200 u. Thus, in general, heavier atoms are generally better analyzed by heavier probe ions, a fact that can be deduced directly from Equation 1 in Figure 5.3.

LEIS also provides isotopic information with detection limits in the order of the few % of a monolayer. However, as the LEIS instrument offers maximum surface sensitivity, chemical sample cleaning prior to the analysis is considered imperative in most cases in order to eliminate ambient moisture that could potentially affect the LEIS signal from the target surface. In these cases, atomic oxygen provides the means to remove organic contaminants from the surface without causing structural damage. The oxygen atoms are extremely reactive and will form gaseous molecules like CO, NO or H_2O, which are then pumped off, and thus, most of LEIS instruments are equipped with an atomic oxygen generator (Figure 5.4). The ion scattering processes exploited in LEIS take place on a very short time scale, which leads to the target atoms behaving like free particles. This so–called matrix independence provides the opportunity to obtain absolute quantification values for the elemental composition of the outermost atomic layer of the sample, undisturbed by the chemical environment and the sample roughness, as opposed to SIMS. There are several methods to perform such quantification (using reference samples and/or tabulated sensitivity factors, two component systems, relative quantification, and converting LEIS signals to atomic concentrations), but all of them are based on the analysis of the peak areas of the relevant surface peaks in the LEIS spectrum. These values are directly proportional to the surface coverage of the corresponding element. As the proportionality factors depend on the instrument settings and may vary somewhat from instrument to instrument, reference samples are often used to compare samples to standardized materials with well–known surface compositions. Therefore, quantitative LEIS analysis can be considered to be straightforward in planar oxidic surfaces.[17] However, it should be noted that a good quantification requires the samples to be very flat.

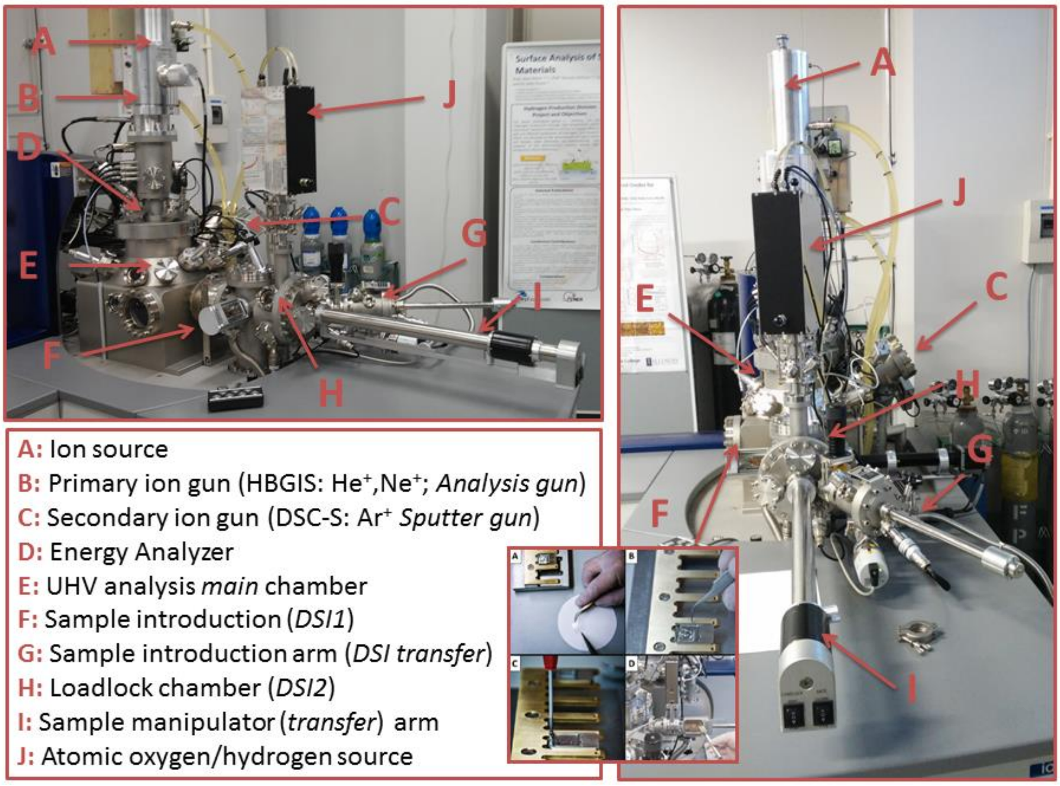

Figure 5.4. LEIS instrument Qtac[100] with locations of key components labelled (I[2]CNER, Kyushu University, Japan). HBGIS = High Brightness Gas Ion Source; DSC–S= Dual Source Column–Sputtering; UHV = Ultra–High Vacuum.

Along with its mono–atomic layer resolution, a LEIS spectrum contains inherently depth profile information about the outer *ca.* 5–10 nm of a material. This is typically referred to as a static depth profile because this information can be obtained without sputtering, which implies that less than 1% of the surface is bombarded during the analysis.[18] Usually the ion fluence can be kept below this “static limit”, which varies depending on the primary ion (He^+, Ne^+,…), and therefore avoids or at least substantially reduces any perturbation in the original composition of the sample material (static LEIS is considered non–destructive). While signals from the sample surface in LEIS result in Gaussian peaks at well–defined energies, the in–depth signal in LEIS appears as a tail on the low–energy side of the surface peak originated from the reionized neutrals (Figure 5.3). As the noble gas ions from the probe beam penetrate the sample surface, they are immediately neutralized due to their high ionization energy. However, they continue to travel through the sample, losing energy from small angle scattering events with atoms below the surface of the sample. At some depth below the surface, backscattering events may occur, sending the noble gas atoms towards the surface while continuing to lose energy as they return to the surface. When these neutral noble gas atoms leave a solid, a fraction of them are reionized and thus, these reionized neutrals can be detected and provide the static depth profile information mentioned above. However, it must be noted that this reionization process depends heavily on the surface chemistry of the sample.[14d]

In contrast, by simultaneous sample erosion using a second, high intensity ion beam (dual beam mode), the composition of the material can be determined as a function of depth within a range of some 100 nm (Figure 5.3). This is known as dynamic depth profile and it is destructive, as opposed to the static regime commented above, since a series of partial spectra are acquired between successive sputter cycles. Each sputter cycle will erode a significant depth of the sample, exposing usually a "fresh" surface that is not influenced by the primary beam bombardment of the previous analysis cycle. This can be assured by sputtering at least 1 or 2 monolayers of material with the low energy sputter beam. Although this will obviously modify the surface, it will at least return it to conditions dominated by low energy sputtering. After the sputtering cycle however, the acquisition dose of the partial spectrum should remain below the static limit to ensure that the primary beam does not change the surface composition while the partial spectrum is being acquired. When doing depth profile experiments, it is important that the two ion beams for analysis and sputtering are aligned relative to each other and that the size of the sputter crater is a little larger than that of the analysis area. These conditions ensure that the secondary ions being counted are being emitted from the flat center of the sputter crater and therefore, crater edge effects can be avoided. In addition to both static and dynamic depth profiling, LEIS also provides 2D imaging of the target surface. However, as the LEIS intensities are often low, the statistics in these images usually are not sufficient to show bright images without applying a destructive dose to the analyzed sample area. Nevertheless, these images could contain valuable lateral information which may be extracted by defining regions of interest and reconstructing the spectra from these areas to compare the elemental surface composition of different lateral phases.

It is important to note that the surface of non–conducting samples will charge during the course of bombardment with positive ions, generating charged secondary particles, which are mainly secondary electrons. This fact leads to the surface acquiring an overall positive charge. Consequently, the spread in scattered ion energy is also increased compared to a conductive sample, shifting and compressing the LEIS spectra towards higher energies. The charge compensation showers the sample with low energy electrons to negate these charging effects, resulting in a surface potential close to 0 V. However, as the current density of the sputter ion beam is typically much higher than that of the analysis beam, it may be advisable to include a pause after each sputter phase to allow some time for compensating the remaining charge from the sputter phase before the acquisition of the next partial spectrum starts.

In summary, LEIS is an exquisitely surface sensitive analytical tool that provides the elemental composition of the outermost atomic layer of a surface. This capability is truly extraordinary and unique. LEIS consists of the bombardment of surfaces with low energy noble gas ions, the scattering of which is quite well described classically. Accordingly, different noble gas ions show different sensitivities to surface atoms with different masses, and heavier atoms are generally better analyzed by heavier probe ions. LEIS also provides depth profile information about the upper *ca.* 5–10 nm of a material without the need of sputtering. As a result, LEIS occupies a space that neither XPS nor ToF–SIMS does.

5.1.3 Time–of–Flight Secondary Ion Mass Spectrometry (ToF–SIMS)

Mass spectrometry (MS) is one of the most widely used chemical analysis techniques. Its prominence originates from the fact that, in many of its embodiments, MS provides low detection limits, high resolution, a large dynamic range, high speed, as well as both molecular and elemental information of all elements and isotopes in the periodic table. As SIMS is the solid–state analogue of MS, it has found extensive use in many highly diverse areas within both industry and academia (material, earth–, bio– and environmental sciences as well as cosmology), in which the distribution of isotopes, elements, and/or molecules on or within a specific region of the substrate is of interest.[19] SIMS has experienced an extensive growth and sophistication within many divergent fields over the past few decades. With its commercialization starting in the late 1960s, numerous instrument types and geometries exist nowadays. Among them, SIMS instruments equipped with Time–of–Flight analyzers (ToF–SIMS) are considered one of the most sensitive surface analysis techniques because they provide essentially parallel detection across the entire mass range, in such a way that a nearly complete mass spectrum is collected from every pulse of primary ions.[20] This feature is extremely important for surface analysis because surfaces have so little material associated with them.[21] As a result, ToF–SIMS allows the characterization of submicron scale regions within planar solids to high sensitivity and dynamic range with detection limits in the range of ppm–ppb levels along with spatial resolutions in the order of the sub–micron (lateral) and nanometer (depth) scales.[19]

In a conventional ToF–SIMS measurement, a sample surface is bombarded with a pulsed energetic beam of primary ions (typically Cs^+, Ga^+, In^+, Au^+, Bi_n^{q+} clusters where n = 1–7, q = 1–3; or C_{60}^+) in the range of 0.1–50 KeV under ultra–high vacuum (UHV) conditions. The pulsing is necessary so that all of the secondary ions have, at least nominally, the same starting time. Upon impact, the primary ion generates an intense but short–lived collision cascade resulting in the reallocation of many atoms of the matrix.[22] Some of the atoms near the surface receive enough energy to leave it; and thus, they are sputtered from the sample (Figure 5.5). Usually, a rather small fraction of these sputtered particles are ionized. These secondary ions are then accelerated to energies of several keV into a flight tube with a pulsed electric field, before being allowed to drift though a field–free region and separated according to their speed using a time–of–flight mass analyzer. The latter operates on the assumption that all incoming ions have the same kinetic energy per unit charge, but that the velocities of the ions differ depending on their masses. Since different velocities result in different flight times, the latter can be measured and used to calculate the masses of the secondary ions.[19]

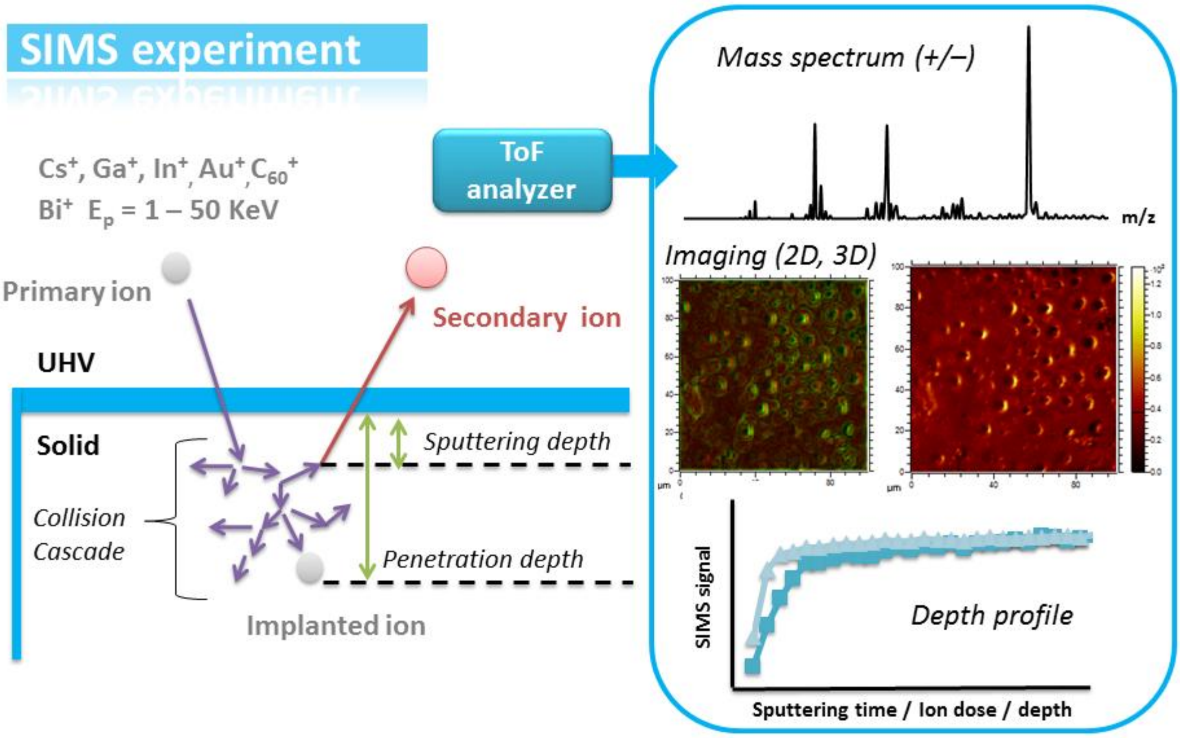

Figure 5.5. Fundamentals of Secondary Ion Mass Spectrometry (SIMS) technique. UHV = Ultra–High Vaccum.

A ToF–SIMS instrument analyzes a sample to a depth of several atomic layers, and is generally more surface sensitive than X–Ray Photoelectron Spectroscopy (XPS), which is the most widely used surface analysis tool.[23] Other noteworthy features of ToF–SIMS are its parts–per–million to parts–per–billion detection limits, its fast data acquisition time (seconds to minutes per sample), and its high spatial resolutions in the order of the sub–micron (lateral) and nanometre (depth) scales. In ToF–SIMS, sample cleaning is very important, but atomic oxygen cleaning is neither common nor necessary as it is in LEIS. Compared to LEIS, ToF–SIMS with its greater sampling depth is much less affected by a small amount of surface hydrocarbons. On top of that, since it provides molecular information, ToF–SIMS is a powerful tool for identifying surface contamination, e.g., polydimethylsiloxane (PDMS),[24] plasticizers,[25] etc... Of course atomic oxygen is ideal for cleaning most metal oxide samples (often analyzed by LEIS), but it would be damaging to most organic materials (often analyzed by ToF–SIMS). Similar to LEIS, the application of SIMS can be subdivided into two modes, those being static and dynamic SIMS.

In surface spectroscopy or static SIMS mode,[19] elemental as well as molecular information about the chemical composition of the surface can be obtained with high sensitivity. In close analogy to the Static LEIS, the former consists on irradiating the sample surface with a very low dose of primary ions so that each primary ion arriving at the sample surface should impact on a previously undamaged site. This can be achieved if the primary ion dose is kept below the static limit, and thus, the contribution of already damaged surface areas can be neglected (static SIMS is considered non–destructive, just like static LEIS). Since the information depth in SIMS is essentially a few monolayers, this mode of analysis yields near atomic resolution on the surface monolayer. The information is usually shown in the form of mass spectra or 2D images. The mass spectrometric imaging can be achieved by focusing and rastering the ion beam over a defined surface area where the secondary ion intensity for a given mass–to–charge ratio (m/z) can be mapped with high lateral resolution. At each pixel of the raster, a full mass spectrum is recorded that can be assigned to a certain position on the sample surface. By selecting certain mass peaks out of the spectra, 2D surface images can be generated for the corresponding species. The low dose of primary ions used in static mode greatly minimizes the damage done to the sample surface at the cost of a decreased sensitivity, compared to that of dynamic SIMS.[19] In addition, since there are not significant sputtering processes in static SIMS, depth profiles as well as 3D imaging are not permitted. The primary parameters of interest in Static SIMS are: a) sensitivity and best possible detection limits; b) high mass resolution; and c) spatial resolution. Unfortunately, optimizing one of the above generally minimizes one or more of the others.

In dynamic SIMS,[19] the primary beam probes the constituents present at the surface and below through the removal or sputtering of many layers per analytical cycle and hence, this mode is destructive. Just like in dynamic LEIS, the sputtering is usually performed by a secondary ion gun while the analysis of the secondary ions is done by the primary gun (dual beam mode), although the primary beam can act as analysis and sputter beam simultaneously (single beam mode). As sputtering removes atoms/molecules present at the outer surface of a solid and damage is of minor concern (opposite to Static SIMS), measurement of the secondary ion signal as a function of sputtering time or ion dose provides the depth distribution of the signal measured, that is, a depth profile. Similar to LEIS, to record a depth profile, the ion beam is scanned over the surface, usually in a square digital pattern, ensuring that both the primary and sputter beam overlap exceeds 50% to avoid potential crater edge effects. This way, depth profiles ranging from several nm up to 10 µm can then be collected. Under ideal conditions, the depth resolution can surpass 1 nm. In addition, 3D images can be also constructed in dynamic mode by overlaying 2D images collected as a function of sputtering time in the same way a depth profile is constructed, which provides additional useful information. The primary parameters of concern in dynamic SIMS are: a) sensitivity along with the best possible detection limits and dynamic range, b) high mass resolution and c) depth resolution. Just like in static SIMS, optimizing one of the above generally comes at the cost of one or more of the others. There are, however, a number of modes under which a SIMS instrument can be operated such as high current bunched mode (HCBM), burst alignment mode (BAM) or collimated mode (CM), with each optimized for a particular type of analysis, whether pertaining to the collection of mass spectra, depth profiles, or images in two or three dimensions. In close analogy to LEIS, surfaces of insulating targets are easily charged up by primary ions, which badly influence the TOF–SIMS measurement. To avoid this, the low–energy electron floodgun (0–21 eV) must be used to compensate the superficial charge of the sample.

Despite the powerful attributes of the technique, ToF–SIMS has unfortunately some important weaknesses.[20] First, sputtering damages surfaces, although in its static mode the degree of damage is small enough that ToF–SIMS can be considered to be non–destructive. In depth profiling, damage from the sputter beam can cause some degree of mixing of atomic layers, which degrades mass resolution. Surface bombardment with ions can also break chemical bonds, causing a loss of molecular information. The choice of sputter beam and sputter conditions can mitigate these effects though. Perhaps the biggest drawback of ToF–SIMS is that it suffers from a strong matrix effect as opposed to LEIS, the effects of which are difficult to account for. That is, the signals from certain species can be enhanced or suppressed depending on what other species are present around them which makes quantifying the recorded signal/s quite difficult. As a result, quantification requires that matrix–matched reference materials be analyzed in concert with the sample of interest which can be quite tedious. Hence, ToF–SIMS is often, at best, semi–quantitative.[20] Figure 5.6 shows the ToF–SIMS instrument with the key components labelled.

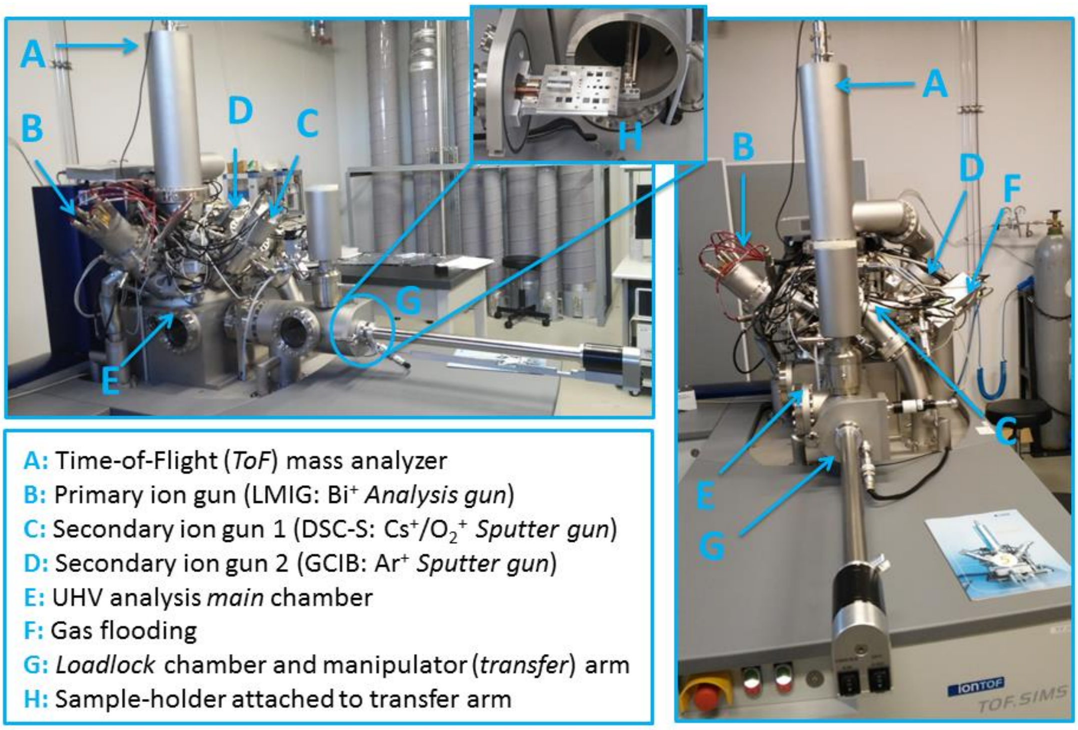

Figure 5.6. ToF–SIMS instrument ION.TOF[5] with locations of key components labelled (I^{2}CNER, Kyushu University, Japan). LMIG = Liquid Metal Ion Gun; DSC–S = Dual Source Column–Sputtering; GCIB = Gas Cluster Ion Beam; UHV = Ultra–High Vacuum.

In summary, ToF SIMS is based on the mass spectrometric detection of the secondary ions emitted from the surface as a consequence of ion bombardment, providing information about the elemental and molecular compositions within two or three atomic layers of the immediate surface. ToF–SIMS is one of the most sensitive surface analysis techniques with limits of detection in the range of ppm–ppb levels with spatial resolutions in the order of the sub–micron (lateral) and nanometre (depth) scales. The main drawback is that it is considered a semiquantitative technique due to a strong matrix effect. Nevertheless, ToF–SIMS along with LEIS, is considered one of the most powerful techniques in surface chemistry due to their analytical performance to provide powerful, comprehensive surface and material characterization when used together (Table 5.1).

Table 5.1. Summary and comparison of the analytical performance of ToF–SIMS and LEIS techniques.

	ToF–SIMS	LEIS
Samples	UHV compatible, flat surfaces	Rough and powdered samples
Mass range	Up to 14 000 u	Z > 3 (for $^3He^+$ scattering)
Chemical information	Elemental and molecular	Elemental
Oxidation state information	Through molecular fragments	None
Primary ions	LMIG: Bi^+, Bi_3^+, Bi_3^{2+}	Noble gas ions (He^+, Ne^+, Ar^+, Kr^+)
Primary ion energy	30 KeV	1–8 KeV
Static DP	No	Inherent, *ca*. 10 nm
Dynamic DP	With sputter gun	With sputter gun
Matrix effect	Strong	Essentially none
Quantitative results	Relatively poor	Excellent
Resolution	unit mass resolution	–
Lateral resolution	Micron to submicron	*ca.* 10 microns
Information depth	2–3 atomic Layers	1st atomic layer
Limit of detection	ppm–ppb	Lighter elements: a few % of a ML Heavier elements: 0.1 –1 %

DP = Depth Profiling; LMIG: liquid metal ion gun; ML = monolayer.

5.1.4 Summary

In this final chapter, the first steps within a new research line established within our group in the *Departamento de Química Inorgánica* together with *Departamento de Química–Física* at the *Facultad de Ciencia y Tecnología* at UPV/EHU have been carried out, which consist in the incorporation of POM clusters into tailored polymeric surfaces for diverse potential applications. In this preliminary work, “breath figures” surfaces were made of polystyrene–*b*–poly(acrylic acid)/polystyrene (PS–b–PAA/PS) blends (**BF**) whereas their functionalization was performed by interfacial migration of the amphiphilic block copolymer toward the interface to expose the anchoring/coordination sites. These carboxylic acid functional groups contained within the PAA blocks were then used to anchor **1–CuV10**, **1–CuV1**, **1–CuMo5** and **1–CuW7** hybrid POMs by immersing the films into aqueous solutions of the *in situ* formed hybrid clusters. Alternatively, during reactivity tests between poly(acrylic acid) (PAA) and the selected POMs, various hybrid gel composites were also synthetized by direct mixing of the carboxylic block PAA and solutions containing the hybrid POMs, from which different hybrid surfaces were prepared (**HS** samples). The superficial characterization of these organic–inorganic composites was carried out by means of ion beam based techniques, such as low–energy ion scattering (LEIS, **HS** samples) and time–of–flight secondary ion mass spectrometry (ToF–SIMS, **BF** samples).

5.2 EXPERIMENTAL SECTION

5.2.1 Materials and Methods

Materials and Methods. Styrene (St) (Aldrich, 99%) and t–butyl acrylate (tBA) (Aldrich, 98%) were distilled under reduced pressure over calcium hydride prior to their use. Polystyrene (PS) [M_w = 300000 g mol^{-1}, polydispersity index (PDI) = 1.80] and poly(acrylic acid) (PAA) (M_w = 450000 g mol^{-1}) were purchased from Polysciences (USA). Copper (I) bromide (CuBr) (Aldrich, 98%), N,N,N',N'',N'',–pentamethyldiethylenetriamine (PMDETA) (Aldrich, 99%), ethyl–2–bromoisobutyrate (EtBr) (Aldrich, 98%) and tetrahydrofuran (THF) (HPLC grade) were purchased from Scharlab (Spain) and used without further purification. All other chemicals were obtained from commercial sources and used without further purification as well. The polymer solutions were cast in a round glass coverslips of 20 mm diameter purchased from Marienfeld (Germany). Water used was MilliQ grade.

^{1}H–Nuclear Magnetic Resonance (1H–NMR). ^{1}H–NMR spectra of the synthetized copolymers were recorded at room temperature on a Bruker Avance 400 MHz spectrometer, using the residual proton resonance of the deuterated solvent as internal standard.

Size Exclusion Chromatography (SEC). Average molar masses and molar mass distributions of the polymers were determined by SEC in DMF in a Waters equipment using two Waters columns. Calibration was obtained using narrowly–distributed polystyrene standards and DMF as the mobile phase at a flow rate of 0.5 mL min^{-1}.

Secondary Electron Microscopy (SEM). The BF samples were coated with gold, prior to scanning, using a Fine coat ion sputter JFC–1100. Scanning electron microscopy (SEM) micrographs were taken using a Hitachi S–4800 (150 s, 20 mA, 5.0 kV, zoom at 2000).

Optical microscope imaging. Optical images of **HS** and **BF** samples were taken using a LEXT 3D measuring laser microscope OLS4000 Olympus in scanning XYZ mode using a MPLAPON LEXT20 lens to check the relative roughness of the samples.

Low Energy Ion Scattering (LEIS). Superficial characterization of **HS** samples was carried out by LEIS measurements. The LEIS instrument (Qtac^{100}) is fitted with an electron ionization source to produce a noble gas beam (e.g.: He^+, Ne^+, and Ar^+). The primary ion beam is incident normal to the surface at a typical energy between 1 to 8 KeV. The backscattered primary ions are analysed using a double toroidal analyser (DTA) which allows parallel energy detection at a scattering angle of 145° over all azimuthal angles, providing improved detection limits and mass resolution compared to conventional instruments.[18a] Although ion fluence during the LEIS analysis is always kept below the static limit, some sputtering of adsorbed species or light atoms on the surface might be produced and then detected by the DTA. These sputtered species give rise to an undesirable exponential background signal at low scattering energies, which hampers the detection of low Z atoms on the surface. Depth profiling was performed using a 1 KeV Ar^+ sputtering beam.

Time of Flight–Secondary Ion Mass Spectrometry (ToF–SIMS). Superficial characterization of **BF** samples was carried out by Tof–SIMS measurements. The ToF–SIMS instrument (TOF.SIMS[5]) is fitted with a 30 keV Bi^+ analytical beam and several sputter sources producing O_2^+, Ar^+ and Cs^+ beams, which can be operated in an energy range between 0.2–2.0 KeV. Both analytical and sputtering beams are incident at 45° to the sample surface, and are alternated during depth profiling analysis in a dual beam mode. The sputtered secondary ions are extracted during the analytical beam pulse and introduced into the ToF analyzer by applying an extraction voltage of 2 KeV. Since the analytical pulse is very short, the ion fluence is kept below the static limit (less than 1% of the surface is sputtered), minimizing surface damage during the analysis. In order to neutralize any charge that might build–up on the surface during the ion bombardment of insulating samples, a low energy (20 eV) electron beam floods the surface during the sputtering cycle. The analysis is performed in a small area at the center of the sputtered crater in order to avoid crater edge effects during depth profiling.

5.2.2 Synthetic Procedure

Synthesis of the Copolymer Polystyrene–b–poly(acrylic acid) (PS_{53}–*b*–PAA_{25}). The synthesis of the diblock copolymer PS–b–PAA have been prepared by Atom Transfer Radical Polymerization (ATRP) in three steps, following previously reported [26] procedures briefly described below:

Synthesis of the Polystyrene (PS–Br) Macroinititator by ATRP. The polystyrene was synthesized by atom transfer radical polymerization (ATRP). The polymerization was performed in a Schlenk flask. ATRP was carried out using the following stoichiometry: [M]/[I]/[CuBr]/[L] = 50:1:1:1, where M = styrene, I = initiator (ethyl–2–bromoisobutyrate), and L = ligand (N,N,N',N'',N''–pentamethyldiethtylentriamine, PMDETA). The reactants were added under N_2. The reaction mixture was then degassed by three freeze–pump–thaw cycles and placed in a thermostated oil bath at 65 °C. When the polymerization was over, the Schlenk flask was introduced in a Dewar container filled with liquid N_2 to freeze the reaction mixture. The mixture was then cooled down to room temperature. The polymeric reaction was diluted in tetrahydrofurane (THF) and passed through a neutral alumina column to remove the copper salt. After that, the solvent was removed by evaporation and the polymers were precipitated in ethanol, filtered, washed and dried under vacuum. Average molar masses and polydispersity index of the polymer were 6620 $g.mol^{-1}$ and 1.04, respectively.

Synthesis of PS–b–PtBA by ATRP. The copolymer was synthesized by ATRP using the same procedure above. In this case, the stoichiometry was [M]/[I]/[CuBr]/[L] = 100:1:1:1, where M = *t*–butyl acrylate, I = macroinitiator PS–Br and L = PMDETA. The PS–Br macroinitiator was dissolved in degassed acetone (5 mL) and added to the mixture with the other reagents. Acetone enhanced the solubility of the CuBr/PMDETA complex. The reaction was carried out at 65 °C. Average molar masses and polydispersity index of the copolymer were 7757 g mol^{-1} and 1.04, respectively. The composition of the block copolymer was determined by ^1H–NMR to be PS_{53}–b–PAA_{25}.

Hydrolysis of the PtBA Block in the PS–b–PAA Copolymer. The copolymers were first dissolved in CH_2Cl_2. Trifluoroacetic acid (TFA) was then added (10 equivalents to *t*–butyl ester units), and the mixture was stirred at room temperature for 3 days. The unprotected polymers precipitated in the reaction media and were filtered, washed with CH_2Cl_2, and finally dried under vacuum.

Preparation of Breath Figure surfaces (BF). Polymer solutions were prepared by dissolving solid commercial PS and the synthetized PS_{53}–b–PAA_{25} copolymer in THF. The total polymer/copolymer concentrations used in this study was 50 mg mL^{-1}. The blend employed contained 10% of PS_{53}–b–PAA_{25} diblock copolymer and 90% w of high molecular weight linear PS. The films were prepared from these solutions by casting onto glass wafers under controlled humidity inside of a closed chamber. The relative humidity (RH) was controlled by saturated salt solutions of KCl and KNO_3 in water to obtain 80 and 90% RH, respectively.

Immobilization of Hybrid POMs into the BFs. The immobilization of the POM components was carried out by immersion of the BF surfaces into the corresponding solutions. After 24 h, the BF were taken out of the solutions, washed with deionized water repeatedly and dried with Ar gas flow.

*Breath Figures Surface 0 (**BF0**).* A solution containing $CuSO_4.2H_2O$ (0.10 mmol) and cyclam ligand (0.10 mmol) in 12 mL of distilled water was prepared. The dark purple solution was stirred for 15 minutes at room temperature, after which a BF surface was immersed in it carefully. After 24 h, the BF was taken out of the solution, washed with deionized water repeatedly and dried with Ar gas flow. Compared to the initial blank BF surface, the resulting **BF0** showed a slight violet color across its surface.

*Hybrid Breath Figures Surface 1 (**BF1**).* Compound **1–CuV10** was generated in situ following the synthesis described in chapter 2. After filtering, the same procedure carried out for **BF0** was applied. Compared to the initial blank BF surface, the resulting **BF1** showed a slight orange color across its surface.

*Hybrid Breath Figures Surface 2 (**BF2**).* Compound **1–CuV** was generated in situ following the synthesis described in chapter 2. After filtering, the same procedure carried out for **BF0** was applied. Compared to the initial blank BF surface, the resulting **BF2** showed a pale purple color across its surface.

*Hybrid Breath Figures Surface 1 (**BF3**).* Compound **1–CuMo5** was generated in situ following the synthesis described in chapter 3. After filtering, the same procedure carried out for **BF0** was applied. Compared to the initial blank BF surface, the resulting **BF3** showed a slight violet color across its surface.

*Hybrid Breath Figures Surface 2 (**BF4**).* Compound **1–CuW7** was generated in situ following the synthesis described in chapter 4. After filtering, the same procedure carried out for **BF0** was applied. Compared to the initial blank BF surface, the resulting **BF4** showed a pale purple color across its surface.

Preparation of Hybrid Surfaces (HS). Hybrid POM/polymer surfaces were prepared by direct mix of both components in commercial methanol (MeOH). The solutions of the hybrid POMs were prepared according to the corresponding synthetic procedures described in previous chapters.

*Poly(acrylic acid) Surface (**PAA**).* 0.250 g of commercial PAA was dissolved in 30 mL of MeOH under heavy stirring at room temperature. After 30 minutes, the colorless solution was added dropwise to 200 mL of cold (ethyl)acetate, and the formation of a white gel was observed. The suspension was stirred at room temperature for another 30 minutes and then the solvent was removed. After the removal of the solvent, a white–colored gel was obtained.

*Hybrid Surface 0 (**HS0**).* 0.250 g of commercial PAA was dissolved in 30 mL of MeOH under heavy stirring at room temperature. Meanwhile, $CuSO_4.2H_2O$ (0.025 g, 0.10 mmol) and cyclam ligand (0.020 g, 0.10 mmol) were dissolved in 12 mL of distilled water at room temperature, which was added to the polymeric solution. After 30 minutes, the resulting purple solution was added dropwise to 200 mL of cold (ethyl)acetate, and the formation of a purple substance was observed. The suspension was stirred at room temperature for another 30 minutes and then the solvent was removed. A dark purple gel was obtained.

*Hybrid Surface 1 (**HS1**).* The preparation is similar to that of **HS0** except that a solution of **1–CuV10** was added instead of the *in situ* generated {Cu(cyclam)} complex. The resulting brownish solution was added dropwise to 200 mL of cold (ethyl)acetate, and the formation of a brownish solid was observed. After solvent removal, a brownish gel was obtained.

*Hybrid Surface 1 (**HS2**).* The preparation is similar to that of **HS1** except that a solution of **1–CuV** was added instead. After the removal of the solvent, a garnet–colored gel was obtained.

*Hybrid Surface 1 (**HS3**).* The preparation is similar to that of **HS1** except that a solution of **1–CuMo5** was added instead. After the removal of the solvent, a violet gel was obtained.

*Hybrid Surface 1 (**HS4**).* The preparation is similar to that of **HS1** except that a solution of **1–CuW7** was added instead. After the removal of the solvent, a dark purple gel was obtained.

5.3 RESULTS AND DISCUSSION

5.3.1 Preparation of the BF and HS Surface Samples

First, the reactivity between the selected {Cu(cyclam)}–containing POMs towards the carboxylic poly(acrylic acid) was assessed by direct mixing of both components in solution (MeOH). After the addition of the precipitant agent (ethylacetate) to the media, the formation of different colored gels was observed (Figure 5.2). The color of each gel closely resembles those shown by the corresponding POM crystals described in previous chapters. As mentioned in the introductory section, these gels were soaked in deionized water, press between two sample holders using a Nd magnet and then they were freezed with liquid N_2 in order to flatten the samples and make them susceptible to be characterized by surface analyses techniques. After cooling down to room temperature, the composite gels were detached from the glass yielding moderately flat surfaces, labelled as **HS0–4** samples.

In the breath figure method, the choice of the solvent is considered crucial for obtaining the desired honeycomb patterns. The solvent should fulfill some requirements such as high vapor pressure (i.e., low boiling point), low solubility in water, and higher density than water.[27] According to these requirements, carbon disulfide and chloroform are the most commonly used solvents. In this work, however, THF was selected as solvent, as it exhibits similar vapor pressure and boiling point, with the advantage of being miscible in water, a lower density, and a more ecofriendly nature than carbon disulfide.

Herein, PS/PS–*b*–PAA porous films were prepared by the static BF method (Figure 5.2). In order to determine the optimum parameters for the formation of such surfaces, solutions with total polymer concentrations of 50, 60, 70, 80, and 90 mg mL^{-1} of two different blends, namely 80/20% w and 90/10% w (PS/PS–*b*–PAA% w), were cast in a moist atmosphere with 80 and 90% relative humidity (RH) using THF as solvent (Figure 5.7). The regularity of the patterned films was evaluated by SEM in a qualitative manner attending to the homogeneity and distribution of the resulting cavities. As can be seen in Figure 5.7, the different conditions under which the BF surface were made resulted in drastically different outcomes in terms of the formation of the cavities, their sizes as well as the homogeneity of their distribution across the surface.

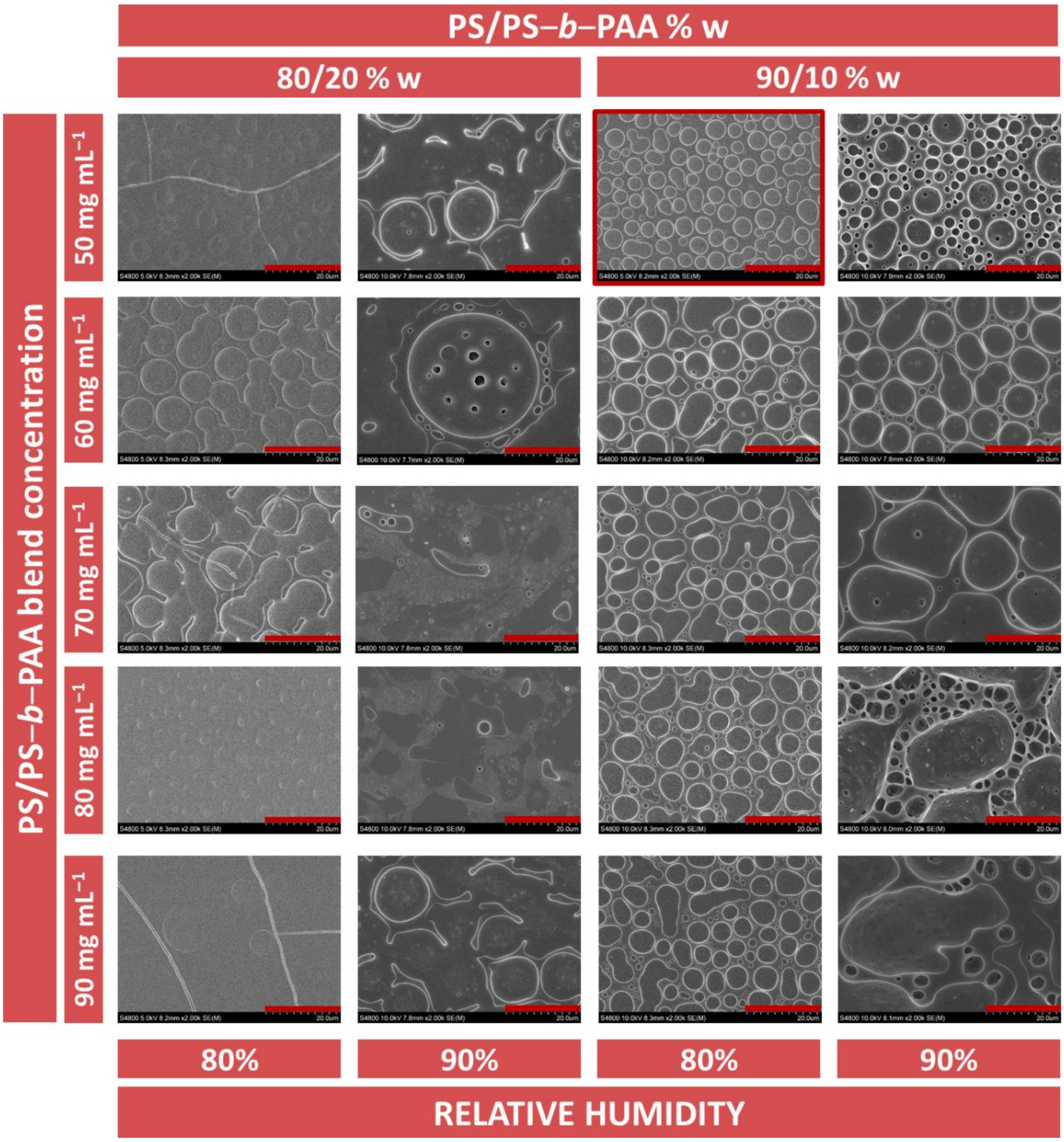

Figure 5.7. SEM images for BF with 50, 60, 70, 80, and 90 mg mL^{-1} in THF at 80% and 90% RH for the tested PS/PS–*b*–PAA blends (80/20 and 90/10% w), highlighting the optimum conditions for their preparation (scale bar = 20 μm).

At first glance, it is noticeable that when using the first polymeric blend 80/20% w in THF at both 80% and 90% RH, no breath figure patterns were formed whatsoever in any tested polymer concentrations. However, when the second polymer blend with a higher relative concentration of the PS was used, hole patterns were successfully formed at different concentrations in both tested relative RH media. In the case of 90% RH, the polymer concentration dramatically determined the regularity of the breath figure patterns, as higher concentration resulted in the formation of larger but more irregular cavities. The effect of the polymer concentration was less accused when the relative humidity of the medium was decreased to 80%, although higher concentration was also accompanied by more irregular distribution of the cavities to those observed in the less concentrated samples at 80% RH. In this sense, the most regular patterns were identified as those obtained for concentrations ranging from 50 to 80 mg mL^{-1}. Among them, the cavities formed in the less concentrated sample were significantly smaller compared to the others but at the same time, this concentration allowed the formation of the most ordered hole patterns in all tested conditions. In view of this results, we selected this polymeric blend PS/PS–*b*–PAA = 90/10% w with a [PS/PS–*b*–PAA]$_{total}$ = 50 mg mL^{-1} at 80% RH as the optimum to prepare the BF samples to carry out the incorporation of the polyoxometalates.

The optimized BF were then immersed on aqueous POM solutions for immobilization of the clusters via entrapment with the poly(acrylic acid) branches located primarily at the cavities as a result of the breath figure patterning method. As mentioned before, we selected hybrid POMs containing copper(II) complexes of cyclam because of the plasticity of the coordination sphere of the Cu^{II} centers so that the cyclam macrocyclic ligand could allow the axial positions of the coordination sphere of the metal to be readily available to coordinate to these carboxylic functions. The selected POM clusters **1–CuV, 1–CuV10**, **1–CuMo5** and **1–CuW7** were generated *in situ* following the corresponding synthetic procedures described in chapters 2, 3 and 4, respectively. The reference solution containing just the metalorganic complex Cu(cyclam) was prepared similarly (**BF0**). After 24 h of immersion of the BFs in these solutions at room temperature, the resulting hybrid surfaces **BF0**–**BF4** were gently washed with deionized water repeatedly to ensure the firm immobilization of the POMs. The characterization of the BF hybrid samples was made using Time of Flight–Secondary Ion Mass Spectrometry (ToF–SIMS) to analyze the sample compositions at the outermost layers and with material depth as well as the distribution of the hybrid POMs across the surface. In contrast, the **HS0**–**HS4** samples were superficially characterized by Low Energy Ion Scattering (LEIS) to analyze the elemental composition at the outermost atomic layer and the distribution of the elements when going deeper into the hybrid material. In addition, optical images were obtained with a 3D Laser microscope to check the roughness of both types **BF0**–**BF4** and **HS0**–**HS4** samples.

5.3.2 Superficial Characterization of HS samples

Low Energy Ion Scattering (LEIS)

The superficial characterization of **HS** samples was carried out by LEIS due to their higher roughness compared to the more flat BF samples. Light He$^+$ projectiles were used to detect light elements (C, O, etc.) whereas Ne$^+$ primary ions were employed to confirm the presence of the heavier atoms (Cu, V, Mo and W). After performing measurements in a virgin spot of the sample surface, cleaning treatment with activated O_2 was carried out and new measurements at the same spot were carried out to confirm if any compositional changes took place as a result of the cleaning process. Depth profiles were acquired using a 1 KeV Ar^+ sputter beam. In this preliminary work, we focused on using LEIS to confirm the presence of the POMs at the outermost atomic monolayer as well as the compositional distribution of the components when going deeper into the material in a qualitative manner.

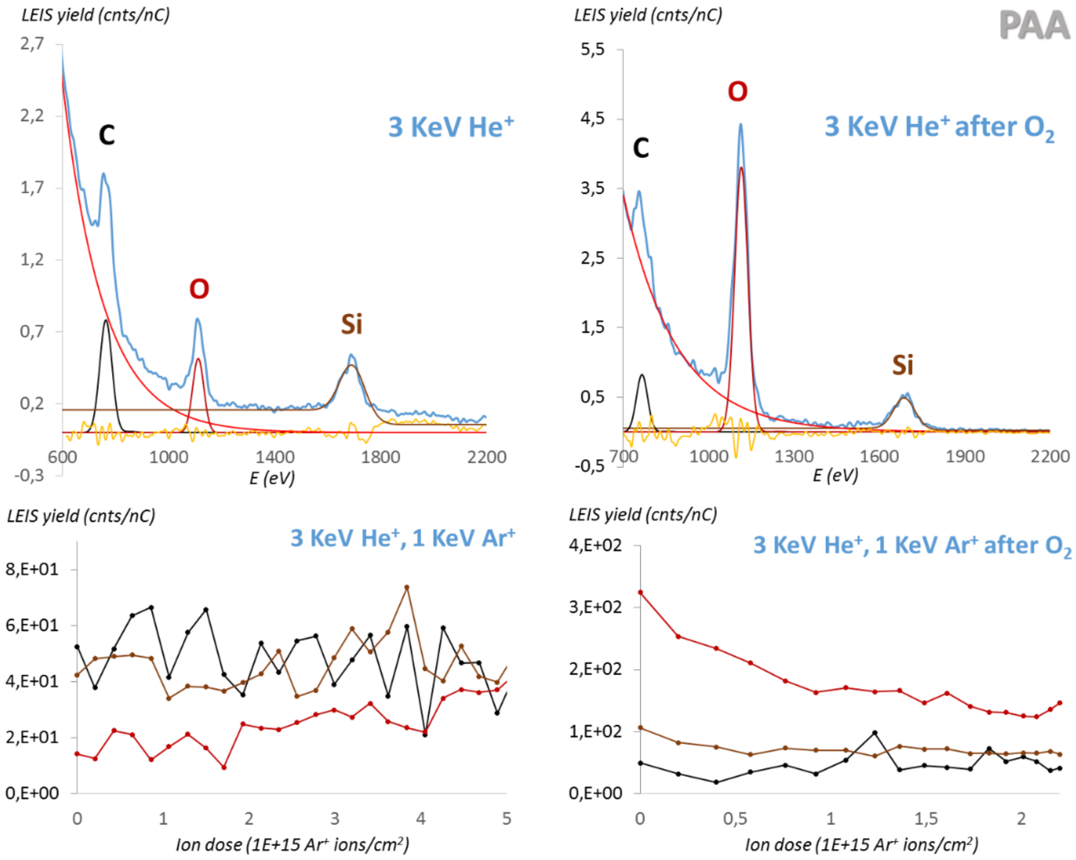

Figure 5.8. 3 KeV He^+ LEIS spectra of the **PAA** (top left) and after cleaning it with activated O_2 (top right) along with the corresponding depth profiles using 1 KeV Ar^+ sputtering (bottom).

The LEIS spectrum of the POM– and Cu(cyclam)–free blank surface made from commercial poly(acrylic)acid (**PAA**) shows the expected peaks for C and O (760 and 1110 eV, respectively) in its outermost layer. In addition, a strong peak belonging to Si at *ca.* 1690 eV was also detected (Figure 5.8). This fact led us to believe that the presence of silicon in this commercial sample must come from the preparation method, specifically when detaching the sample from the glass sample holders (Figure 5.2). As such, we should expect this signal to be present in all samples. A moderately low homogeneity when going deeper into the material was observed, as seen in the fluctuating trend for all the elements in the depth profile. A superficial cleaning treatment was performed with activated O_2 after which another spectra were measured, but no substantial changes in the LEIS signals were observed, except for the obvious increase in the O peak, as seen in both the corresponding LEIS spectrum and depth profile (Figure 5.8).

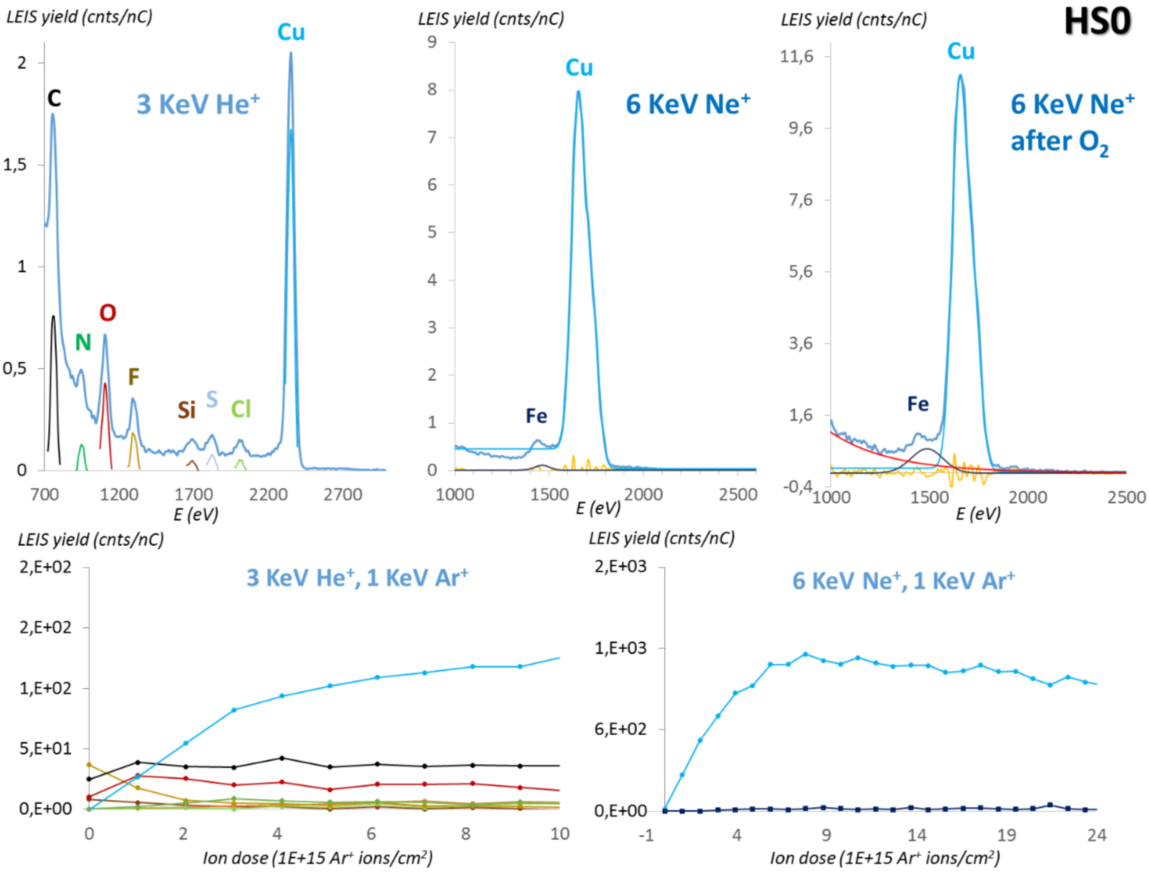

Figure 5.9. 3 KeV He⁺ and 6 KeV Ne⁺ LEIS spectra of the **HS0** (top left) and after cleaning it with activated O_2 (top right) along with the corresponding depth profiles using 1 KeV Ar⁺ sputtering (bottom).

The POM–free Cu(cyclam) reference **HS0** sample shows several peaks in the LEIS spectrum when using light He^+ ions as projectiles. Apart from the expected C, N and O peaks at ca. 765, 960 and 1115 eV respectively (as well as Si at around 1700 eV), the presence of F, S and Cl was also confirmed at the final layers of the material with peaks appearing at 1310, 1835 and 2030 eV, respectively (Figure 5.9). These impurities could be coming from elemental traces found in the $CuSO_4.2H_2O$ reactant. A very strong peak corresponding to Cu at 2355 eV could be detected with He^+, as well as when using heavier projectiles in the Ne^+ LEIS spectrum at *ca*. 1660 eV. In the latter, traces of Fe were also detected in the small peak at 1440 eV which should be coming from the impurities of the Cu(II) salt. All in all, the LEIS spectra indicate that the Cu(Cyclam) units are present at the outermost layer of **HS0** sample. However, while the depth profile shows a regular trend for all light elements a significant increase in the heavier Cu signal within the first sputtering cycles was observed, indicating that the presence of Cu(cyclam) units increases with depth. In close analogy to PAA surface, the O_2 cleaning of the surface did not result in any modifications of the spectrum as can be seen in (Figure 5.9).

Superficial analysis of **HS1** confirms the presence of C, O and Si elements just like previous samples with signals at approximately 770, 1110 and 1700 eV (Figure 5.10). Since the synthesis of **1–CuV10** was carried out in NaCl 1M medium, the Na and Cl peaks at 1510 and 2030 eV were also expected. In addition, He^+ projectiles allowed the detection of peaks at 2190 and 2360 eV associated to heavier V and Cu atoms respectively, which suggest the presence of the decavanadate species at the outermost layers. As expected, these two signals are more clearly defined in the Ne$^+$ LEIS spectrum as shown by the strong peaks associated to them at 1180 and 1655 eV, respectively. Regarding the homogeneity of the hybrid sample, C, O and Si seems to be evenly distributed with depth whereas a slightly more fluctuating trend was observed for the remaining elements (Na, Cl, V and Cu). The depth profile obtained when using Ne$^+$ primary ions shows an overall increase of the LEIS signal for both V and Cu peaks, suggesting that the presence of the hybrid decavanadate species is higher when going deeper into the hybrid material.

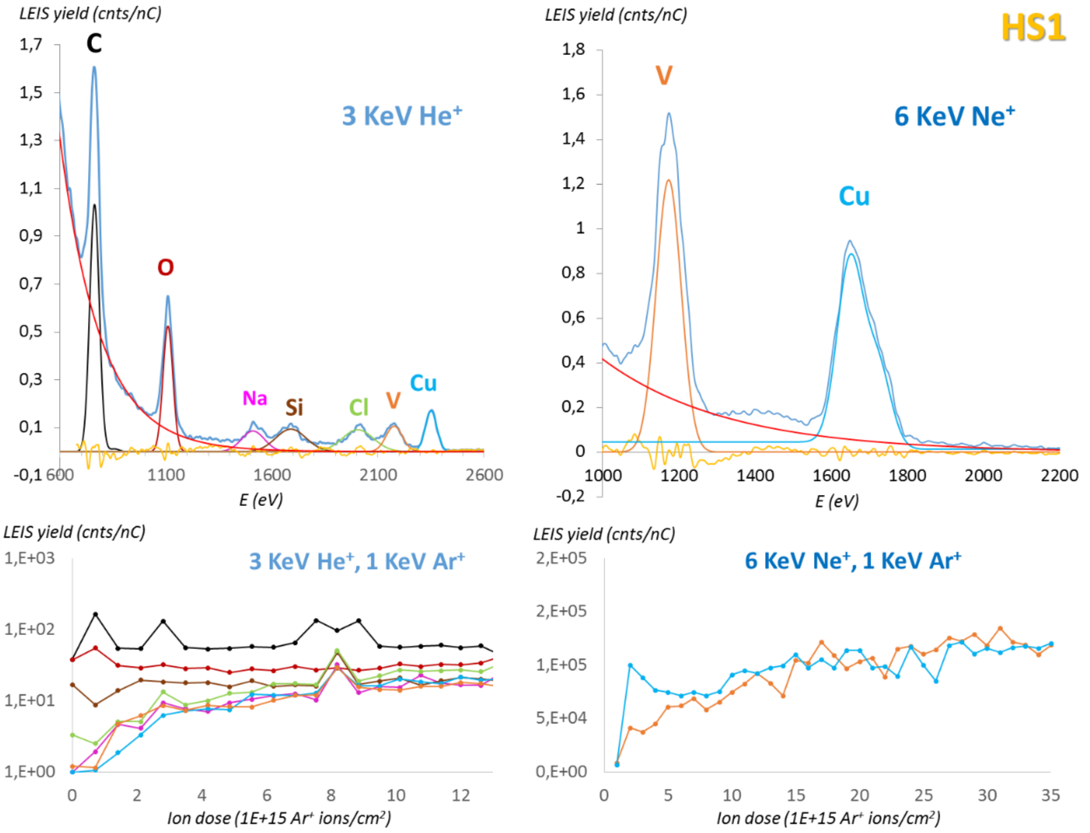

Figure 5.10. 3 KeV He$^+$ and 6 KeV Ne$^+$ LEIS spectra (top) of the **HS1** along with the corresponding depth profiles using 1 KeV Ar$^+$ sputtering (bottom).

The LEIS spectrum of **HS2** is highly reminiscent of that observed in the previous **HS1**, as the immobilized POMs belongs to the polyoxovanadate family for both surfaces, although some peaks corresponding to lighter elements (Na, Cl) as well as V are poorly defined in the He$^+$ LEIS spectrum (Figure 5.11), which appear as small signals at 1520, 2020 and 2180 eV, respectively. Measurement with heavier Ne$^+$ projectiles results in a spectrum with considerable noise although the signals for both V and Cu can be clearly identified at eV values of 1180 and 2365 eV approximately. The poor shape of the LEIS spectra can be explained attending to the roughness of the **HS2** sample, which was significantly more accused compared to the surface of **HS0** and **HS1** samples (Figure 5.12). Depth profiles of **HS2** indicate a relatively good homogeneity with material depth for the lighter elements although the presence of Cu increases with each sputtering cycle evidencing an inhomogeneous distribution. In contrast, the intensity of the peak associated to V remained nearly constant with depth suggesting a homogeneous distribution for the **1–CuV** polyoxovanadate. The fact that Cu signal increase while V remained constant could be indicative of free Cu(cyclam) moieties that are not grafted to the polyanion located within the material (Figure 5.11).

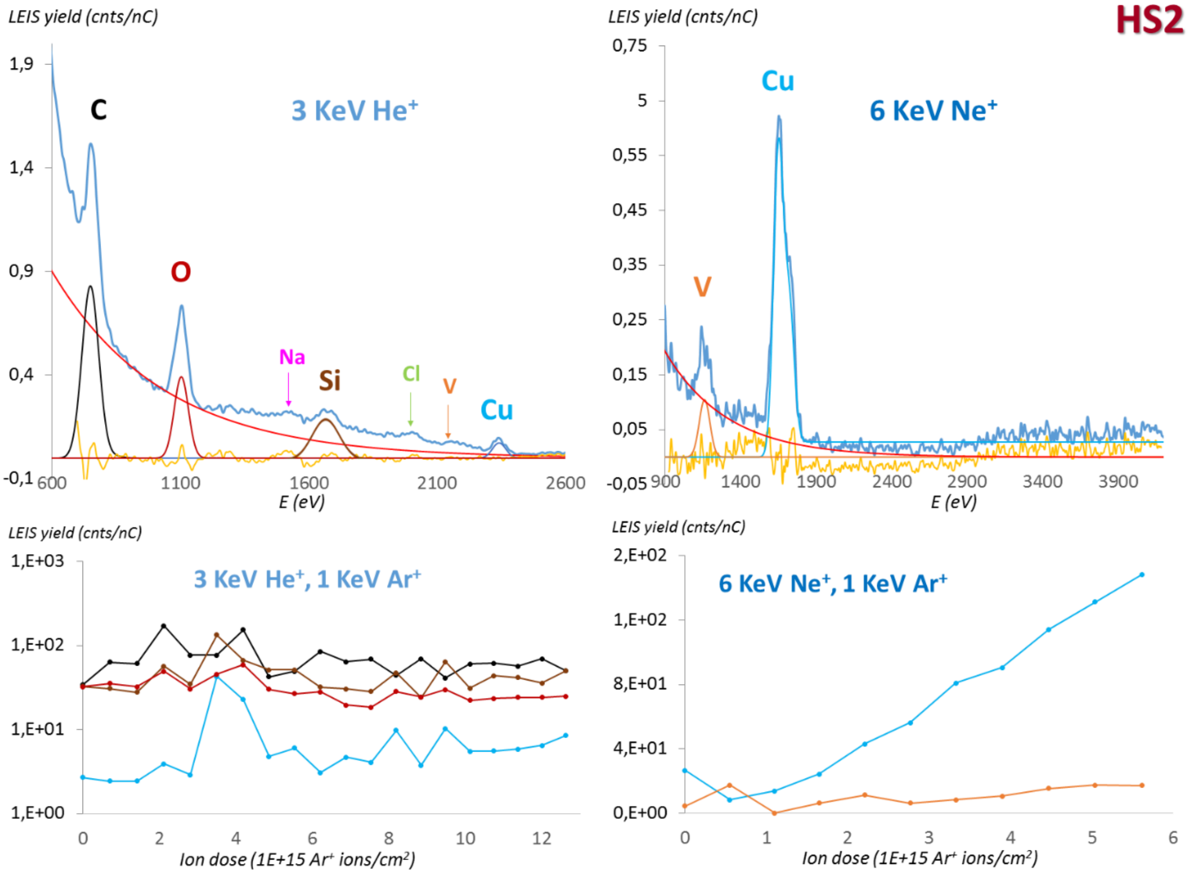

Figure 5.11. 3 KeV He$^+$ and 6 KeV Ne$^+$ LEIS spectra (top) of the **HS2** along with the corresponding depth profiles using 1 KeV Ar$^+$ sputtering (bottom).

Unfortunately, the roughness of the **HS3** sample was too accused to be appropriately measured and as a result, the obtained statistics were of very poor quality. Finally, LEIS measurements on **BF4** sample confirm the presence of C, O, Si with peaks at 770, 1110 and 1710 eV as well as Na and Cl as seen in the signals at 1510 and 2020 eV (Figure 5.13). Just like in **BF1**, the latter signals can be considered a direct consequence of the synthesis medium of the **1–CuW7** whereas the Si peak can be associated to the preparation method as mentioned previously. Small peaks at *ca.* 2360 and 2710 eV corresponding to Cu and W respectively could also be fitted in the LEIS He$^+$ 3 KeV spectrum although those can be seen more clearly with a heavier projectile for obvious reasons at around 1900 and 3900 eV, respectively. Much like the results observed in the previous samples, the cleaning treatment with activated O_2 did not result in any changes whatsoever. Depth profiles indicate a significant increase in the signals of all elements within the first few sputtering cycles evidencing a lack of homogeneity for the first monolayers of the material, in particular for Na and Cl as well as for the heavier elements Cu and W (Figure 5.13). The latter suggest that the presence of **1–CuW7** increases when going deeper into the hybrid material, similar to the results observed for **HS1**.

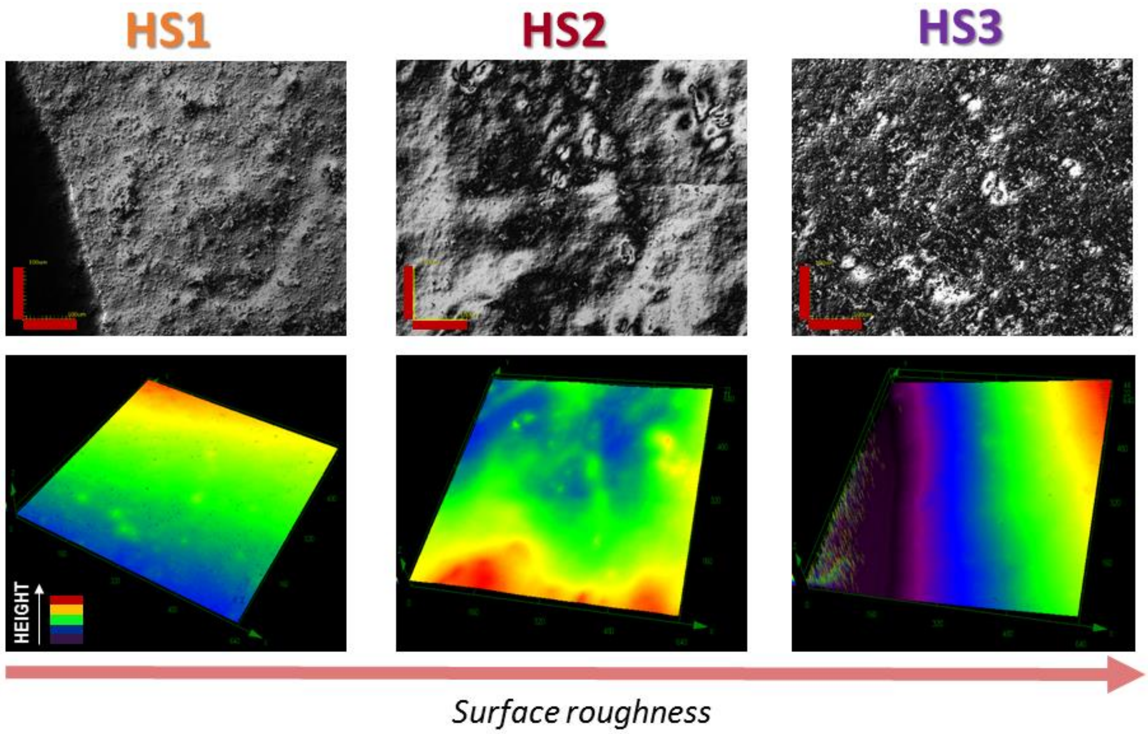

Figure 5.12. Optical microscope images showing the difference in roughness of the **HS1–HS3** (scale bar = 100 µm).

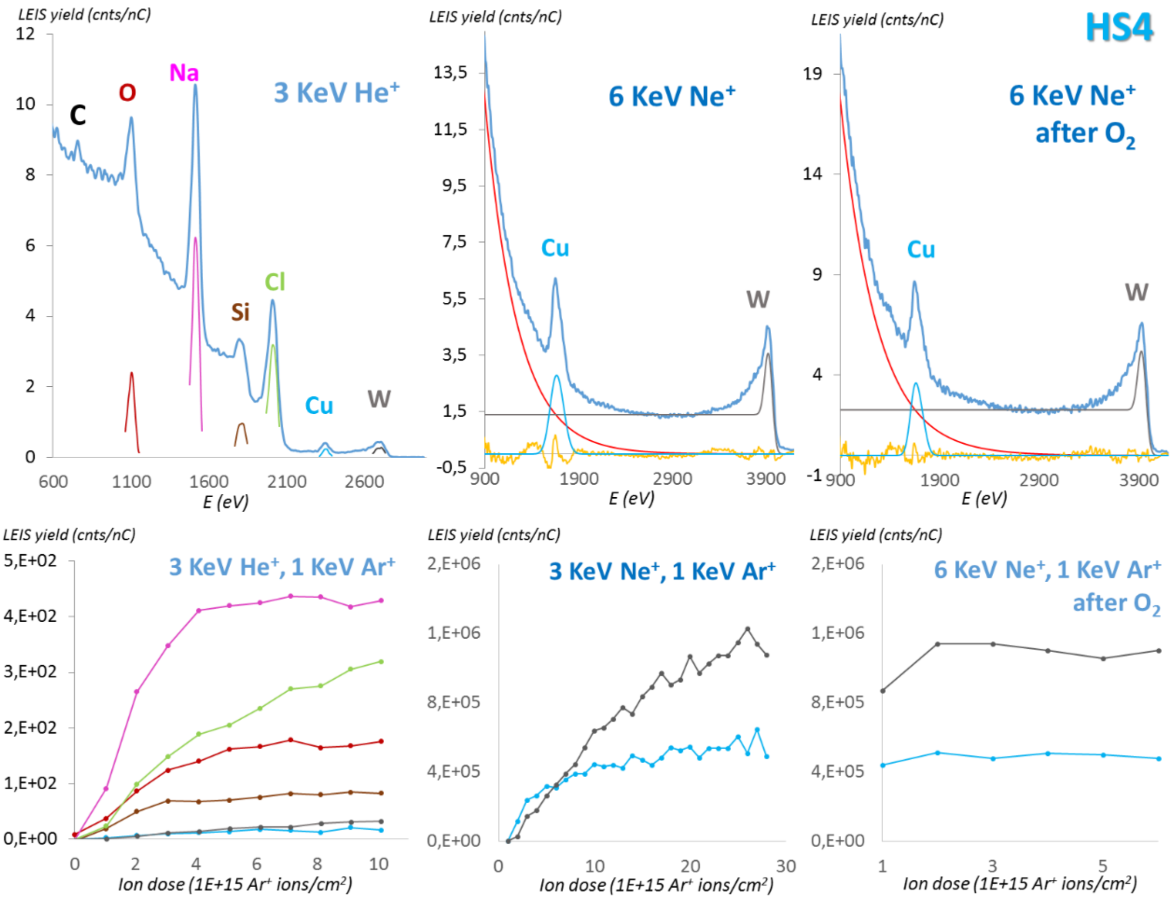

Figure 5.13. 3 KeV He$^+$ and 6 KeV Ne$^+$ LEIS spectra (top) of the **HS4** and after cleaning it with activated O_2 (top right) along with the corresponding depth profiles using 1 KeV Ar$^+$ sputtering (bottom).

In summary, LEIS is a surface sensitive analytical tool that provides the elemental composition of the outermost atomic layer of a surface as well as their distribution with the depth of the material. In this preliminary work, LEIS provided valuable information of qualitative nature about our hybrid model POM–polymer surfaces. A fine example of the latter would be the Si peaks observed in all surfaces, which makes us believe that its origin lies in the preparation method so modifications in that regard must be undertaken. Similarly, traces of Fe could be detected in **HS0** surface owing to the sensibility of the technique and the presence of uncoordinated free–Cu(cyclam) moieties within **HS2** is hinted because of the drastic different distribution of Cu and V with the material depth. However, the important expected peaks (Cu and V, W) were observed at the outermost atomic layer for all **HS** samples which was one of our primary goals regarding the superficial characterization of the hybrid POM–polymer materials, as their presence heavily implied the that both inorganic clusters and the anchoring metalorganic Cu(cyclam) units are in fact located there. Hopefully, these initial results will prove helpful for more elaborated studies within this new interesting research line in the near future.

5.3.3 Superficial Characterization of BF samples

Time of Flight–Secondary Ion Mass Spectrometry (ToF–SIMS)

In comparison to **HS0–HS4**, the more flat **BF0–BF4** samples permitted their superficial analysis by ToF–SIMS technique (Figure 5.14). The main objectives of this preliminary work were the confirmation of both the immobilized polyoxometalates and Cu(cyclam) moieties as well as the qualitative distribution of the components with the depth of the material and their preferential location across the sample surfaces. To achieve these goals, we conducted SIMS experiments in different modes to collect the corresponding mass spectra, depth profiles and SIMS images.

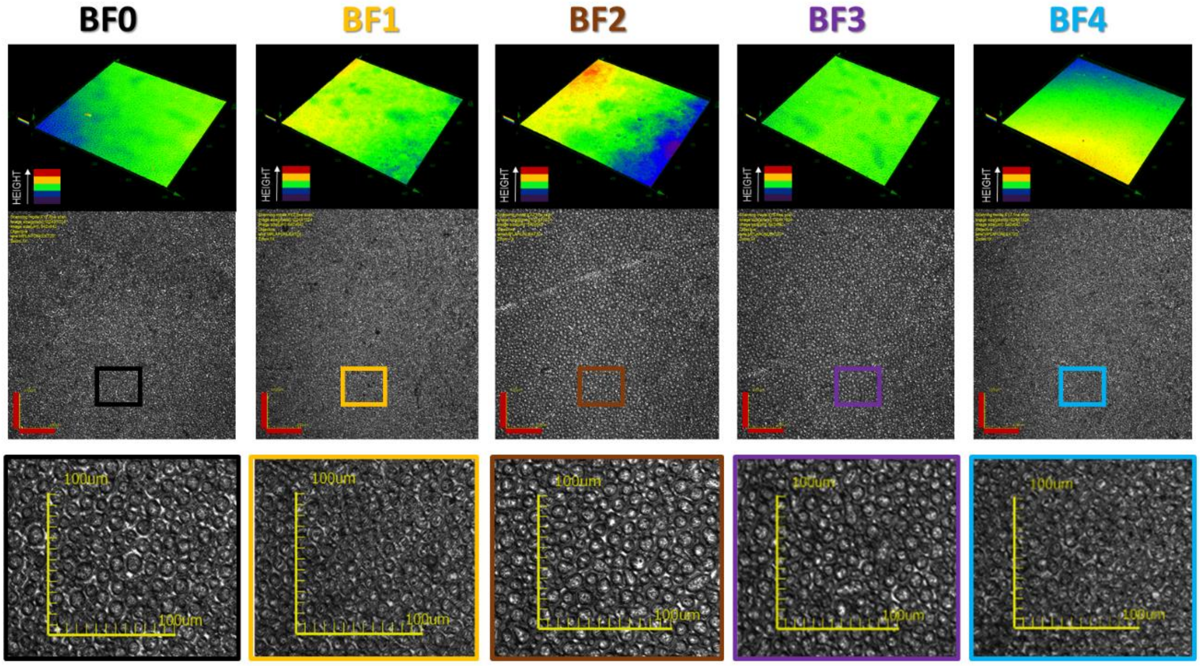

Figure 5.14. Optical microscope images showing the difference in roughness of the **BF0**–**BF4** samples as well as a zoom at the carboxylic–functionalized cavities (scale bar = 100 µm).

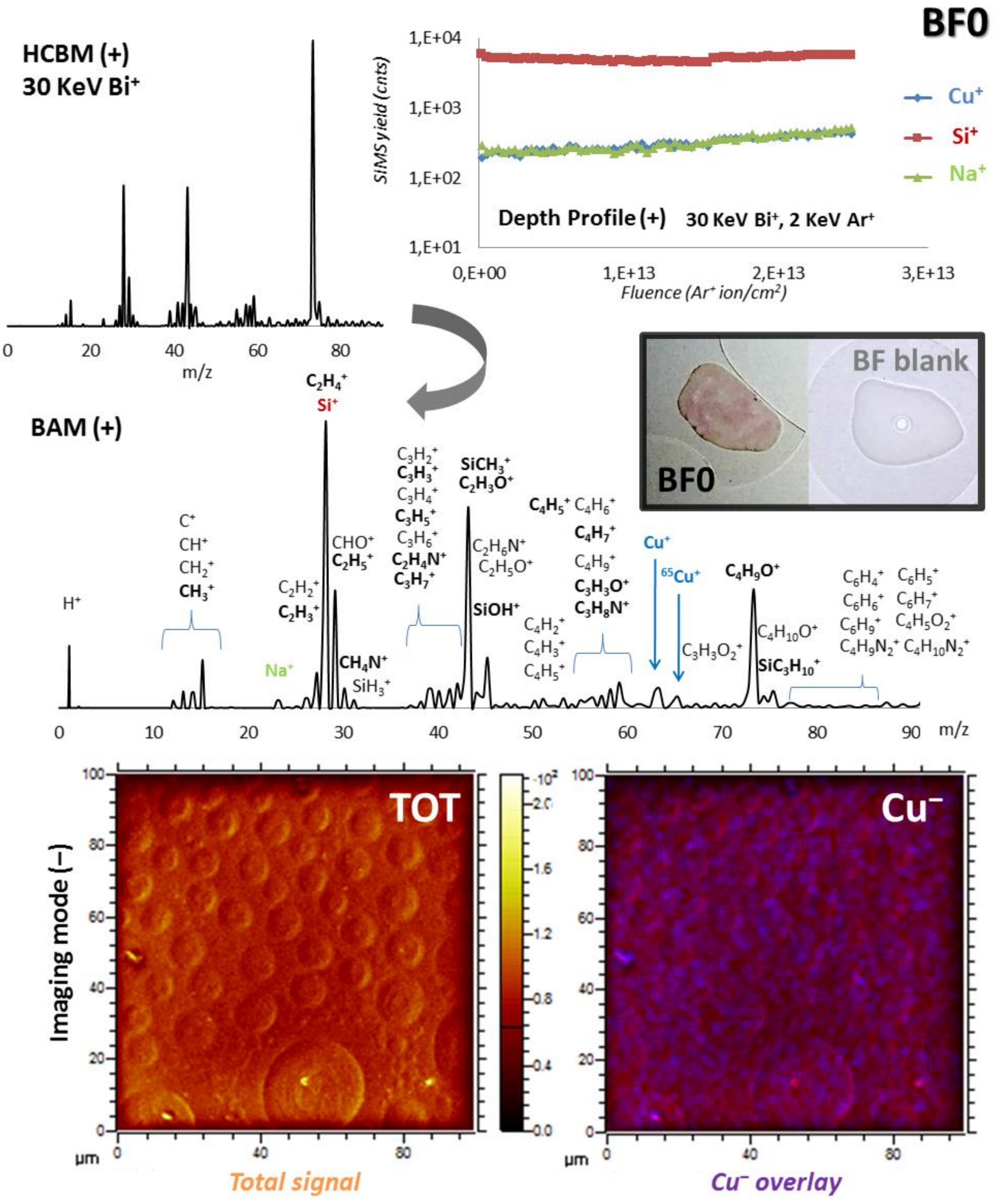

Figure 5.15. 30 KeV Bi^+ SIMS (+) spectrum recorded in HCBM (top left) and BAM with assignment of the most probable fragments of the organic components and metals highlighting the strongest signals (bottom) along with the depth profile (+) using 2 KeV Ar^+ sputtering (top right) for **BF0**. Surface images obtained in imaging mode (–) are also shown indicating the spatial distribution of the signals arising from the Cu^- peaks, as well as digital photographs of **BF0** and a BF blank. HCBM = High Current Bunch Mode; BAM = Burst Alingment mode.

First, the **BF0** sample was measured and used as reference as only the metalorganic anchoring units Cu(cyclam) was used for its preparation (Figure 5.15). Among the numerous signals observed in the mass spectrum in positive mode, those belonging to the most probable fragmentation modes of the organic components could be assigned which would evidence the presence of the cyclam ligands at the outer layers of the samples. Similarly, the presence of copper was confirmed by the characteristics peaks of Cu^+ and its isotope ^{65}Cu. Strong signals belonging to Si^+ and related peaks (SiH_3^+, $SiOH^+$,…) were also found which could be coming from the preparation method as they are present in all **HS** and **BF** samples, even in the **PAA** sample discussed in the LEIS results (Figure 5.8). In close analogy, a small peak corresponding to Na$^+$ could also be identified, which is a common contaminant that is often detected when measuring in positive mode. The dynamic depth profile shows a regular trend for all Cu, Na and Si elements with the depth of the material which indicates a good homogeneity and distribution of the elements at the first few monolayers. The SIMS images obtained in negative mode show the pores of the surface that did not suffer notable changes compared to the blank surfaces observed in SEM prior to the immobilization of the POMs. Interestingly, the overlay of the Cu$^-$ signal versus the total signal suggest that the positions where the Cu signal originate are mainly located at the pores, as we intended (Figure 5.15).

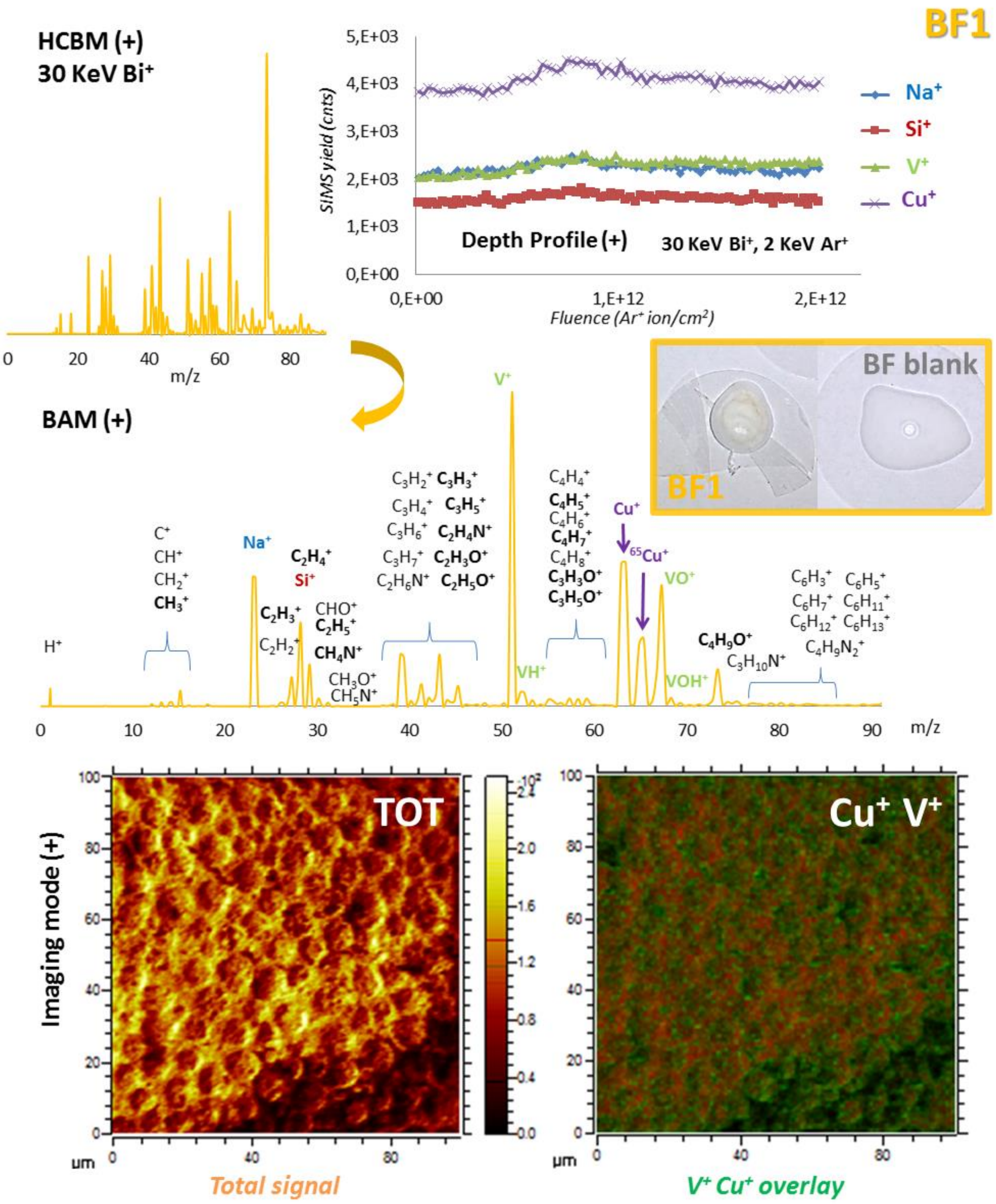

Figure 5.16. 30 KeV Bi$^+$ SIMS (+) spectrum recorded in HCBM (top left) and BAM with assignment of the most probable fragments of the organic components and metals highlighting the strongest signals (bottom) along with the depth profile (+) using 2 KeV Ar$^+$ sputtering (top right) for **BF1**. Surface images obtained in imaging mode (+) are also shown indicating the spatial distribution of the signals arising from the Cu$^+$ and V$^+$ peaks, as well as digital photographs of **BF1** and a BF blank. HCBM = High Current Bunch Mode; BAM = Burst Alingment mode.

Some notable changes in the SIMS (+) spectrum of **BF1** were observed compared to the reference **BF0**. The most important change lies in the numerous peaks associated to V (V^+, VH^+, VO^+ and VOH^+) which imply that the $\{V_{10}O_{28}\}$ species should be located at the outermost layers of the material and hence, suggest that the incorporation of the POM met some success (Figure 5.16). The intensity of the Na^+ peak increased various times that observed in the **BF0**, which was expected since **1–CuV10** was synthetized in NaCl 1 M medium. In a similar fashion, a significant increase in the intensity of the Cu^+ and $^{69}Cu^+$ was also observed in comparison to **BF0**. In contrast, the Si^+ and related peaks decreased significantly. The depth profile confirms a regular distribution of both Cu^+ and V^+ signals indicating a good homogeneity when going deeper into the material. SIMS imaging also provided useful information: the overlay of the Cu^+–V^+ signals versus the total signal show that the most intense positions were these peaks originate are primarily located at the carboxylate–filled cavities (Figure 5.16).

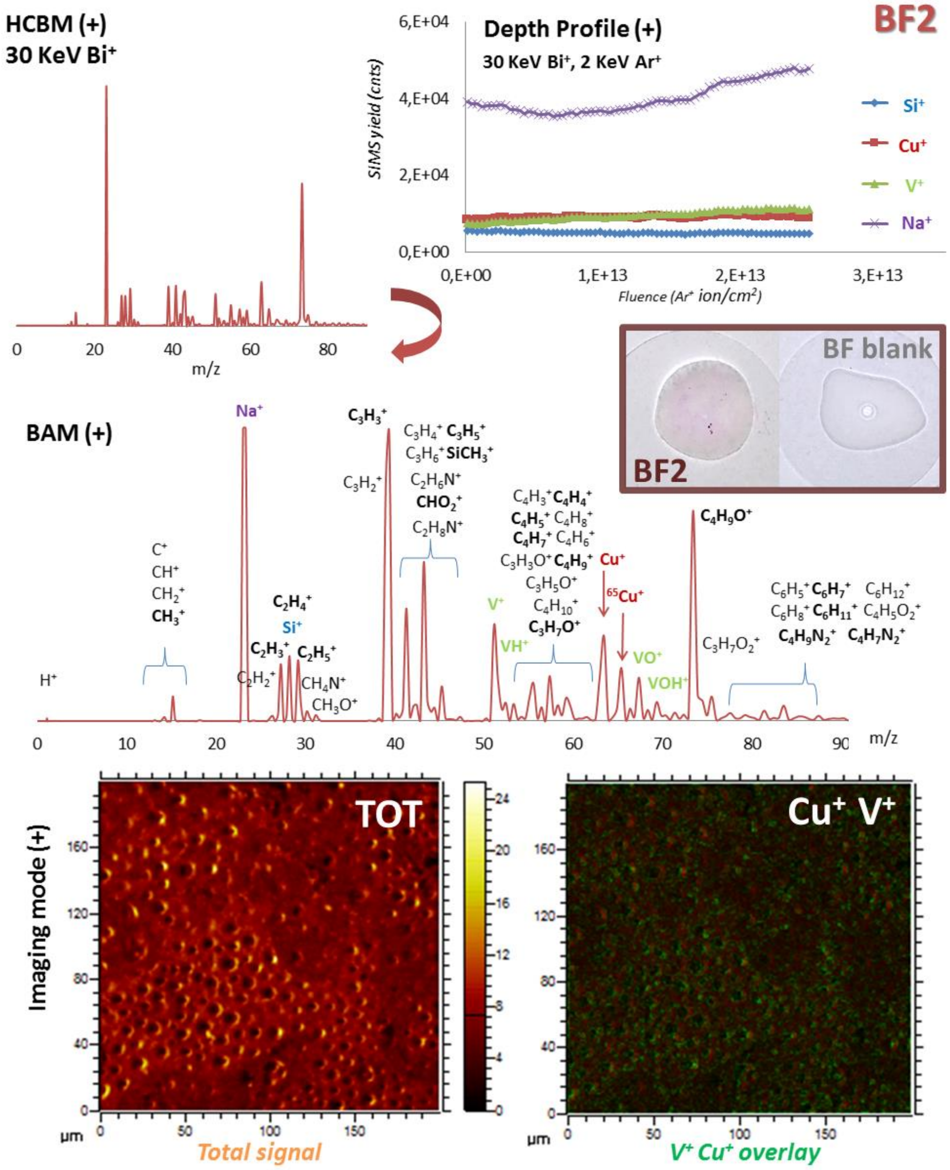

Figure 5.18. 30 KeV Bi^+ SIMS (+) spectrum recorded in HCBM (top left) and BAM with assignment of the most probable fragments of the organic components and metals highlighting the strongest signals (bottom) along with the depth profile (+) using 2 KeV Ar^+ sputtering (top right) for **BF2**. Surface images obtained in imaging mode (+) are also shown indicating the spatial distribution of the signals arising from the Cu^+ and V^+ peaks, as well as digital photographs of **BF2** and a BF blank. HCBM = High Current Bunch Mode; BAM = Burst Alingment mode.

BF2 shows a very similar SIMS (+) spectrum to that of **BF1** showing the characteristic peaks of V^+ and Cu^+ as well as the organic fragments observed in the latter, suggesting that **1–CuV** was successfully incorporated into the sample (Figure 5.17). The intensity of the V^+ and related peaks decreased considerably, which is in good agreement with the fact that the vanadium content per formula in **1–CuV** is much lesser than that of **1–CuV10** in the previous **BF1** surface. While a good homogeneity for Cu, V and Si elements is observed with depth, a slightly more irregular trend for Na^+ was obtained in the depth profile, which slightly increases when going deeper into the material. In close analogy to **BF1**, however, the SIMS images show that the most intense positions were the Cu^+–V^+ signals originate are mainly located at the carboxylic–functionalized pores (Figure 5.17).

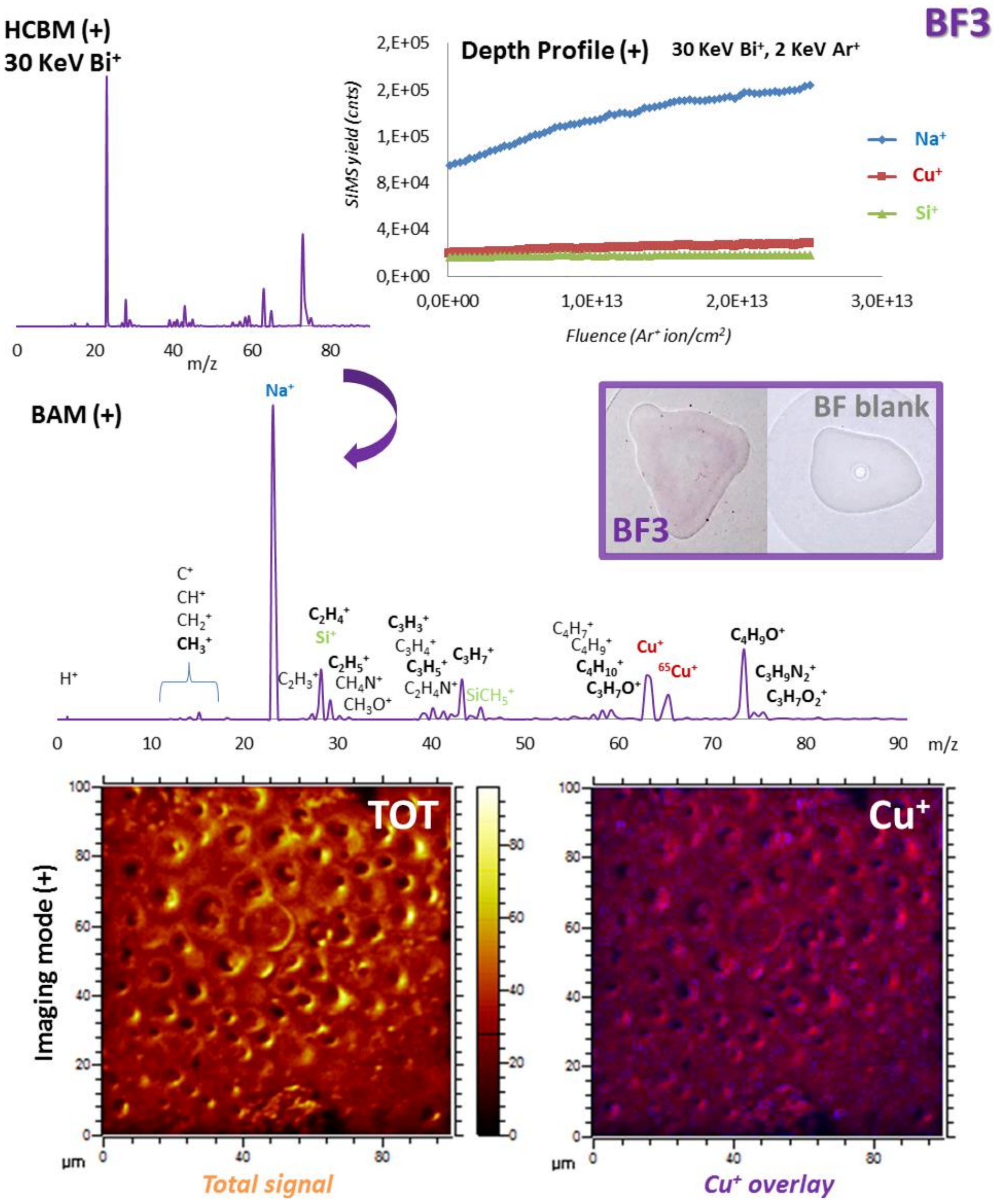

Figure 5.18. 30 KeV Bi^+ SIMS (+) spectrum recorded in HCBM (top left) and BAM with assignment of the most probable fragments of the organic components and metals highlighting the strongest signals (bottom) along with the depth profile (+) using 2 KeV Ar^+ sputtering (top right) for **BF3**. Surface images obtained in imaging mode (+) are also shown indicating the spatial distribution of the signals arising from the Cu^+ peaks, as well as digital photographs of **BF3** and a BF blank. HCBM = High Current Bunch Mode; BAM = Burst Alingment mode.

Compared to **BF1** and **BF2** drastic differences were found in the SIMS (+) spectrum of **BF3**. First, no signal for Mo could be found at all and secondly, the overall spectra is highly reminiscent to that seen for the reference **BF0** (Figure 5.18). These two facts unequivocally confirm the absence of **1–CuMo5** at the surface of the sample so no POM functionalization took place, as opposed to **BF1** and **BF2**. Depth profile indicates that Cu and Si are evenly distributed with depth whereas a gradual increase for Na^+ can be seen Figure 5.18. Similar results were obtained for **BF4**, those being an almost identical fragmentation profile and the absence of the characteristic W peak of the POM (Figure 5.19), corroborating the absence of **1–CuW7** at the first atomic monolayers of the material. In comparison to the previous **BF3**, the depth profile of **BF4** shows a good homogeneity at the material surface. Interestingly, the SIMS imaging for both surfaces indicate that the copper is also mainly located at the carboxylic pores (Figures 5.18 and 5.19), much like the reference **BF0** surface.

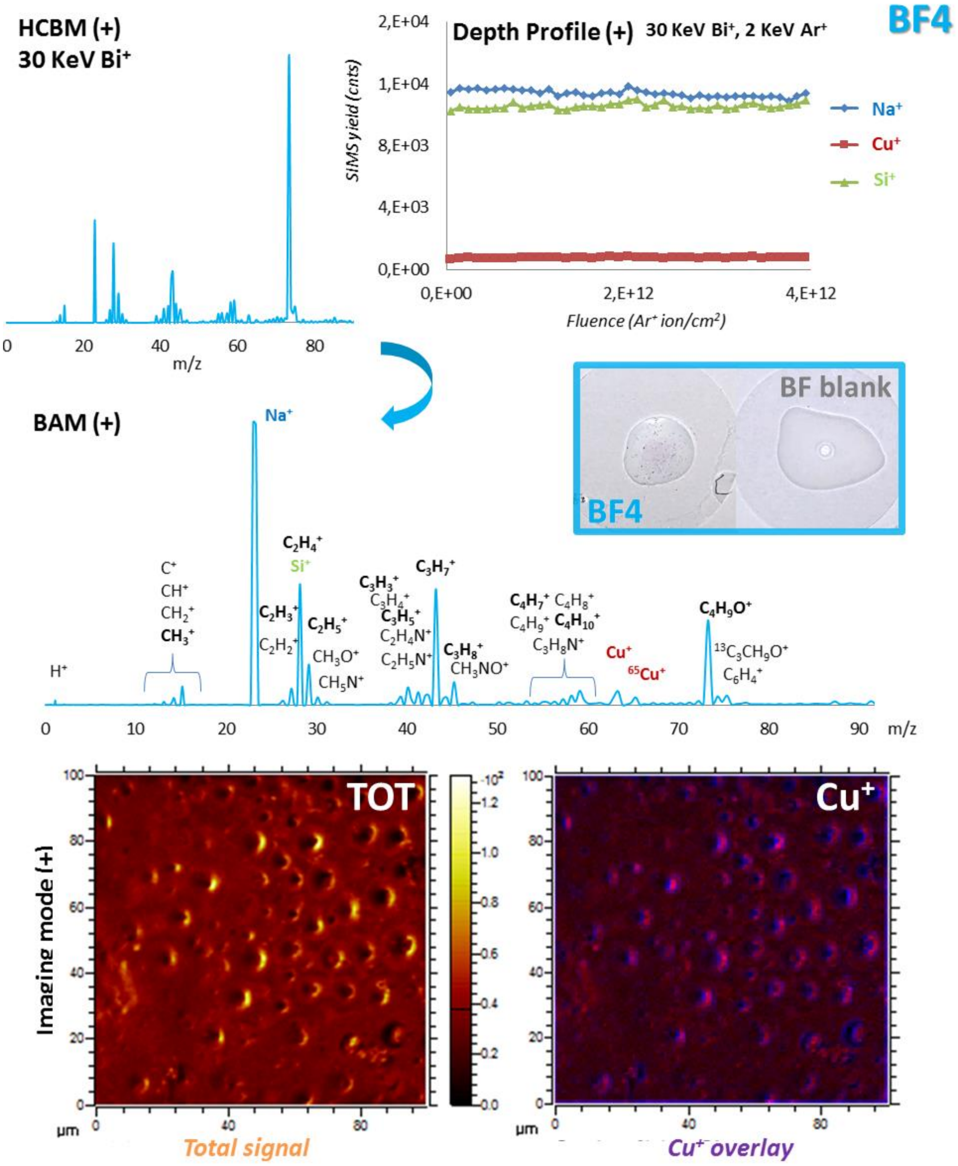

Figure 5.19. 30 KeV Bi^+ SIMS (+) spectrum recorded in HCBM (top left) and BAM with assignment of the most probable fragments of the organic components and metals highlighting the strongest signals (bottom) along with the depth profile (+) using 2 KeV Ar^+ sputtering (top right) for **BF3**. Surface images obtained in imaging mode (+) are also shown indicating the spatial distribution of the signals arising from the Cu^+ peaks, as well as digital photographs of **BF4** and a BF blank. HCBM = High Current Bunch Mode; BAM = Burst Alingment mode.

SIMS (+) spectra in BAM for the reference and all four samples are grouped in Figure 5.20 for comparative purposes. A quick glance at the highlighted m/z ranges shows notable differences for **BF1** and **BF2** compared to the others, which indicate that the fragmentation modes of the components differs. This fact indicates that significant changes in the chemical composition at the outermost layers must exist and thus, it further corroborates that the POM immobilization succeeded in the case of **BF1** and **BF2,** while **BF3** and **BF4** samples display a virtually identical fragmentation patterns to those observed in the reference **BF0**. These similarities together with the absence of POM–related peaks (Mo and W for **BF3** and **BF4**, respectively) indicate that only free, uncoordinated–Cu(cyclam) moieties were immobilized into the surface of **BF3** and **BF4** samples.

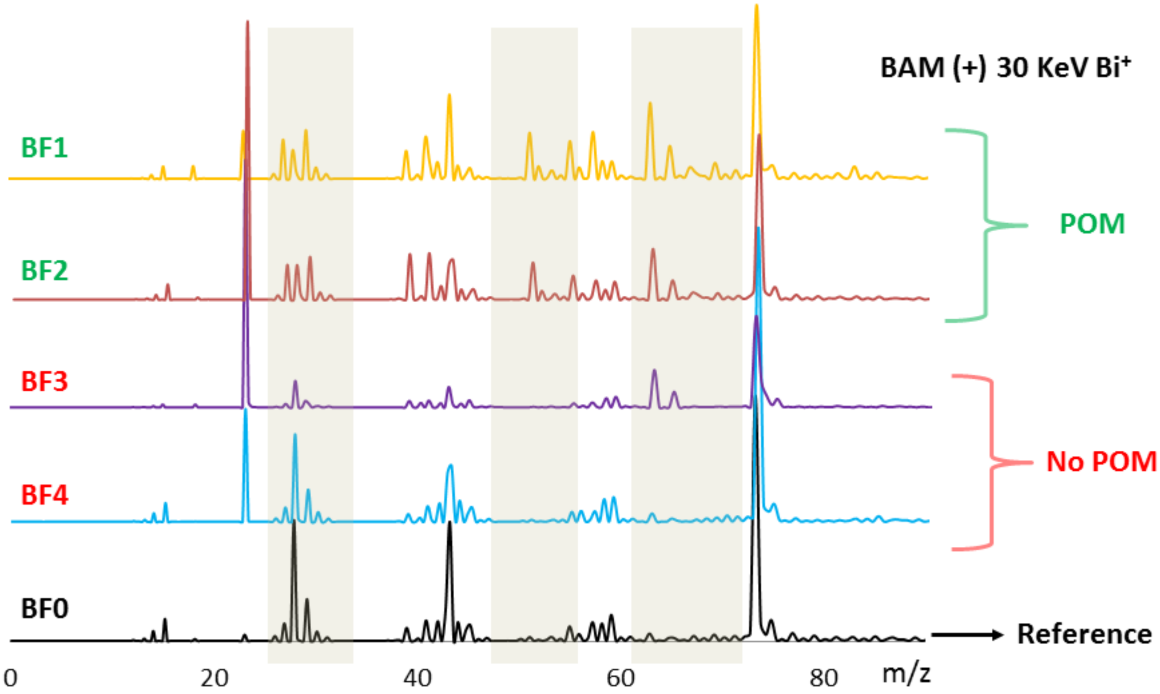

Figure 5.20. Comparison of the 30 KeV Bi$^+$ SIMS (+) spectra recorded in BAM for all **BF** samples and the reference, highlighting the different fragmentation modes in the highlighted m/z regions. BAM = Burst Alingment Mode.

Similar results can be observed for the SIMS spectra recorded in negative mode (–) that are shown in Figure 5.21. For instance, several peaks found in the 20–45, 59–64 and 70–80 m/z ranges are practically identical for **BF3** and **BF4** surfaces to those found in the reference **BF0** while slightly different fragmentation peaks can be seen in the SIMS (–) spectra belonging to **BF1** and **BF2** samples. These observations further reinforces the conclusions reached above.

In summary, SIMS measurements carried out in this preliminary work strongly suggest that the POM incorporation to the breath figure polymeric surfaces was successful for **BF1** and **BF2** samples, while no POM components were found at the first monolayers in the case of **BF3** and **BF4** samples. The latter is corroborated by the absence of Mo and W related peaks as well as the virtually identical fragmentation modes observed in both BAM (+) and BAM (–) to those observed in the POM–free **BF0** reference surface. Interestingly, SIM imaging provided useful information about the preferential location of the metal atoms at the surface of the samples. In all cases, signals arising from Cu peaks are mainly distributed at the pores of the breath figure surfaces whereas **BF1** and **BF2** also show V^+ signals coming from the pores, potentially suggesting that the POMs are indeed preferentially located there.

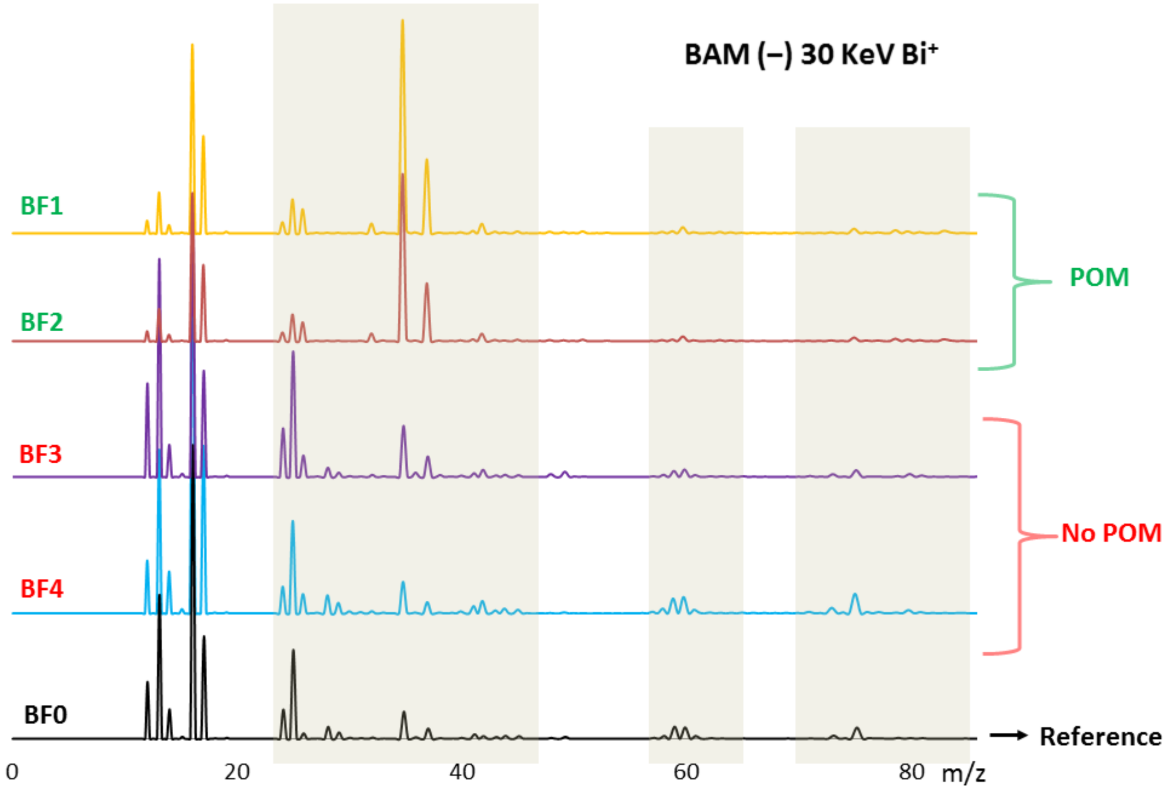

Figure 5.21. Comparison of the 30 KeV Bi^+ SIMS (–) spectra recorded in BAM for all **BF** samples and the reference, highlighting the different fragmentation modes in the highlighted m/z regions. BAM = Burst Alingment Mode.

5.4 CONCLUSIONS

This preliminary work describes a very facile approach to obtain various polymer–polyoxometalate (POM) hybrid surfaces by either immobilization of POM species on tailored “breath figures” films made by poly(styrene)–poly(acrylic acid) copolymers (**BF**) or by direct mixing of POM–containing solutions with solid poly(acrylic acid) hydrophilic polymer (**HS**). Highly sensitive ion beam–based techniques were used to carry out the superficial characterization of such hybrid composites to obtain useful information about the composition at the outermost atomic layers of the materials and elemental distribution when going deeper into the materials.

On one hand, LEIS measurements on **HS** samples provided valuable information of qualitative nature about our hybrid model POM–polymer surfaces. A fine example of the latter would be the Si peaks observed in all samples, which makes us believe that its origin lies in the preparation method so modifications in that regard must be undertaken. Similarly, traces of Fe could be detected in **HS0** surface owing to the sensibility of the technique and the presence of uncoordinated free–Cu(cyclam) moieties within **HS2** is hinted because of the drastic different distribution of Cu and V with the material depth. In contrast, the depth profiles of **HS1** (and **HS4**) show an even distribution of both Cu and V (and W) peaks that increases with depth, suggesting that the presence of the incorporated POM species increases when going deeper into the hybrid material. All in all, the important expected peaks (Cu and V, W) were observed at the outermost atomic layer for all **HS** samples which was one of our primary goals regarding the superficial characterization of these hybrid POM–polymer materials, as their presence heavily implied the that both inorganic clusters and the anchoring metalorganic Cu(cyclam) units are in fact located there.

On the other hand, SIMS measurements on **BF** samples strongly suggest that the POM incorporation onto the breath figure polymeric surfaces was successful for **BF1** and **BF2** samples (**1–CuV** and **1–CuV10**, respectively), while no POM components were found at the first monolayers in the case of **BF3** and **BF4** samples (**1–CuMo5** and **1–CuW7**, respectively). The latter is corroborated by the absence of Mo and W related peaks as well as the virtually identical fragmentation modes observed in both SIMS (+) and SIMS (–) to those observed in the POM–free **BF0** reference surface. Interestingly, SIM imaging provided useful information about the preferential location of the metal atoms at the surface of the samples. In all cases, signals arising from Cu peaks are mainly distributed at the pores of the breath figure surfaces whereas **BF1** and **BF2** also show V^+ signals coming from the pores, potentially suggesting that the POMs are indeed preferentially located there.

To our knowledge, this is the first time that these beam–based techniques are applied to characterize the immediate surface of such POM–polymer hybrid films. LEIS and SIMS are appropriate techniques to characterize these types of materials as they provide useful information with high sensitivity about the composition at the outermost layers and distribution of the different elements with material depth as well as the preferential location of specific signals across the target surface. This is of outmost importance as these final atoms of a surface often govern the chemical interaction with other materials and thus, these type of information should help understand better the potential applications of these hybrid materials. Hopefully, these preliminary results will help pave the way for more elaborated studies within this new interesting research line in the near future.

5.5 REFERENCES

---

[1] For some books on POMs see: (a) Pope, M. T. *Heteropoly and Isopoly Oxometalates*; Springer-Verlag: Berlin, Germany, 1983. (b) *Polyoxometalates: from Platonic Solids to Anti-Retroviral Activity*; Pope, M. T., Müller, A., Eds.; Kluwer: Dordrecht, The Netherlands, 1994. (c) *Polyoxometalate Chemistry: From Topology via Self-Assembly to Applica-tions*; Pope, M. T., Müller, A., Eds.; Kluwer: Dordrecht, The Netherlands, 2001. (d) *Polyoxometalate Chemistry for Nanocomposite Design*; Pope, M. T., Yamase, T., Eds.; Kluwer: Dordrecht, The Netherlands, 2002. (e) *Polyoxometalate Molecular Science*; Borrás-Almenar, J. J., Coronado, E., Müller, A., Pope, M. T., Eds.; Kluwer: Dordrecht, The Netherlands, 2003. (f) *Polyoxometalate Chemistry. Some Recent Trends*; Sécheresse, F., Ed.; World Scientific: Singapore, 2013.

[2] For some thematic issues on POMs see: (a) Hill, C. L., Guest Ed. *Chem. Rev*. **1998**, *98*, issue 1. (b) Kortz, U., Guest Ed. *Eur. J. Inorg. Chem*. **2009**, issue 34. (c) Cronin, L., Long, D.-L., Guest Eds. *Dalton Trans*. **2012**, *41*, issue 33. (d) Cronin, L., Müller, A., Guest Eds. *Chem. Soc. Rev*. **2012**, *41*, issue 22. (e) Kortz, U., Liu, T., Guest Eds. *Eur. J. Inorg. Chem*. **2013**, issue 10-11.

[3] For some recent reviews see: (a) Long, D.-L.; Tsunashima, R.; Cro-nin, L. *Angew. Chem. Int. Ed*. **2010**, *49*, 1736. (b) Dolbecq, A.; Dumas, E.; Mayer, C. R.; Mialane, P. *Chem. Rev*. **2010**, *110*, 6009. (c) Song, Y.-F.; Tsunashima, R. *Chem. Soc. Rev*. **2012**, *41*, 7384. (d) Proust, A.; Matt, B.; Villanneau, R.; Guillemot, G.; Gouzerh, P.; Izzet, G. *Chem. Soc. Rev*. **2012**, *41*, 7605.

---

[4] See for example: (a) Liu, S. Q.; Tang, Z. Y. *Nano Today* **2010**, *5*, 267 and references therein. (b) Li, D.; Yin, P.; Liu, T. *DaltonTrans*. **2012**, *41*, 2853. (c) Nisar, A.; Lu, Y.; Zhuang, J.; Wang, X. *Angew. Chem. Int. Ed.* **2011**, *50*, 318. (d) Kurth, D. G.; Lehmann, P.; Volkmer, D.; Cölfen, H.;Müller, A.; Du Chesne, A. *Chem. Eur. J.* **2000**, *6*, 385. (e) Li, H.; Sun, H.; Qi, H.; Xu, M.; Wu L. *Angew. Chem. Int. Ed*. **2007**, *46*, 1300. (f) Landsmann, S.; Lizandara-Pueyo, C.; Polarz, S. *J. Am. Chem. Soc*. **2010**, *132*, 5315. (g) Zhang, J.; Song, Y. F.; Cronin, L.; Liu, T. *J. Am. Chem. Soc*. **2008**, *130*, 14408. (h) Rosnes, M. H.; Musumeci, C.; Pradeep, C. P.; Mathieson, J. S.; Long, D.-L.; Song, Y.-F.; Pignataro, B.; Cogdell, R.; Cronin, L. *J. Am Chem. Soc*. **2010**, *132*, 15490.

[5] See for example: (a) Toma, F. M.; Sartorel, A.; Iurlo, M.; Carraro, M.; Parisse, P.; Maccato, C.; Rapino, S.; Rodriguez Gonzalez, B.; Ame-nitsch, H.; Da Ros, T.; Casalis, L.; Goldoni, A.; Marcaccio, M.; Scorrano, G.; Scoles, G.; Paolucci, F.; Prato, M.; Bonchio, M. *Nat. Chem*. **2010**, *2*, 826. (b) Giusti, A.; Charron, G.; Mazerat, S.; Compain, J.-D.; Mialane, P.; Dolbecq, A.; Rivière, E.; Wernsdorfer, W.; Ngo Biboum, R.; Keita, B.; Nadjo, L.; Filoramo, A.; Bourgoin, J.-P.; Mallah, T. *Angew. Chem. Int. Ed*. **2009**, *121*, 5049. (c) Tessonnier, J.-P.; Goubert-Renaudin, S.; Alia, S.; Yan, Y.; Barteau, M. A. *Langmuir* **2013**, *29*, 393. (d) Li, H.; Pang, S.; Wu, S.; Feng, X.; Müllen, K.; Bubeck, C. *J. Am. Chem. Soc*. **2011**, *133*, 9423. (e) Song, J.; Luo, Z.; Britt, D. K.; Furukawa, H.; Yaghi, O. M.; Hardcastle, K. I.; Hill, C. L. *J. Am. Chem. Soc*. **2011**, *133*, 16839. (f) Mayer, C. R.; Thouvenot, R.; Lalot, T. *Chem. Mater*. **2000**, *12*, 257. (g) Han, J. W.; Hill, C. L. *J. Am. Chem. Soc*. **2007**, *129*, 15094. (h) Geisberger, G.; Paulus, S.; Carraro, M.; Bonchio, M.; Patzke, G. R. *Chem. Eur. J*. **2011**, *17*, 4619. (i) Bu, W.; Uchida, S.; Mizuno, N. *Angew. Chem. Int. Ed*. **2009**, *48*, 8281. (j) Li, H.; Qi, W.; Li, W.; Sun, H.; Bu, W.; Wu, L. *Adv. Mater*. **2005**, *17*, 2688.

[6] Ammam, M. *J. Mater Chem. A* **2013**, *1*, 6291

[7] See for example: (a) Carraro, M.; Gardan, M.; Scorrano, G.; Drioli, E.; Fontananova, E.; Bonchio, M. *Chem. Commun*. **2006**, 4533. (b) Fontananova, E; Donato, L.; Drioli, E.; Lopez, L. C.; Favia, P.; d'Agostino, R. *Chem. Mater*. **2006**, 18, 1561.

[8] See for example: (a) Alam, M. S.; Dremov, V.; Müller, P.; Postnikov, A. V.; Mal, S. S.; Hussain, F.; Kortz, U. *Inorg. Chem*. **2006**, *45*, 2866. (b) Musumeci, C.; Luzio, A.; Pradeep, C. P.; Miras, H. N.; Rosnes, M. H.; Song, Y.-F.; Long, D.-L.; Cronin, L.; Pignataro, B. *J. Phys. Chem. C* **2011**, *115*, 4446. (c) Inumaru, K.; Ishihara, T.; Kamiya, Y.; Okuhara, T.; Yamanaka, S. *Angew. Chem. Int. Ed*. **2007**, *46*, 7625. (d) Li, H.-L.; Perkas, N.; Li, Q.-L.; Gofer, Y.; Koltypin, Y.; Gedanken, A. *Langmuir* **2003**, *19*, 10409. (e) Kasai, J.; Nakagawa, Y.; Uchida, S.; Yamaguchi, K.; Mizuno, N. *Chem. Eur. J*. **2006**, *12*, 4176. (f) Song, I. K.; Kaba, M. S.; Nomiya, K.; Finke, R. G.; Barteau, M. A. *J. Mol. Catal. A* **2007**, *262*, 216. (g) Zhong, D.; Sousa, F. L.; Müller, A.; Chi, L.; Fuchs, H. *Angew. Chem. Int. Ed*. **2011**, *50*, 7018.

[9] See for example: (a) Errington, R. J.; Petkar, S.S.; Horrocks, B. R.; Houlton, A.; Lie, L. H.; Patole, S. N. *Angew. Chem. Int. Ed*. **2005**, *44*, 1254. (b) Schroden, R. C.; Blanford, C. F.; Melde, B. J.; Johnson, B. J. S.; Stein, A. *Chem. Mater*. **2001**, *13*, 1074. (c) Zhang, R.; Yang, C. *J. Mater. Chem*. **2008**, *18*, 2691.

[10] (a) Mercier, D.; Boujday, S.; Annabi, C.; Villanneau, R.; Pradier, C.-M.; Proust, A. *J. Phys. Chem. C* **2012**, *116*, 13217. (b) Villanneau, R.; Marzouk, A.; Wang, Y.; Djamaa, A. B.; Laugel, G.; Proust, A.; Launay, F. *Inorg. Chem*. **2013**, *52*, 2958. (c) Song, Y.-F.; McMillan, N.; Long, D.-L.; Kane, S.; Malm, J.; O Riehle, M.; Pradeep, C. P.; Gadegaard, N.; Cronin, L. *J. Am. Chem. Soc*. **2009**, *131*, 1340

[11] (11) (a) Johnson, B. J. S.; Stein, A. *Inorg. Chem*. **2001**, *40*, 801. (b) Yang, Y.; Guo, Y.; Hu, C.; Wang, Y.; Wang, E. *Appl. Catal. A* **2004**, *273*, 201.

[12] Lunkenbein, T.; Kamperman, M.; Li, Z.; Bojer, C.; Drechsler, M.; Förster, S.; Wiesner, U.; Müller, A. H. E.; Breu, J. *J. Am. Chem. Soc*. **2012**, *134*, 12685

[13] (a) Kilner, J. A.; Tellez-Lozano, H.; Burriel, M.; Cook, S.; Druce, J. *ECS Trans.* **2013**, *57*, 1701. (b) Kilner, J. A.; Skinner, S. J.; Brongersma, H. H. *J. Solid State Electrochem*. **2011**, *15*, 861. (c) *Surface Analysis: The Principal Techniques*; Vickerman, J. C.; Gilmore, I., Eds.; John Willey & Sons, 2009.

[14] (a) Smith, D. P. *J. Appl. Phys.* **1967**, *38*, 340. (b) Brongersma, H. H.; Mul, P. M. *Surf. Sci.* **1973**, *35*, 393. (c) Brongersma, H. H.; Grehl, T.; van Hal, P. A.; Kuijpers, N. C. W.; Mathijssen, S. G. J.; Schofield, E. R.; Smith, R. A. P.; ter Veen, H. R. J. *Vacuum* **2010**, *84*, 1005. (d) Brongersma, H.; Draxler, M.; Deridder, M.; Bauer, P. *Surf. Sci. Rep.* **2007**, *62*, 63.

[15] (a) Brongersma, H. H.; de Ridder, M.; Gildenpfennig, A.; Viitanen, M. M. *J. Eur. Ceram. Soc.* **2003**, *23*, 2761.

[16] (a) Stamenkovic, V. R.; Fowler, B.; Mun, B. S.; Wang, G.; Ross, P. N.; Lucas, C. A.; Marković, N. M. *Science* **2007**, *315*, 493. (b) Tellez, H.; Aguadero, A.; Druce, J.; Burriel, M.; Fearn, S.; Ishihara, T.; McPhail, D. S.; Kilner, J. A. *J. Anal. At. Spectrom.* **2014**, *29*, 1361. (c) Burriel, M.; Wilkins, S.; Hill, J. P.; Munoz-Marquez, M. A.; Brongersma, H. H.; Kilner, J. A.; Ryan, M. P.; Skinner, S. J. *Energy Environ. Sci.* **2014**, *7*, 311. (d) de Rooij-Lohmann, V. I. T. A.; Kleyn, A. W.; Bijkerk, F.; Brongersma, H. H.; Yakshin, A. E. *Appl. Phys. Lett.* **2009**, *94*, 063107.

---

[17] Shin, H. H.; McIntosh, S. *J. Mater. Chem. A* **2013**, *1*, 7639.

[18] (a) Brongersma, H. H.; Grehl, T.; van Hal, P. A.; Kuijpers, N. C. W.; Mathijssen, S. G. J.; Schofield, E. R.; Smith, R. A. P.; ter Veen, H. R. *J.* Vacuum, **2010**, *84*, 1005. (b) Rafati, A.; ter Veen, H. R.; Castner, D. G. *Surf. Interface Anal*. **2013**, *45*, 1737.

[19] van der Heide, P. *Secondary Ion Mass Spectrometry: An Introduction to Principles and Practices*, John Wiley & Sons, Hoboken, New Jersey, 2014.

[20] Cushman, C. V.; Brüner, P.; Zakel, j.; Major, G.; Lunt, B. M.; Grehl, T.; Smith, N. J.; Linford, M. R. *Technology & Coating Vacuum* **2016***, 27-35.*

[21] (a) Benninghoven, A. *Angew. Chem., Int. Ed. Engl.* **1994**, *33*, 1023. (b) Benninghoven, A., *Surf. Interface Anal.* **2011**, *43*, 2.

[22] *ToF-SIMS: Surface analysis by mass spectrometry*, J. C. Vickerman; Briggs, D., Eds.; IM Publications, 2001.

[23] Powell, C. J. *J. Surf. Anal.* **2014**, *20*, 155.

[24] Yang, L.; Shirahata, N.; Saini, G.; Zhang, F.; Pei, L.; Asplund, M. C.; Kurth, D. G.; Ariga, K.; Sautter, K.; Nakanishi, T. *Langmuir* **2009**, *25*, 5674.

[25] Chen, C.-Y.; Ghule, A. V.; Chen, W.-Y.; Wang, C.-C.; Chiang, Y.-S.; Ling, Y.-C. *Appl. Surf. Sci.* **2004**, *231*, 447.

[26] Bousquet, A.; Pannier, G.; Ibarboure, E.; Papon, E.; Rodríguez-Hernández, J. *J Adhes.* **2007**; *83*, 335.

[27] Escalé, P.; Rubatat, L.; Billon, L.; Save, M. *Eur. Polym. J.* **2012**, *48*, 1001.

SUPPORTING INFORMATION

APPENDIX

APPENDIX

2. Thermo-Structural Studies in Vanadate–Metalorganic Hybrid Compounds: Dynamic vs. Robust Open-Framework Materials

FIGURES 2A:

3. Thermally triggered SCSC transformations upon gradual dehydration in iso– and lanthanide–substituted hetero–polyoxotungstates

FIGURES 3A:

TABLES 3A:

4. Thermostructural studies in multidimensional Strandberg and Anderson-Evans type hybrid heteropolyoxomolybdates

FIGURES 4A:

2. Thermo-Structural Studies in Vanadate–Metalorganic Hybrid Compounds: Dynamic vs. Robust Open-Framework Materials

Figures A2:

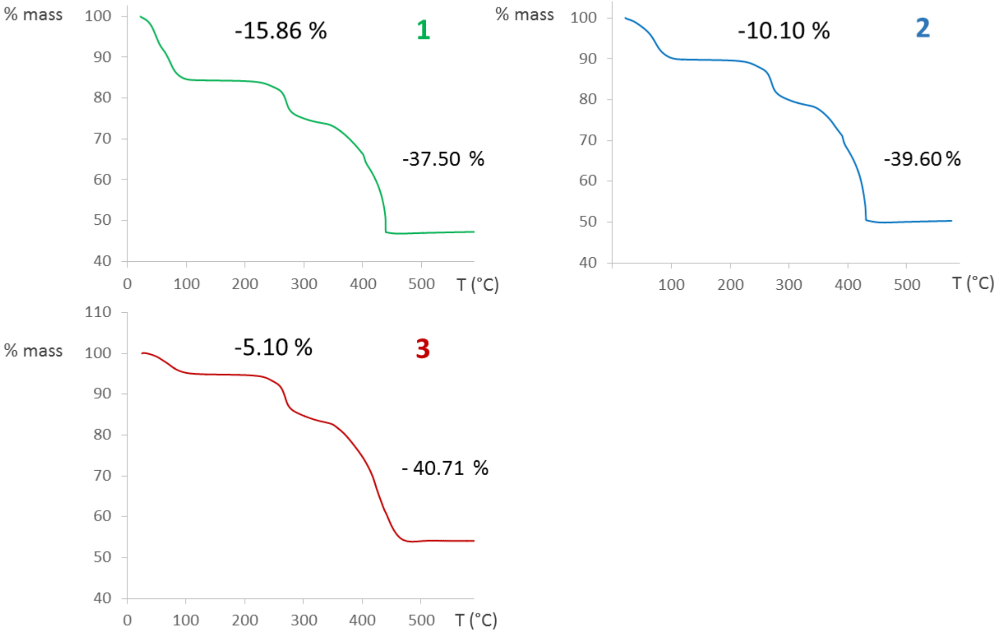

Fig. A2.1. TGA curves for freshly prepared **1–3–CuV** compounds.

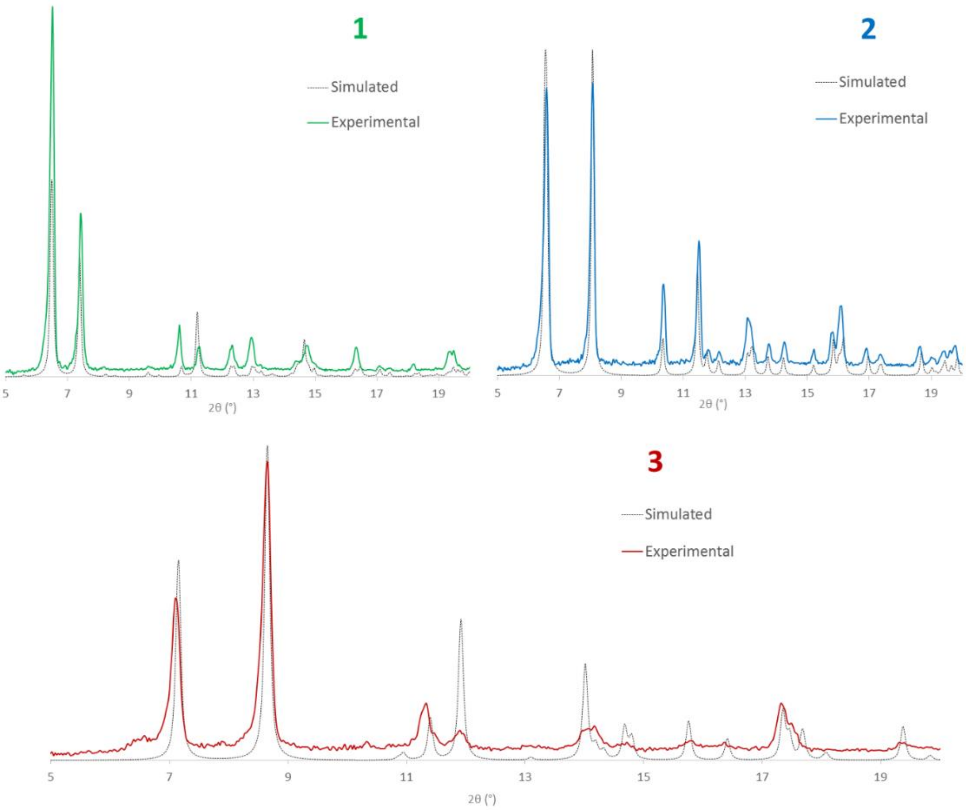

Figure A2.2. Comparison between the experimental PXRD patterns of freshly prepared **1–3–CuV** and those simulated from single-crystal X-ray diffraction data.

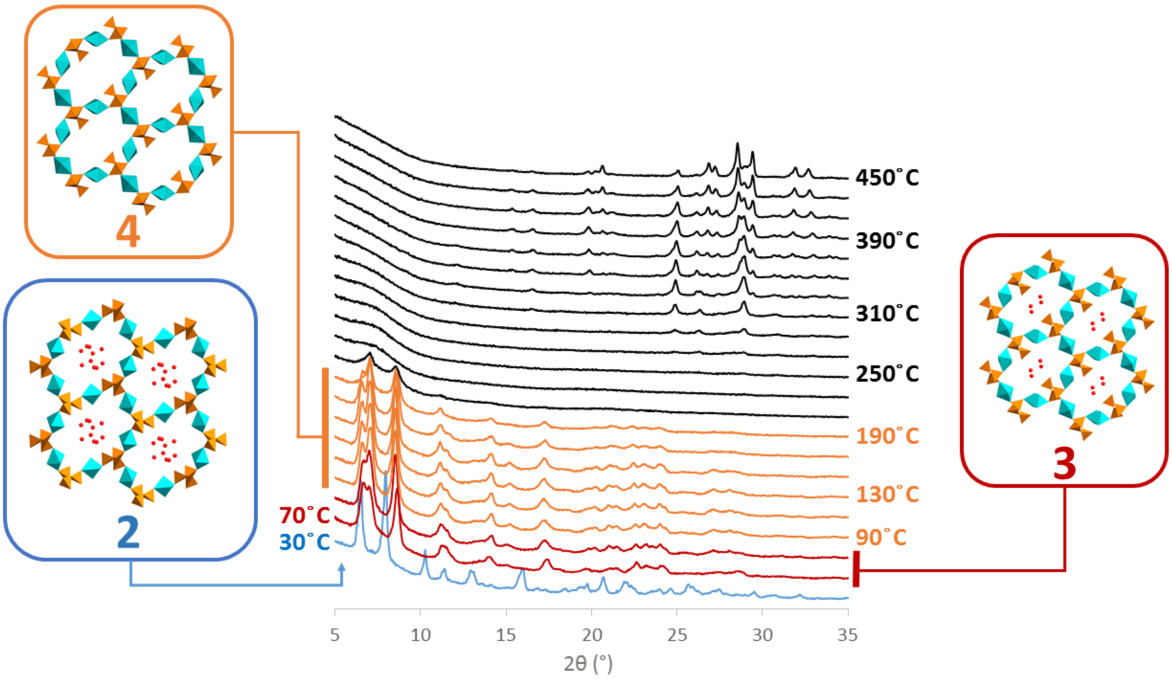

Figure A2.3. Variable temperature PXRD patterns of **1–CuV** from 30 to 450 °C.

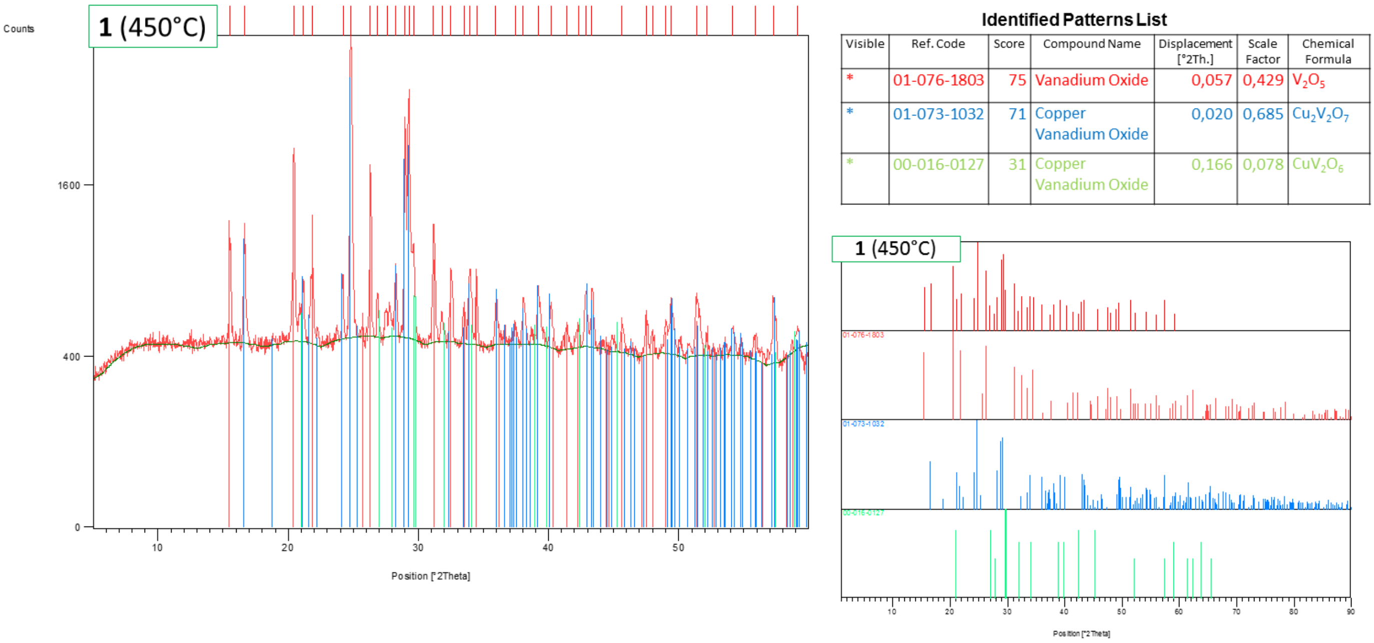

Identified Patterns List

Visible	Ref. Code	Score	Compound Name	Displacement [°2Th.]	Scale Factor	Chemical Formula
*	01-076-1803	75	Vanadium Oxide	0,057	0,429	V_2O_5
*	01-073-1032	71	Copper Vanadium Oxide	0,020	0,685	$Cu_2V_2O_7$
*	00-016-0127	31	Copper Vanadium Oxide	0,166	0,078	CuV_2O_6

Figure A2.4. Identification of the phases that constitute the final residue of the variable temperature PXRD experiments for compound **1–CuV.**

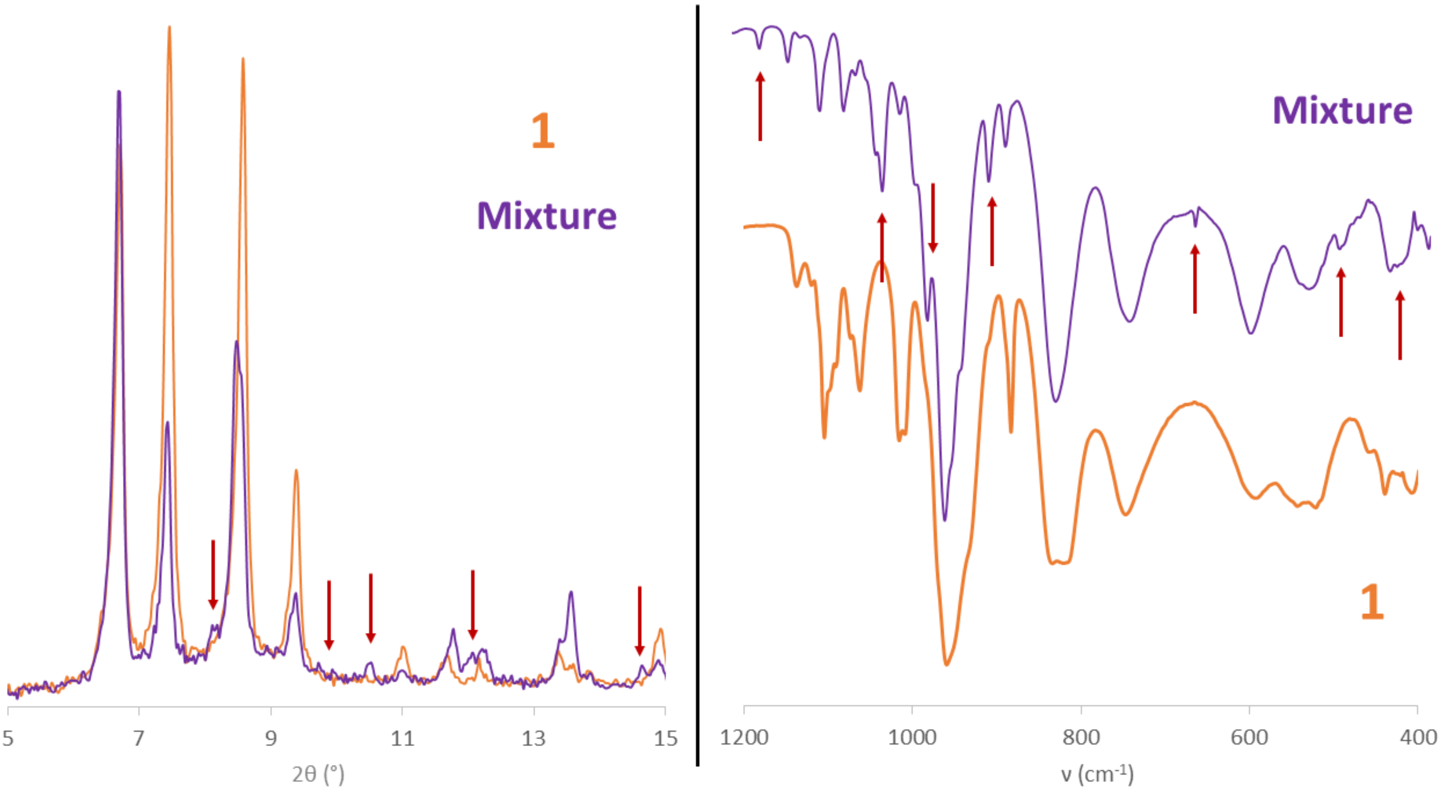

Figure A2.5. Experimental powder X–ray diffraction pattern (left) and FT-IR spectrum (right) of the brown precipitate obtained from the reaction of VO_3^- and $\{Cu(cyclam)\}^{2+}$ complexes in water (pH = 4.6–4.7) compared to those of compound **1–CuV10** in crystalline form. Arrows highlight the signals corresponding to impurities of the bulk material.

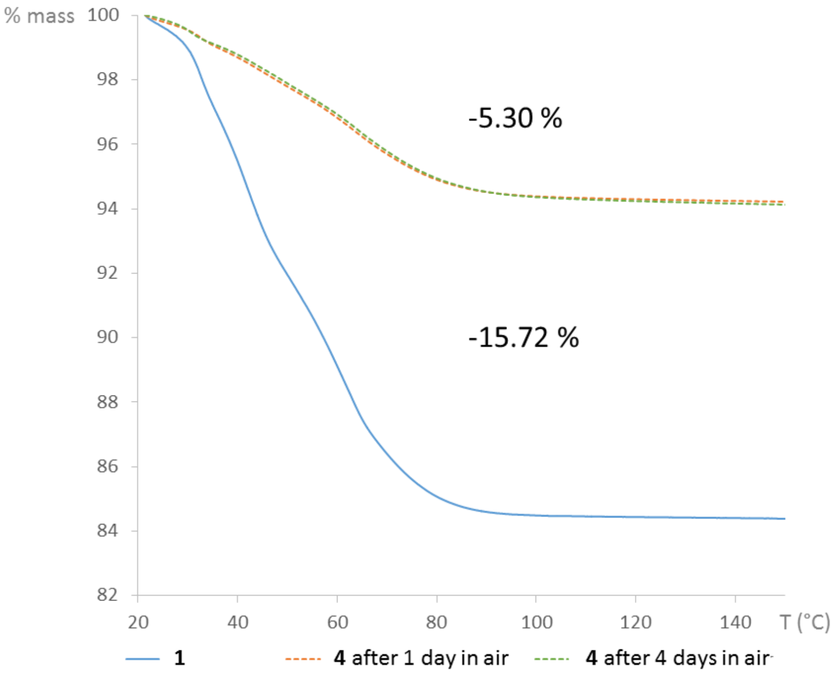

Figure A2.6. Comparative TGA curves for the dehydration of **1–CuV** and the resulting anhydrous **4–CuV** after being exposed to air for 1 and 4 days**.**

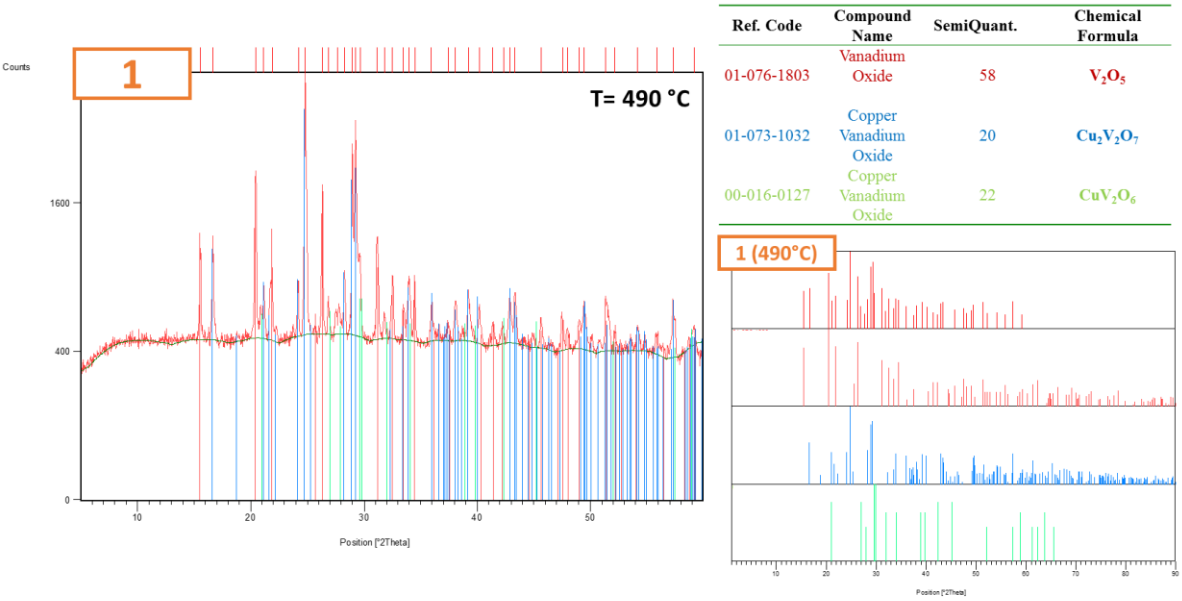

Ref. Code	Compound Name	SemiQuant.	Chemical Formula
01-076-1803	Vanadium Oxide	58	V_2O_5
01-073-1032	Copper Vanadium Oxide	20	$Cu_2V_2O_7$
00-016-0127	Copper Vanadium Oxide	22	CuV_2O_6

Figure A2.7. Identification by powder X–ray diffraction of the phases forming the final residue in the thermal decomposition of compound **1–CuV10.**

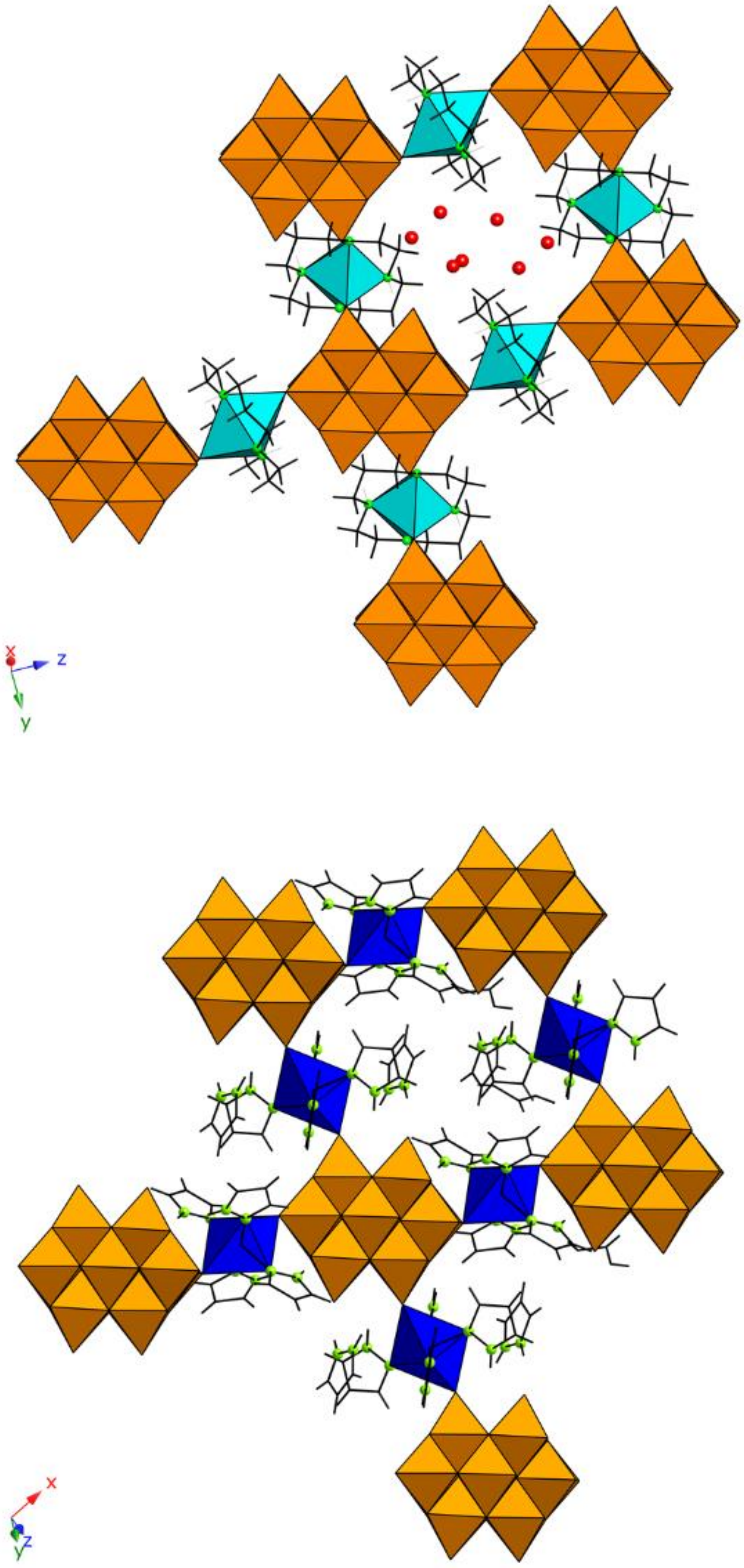

Figure A2.8. Structural relationship between the hybrid layers in **1–CuV10** and those described for $(Hpz)_2[\{Cu(pz)_4\}_2(V_{10}O_{28})]\cdot 2H_2O$ (pz = pyrazole). See the following reference for more information: Thomas, J.; Agarwal, M.; Ramanan, A.; Chernova, N.; Whittingham, M. S. *CrystEngComm* **2009**, *11*, 625–631.

3. THERMALLY TRIGGERED SCSC TRANSFORMATIONS UPON GRADUAL DEHYDRATION IN ISO– AND LANTHANIDE-SUBSTITUTED HETERO–POLYOXOTUNGSTATES

Figures A3:

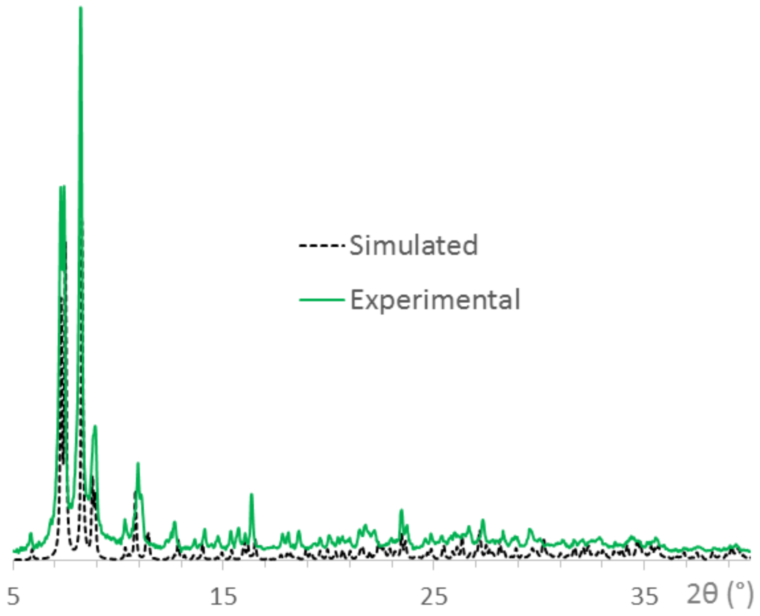

Figure A3.1. Comparison between the experimental powder X–ray diffraction pattern of **1-CuW7** and that simulated from single–crystal X–ray diffraction data.

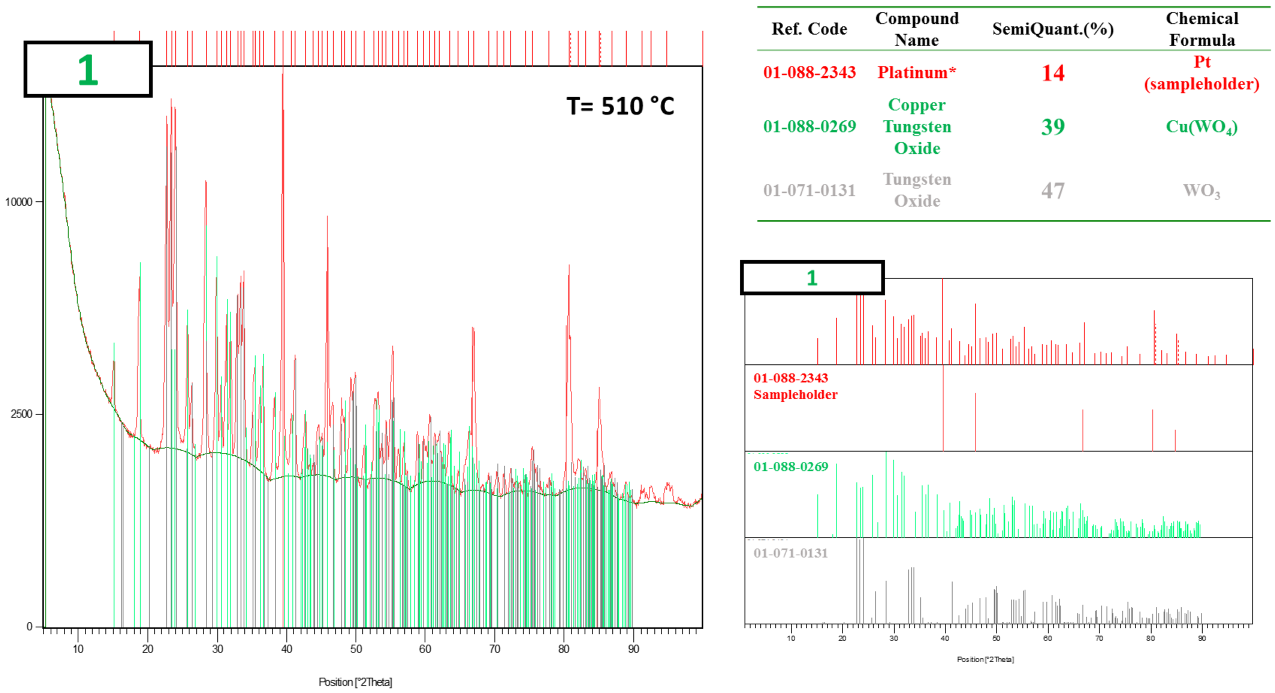

Ref. Code	Compound Name	SemiQuant.(%)	Chemical Formula
01-088-2343	Platinum*	14	Pt (sampleholder)
01-088-0269	Copper Tungsten Oxide	39	$Cu(WO_4)$
01-071-0131	Tungsten Oxide	47	WO_3

Figure A3.2. Identification of the phases forming the final residue in the thermal decomposition of **1–CuW7.**

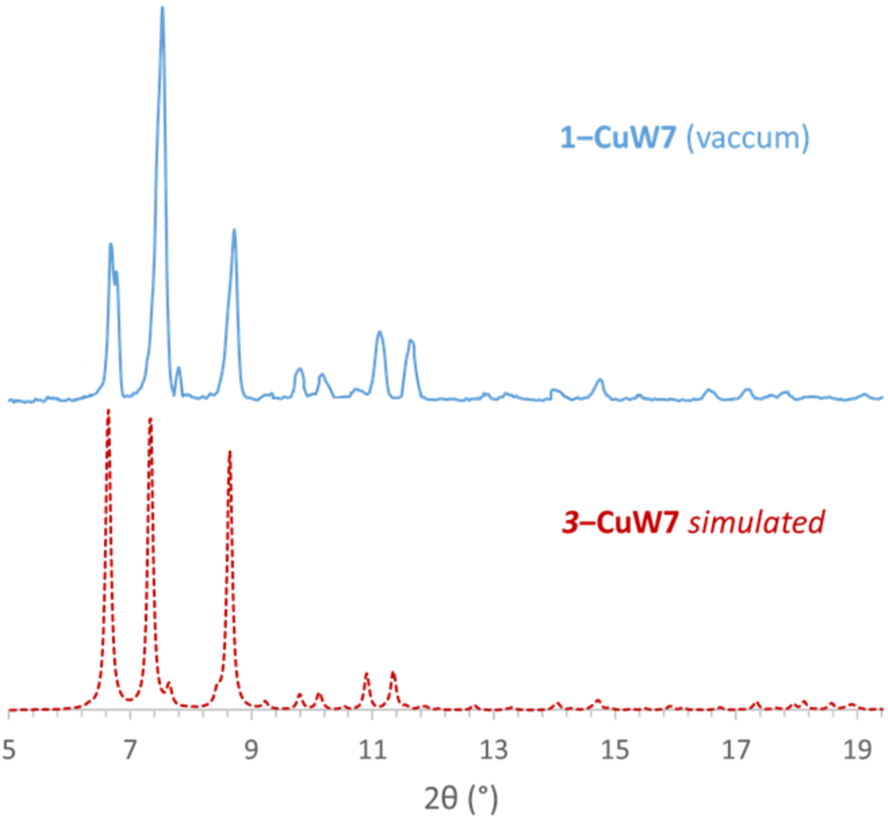

Figure A3.3. Comparison of the PXRD patterns of a sample of **1–CuW7** under vaccumm with that simulated for **3-CuW7.**

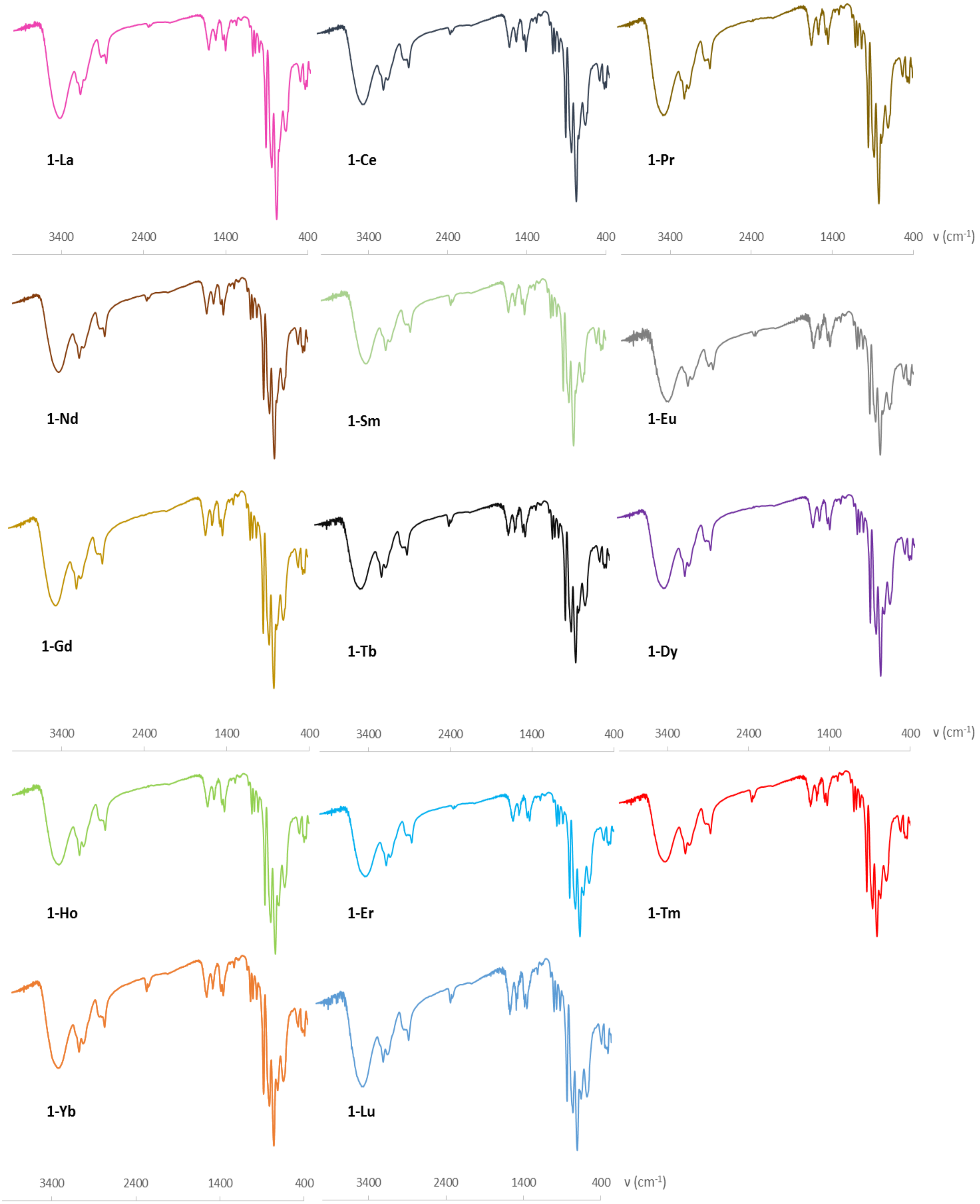

Figure A3.4. FT–IR spectra of **1–Ln** compounds.

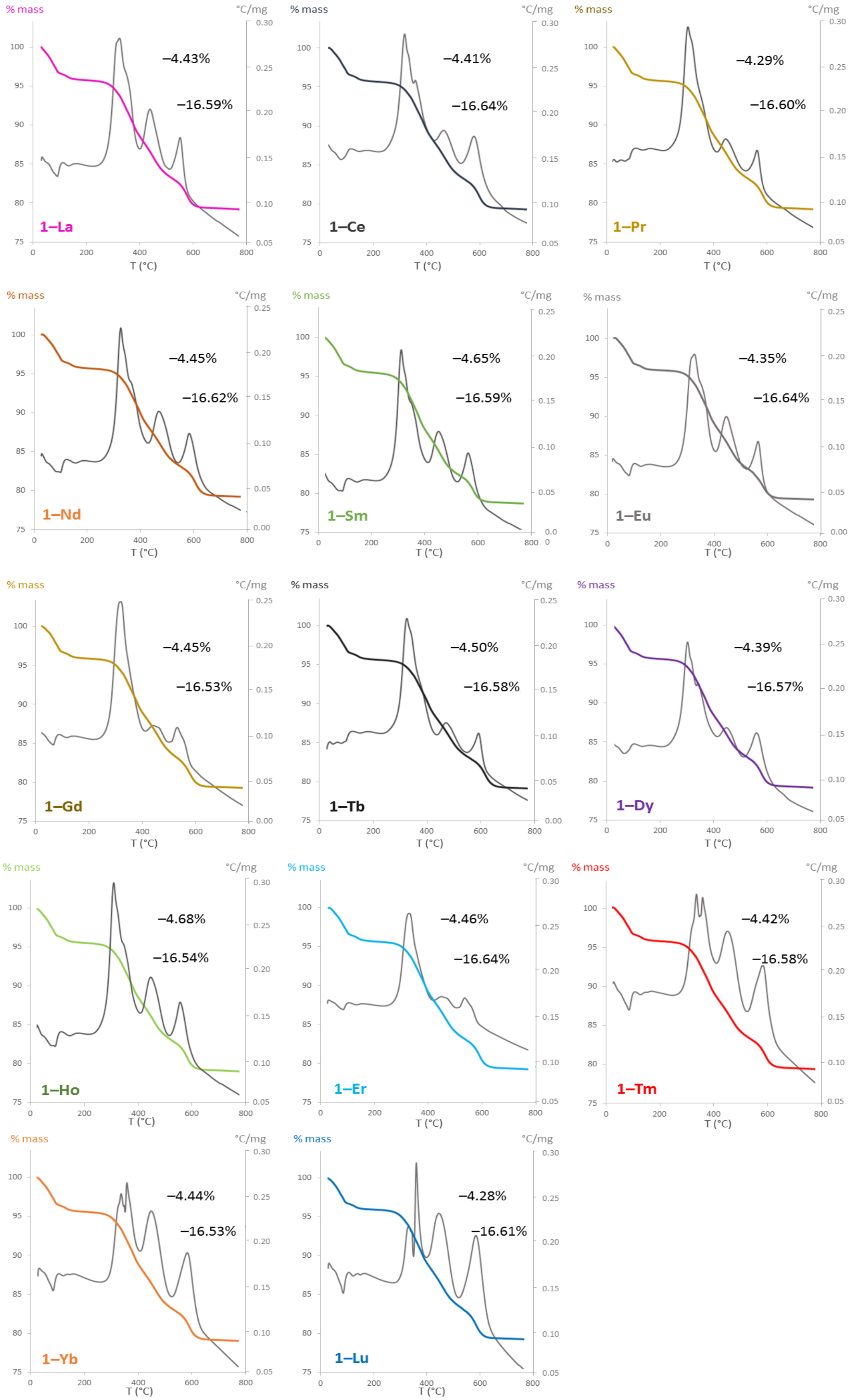

Figure A3.5. TGA/DTA curves of **1–Ln** compounds.

Figure A3.6. Comparison between the experimental powder X–ray diffraction patterns of **1–Ln** compounds with the corresponding simulated PXD patterns from single–crystal X–ray diffraction data.

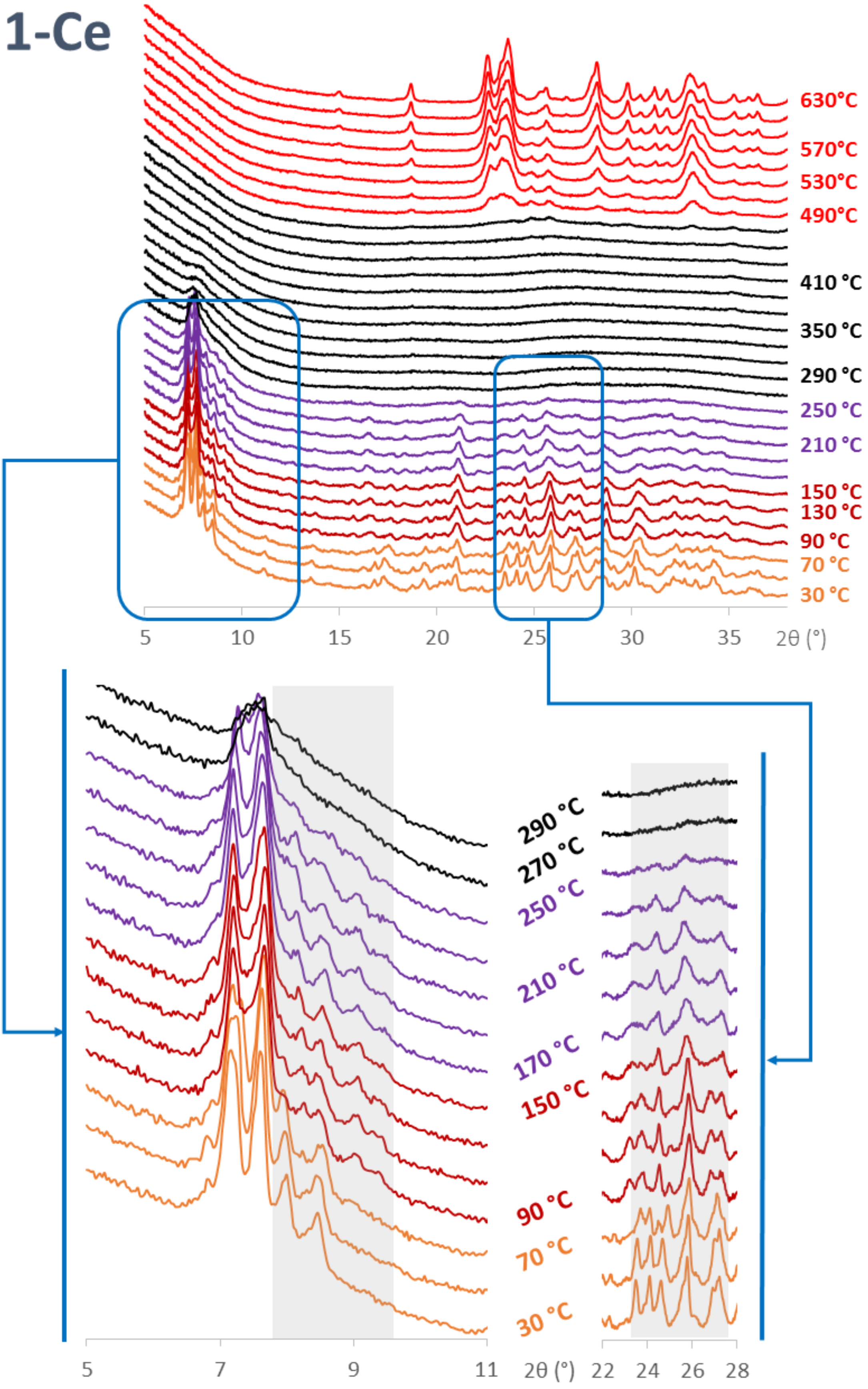

Figure A3.7. Details of the variable–temperature PXD patterns of **1–Ce.**

1-Eu

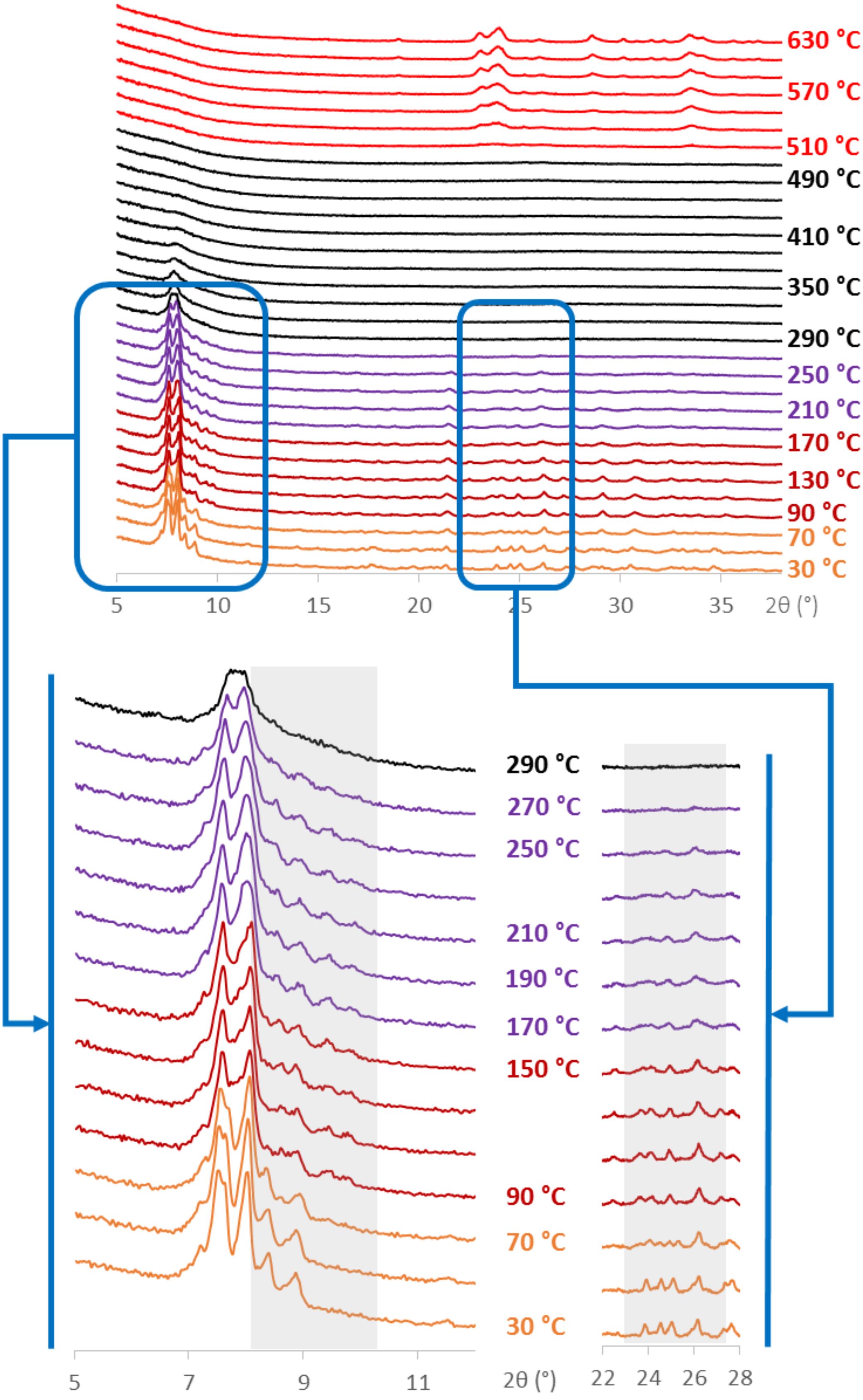

Figure A3.8. Details of the variable–temperature PXD patterns of **1–Eu.**

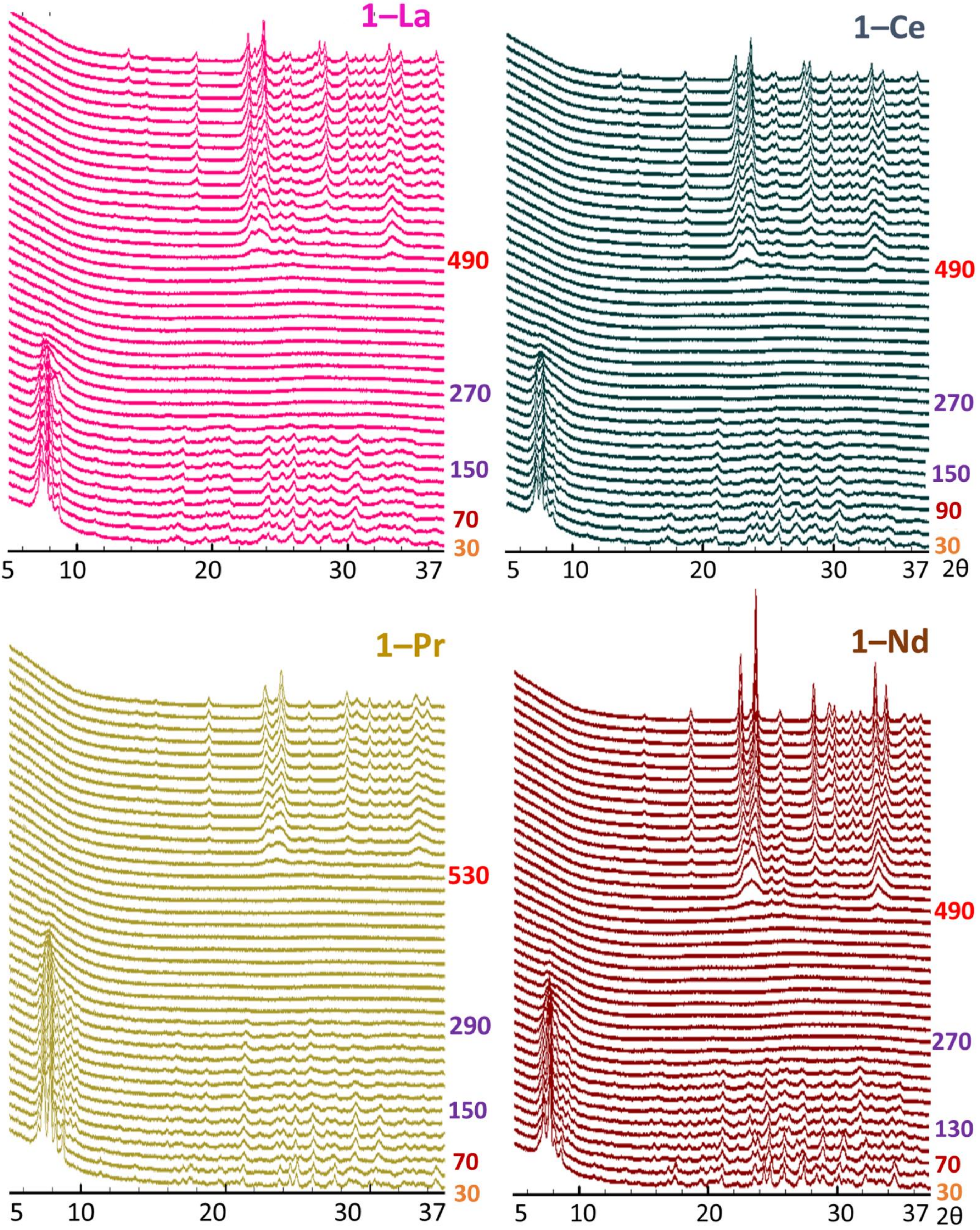

Figure A3.9. Variable–temperature PXD patterns of **1–Ln** (Ln = La–Nd).

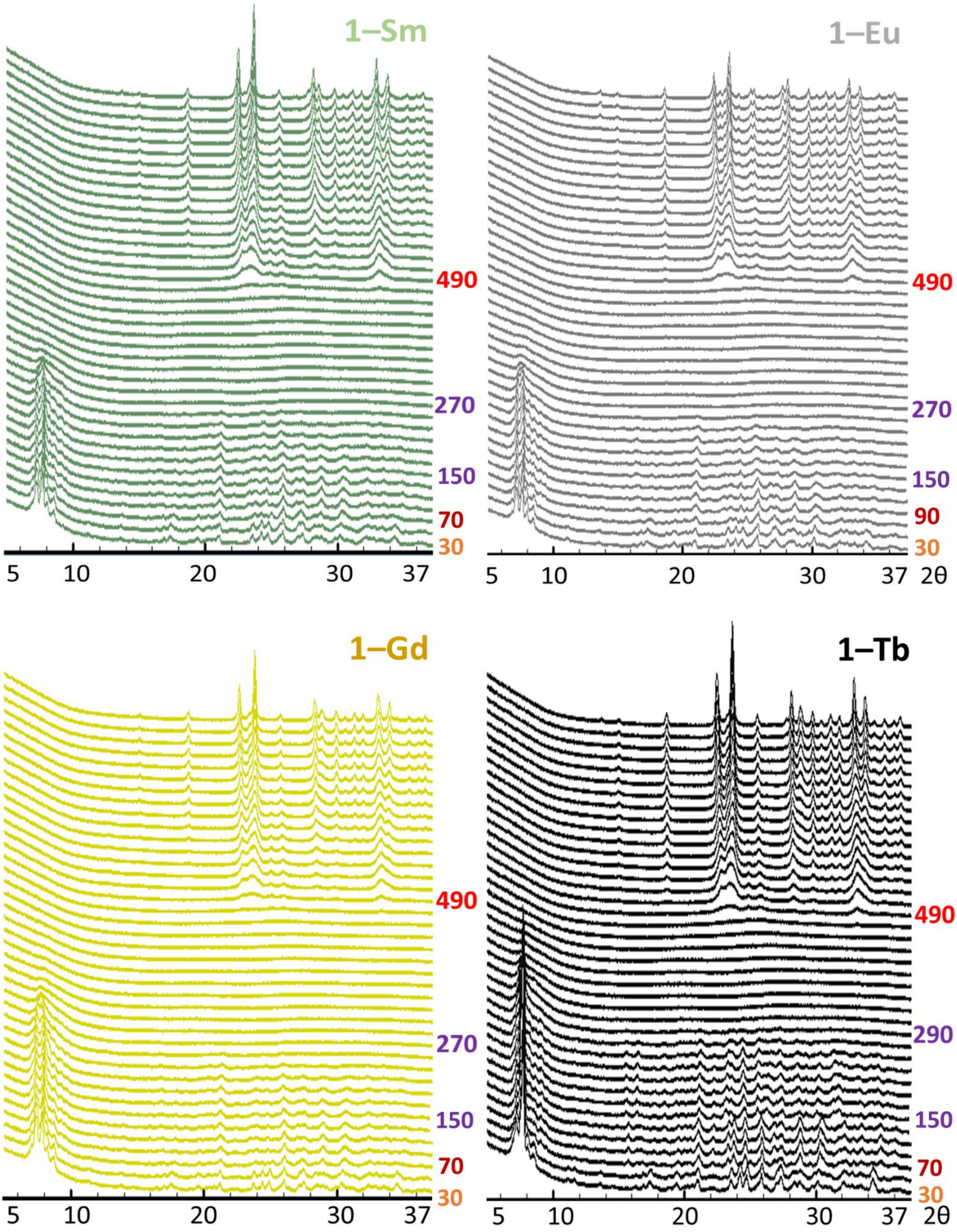

Figure A3.10. Variable–temperature PXD patterns of **1–Ln** (Ln = Sm–Tb).

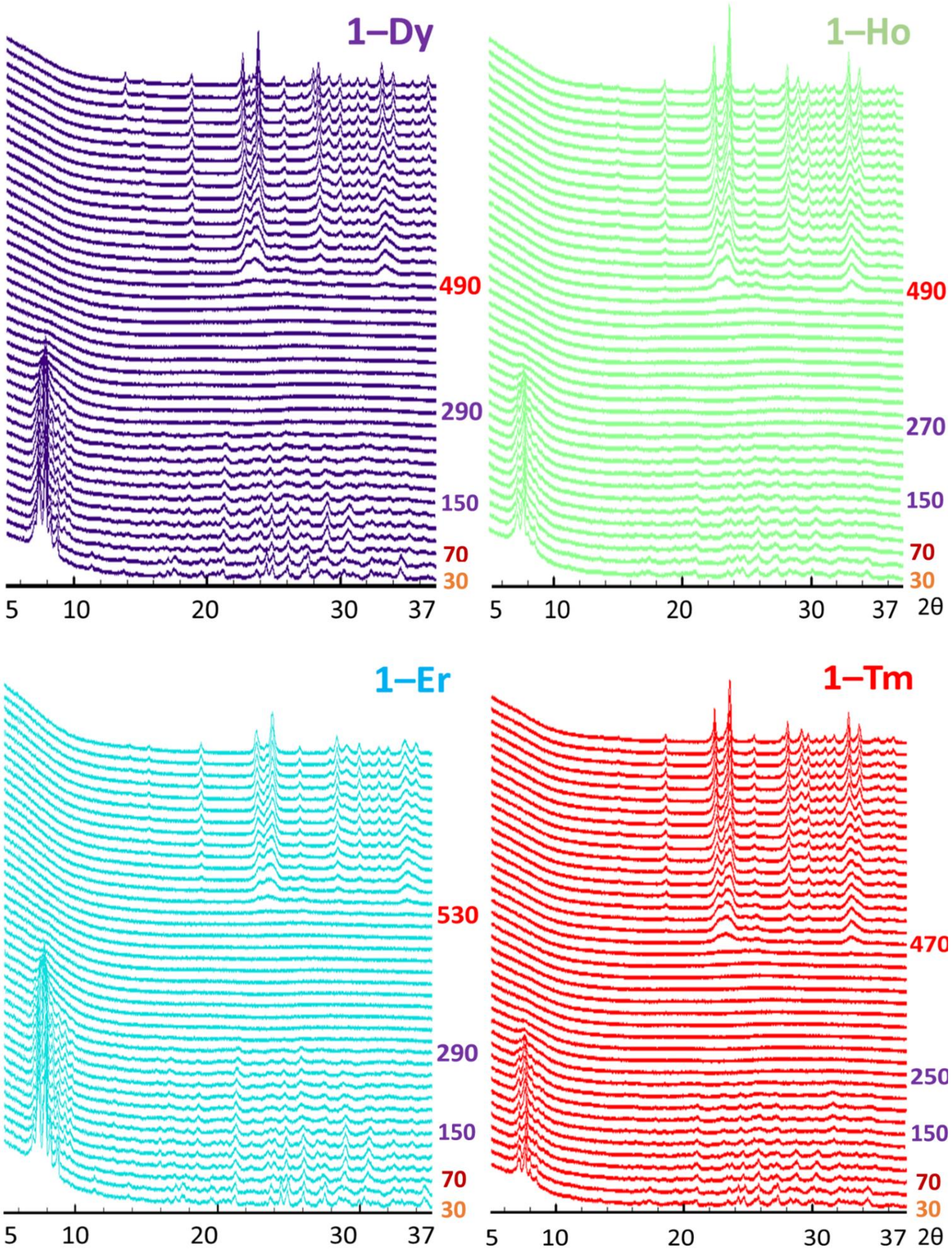

Figure A3.11. Variable–temperature PXD patterns of **1–Ln** (Ln = Dy–Tm).

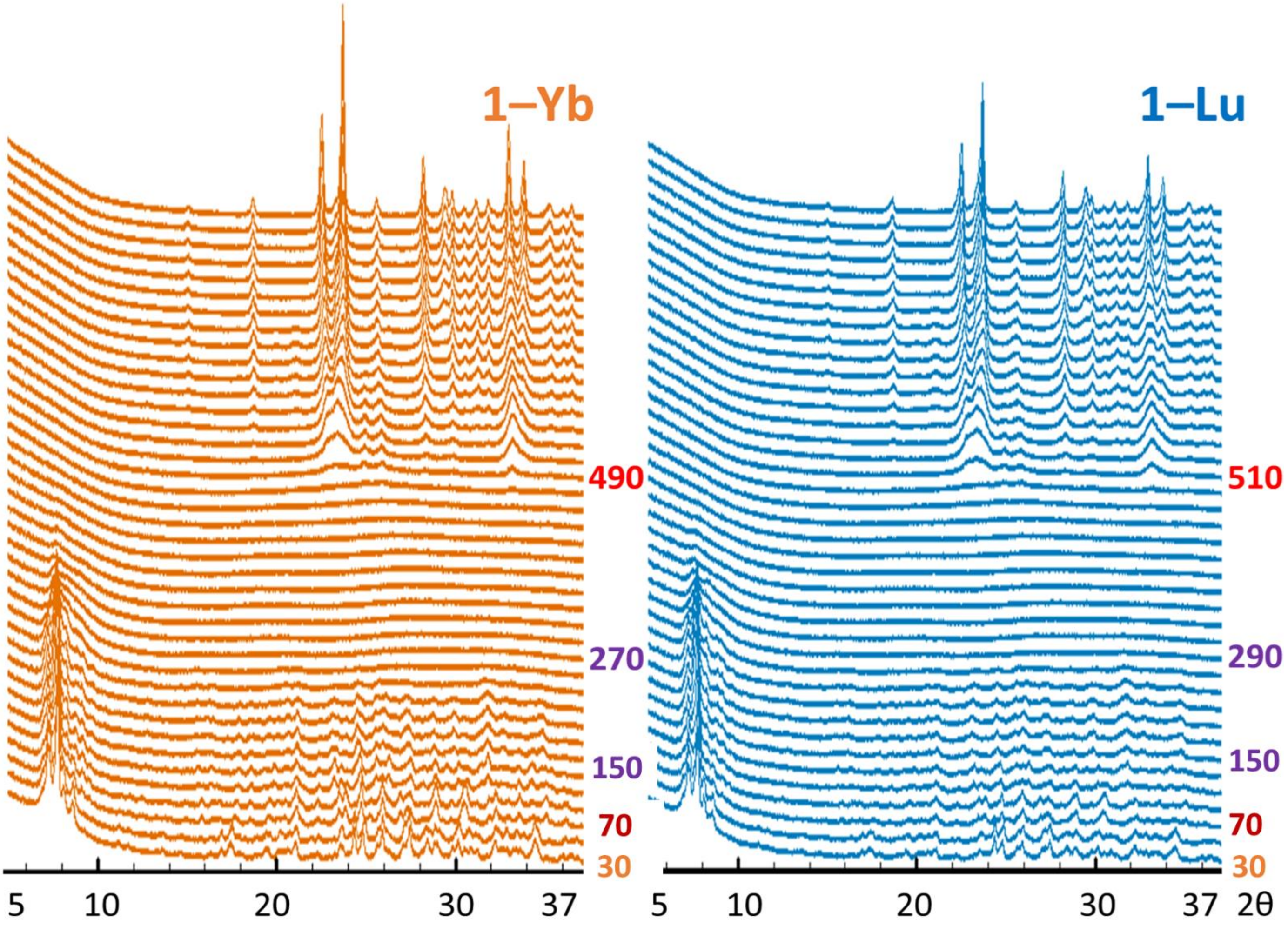

Figure A3.12. Variable–temperature PXD patterns of **1–Ln** (Ln = Yb–Lu).

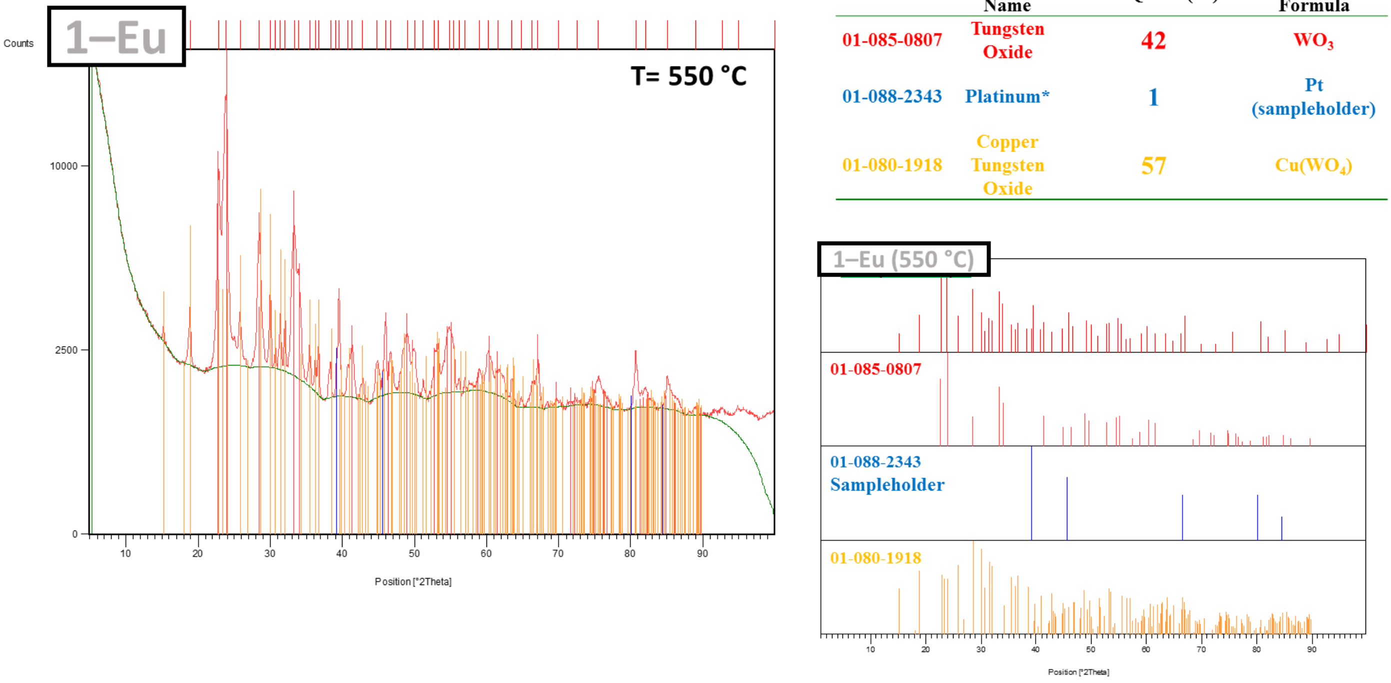

Ref. Code	Compound Name	SemiQuant.(%)	Chemical Formula
01-085-0807	Tungsten Oxide	42	WO_3
01-088-2343	Platinum*	1	Pt (sampleholder)
01-080-1918	Copper Tungsten Oxide	57	$Cu(WO_4)$

Figure A3.13. Identification of the phases forming the final residue in the thermal decomposition of **1–Eu.**

Ref. Code	Compound Name	SemiQuant.(%)	Chemical Formula
01-085-0807	Tungsten Oxide	36	WO_3
01-088-0269	Scheelite (Cu-exchanged)	56	$Cu(WO_4)$
01-088-2343	Platinum*	8	Pt (sampleholder)

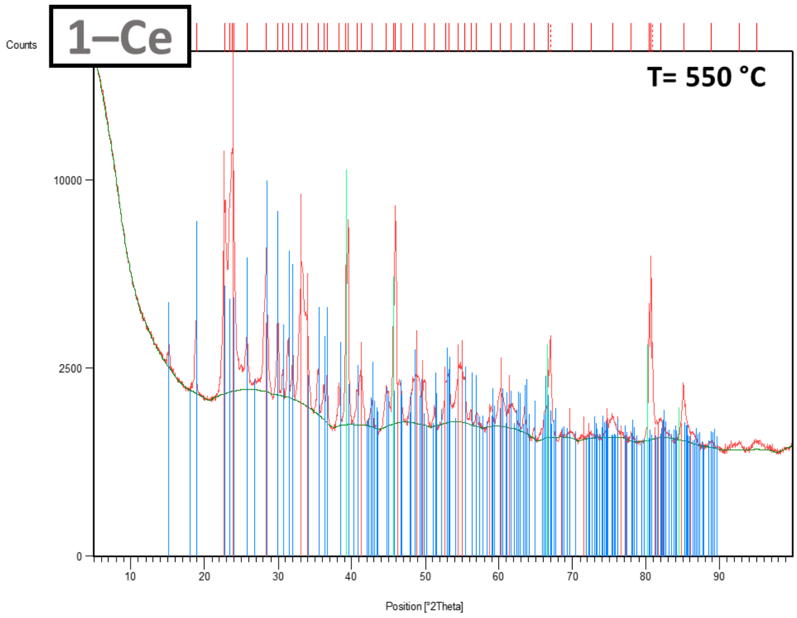

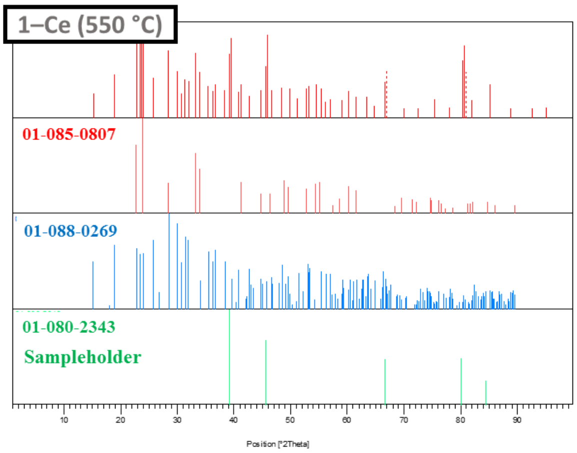

Figure A3.14. Identification of the phases forming the final residue in the thermal decomposition of **1–Ce.**

Ref. Code	Compound Name	SemiQuant.(%)	Chemical Formula
01-070-1732	Copper Tungsten Oxide	55	$Cu(WO_4)$
01-085-0807	Tungsten Oxide)	45	WO_3

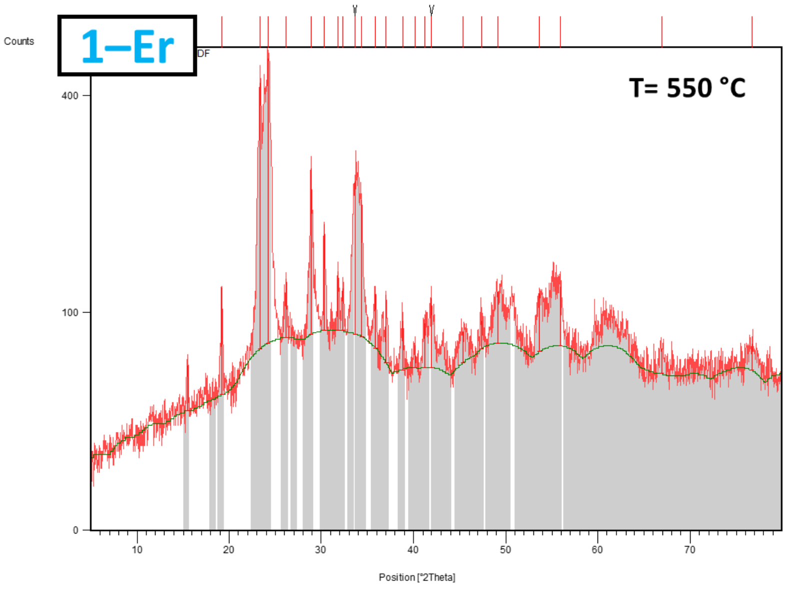

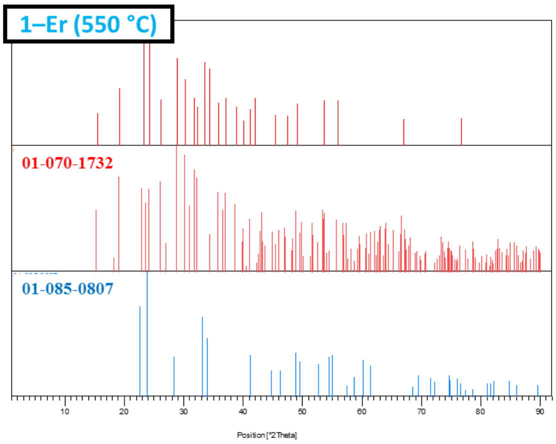

Figure A3.15. Identification of the phases forming the final residue in the thermal decomposition of **1–Er.**

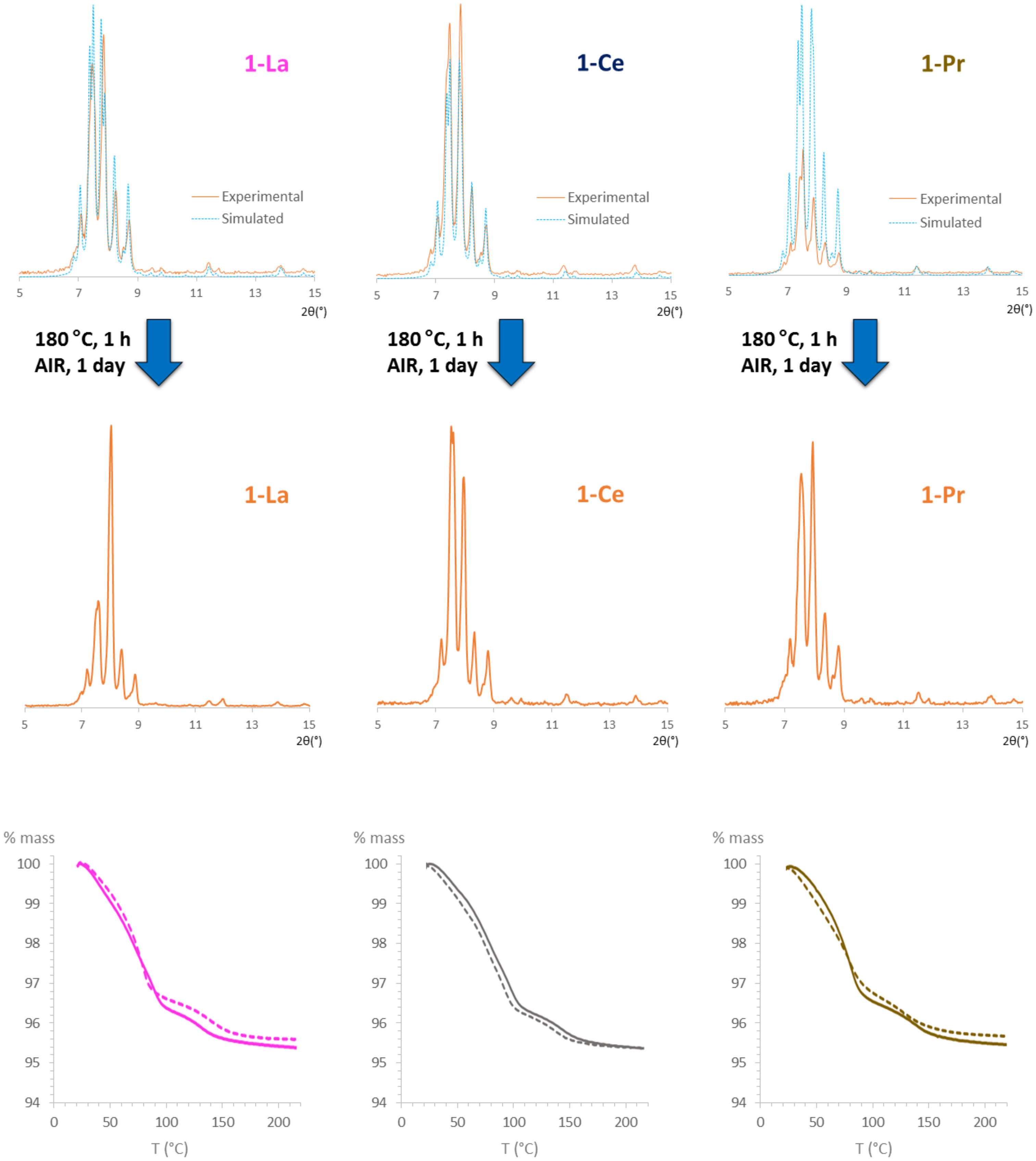

Figure A3.16. PXRD patterns and TGA curves for dehydration/rehydration processes for dehydrated **1–Ln** samples heated to 180 °C one day prior to the measurements (Ln = La–Pr). Dashed line represents the dehydration curve 1 day after the sample was heated.

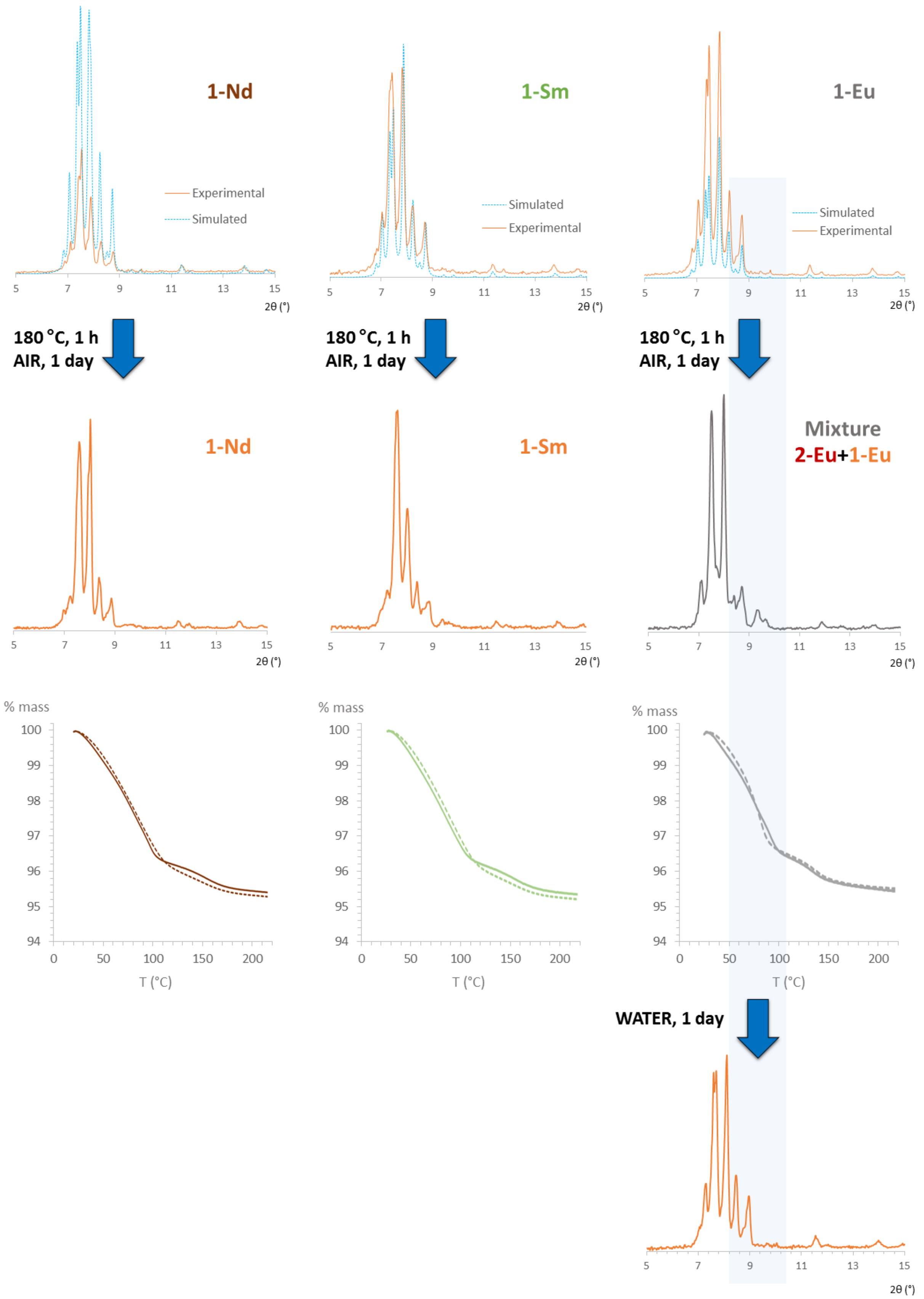

Figure A3.17. PXRD patterns and TGA curves for dehydration/rehydration processes for dehydrated **1–Ln** samples heated to 180 °C one day prior to the measurements (Ln = Nd–Eu). Dashed line represents the dehydration curve 1 day after the sample was heated.

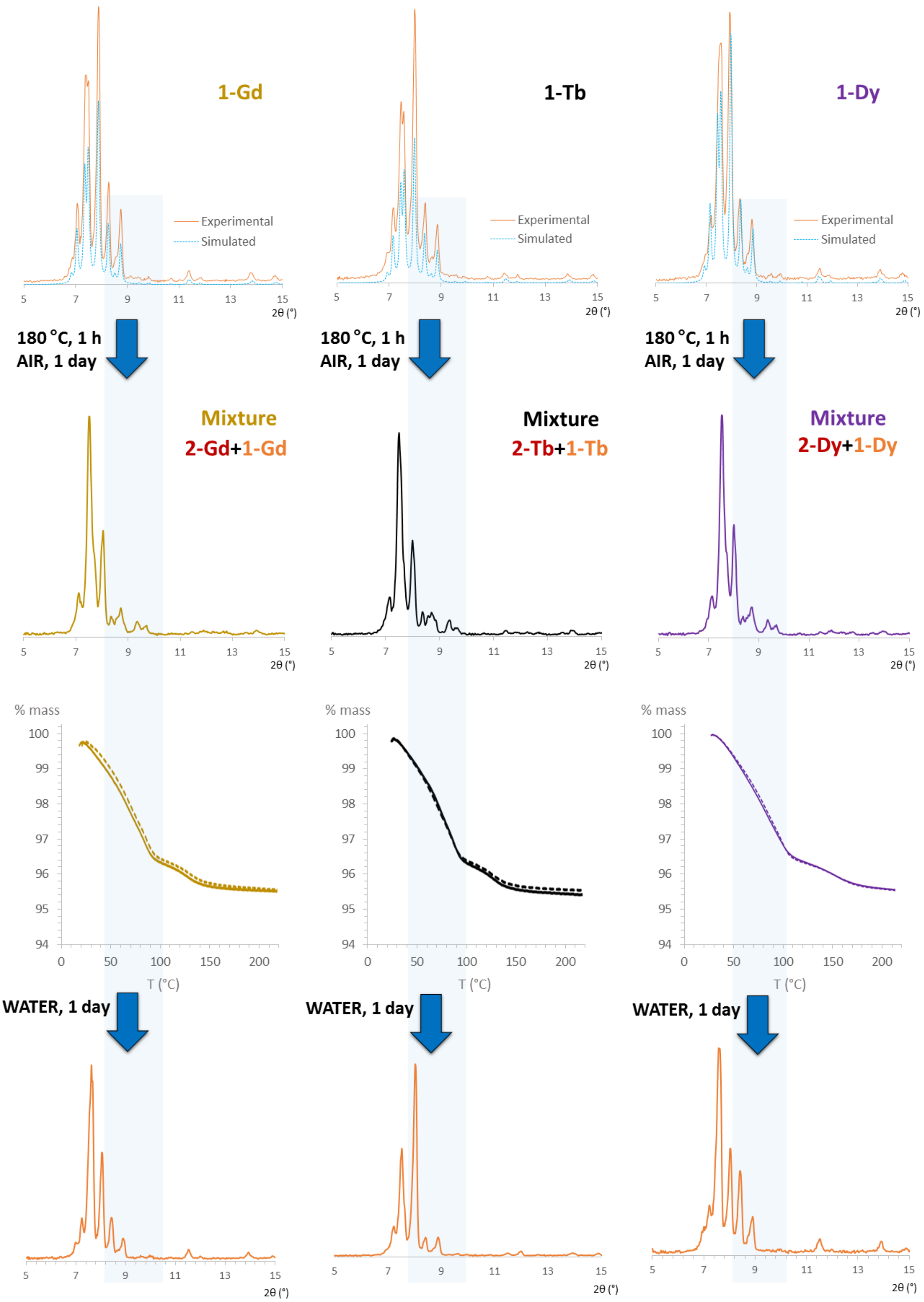

Figure A3.18. PXRD patterns and TGA curves for dehydration/rehydration processes for dehydrated **1–Ln** samples heated to 180 °C one day prior to the measurements (Ln = Gd–Dy). Dashed line represents the dehydration curve 1 day after the sample was heated.

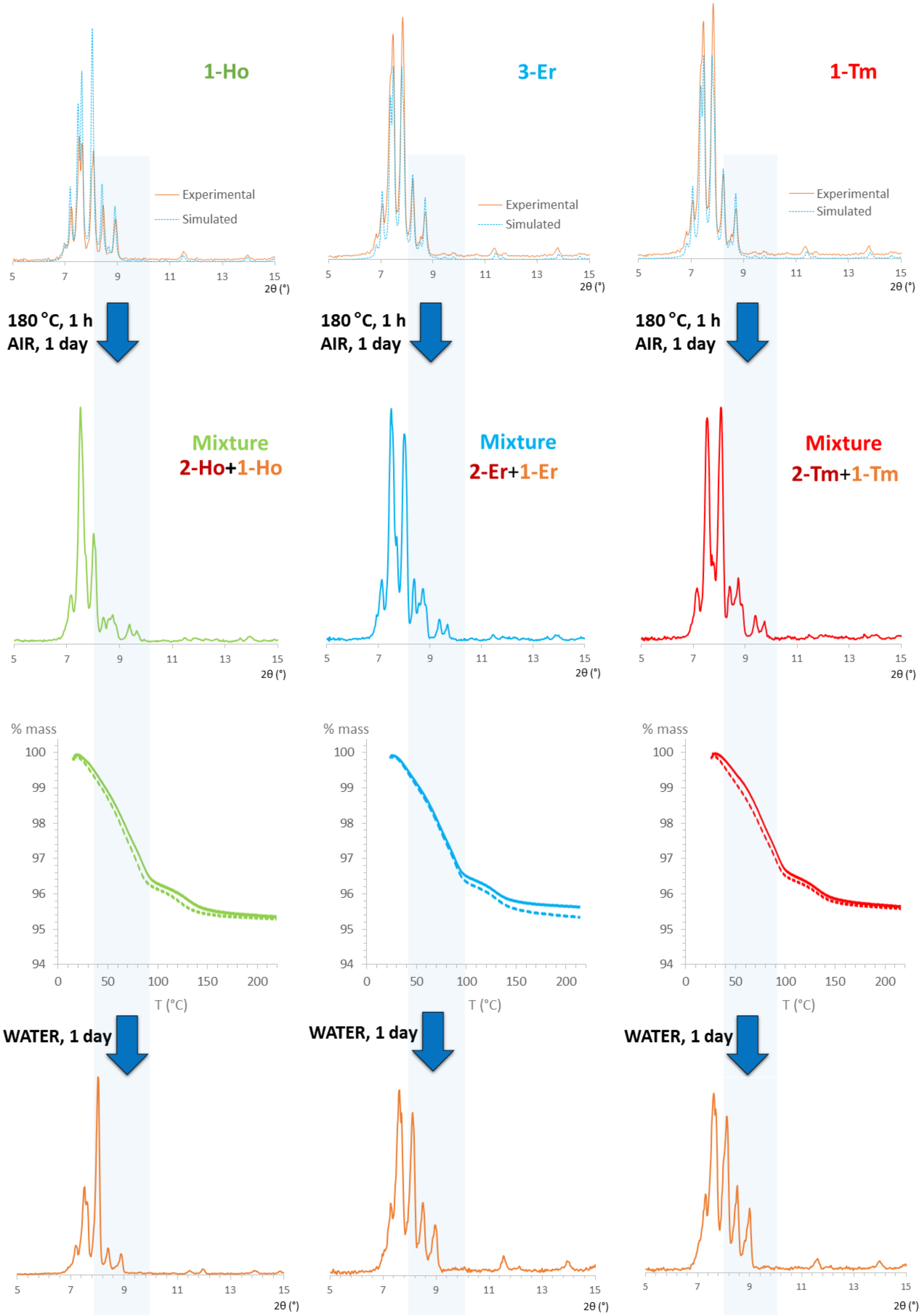

Figure A3.19. PXRD patterns and TGA curves for dehydration/rehydration processes for dehydrated **1–Ln** samples heated to 180 °C one day prior to the measurements (Ln = Ho–Tm). Dashed line represents the dehydration curve 1 day after the sample was heated.

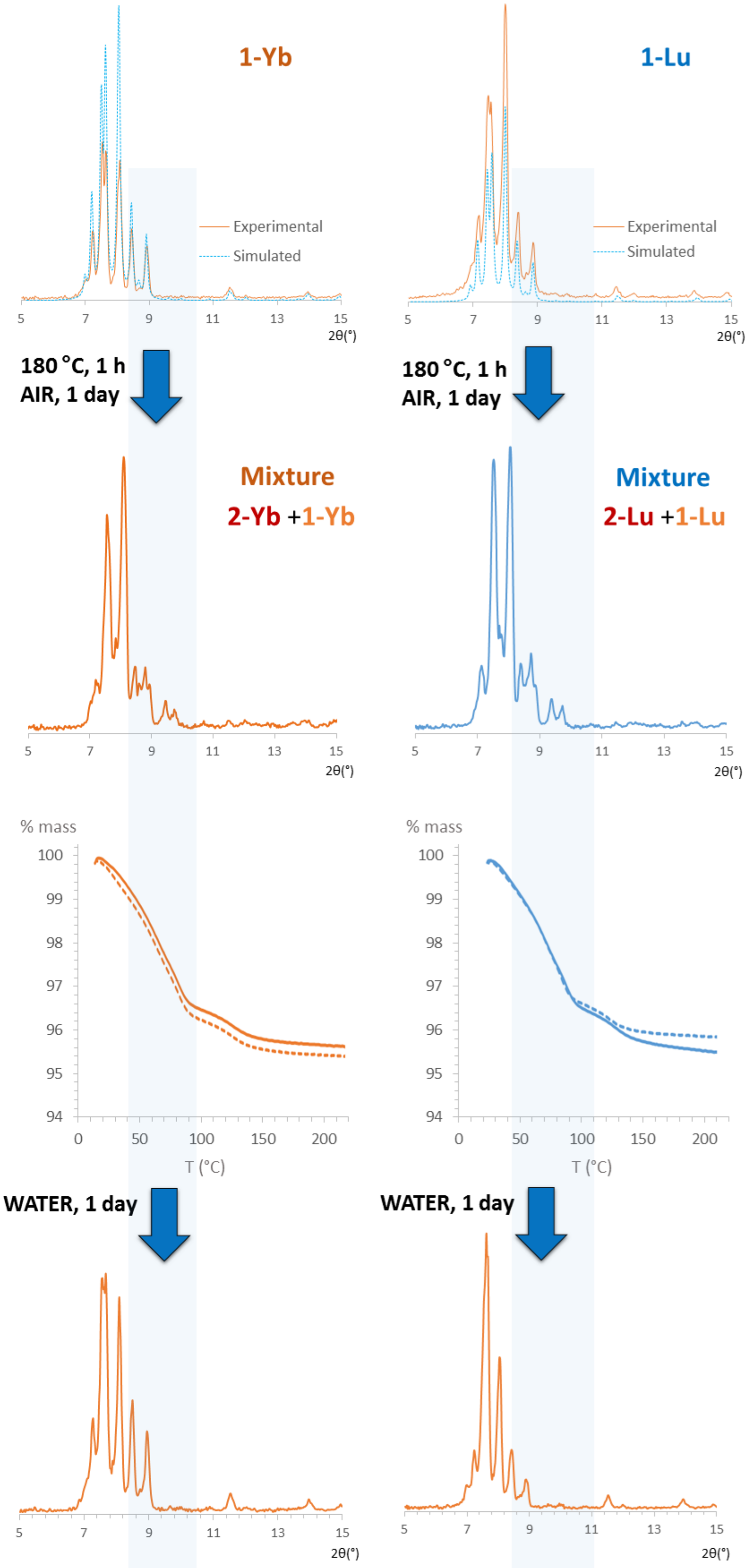

Figure A3.20. PXRD patterns and TGA curves for dehydration/rehydration processes for dehydrated **1–Ln** samples heated to 180 °C one day prior to the measurements (Ln = Yb–Lu). Dashed line represents the dehydration curve 1 day after the sample was heated.

Tables A3:

Tables A3.1. Crystallographic data for **1-Ln** and the rehydrated crystals **1R-Ln** (Ln = Ce, Eu and Er).

	1-Ce	**1R–Ce**	**1-Eu**	**1R–Eu**	**1-Er**	**1R–Er**
Empirical formula	$C_{64}H_{190}Cu_6Ce_2Ge_2N_{24}O_{102}W_{22}$	$C_{64}H_{190}Cu_6Ce_2Ge_2N_{24}O_{102}W_{22}$	$C_{64}H_{188}Cu_6Eu_2Ge_2N_{24}O_{101}W_{22}$	$C_{64}H_{188}Cu_6Eu_2Ge_2N_{24}O_{101}W_{22}$	$C_{64}H_{190}Cu_6Er_2Ge_2N_{24}O_{102}W_{22}$	$C_{64}H_{190}Cu_6Er_2Ge_2N_{24}O_{102}W_{22}$
fw (g mol^{-1})	7779.76	7779.75	7785.42	7785.42	7834.03	7834.03
crystal system	triclinic	triclinic	triclinic	triclinic	Triclinic	Triclinic
space group	P–1	P–1	P–1	P–1	P–1	P–1
T (K)	100(2)	100(2)	100(2)	100(2)	100(2)	100(2)
a (Å)	13.5968(3)	13.5049(6)	13.5580(3)	13.6301(2)	13.6108(4)	13.6233(2)
b (Å)	13.8641(3)	13.7493(4)	13.8266(3)	13.8798(2)	13.8628(3)	13.8868(2)
c (Å)	23.1308(4)	22.9427(8)	22.9904(6)	23.0003(4)	22.8601(5)	23.1054(4)
α (°)	92.4830(16)	92.277(3)	92.667(2)	92.7678(14)	92.7378(19)	92.7908(14)
β (°)	99.6151(18)	100.038(4)	99.921(2)	99.8584(13)	100.061(2)	99.6928(14)
γ (°)	110.184(2)	110.147(4)	110.057(2)	110.0622(14)	110.005(2)	110.0975(15)
V (Å^3)	4010.96(14)	3915.2(3)	3961.79(17)	3999.86(12)	3963.69(18)	4019.50(12)
ρ_{calc} (g cm^{-3})	3.221	3.300	3.263	3.232	3.282	3.236
K_α (Å)	1.54184	0.71073	0.71073	1.54184	1.54184	1.54184
μ (mm^{-1})	34.661	17.927	17.932	35.965	32.602	32.149
collected reflns	31190	29360	27080	29896	30567	30227
unique reflns (R_{int})	14298 (0.059)	13597 (0.0832)	13965 (0.034)	14220 (0.0681)	14114 (0.040)	14310 (0.0693)
obsd reflns [$I > 2\sigma(I)$]	12415	10050	11766	11883	12701	12457
parameters	541	512	530	530	540	536
$R(F)^a$ [$I > 2\sigma(I)$]	0.048	0.0855	0.039	0.0733	0.041	0.0772
$wR(F^2)^b$ [all data]	0.129	0.2006	0.090	0.2099	0.103	0.2141
GoF	0.129	1.048	1.059	1.221	1.103	1.075

[a] $R(F)=\Sigma||F_o-F_c||/\Sigma|F_o|$; [b] $wR(F^2)=\{\Sigma[w(F_o^2-F_c^2)^2]/\Sigma[w(F_o^2)^2]\}^{1/2}$

4. Thermostructural studies on multidimensional Strandberg and Anderson-Evans type hybrid heteropolyoxomolybdates

FIGURES 4A:

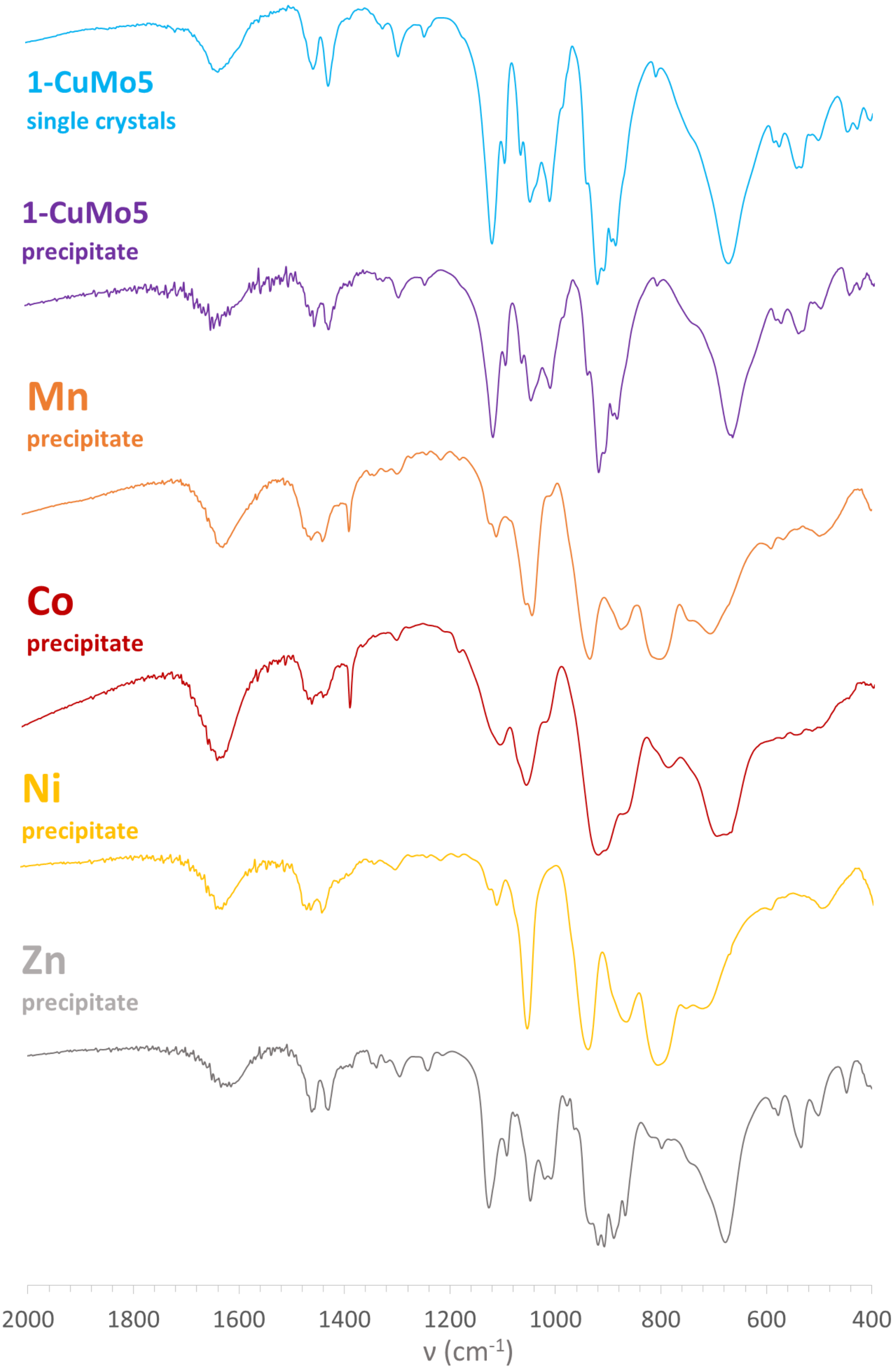

Figure A4.1. Comparison between the FT–IR spectra of single crystal and the precipitate that forms during the reaction of **1–CuMo5** with the precipitate obtained when using other transition metal source.

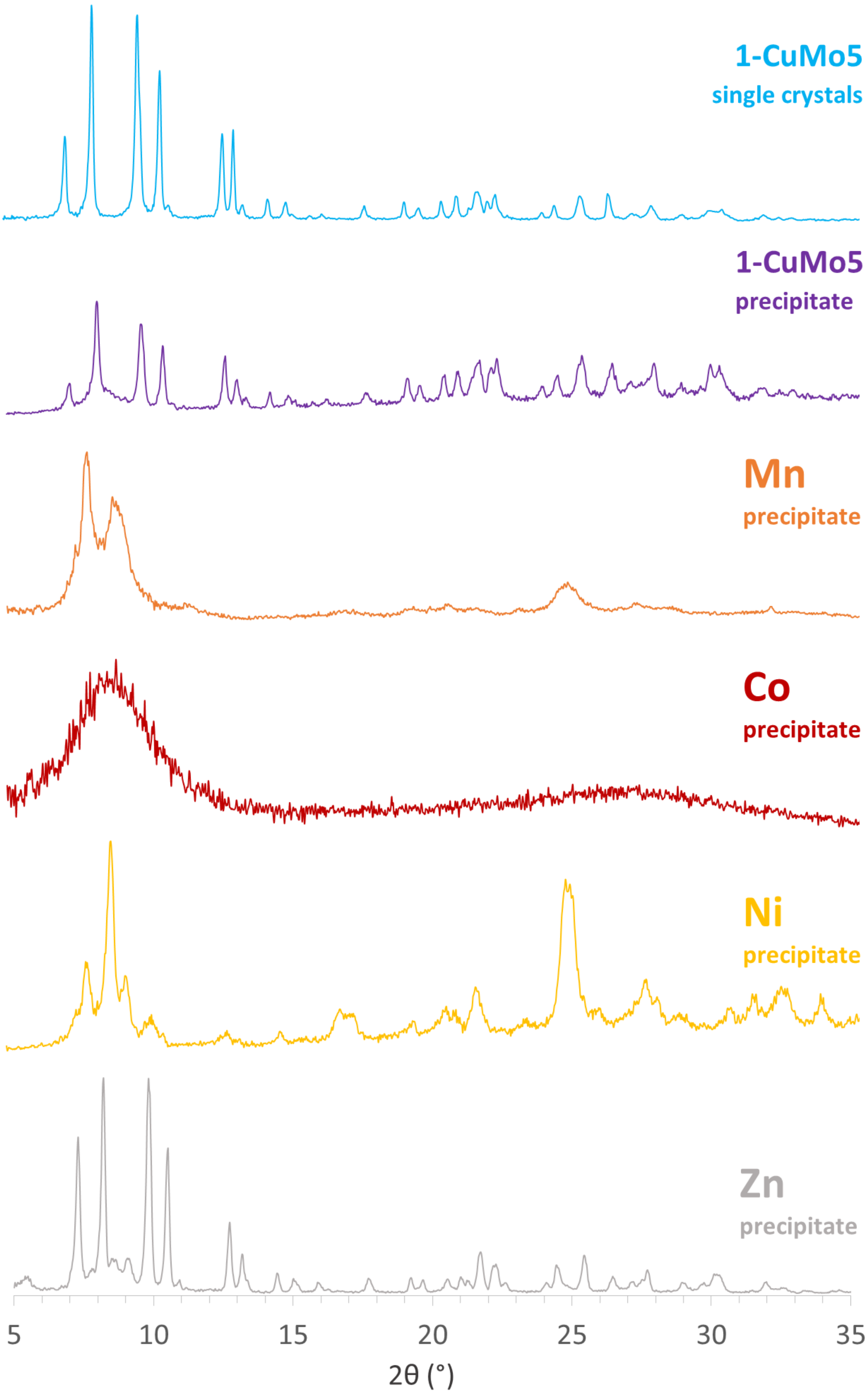

Figure A4.2. Comparison between the PDX patterns of the crystals and the precipitate that forms during the reaction of **1–CuMo5** with the precipitate obtained when using other transition metal source.

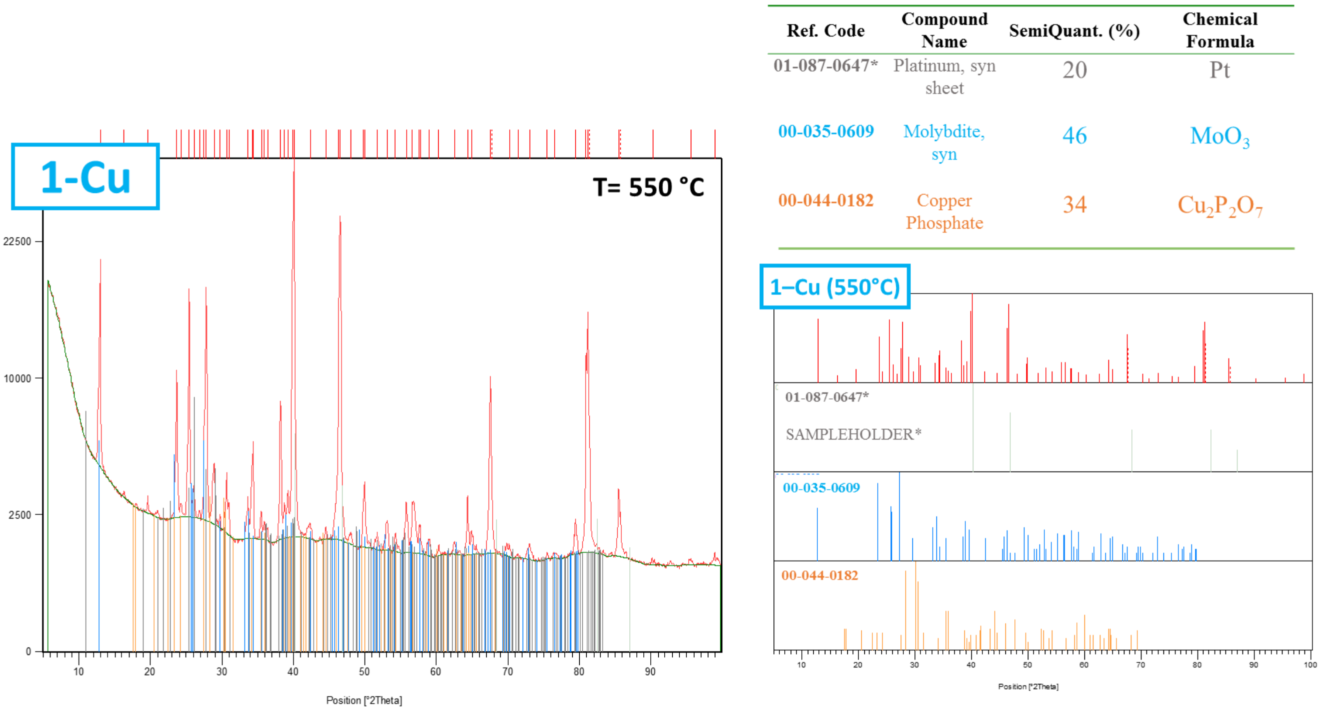

Ref. Code	Compound Name	SemiQuant. (%)	Chemical Formula
01-087-0647*	Platinum, syn sheet	20	Pt
00-035-0609	Molybdite, syn	46	MoO_3
00-044-0182	Copper Phosphate	34	$Cu_2P_2O_7$

Figure A4.3. Identification of the phases that constitute the final residue of the variable temperature PXRD experiments for compound **1–CuMo5.**

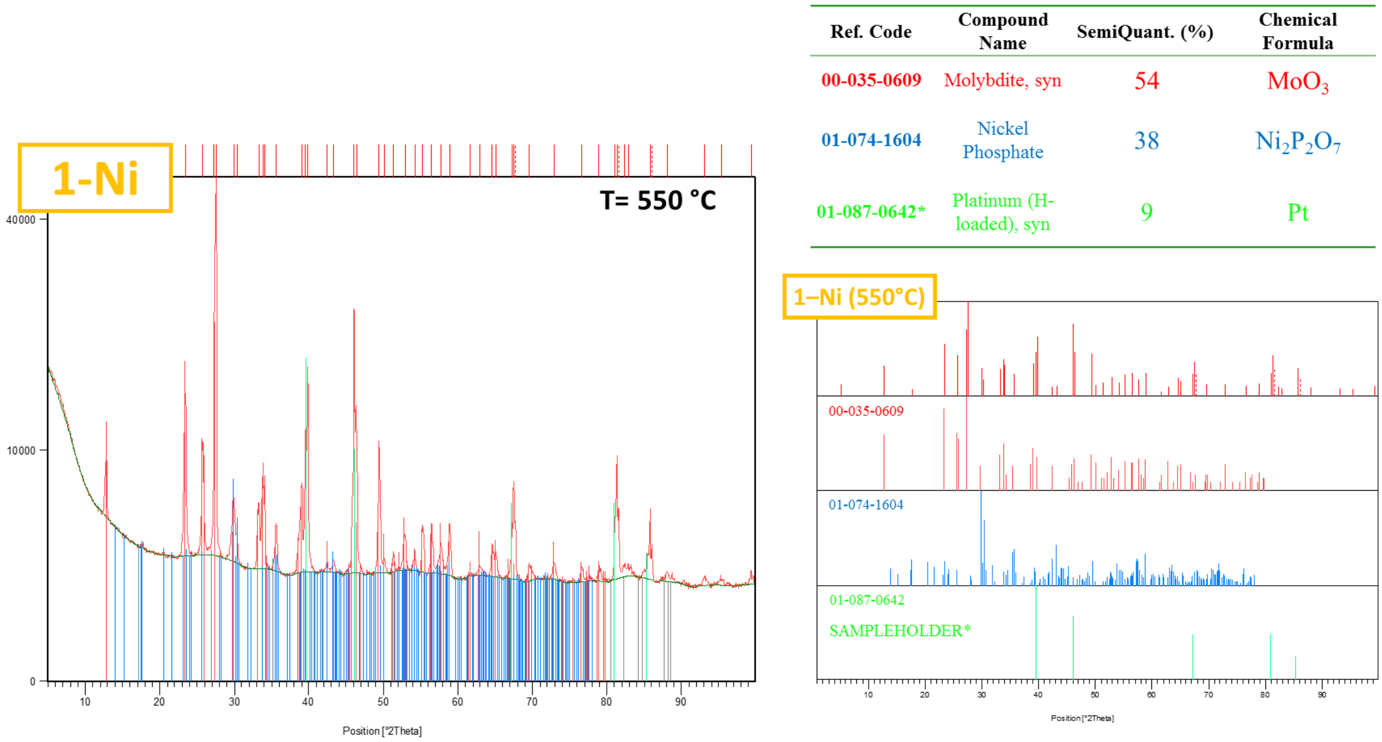

Ref. Code	Compound Name	SemiQuant. (%)	Chemical Formula
00-035-0609	Molybdite, syn	54	MoO_3
01-074-1604	Nickel Phosphate	38	$Ni_2P_2O_7$
01-087-0642*	Platinum (H-loaded), syn	9	Pt

Figure A4.4. Identification of the phases that constitute the final residue of the variable temperature PXRD experiments for compound **1–NiMo5.**

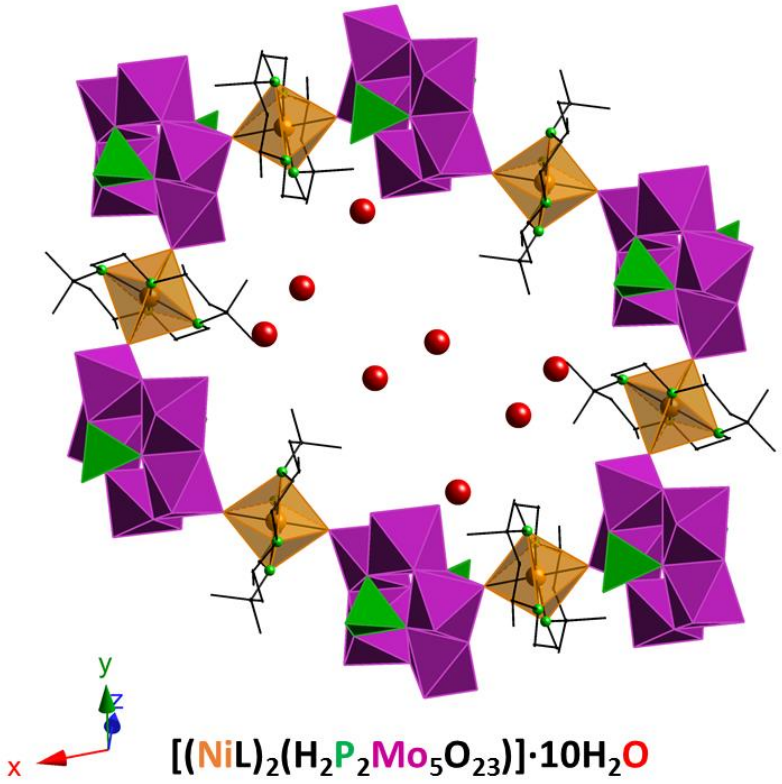

$[(NiL)_2(H_2P_2Mo_5O_{23})]\cdot 10H_2O$

Figure. A4.5. Polyhedral representation of the channels found in the compound reported by Ou and coworkers (L = 5,5,7,12,12,14-hexamethyl-1,4,8,11-tetraazacyclotetradecane). Color code: orange (Ni), violet (Mo), green (P), red (O). Reference 36: Ou, G.-C.; Yuan, X.-Y.; Li, Z.-Z.; Ding, M.-H. *J. Coord. Chem* **2013**, *66*, 2065–2075.

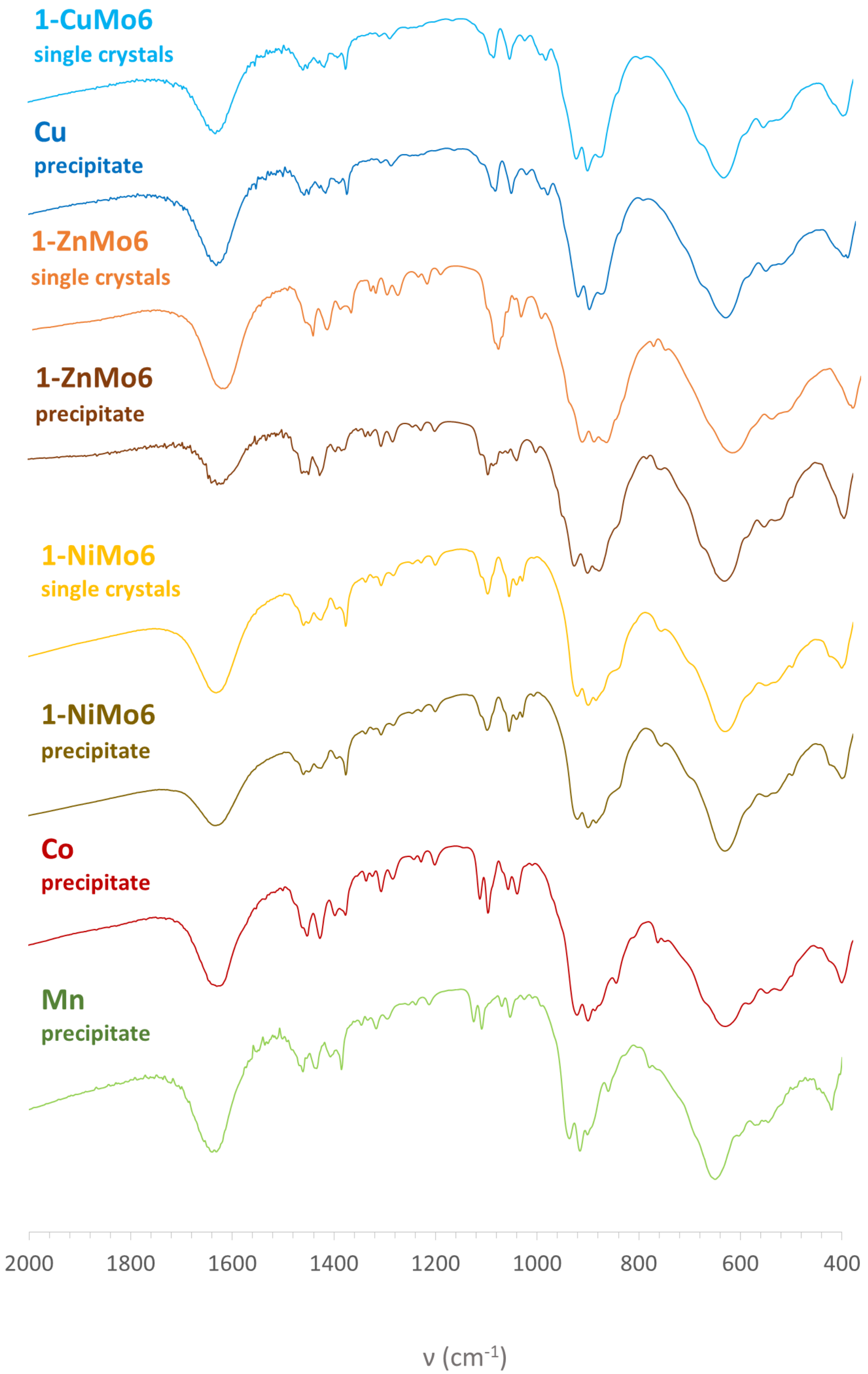

Figure A4.6. Comparison between the FT–IR spectra of single crystal and the precipitate that forms during the reaction of **1–CuMo6** with the precipitate obtained when using other transition metal source.

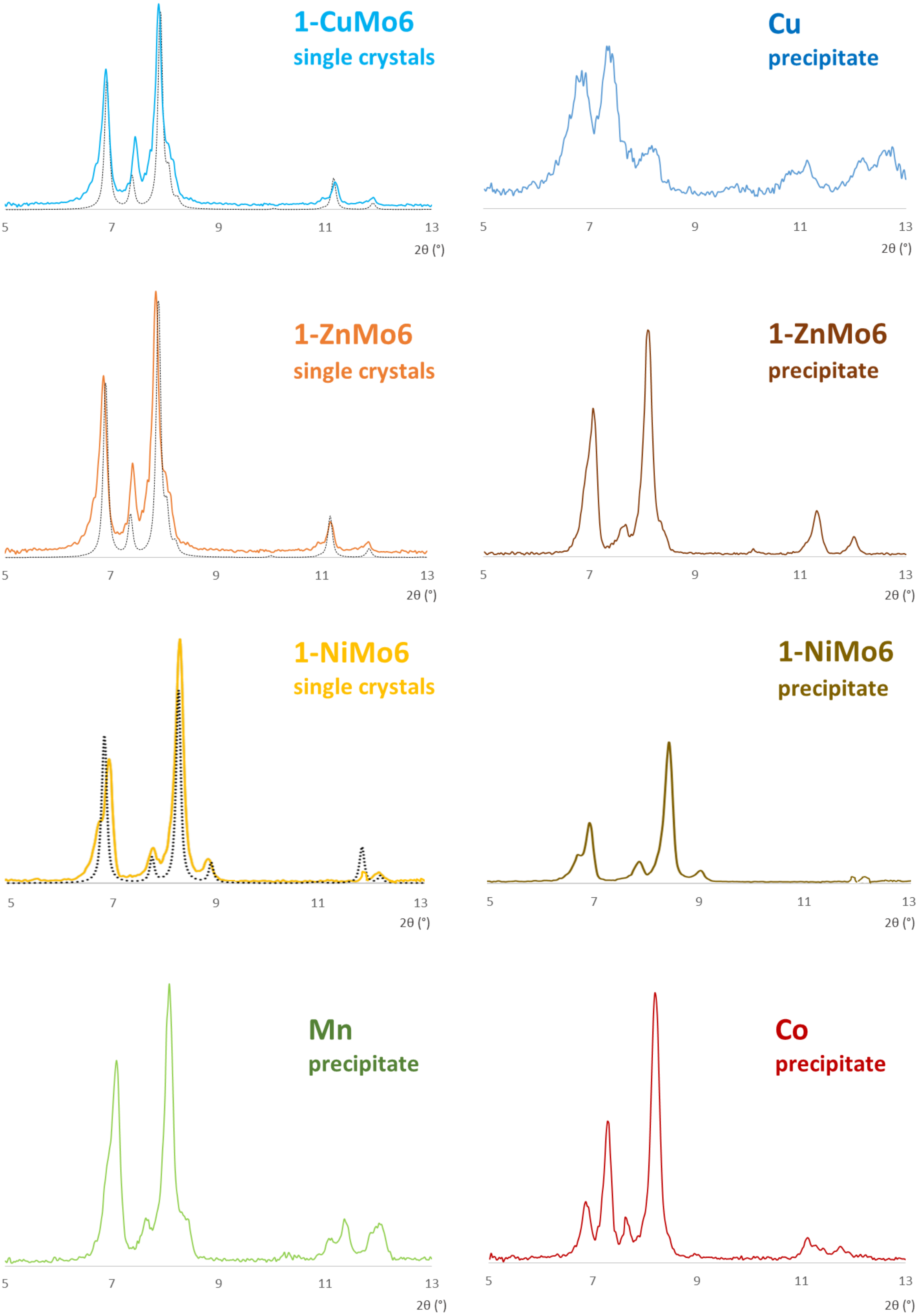

Figure A4.7. Comparison between the PDX patterns of the crystals and the precipitate that forms during the reaction of **1–CuMo6** with the precipitate obtained when using other transition metal source (black dotted line = simulated pattern from single-crystal XRD data).

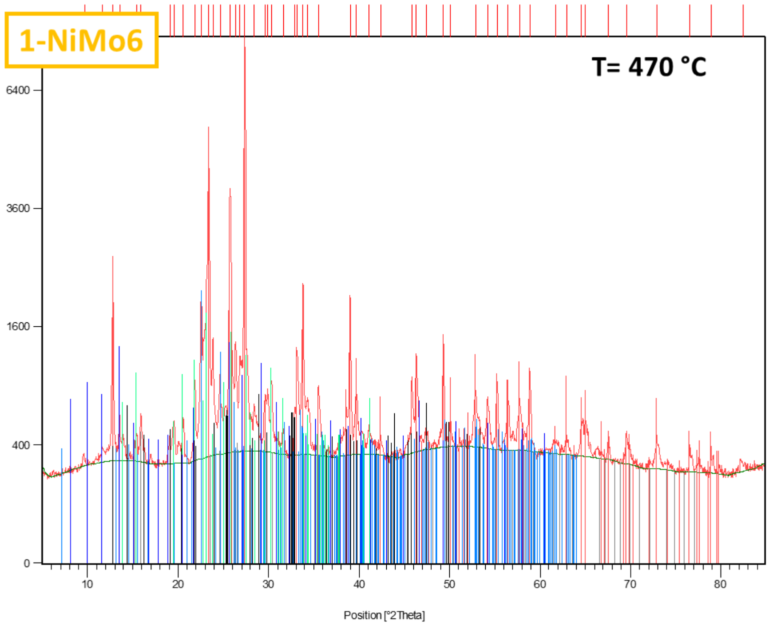

Ref. Code	Compound Name	Chemical Formula
00-035-0609	Molybdite, syn	MoO_3
01-072-0447	Molybdenum Oxide	Mo_4O_{11}
00-020-0310	Chromium Molybdenum Oxide	$Cr_2Mo_3O_{12}$
00-032-0692	Nickel Molybdenum Oxide	$NiMoO_4$
00-001-0125	Molybdenum Hydrogen Oxide	H_2MoO_4

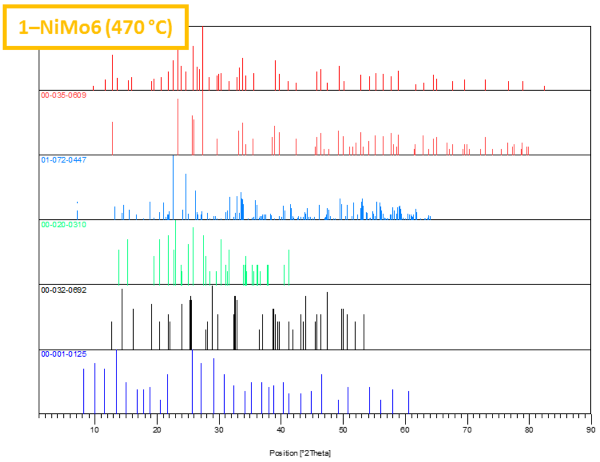

Figure A4.8. Identification of the phases that constitute the final residue of the variable temperature PXRD experiments for compound **1–NiMo6.**

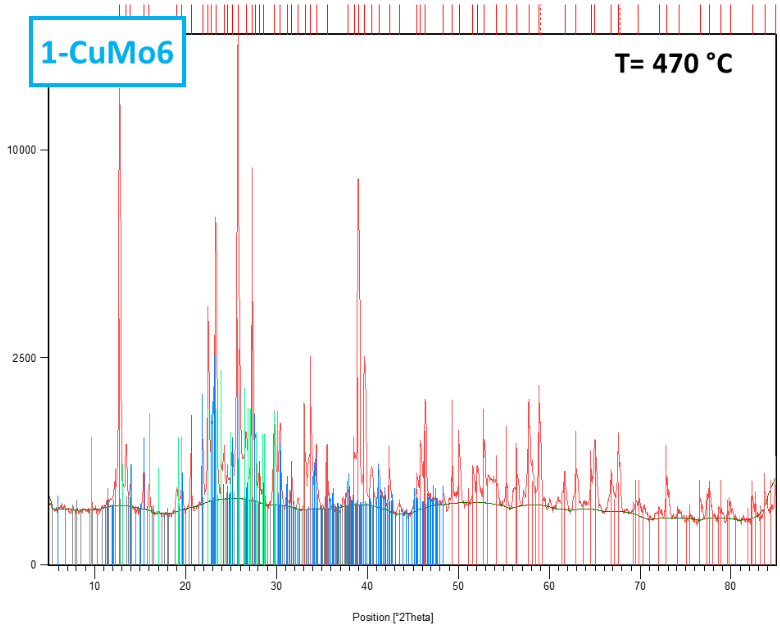

Ref. Code	Compound Name	Chemical Formula
01-076-1003	Molybdite, syn	MoO_3
01-078-1654	Chromium Molybdenum Oxide	$Cr_2(MoO_4)_3$
00-022-0242	Copper Molybdenum Oxide	$CuMoO_4$

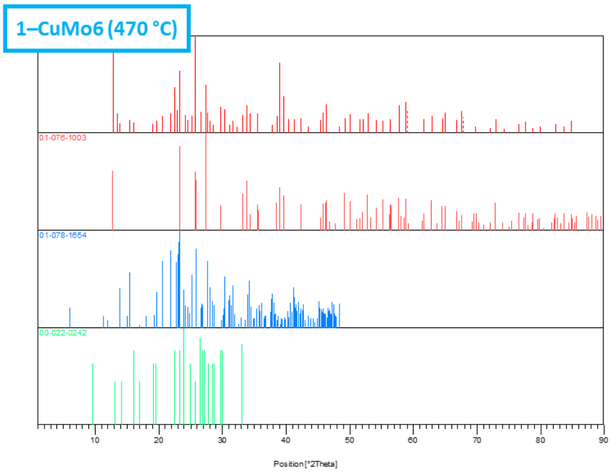

Figure A4.9. Identification of the phases that constitute the final residue of the variable temperature PXRD experiments for compound **1–CuMo6.**

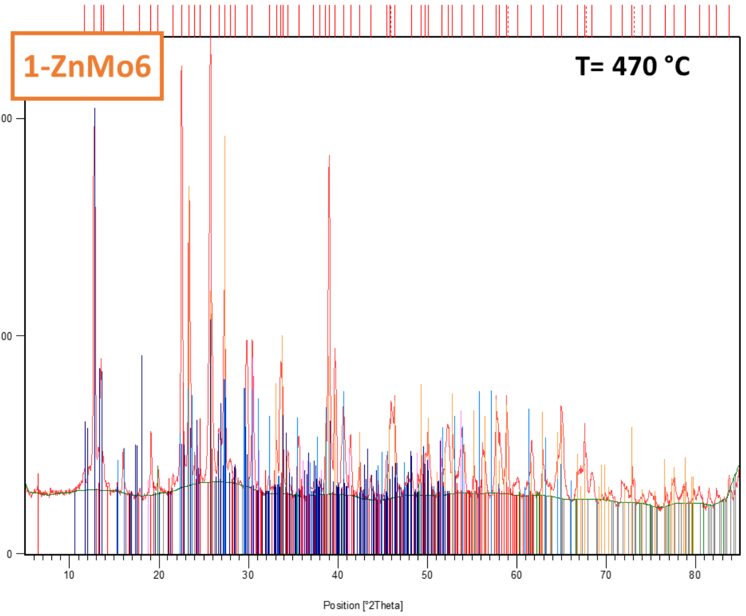

Ref. Code	Compound Name	Chemical Formula
00-035-0609	Molybdite, syn	MoO_3
00-016-0310	Zinc Molybdenum Oxide	$ZnMoO_4$
01-081-1263	Molybdenum Oxide	Mo_9O_{25}
01-085-1373	Grimaldiite	$CrO(OH)$
00-020-1437	Zinc Hydroxide	$Zn(OH)_2$
01-070-1513	Molybdenum Oxide Hydrate	$MoO_3(H_2O)_2$

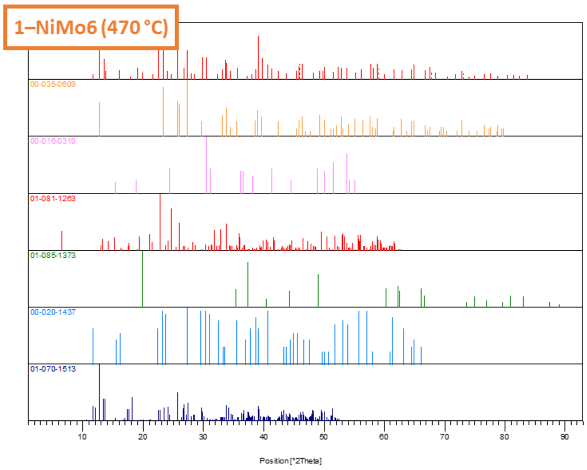

Figure A4.10. Identification of the phases that constitute the final residue of the variable temperature PXRD experiments for compound **1–ZnMo6.**